

学位論文

Search for Gluinos using Final States
with One Isolated Lepton in the LHC-
ATLAS Experiment

(LHC-ATLAS 実験における 1 レプトン終状態を
用いたグルイーノ探索)

平成 29 年 7 月博士(理学)申請

東京大学大学院理学系研究科
物理学専攻

陳 詩遠

Search for Gluinos using Final States with One Isolated Lepton in the LHC-ATLAS Experiment

Ph. D dissertation

Shion Chen

Department of Physics,
School of Science,
The University of Tokyo
7-3-1, Hongo, Bunkyo-ku, 113-0033, Tokyo, Japan

July 2017

Abstract

Despite the enormous success of the Standard Model in particle physics, there are still a number of problems left to be solved such as the fine tuning problem of the higgs mass, or the unaccounted presence of dark matter and so on. It is then strongly motivated to extend the Standard Model, and the Minimal Super-symmetric Standard Model (MSSM) has been one of the most appealing candidates, where a boson-fermion symmetry (super-symmetry; SUSY) is introduced. Experimental searches of SUSY particles predicted by MSSM has been widely performed over the decade in collider experiments. Though no evidence has been claimed so far, searches in the Large Hadron Collider (LHC) are anticipated with the unprecedented high center-of-mass energy and increased data statistics, allowing one to probe heavier SUSY particles. Gluino is one of the SUSY particles of which search is increasingly motivated after the discovery of higgs boson with its mass of 125 GeV.

This thesis presents the updated search for gluinos via proton-proton collisions with the center-of-mass energy of $\sqrt{s} = 13$ TeV at LHC, by focusing on the final state with exactly one lepton. With respect to the past searches, the sensitivity to heavier gluino is drastically gained using the improved analysis technique and updated data statistics (36.1 fb^{-1} of integrated luminosity) collected in the ATLAS detector. No significant data excess is found in the unblinded dataset, and the exclusion limits are set on all the targeted gluino decay scenarios. As a general conclusion, it is confirmed that up to $1.7 \text{ TeV} \sim 2.0 \text{ TeV}$ in gluino mass and up to $\sim 1 \text{ TeV}$ in the lightest neutralino mass is excluded for typical mass spectra, while the limit extends up to $1.5 \text{ TeV} \sim 1.9 \text{ TeV}$ in gluino mass for the case of the dark matter oriented mass spectra.

Contents

1	Introduction	1
2	Theoretical Backgrounds and Search Strategy	3
2.1	The Standard Model of Elementary Particles	3
2.1.1	The Gauge Principle and Particle Interaction	3
2.1.2	Perturbation and Renormalization	5
2.1.3	QED, QCD, and the Electroweak Theory	6
2.1.4	Electroweak Symmetry Breaking and the Higgs boson	9
2.2	Remained Problems for the Standard Model and the SUSY Solution	11
2.2.1	The Fine-tuning Problem in Higgs Mass	11
2.2.2	Grand Unification	12
2.2.3	Dark Matter	13
2.3	Super-Symmetry and the MSSM	14
2.3.1	Particle Contents in MSSM	14
2.3.2	The MSSM Lagrangian	15
2.3.3	Mass Spectra	17
2.3.4	Running Masses and GUT	19
2.4	Experimental Constraints on SUSY so far	21
2.4.1	Constraints from Observed Standard Model Higgs Mass	21
2.4.2	Constraint from Dark Mater Relic Density	23
2.4.3	Constraint from Direct Search at Collider Experiments	25
2.5	Target SUSY Scenario and the Search Strategy	30
2.5.1	Target SUSY Scenario	30
2.5.2	The Strategy of Decay Chain Based Search	31
2.5.3	Target Gluino Decay Chains	31
2.5.4	Target Signal Models for 1-lepton Final State	33
3	Experiment Apparatus: The ATLAS Detector at the LHC	37
3.1	The Large Hadron Collider	37
3.2	The ATLAS Detector	39
3.2.1	Overview	39
3.2.2	Coordinate System	40
3.2.3	Inner Detectors	41
3.2.4	Calorimetry	45

3.2.5	Muon Spectrometer	50
3.2.6	Luminosity Detectors	53
3.2.7	Trigger and Data Acquisition System	53
3.3	Recorded Data by ATLAS	55
4	Object Reconstruction and Identification	57
4.1	Tracks	58
4.2	Primary Vertices	58
4.3	Topo-clusters	59
4.4	Electrons	60
4.4.1	Reconstruction	60
4.4.2	Identification	61
4.4.3	Calibration	61
4.5	Muons	63
4.5.1	Reconstruction	63
4.5.2	Identification	63
4.5.3	Calibration	64
4.6	Jet	65
4.6.1	Jet Clustering	65
4.6.2	Energy Calibration	65
4.6.3	Flavor Tagging	67
4.6.4	Pile-up Jet Tagging and Rejection	68
4.7	Overlap Removal between the Reconstructed Objects	70
4.8	Fake Leptons and the Isolation Requirement	71
4.9	Missing Transverse Energy	73
4.10	Object Definition in the Analysis	74
5	Monte-Carlo Simulation	75
5.1	Phenomenology of a pp -collision	75
5.2	Implementation of pp -collisions in Simulation	77
5.2.1	Parton Distribution Function	77
5.2.2	Fixed-Order QCD Calculation	77
5.2.3	Parton Showering	78
5.2.4	Hadronization	80
5.3	Setup of the Simulated Dataset	80
5.3.1	Event Generation	80
5.3.2	Pileup simulation	81
5.3.3	Detector Simulation and Emulation	81
5.4	Design of SUSY Signal Grid for Interpretation	82
6	Event Selection	85
6.1	Trigger Selection	85
6.2	Event Cleaning and the Pre-selection	86
6.3	Signal Region Definition	88

6.3.1	Binning Strategy	88
6.3.2	Discriminating Variables for Background Rejection	95
6.3.3	Cut Optimization	100
6.3.4	Expected Sensitivity	108
7	Background Estimation	111
7.1	Background Breakdown in the Signal Regions	112
7.2	The Kinematical Extrapolation Method	116
7.2.1	MC vs Data Comparison and the MC mis-modeling	116
7.2.2	Definition of Control Regions and Validation Regions	128
7.2.3	Result of the Normalization	131
7.3	The Object Replacement Method	136
7.3.1	The Replacement Procedure and the Per-event Logic	139
7.3.2	Closure Test using $t\bar{t}$ MC Samples	150
7.3.3	Subtraction of Bogus Sub-events	158
7.3.4	Closure Test using Data	160
7.4	Unblinded Validation Regions	162
8	Systematic Uncertainties	167
8.1	Instrumental Uncertainty	167
8.2	Theoretical Uncertainty	169
8.2.1	Normalized Backgrounds: $W+jets$ and Tops	171
8.2.2	Non-normalized Backgrounds: $Z+jets$, di-bosons and $t\bar{t} + W/Z/WW$	172
8.2.3	SUSY Signals	173
8.3	Other Uncertainties	174
8.3.1	Generaic Uncertainty on the BG Estimation Methods	174
8.3.2	Control region statistics	175
8.3.3	MC statistics	176
9	Result	177
9.1	Statistical Analysis and Hypothetical Test	177
9.2	Unblinded Signal Regions with Background-only Hypothesis	181
9.3	Constraints on the Benchmark Models	193
9.4	Obtained Cross-section Upper-limit	202
10	Discussion	205
10.1	Comparison with the Other Up-to-date LHC Searches	205
10.2	What is Unique/Important in This Study?	206
10.3	Future Prospect	208
11	Conclusion	211

Acknowledgement	212
Appendix	215
A Auxiliary Materials for MC Simulation	216
A.1 Detail Configuration of Event Generation	216
A.2 Fast Simulation vs Detector Emulation	218
B Auxiliary Materials for Event Selection	222
B.1 Kinematics vs SUSY Masses	222
B.2 N-1 Plots for the Optimized Signal Regions	226
C Auxiliary Materials for Background Estimation	235
C.1 Data vs Reweighted MC in the Pre-selection Regions	235
C.2 MC Closure Test for the Object Replacement Method Estimating the Soft-Lepton Regions	243
C.3 Validation of Fake-Lepton Background Esmation	246
C.4 Post-fit Distributions in CRs and VRs	247
C.5 Comparison between Kinematical Extrapolation and Object Replacement	259
D Auxiliary Materials for Systematic Uncertainties	264
D.1 Extrapolation Error due to the MC Mis-modeling	264
E Tips	273

Chapter 1

Introduction



Figure 1.1: What is *matter* made of? The answer is quarks and leptons [1].

The origin of *things* has been an ultimate question of human beings since civilization. The pursue by modern science dates from the establishment of the atomic theory, and the quest towards the fundamental element has been continuously proceeded, together with the development of theory of forces acting between the them. A great milestone is set in recent years by the theoretical and experimental establishment of the Standard Model (SM). With this, today we understand a kitten (Figure 1.1) is made of $O(10^{27})$ atoms (bounded by the electric force); each of which accommodates a nucleus and electrons inside; and the a nucleus consists of a bunch of protons and neutrons (bounded by the strong force); which are made of a couple of quarks and numerous virtual partons. No any further elements are needed. With the quarks and leptons that form matter, gauge bosons mediating forces and a Higgs boson feeding the masses, the SM succeeds in explaining the origin of *matter* that we are familiar with and most of the phenomena at microscopic level.

Though it could be the end of the story, we are greedy enough to move forward. SM is a nice theory, however not perfect either in terms of the unaccountability to some observational facts such as dark matter or neutrino masses, or its problems to be solved towards an ultimate theory, for example the unification of the three gauge forces (grand unification) and inclusion of gravity. SM is awaiting for next breakthrough, just like the paradigm shift that the quantum mechanics and the relativistic theory brought about out of classical mechanics, and both theoretical and experimental approaches towards beyond-the-SM (BSM) has been actively going on. This work is done in context of the pursue, which is an experimental search of new particles predicted by

super-symmetry (SUSY) theory, using the proton-proton collisions in the Large Hadron Collider (LHC) at a center-of-mass energy of $\sqrt{s} = 13$ TeV. SUSY is known as one of the most motivating BSM frameworks, in which a set of partner particles of the SM are introduced, providing good dark candidates as well as prospect towards grand unification. Since it works particularly well when the SUSY particles are at a few TeV in their masses, the direct production in LHC is feasible in a number of scenarios. This thesis describes the search for unprecedentedly heavy gluino with the mass around $1.5 \text{ TeV} \sim 2 \text{ TeV}$, using the updated LHC dataset and advanced analysis technique.

Organization of the dissertation

The first part involves the introductory chapters describing the theoretical background, experimental apparatus, and toolkits used in the analysis:

- Chapter 2 provides the backgrounds necessary to motivate the study in the thesis and the status quo of gluino search, as well as an analysis of motivated SUSY scenarios today.
- Chapter 3 overviews the experiment apparatus used in the study; the LHC and the ATLAS detector.
- Chapter 4 describes the reconstruction algorithms used for particle identification and jet clustering.
- Chapter 5 outlines the method of event simulation and the setup employed in the analysis.

The main description of the analysis is given by:

- Chapter 6 describes the event selection of signal regions in which gluino is enhanced and background suppressed in an optimal manner.
- Chapter 7 comprehensively discusses the background estimation procedure and its validation.
- Chapter 8 overviews and evaluates the systematic uncertainties associated with background estimation and signal modeling.

Result and the discussion are provided by:

- Chapter 9 summarizes the results and resultant limits.
- Chapter 10 discusses the impact of the obtained result.
- Chapter 11 close the thesis with concluding remarks.

Chapter 2

Theoretical Backgrounds and Search Strategy

This chapter provides the backgrounds necessary to motivate the study in the thesis. It starts with an introduction of the theoretical framework, the status-quo of the SUSY searches. In the latter part of the chapter, a class of the most motivated SUSY scenarios are analyzed and the search strategy towards it is discussed.

2.1 The Standard Model of Elementary Particles

Before jumping to SUSY, the Standard Model (SM) of particle physics, current our best validated knowledge about the universe, is quickly reviewed (widely referred from the discussion in Peskin & Schröder [2], and Halzen & Martin [3]).

The particle content of the SM is shown in Table 2.1 and Table 2.2. There are three types of particles: fermions with the spin of 1/2 that consist matter; gauge bosons with the spin of 1 mediating the interaction acting between particles; and the spin-0 Higgs boson feeding their masses through the Brout-Englert-Higgs (or BEH) mechanism [4, 5].

The three types of gauge bosons; gluon (g); weak bosons (W^\pm, Z) and photon (γ) respectively characterize strong interaction, weak interaction and electromagnetic interaction. Fermions have two families; quarks which sense all the three gauge interactions; leptons which couple only via weak and electromagnetic interaction. Both families have up- and down-type. There are also two more duplications of them (“2nd / 3rd generation”) with exactly the same properties except the masses. Each fermions furthermore have the charge conjugated partner called anti-fermions.

2.1.1 The Gauge Principle and Particle Interaction

A successful theory for elementary particles must be quantum and relativistic. The theory of SM is constructed in a relativistic framework of field theory, fully exploiting the virtue that time (t) and position (\mathbf{x}) are treated equivalently in that both are coordinates rather than observables. It is characterized by a Lorentz-invariant Lagrangian in which particles are described by a function in

Table 2.1: Fermion contents in the SM. The quantum numbers Q , T , T^3 and Y are respectively electric charge, weak iso-spin number, the third component of weak iso-spin and weak hyper charge. N_C represents the number of color states. The subscripts L, R indicate the chirality (left- or right-handed respectively), and the parentheses denote the $SU(2)_L$ doublet.

	Generation			Q	T	T^3	Y	N_C
	1st	2nd	3rd					
Quarks	$\begin{pmatrix} u \\ d \end{pmatrix}_L$	$\begin{pmatrix} c \\ s \end{pmatrix}_L$	$\begin{pmatrix} t \\ b \end{pmatrix}_L$	$\begin{pmatrix} 2/3 \\ -1/3 \end{pmatrix}$	$1/2$	$\begin{pmatrix} 1/2 \\ -1/2 \end{pmatrix}$	$1/3$	3
	u_R	c_R	t_R	$2/3$	0	0	$4/3$	3
	d_R	s_R	b_R	$-1/3$	0	0	$-2/3$	3
	$\begin{pmatrix} \nu_e \\ e^- \end{pmatrix}_L$	$\begin{pmatrix} \nu_\mu \\ \mu^- \end{pmatrix}_L$	$\begin{pmatrix} \nu_\tau \\ \tau^- \end{pmatrix}_L$	$\begin{pmatrix} 0 \\ -1 \end{pmatrix}$	$1/2$	$\begin{pmatrix} 1/2 \\ -1/2 \end{pmatrix}$	-1	0
	e_R	μ_R	τ_R	-1	0	0	-2	0
Leptons								

Table 2.2: Gauge bosons and higgs in the SM. The notation for the quantum numbers are the same with Table 2.1.

		Q	T	T^3	Y	N_C
gluon	g	0	0	0	0	8
weak bosons	W^\pm	± 1	1	± 1	0	0
	Z	0	0	0	0	0
photon	γ	0	0	0	0	0
higgs	h	0	$1/2$	$-1/2$	1	0

terms of x^μ (“fields”) following the Lorentz transformation law of corresponding spin expression. The free Lagrangian for a fermion are given by:

$$\mathcal{L} = i\bar{\psi}\gamma^\mu\partial_\mu\psi - m\bar{\psi}\psi + \text{h.c.} \quad (2.1)$$

where ψ is a spinor field with the mass of m , and γ^μ is the 4-dimensional gamma matrices. The first term corresponds to the kinetic terms and the second is to the mass term of the fermion.

Interaction between particles are ruled by a local symmetries referred as “gauge symmetry”. The interaction terms are obtained by imposing on the free Lagrangian an invariant nature against the gauge transformation. In case of electromagnetic interaction, for instance, the gauge transformation is given by:

$$\psi \rightarrow e^{i\theta(x)Q}\psi = e^{i\theta(x)q}\psi \quad (2.2)$$

where Q is the generator of the $U(1)$ transformation, q is charge that the fermion f has, and $\theta(x)$ is an arbitrary time-space dependent phase. The free Lagrangian in Eq. (2.5) is not invariant under this transformation, however can be fix by a small hack in the differential in the free Lagrangian (∂_μ) such as:

$$\partial_\mu \rightarrow D_\mu := \partial_\mu - ieA_\mu(x) \quad (2.3)$$

where e is the elementary charge and $A(x)$ is a vector field transformed by the gauge transformation:

$$A_\mu \rightarrow A_\mu + \frac{1}{e} \partial_\mu \theta(x). \quad (2.4)$$

The interaction term then emerges as the extra terms in the Lagrangian:

$$\mathcal{L}_{\text{int.}} = e \bar{\psi} \gamma^\mu \psi A_\mu. \quad (2.5)$$

From the consistency with classical Maxwell equation, this describes the electromagnetic force acting on the fermion, and A_μ corresponds to the electromagnetic potential in the classical electromagnetism or the particle field for photon.

2.1.2 Perturbation and Renormalization

The effect of interaction is often characterized via transition amplitude from an initial state (i) to a final state (f):

$$\langle f | e^{-i\mathcal{H}_{\text{int.}} t} | i \rangle, \quad (2.6)$$

where $\mathcal{H}_{\text{int.}}$ is the interaction Hamiltonian obtained by a Legendre transformation of interaction Lagrangian. The amplitude is often a basic building block of phenomenological predictions such as interaction cross-section or decay branch, however it is in most of the cases not analytically calculable. It is therefore done through a perturbation expansion in terms of the coupling constant of the interaction, for which $\alpha := e^2/4\pi$ is conventionally used for electromagnetic interaction.

The small coupling constant of electromagnetic interaction ($\alpha \sim 1/137$) may sound to guarantee a good convergence behavior of the expansion in which the impact from the truncated orders in the series is small enough. It is however found that the higher-order contribution immediately leads to divergence quite everywhere in cross-section calculation (infrared / ultraviolet divergences), causing the theory unpredictable. This problem was solved by a procedure called “renormalization” where theory parameters (i.e. the masses and coupling constants) are redefined to absorb the infinities, maintaining a finite cross-section calculation. Historically, this formulation firstly succeeded in QED, and then understood by that the gauge symmetry played an important role in cancelling the divergence [6, 7]. From this moment, gauge symmetry started establishing the status as a guidance principle in constructing theories, beyond merely a prescription. It is also shown with considerable generality that well-behaving theory (“renormalizable theory”) must respect gauge symmetry [8].

The consequence of renormalization also provided a critical insight that the magnitude of theory parameters effectively vary depending on the energy scale with which the interaction happen. The evolution is characterized by the renormalization group equation (RGE), for example, as for the coupling constant (α):

$$\frac{1}{\alpha(Q)^2} - \frac{1}{\alpha(Q_0)^2} = -\frac{\beta(\alpha)}{2\pi} \log\left(\frac{Q}{Q_0}\right), \quad (2.7)$$

where Q is the scale defined by the typical momentum transfer of the interaction process, and $\beta(\alpha)$ is the beta function, proportional to α^2 at 1-loop level. This evolution is known as the “running”

effect, which is an useful proxy for exploring the behavior of theory over the scale.

2.1.3 QED, QCD, and the Electroweak Theory

The Lagrangian for Quantum Electromagnetic Theory (QED) is given by adding the kinetic terms of photon ($-\frac{1}{4}F_{\mu\nu}F^{\mu\nu}$) to one obtained in Sec. 2.1.1:

$$\mathcal{L} = -\frac{1}{4}F_{\mu\nu}F^{\mu\nu} + i\bar{\psi}\gamma^\mu\partial_\mu\psi - m\bar{\psi}\psi + \text{h.c.} \quad (2.8)$$

with $F_{\mu\nu}$ being the field strength:

$$F_{\mu\nu} := \partial_\mu A_\nu - \partial_\nu A_\mu. \quad (2.9)$$

Similar to what is done in QED with the gauge group of $U(1)$, the Lagrangian for strong and weak interaction can be generated by considering gauge groups of $SU(2)_L$ and $SU(3)$:

$$\psi \rightarrow e^{i\theta_a(x)\lambda^a}, \psi \quad a = 1, 2, \dots (N^2 - 1) \quad (\text{for } SU(N))$$

with λ^a being the generators of the gauge group. The choice of the gauge groups are motivated by:

- ($SU(2)$ for weak interaction) the observation of approximate iso-spin symmetry in theories of nucleus decay,
- ($SU(3)$ for strong interaction) the factor of 3 enhancement in cross-section of the Drell-Yan process for quark-antiquark production with respect to muon pair production: $\sigma(ee \rightarrow q\bar{q})/\sigma(ee \rightarrow \mu\mu) = 3N_q$ where N_q is number quark species (see Figure 2.1).

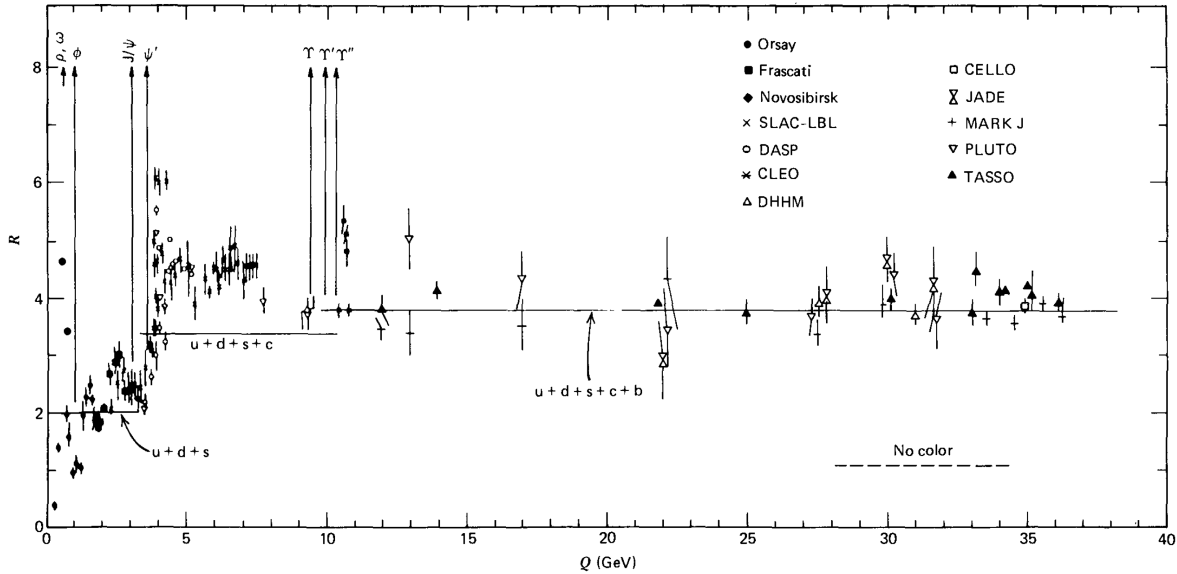


Figure 2.1: Measurement of the R -factor ($:= [d\sigma(ee \rightarrow q\bar{q})/dQ]/[d\sigma(ee \rightarrow \mu\mu)/dQ]$) versus the center-of-energy of the ee -collision (Q). The factor of 3 enhancement by the color factor is needed in addition to number of opened channels of quark-antiquark production to account for the observation.

Strong Interaction

The Lagrangian for strong interaction is:

$$\begin{aligned}\mathcal{L}_{\text{QCD}} &= -\frac{1}{4}\hat{\mathbf{G}}_{\mu\nu}\hat{\mathbf{G}}^{\mu\nu} + \bar{q}(i\gamma^\mu D_\mu - m)q + \text{h.c.}, \\ D_\mu &:= \partial_\mu + ig_s \sum_{a=1}^8 G_\mu^a \frac{\lambda_a}{2} \\ \hat{\mathbf{G}}_{\mu\nu} &:= \partial_\mu \mathbf{G}_\nu - \partial_\nu \mathbf{G}_\mu - g_s \mathbf{G}_\mu \times \mathbf{G}_\nu, \\ \mathbf{G}_\mu &:= \{G_\mu^a; a = 1, 2, \dots, 8\}\end{aligned}\tag{2.10}$$

where G_μ^a and q represent the fields for gluons and quarks respectively. g_s is related to the strong coupling constant α_s by $\alpha_s = g_s^2/4\pi$. The charge of strong interaction is called “color”, and the theoretical framework is referred to Quantum Chromo Dynamics (QCD). Quarks are in the triplet and gluons are in the octet expression with 3 and 8 degenerated states respectively. In addition, due to the non-Abelian nature of $SU(3)$, gluon has self-interaction with coupling to itself. One distinct consequence of this is the negative running coupling:

$$\alpha_s(Q) = \frac{4\pi\alpha_s(\mu_R)}{4\pi + \beta_0\alpha_s(\mu_R)\log(Q^2/\Lambda_{\text{QCD}}^2)}\tag{2.11}$$

where $\beta = 11 - 2n_f/3$ (n_f is number of quarks with the mass above Q), μ_R the renormalization scale (a reference scale of renormalization, different from the physical energy scale Q), and Λ_{QCD} the QCD cut-off scale at ~ 200 MeV. The indication of $\beta < 0$ is decreasing coupling constant with increased energy scale Q . Despite of the generally larger coupling than that of electromagnetic interaction, in the energy scale interested in LHC ($Q > 100$ GeV), α_s typically about 0.1, which is small enough to recover the perturbative picture (“asymptotic freedom”). On the other hand, the coupling becomes increasingly strong as approaching to Λ_{QCD} , leading to an immediate catastrophe of the perturbation picture. As a result of this strong coupling, colored particles are forced to combine each other to form a color singlet state (“confinement”),

Electro-weak interaction

Weak interaction is described by a larger gauge group $SU(2)_L \times U(1)_Y$, in a manner where weak and electromagnetic interaction reside altogether [9–11]. The basic idea is that they share the common origin at high energy scale and branch into separate interactions at some point through a spontaneous symmetry breaking $SU(2)_L \times U(1)_Y \rightarrow U(1)_Q$. The regime of unified interaction is commonly referred as electroweak (EW) interaction.

The gauge transformation distinguishes chirality of fermions, in that $SU(2)_L$ selectively acts to the left-handed component, accounting for the observed parity violating nature of weak interaction [12, 13]:

$$\psi_L \rightarrow e^{i\theta T_3 + i\Theta Y} \psi_L\tag{2.12}$$

$$\psi_R \rightarrow e^{i\Theta Y} \psi_R.\tag{2.13}$$

The Lagrangian arrives at:

$$\begin{aligned}\mathcal{L}_{\text{EW}} &= -\frac{1}{4}\hat{\mathbf{W}}_{\mu\nu}\hat{\mathbf{W}}^{\mu\nu} - \frac{1}{4}B_{\mu\nu}B^{\mu\nu} + \bar{\psi}(i\gamma^\mu D_\mu - m)\psi + \text{h.c.}, \\ D_\mu &:= \partial_\mu + ig \sum_{a=1}^3 W_\mu^a \tau_a + ig' \frac{Y}{2} B_\mu \\ \hat{\mathbf{W}}_{\mu\nu} &= \partial_\mu \mathbf{W}_\nu - \partial_\nu \mathbf{W}_\mu - g \mathbf{W}_\mu \times \mathbf{W}_\nu \\ \mathbf{W}_\mu &:= \{W_\mu^a; a = 1, 2, 3\} \\ B_{\mu\nu} &= \partial_\mu B_\nu - \partial_\nu B_\mu\end{aligned}\tag{2.14}$$

where W_μ^a and B_μ are the fields of EW gauge bosons, and g, g' are the coupling respectively for $SU(2)_L$ and $U(1)_Y$. $\tau (= \sigma/2)$ are generators of $SU(2)$.

The Lagrangian can be also re-written by introducing weak currents J_μ :

$$\begin{aligned}\mathcal{L}_{\text{EW}} &= -\frac{1}{4} \sum_{a=1}^3 W_{\mu\nu}^a W^{a\mu\nu} - \frac{1}{4}B_{\mu\nu}B^{\mu\nu} \\ &\quad - \frac{g}{2}(J_\mu^+ W^{-\mu} + J_\mu^- W^{+\mu}) - g J_\mu^3 W^{3\mu} - \frac{g'}{2} J_\mu^Y B^\mu + \text{h.c.} \\ J_\mu^\pm &:= \frac{1}{\sqrt{2}}(W_\mu^1 \mp iW_\mu^2) \\ J_\mu^a &:= \bar{\psi}_L \gamma^\mu \tau_q W_\mu^a \psi_L \ (a = 1, 2, 3) \\ J_\mu^Y &:= Y \bar{\psi}_L \gamma^\mu \psi_L.\end{aligned}\tag{2.15}$$

J_μ^\pm represent currents changing T_3 , while J_μ^0 and J_μ^Y neutral current conserving either T_3 and Y .

The EW symmetry breaking is expressed by mixing the fields (W_μ^3, B_μ) into (Z_μ, A_μ) :

$$\begin{pmatrix} Z_\mu \\ A_\mu \end{pmatrix} := \begin{pmatrix} \cos \theta_W & -\sin \theta_W \\ \sin \theta_W & \cos \theta_W \end{pmatrix} \begin{pmatrix} W_\mu^3 \\ B_\mu \end{pmatrix}\tag{2.16}$$

with a mixing angle (Weinberg angle θ_W) of:

$$\tan \theta_W := \frac{g'}{g}.\tag{2.17}$$

The current terms in the Lagrangian Eq. (2.15) then becomes:

$$\begin{aligned}&- \frac{g}{2}(J_\mu^+ W^{-\mu} + J_\mu^- W^{+\mu}) \\ &+ \frac{g}{\cos \theta_W} \left(-\cos^2 \theta_W J_\mu^3 + \frac{\sin^2 \theta_W}{2} J_\mu^Y \right) Z^\mu \\ &- g \sin \theta_W \left(J_\mu^3 + \frac{1}{2} J_\mu^Y \right) A^\mu\end{aligned}\tag{2.18}$$

By choosing $Y := 2(Q - T^3)$, A_μ becomes associated with the gauge field of electromagnetic interaction, and the electric charge is found to be related to the weak coupling constant by the Weinberg angle: $e = g \sin \theta_W$.

2.1.4 Electroweak Symmetry Breaking and the Higgs boson

One outstanding problem in the EW Lagrangian is the prohibition of mass terms, for both gauge bosons and fermions, since they explicitly violates the gauge invariance. The BEH mechanism [4, 5] is then employed to solve the problem, where assuming a $SU(2)$ doublet ϕ ($Y = -1, T = 1/2$) with scalar fields $\phi = (\phi_1, \phi_2) = (\phi^+, \phi^0)$, and a potential $V(\phi)$ added in the Lagrangian:

$$\begin{aligned}\mathcal{L}_{\text{Higgs}} &:= (D_\mu \phi)^\dagger (D^\mu \phi) - V(\phi) \\ V(\phi) &:= \mu^2 \phi^\dagger \phi + \lambda (\phi^\dagger \phi)^2.\end{aligned}\quad (2.19)$$

While the minimum of the potential is always found in $\phi = (0, 0)$ in the $\phi_1 - \phi_2$ plane when $\mu^2 > 0$, negative μ^2 leads to non-trivial minima in $v := |\phi|^2 = -\mu^2/2\lambda$. This causes a shift of the vacuum expectation value : $\langle 0 | \phi | 0 \rangle = 0 \rightarrow v$ (spontaneous symmetry breaking).

Redefining the field ϕ by the variation around the new vaccum $(0, v)$ $h(x)$:

$$\phi = \begin{pmatrix} 0 \\ v + h(x) \end{pmatrix} \quad (2.20)$$

and applying the $\partial_\mu \rightarrow D_\mu$ prescription to Eq. (2.19), one finds the mass terms for W, Z as:

$$\begin{aligned}m_W &= gv/2 \\ m_Z &= \sqrt{g^2 + g'^2}v/2,\end{aligned}$$

where the mass for W and Z is successfully provided.

The mass for scalar field h is also found to be:

$$m_h = \sqrt{-2\mu^2}.$$

thus h can be also regarded is physical mode, referred as higgs particle.

The fermion masses are fed by adding following Gauge invariant terms to Lagrangian:

$$\begin{aligned}\mathcal{L}_{\text{Yukawa}} &:= -\bar{\psi}_{i,L} y_u^{ij} \phi \psi_{j,R} - \bar{\psi}_{i,R} y_u^{ij} \phi^\dagger \psi_{j,L} \\ &\quad - \bar{\psi}_{i,L} y_d^{ij} \phi^c \psi_{j,R} - \bar{\psi}_{i,R} y_d^{ij} \phi^{c\dagger} \psi_{j,L} \\ &\quad - \bar{\psi}_{i,L} y_e^{ij} \phi \psi_{j,R} - \bar{\psi}_{i,R} y_e^{ij} \phi^\dagger \psi_{j,L}\end{aligned}\quad (2.21)$$

where $i, j = 1, 2, 3$ index the generations of fermions. y_u^{ij} , y_d^{ij} , and y_e^{ij} are the components of Yukawa matrices respectively for up-, down-type quarks and down-type leptons. The Yukawa matrices are 3×3 matrices spanning over the family space, in which Yukawa couplings for each fermion are accommodated. The off-diagonal components are also responsible for the mixing between generations, which are set all zero for down-type leptons, while they are non-zero in case of quarks characterized by the CKM matrix [14].

Inserting Eq. (2.20), $\mathcal{L}_{\text{Yukawa}}$ is finally reduced to:

$$\begin{aligned}\mathcal{L}_{\text{Yukawa}} &= \sum_f y_f v \bar{\psi} \psi + y_f \bar{\psi} \psi h \\ &= \sum_f m_f \bar{\psi} \psi + y_f \bar{\psi} \psi h,\end{aligned}\quad (2.22)$$

where f is the index of fermions, with y_f (ϕ_f) being the mass eigenvalues (eigenstates) of the Yukawa matrices.

Higgs boson was discovered in LHC in 2012 [15, 16], bringing the last piece of the Standard Model in human knowledge. Measurements on its properties including the mass, spin [17, 18] and couplings [19, 20] are underway, which is all consistent with the SM so far. Figure 2.2 shows the coupling measurement by ATLAS and CMS in LHC Run1. Further Precision measurement is planned in the later stages in LHC as well as the future linear collider projects such as ILC (International Linear Collider).

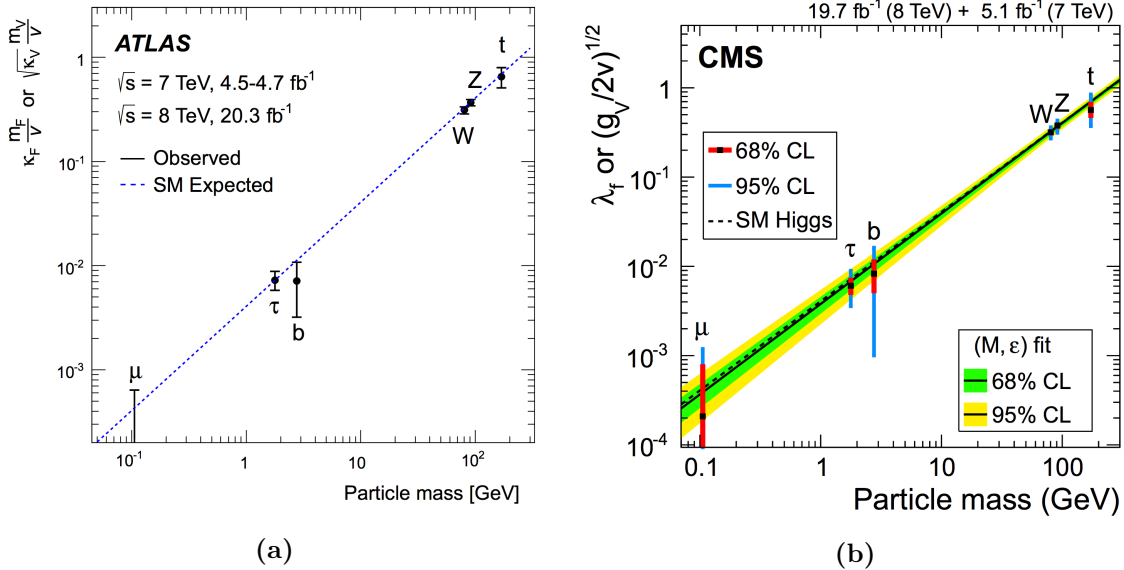


Figure 2.2: Higgs coupling measurement in LHC Run1 carried out by (a) ATLAS [19] and (b) CMS [20].

2.2 Remained Problems for the Standard Model and the SUSY Solution

Despite the enormous sucess of the SM, there are still couple of problems left to be solved, from phenomenological ones such as the inaccountability to dark matter, to conceptual ones towards the ultimate theory (e.g. the too many parameters, the naturalness as a theory etc.). This section will overview several most notable ones, enough motivating the beyond-the-SM (BSM) theoriees including SUSY. A particular emphasis is put on that TeV-scale SUSY is preferred in order to being the solution of the problems. Also, an example is shown to illustrate why SUSY is particularly important among the candidates of the solutions.

2.2.1 The Fine-tuning Problem in Higgs Mass

Though divergences appearing in higher-order calculations in SM are universaly cured in renormalization by the cenceling with the counter terms, it has been pointed that the magnitude of the cancelling terms are unnaturally large in case of the radiation correction on the higgs mass [21–24]. For instance, the 1-loop correction given by a top-quark loop (Figure 2.3 (a)) before renormalization is:

$$\Delta m_h^2 = -\frac{3|\lambda|^2}{8\pi^2} \Lambda^2 + O(\log \Lambda), \quad (2.23)$$

which is related by the renormalized mass ($m_{h,\text{obs.}}$) and the bare mass ($m_{h,\text{bare}}$) with:

$$m_{h,\text{obs.}}^2 = m_{h,\text{bare}}^2 + \Delta m_h^2. \quad (2.24)$$

The magnitude of the correction term Δm_h^2 can be order of $10^{38}(\text{GeV})^2$ assuming SM is valid upto the Planck scale: $\Lambda \sim 10^{19}(\text{GeV})^2$, while the observed mass is 125 GeV. Naively thinking this implies that the bare mass $m_{h,\text{bare}}$ and the correction Δm_h has to cancel in a precision of 10^{-17} (“fine tuning problem” or “naturalness problem”). It is highly unnatural for a theory to contain such extraordinary scale hierarchy in it, therefore it is preferred to conceive the underlying mechanism behind it.

The simplest solution is to add a partner particle yielding the opposite loop contribution to cancel it (Figure 2.3 (b)). In SUSY, this is done by introducing scalar-top (bosonic partner of top-quark “stop”) with the mass of m_S and the same couplings as tops. The quadratic terms cancel out as:

$$\begin{aligned} \tilde{\Delta}m_h^2 &= 2 \times \frac{3|\lambda|^2}{16\pi^2} \Lambda^2 + O(\log \Lambda) \\ \Delta m_{h,\text{stop}}^2 &= \Delta m_h^2 + \tilde{\Delta}m_h^2 = O(\log \Lambda) \end{aligned} \quad (2.25)$$

where the 10^{-34} order of fine-tuning is no longer needed.

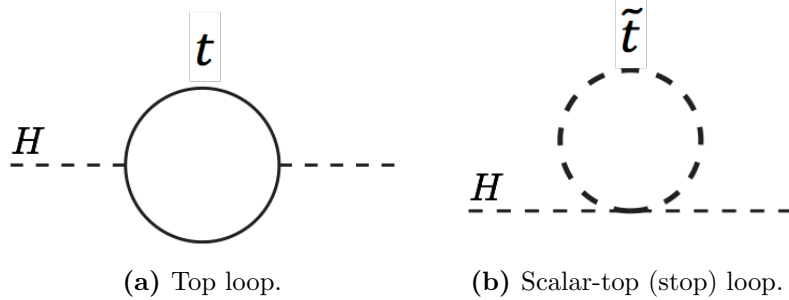


Figure 2.3: Feynman diagrams of 1-loop processes contributing to higgs mass by (a) top and (b) scalar-top.

2.2.2 Grand Unification

It is the ultimate desire for physicists to explain all phenomena in the universe by a single principle. While in the SM, the EW symmetry breaking $SU(2)_L \times U(1) \rightarrow SU(2) \times U(1)_Q$ implies a common origin of electromagnetic and weak interaction, this encourages physicists to conceive another unification together with strong interaction at a higher scale (Grand Unification Theory; GUT).

Running coupling constants are useful proxies to analyze the possibility of such unification. The evolution of coupling constants along scale is given by the RGE:

$$\frac{1}{\alpha_i(Q)^2} - \frac{1}{\alpha_i(Q_0)^2} = -\frac{\beta_i}{2\pi} \log\left(\frac{Q}{Q_0}\right), \quad (2.26)$$

with the indices $i = 1, 2, 3$ denote strong, weak and electro-magnetic interaction respectively. β_i are the beta functions. In the SM at 1-loop level, these are:

$$\begin{pmatrix} b_1 \\ b_2 \\ b_3 \end{pmatrix} = \begin{pmatrix} 1/10 \\ -43/6 \\ -11 \end{pmatrix} + n_{\text{gen}} \begin{pmatrix} 4/3 \\ 4/3 \\ 4/3 \end{pmatrix}, \quad (2.27)$$

where n_{gen} is the number of generation of fermions, which is equal to 3 for $Q > m_t$. One naively expects a convergence of the three couplings at a certain scale (μ_{GUT}) in case of the grand unification. Unfortunately, this does not happen in the SM, as illustrated in Figure 2.4 (a). However, it can be relatively easily realized in the SUSY regime, where more fermion particles can participate in the game changing the slope of the running. For instance, the beta function for MSSM is:

$$\begin{pmatrix} b_1 \\ b_2 \\ b_3 \end{pmatrix} = \begin{pmatrix} 3/5 \\ 1 \\ -3 \end{pmatrix}, \quad (2.28)$$

and the coupling unification is achieved at $\mu_{\text{GUT}} \sim 10^{16}$ GeV, as shown in Figure 2.4 (b). This is superizing given that the convergence can be easily violated with even a little different particle content, and this is one of the reasons that SUSY is particularly special among the BSM frameworks.

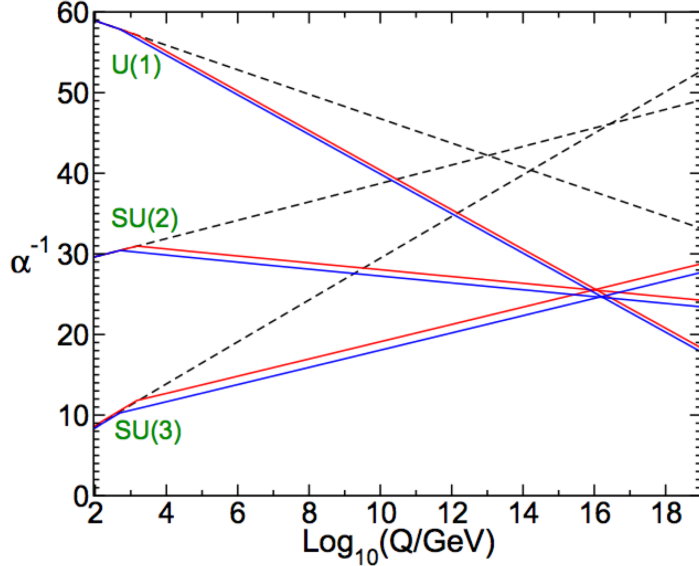


Figure 2.4: Two-loop renormalization group evolution of the inverse gauge coupling $1/\alpha_i$ in case of SM (dashed lines), and a scenario in MSSM (solid lines) where the masses of SUSY partners are set between 500 GeV and 1.5 TeV [25].

2.2.3 Dark Matter

Historically, the argument of dark matter (DM) originated from observations on velocity of galaxy rotation, implying excessive masses in galaxy center beyond the expectation from spectroscopy [26, 27]. The non-baryonic dark matter hypothesis has been strongly supported by the a number of observatory facts that comes up later such as the mass tomography on The Bullet Cluster using the gravitational lensing effect and so on. Currently the most commonly considered framework of dark matter is the Λ -CDM model (Cold Dark Matter) in which DM is assumed to:

- only sense very weak interaction such as gravity (Weakly Interacting Massive Particles; WIMPs)¹
- be non-relativistic, given that DM is relatively spatially localized such as in galaxy center.

The density abundance is dedicatedly measured via cosmic microwave background (CMB) by WMAP [29] and Planck [30] under the Λ -CDM regime:

$$\Omega_{\text{CDM}} h^2 = \begin{cases} 0.1138 \pm 0.0045 & (\text{WMAP}) \\ 0.1186 \pm 0.0020 & (\text{Planck, TT+lowP+lensing}), \end{cases} \quad (2.29)$$

While the SM has no candidates for DM, SUSY provides several attractive candidates when assuming the R-parity conservation (Sec 2.3.2) in which the lightest SUSY particle (LSP) becomes stable. It is worth noting that the LSP mass will be constrained by an upper bound about 3 TeV, when trying to explain the whole abundance by SUSY. This makes SUSY as a phenomenologically important model rather than a purely theoretical framework, this is a strong motivation of considering TeV-scale SUSY.

¹This almost requires electrically neutral, but completely forbidden [28].

2.3 Super-Symmetry and the MSSM

Minimal Super-Symmetric Standard Model (MSSM) is a SUSY framework where minimum matter contents and degrees of freedom are newly introduced with respect to the SM such as:

- Only one set of SUSY partners is employed ($\mathcal{N}_{\text{SUSY}} = 1$),
- SUSY partners of SM fermions have the spin of 0, while the partners for boson in SM (gauge boson and higgs) are spin-1/2
- Use only two higgs doublets to construct the higgs sector.²

Though it is called “minimal”, MSSM is a framework general enough to expressing the typical natures of SUSY at phenomenology level, therefore this thesis will confine the scope within MSSM. An overview on MSSM is given in the rest of the section, widely based on the reference [25].

2.3.1 Particle Contents in MSSM

Table 2.3: Matter content of MSSM. The left column defines the naming convention for SUSY particles. $n[SU(3)_C](n[SU(2)_L])$ represents the degree of freedom of the $SU(3)_C(SU(2)_L)$ multiplet that the field(s) belongs to. All of them belongs to the single of $U(1)_Y$, thus the $U(1)$ charge Y is shown instead. There are also two set of replications for the 2nd and 3rd generation of (s)quarks/(s)leptons, which are not shown here.

Super-multiplet		SM sect.	SUSY partner	$n[SU(3)_C]$	$n[SU(2)_L]$	Y
gluon/gluino	G	g	\tilde{g}	8	1	0
EW gauge boson /	W	W^\pm, W^0	$\tilde{W}^\pm, \tilde{W}^0$	1	3	0
EW gaugino	B	B^0	\tilde{B}^0	1	1	0
lepton / slepton	L	$(\nu_e, e)_L$	$(\tilde{\nu}_e, \tilde{e})_L$	1	2	-1
	E	\tilde{e}_R	e_R	1	1	-2
quark / squark	Q	(u_L, d_L)	$(\tilde{u}_L, \tilde{d}_L)$	3	2	1/3
	U	u_R	\tilde{u}_R	3	1	4/3
	D	d_R	\tilde{d}_R	3	1	-2/3
Higgs boson /	H_u	(H_u^+, H_u^0)	$(\tilde{H}_u^+, \tilde{H}_u^0)$	1	2	1
higgsino	H_d	(H_d^0, H_d^-)	$(\tilde{H}_d^0, \tilde{H}_d^-)$	1	2	-1

The particle contents are summarized in Table 2.3. Note that scalar-fermions (sfermions) have two modes indexed by L, R indicating that they are the SUSY partners of left-handed or right-handed SM fermions respectively. On the other hand, gauginos are all Majorana, in order to match

²Introducing multiple VEV is the simplest solution against the quantum anomalies that newly arise when extending to SUSY.

the degree of freedom with either the partner gauge bosons and higgs bosons.

MSSM higgs sector has two higgs doublets ($\mathbf{H}_u := (H_u^+, H_u^0)$, $\mathbf{H}_d := (H_d^-, H_d^0)$) with their own vacuum expectation values (VEV):

$$v_u := \langle H_u^0 \rangle, \quad v_d := \langle H_d^0 \rangle,$$

where each provides the masses for up- or down-type fermions respectively. Their splitting is commonly parametrized using a mixing angle β as:

$$\tan \beta := v_u/v_d. \quad (2.30)$$

The consistency with SM is ensured by relating the VEVs as:

$$v_{\text{SM}}^2 = v_u^2 + v_d^2. \quad (2.31)$$

Note that if gravity is quantized in the picture of QFT, there should be also the corresponding gauge boson "graviton" and its SUSY partner "gravitino" along a natural extension. In some SUSY scenarios, gravitino do act a important role such as in GMSB (Gauge Mediated SUSY Breaking), however we do not assume them in the study of this thesis.

2.3.2 The MSSM Lagrangian

Construction of a super-symmetric Lagrangian is commonly done by the method of super-potential or super-space. Though the procedure is skipped here, it may worth noting that it is not as a simple extension from SM Lagrangian as just adding terms accounting for the extra particle contents. The MSSM Lagrangian can be divided into two parts:

$$\mathcal{L}^{\text{MSSM}} = \mathcal{L}_{\text{SUSY}}^{\text{MSSM}} + \mathcal{L}_{\text{soft}}^{\text{MSSM}}. \quad (2.32)$$

The first term is the SUSY invariant part of the Lagrangian which is given by:

$$\begin{aligned} \mathcal{L}_{\text{SUSY}}^{\text{MSSM}} &= \frac{1}{4} F_{a\mu\nu} F^{a\mu\nu} + D^\mu \phi^* D_\mu \phi + \psi^\dagger \bar{\sigma}^\mu D_\mu \psi + i \lambda^\dagger a \bar{\sigma} D_\mu \lambda_a && \text{(Kinetic terms)} \\ &- \frac{1}{2} W^{ij} \psi_i \psi_j + h.c. && \text{(Yukawa interaction terms)} \\ &- \sqrt{2} g (\phi^* T^a \psi) \lambda_a + h.c. && \text{(Gaugino interaction terms)} \\ &- \sum_i \left| \frac{\delta W}{\delta \phi_i} \right|^2 + \frac{1}{2} (g_a \phi^* T^a \phi)^2 && \text{(Residual terms from the aux. fields)} \end{aligned}$$

where ψ is SM fermions are ϕ is the corresponding spin-0 SUSY partners, while λ are gauginos. W_{ij} is the second derivative of super-potential W , with W being defined by:

$$\begin{aligned} W_{ij} &:= \frac{\delta^2 W}{\delta \phi_i \delta \phi_j}, \\ W &:= U \mathbf{y}_u Q H_u - D \mathbf{y}_d Q H_d - E \mathbf{y}_e L H_d + \mu H_d H_u. \end{aligned} \quad (2.33)$$

\mathbf{y}_u , \mathbf{y}_d and \mathbf{y}_e are the same Yukawa matrices in Eq. (2.21). Note that no theory parameters are newly introduced compared with SM in $\mathcal{L}_{\text{SUSY}}^{\text{MSSM}}$. The soft SUSY breaking term $\mathcal{L}_{\text{soft}}^{\text{MSSM}}$ is SUSY variant part of the Lagrangian. Further caveats are provided as below:

SUSY breaking While an exact super-symmetry requires the SUSY partners being in the identical masses with respect to the SM particles, it is not the case at least in the energy scale of current our universe since no SUSY particles have been discovered so far. Therefore, a realistic SUSY model as an effective theory at the EW scale, must contain a scheme of SUSY breaking in its Lagrangian ($\mathcal{L}_{\text{soft}}^{\text{MSSM}}$). On the other hand, we don't want to ruin the desired features in SUSY at the cost of it, particularly as the solution of the higgs mass fine-tuning problem (Sec. 2.2.1). Therefore, it is common to restrict the SUSY breaking in a form of “soft breaking” where the cancelation of the quadratic divergence in the higgs mass loop correction Eq. (2.25) is maintained.

The most general form of the soft breaking terms is given by:

$$\mathcal{L}_{\text{soft}}^{\text{MSSM}} = \frac{1}{2} \left(M_3 \tilde{g}\tilde{g} + M_2 \tilde{W}\tilde{W} + M_1 \tilde{B}\tilde{B} + \text{c.c.} \right) \quad (\text{gaugino mass terms}) \quad (2.34)$$

$$- Q^\dagger \mathbf{m}_Q^2 Q - L^\dagger \mathbf{m}_L^2 L - U \mathbf{m}_U^2 U^\dagger - D \mathbf{m}_D^2 D^\dagger - E \mathbf{m}_E^2 E^\dagger \quad (\text{sfermion mass terms}) \quad (2.35)$$

$$- (U \mathbf{a}_u Q H_u - D \mathbf{a}_d Q H_d - E \mathbf{a}_e L H_d + \text{c.c.}) \quad (\text{trilinear coupling}) \quad (2.36)$$

$$- m_{H_u}^2 H_u^\dagger H_u - m_{H_d}^2 H_d^\dagger H_d - (b H_u H_d + \text{c.c.}) \quad (\text{Higgs potential}) \quad (2.37)$$

The notation of the particle fields ($\tilde{g}, \tilde{W}, \tilde{B}$) and super-multiplet (Q, L, U, D, E, H_u, H_d) follow the definition in Table 2.3. The first line (Eq. (2.34)) show the mass terms for gauginos, with M_1 , M_2 and M_3 are respectively bino, wino and gluino mass. Eq. (2.35) involves the Yukawa terms for SUSY particles where the former are the standard sfermion mass terms, and Eq. (2.36) the trilinear terms describing the Yukawa interaction coupling left-handed and right-handed sfermions, emerged as the cross terms of super-multiplet. The mass matrices (\mathbf{m}_Q , \mathbf{m}_L , \mathbf{m}_U , \mathbf{m}_D , \mathbf{m}_E), and the A terms (\mathbf{a}_u , \mathbf{a}_d and \mathbf{a}_e) are 3×3 matrices spanned in family space, equivalent to the CKM matrix in the SM sector multiplied by sparticles masses. The last terms are the MSSM higgs potential, controlling the EW symmetry breaking.

Though not specifically targeted in the thesis, there are a number of models in the market offering explicit mechanisms of the soft SUSY breaking. The most minimal models are known as GMSB (Gauge-Mediated SUSY Breaking [31]), AMSB (Anomaly-Mediated SUSY Breaking [32, 33]) or mSUGRA (minimal SUper Gravity [34]).

R-parity A quantum number R associated with the number of “SUSY partner” (analogous to the lepton number or baryon number etc.) can be defined by the spin, baryon number and lepton number as:

$$R := (-1)^{3(B-L)+2S}. \quad (2.38)$$

The corresponding symmetry is referred to R-parity, which conservation law will prohibit single production of SUSY particles, as well as SM particles annihilating into a resonance of a SUSY particle. This leads a set of spectacular phenomenological advantages:

- The lightest SUSY particles (LSP) become the DM candidates if they are electric neutral, in particular the lightest neutralino is the most commonly assumed.

- Proton decays via diagrams in Figure 2.5 are prohibited, naturally reconciling with the constraints set by experiments [35].

In the framework of MSSM, the R-parity conservation (RPC) is explicitly assumed, which is equivalent to discard following terms in the most general soft breaking Lagrangian:

$$\begin{aligned} W_{\Delta L=1} &= \frac{1}{2} \lambda^{ijk} L_i L_j \bar{e}_k + \lambda'^{ijk} L_i Q_j \bar{d}_k + \mu'^i L_i H_u \\ W_{\Delta B=1} &= \frac{1}{2} \lambda''^{ijk} \bar{u}_i \bar{d}_j \bar{d}_k. \end{aligned} \quad (2.39)$$

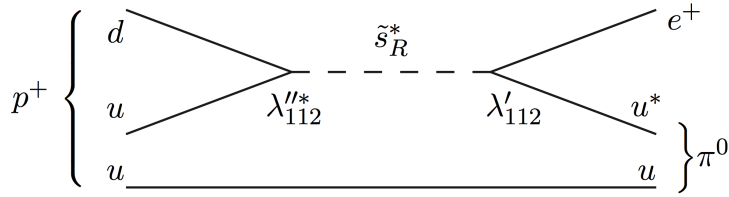


Figure 2.5: An example process of a proton decay triggered by intermediate SUSY particles (scalar-strenge quark here). λ''_{112} and λ'_{112} are couplings for corresponding interaction vertices which violate R -parity.

2.3.3 Mass Spectra

The masses of SUSY particles are derived by specifying the coefficient associated with mass terms (e.g. m in $m\phi\phi$), after a full expansion of the Lagrangian in Eq. (2.32). This is effectively done by extracting relevant terms and performing the diagonalization on the mass matrices, accounting for the mixing between eigenstates of interactions.

Squarks and sleptons Sfermion masses are fed solely from the soft Lagrangian. Generally, they are allowed to mix between different generations via the off-diagonal components either in the mass matrices or the A terms. These are however known to lead to a significant rate of flavor changing natural current which are experimentally highly disfavored thus usually set to zero:

$$\begin{aligned} \mathbf{m}_Q^2 &= m_Q^2 \mathbf{1}, & \mathbf{m}_L^2 &= m_L^2 \mathbf{1}, & \mathbf{m}_{\bar{u}}^2 &= m_{\bar{u}}^2 \mathbf{1}, & \mathbf{m}_{\bar{d}}^2 &= m_{\bar{d}}^2 \mathbf{1}, & \mathbf{m}_{\bar{e}}^2 &= m_{\bar{e}}^2 \mathbf{1}, \\ \mathbf{a}_u &= A_u \mathbf{1}, & \mathbf{a}_d &= A_d \mathbf{1}, & \mathbf{a}_e &= A_e \mathbf{1} \end{aligned} \quad (2.40)$$

In addition, it is also allowed to mix left-handed sfermion and right-handed sfermion since they share the same gauge quantum numbers. Ignoring the off-diagonal components of the Yukawa matrix, the mass matrix for sfermion \tilde{f} reduces to:

$$\begin{aligned} v_f &= \begin{cases} v_u & (\tilde{f} = \tilde{u}, \tilde{c}, \tilde{t}) \\ v_d & (\tilde{f} = \tilde{d}, \tilde{s}, \tilde{b}) \end{cases} \\ &\left(\begin{array}{cc} m_{\tilde{f}_L}^2 + m_Z^2 (T_{3,f} - Q_f \sin \theta_W)^2 \cos 2\beta + m_f^2 & v_f (A_f - \mu y_f) \\ v_f (A_f - \mu y_f) & m_{\tilde{f}_R}^2 + m_Z^2 Q_f \sin \theta_W^2 \cos 2\beta + m_f^2 \end{array} \right), \end{aligned} \quad (2.41)$$

where $T_{3,f}$ and Q_f are the iso-spin and electric charge of \tilde{f} . As the magnitude off-diagonal component scales with the Yukawa coupling, the effect of the mixing can be only sizable in case of third generation sfermions (stop, sbottom and stau). This is why the third generation sfermions are particularly phenomenologically important, since the masses of lighter eigenstates can be significantly lowered, enhancing the chance of being within experimental reach.

Gauginos The mass terms of EW gauginos and higgsinos are sourced by $\mathcal{L}_{\text{SUSY}}^{\text{MSSM}}$. The eigenstate of charged EW gauginos (charginos; $\tilde{W}^\pm, \tilde{H}_u^+, \tilde{H}_d^-$) in the same signs will mix each other. The mass matrices are common and described as:

$$\begin{pmatrix} M_2 & \sqrt{2}m_W \sin \beta \\ \sqrt{2}m_W \sin \beta & \mu \end{pmatrix}.$$

The diagonalized mass eigenstates are then:

$$m_{\tilde{\chi}_{1,2}^\pm}^2 = \frac{1}{2} \left[(M_2^2 + \mu^2 + 2m_W^2) \mp \sqrt{(M_2^2 + \mu^2 + 2m_W^2)^2 - 4(\mu M_2 - m_W^2 \sin 2\beta)^2} \right]. \quad (2.42)$$

The mass matrix for neutral EW gauginos (neutralinos; $\tilde{B}, \tilde{W}^0, \tilde{H}_u^0, \tilde{H}_d^0$) are given as:

$$\begin{pmatrix} M_1 & 0 & -\cos \beta \sin \theta_W m_Z & \sin \beta \sin \theta_W m_Z \\ 0 & M_2 & \cos \beta \cos \theta_W m_Z & -\sin \beta \cos \theta_W m_Z \\ -\cos \beta \sin \theta_W m_Z & \cos \beta \cos \theta_W m_Z & 0 & -\mu \\ \sin \beta \sin \theta_W m_Z & -\sin \beta \cos \theta_W m_Z & -\mu & 0 \end{pmatrix}.$$

The eigenfunction is quartic and the solutions are:

$$\begin{aligned} m_1 &= M_1 + \frac{m_Z^2 \sin^2 \theta_W}{M_1^2 - \mu^2} (M_1 + \mu \sin 2\beta) \\ m_2 &= M_2 + \frac{m_Z^2 \cos^2 \theta_W}{M_2^2 - \mu^2} (M_2 + \mu \sin 2\beta) \\ m_3 &= \mu + \frac{m_Z^2 (1 + \sin 2\beta)}{2(\mu - M_1)(\mu - M_2)} (\mu - \cos \theta_W M_1 - \sin \theta_W M_2) \\ m_4 &= \mu + \frac{m_Z^2 (1 - \sin 2\beta)}{2(\mu + M_1)(\mu + M_2)} (\mu + \cos \theta_W M_1 + \sin \theta_W M_2) \end{aligned} \quad (2.43)$$

The conventional notation for neutralino masses $m_{\tilde{\chi}_{1-4}^0}$ are defined by sorting these eigenvalues as $m_{\tilde{\chi}_1^0} < m_{\tilde{\chi}_2^0} < m_{\tilde{\chi}_3^0} < m_{\tilde{\chi}_4^0}$.

Finally, gluinos are color-octet fermions and do not mixed to any other sfermions.

The MSSM Higgs sector Due to the two higgs doublets with 4 real and 4 imaginary parts, there are in total five degree of freedoms as physical particles after the gauge fixing. The MSSM

higgs potential is given by:

$$\begin{aligned}
V = & \left(|\mu|^2 + m_{H_u}^2 \right) \left(|H_u^0|^2 + |H_u^+|^2 \right) \\
& + \left(|\mu|^2 + m_{H_d}^2 \right) \left(|H_d^0|^2 + |H_d^-|^2 \right) \\
& + [b(H_u^+ H_d^- - H_u^0 H_d^0) + \text{c.c.}] \\
& + \frac{1}{8} (g^2 + g'^2) \left(|H_u^0|^2 + |H_u^+|^2 - |H_d^0|^2 - |H_d^-|^2 \right)^2 \\
& + \frac{1}{2} |H_u^+ H_u^{0*} + H_d^+ H_d^{-*}|.
\end{aligned} \tag{2.44}$$

Similarly to the case in SM, implementing the spontaneous symmetry breaking by plugging $H_{u,d} \rightarrow v_{u,d} + \eta_{u,d}$ into Eq. (2.44), and requiring $dV/dv_u = dV/dv_d = 0$, one arrives:

$$\sin 2\beta = \frac{2b}{m_{H_u}^2 + m_{H_d}^2 + 2|\mu|^2} \tag{2.45}$$

$$\frac{1}{2} m_Z^2 = -|\mu|^2 + \frac{m_{H_u}^2 - m_{H_d}^2 \tan^2 \beta}{\tan^2 \beta - 1} \tag{2.46}$$

The higgs masses are found by the masses terms with inserting Eq. (2.45)-(2.46) back to Eq. (2.44):

$$\begin{aligned}
m_A^2 &= 2|\mu|^2 + m_{H_u}^2 + m_{H_d}^2, \\
m_{H^\pm}^2 &= m_{A^0}^2 + m_W^2 \\
m_{h,H}^2 &= \frac{1}{2} \left(m_{A^0}^2 + m_Z^2 \mp \sqrt{(m_{A^0}^2 + m_Z^2)^2 - 4m_Z^2 m_{A^0}^2 \cos^2 2\beta} \right),
\end{aligned} \tag{2.47}$$

where H^\pm is the charged, A the CP-odd higgs respectively. H and h are the mass eigenstates of CP-even neutral higgs, where the lighter one h is often associated with the SM higgs. Given that no observation of H has been claimed upto 400 GeV – 1 TeV, it is generally preferred to have large mass splitting between h and H , which implies a large $\tan \beta$.

2.3.4 Running Masses and GUT

Though the SUSY masses are mostly free parameters in MSSM, an useful insight can be obtained from an quick analysis under the GUT regime in which the coupling constants are unify at the GUT scale: $\mu_{\text{GUT}} \sim 10^{16-17}$ GeV. In the SUSY context, the mass unification is often in addition considered, typically under the regime where:

- all sfermions masses converge to $m_{1/2}$
- all gaugino masses converge to m_0
- all higgs boson (H_u, H_d) masses converge to $(\mu^2 + m_0^2)^{1/2}$.

This configuration is particular advantageous in that it naturally causes EW symmetry breaking at the EW scale, and adopted in many minimal models including SUGRA and so on.

Starting with gaugino masses, using the general condition satisfied in the 1-loop renormalization:

$$\frac{d(M_i/\alpha_i)}{d\mu} = 0, \quad (i = 1, 2, 3),$$

it turns that (M_i/α_i) is constant in arbitrary scales. Therefore, one obtains:

$$\frac{M_i}{\alpha_i}|_{\mu=\mu_{\text{EW}}} = \frac{M_i}{\alpha_i}|_{\mu=\mu_{\text{GUT}}} = \frac{m_{1/2}}{\alpha_{\text{GUT}}}, \quad (2.48)$$

resulting in an univeral ratio in gaugino masses valid in any scale:

$$M_1 : M_2 : M_3 \sim 6 : 2 : 1. \quad (2.49)$$

This is the reason this mass hierarchy between gluino, wino and bino are especially motivated and commonly assumed in SUSY phenomenology, though it is true that the assumption of mass unification may be too strong.

As for sfermions, the running masses also provide some idea about the mass spectra at the EW scale. The running masses are calculated unambiguously using the renormalization group equations:

$$\begin{aligned} m_{d_L}^2 &= m_0^2 + K_3 + K_2 + \frac{1}{36}K_1 + \Delta_{\tilde{d}_L} \\ m_{\tilde{u}_L}^2 &= m_0^2 + K_3 + K_2 + \frac{1}{36}K_1 + \Delta_{\tilde{u}_L} \\ m_{d_R}^2 &= m_0^2 + K_3 + \frac{1}{9}K_1 + \Delta_{\tilde{d}_R} \\ m_{\tilde{u}_R}^2 &= m_0^2 + K_3 + \frac{4}{9}K_1 + \Delta_{\tilde{u}_R} \\ m_{\tilde{e}_L}^2 &= m_0^2 + K_2 + \frac{1}{4}K_1 + \Delta_{\tilde{e}_L} \\ m_{\tilde{\nu}_L}^2 &= m_0^2 + K_2 + \frac{1}{4}K_1 + \Delta_{\tilde{\nu}_L} \\ m_{\tilde{e}_R}^2 &= m_0^2 + K_1 + \Delta_{\tilde{e}_R} \end{aligned}$$

where K_1 , K_2 and K_3 respectively denotes the contribution from the interaction of $U(1)_Y$, $SU(2)_L$ and $SU(3)_C$, which are approximately:

$$K_1 \sim 0.15 m_{1/2}^2, \quad K_2 \sim 0.5 m_{1/2}^2, \quad K_3 \sim 6 m_{1/2}^2, \quad (2.50)$$

and the correction factors $\Delta_{\tilde{f}}$ are given by:

$$\begin{aligned} \Delta_{\tilde{f}_L} &= (T_3 - Q \sin^2 \theta_W) m_Z^2 \cos 2\beta + m_f^2 \\ \Delta_{\tilde{f}_R} &= Q \sin^2 \theta_W m_Z^2 \cos 2\beta + m_f^2. \end{aligned}$$

Since the effect of running masses are always larger for squarks than sleptons due to the $SU(3)_C$ interaction, it generally implies lighter masses for sleptons. The typical running mass spectra is shown in Figure 2.6.

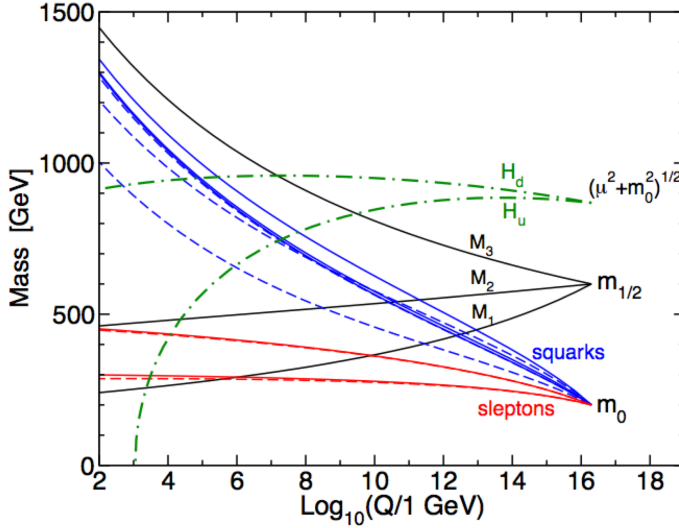


Figure 2.6: Evolution of scalar and gaugino mass parameters in the MSSM with mSUGRA boundary conditions [25]. The parameters are $m_0 = 200$ GeV, $m_{1/2} = 600$ GeV, $A^0 = -600$ GeV, $\tan \beta = 10$ and $\text{sign}(\mu) > 0$.

2.4 Experimental Constraints on SUSY so far

2.4.1 Constraints from Observed Standard Model Higgs Mass

It is a striking fact that in MSSM the mass of 125 GeV higgs (h) is bounded by:

$$m_h < m_Z \cos 2\beta < m_Z = 91.2 \text{ GeV}, \quad (2.51)$$

according to Eq. (2.47). Therefore, a sizable radiation correction is needed to achieve 125 GeV. The 1-loop correction is dominantly given by the remnant of cancellation of top and stop loop in Eq. (2.25):

$$\Delta m_h^2 := \frac{3}{4} \frac{m_t^4}{v_{\text{SM}}^2} \left[\log \frac{m_{\tilde{t}}^2}{m_t^2} + \frac{X_t^2}{m_{\tilde{t}}^2} \left(1 - \frac{X_t^2}{12m_{\tilde{t}}^2} \right) \right], \quad (2.52)$$

which has to accord with

$$\sqrt{(125 \text{ GeV})^2 - m_Z^2} \sim 85 \text{ GeV}. \quad (2.53)$$

This is a tremendously powerful constraint that forces either of following two ambivalent choices:

1. without assuming anything on stop mixing (e.g. X_t is free) and $O(10 \text{ TeV})$ of stop mass, with relatively large fine tuning ($\Delta m_h > 1000$), as shown in Figure 2.7.
2. maximal stop mixing ($X_t \sim \sqrt{6}m_{\tilde{t}}$), and 500 GeV – 1 TeV of stop mass, with mild fine tuning ($\Delta m_h \sim 100$).

The consequent implication from the former choice is that all the squarks and sleptons are heavy, and only gauginos could be explored in LHC, while the latter leads to light stop (or sbottom)

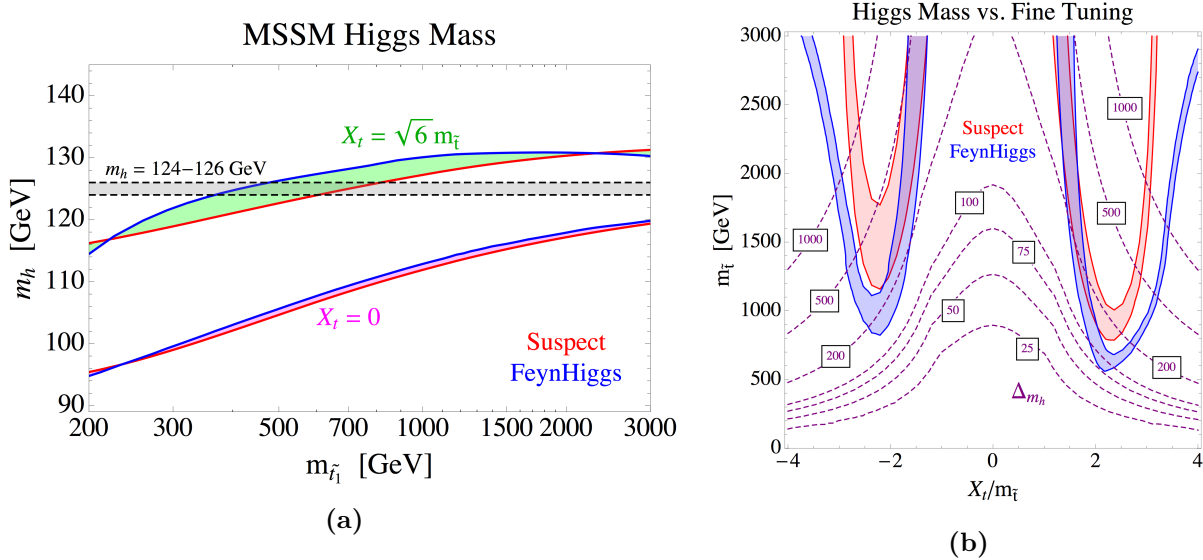


Figure 2.7: Relation of mass of SM-like higgs and stop mass in MSSM [36]. (a) The SM-like higgs mass as a function of lightest stop mass ($m_{\tilde{t}}$), with the no ($X_t = 0$) or maximal stop mixing ($X_t \sim \sqrt{6}m_{\tilde{t}}$). Red/blue solid lines correspond the computation using Suspect/FeynHiggs. (b) A 2D-constraint on the stop mass and stop mixing $X_t/m_{\tilde{t}}$ by observed SM-like higgs mass, with $m_{\tilde{Q}} = m_{u_3} = m_{\tilde{t}}$ and $\tan\beta = 20$. The dashed contour shows the gauge of fine tuning Δ_{m_h} defined by Eq. (2.54).

accessible by the LHC energy while the others are not necessarily so.

The higgs mass fine tuning argument in MSSM is rather subtle, since the observed m_h is no longer as straightforwardly associated with its own mass parameter H_u as in the case in SM (Sec. 2.2.1), but also involved by the other MSSM parameters as seen in Eq. (2.47). The magnitude of fine tuning is usually quoted by the linear response of any arbitrary MSSM parameters p_i [36]:

$$\Delta_{m_h} := \max_i \left| \frac{\partial \log[m_h^2(1\text{-loop})]}{\partial \log p_i} \right|. \quad (2.54)$$

In scenario 1. above, the resultant fine tuning is typically $1/\Delta_{m_h} \sim O(10^{-3})$, while $\sim 1\%$ is achievable in the scenario 2 in the most optimistic case with ~ 500 GeV stop.

As a level of $\sim O(10^{-3})$ of the fine tuning is not as fatal as that in the SM (10^{-34}), in the thesis, we pursue the former scenario, and probing gluinos in the experiment assuming all the squarks are all decoupled.

2.4.2 Constraint from Dark Mater Relic Density

The main stream of current DM theory is based on the “cold matter” regime in which DM used to be in a thermal equilibrium at the beginning of the universe, and cooled down according to the cosmic expansion later on, and being decoupled at a certain scale, fixing the abundance upto now. The relics is strongly related by the annihilation cross-section, which can be calculated within the MSSM framework.

Phenomenologically there are a couple of major classes of DM scenarios depending on the component of LSP. The case of pure bino-LSP can be almost immediately excluded, in a limit where all the squarks are decoupled, since it has to then rely on the annihilation channel via sleptons [37], where $m_{\tilde{\ell}} < 110$ GeV is needed to achieve the observed relic abundance (Eq. (2.29)) which is actually already excluded by LEP2. On the other hand, the annihilation cross-section tends to be too large in case of pure-wino or pure-higgsino LSP, where roughly ~ 3 TeV of wino mass or ~ 1 TeV of higgsino mass is needed to match with the observed relic Eq. (2.29), which is unfortunately beyond the LHC reach. What if the mixed case? It is particular interesting to consider doping a bit of wino or higgsino component into bino-dominated LSP, where moderated annihilation cross-section and experimental accessible LSP mass can be achieved simultaneously. This type of LSP is called “well-tempered” neutralino LSP [37], typically predicting a moderately small mass splitting between the next-to-the-lightest SUSY particle (NLSP) and the LSP with $20 - 60$ GeV [38, 39].

Note that a number of caveat remarks are to be added on the discussion:

- The observed relics is always based on Λ -CDM within the cold DM regime. The constraint on SUSY could therefore drastically different if DM is “warm” produced non-thermally.
- The DM annihilation cross-section calculation so far is dominantly done at the lowest-order (LO) in the perturbation. The contribution of higher order terms will generally increase annihilation cross-section.
- Non-perturbative effects (continuous interaction) in a collision of non-relativistic particles often lead to a sizable increase in annihilation cross-section (“Sommerfeld enhancement”).
- Is is a bit awkward though, it is possible for other new physics to supply the DM relics when SUSY is not capable of explaining the entire relic.

Given these too many uncertainties, it is sensible to regard the relic constraint as soft constraint. However, generally it is more fatal to have excessive relics than the opposite case, here we promise to respect the observed relic more as upper bound.

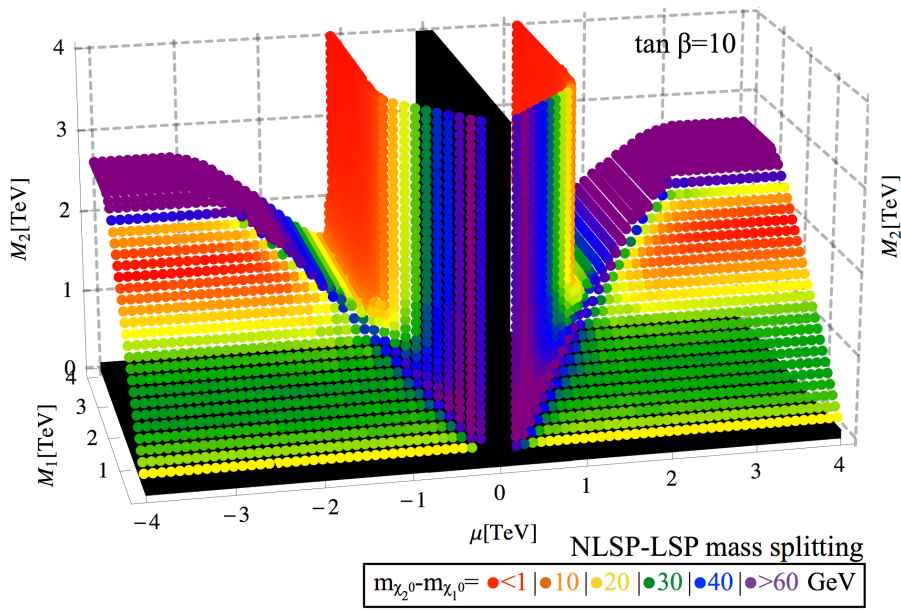


Figure 2.8: Mass splitting between NLSP (next-to-the-lightest SUSY particle) and LSP, as function of M_1 , M_2 and μ when assigning the DM relic constraint [39]. The effect of Sommerfeld enhancement is taken into the calculation. Within the reach by the LHC energy ($\min(M_1, M_2) < 1$ TeV), the resultant NLSP-LSP mass splitting is about 20 GeV ~ 30 GeV. Black points correspond to parameter space excluded by LEP.

2.4.3 Constraint from Direct Search at Collider Experiments

The direct search of SUSY had been widely performed in collider experiments including LEP, Tevatron and LHC covering over a number of signatures and scenarios. Unfortunately no evidence has been claimed, it is interpreted into constraints either on specific full models (mainly SUGRA-type models, GMSB and cMSSM), or on particular production and decay chains (“simplified model” as discussed in Sec 2.5.2). This sub-section overviews the status of constraints placed on simplified models.

Gluinos The best job is done by hadron collider experiments due to its outstandingly high production cross-section. It is particularly the case in LHC Run2, dominating the sensitivity in most of the scenarios in terms of the mass spectra and gluino decays.

The exclusion limits on the most typical gluino decays set by ATLAS and CMS are shown in Figure 2.9, namely (a) the direct decay where gluino directly fall into LSP with emitting two quarks, or (b) the 1-step decay via NLSP chargino. Up to ~ 2 TeV in gluino mass is excluded for case with large mass splitting between gluino and LSP, and $1.2 \sim$ TeV for the most pessimistic case where gluino and LSP are highly compressed. Note that the listed limits are all up-to-date published results as of July 2017. While most of them is with full 2016 dataset (integrated luminosity of $\mathcal{L} \sim 36 \text{ fb}^{-1}$), the ATLAS 1-lepton analysis (ATLAS-CONF-2016-054) is with smaller dataset ($\mathcal{L} = 14.8 \text{ fb}^{-1}$). **This study is meant for the update of it with the up-to-date dataset ($\mathcal{L} = 36.1 \text{ fb}^{-1}$) as well as the improved analysis method.**

Gluino decaying with top quarks addresses particular importance since it can be enhanced by the light stop which is motivated by naturalness. They are exclusively searched with dedicated signal regions, and the resultant limit is given in Figure 2.10. **This type of models are also the scope of the thesis, for which an improved result will be provided with respect to the existing ones.**

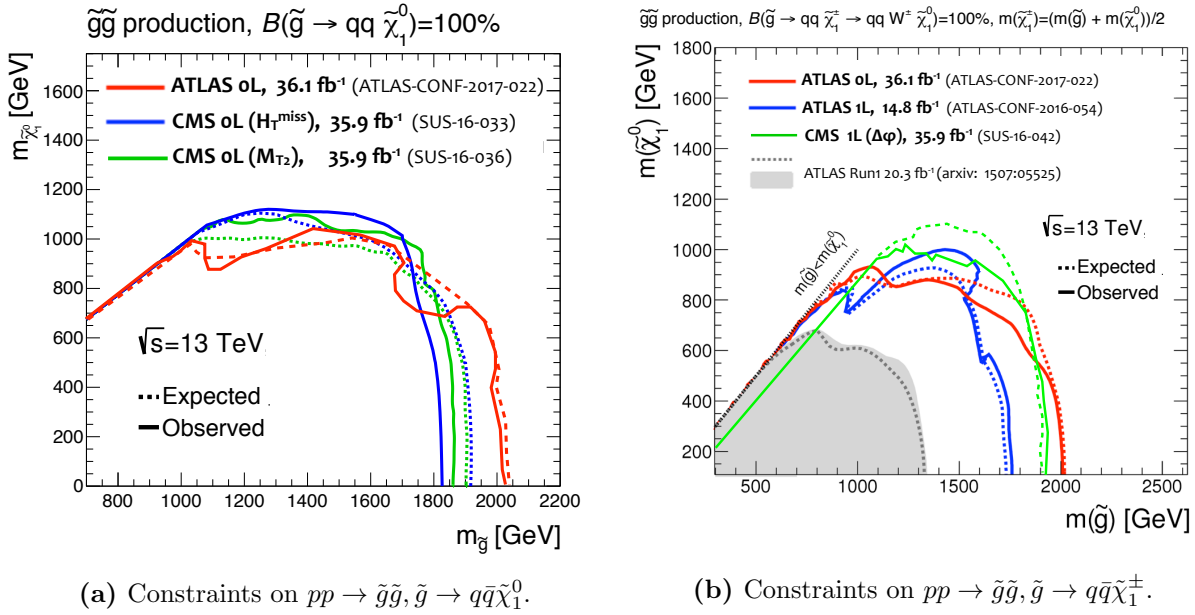


Figure 2.9: Up-to-date constraints set by ATLAS and CMS on (a) direct gluino decay: $\tilde{g} \rightarrow q\bar{q}\tilde{\chi}_1^0$, and (b) the 1-step chargino-mediated gluino decay: $\tilde{g} \rightarrow q\bar{q}\tilde{\chi}_1^\pm$ with the mass being in the middle between gluino and the LSP. The article numbers for corresponding references are labeled on the plots. “0L” and “1L” respectively denote searches with 0-lepton and 1-lepton final state.

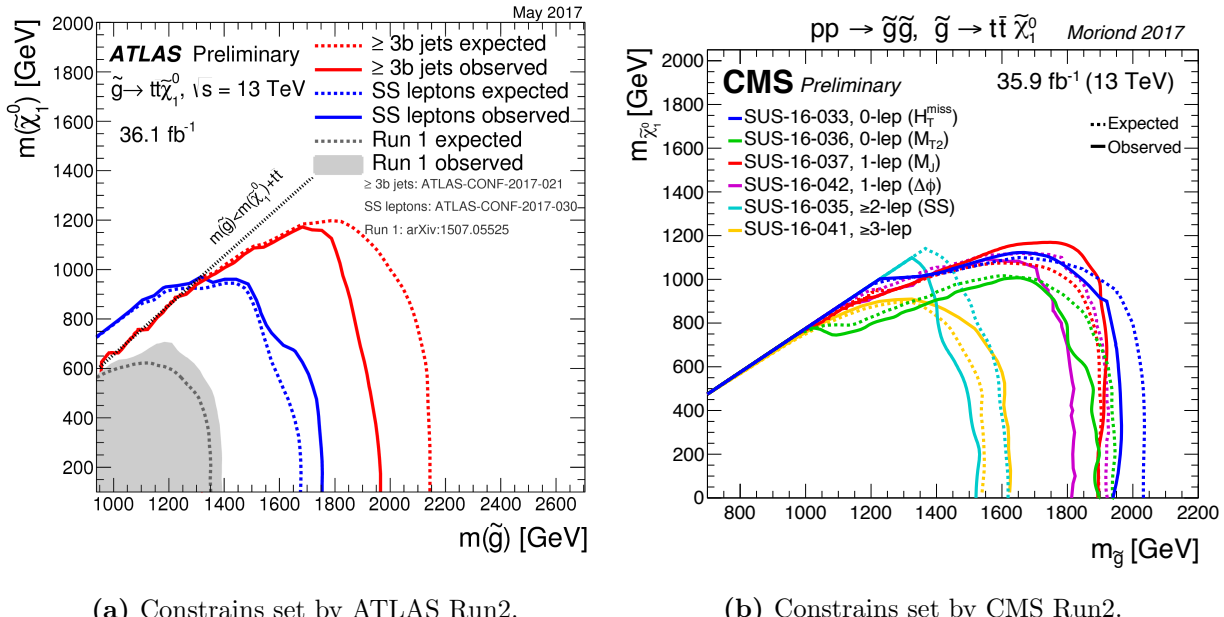


Figure 2.10: Up-to-date constraints on pair produced gluinos directly decaying with top quarks ($\tilde{g} \rightarrow t\bar{t}\tilde{\chi}_1^0$) set by (a) ATLAS and (b) CMS. The summary plots are referred from [40] (ATLAS) and [41] (CMS).

Squarks A class of analyses are dedicated for direct stop production with numerous stop decay scenarios and mass configurations. The strongest limits are provided by LHC, and up to about 400 GeV \sim 1 TeV in stop mass is generally excluded. Figure 2.11 presents the example limits on the direct stop decay scenario: $\tilde{t} \rightarrow t\tilde{\chi}_1^0$ provided by ATLAS and CMS.

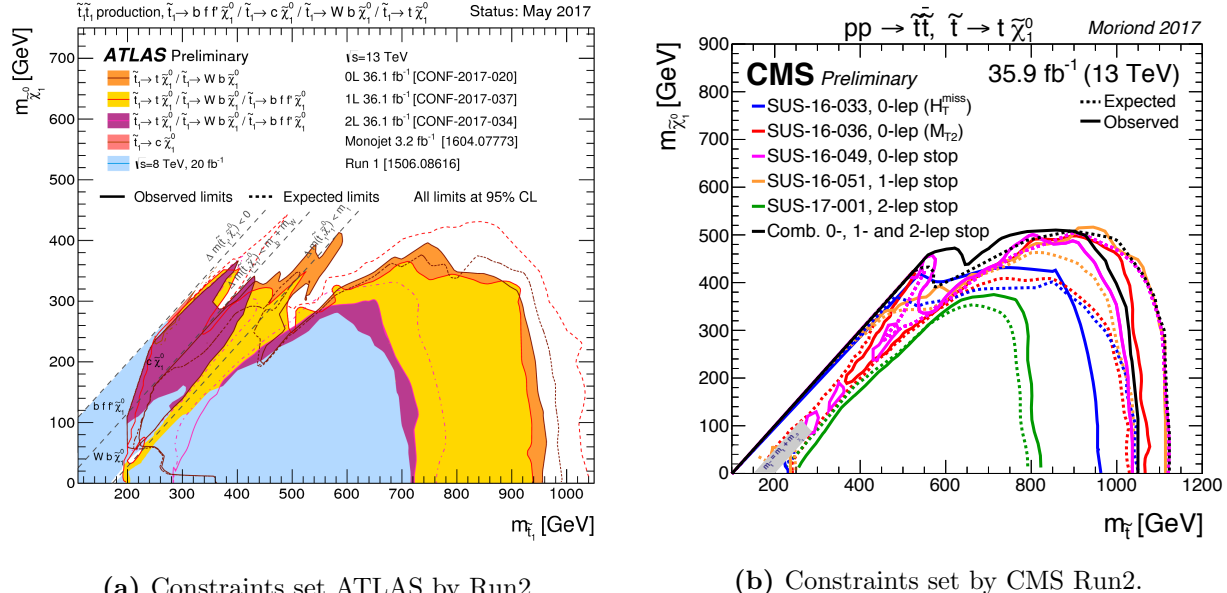


Figure 2.11: Up-to-date constraints on stop pair production with direct decay $\tilde{t} \rightarrow t\tilde{\chi}_1^0$ set by (a) ATLAS and (b) CMS. The summary plots are referred from [40] (ATLAS) and [41] (CMS).

Electroweak Gauginos A number of searches for direct EW gaugino production have been performed in LEP, Tevatron and LHC, and LHC provides the majority of current strongest limits. The targeted signature is mostly pair produced NLSPs ($\tilde{\chi}_1^\pm$ or $\tilde{\chi}_2^0$) decaying to LSP, where decoupled squarks are often assumed.³

Bino-LSP/wino-NLSP is the most commonly assumed configuration since it is easily explored; the signal typically leaves multiple leptons and large missing E_T in the final states. The exclusion limits set by ATLAS and CMS are shown in Figure 2.12. About up to 600 GeV of NLSP mass is excluded for cases with large NLSP-LSP mass splitting, and 150 – 250 GeV for small splitting.

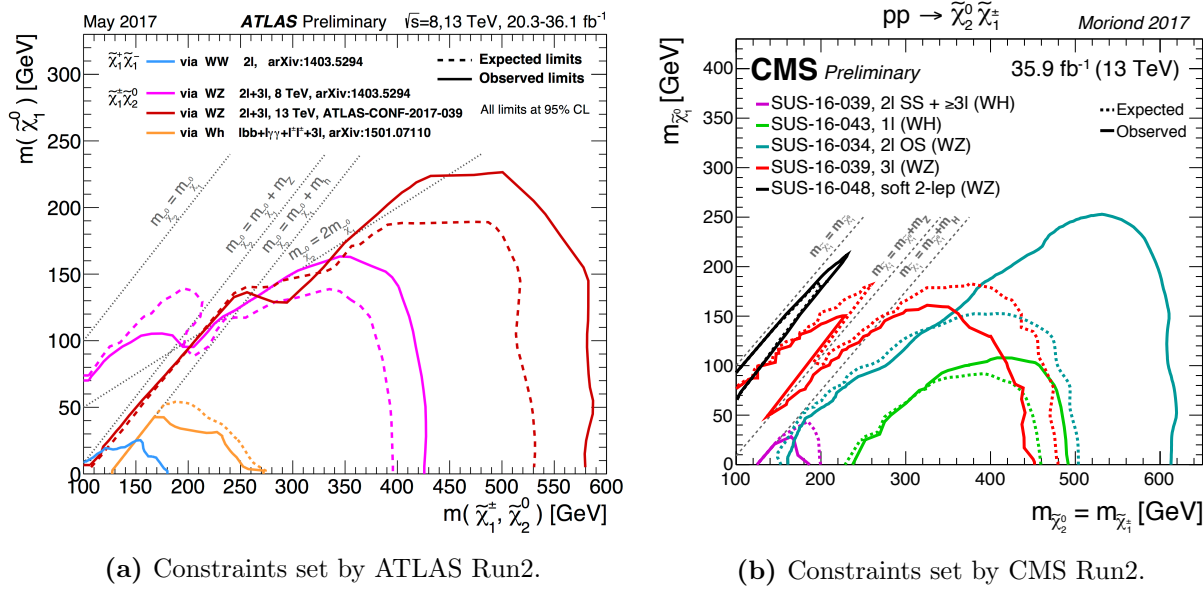


Figure 2.12: Up-to-date constraints on direct EW gaugino production with decays via $W/Z/h$ set by (a) ATLAS [42] and (b) CMS [43]. The summary plots are referred from [40] (ATLAS) and [41] (CMS).

The wino-LSP scenario is explored using a strikingly different approach. Since the mass splitting between NLSP wino-chargino and the wino-LSP is extremely compressed ($150 \sim 160$ MeV), wino-chargino retains $O(ns)$ of moderately long lifetime, resulting in a characteristic disappearing track signature where a traveling chargino track stops halfway in the tracker due to the decay into a soft pion. The results from ATLAS (Run2) and CMS (Run1) are given in Figure 2.13. The exclusion runs up to 300 – 500 GeV in wino mass at the lifetime (or the NLSP-LSP mass splitting) predicted by MSSM.

Although motivated by in light of naturalness, almost no constraint is set for direct higgsino production so far by LHC, due to the marginal production cross-section ($\sim 1/4$ of that of the wino production) as well as the experimentally challenging small NLSP-LSP splitting generally predicted in case of higgsino LSP. The strongest limit on direct higgsino production is still held by LEP2. The limit is shown in Figure 2.14, where up to ~ 90 GeV of LSP mass is excluded.

³Under the decoupled squark scenario, bino production is strongly suppressed.

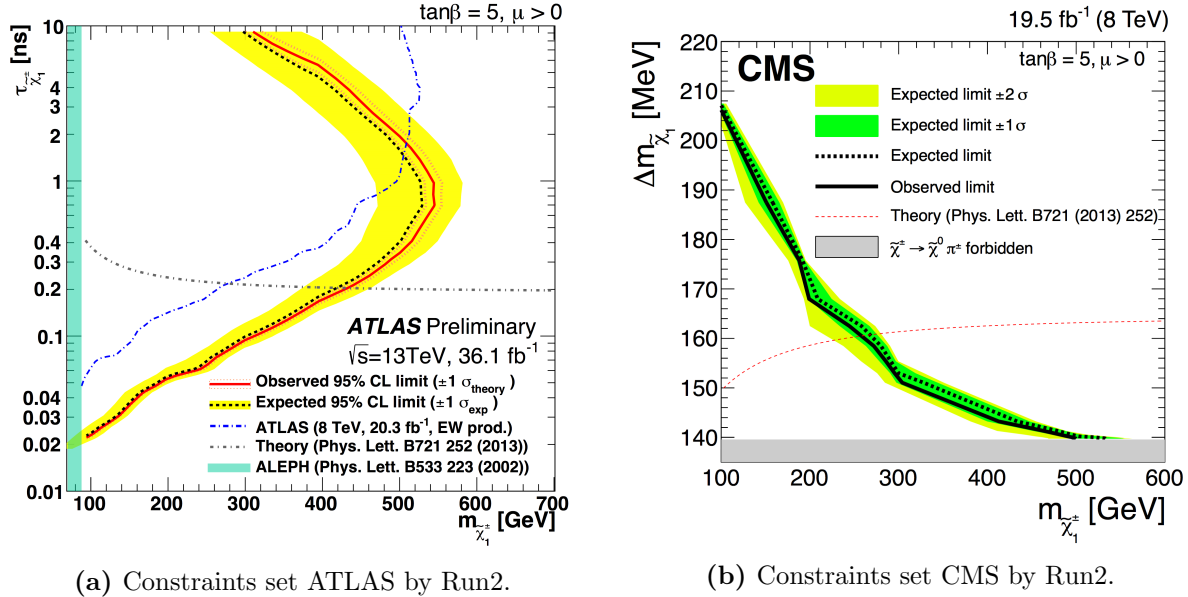


Figure 2.13: Constraints on the wino-LSP scenario set by (a) ATLAS [44] and (b) CMS [45].

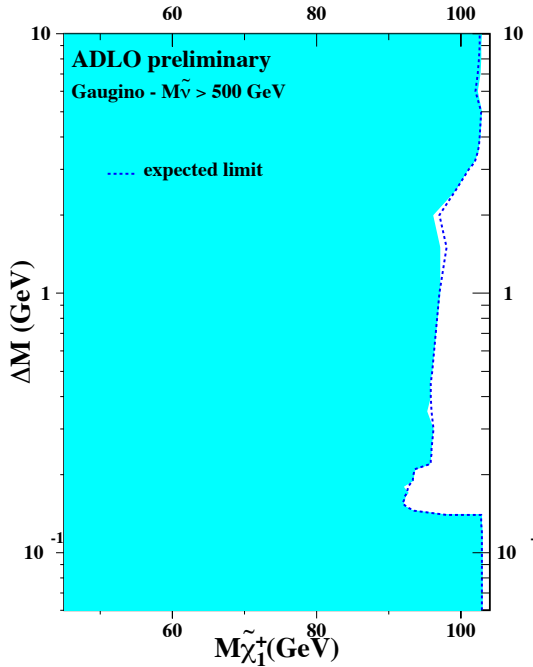


Figure 2.14: Exclusion limit on direct production of higgsino pairs set by LEP2. Combined result from all the four experiments is shown [46].

2.5 Target SUSY Scenario and the Search Strategy

2.5.1 Target SUSY Scenario

To summarize the discussion above, thesis focuses on the MSSM scenarios where:

- Squarks are all heavy (> 3 TeV).
- Allow the higgs mass fine tuning at order of 10^{-3} .
- LSP is neutralino.
- Loosely respect the observed DM relic (Eq. (2.29)).

The targeted experimental signature is the pair production of gluinos (Figure 2.15) with the mass of 800 GeV – 2 TeV. Although the search is inclusively carried out with no particular assumption on the mass spectra, a special attention will be made for the case of $\Delta m(\tilde{\chi}_1^\pm/\tilde{\chi}_2^0, \tilde{\chi}_1^0) = 20$ GeV ~ 30 GeV motivated by the well-tempered neutralino DM scenario.

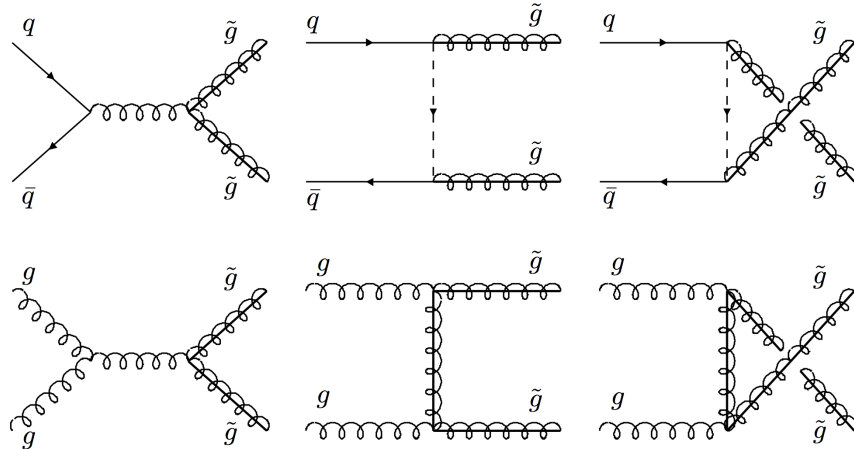


Figure 2.15: Feynmann diagrams for tree-level gluino pair production in LHC [47].

2.5.2 The Strategy of Decay Chain Based Search

Though minimality is still respected in principle, it would be more sensible to extend the scope of the search to a more general direction with respect to past analyses, given that the most straightforward scenarios has already been largely excluded by LHC so far. Ideally, we prefer to consider as general as possible e.g. MSSM, but constraining the full parameter spaces is not realistic (e.g. > 100 parameters for the most general MSSM). However, it is also true that most of the MSSM parameters only affect the spins or decay branchings of SUSY particles, rather than kinematics i.e. they do not change the signal acceptance. On the other hands, kinematics of SUSY signatures are dominantly determined by SUSY mass spectra. Therefore, we only have to care about the mass dependence, once a full decay chain is specified. In other words, setting the cross-section upper limit on each decay chain and mass spectra is no less general than considering the full parameter space of the MSSM⁴.

Placing an upper limit on particular a decay chain $A \rightarrow B$ is essentially equivalent to setting an exclusion limit on following model called “simplified model” where:

- $\text{Br}(A \rightarrow B)$ is 100%.
- Parameters other than SUSY masses are fixed to an arbitrary configuration. For instance, in LHC analysis, the EW gaugino mixing is usually set so that NLSP and LSP become wino- and bino-dominant.

Though interpretation has already been widely employed based on the simplified model in LHC searches, the critical problem is that the coverage of decay chains and mass spectra is far from complete, for instance, in case of gluino, only a few decays are considered. In this thesis, all the viable gluino decay chains will be considered, and setting the limit on each of them with full coverage of mass assumption on gluino and EW gauginos. In the following sub-section, the target decay chains are explicitly specified.

2.5.3 Target Gluino Decay Chains

Under the decoupled squarks scenario, gluino always decays 3-body; 2 SM quarks and a EW gaugino via heavy virtual squarks:

$$\tilde{g} \rightarrow \begin{cases} (u\bar{d}, c\bar{s}, t\bar{b}) \times (\tilde{\chi}_{1,2}^-) \\ (d\bar{u}, s\bar{c}, b\bar{t}) \times (\tilde{\chi}_{1,2}^+) \\ (u\bar{u}, d\bar{d}, s\bar{s}, c\bar{c}, b\bar{b}, t\bar{t}) \times (\tilde{\chi}_{1-4}^0). \end{cases}$$

Including the subsequent EW gaugino decays, it leads to an enormous number of final states. However kinematically some the them are approximately equivalent which can be merged or trimmed. For instance, since the acceptance is nearly invariant between light quark flavors (u, d, s, c), they are merged into a single simplified model where gluino has equal decay branches into u, d, s, c .

⁴This is equivalent to admit our search has no sensitivity in determining model parameters other than masses.

In addition, the four higgsino (or two wino) states can be regarded as a single state since their masses are highly compressed each other⁵ leading the same kinematics. The mass spectra can be eventually reduced into either the three scenario schematized in Figure 2.16, involving three types of gluino decays:

- “direct” decay in which gluino directly de-excites into LSP,
- “1-step” decay with one intermediate EW gaugino state,
- “2-step” decay in which gluino decays via two resolved intermediate EW gauginos mass states.

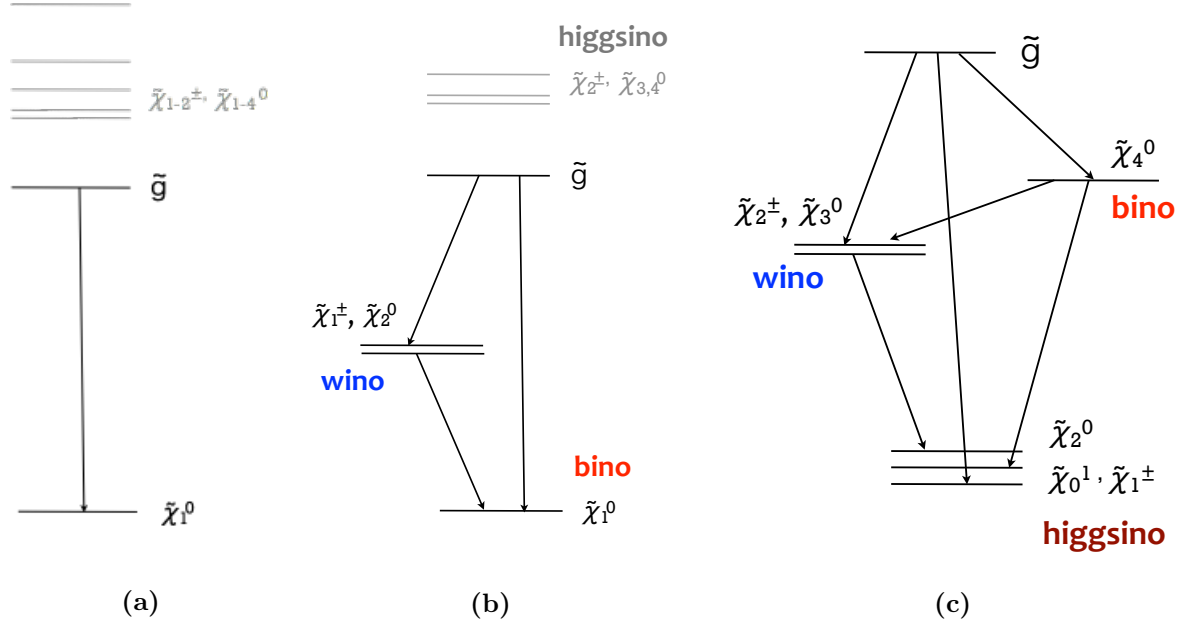


Figure 2.16: Illustration of possible gluino decay paths under various scenario of the mass spectra. (a) All the EW gauginos are heavier than gluino except the LSP (gluino decay: direct). (b) One of the EW gauginos (bino, wino, higgsino) is heavier than gluino while the other EW gauginos are lighter (gluino decay: direct or 1-step). (c) All the EW gauginos are below gluino mass (gluino decay: direct or 1-step or 2-step).

As for the scenario (c) in Figure 2.16, a numerous MSSM parameters scans demonstrate that the probability of 2-step decays are generally much lower than that of direct or 1-step decays, except for some of the cases where each of the intermediate masses are aligned with relatively equal distance. Therefore, in the analysis, we confine our scope within the direct and 1-step decays.

For subsequent EW gaugino decays, charginos are always assumed to emit on-shell or off-shell W -boson, while there are two options for neutralino decays i.e. via Z or h . The decays into slepton is ignored here, majorly for convenience sake of restricting the number of final states, however with a few justifications; under the regime of sfermion mass unification (Sec. 2.3.4), slepton masses are in the same order of squark masses which are assumed to be decoupled here ; when respecting the

⁵The splitting will be rarely greater than 50 GeV even when all M_1 , M_2 and μ are at the same mass leading to the maximum mixing.

observed DM relic abundance, the mass splitting between NLSP and LSP becomes generally small (typically < 50 GeV). Decays via sleptons then requires slepton masses to be just within the small gap between the NLSP and LSP, which is however very unnatural.

With all the consideration, the targeted gluino decay chains are reduced into Table 2.4 with corresponding Feynmann diagrams shown in Figure 2.17.

Table 2.4: Summary of targeted gluino decay chains. The number in the pharenthese indicates the numbers of chains in the category.

Direct decay (3)	$\tilde{g} \rightarrow (q\bar{q}, b\bar{b}, t\bar{t}) \tilde{\chi}_1^0$
1-step decay (8)	$\tilde{g} \rightarrow (q\bar{q}', b\bar{b}(t\bar{t})) \tilde{\chi}_1^\mp, \tilde{\chi}_1^\mp \rightarrow W^\mp \tilde{\chi}_1^0$ $\tilde{g} \rightarrow (q\bar{q}, b\bar{b}, t\bar{t}) \tilde{\chi}_2^0, \tilde{\chi}_2^0 \rightarrow Z \tilde{\chi}_1^0$ $\tilde{g} \rightarrow (q\bar{q}, b\bar{b}, t\bar{t}) \tilde{\chi}_2^0, \tilde{\chi}_2^0 \rightarrow h \tilde{\chi}_1^0$

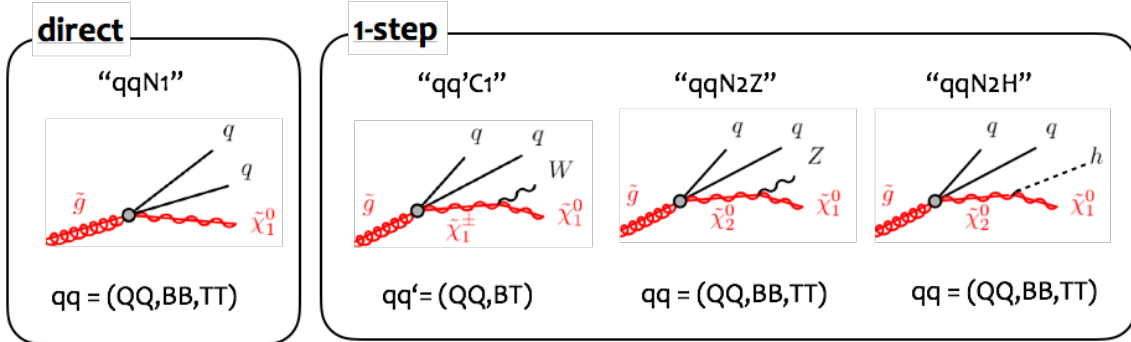


Figure 2.17: Target gluino decay chains.

The full decay chains of pair produced gluinos become increasingly complicated: 11 symmetric decays (two gluinos experience the same decay chains), 55 symmetric decays (two gluinos experience different decay chains). In total, 66 decay chains are identified as the candidate for the targets.

2.5.4 Target Signal Models for 1-lepton Final State

In LHC, analyses are conventionally divided based on number of hard leptons in the final state, since either signal kinematics and the background strategy are drastically different. In gluino decays, when ignoring the decays into sleptons, leptons are always generated via decays of W/Z/H bosons. Therefore, giving their small leptonical branching ratio, 0-lepton or 1-lepton final state are the most promising channels for inclusive search, while 2/3-leptons final states are more specialized in specific types of scenarios such as long-chain multi-step gluino decays involving a large number of W/Z/H bosons.

This thesis focuses on the final state with exactly one lepton. After excluding the decay chains with marginal branching ratio into final state with exactly 1-lepton, 45 decay chains are selected

as the benchmark models for the thesis. The full list are shown in Table 2.5 - Table 2.7, with the naming convention for each decay chain defined as:

$$\begin{aligned} \text{Model name} &:= [aaXX][bbYY] \\ aa, bb &= \text{"QQ", "BB", "TT", "BT"} \\ XX, YY &= \text{"N1", "C1", "N2Z", "N2H"} \end{aligned} \quad (2.55)$$

where each sub-block ($[aaXX], [bbYY]$) denotes the full chain of one gluino decay, corresponding to either of the topology shown in Figure 2.17.

Since the signal regions will be segmented based on the number of b -tagged jets, the benchmark models are further categorized (BV/BT/3B) based on the number of expected b -quarks in the final state. The reference models for each b -categories are respectively chosen as **QQC1QQC1**, **QQC1BTC1** and **TTN1TTN1** for BV, BT and 3B (Figure 2.18), which will be used as the reference in designing signal regions and other various studies. The Feynman diagrams for the reference models are illustrated in Figure 2.18.

Note that simplified models with asymmetric gluino decays are not realistic due to the assumption of 100% branching ratio, since there is always branching to symmetric decays when asymmetric decays happen. However, this is in fact a more user friendly presentation since it provides the upper limit on the acceptance for each decay chain so that the compatibility between observation and models can be easily tested using it, which is not the case in case of an interpretation with a realistic models where many sorts of decays are mixed.

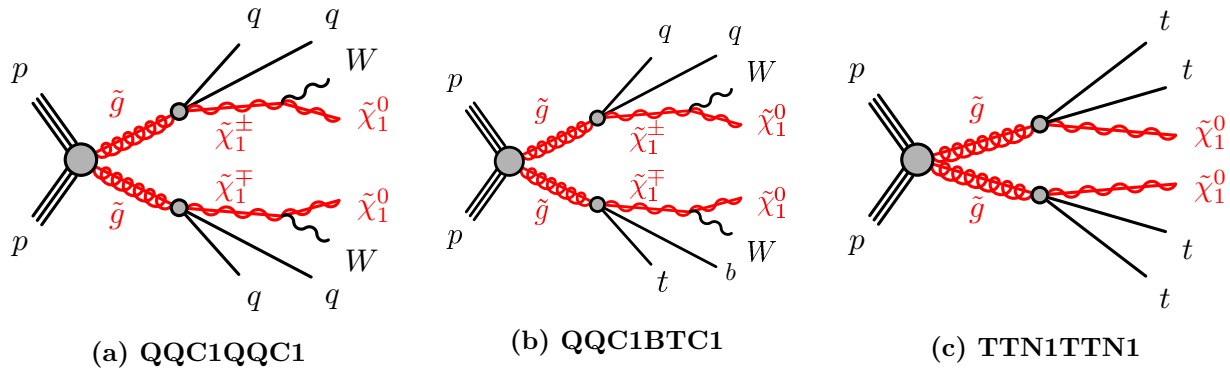


Figure 2.18: Feynman diagrams for the reference models.

Table 2.5: Target models with no b-jets at tree level (BV models). The average jet multiplicity (n_J) and b-jet multiplicity (n_B) are calculated based on number of quarks and b-quarks appearing in the final state. The PDG values [48] are referred for branching ratio of top, W/Z/h bosons. “✓” specifies the models with the final result derived using the samples with the fast detector simulation (ATLFast 2 [49]), while the others are with emulated truth samples.

1-step decay	n_J	n_B	$\text{Br}(1\text{L})/\text{Br}(0\text{L})$	$\text{Br}(1\text{L})/\text{Br}(2\text{L})$	det sim.?
QQN1QQC1	5.5	0.0	0.33	-	
QQC1QQC1	7.0	0.0	0.67	6	✓
QQC1QQN2Z	7.3	0.3	0.35	3.86	✓

Table 2.6: Target models with 1 or 2 b-jets at tree level (BT models). Definition of $n_{B,J}$, branching and “✓” are the same as Table 2.5.

Direct decay	n_J	n_B	$\text{Br}(1\text{L})/\text{Br}(0\text{L})$	$\text{Br}(1\text{L})/\text{Br}(2\text{L})$	det sim.?
QQN1TTN1	7.0	2.0	0.67	6	
1-step decay	n_J	n_B	$\text{Br}(1\text{L})/\text{Br}(0\text{L})$	$\text{Br}(1\text{L})/\text{Br}(2\text{L})$	det sim.?
QQC1QQN2H	7.4	1.1	0.46	7.07	✓
QQN1BTC1	7.0	2.0	0.67	6	
QQN1TTN2Z	8.8	2.3	0.68	3.30	
QQC1BTC1	8.5	2.0	1.0	3	✓
QQC1BBN2Z	7.3	2.3	0.35	3.86	
QQC1TTN2Z	10.3	2.3	1.02	2.34	
QQN2ZTTN2Z	10.7	2.6	0.7	2.31	
BBN1QQC1	5.5	2.0	0.33	-	
BTC1QQN2Z	8.8	2.3	0.68	3.30	
TTN1QQC1	8.5	2.0	1.0	3	
TTN1QQN2Z	8.8	2.3	0.68	3.30	

Table 2.7: Target models with 3 or more b-jets at tree level (3B models). Definition of $n_{B,J}$, branching and “✓” are the same as Table 2.5 and 2.6.

Direct decay	n_J	n_B	$Br(1L)/Br(0L)$	$Br(1L)/Br(2L)$	det sim.?
BBN1TTN1	7.0	4.0	0.67	6	
TTN1TTN1	10	3.9	1.33	2	✓
1-step decay	n_J	n_B	$Br(1L)/Br(0L)$	$Br(1L)/Br(2L)$	det sim.?
QQN1TTN2H	8.9	3.1	0.79	3.64	
QQC1BBN2H	7.4	3.1	0.46	7.07	
QQC1TTN2H	10.4	3.1	1.12	2.34	
QQN2ZTTN2H	10.8	3.4	0.8	2.56	
QQN2HTTN2H	10.8	4.3	0.91	2.70	
BBN1BTC1	7.0	4.0	0.67	6	
BBN1TTN2Z	8.8	4.3	0.68	3.30	
BBN1TTN2H	8.9	5.1	0.79	3.64	
BBN2ZTTN2Z	10.7	4.6	0.7	2.31	
BBN2ZTTN2H	10.8	5.4	0.8	2.56	
BBN2HTTN2H	10.8	6.3	0.91	2.70	
BTC1QQN2H	8.9	3.1	0.79	3.64	
BTC1BTC1	10	4.0	1.33	2	
BTC1BBN2Z	8.8	4.3	0.68	3.30	
BTC1BBN2H	8.9	5.1	0.79	3.64	
BTC1TTN2Z	11.8	4.3	1.35	1.75	
BTC1TTN2H	11.9	5.1	1.46	1.70	
TTN1QQN2H	8.9	3.1	0.79	3.64	
TTN1BTC1	10	4.0	1.33	2	
TTN1BBN2Z	8.8	4.3	0.68	3.30	
TTN1BBN2H	8.9	5.1	0.79	3.64	
TTN1TTN2Z	11.8	4.2	1.35	1.75	
TTN1TTN2H	11.9	5.1	1.46	1.70	
TTN2ZQQN2H	10.8	3.4	0.8	2.56	
TTN2ZBBN2H	10.8	5.4	0.8	2.56	
TTN2ZTTN2Z	13.7	4.5	1.36	1.55	
TTN2ZTTN2H	13.8	5.4	1.47	1.53	
TTN2HTTN2H	13.8	6.2	1.58	1.49	

Chapter 3

Experiment Apparatus: The ATLAS Detector at the LHC

3.1 The Large Hadron Collider

The Large Hadron Collider (LHC) [50] is a 27 km long circular proton accelerator embedded underground of the Geneva area. It is designed to collide protons at a center-of-mass energy of $\sqrt{s} = 14$ TeV, at the four detector sites (ATLAS[51], CMS[52], ALICE[53] and LHCb[54]) built on the accelerator ring. ATLAS and CMS are general purpose detectors designed to study a vast range of physics programs, while LHCb and ALICE are specialized in studying b -hadrons and heavy-ion collisions respectively. The operation started in 2010, offering proton-proton (pp) collisions at a center-of-mass energies of 7 TeV and 8 TeV with 4.7fb^{-1} and 20.3fb^{-1} of integrated luminosity until 2012 (Run1). The center-of-mass energies has been almost doubled to 13 TeV in the runs starting from 2015 (Run2). The LHC has also delivered lead-ion (Pb-Pb) collisions with a center-of-mass energy of $\sqrt{s_{NN}} = 2.76$ TeV and proton-lead (p-Pb) collisions with $\sqrt{s_{NN}} = 5.02$ TeV.

The acceleration of protons with various steps: Protons are firstly seeded from hydrogen gas, by blowing the electrons off the hydrogen atoms using electric field. They are injected in the linear accelerator LINAC2 accelerated up to 50 MeV, and sent to the Proton Synchrotron Booster (PSB) with being accelerated up to an energy of 1.4 GeV. The subsequent accelerator is the Proton Synchrotron (PS) elevating the energy of the protons to 25 GeV, and injecting them into the Super Proton Synchrotron (SPS). After being accelerated to 450 GeV in SPS, the protons finally enter the two LHC pipes running the beam oppositely each other. The whole acceleration chain is illustrated in Figure 3.1.

The LHC accelerator consists of octant-shaped 2.45 km arcs with 1232 superconducting magnets located at the curves, providing 8.33T of magnetic field to bend the proton trajectory. In total, 39 bunch-trains can be filled simultaneously at the design condition, and 2808 bunches per beam are brought to collision in the LHC. Each bunch contains about 10^{11} protons. The beam bunches are collided with a crossing angle of 285 mrad. The peak luminosity amounts upto $L = 0.7 - 1.4 \times 10^{34}\text{cm}^2\text{s}^{-1}$ in the 2015-2016 runs, as shown in Figure 3.2 (a).

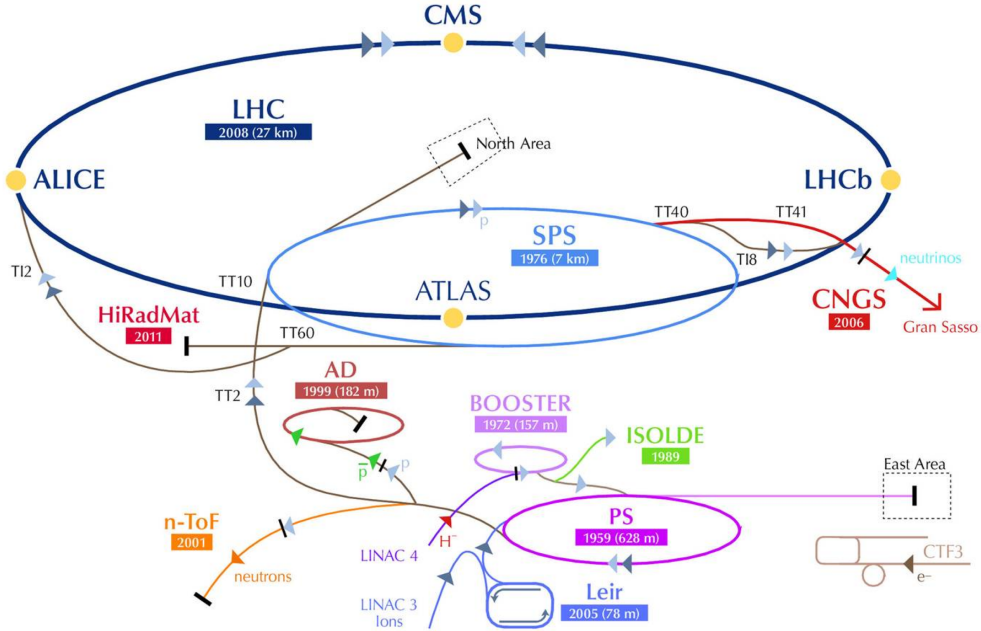


Figure 3.1: The LHC and associated booster accelerator system. [55]

Due to the high frequency of collisions and the dense proton bunches, multiple proton collisions can take place within the same bunch crossing, referred as “pile-up”. The average pile-up μ , defined as the mean number of interactions per bunch crossing, has been evolved according to the peak luminosity increase. The μ profile in Run2 is shown in Figure 3.2 (b) where $\mu = 20 \sim 40$ is typically achieved.

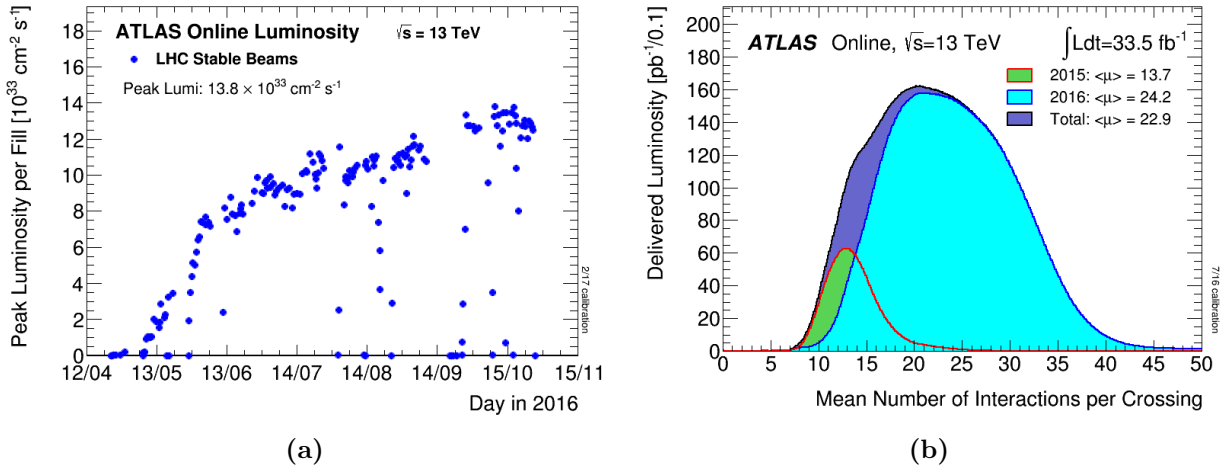


Figure 3.2: (a) Peak luminosity evolution in 2016 runs [56], and (b) the pile-up profile obtained in 2015-2016 runs [57].

3.2 The ATLAS Detector

3.2.1 Overview

ATLAS (A Toroidal LHC ApparatuS) is a general purpose detector, aiming to a wide range of physics programs from precision measurements to the energy frontier experiments, through a dedicated measurement of particles produced in the pp collisions. The detector extends over 44m in width and 25m in height weighing 7000 tons in total, covering the interaction point (IP) by a cylindrical barrel and two end-caps, achieving a nearly full solid angle coverage. The cut-away image is shown in Figure 3.3.

The purposes of the detector are mainly two-fold:

- identification of particle species,
- determination of particle's energy and momentum,

with two complementary concepts of measurement:

- fast measurement to provide triggers
- precision measurement for physics analyses

To satisfy these functionalities at the same time, following sub-detectors are arranged in a designed order from the inner to the outer with respect to the IP.

- Inner detector (and magnets) to identify and measure electrically charged particles, as well as to define the primary vertices.

Charged particle can easily interact with materials by ionizing the molecules inside. The path of flight can be “imaged” as a track, by recording the position of ionization. In ATLAS, a complex of discrete layers of silicon sensors and a continuously volumed gas chambers are placed in the innermost part. The momentum can be measured by applying a magnetic field, and quantifying the curvature of the bent trajectory.

- Calorimeters to measure the energy of electron, photon and hadrons.

Electrons and photons traveling inside materials above certain energy ¹ lose their energy through electromagnetic showering; photons create e^+e^- pairs and electrons spew bremsstrahlung photons; the daughter electrons and photons are multiplicatively split by the recursive splitting; ending up in a particle shower. Most of the energy are absorbed after traversing about 20 radiation lengths (X_0) of material. Hadrons (mostly pions) also cause similar cascade reactions. The shower branch evolves by interacting with nucleus in the material via strong interaction, meanwhile produced π_0 s promptly decay into two photons which shower electromagnetically. The resultant shower is a combination of a long hadronic shower and small local EM clusters in it. Electromagnetic and hadronic calorimeters are set as the outer layers of the trackers.

¹Referred to the critical energy. ~ 800 MeV for typical material.

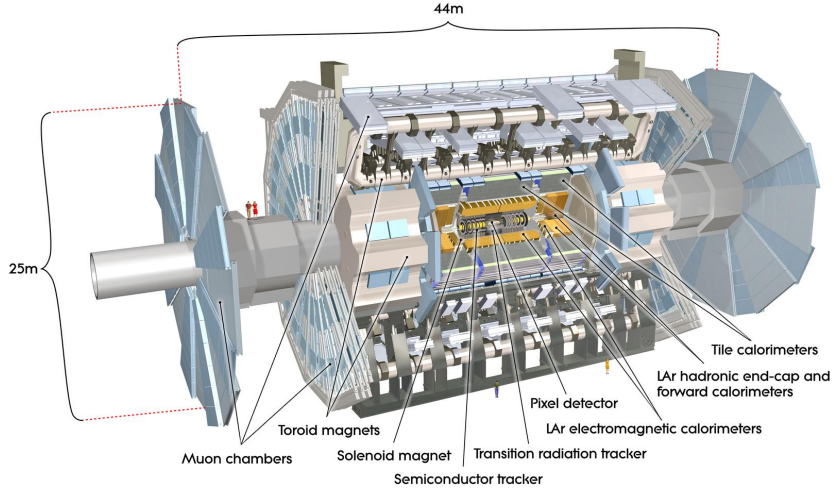


Figure 3.3: Full-body view of the ATLAS detector [59]. The geometry is completely forward-back symmetric.

- Muon spectrometer (and the magnet) to measure the muons penetrating the detector.
Among all the particles that interact with material, muons are only exception that do not seriously deposit the energy in the calorimeter. This is due to the fact that muons are the leptons happening to have the mass realizing the minimum EM interaction with material (Minimum Ionizing Particle; MIP), and the corresponding critical energy for EM showering is usually at several TeV level. This is actually a lovely coincident for human being (or poor particle physicists), since they can be easily identified i.e. particles punching through the calorimeter are automatically muons. The muon spectrometer located the outermost serves for identifying such muons as well as measuring the tracks together with the information from the inner tracker.
- Given the total momentum conservation in the transverse direction in each collision, the presence of non-interacting particles such as neutrinos and hypothetical new particles can be indirectly detected through the transverse momentum imbalance; This is referred to missing E_T (E_T^{miss}), ² defined by the negative of the vectoral sum of transverse momentum of all detected particles.

In the following sections, each of the sub-detector system is overviewed, comprehensively based on references [51] and [58].

3.2.2 Coordinate System

For referencing the position of the detector as well as the orientation of particles, a right-handed Cartesian coordinate system is defined where the interaction point is the origin; the x -axis pointing to the center of the LHC ring; the y -axis and z -axis are accordingly the direction of sky or the

²The “ E_T ” in the name is due to a historical reason; it used to be calculated only using calorimeter deposits, which is now actually outdated

beam direction respectively. Polar angle θ and azimuthal angle ϕ are defined by the cylindrical representation (θ, ϕ, z) : θ ranges from 0 to π with respect to the z -axis, and ϕ runs from $-\pi$ to π from the x -axis. The two end-caps in the ATLAS detector are referred as “A-side” and “C-side”,³ corresponding to the position of positive and negative coordinate in the z -axis.

It is the unfortunate fate for hadron colliders that particles generated by collisions are usually highly boosted along z -axis, since the energy of the initial interacting partons inside the hardons are asymmetric. From this point of view, a set of variables with Lorentz-invariant nature are introduced for describing the momentum or position for such particles. In particular, it is useful to define the transverse component of variables, such as transverse momentum $p_T := p \sin \theta$ or transverse energy $E := E \sin \theta$. The advantage over the use of p or E is obvious that they do express the intrinsic hardness of the particles in the center-of-mass frame of the reaction, and also that the vectorial sum of all particles conserves before and after the collision.

Similarly, pseudo-rapidity η is defined below, serving as the coordinate of polar angle:

$$\eta := -\ln \left(\tan \frac{\theta}{2} \right). \quad (3.1)$$

It has two practical advantages over θ ; the difference in pseudo-rapidity between particles $\Delta\eta$ are invariant against the boost towards z -direction.⁴; η has an effectively wider dynamic range upto a very forward region thanks to the finer measure, where θ suffers from the degeneracy in $\cos \theta \sim 1$, thus more convenient in expressing the orientation of forward particles.

Angular distance between two particles are commonly expressed by R , defined as:

$$\Delta R := \sqrt{(\Delta\eta)^2 + (\Delta\phi)^2}. \quad (3.2)$$

3.2.3 Inner Detectors

The inner detector (ID) is placed the inner-most of the ATLAS detector, designed to measure the tracks of charged particles, as well as precisely determining the position of vertices of the hardest scattering in interest. It consists of a silicon tracker (the pixel detector and the semiconductor tracker ;SCT) at the inner radii, and the Transition Radiation Tracker (TRT) for continuous tracking at the outer radii. The detector arrangement is illustrated in Figure 3.4 and Figure 3.5. The outer radius is surrounded by the central solenoid, providing a magnetic field of 2T along the z -axis, to bend the tracks traveling inside the ID volume. As a general requirement, ID has to contain material as less as possible, to avoid disturbing the measurement downstream by the energy loss. Figure 3.6 shows the total material profile of the ID as function of $|\eta|$. The material volume is suppressed below 2.5 radiation length and 1 nucleus interaction length, which is low enough compared with energy dropped in the calorimeter.

³Reportedly named after the direction towards (Geneva) Airport and the Charlie’s Pub in St. Genis-Pouilly from the ATLAS respectively.

⁴ This is true when the particles are massless, which is approximately valid given that the boos along z -axis is sourced by the momentum of order of the beam energy.

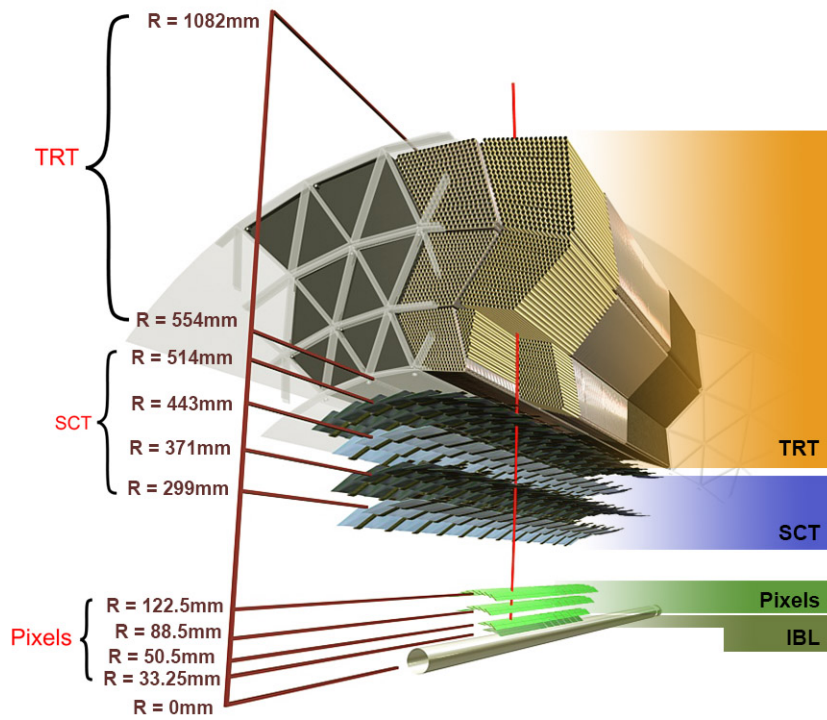


Figure 3.4: Cross-section of the ATLAS inner detectors [51].

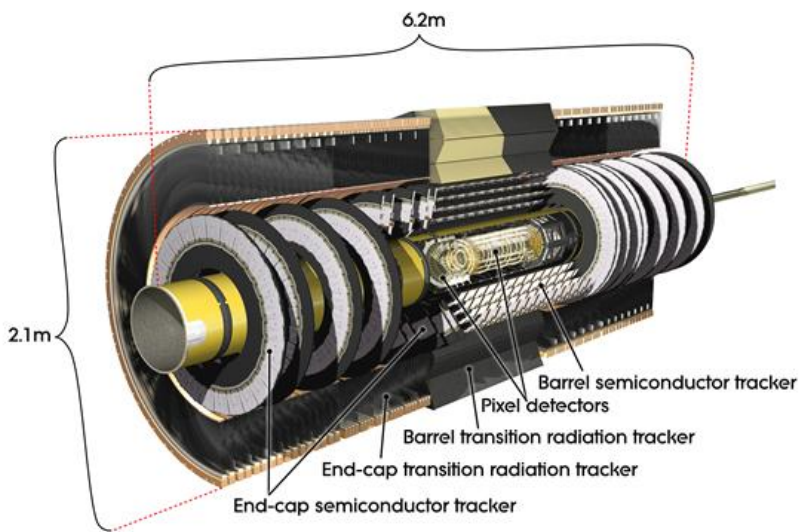


Figure 3.5: Cut-away view of the ATLAS inner-detector [51].

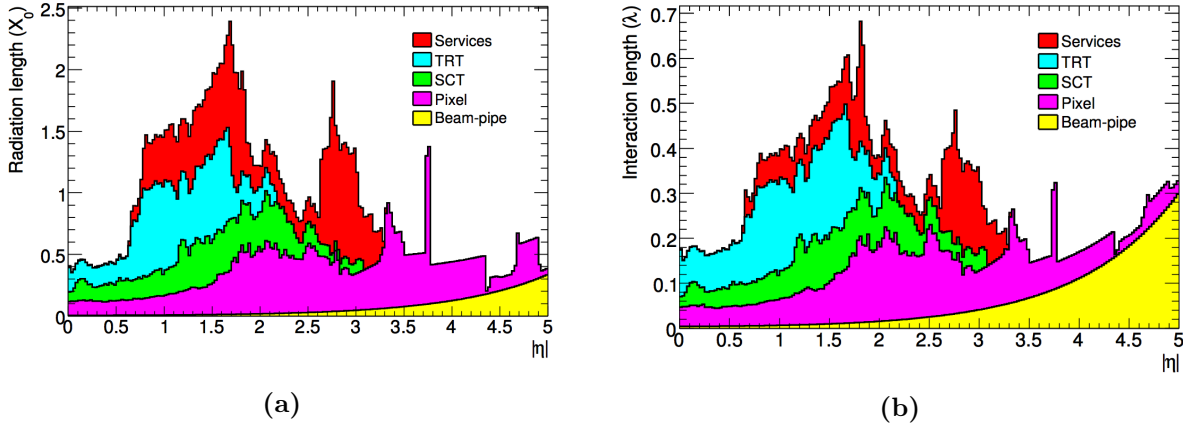


Figure 3.6: Simulated material profile of whole ID in unit of (a) electro-magnetic radiation length and (b) nucleus interaction length [51]. The peak in $|\eta| \sim 1.5$ corresponds to the barrel-end-cap transition area through which service cables travel.

The silicon trackers: Pixel and SCT The detection principle of silicon detector is based on the electron-hole pair creation induced by a traverse of a charged particle. Those electron-hole pairs are then inhaled by the bias voltage applied on the sensor, and transferred into an electric signal. The choice of silicon is largely due to its radiation hardness sufficient to endure the enormously high radiation around the IP. On the other hand, the performance (e.g. noise level, gain) is relatively sensitive to temperature, therefore they are kept in low temperature ($-5 \sim 0^\circ\text{C}$) during the operation.

The pixel detector is the unit of layers of pixelated silicon sensors located closest to the IP of all the detector component. Oxygen enriched n -in- n silicon semiconductor is used for the sensors. Four cylindrical layers are placed in the barrel at the radial distance of $31 \text{ mm} \sim 122.5 \text{ mm}$ with respect to the IP, and 3 disk layers cover each side of the end-cap, providing an acceptance of $|\eta| < 2.5$. The innermost layer in the barrel provides the highest precision referred as the “insertable b-layer” (IBL) installed during the long shutdown between Run1 and Run2. The pixels are in the $50 \times 250 \mu\text{m}$ granularity in the IBL, and $50 \times 400 \mu\text{m}$ in the other layers. The resolution is purely determined by the pixel size. A spatial resolution of $4 \mu\text{m}$ and $115 \mu\text{m}$ is achieved along the radial and beam z -direction respectively, by combining the hit information from the four layers.

The SCT is located outside of the pixel detector. The sensors are made by single-sided p -on- n silicon semiconductors. The strips of barrel SCT aligning along the z -axis with $80 \mu\text{m}$ pitch, giving a precision position in the $r - \phi$ plane. A slight angle stereo (40 mrad) alternated by layers is applied to the arrangement, providing decent z -position determination in addition. The barrel region is surrounded by four layers, while nine discs are placed in each end-cap. The intrinsic resolution is $17 \mu\text{m}$ ($580 \mu\text{m}$) in $r - \phi(z)$ direction respectively. The strips in the end-cap SCT are aligned in a mesh in terms of $x - y$, capable of 3D position determination together with the z -coordinate of the disks.

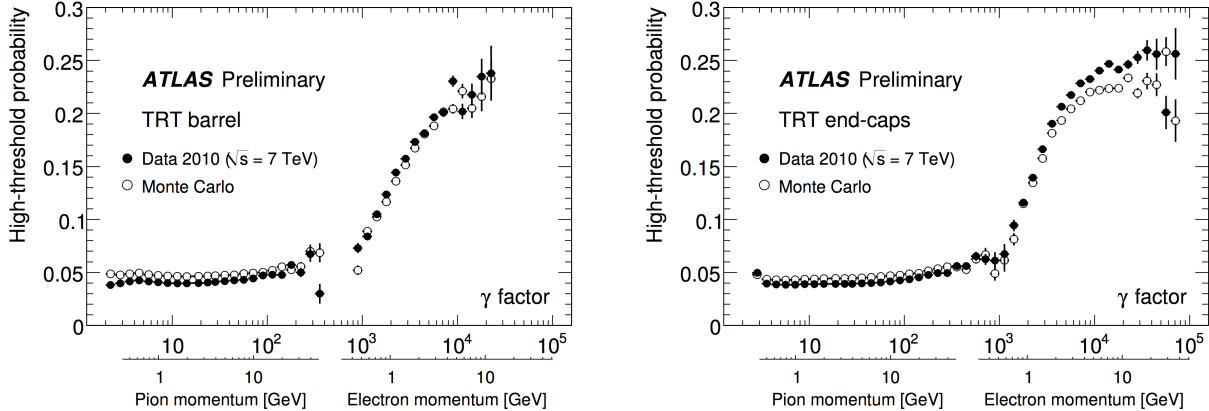


Figure 3.7: TRT high threshold rate as function of Lorentz factor ($\gamma = E/m$) of incident particles [60]. The γ scale of typical pions and electrons are labeled aside. The left (right) plot corresponds to the rate in barrel (end-caps) respectively.

Trasition radiation tracker (TRT) TRT is a gaseous detector designed for tracking particles as well as identifying the species using the characteristic transition radiation. The detector is filled with 4mm-diameter straw tubes in which xenon-based active gas is confined. Ionized secondary electrons are collected by the 30 μm -diameter gold-plated tungsten-Rhenium anode wire in the center of each straws. 73 layers of aligned straw tubes are arranged in the barrel, and 160 layers in the end-cap sectors. The tube length is 144 cm (37 cm) in the barrel (end-cap) region. The barrel tubes are arranged in parallel along the beam pipe, with 7 mm of interval between layers. The intrinsic position resolution per straw is about 130 μm . A traverse of charged particle fires 36 straws on average.

Transition material is inserted between the straws. 19 μm -diameter polypropylene fibers are used in barrel, and 15 μm -thick polypropylene radiator foils isolated by a polypropylene net are set for the end-caps. Transition radiation can address unique sensitivity in particle identification, particularly to e/π separation, since the intensity is sensitive to incident particle's velocity (proportional to $\gamma = E/m$) rather than the energy or momentum. Given that the signal of transition radiation typically yield more amplitude than the nominal gas ionization, two different thresholds are set in the TRT ; the lower threshold to collect the signal of ionization caused by a particle traverse; the high threshold defining the signal of transition radiation. The high threshold is carefully designed so that only electrons in the typical range of energy (0.5 GeV – 150 GeV) can fire while pions are inert to it.

Figure 3.7 shows the γ -dependence of high threshold rate, demonstrating a good separation of particles in the electron-like momentum and pion-like momentum.

Combined Tracking Performance The combined tracking performance has been validated via the measurement of cosmic muons [59]. The resolution for a single muon track is obtained as

function of muon transverse momentum:

$$\frac{\sigma_{p_T}}{p_T} = 1.6\% \oplus \frac{0.053\%}{\text{GeV}} \times p_T. \quad (3.3)$$

3.2.4 Calorimetry

The ATLAS calorimetry located outside the ID is composed of the electromagnetic calorimeter (EM calorimeter), the hadronic calorimeter (HC), and the forward calorimeter. The whole view is given by Figure 3.8. The calorimeters employ two detector technologies:

- Liquid-Argon sampling calorimeter (LAr) with alternately sandwiching the lead absorber layers and the sensor layer filled with liquid-argon.
- “Tile calorimeter” consisting of the sensor layers with scintillator tiles and steel absorber.

The detector technology and the spatial segmentation in each pseudo-rapidity coverage are summarized in Table 3.9. Thanks to the fast response of the readout, calorimeter can provide the function of trigger, based on the fast processing of particle identification and the energy measurement using the information of individual showers, as detailed in Sec. 3.2.7.

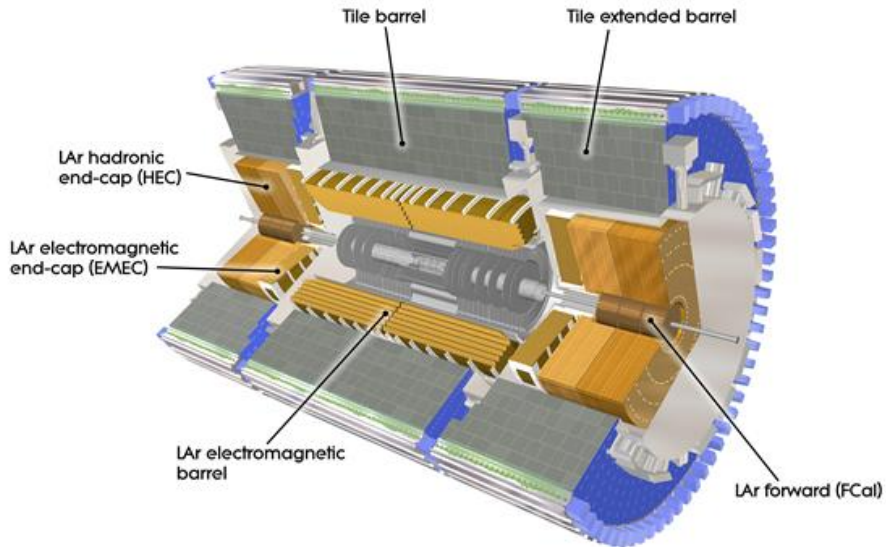


Figure 3.8: Cut-away view of the ATLAS calorimetry [51].

EM CALORIMETER	Barrel	End-cap			
Coverage	$ \eta < 1.475$	$1.375 < \eta < 3.2$			
Longitudinal segmentation	3 samplings	3 samplings	$1.5 < \eta < 2.5$		
		2 samplings	$1.375 < \eta < 1.5$		
			$2.5 < \eta < 3.2$		
Granularity ($\Delta\eta \times \Delta\phi$)					
Sampling 1	0.003×0.1	0.025×0.1	$1.375 < \eta < 1.5$		
		0.003×0.1	$1.5 < \eta < 1.8$		
		0.004×0.1	$1.8 < \eta < 2.0$		
		0.006×0.1	$2.0 < \eta < 2.5$		
		0.1×0.1	$2.5 < \eta < 3.2$		
Sampling 2	0.025×0.025	0.025×0.025	$1.375 < \eta < 2.5$		
		0.1×0.1	$2.5 < \eta < 3.2$		
Sampling 3	0.05×0.025	0.05×0.025	$1.5 < \eta < 2.5$		
PRESAMPLER	Barrel	End-cap			
Coverage	$ \eta < 1.52$	$1.5 < \eta < 1.8$			
Longitudinal segmentation	1 sampling	1 sampling			
Granularity ($\Delta\eta \times \Delta\phi$)	0.025×0.1	0.025×0.1			
HADRONIC TILE	Barrel	Extended barrel			
Coverage	$ \eta < 1.0$	$0.8 < \eta < 1.7$			
Longitudinal segmentation	3 samplings	3 samplings			
Granularity ($\Delta\eta \times \Delta\phi$)					
Samplings 1 and 2	0.1×0.1	0.1×0.1			
Sampling 3	0.2×0.1	0.2×0.1			
HADRONIC LAr	End-cap				
Coverage	$1.5 < \eta < 3.2$				
Longitudinal segmentation	4 samplings				
Granularity ($\Delta\eta \times \Delta\phi$)	0.1×0.1	$1.5 < \eta < 2.5$			
	0.2×0.2	$2.5 < \eta < 3.2$			
FORWARD CALORIMETER	Forward				
Coverage	$3.1 < \eta < 4.9$				
Longitudinal segmentation	3 samplings				
Granularity ($\Delta\eta \times \Delta\phi$)	$\sim 0.2 \times 0.2$				

Figure 3.9: Summary of partition and geometry of the ATLAS calorimetery [58].

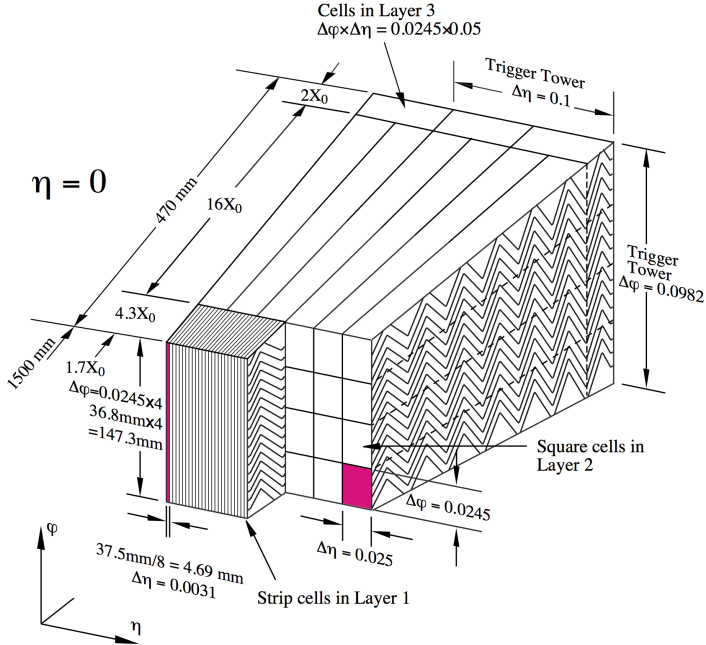


Figure 3.10: Geometry of barrel LAr sampling layers. Position resolution is addressed by the innermost sampling layer by the highest $\eta \times \phi$ granularity of 0.0031×0.098 , and the energy measurement is mainly provided by the second layer with the largest volume. The third layer standing behind in the plot is the tail catcher providing information of the shower profile. [58].

Electromagnetic calorimeter The basic unit of LAr calorimeter consists of a gap filled with liquid argon (gap width: 1.1-2.2mm) generating the ionized electrons, a copper-kapton electrodes to collect the ionized charge, and a steel-clad lead absorber layer to develop the EM shower (layer width: 1.13-1.53mm). A bias voltage of 2000V between the electrodes and the absorbers is applied, achieving the drift time of 450ns. The readout signal is amplified by a pre-amplifier, and shaped into a 13 ns width signal pulse by a bi-polar shaper managing the 25 ns width bunch crossings. The detector is maintained at a constant temperature of 88K by cryostats surrounding the barrel EM calorimeter.

The geometry and cell segmentation varies between barrel and end-cap depending on the desired function. Figure 3.10 illustrates the segmentation in the barrel ECM. 3 sampling blocks are placed along shower with different $\eta \times \phi$ segmentation. The first sampling layer has the finest $\eta \times \phi$ granularity (0.0031×0.098) identifying the precise angular position of the incident particle. The second sampling addresses the largest volume ($16X_0$) containing the most of shower in which the energy is mainly measured. The third sampling layer is intended to measure the tail of EM showers, providing information about the longitudinal profile together with the other layers. The layer units are arranged in an accordion geometry, which is the characteristic to the barrel ECM, designed to be fully hermetic in terms of angular acceptance. In order to compensate the upstream energy loss, a presampling layer is additionally placed in front of the first layer of the EM calorimeter for both barrel and the end-caps. The total thickness amounts to $> 22X_0$ in the barrel and $> 24X_0$

in the end-cap, which can fully accommodate the EM showers of photons or electrons in an energy of upto a few TeV. The transition region between the barrel and end-caps ($1.37 < |\eta| < 1.52$) is dedicated to detector services and therefore not fully instrumented.

The designed resolution is given in Eq. 3.6 [61]:

$$\frac{\sigma_E}{E} = \frac{10\%}{\sqrt{E}} \oplus \frac{17\%}{E} \oplus 0.7\%. \quad (3.4)$$

The energy resolution for the off-line objects can be further improved through the dedicated calibration exploiting the full detail of the shower and information from the other detector.

Hadronic Calorimeter The ATLAS hadronic calorimeter consists of the barrel Tile HC ($|\eta| < 1.7$) and end-cap LAr HC. Barrel Tile HC is segmented into three sections, the central barrel section ($|\eta| < 1.0$) and the two extended barrel sections ($1.0 < |\eta| < 1.7$), using different channel dimensions. There are three sampling layers along the shower development with the thickness of 1.5λ , 4.1λ and 1.8λ for barrel, and 1.5λ , 2.6λ and 3.3λ for extended barrel respectively. Figure 3.11 (a) schematizes one module in the Tile HC. Generated scintillation photons are read out by the photo-multiplier tubes equipped at the ends of the module via wavelength shifting fibers. The end-cap HC is the sampling calorimeter with liquid-argon sensor layers and copper absorber. The choice of material is dominantly based on the durability against the extremely high radiation flux in the forward region.

The intrinsic resolution of barrel Tile HC and end-cap LAr HC for an individual hadron jet is given by Eq. 3.6 [62]:

$$\frac{\sigma_E}{E} = \frac{50\%}{\sqrt{E}} \oplus 3\%, \quad (\text{Tile HC}) \quad (3.5)$$

$$\frac{\sigma_E}{E} = \frac{100\%}{\sqrt{E}} \oplus 10\%, \quad (\text{End-Cap LAr HC}) \quad (3.6)$$

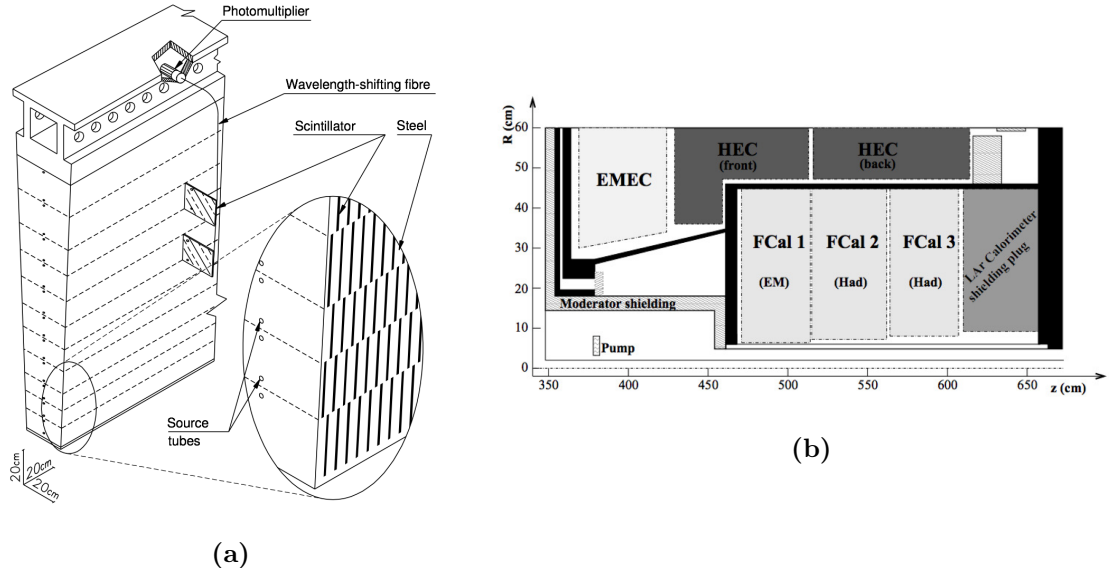


Figure 3.11: (a) Illustration of a Tile HC module. (b) Alignment of each detectors in an end-cap; end-cap LAr EM calorimeter (EMEC); end-cap LAr Hadronic calorimeter (HEC); and the Forward calorimeter (FCal)) [51].

Forward Calorimeter A set of LAr calorimeter layers are arranged in a very forward region close to the beam axis covering $3.1 < |\eta| < 4.9$, designed to capture the full content of jets or particles from hard scattering particles from extremely boosted center-of-mass. The location with respect to the adjacent calorimeter systems are illustrated as Figure 3.11 (b). Forward calorimeter is made by three sampling layers in which both functions of EM calorimeter and hadronic calorimeter are integrated; The first layer is with copper absorber working as EM calorimeter, and the later two layers are with tungsten functioning as EM calorimeter. The overlap region with respect to the end-cap HC is deliberated to realize smooth transition.

3.2.5 Muon Spectrometer

Muon spectrometers are located outermost in the ATLAS, consisting of four sub-detectors; Monitored Drift Tube (MDT); Cathode Strip Chamber (CSC); Resistive Plate Chamber (RPC); and the Thin-Gap Chamber (TGC). The former two are dedicated to precision measurement of muon tracks and the latter two are to triggering. The spectrometer covers the pseudo-rapidity range $|\eta| < 2.7$ and allows identification of muons with momenta above 3 GeV and precise determination of p_T up to about 1 TeV with 10% momentum resolution.

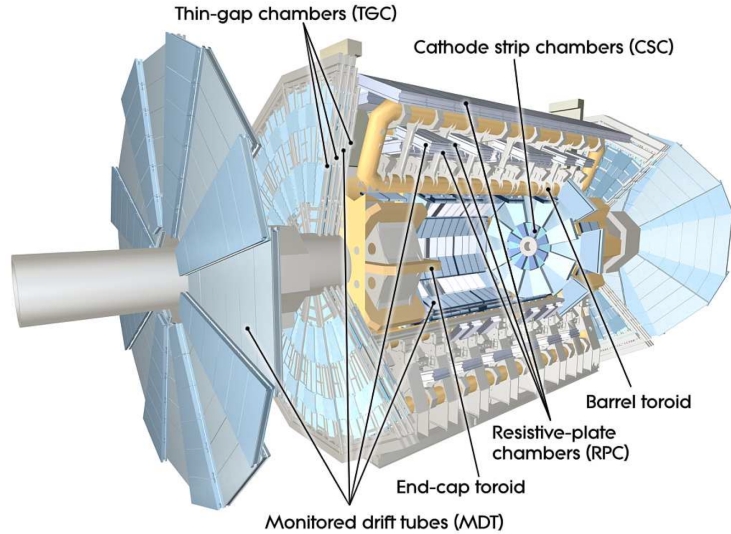


Figure 3.12: Global view of the ATLAS muon spectrometers [51].

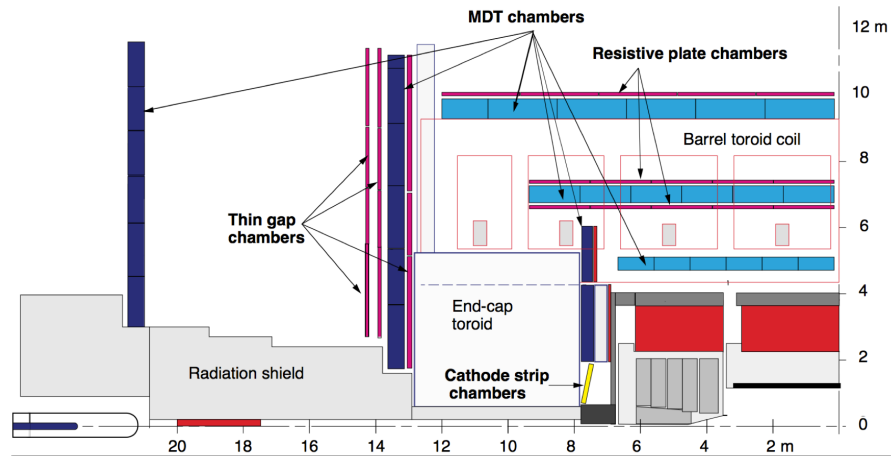


Figure 3.13: Cross-section of the ATLAS Muon spectrometer [59].

The magnetic field for tracking is sourced by the three pieces of toroidal superconducting magnets i.e. two end-cap toroids and a barrel toroid embedded in the space inside the muon spectrometers. $3.9T$ and $4.1T$ B-field is provided in the barrel and end-cap region respectively. The internal volume of toroidal coils are vacant (“air-core”), in order to reduce the material with which muons experience the multiple scattering. The integrated B-filed profile at the position of MDT is shown in Figure 3.15, while the global schematic of the magnet system is given in Figure 3.14.

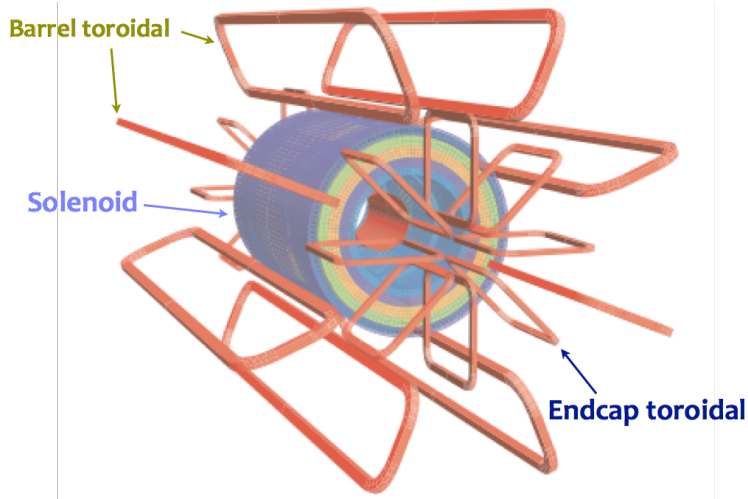


Figure 3.14: Schematic of the ATLAS magnet system with one central solenoid and 3 toroidals (barrel+2 end-caps) [51].

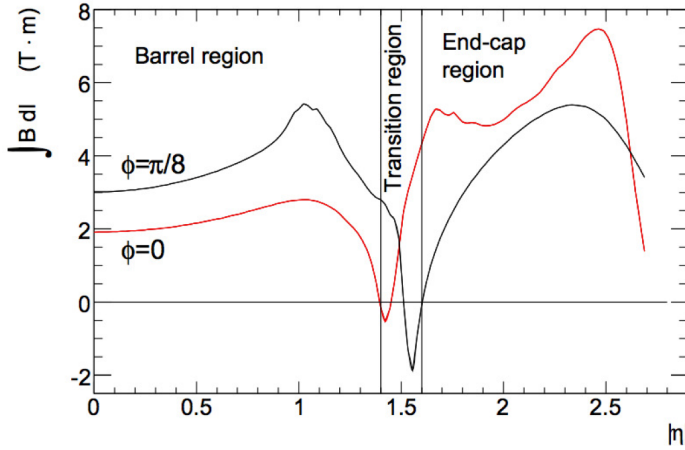


Figure 3.15: Simulated magnetic field integral provided by a single troid octant, from the innermost MDT layer to the outermost. [51].

Monitor Drift Tubes (MDT) MDT is a gaseous drift chamber filled with the basic detection elements of 30 mm-diameter aluminum tubes that are covered by a 400 μm -thick wall. Drifting electrons are absorbed by a 50 μm -diameter tungsten-Rhenium wire in the center of a tube with a bias voltage of 3080 V is applied, and read out by a low-impedance current sensitive preamplifier. The gas mixture is with Ar (93%) and CO₂ (7%), maintaining the maximum drift time of 700 ns. The position resolution by a single wire is about 80 μm . There are three layers of MDT chambers located both in barrel and end-cap, covering a pseudo-rapidity range of $|\eta| < 2.0$. The limitation in the η -coverage is determined by its maximum durable rate ($150\text{cm}^{-1}\text{s}^{-1}$). CSC takes over the role in such forward region.

Cathode Strip Chamber (CSC) The CSCs are multi-wire proportional chambers covering the forward region ($|\eta| > 2.0$) in the end-caps, providing 2D position of incident particles. It is operated with a gas mixture of Ar (80%) and CO₂ (20%) and with a bias voltage of 1900 V applied. The cells are symmetric in terms of the pitch of readout cathodes and the anode-cathode spacing, which is equally set to 2.54 mm. Since the spatial resolution of the CSCs is sensitive to the inclination of tracks and the Lorentz angle, the chamber is fixed at tilted posture so that tracks originating from the IP become approximately orthogonal to the chamber surface.

Resistiv Plate Chamber (RPC) The RPCs are digital gaseous detectors specialized in fast timing response for triggering. They are mechanically mounted on the surface in the barrel MDT, covering the pseudo-rapidity range of $|\eta| > 1.05$. The elementary detection unit is a gas gap filled with non-flammable gas mixture (94.7% C₂H₂F₄, 5% Iso-C₄H₁₀, 0.3% SF₆). An uniform high electric field ($\sim 4900 \text{ V/mm}$) is applied so that the ionized electrons amplitude by themselves via the avalanches. Signals are read out by a metal strip attached on both ends of the gaps, arranged with a pitch of 30 mm \sim 39.5 mm. The typical spatial and timing resolution achieved by a RPC chamber are 1 cm and 2 ns respectively.

Thin-Gap Chamber (TGC) The TGCs are a special type of multi-wire proportional chambers characterized by the notably small distance between the anode wires and the read out cathode strips (1.4mm). A quick drain of secondary electrons is achieved by the quenching gas mixture of CO₂ (55%) and n-pentan (45%), yielding the timing response of 5 ns. TGCs also contribute to the momentum determination by supplementing the measurement in ϕ by MDT. Three modules are placed per end-cap, covering $1.05 < |\eta| < 2.7$ by the innermost one and $1.05 < |\eta| < 2.4$ by the two behind. Trigger is generated using tracks in $1.05 < |\eta| < 2.4$, while all tracks are subjected to the momentum measurement.

3.2.6 Luminosity Detectors

Luminosity determination is particularly important since it provides the reference of normalizing simulated dataset which enables the comparison to data. The instantaneous luminosity is calculated by the formula below:

$$\mathcal{L} = \frac{\mu n_b f_b}{\sigma}, \quad (3.7)$$

where n_b is the number of colliding bunches and f_b the frequency of the beam circulation. σ is total fiducial cross-section of pp -interaction including both elastic and inelastic scattering, and μ is the average number of such interaction per bunch crossing. While σ is provided by a dedicated calibration (van der Meer scan [63]) measuring the lateral beam profile using overlapping two beams, μ is obtained directly by exploiting the rate information from luminosity detectors located in the very forward region nearby the beam pipe. Dedicated calibration and luminosity determination algorithm studied in [64]. Two luminosity detectors mainly contribute to the luminosity measurement:

LUCID (LUminosity measurements using Cherenkov Integrating Detector)

LUCIDs are located at the both ends of the ATLAS detector at a distance of 17m from the IP, covering the pseudo-rapidity range of $5.6 < |\eta| < 6.0$. The LUCID detector consists of 16 aluminum tubes filled with C_4F_{10} gas filled inside, designed to count the Cherenkov photons kicked out by charged particles flying along the beam axis which are mainly generated by proton-proton inelastic scattering in the IP.

ALFA (Absolute Luminosity For ATLAS)

ALFA is located beyond the ATLAS envelope at $z = \pm 240$ m, sandwiching the beam pipe from top and bottom. The detectors are composed of 8 scintillating fibers, designed to measure the elastic scattering component of the pp -interaction.

3.2.7 Trigger and Data Acquisition System

While ATLAS enjoys incredibly high collision rate of about 100 MHz (40 MHz beam bunch crossing together with pile-up), these data cannot entirely read out due to the limitation from data transmission as well as the computation resource. Luckily or unluckily, most of them are junk QCD reactions resulting in cheap low p_T jets, the rate can be drastically suppressed by requiring hard jets, leptons or E_T^{miss} in the events.

The ATLAS Trigger and Data Acquisition System (TDAQ) [65] is the data acquisition system handling the trigger and readout. The schematic of the readout streams are shown in Figure 3.16. It consists of a two-staged trigger pipeline served by the hardware-based Level-1 Trigger (L1) and the software-based High-Level Trigger (HLT). The idea is to reject the major trivial QCD events in L1, based on a fast particle reconstruction with coarse resolution, and perform further filtering in HLT using more sophisticated reconstruction and energy measurement benefited by the timing latency that L1 earns. The benchmark of rate suppression is 100 kHz at the end of L1 and down to 1 kHz after the HLT on average.

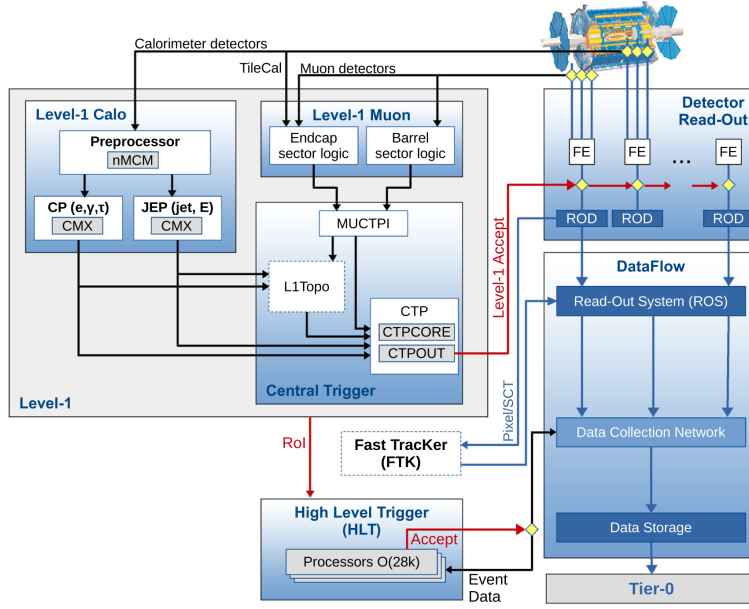


Figure 3.16: The logic of ATLAS trigger system [65]. Trigger detectors have separated readout line for trigger, sending input information for trigger decision to CTP. The CTP reconstructs L1 objects and issue a global accept signal relieving the buffered data, once the trigger criteria are satisfied. The (η, ϕ) position of identified trigger object is sent to downstream HLT, in which offline-like software-based triggers run to filter events further. L1 topological trigger (L1 Topo) and Fast Tracker (FTK) have been in commissioning since 2015.

The L1 consists of two independent sub-trigger systems; L1Calo identifying the EM or hadronic clusters in calorimeter and reconstruct primitive jets, electrons, photons and taus (L1 objects) with calibrated energy in EM scale; L1Muon identifying and measuring the tracks in the muon spectrometer designed to accept events with muons. The object reconstruction is based on the coarsely segmented blocks of combined detector channel called “trigger tower” with $\eta \times \phi$ granularity of 0.1×0.1 . E_T^{miss} is also calculated at the L1 stage by the vectoral sum of the calorimeter deposits, referred as L1XE. Trigger accept is issued by the Central Trigger Processors (CTP) when the L1 objects meet certain criteria in terms of p_T threshold and number of objects.

In the HLT, offline-like algorithms are employed to refine the energy of L1 objects, or recover the mis-identified objects (low- p_T muons most typically) by scanning over whole detector. This is performed by a set of custom farmwares with a processing time of 0.2s on an average. The event triggered by the HLT is subsequently sent to event storage infrastructures outside the ATLAS. Figure 3.17 illustrates the rate of HLT acceptance in 2016 operation. The performance of triggers relevant to the analysis is dedicatedly overviewed in Sec. 6.1.

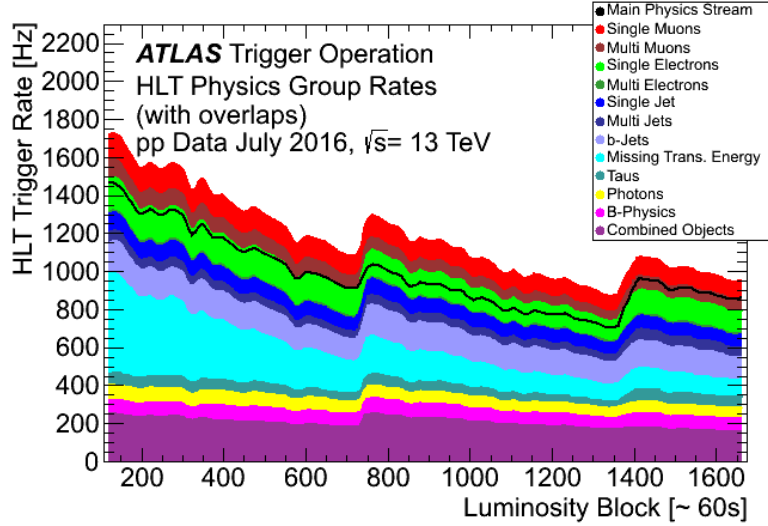


Figure 3.17: Rate of HLT streams for physics analyses during the 2016 data-taking [66]. Horizontal axis is in unit of lumi-clock, the smallest unit of data-taking in the same configuration.

3.3 Recorded Data by ATLAS

The pp -collision data analyzed in this study has been collected by ATLAS during 2015 and 2016. Quality requirements are applied for the recorded data base on each lumi-block which is the smallest unit of data-taking defined as a period in the same run configuration and conditions of beam and detector. Rejected data is typically at the periods with more than a certain fraction of modules in the sub-detectors being disabled or in a wrong operation configuration (e.g. voltage or temperature etc.). After the quality requirement, the total integrated luminosity available for the analysis is 36.1 fb^{-1} with the measurement error of 3.2%.

Chapter 4

Object Reconstruction and Identification

The raw detector-level information is translated into physics quantities through the sequence of particle reconstruction, identification and calibration. Though this is partially done at the trigger level, the recorded events are further elaborated by the sophisticated off-line algorithms. These off-line reconstructed particles refer to “object”. In this analysis, electrons, muons, jets and missing transverse energy (MET) are defined, and Figure 4.1 schematizes the workflow of the formation of these analysis-level objects from the detector information via low-level objects such as tracks and vertices. This section will overview the procedures regarding to the object definition (reconstruction, identification, calibration etc.) for each involved object.

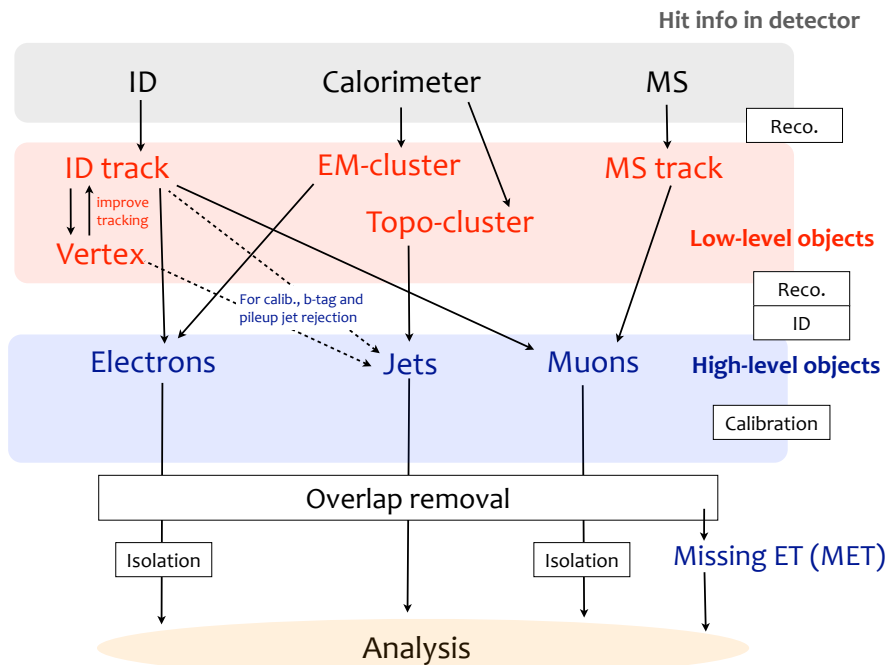


Figure 4.1: Schematic flow of the formation of analysis-level objects from the detector-level infomation. Black squares symbolize the procedures that dedicated off-line algorithms are working on.

4.1 Tracks

Charged tracks are the fundamental units seeding various off-line particle reconstruction and calibration. Standard tracks used in ATLAS refers to ID tracks, reconstructed by the hits created in the inner detector (ID). The MS tracks for muon identification are separately reconstructed, which is described in Sec. 4.5.1. The reconstruction algorithm mainly consists of following four steps (the detail can be found in [67]):

- Based on the 3-dimensional position information and the readout charge associated to each hit in the silicon detectors, spatial charge profile is constructed. Hits from the same particle traverse are identified and merged, using a combination of a pattern recognition technique called connected component analysis (CCA) [68] and a neural network classifier [69]. Seed tracks are then reconstructed from three aligned clusters.
- The seed tracks are extrapolated outward, and the association with the TRT hits are tested using the Kalman Filter [70] characterized by five tracking parameters, with a pion track hypothesis assuming the MIP energy loss in the ID material.
- If the first pattern recognition fit fails, a second fit is attempted based on the electron hypothesis where the energy loss at each hit surface is allowed, recovering the electrons with significant bremsstrahlung.
- Successful tracks from the Kalman Filter are rerun using the ATLAS Global χ^2 -Track Fitter [71]. A pion or an electron hypothesis is used, depending on which was used successfully in the previous step.

A further refined algorithm (Tracking In Dense Environment; TIDE) is used from Run2 [67], to cope with the denser particle environment due to the increased pile-up and collision energy. The performance is shown red lines in Figure 4.2 where the efficiency is shown as function of the proximity to the closest jet. Typically over 95% of efficiency is maintained.

4.2 Primary Vertices

The positions of pp -collisions are identified using the reconstructed ID tracks. These vertices refers to “primary vertices” (PV)¹ and are important for providing reference point of re-tracking and objects calibrations. PVs are reconstructed using the Iterative Vertex Finding algorithm [72][73], identifying the peak in the z -distribution of extrapolated tracks. The position of identified PVs are further elaborated using the adaptive vertex fitting algorithm [74]. The ID tracks are then re-fit taking advantage of these reconstructed PVs. The re-tracking procedure in principle lasts until all the tracks are associated to either of the PVs. PVs with less than two associated tracks are discard. Though 10 ~ 30 PVs are reconstructed per bunch crossing, usually there is only one PV causing meaningful scattering, for instance firing the trigger. This PV is referred by the “hard-scatter” vertex identified as the PV with the highest sum of associated track p_T , and the position is used

¹The “primary” is meant to distinguish against the vertices generated by late decaying particles known as “secondary-vertices”.

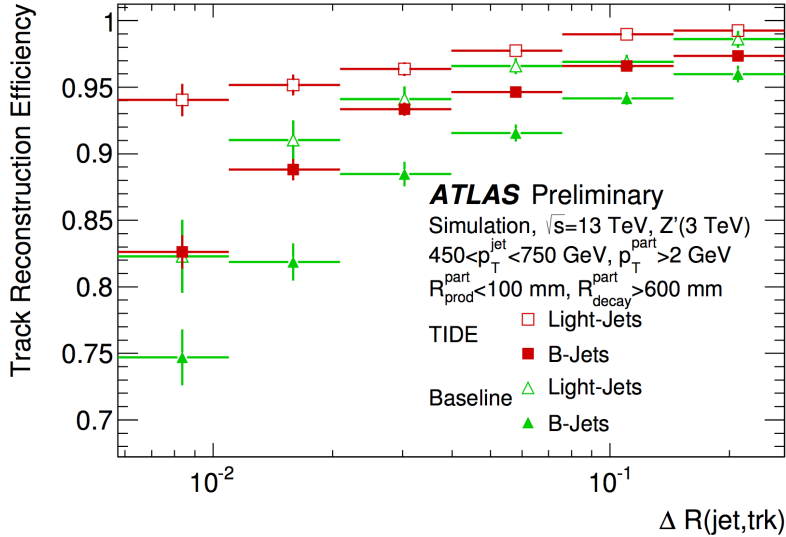


Figure 4.2: Reconstruction efficiency of tracks in jets as function of angular distance with respect to barycenter of the jet [67]. Red points corresponds to the tracking algorithm used from Run2.

as the origin for object calibration.

4.3 Topo-clusters

Topo-cluster (or TC) is the basic unit of energy measurement in calorimeter and used as the input for jet clustering (Sec. 4.6.1) as well as in computing the isolation variables (Sec. 4.8). It is formed by three-dimensionally grouping the cells with significant energy deposit. The clustering algorithm proceeds as follow [75]:

- Find cells with energy deposit exceeding 4σ from the expected noise level. These cells are identified as seed cells.
- Neighboring cells touching the boundary of seed cells with energy deposit exceeding 2σ from the expected noise level are added to the cluster and become the seed cells for the next iteration.
- Iterate the previous step until the cluster stops growing.
- Split the cluster if there are two or more local maxima with $E_{\text{cell}} > 500 \text{ MeV}$ inside the TC.

EM-scaled energy is assigned for TCs.

4.4 Electrons

4.4.1 Reconstruction

The electron reconstruction algorithm proceeds as following (widely referred from [76]):

- **Reconstruction of a EM cluster from energy deposit in the EM calorimeter.**

This is done by the sliding window algorithm. Cells in the all four layers in the EM calorimeter are grouped into $\eta \times \phi$ towers of 0.025×0.025 , and a window defined by the 3×5 units of towers are slided over the detector. A local maximum in the window energy above 2.5 GeV is identified an EM the cluster. About 95% (99%) of clustering efficiency are maintained with electrons in $E_T = 7$ GeV (> 15 GeV).

- **Track-Cluster matching and refitting.**

The EM cluster is matched with a ID track reconstructed based on the electron hypothesis (see Sec. 4.1) in the angular distance $\Delta R = \sqrt{(\Delta\eta)^2 + (\Delta\phi)^2}$. Closest track in ΔR with respect to the EW cluster is chosen if multiple tracks satisfy the matching criteria. The matched track enjoys further correction by a re-tracking using the Gaussian Sum Fitter (GSF) [77] algorithm in which Bremsstrahlung is dedicated modeled.

- **Energy determination.**

The information from track momentum and calibrated EM cluster energy are combined using a multivariate algorithm [78].

The reconstruction efficiency is measured by $Z \rightarrow ee$ events. Figure 4.3 presents the result together with the prediction by MC. Over 96% – 98% of efficiency is achieved for $E_T > 20$ GeV.

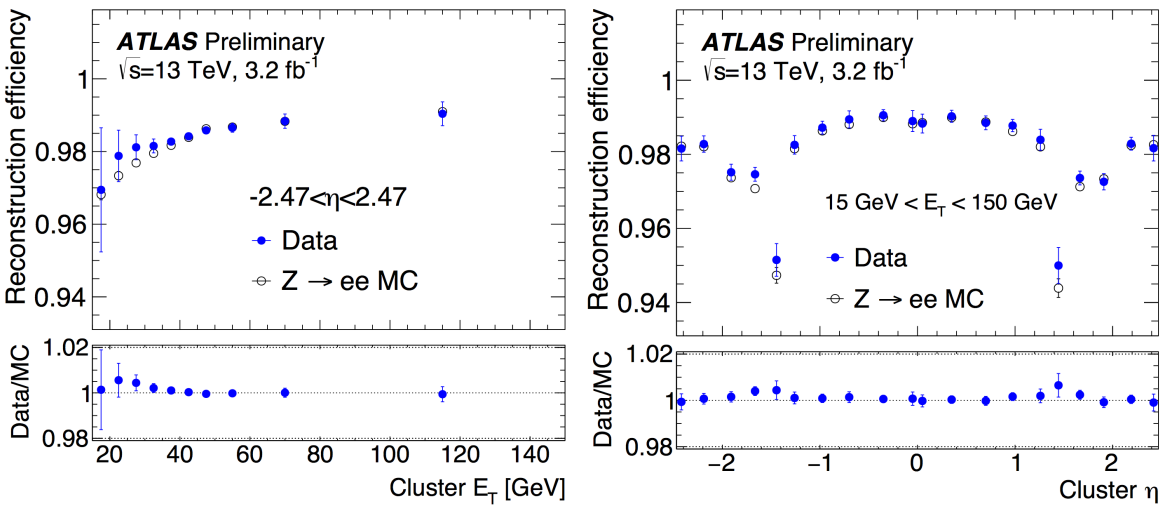


Figure 4.3: Reconstruction efficiency simulated (grey) or measured (blue) using $Z \rightarrow ee$ events [76] as function of (a) E_T , and (b) pseudo-rapidity of reconstructed EM clusters.

4.4.2 Identification

Reconstructed electron candidates are dominated by backgrounds from pions in the jets, particularly when they are low- E_T . Therefore, a powerful identification algorithm is employed, using a multi-dimensional likelihood exploiting all the relevant detector information. 17 variables in total are input into the likelihood, including the longitudinal or transverse EM shower profile and the number of high-threshold hits in TRT and so on. The full list of input variables is found in [76]. The discriminant is given by a form of likelihood ratio, which is known to generally provide the best separation between the hypotheses [79]. The signal and background PDF is modeled using the simulated events of $Z \rightarrow ee$ and di-jet respectively. Figure 4.4 shows the efficiency of the electron identification. Multiple working points are available with different cut value in the likelihood ratio. In the analysis, two working points; **Loose** and **Tight** are used, corresponding about 90% and 70% of efficiency at $E_T = 30$ GeV.

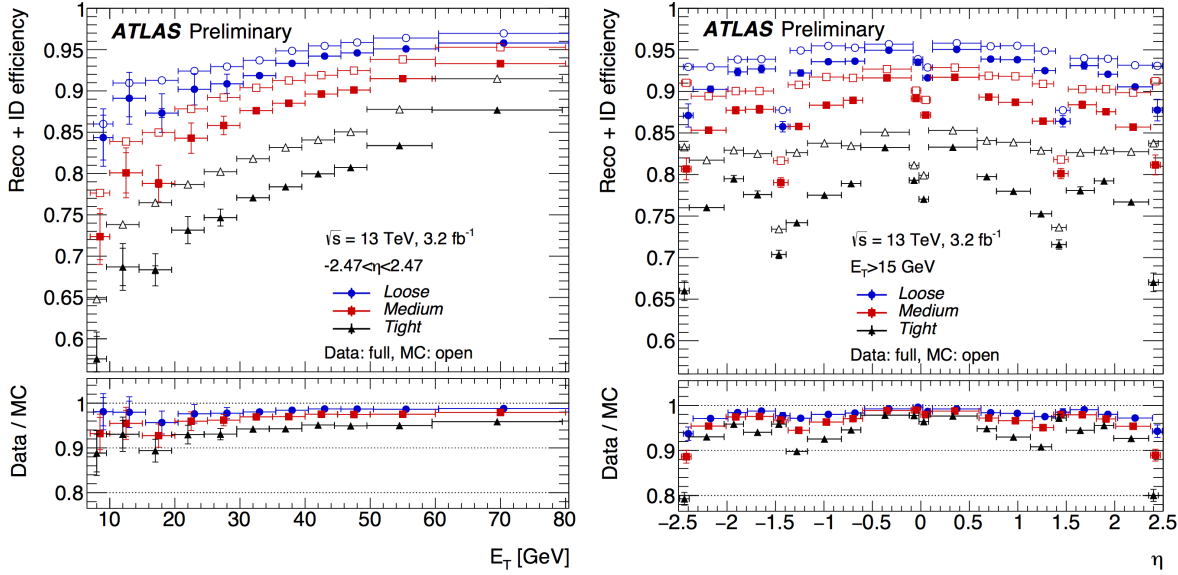


Figure 4.4: Electron identification efficiency as function of (a) E_T , or (b) pseudo-rapidity of reconstructed electron candidates [76]. $Z \rightarrow ee$ events are used for both MC and data.

4.4.3 Calibration

The electron calibration consists of several different procedures. Different treatments are applied between simulation and data. The workflow is illustrated in Figure 4.5.

A MC-based calibration using BDT

Though the energy of cell deposit in EM calorimeter and electron cluster is already calibrated in EM scale, it still suffers from the residuals due to the energy loss in the material upstream of the calorimeter, energy leakage out of the envelope of the cluster or the EM calorimeter, and so on. A multi-variate algorithm (BDT regression) is employed to account for these numerous effects and correct them. This is done by constructing a mapping function to the true energy from the raw energy as well as other information such as the angular position,

shower profile, and the hit information from the other auxiliary detectors such as hadronic calorimeter. The full detail can be found in [78] [80].

Longitudinal calorimeter layer inter-calibration

The scales along longitudinal layers is equalized in data with respect to simulation, prior to the determination of the overall energy scale, in order to ensure the correct extrapolation of the response in the full p_T range. This is only applied in data.

Non-uniformity correction in ϕ

A set of corrections are applied to data, to account for the ϕ -inuniformity due to various on-line instrumental effects that are not included in simulation, such as non-optimal high voltage setting, geometrical effects (e.g. inter-module widening) or biases in the LAr calorimeter electronics calibration.

Residual scale calibration on data / Resolution correction on simulated electrons.

The residual mis-calibration in data is corrected by shifting the energy scale so that it agrees with the expectation from simulation. This is done by comparing the mass of Z-peak in $Z \rightarrow ee$ events.

It is found that the resolution in data is slightly worse than that in simulation using the same event sample. The corrections are derived and applied to simulation to match the data.

Numerous minor corrections follow additionally, which is detailed in [78]. The calibration is widely validated using the data events of $J/\psi \rightarrow ee$ and $Z \rightarrow ee$.

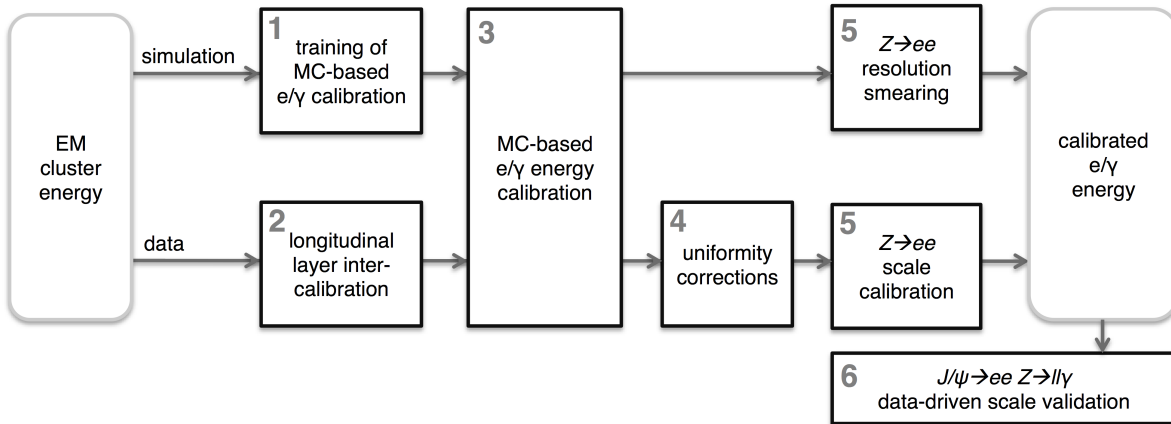


Figure 4.5: Flow chart of electron calibration applied for MC and data [78].

4.5 Muons

4.5.1 Reconstruction

Muon tracks are reconstructed independently from ID, referred as MS-tracks. The tracking begins with finding the hits inside each MDT/CSC chamber and forming small track segments per chamber. A Hough transform is employed to convert the bending detector plane geometry into flat plane. A straight-line fit are then performed on the flattened plane for the track segments. The hits in RPC and TGC are used to determine the coordinate orthogonal to the MDT/CSC detector plane. The search algorithm employ a loosened requirement on the compatibility of the track and the hits, to account for the muon energy loss by interaction with material.

The trajectory and momentum of muons are decided by a synergy between the reconstructed MS track and the measurement by the other detectors. There are four different schemes of the combination [81]:

Combined muons: A MS track is matched to a reconstructed track in the ID, and the measurements of the momenta are statistically combined.

Segment-tagged muons: A fragmet of MS track is matched with an ID track, with the momentum taken from the ID track.

Standalone muons: MS tracks found outside the ID acceptance ($2.5 < |\eta| < 2.7$), with the momentum quoted from the MS track.

Calorimeter-tagged muons: A special type of reconstruction dedicated to muons traveling to the inactive ‘crack of the MDT at $|\eta| < 0.1$. The ID tracks with $p_T > 15$ GeV associated calorimeter deposit consistent with a minimum ionizing particle are tagged, with the momentum of ID track.

In this analysis, the combined muons is always in defining muons, while the segment-tagged muons are used for correcting the MET calculation as described in Sec. 4.9.

4.5.2 Identification

Additional identification requirements are imposed to purify the sample of reconstructed muons. Cuts on variables listed in Table 4.1 are applied. The **Medium** working point defined in [82] is used

Table 4.1: Variables used for the muon identification selection.

Variable	Description
$\sigma(q/p)$	Fitting error of a tracking parameter q/p associated with the quality of measurement.
ρ'	p_T difference between ID and MS track normalized by the p_T of the combined track.
χ^2	A generic measure of fit quality defined as normalized χ^2 of the combined track fit.

throughout the analysis, where only $\sigma(q/p) < 7$ is required. Figure 4.6 summarizes the performance

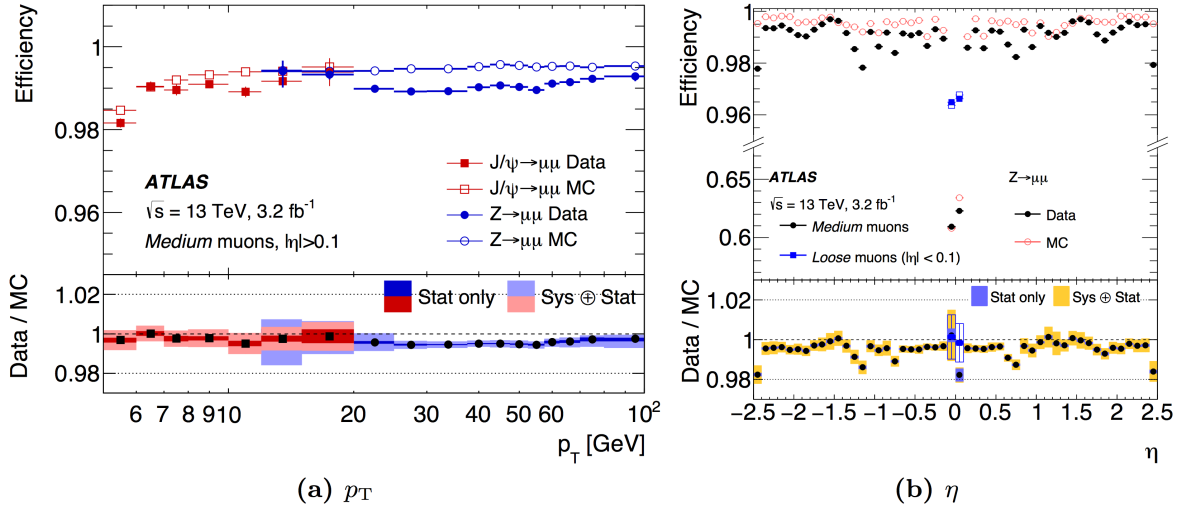


Figure 4.6: Simulated / measured efficiency for reconstruction and identification of muons, using $J/\psi\mu\mu$ and $Z \rightarrow \mu\mu$ events [82].

of reconstruction and ID for muons.

4.5.3 Calibration

As the momentum of a muon track is already well-representing the particle-level momentum of the muon, the scale calibration only subjects to a series of minor corrections, accounting for the imperfect knowledge on the magnetic field integral inside the detector, the material profile between the interaction point and the MS and so on.

The momentum correction is performed on each muon in MC based on the formula below [81]:

$$p_T^{\text{Cor.}} = \frac{s_0 + p_T^{\text{MC}}(1 + s_1)}{1 + \Delta r_0 g_0 + \Delta r_1 p_T^{\text{MC}} g_1 + \Delta r_2 (p_T^{\text{MC}})^2 g_2} \quad (4.1)$$

where p_T^{MC} and $p_T^{\text{Cor.}}$ respectively represent the momentum before and after the correction, and $g_m (m = 0, 1, 2)$ are random numbers generated by an uniform PDF ranging from 0 to 1. Numerator corresponds to the scale correction, and denominator is responsible for the resolution correction. The parameterization of denominator is based on the fact that muon resolution obeys a p_T dependence of:

$$\frac{\sigma(p_T)}{p_T} = \frac{a}{p_T} \oplus b \oplus c \cdot p_T. \quad (4.2)$$

The coefficients s_i , Δr_i are determined bin-by-bin in (η, ϕ) , by applying a template fit on $J/\psi \rightarrow \mu\mu$ and $Z \rightarrow \mu\mu$ events in data.

4.6 Jet

4.6.1 Jet Clustering

Jet reconstruction employs the anti- k_T algorithm [83] using the topo-clusters (TCs) calibrated with EM scale as input. The basic step of the algorithm is to merge the proximate two TCs based on a distance measure defined by:

$$d_{i,j} = \min(p_{T,i}^{-2}, p_{T,j}^{-2}) \frac{\Delta R_{i,j}^2}{r^2} \quad (4.3)$$

where i and j denote the index of TCs, and $\Delta R_{i,j}^2$ is the angular distance between them. $p_{T,i}$ denotes the transverse energy of TC i . r is the cone parameter dictating the typical size of resultant jets, which is set to $r = 0.4$ in the analysis. The two TCs with the smallest $d_{i,j}$ are merged in each step, and the iteration continues until:

$$\min_{i,j} [d_{i,j}] > \min_i [p_{T,i}^{-2}] . \quad (4.4)$$

The anti- k_T jet clustering is characterized by the negative power index on p_T in the metric $d_{i,j}$, where soft clusters are always added to hard components instead of being merged with the other soft cluster. This results in a well boundary behavior of jets, giving an insensitive nature to the soft jet component on which perturbative QCD does not provide robust prediction. This so-called collinear- and infrared-safety is an extremely welcomed feature for jet clustering since it allows one to straightforwardly compare the theory and data, on which the jet calibration significantly relies.

4.6.2 Energy Calibration

As the energy of TC is calibrated in the EM scale, clustered jet needs extra calibration to account for the hadronic interaction activity. Particle-level jets in simulated events (referred as “truth jets”) are used for the reference of the truth energy. They are clustered by the same algorithm (anti- k_T , $r = 0.4$) using only stable, final-state particles as input. The input particles are required to have a life-time of $c\tau > 10$ m. Muons, neutrinos, and particles from pile-up activity are excluded. Truth jets with $p_T > 7$ GeV and $|\eta| < 4.5$ are used for the calibration. In simulated events, corresponding detector-level jets can be found by geometrically matching in terms of the $\Delta R := \sqrt{(\Delta\eta)^2 + (\Delta\phi)^2}$

A series of dedicated calibration procedures is employed aiming to restore the energy to that of the truth jets reconstructed at the particle-level energy scale. It mainly proceeds as following stages (detailed in [84]):

Origin correction

Angular coordinate assigned to each topo-cluster is based on the origin defined by the designed IP position with which the actual hard-scatter vertex is displaced in z -axis direction. The jet orientation is recalculated based on the refined origin defined with the reconstructed primary vertex that the jet is associated with (see [85]).

Pileup subtraction

The contribution of particles from pile-up jets is removed using the method of area-based

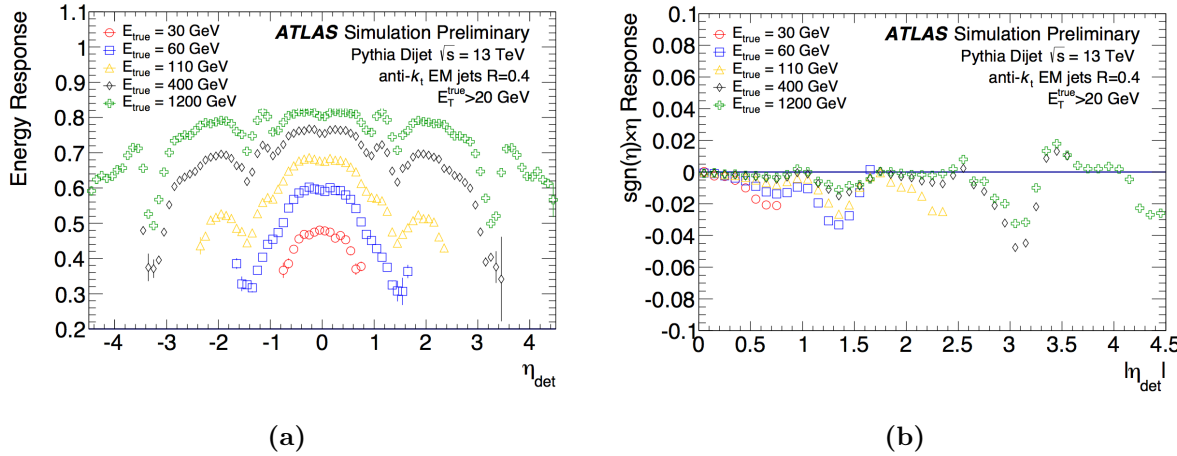


Figure 4.7: Response functions; (a) R_{p_T} ; (b) R_η defined in Eq. 4.7 before the MC-based calibration. [84]

density subtraction [86]:

$$p_T^{\text{corr.}} = p_T^{\text{reco.}} - \rho \times A, \quad (4.5)$$

where $p_T^{\text{reco.}}$ and $p_T^{\text{corr.}}$ are the jet transverse momentum before and after the correction respectively. A is the jet area defined by the area that energy deposit distributes in $\eta - \phi$ plane calculated using the ghost-association [87]. ρ is the average p_T density from the contribution of pile-up jets. The idea is to treat the pile-up as an uniform noise level over the detector, and the contribution is proportional to the area the jet is overlaying to it.

There are residual pile-up dependencies found to be linear in terms of the number of reconstructed primary vertices (N_{PV}) and the average number of interactions per bunch crossings (μ). These are corrected by:

$$p_T^{\text{corr.}} = p_T^{\text{reco.}} - \rho \times A - \alpha(p_T, \eta) \times (N_{\text{PV}} - 1) - \beta(p_T, \eta) \times \mu, \quad (4.6)$$

where the linear coefficients α and β are determined using the simulation as function of p_T and η of the jet.

MC-based calibration

The main calibration is provided by comparing the energy (or p_T) of detector-level jets to the corresponding truth jets in the simulated di-jet events from PYTHIA. The response functions R_{p_T}, R_η are defined by:

$$R_{p_T}(p_T, \eta) := \left\langle \frac{p_T^{\text{reco.}}}{p_T^{\text{truth}}} \right\rangle, \quad R_\eta(p_T, \eta) := \left\langle \frac{\eta^{\text{reco.}}}{\eta^{\text{truth}}} \right\rangle, \quad (4.7)$$

calculated in various p_T and η bins, and are applied for the detector-level jets so that the energy and η are adjusted to the particle-level scale. The conversion from the EM scale to the hadronic scale is mainly done in this stage.

Global Sequential Calibration

While only the topo-clusters level information is used for the jet energy determination so far, further improvements are achieved by applying corrections exploiting the global detector information from the calorimeter and muon spectrometer, as well as the reconstructed tracks from the inner detector.

The procedure involves 5 independent stages, referred as the Global Sequential Calibration (GSC) [88], killing residual dependence of jet energy scale on the number of associated tracks or the spatial energy profile of the jet and etc.

The most important function of the GSC is adding robustness against varying jet flavors in jet energy measurement, in particular between quark-initiated jets and gluon-initiated.

Residual in-situ calibration

A residual calibration is derived by the in-situ measurements applied only to data, accounting for the differences in the jet response between data and MC simulation. The differences is quantified using data events of $\gamma + \text{jet}$ and $Z \rightarrow \mu\mu + \text{jet}$, by balancing the p_T of a jet against the well-measured counterpart objects as reference.

4.6.3 Flavor Tagging

Hadron jets originating from b -quarks can be exclusively identified by taking advantage of the long lifetime ($c\tau \sim 450 \mu\text{m}$) of b -hadrons, creating distinct secondary decay vertices. Four independent sub-algorithms (IP2D, IP3D, SV, JetFitter) exist addressing unique b -finding power. Their outcomes are combined by inputting into a BDT classifier (MV2), and the output is used as the final discriminant. Each sub-algorithm works as following (widely referred from [89] [90] [91]):

Impact parameter based algorithm: IP2D and IP3D IP2D and IP3D are the likelihood based classifiers using the impact parameter information of tracks associated to the jet. The track-level likelihood is defined in terms of the transverse impact parameter d_0 and its error $\sigma(d_0)$ (and longitudinal impact parameter z for the case of IP3D), and modeled by MC respectively for b -jets and light-flavor jets. The jet-level likelihood is calculated by taking the product over the track-level likelihoods of associated tracks to the jet. The IP2D (IP3D) is then defined by the likelihood ratio between the b -jet and light-flavor jet hypothesis.

Secondary vertex finding algorithm: SV The SV is an algorithm [92] explicitly exploring a secondary vertex. After a set of qualification requirements on tracks in the jet, remained seed tracks are paired testing the consistency with the two-track vertex hypotheses. Found vertices consistent with the decays of other long-lived particles (such as K_s or Λ), photon conversions or hadronic interaction with a material are rejected. As further requirements, the sum of the two impact parameter significances of the two tracks is required greater than 2, and vertices with the invariant masses exceeding 6 GeV are removed given the masses of the b - or c -hadrons. Vertex with the highest invariant mass is chosen if multiple candidates are found.

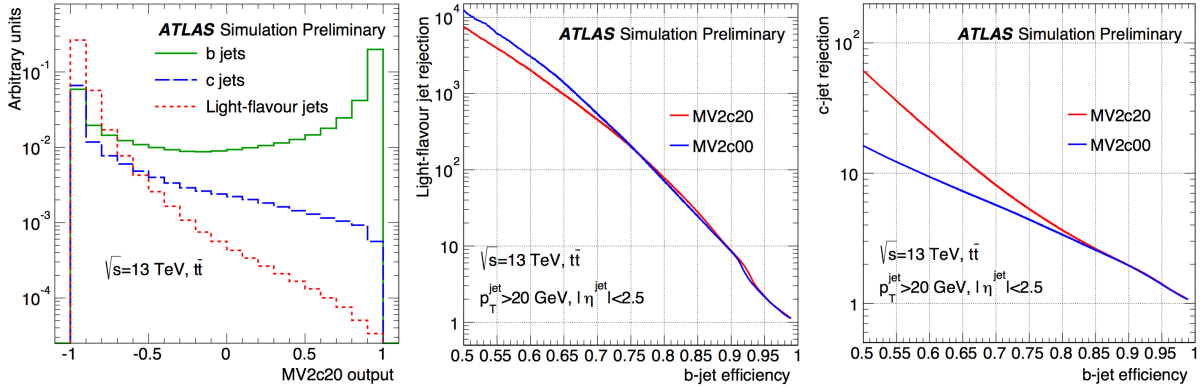


Figure 4.8: Left distributions present the output BDT score (MV2c20) of the signal (b -quark jets) and background (light-flavor and c -quark jets) samples. The middle and right curves respectively show the signal efficiency vs light-flavor jet rejection, and vs c -jet rejection. [89]

Decay chain multi-vertex algorithm: JetFitter **JetFitter** [93] is a kinematic fitting algorithm, exploiting the topological structure of weak b - and c -hadron decays inside the jet and attempt to reconstruct the full b -hadron decay chain. Using the Kalman Filter [70], JetFitter finds a common line to which the PV and the bottom and charm vertices belong, approximating the b -hadron flight path, as well as their positions. The notable advantage of this approach is that the vertices of b - and c -hadron can be reconstructed, even if only a single track is associated to any of them.

Combining algorithm: MV2 A Boosted Decision Tree (BDT) is used to combine the output from the four algorithms. The input variables includes the likelihood values from IP2D and IP3D, properties of reconstructed secondary vertex (mass, position etc.) and the associated tracks providing by SV, and the information of fitted vertices including subsequent decays of b -hadrons from JetFitter. The full list can be found in [89].

The output distribution and the performance is presented in Figure 4.8. Although the input information between the algorithms is highly correlated, it is shown that the combined algorithm drastically outperforms over either single algorithm.

Multiple working points are defined to provide different relative discrimination power against light-flavor jets and c -jets. For example, MV2c10 (MV2c20) are designed to address more rejection power towards c -jets, trained using the background sample with light-flavor jets admixed with c -jets by 10% (20%). The MV2c10 working point is used in the analysis.

4.6.4 Pile-up Jet Tagging and Rejection

Significant fraction of reconstructed jets are originated from pile-up, particularly when they are low- p_T . In order to suppress the contamination, a pile-up jet rejection is applied using the Jet Vertex Tagger (JVT) discriminant [94] exploiting the vertex information.

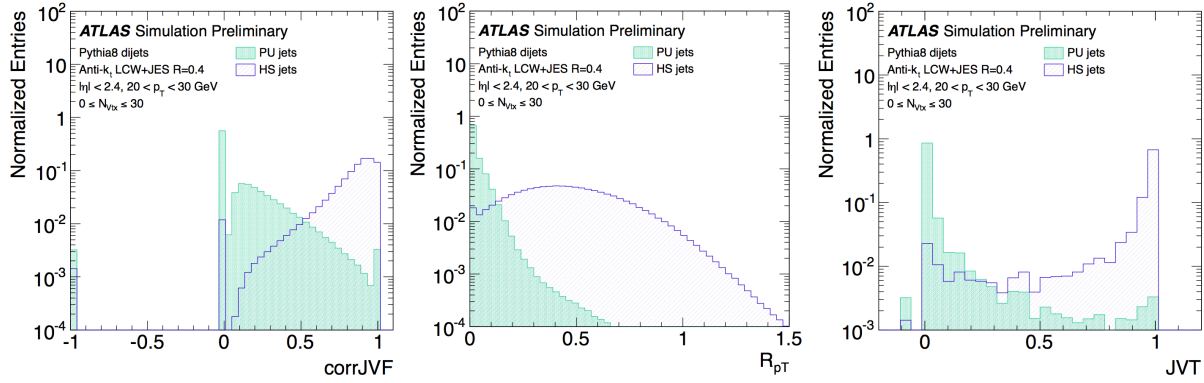


Figure 4.9: Left two plots display the distribution of the input variables of JVT; corrJVF and R_{pT} . corrJVF = -1 represents jets with no associated tracks. The right plot is resultant output likelihood score, JVT [94].

JVT is based on a 2D-likelihood function in terms of the corrected Jet Vertex Fraction (corr. JVT) and R_{pT} :

$$\text{corrJVF} := \frac{\sum_k p_T^{\text{trk}_k}(\text{PV}_0)}{\sum_l p_T^{\text{trk}_l}(\text{PV}_0) + \sum p_T(\text{PU})/(\kappa \cdot n_{\text{trk}}^{\text{PU}})}, \quad \sum p_T(\text{PU}) := \sum_{n \geq 1} \sum_k p_T^{\text{trk}_k}(\text{PV}_n)$$

$$R_{pT} := \frac{\sum_k p_T^{\text{trk}_k}(\text{PV}_0)}{p_T^{\text{jet}}}, \quad (4.8)$$

where PV₀ denotes the hard-scatter vertex and PV_j ($j \geq 1$) are the other primary vertices presumably due to the pile-up interaction. JVF (Jet Vertex Fraction) was a variable originally used for the pile-up suppression in Run1 [95] defined by the fraction of charged tracks associated to the hard-scatter vertex:

$$\text{JVF} := \frac{\sum_k p_T^{\text{trk}_k}(\text{PV}_0)}{\sum_l p_T^{\text{trk}_l}(\text{PV}_0) + \sum p_T(\text{PU})}. \quad (4.9)$$

While the performance of JVF is sensitive to the pileup since $\sum p_T(\text{PU})$ scales linearly according to number of pileup, $\sum p_T(\text{PU})$ is divided by the number of PU tracks $n_{\text{trk}}^{\text{PU}}$ in the corrJVF to kill the linear dependency, together with the scale factor $\kappa = 0.01$ restoring the absolute normalization of the PU term. R_{pT} is the charged energy fraction in the jet, designed to address to the jets with small number of tracks leading to low corrJVF value. A 2D-likelihood profile in terms those two variables is respectively modeled for hard-scatter jets and pile-up jets, and the JVT is defined as likelihood ratio.

Figure 4.9 demonstrates the typical separation. The JVT selection $\text{JVT} > 0.57$ is applied for jets with ($20 \text{ GeV} < p_T < 60 \text{ GeV}$ and $|\eta| < 2.4$), in which the pile-up jets dominantly populates.

4.7 Overlap Removal between the Reconstructed Objects

Electrons, muons and jets are reconstructed in parallel, allowing the ambiguity that a single particle is reconstructed or identified as multiple objects simultaneously (for instance, an electron is typically reconstructed both as an electron object and a jet). ² A sequence of “overlap-removal” procedure is applied to resolve the double-counting, based on the angular distance $\Delta R = \sqrt{\Delta\eta^2 + \Delta\phi^2}$ between them.

The algorithm begins with the electron-jet overlap removal. Any light-flavor jet ³ reconstructed within $\Delta R < 0.2$ with respect to identified electrons is rejected. The electron is otherwise removed if the overlapping jet is b -tagged jet, to avoid rejecting b -jets due to the non-prompt lepton nearby caused by the decays of b -hadrons. Next, to remove bremsstrahlung from muons followed by a photon conversion into electron pairs, electrons lying within $\Delta R < 0.01$ of a preselected muon are discarded. Subsequently, the contamination of muons from heavy-flavored hadron decays is suppressed by removing muons that lie within $\Delta R < \min(0.04 + (10 \text{ GeV})/p_T(\mu), 0.4)$ of any remaining jet, or within $\Delta R < 0.2$ of a b -tagged jet or a jet containing more than three tracks with $p_T > 500 \text{ MeV}$. In the former case, the p_T -decreasing angular separation mitigates the rejection of energetic muons close to jets in boosted event topologies. Finally, jets reconstructed within $\Delta R < 0.2$ of remaining electrons or muons are excluded.

The identification of hadronically decaying taus and photons are not exploited in the analysis, since they are not explicitly used as objects in event selections. Instead, those with sufficiently high transverse momentum can pass the jet reconstruction and the JVT requirement, treated as jets in the analysis.

²The “overlap removal” procedure is purposely left to users, to accommodate various preference in object selection between analyses.

³A working point with 85% efficiency is used for the b -tagging in the overlap removal, while 77% efficiency working point is used for the b -jet selection in the analysis, in order to save as many b -jets as possible in the stage.

4.8 Fake Leptons and the Isolation Requirement

Light-flavor leptons (electrons or muons) produced in LHC subject to two types; “prompt leptons” directly originated from the hard scattering via decays of real and virtual gauge bosons; “non-prompt leptons” generated via decays of long-lived particles such as heavy flavor hadrons or tau leptons, or pair creation of photons (mostly stemming from π_0 in jets). The leptons interested in the new physics or EW physics always subject to the prompt leptons, while non-prompt leptons are trivial and often disturbing. There are also a type of reconstructed leptons by wrongly identified pions in jets. In the thesis, these unwilling leptons (non-prompt leptons and wrongly identified pions) are collectively referred as “fake leptons”. There are couple of requirements designed for rejecting them, which are described in the following.

Impact parameter requirement Non-prompt leptons are generated in relatively displaced position with respect to the primary vertex, therefore the information of transverse impact parameters is helpful rejecting them. The selection used in the analysis is as Table 4.2. While the d_0 and $z_0|\sin\theta|$ of prompt-leptons populate close to 0, those for non-prompt leptons result in a wider distribution, leading many of them to be rejected.

Table 4.2: Impact parameter requirements used in the analysis. d_0 and (z_0) is the transverse (longitudinal) impact parameter. $\sigma(d_0)$ is the fitting error of d_0 in the track fit.

	Electron	Muon
$ d_0 /\sigma(d_0)$	< 5	< 3
$z_0 \sin\theta $	< 0.5 mm	< 0.5 mm

Isolation While fake leptons generally fly closely by jets because of their origin, the path of flights of prompt-leptons rarely overlap with other particles. Therefore, the isolation requirement with respect to proximate cluster or tracks provide significant rejecting power of fake leptons. Two isolation variables are defined:

Calorimeter isolation ($E_T^{\text{cone} \ 0.2}$): Sum of transverse energies by the calibrated topo-clusters with $\Delta R < 0.2$ with respect to the lepton. An E_T, η dependent pileup correction is applied. For electron, the energy leakage due to the bremsstrahlung is compensated.

Track isolation ($p_T^{\text{cone} \ 0.2}$): Sum of transverse momentum of tracks within the angular distance of $R = \min(0.2, 10 \text{ GeV}/p_T)$ with respect to the lepton. The variable cone size is intended to loosen the isolation cut for high- p_T leptons, based on the fact that most of fake leptons are below 20 GeV.

The isolation requirement is performed by applying a cut in a 2D-plane of $E_T^{\text{cone} \ 0.2}$ and $p_T^{\text{cone} \ 0.2}$. In the analysis, the **GradientLoose** working point is chosen, in which a p_T -dependent cut is applied designed to recover the efficiency in high- p_T . Figure 4.10 shows the isolation efficiency respectively for electrons and muons.

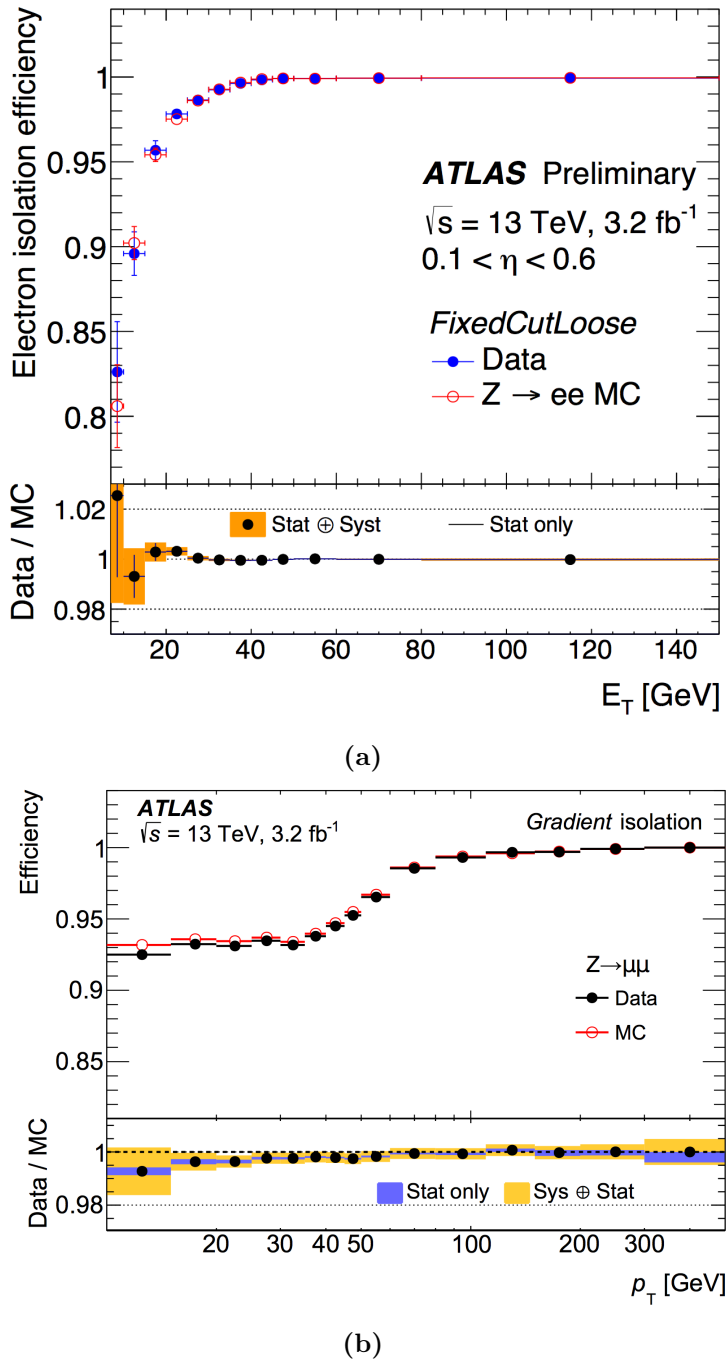


Figure 4.10: Measured and simulated efficiency of the isolation requirement in case of (a) electrons [76] and (b) muons [82]. The $Z \rightarrow ee/\mu\mu$ events are used for both MC and data. The **FixedCutLoose** working point is shown for the electrons where $E_T^{\text{cone}\,0.2}/E_T < 0.2$ and $p_T^{\text{cone}\,0.2}/E_T < 0.15$ is applied, while the case with **GradientLoose** is shown for muons.

4.9 Missing Transverse Energy

Missing Transverse Energy (E_T^{miss}) is an extremely important proxy to new physics since it is directly related with the activity of invisible particles. E_T^{miss} is calculated by the transverse momentum imbalance of visible particles, using the reconstructed objects as well as isolated tracks that are not associated with any objects (“soft term”). It is constructed by four independent terms as shown in Eq. (4.10):

$$E_T^{\text{miss.}} := - \sum \not{E}_T^e - \sum \not{E}_T^\mu - \sum \not{E}_T^{\text{jet}} - \not{E}_T^{\text{soft}}. \quad (4.10)$$

where the first three terms (electron term / muon term / jet term) are the vectorial sum of E_T of the objects after the calibration and the overlap removal.⁴ The last term is the soft term accounting for the residual visible momentum mainly from soft jets ($p_T < 20$ GeV) and mis-identified muons. It is calculated by the track soft term algorithm (TST) [96], summing over the momenta of tracks that are not associated to any jets, and are isolated by $\Delta R > 0.2$ from any reconstructed EM clusters. Tracks with the momentum uncertainties larger than 40%, and the high- p_T tracks ($p_T > 200$ GeV in $|\eta| < 1.5$ or $p_T > 150$ GeV in $|\eta| > 1.5$) with questionable quality of momentum measurement satisfying following conditions are removed to prevent potential large error in the calculation:

$$p_T^{\text{cone } 0.2}/p_T > 0.1, \text{ and } \frac{E_T^{\text{cone } 0.2}}{p_T + p_T^{\text{cone } 0.2}} < 0.6, \text{ and } \frac{p_T^{\text{cone } 0.2}}{p_T + p_T^{\text{cone } 0.2}} < 0.6. \quad (4.11)$$

One of the biggest advantages to calculating the soft term using tracks instead of clusters is the robustness against pile-up. Figure 4.11 show the resolution of TST as function of pile-up, where the bias due to pile-up is shown to be highly suppressed.

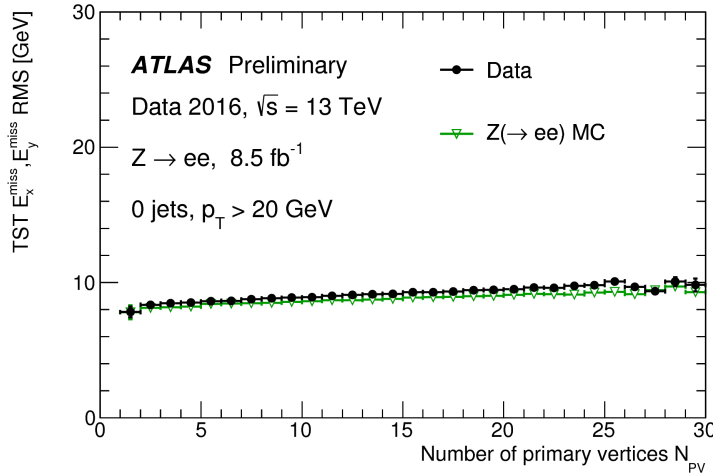


Figure 4.11: Simulated and measured resolution of the TST as function of number of reconstructed primary vertices per event, using the $Z \rightarrow ee$ events without jets with $p_T > 20$ GeV [97].

⁴JVT selection for jets in addition to prevent the contribution from pile-up.

4.10 Object Definition in the Analysis

The requirements for objects used in the analysis are summarized in Table 4.3. For electrons and muons, two types of working point are defined; “baseline” is the loose selection criteria oriented to veto extra prompt leptons in the event; “signal” is the tighter working point aiming to reject fake leptons where tighter identification, the impact parameter cut, and the isolation requirement are imposed in on top of the baseline requirement. Signal regions are defined with exactly one baseline and signal lepton, given that the targeted signal events contain exactly one prompt lepton.

Table 4.3: Summary of object definition used in the analysis. In addition to the listed criteria, objects are required to pass the reconstruction, identification and the overlap removal. The p_T requirements are based on the transverse momentum after the calibrations.

Electrons	Baseline	Signal
p_T	$> 7 \text{ GeV}$	$> 7 \text{ GeV}$
Identification	Loose	Tight
Isolation	-	GradientLoose
Impact parameter cuts	-	$z_0 \sin \theta < 0.5 \text{ mm}, d_0 /\sigma(d_0) < 5$
Muons	Baseline	Signal
p_T	$> 6 \text{ GeV}$	$> 6 \text{ GeV}$
Identification	Medium	Medium
Isolation	-	GradientLoose
Impact parameter cuts	-	$z_0 \sin \theta < 0.5 \text{ mm}, d_0 /\sigma(d_0) < 3$
Jets		
Clustering Algorithm		anti- k_T ($r = 0.4$)
p_T		$> 30 \text{ GeV}$
JVT		> 0.57 for $p_T < 60 \text{ GeV}$
b -tag		MV2c10 algorithm, 77% efficiency working point

Chapter 5

Monte-Carlo Simulation

Monte-Carlo (MC) simulation is a highly powerful toolkit providing theoretical prediction on event kinematics as well as the detector response, which is used extensively from studying signal/background separation, performance evaluation to background estimation.

This chapter discusses how the events are simulated, from some basics about the phenomenology in pp -collision, to the actual implementation in simulation where numerous approximations and simplifications are introduced. Reference [98] and [99] are widely referred. Finally, the detailed configuration of each samples used in the analysis is overviewed.

5.1 Phenomenology of a pp -collision

A typical pp -collision at the LHC energy can be understood and factorized by a number of different sub-processes:

Parton-level hard scattering

The main process dominating the entire collision is the hard scattering where constituent partons in protons interact each other. The cross-section can be constructed by the matrix-element ($\mathcal{M}_{a,b \rightarrow F}$; ME) from an initial state with the two partons (a, b) into a certain final state (F):

$$\frac{d\hat{\sigma}_{a,b \rightarrow F}}{d\mathbf{y}} = \frac{1}{2\hat{s}_{ab}} \frac{d\Phi}{d\mathbf{y}} |\mathcal{M}_{a,b \rightarrow F}|^2 \quad (5.1)$$

where \mathbf{y} represents momenta of final state particles; $d\Phi/d\mathbf{y}$ is the differential phase space; and the flux factor $1/2\hat{s}_{ab}$. The ME is the sum of transition amplitude of all relevant processes with different intermediate states ($a, b \rightarrow X \rightarrow F$) characterized by different Feynman diagrams.

Parton pick-up from a proton

To translate the parton-level hard scattering into a pp -interaction, one has to convolute with the parton distribution in a proton, for instance, the parton-level cross-section Eq. 5.1 is

encapsulated by the parton distribution function (PDF):

$$\frac{d\sigma_{pp \rightarrow F}}{dy} = \sum_{i,j \in (q,\bar{q},g)} \int_0^1 dx_a \int_0^1 dx_b f_i(x_a) f_j(x_b) \frac{d\hat{\sigma}_{a,b \rightarrow F}}{dy}. \quad (5.2)$$

$x_{a,b}$ denotes the momentum fraction of protons carried by the constituent parton a, b , and $f_i(x)$ is the PDF for parton flavor i namely the probability density that one finds parton i in the momentum fraction of x . a and b are finally added up with possible parton flavors, reflecting our ignorance on them. Note that this convolution is not in terms of amplitude (\mathcal{M}) but rather a statistical addition, ignoring the interference between the parton-level hard scattering and proton dynamics, which is justified by the factorization theorem [100].

Additional parton radiation (ISR/FSR)

Furthermore, additional jets often accompany from the splitting legs of initial and final state partons. They are referred as initial state radiation (ISR) or final state radiation (FSR). In principle, this effect should be counted as a part of parton-level hard scattering, however practically it is often useful to treat it as a separated auxiliary effect, as will be shown later.

Hadronization

Resultant quarks and gluons in the final state are transformed into collections of fragmented hadrons (“hadronization”). This is particularly the nature about the strong interaction known as “confinement” where the running coupling constant becomes stronger for longer distance scatterings and eventually diverges at the Landau pole $Q^2 \sim (200 \text{ MeV})^2$. Naively this will lead to an infinite cross-section for processes with $Q^2 \sim (200 \text{ MeV})^2$, including quark and anti-quark pair productions out of the vacuum.¹ Those instantaneously generated partons are recombined eventually into hadrons with the singlet color state. This hadronization procedure can be understood using the universal fragmentation function $D(z)$ in the same internal structure with PDF, representing the probability of finding a hadron with momentum fraction of z with respect to that of seed parton.

Underlying events

Protons from which the hard scattering partons are kicked out are completely destroyed, no longer keeping the form as protons. The remnants will experience their own hadronization, resulting in a splash of permeating hadronic background known as “beam remnant”. In addition, multiple parton-level scatterings (multiple parton interaction; MPI) occasionally take place within a single proton-proton interaction, where usually at least one of them ends up in a cheap QCD scattering leaving low- p_T jets. These sub-processes resulting in soft remnants as the background of the main hard scattering are inclusively referred to “underlying events”.

Figure 5.1 is the schematic of the pp -collision with the sub-process.

¹This picture is incorrect giving the breakdown of perturbation, nevertheless enough to give an idea of the transition toward non-perturbative region.

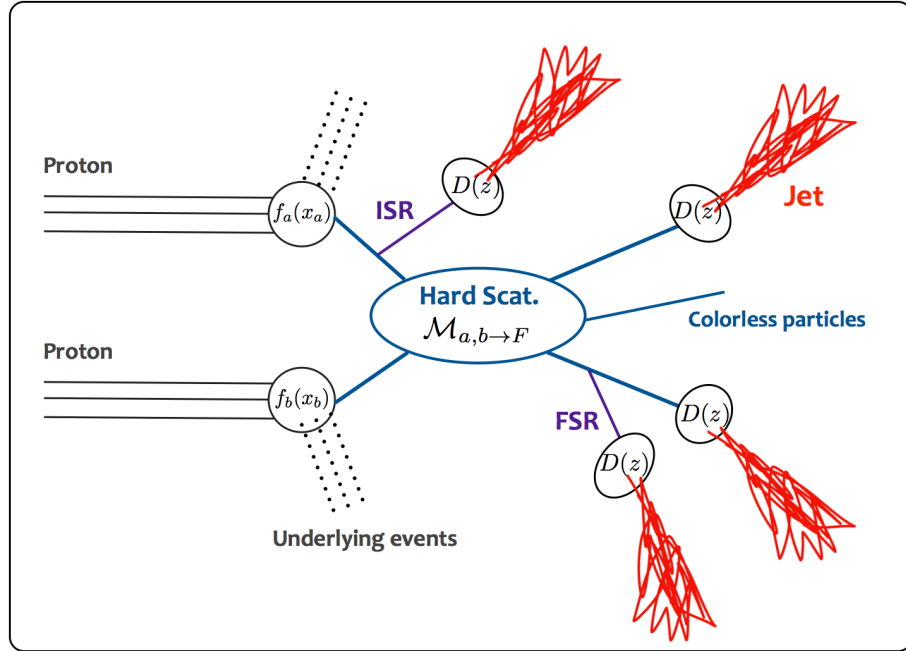


Figure 5.1: Schematic of involved phenomenology in a pp -collision.

5.2 Implementation of pp -collisions in Simulation

Since it is practically non-calculable with the rigid formulation, what is implemented in the simulation is drastically simplified by employing numerical approach or approximation techniques. The detail for each sub-processes is described in this section.

5.2.1 Parton Distribution Function

Since the PDF is determined purely by non-perturbative dynamics, it is much easier to take the result of QCD measurement as the input rather than by first principle calculation. A number of collaborations have performed a global fit on the experimental data of deep inelastic scatterings (DIS) or hadron-hadron collision mostly provided from HERA and Tevatron, with different parameterization and fitting scheme. Most frequently used sets in the LHC analyses are PDF4LHC [101], NNPDF [102], CT14 [103], MSTW [104]. The uncertainties mainly results from instrumental uncertainties in the input data, uncertainties on the strong coupling constant and the functional form of parameterization.

5.2.2 Fixed-Order QCD Calculation

The matrix-element in Eq. (5.1) is computed based on the QCD and EW theory, with the truncated orders of perturbation series. While the leading term in the perturbation (lowest order; “LO”) dominates over the phase space, the inclusion of higher-order terms is significantly important for new physics searches. This is because of the much smaller signal cross-section with respect to the SM backgrounds, forcing one to explore the phase space where the bulk SM component is largely

suppressed, in order to achieve a reasonable S/N. In such regions, typically the LO contribution is relatively more suppressed and the higher-order effects become addressing.

The calculation of higher-order terms are generally challenging giving the skyrocketing increased number of involved diagrams. Currently, the cross-section calculation is available upto next-to-next-to-leading order (NNLO) for typical SM processes in LHC, and upto NLO level in event generation. Since the most phenomenologically important higher-order effect is the additional parton emission (ISR and FSR), there are also a class of generators dedicated for computing diagrams with the additional radiations (“multi-leg generators”) in the market, which can typically afford upto 4-9 additional partons at maximum, saving the computing resources by omitting the loop diagrams.

5.2.3 Parton Showering

On top of the straightforward QCD matrix-element calculation, the parton shower (PS) approximation is further applied to supplement the description of the additional partons emission. The concept is based on following two notions:

- Soft or collinear emission provide dominant contribution to the extra parton emission from a parton. For instance, in $ee \rightarrow q\bar{q}g$ as the minimal demonstration, the differential cross-section can be expressed:

$$\frac{d\sigma_{q\bar{q}g}}{dx_1 dx_2} = \sigma_{q\bar{q}} \times \frac{\alpha_s}{2\pi} \frac{4}{3} \frac{x_q^2 + x_{\bar{q}}^2}{(1-x_q)(1-x_{\bar{q}})}, \quad x_i := 2E_i/\sqrt{s} \quad (5.3)$$

with \sqrt{s} being the center-of-mass energy of the ee system. The appeared singularities correspond to the collinear emission of a gluon ($x_q \rightarrow 1$ or $x_{\bar{q}} \rightarrow 1$) or the soft gluon emission ($x_q \rightarrow 1$ and $x_{\bar{q}} \rightarrow 1$). These collinear and soft singularities are universal to QCD, independent from type of processes.

- In the soft/collinear regime, the cross-section with an additional parton radiation ($d\sigma_{n+1}$) can be approximately factorized into the product of the original cross-section ($d\sigma_n$) and the probability of the splitting $P_{i \rightarrow jk}$:

$$d\sigma_{n+1} = d\sigma_n \left[\sum_{j,k} \frac{\alpha_s}{2\pi} \frac{dq}{q} \frac{dz}{z} P_{i \rightarrow jk}(z) \right], \quad (5.4)$$

where the indices i, j represent respectively the parent parton before and after the splitting, and k the emitted parton. z is the momentum fraction that the emitted parton k carries from the parent i , and q is the invariant mass (“virtuality” when ignoring the quark mass) for the

4-momentum of the parton i . $P_{i \rightarrow jk}$ is calculated as:

$$\begin{aligned} P_{q \rightarrow qg} &= \frac{4}{3} \frac{1+z^2}{1-z}, \\ P_{q \rightarrow qq} &= \frac{4}{3} \frac{1+(1-z)^2}{z}, \\ P_{q \rightarrow gg} &= 3 \frac{z^4+1+(1-z)^4}{z(1-z)}, \\ P_{q \rightarrow q\bar{q}} &= \frac{z^2+(1-z)^2}{2}, \end{aligned} \quad (5.5)$$

known as the Dokshitzer-Gribov-Lipatov-Altarelli-Parisi (DGLAP) evolution equations [105–107].

The parton shower technique is an emulation of the recursive parton splitting (“parton shower”) in a picture of stepwise evolution, in contrast to that in the matrix-element calculation where either initial and final state must be defined beforehand. The probability of emitting an extra parton at each step can be represented using Eq. (5.4) and Eq. (5.5) analogous to the life-time of unstable particle decay :

$$S_i(q_1, q_2) = 1 - \exp \left(- \sum_{j,k} \int_{q^2}^{q_{\max}^2} \frac{dQ^2}{Q^2} \int_{z_{\min}}^{z_{\max}} \frac{\alpha_s}{2\pi} P_{i \rightarrow jk}(\hat{z}) d\hat{z} \right) \quad (5.6)$$

which is known as the Sudakov form factor [108]. q_1 (q_2) denotes the virtuality of parent parton before (after) the splitting. FSRs are simulated by the evolution of final state parton legs with the splitting probability Eq. (5.6), with an arbitrary initial virtuality. The evolution continues until the virtuality becomes the termination scale which is typically set to ~ 1 GeV. ISRs are simulated in a similar manner but with a backward evolution with increasing virtuality. Generated sub-branches during the backward evolution are then evolved forward. The procedure is schematized as Figure 5.2.

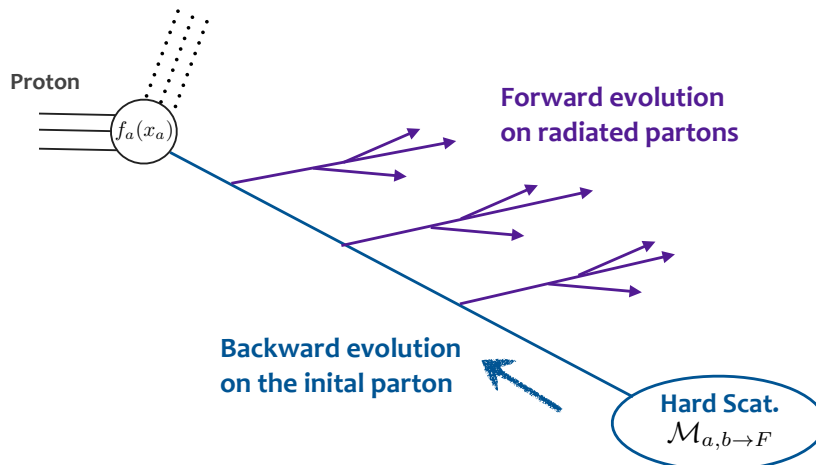


Figure 5.2: Schematic of the backward evolution in the ISR simulation. The evolution starts with the parton entering the hard-scattering, with increasing the virtuality along the evolution. Partons split from the initial line are then evolved forward, in the same manner as the FSRs being generated.

Various implementation for the evolution exist, leading to a subtle difference in the final state kinematics. The impact are quoted as theoretical uncertainty in the analysis (see Sec. 8.2).

Note that this shower evolution is fully perturbative though, it does include the contribution from arbitrarily higher order terms in the perturbation series (upto n -th order, where n is number of parton splittings). Nevertheless, the imperfection of this approximation is that it only accounts for the contribution from collinear and soft singularity. Therefore, a practical approach is commonly employed; generating as many ME-level partons as possible, and complementing the residual higher-order contributions by parton showering. One issue about this combined approach is the potential double-counting. The correction procedure commonly refers to “matching” or “merging”. There are largely two types of correction; separating the region that each ME and PS is responsible for, in terms of phase space or scale. The most widely used algorithm is the Catani-Krauss-Kuhn-Webber (CKKW) [109] algorithm or Michelangelo-L. Mangano algorithm (MLM) [110]. ; Generating all jets by PS, and correct it by normalizing into the ME differential cross-section (ME correction).

5.2.4 Hadronization

A phenomenological approach is usually preferred for simulating hadronization. The most famous model is the Lund string model [111] where the interaction between the combining partons is characterized by a gluonic string. For a quark-antiquark pair, as the partons move apart, the string is stretched leading to an increase in the potential energy. When the energy becomes of the order of hadron masses, it becomes energetically favorable for the string to break and create a new quark-antiquark pair. The two segments of string will be repeatedly pulled and break again, until all energy of initial quarks is converted into newly generated fragments.

5.3 Setup of the Simulated Dataset

5.3.1 Event Generation

Events of the signal and background processes are generated using preferred generators and setups. Table 5.1 summarizes the configurations for the simulated datasets. Given that the analysis typically explores the phase space with many jets, physics processes with few hard tree-level jets (e.g. $W/Z + \text{jets}$, gluino production with compressed mass spectra etc.) need a dedicated modeling on ISRs and FSRs, for which the multi-leg generators (SHERPA, MADGRAPH) are preferred. For the other processes, events are simulated using the NLO generator POWHEG.

The simulated events are normalized by the total cross-sections that are separately calculated at a higher precision such as by including higher orders or the soft gluon resummation. Table 5.2 presents the summary of the total cross-sections and the configuration on which they are calculated.

Further caveats particular to each process are noted in the appendix A.1.

Table 5.1: Setup of simulated SUSY signal and the Standard Model background samples. $n_{\text{ME}}^{\text{a.p.}}$ denotes the number of simulated additional partons in the higher-order QCD processes. The column of “PS/UE” shows the programs in which parton showers and underlying events are generated.

Physics process	Generator	$n_{\text{ME}}^{\text{a.p.}}$	PDF set	PS/UE
SUSY processes	MADGRAPH 2.3 ^a	2	NNPDF2.3 LO	PYTHIA 8 ^d
$W/Z + \text{jets}$	SHERPA ^b	2(NLO)+2(LO)	NNPDF3.0 NNLO[112]	SHERPA
$t\bar{t}$	POWHEG ^c	1	CT10 [113]	PYTHIA 6 ^{d'}
Single-top ($Wt\text{-ch.}$)	POWHEG v2	1	CT10	PYTHIA 6
Single-top ($s\text{-ch.}$)	POWHEG v2	1	CT10	PYTHIA 6
Single-top ($t\text{-ch.}$)	POWHEG v1 ^{c'}	1	CT10f4	PYTHIA 6
Di-bosons	SHERPA	1-2(NLO)+2-3(LO)	CT10	SHERPA
$t\bar{t} + W$	MADGRAPH 2.2 ^{a'}	2	NNPDF2.3 LO	PYTHIA 8
$t\bar{t} + Z$	MADGRAPH 2.2	1	NNPDF2.3 LO	PYTHIA 8
$t\bar{t} + WW$	MADGRAPH 2.2	0	NNPDF2.3 LO	PYTHIA 8

^a MADGRAPH5_aMC@NLO 2.3.3 [114], NLO

^{a'} MADGRAPH5_aMC@NLO 2.2.3, LO

^b SHERPA 2.2.1[115], NLO

^c POWHEG-BOX v2 [116], NLO

^{c'} POWHEG-BOX v1 [116], LO

^d PYTHIA 8.186[117], LO, CKKW matching

^{d'} PYTHIA 6.428[118], LO, ME correction

5.3.2 Pileup simulation

All simulated events are generated with a varying number of proton-proton collisions with soft QCD processes (minimum-bias interaction) overlaid on the hard-scattering event, to account for the pile-up in the same and the nearby crossing crossings. The minimum-bias interactions are simulated with by PYTHIA 8.186 using the A2 tune [131] and the MSTW2008LO PDF set [104].

5.3.3 Detector Simulation and Emulation

The detector response is simulated by a full ATLAS detector simulation model [132] based on GEANT4 [133], for the background samples.

The ATLAS fast simulation [49] is used as the economical alternative for part of the gluino signal processes (models marked as ✓ in Table 2.5-2.7 in Sec. 2.5.3). This is based on a parametrization of the performance of the electromagnetic and hadronic calorimeters measured in the test-beam or on GEANT4. The difference between the full simulation is found to be marginal after examining a number of reference signal points. The subsequent procedures are identical to what is processed for the data sample.

For the signal models without ✓ in Table 2.5-2.7, no detector simulation nor reconstruction is performed. Instead the effect is emulated by smearing the energy of truth-level particles and clustered jets, based on the resolution parameterized using the full simulated samples. The object identification is emulated by randomly accepting the candidates at the rate of the parameterized

Table 5.2: Cross-section used for the simulated processes. “(N)NLL” denotes the order upto which the soft gluon resummartion is taken into account.

Physics process	Cross-section [pb]	Order	Authors
SUSY processes	See Figure 5.3	NLO+NLL	[119–123]
$W + \text{jets}(\rightarrow \ell\nu)$	20079	NNLO	[124]
$Z + \text{jets}(\rightarrow \ell\ell)$	1950	NNLO	[124]
$t\bar{t}$	993.8	NNLO+NNLL	[125]
Single-top (Wt -channel)	75.57	NNLO+NNLL	[126]
Single-top (s -channel)	10.32	NLO	[127]
Single-top (t -channel)	216.95	NLO	[127]
Di-bosons	45.42	NLO	[128]
$t\bar{t} + W/Z/WW$	1.36	NLO	[129, 130]

efficiency. The modeling is extensively tested by comparing the kinematic distributions with the fast simulated samples (see Sec. A.2 in the appendix). The discrepancy is found sufficiently small, generally staying within $10\% \sim 20\%$, which is acceptable given that the $15\% \sim 35\%$ cross-section uncertainty on the gluino pair production.

5.4 Design of SUSY Signal Grid for Interpretation

Obtained exclusion limits are presented in a form of contours in a 2-dimensional plane, usually in terms of SUSY masses. This is done by generating a set of signal samples with various SUSY masses covering the whole plane with discrete steps, referred as a signal grid. The results of the hypothetical test on each point are eventually interpolated into a continuous profile.

For limits on the direct decay models, $m_{\tilde{g}}$ and $m_{\tilde{\chi}_1^0}$ are chosen as the x - and y -axis respectively (“**Direct**” grid). The case with the 1-step decay models is a bit tricky, since they involve the third mass; the mass of the intermediate EW-gaugino ($m_{\tilde{\chi}_1^\pm}$ or $m_{\tilde{\chi}_2^0}$). The full 3-dimensional presentation is not realistic from the computational cost of view. Therefore, a couple of sensible 2D-slices are made that sufficiently capture the essence of the 3D-grid. “**x=1/2**” is the grid with the intermediate EW-gaugino mass is set to the midmost between $m_{\tilde{g}}$ and $m_{\tilde{\chi}_1^0}$, while the splitting parameter x is defined as the relative mass splitting:

$$\begin{aligned}\Delta m_{A,B} &:= m_A - m_B \\ x &:= \Delta m(\tilde{\chi}_1^\pm/\tilde{\chi}_2^0, \tilde{\chi}_1^0)/\Delta m(\tilde{g}, \tilde{\chi}_1^0), \quad x \in [0, 1].\end{aligned}\tag{5.7}$$

The “**LSP60**” grid is designed to complement the hole in high- x or low- x , where the LSP mass is fixed to 60 GeV while the masses of gluino and the intermediate EW-gaugino are set free. There are two additional DM-oriented grids (“**DM20**” and “**DM30**”) are defined in which the masses of the intermediate EW-gaugino and the LSP are compressed so that $\Delta m(\tilde{\chi}_1^\pm/\tilde{\chi}_2^0, \tilde{\chi}_1^0) = 20, 30$ GeV respectively, motivated by the dark matter relic constraint discussed in Sec. 2.4.2. Note that the DM-oriented grids are not considered in models with $\tilde{\chi}_2^0$ decaying to higgs, since higgs is too far

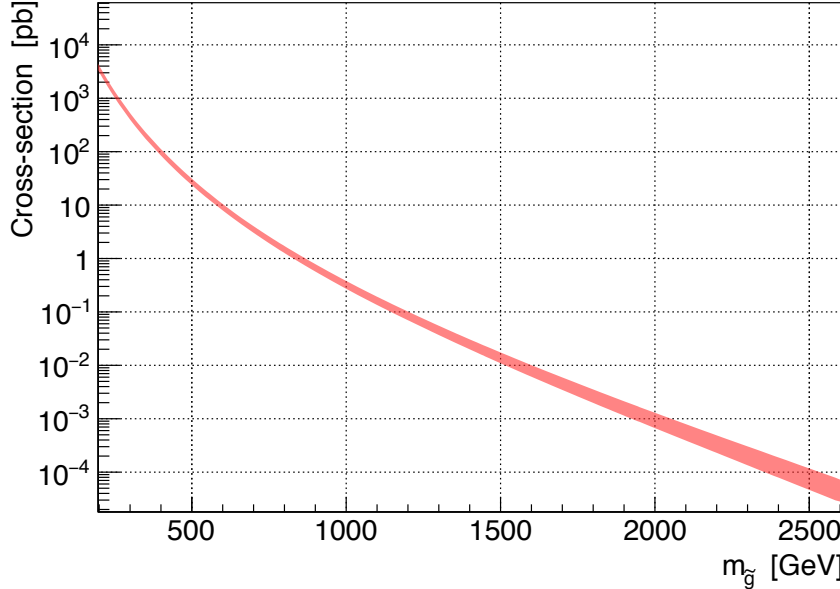


Figure 5.3: Cross-section of gluino pair production as function of gluino mass, at the NNLO+NNLL accuracy. The pink band corresponds to the calculation error.

off-shell thus $\tilde{\chi}_2^0$ almost never decays via higgs in the situation. Table 5.3 summarizies the designed signal grids in the analysis.

Table 5.3: Types of the signal grids used for limit setting. **Direct** is for the direct decay model, and the others are for the 1-step decay models. The latter is four-fold; **x=1/2** where the intermediate EW gaugino mass is fixed to the midmost between $m_{\tilde{g}}$ and $m_{\tilde{\chi}_1^0}$; **LSP60** in which the LSP mass is fixed to 60 GeV; **DM20** and **DM30** are grids with $\Delta m(\tilde{\chi}_1^\pm/\tilde{\chi}_2^0, \tilde{\chi}_1^0) = 20, 30$ GeV which are considered only in models without $\tilde{\chi}_2^0$ decay into higgs.

Grid name	x-axis	y-axis	Slicing	Note
Direct	$m_{\tilde{g}}$	$m_{\tilde{\chi}_1^0}$	-	-
x=1/2	$m_{\tilde{g}}$	$m_{\tilde{\chi}_1^0}$	$\Delta m(\tilde{g}, \tilde{\chi}_1^0)/2 = \Delta m(\tilde{\chi}_1^\pm/\tilde{\chi}_2^0, \tilde{\chi}_1^0)$	-
LSP60	$m_{\tilde{g}}$	$\Delta m(\tilde{\chi}_1^\pm/\tilde{\chi}_2^0, \tilde{\chi}_1^0)/\Delta m(\tilde{g}, \tilde{\chi}_1^0)$	$m_{\tilde{\chi}_1^0} = 60$ GeV	-
DM20, DM30	$m_{\tilde{g}}$	$m_{\tilde{\chi}_1^0}$	$\Delta m(\tilde{\chi}_1^\pm/\tilde{\chi}_2^0, \tilde{\chi}_1^0) = 20, 30$ GeV	For models without h -mediated $\tilde{\chi}_2^0$ decays.

Chapter 6

Event Selection

The goal of this chapter is to define the signal regions in which the compatibility between data and background-only or SUSY signal hypotheses are tested. Different level of event selection will be discussed from the pre-selection including trigger selection, event cleaning selection, design of the signal region binning, and the optimization of background rejection cuts. Finally the decided signal regions are validated via inspecting the expected limits, which is shown in Sec. 6.3.4.

6.1 Trigger Selection

The missing E_T trigger (MET trigger) is primarily used throughout the analysis. Since the lowest unprescaled trigger kept evolved according to the increased instantaneous luminosity during the data taking, a number of different triggers are used in combination. The list of relevant triggers are shown in Table 6.1,

Table 6.1: Summary of MET triggers used in the analysis along the peak luminosity evolution. Corresponding on-line and off-line threshold are shown in the rightest column.

Period	Peak lumi. [$\text{cm}^{-2} \text{s}^{-1}$]	Int. lumi. [fb^{-1}]	L1 (HLT) item	L1/HLT/Off-line thres. [GeV]
2015	0.50×10^{34}	3.19	L1XE50 (xe70_mht)	50 / 70 / 200
2016 A-D1	0.99×10^{34}	6.12	L1XE50 (xe90_mht)	50 / 90 / 200
2016 D1-F1	1.03×10^{34}	6.55	L1XE50 (xe100_mht)	50 / 100 / 200
2016 F2-	1.21×10^{34}	20.2	L1XE50 (xe110_mht)	50 / 110 / 200

The efficiency curve as function of off-line E_T^{miss} is shown in Figure 6.1, taking HLT_xe100_mht as an example. Thanks to the fact that E_T^{miss} is calculated from the global information of an event, rather than the local feature around a single particle, the plateau efficiency achieves almost 100 %. This is a significant advantage over the use of particle-based trigger (e.g. single-lepton trigger) where efficiency is typically 70% \sim 90%. Generally the downside of MET trigger is on the other hand its slow turn-on in terms of the off-line MET that needs nearly 200 GeV to assure the plateau efficiency despite much lower trigger threshold (< 110 GeV). This is due to the deteriorated resolution of on-line MET calculated only with calorimeter deposit, with respect to the off-line one which in addition takes muons and soft tracks into account. The signal acceptance by the MET trigger requirement is $> 95\%$ only except when the masses of gluino and LSP are compressed. This

is however not problematic eventually, since it turns that large- E_T^{miss} is anyway necessary for such signal to be discriminated against the background.

The single-lepton trigger (SLT) is also used for supplemental purpose, including the efficiency measurement of MET trigger and data-driven background estimation. The trigger turn-on is about 28 GeV (26 GeV) for single-electron (muon) in its transverse momentum and 30 GeV (28 GeV) is required as off-line threshold.

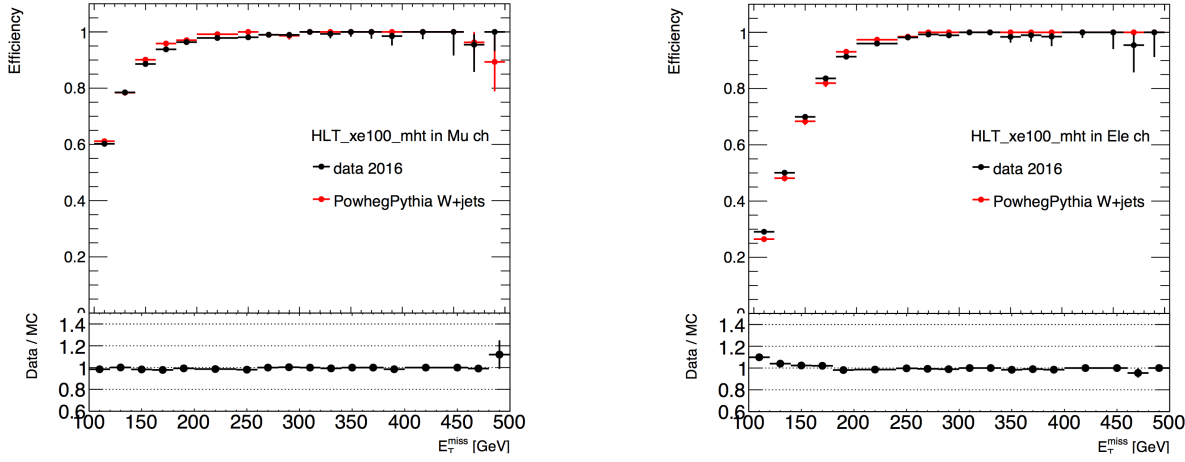


Figure 6.1: Measured and simulated efficiency for HLT_xe100_mht performing the tag-and-probe technique on $W + \text{jets}$ events. The efficiencies in events with (a) exactly one muon, and (b) exactly one electron are shown (by Huajie Cheng).

6.2 Event Cleaning and the Pre-selection

Event cleaning is then applied to get rid of funky data events such as ones in bad detector condition or with unqualified objects including cosmic muons and the beam-induced background. Since those events could result in extraordinary observables, for instance extremely high jet p_T or E_T^{miss} , the contamination in signal regions can be critical even with a few events for the analyses that probes the high-end of kinematics where only a few background events in are expected. The list of cleaning cuts and the efficiencies are shown in Table 6.2.

Firstly, lumi-blocks with more than 10% of any of the sub-detector in the inappropriate status are removed. Events affected by noise bursts in LAr and SCT, corrupted data transmission in LAr and the Tile calorimeter are then vetoed subsequently. Cosmic muon are vetoed by requiring the muon track passing reasonably close-by the primary vertex i.e. $|z_0| < 1 \text{ mm}$, $d_0 < 0.2 \text{ mm}$. The beam induced backgrounds are events with muons that are generated by the secondary cascades of protons traveling upstream of the interaction point. The energy depositions created by these muons can be reconstructed as jets with energy as high as the beam energy therefore becomes highly signal-like. To reject the fake jets, event with jets flagged as “BadLoose” described in [134] are vetoed. High energy muons with poor momentum measurement quality are also a source of fake high MET ranging upto a few TeV. Those are defined by $\sigma(q/p)/(q/p) > 0.2$ where q is muon

Table 6.2: List of event cleaning requirements. Data and MC shows different efficiencies up-to the top four since MC does not emulate bad data quality and cosmic muons in it.

Cut	Efficiency (Data) [%]	Efficiency (MC, $t\bar{t}$) [%]
Veto bad lumi-clocks	95.12	100.0
Veto bad DAQ events	99.81	100.0
Veto events with no primary vertex	100.0	100.0
Veto events with cosmic muons	95.83	98.52
Veto events with badly measured jets	99.49	99.65
Veto events with badly measured muons	99.99	98.56

charge, p the momentum and $\sigma(q/p)$ is the fitting error. The entire events will be vetoed if containing at least one such bad muon. Figure 6.2 demonstrate the performance of the bad muon veto. While the bad muon events typically peak at $\Delta\phi(l, E_T^{\text{miss}}) \sim \pi$ since the fake MET aligns with the muon, it is not the case anymore after the veto.

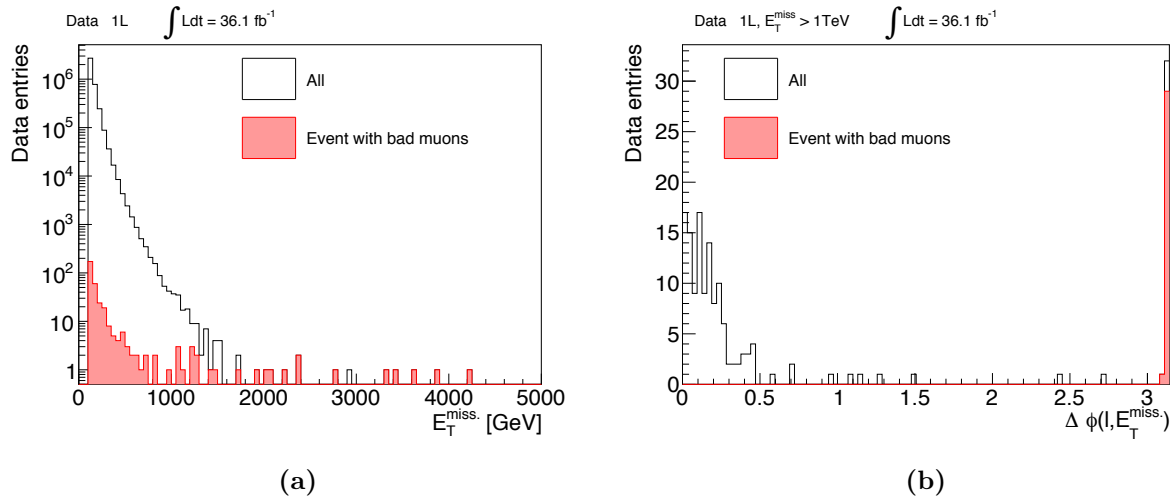
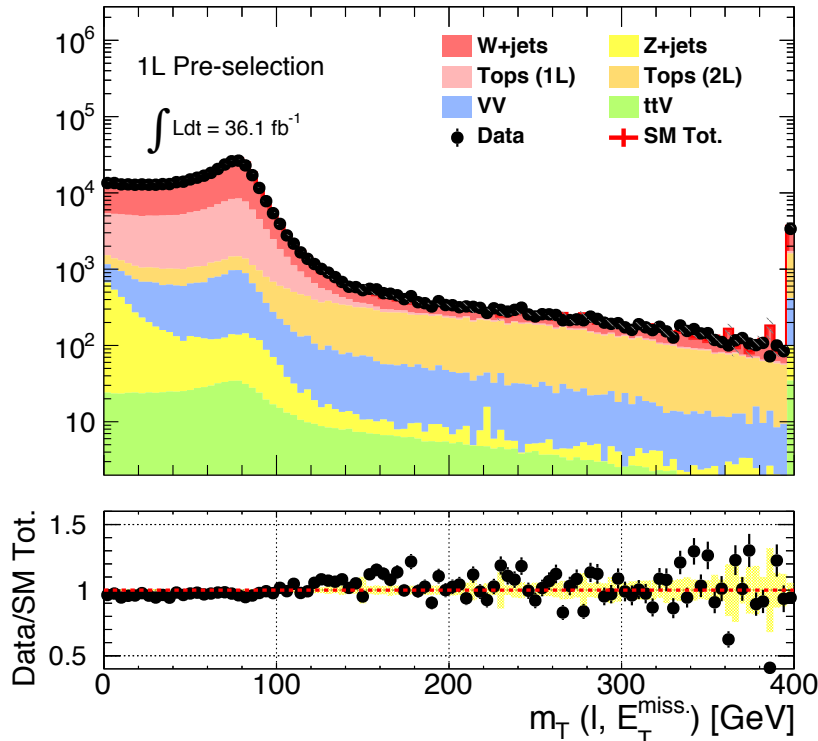


Figure 6.2: (a) E_T^{miss} distribution after requiring exactly one signal muon and MET trigger, and (b) $\Delta\phi(l, E_T^{\text{miss}})$ distribution with $E_T^{\text{miss}} > 1$ TeV being applied. The pink histogram corresponds to events dropped by the bad muon veto. It is shown that the 1-muon high MET phase space generally suffers from severe contamination by bad muon events up to about 20% (90%) with $E_T^{\text{miss}} > 1(2)$ TeV.

The pre-selection is the common selection for all the signal regions in the analysis, which is defined as Table 6.3. Figure 6.3 is a validation plot showing transverse mass (m_T ; invariant mass of lepton p_T and MET) of the data and MC, after the pre-selection being applied.

Table 6.3: List of requirements for the 1-lepton pre-selection.

Event cleaning
Pass the MET trigger and $E_T^{\text{miss}} > 250 \text{ GeV}$
Exactly one signal electron (muon) with $p_T > 7(6) \text{ GeV}$.
At least two jets with $p_T > 30 \text{ GeV}$.

**Figure 6.3:** Transverse mass (m_T ; invariant mass of lepton p_T and MET) distribution after the pre-selection (Table 6.3). The Jacobian peak and the cut-off structure at $m_T \sim m_W$ are clearly seen.

6.3 Signal Region Definition

6.3.1 Binning Strategy

To inclusively address to all the 45 decay chains and all possible mass spectra, a set of tailored multi-bin signal regions (SRs) are employed, based on the following binning strategy:

- split SRs in terms of b -jet multiplicity (“ b -categories”) to cover different gluino decays,
- split SRs in terms of number of jets and lepton- p_T (“towers”) to cover various patterns of the mass spectra.
- split SRs in terms of $m_{\text{eff}} (= E_T^{\text{miss}} + \sum p_T^\ell + \sum p_T^{\text{jet}})$ (“ m_{eff} -bins”) to cover different absolute mass splitting between gluino and LSP.

The SRs are in principle designed to be exclusive for each other, aiming at an easy combination afterward so that no signals are lost due to the binning.

b-categories

The “categories” are defined based on *b*-multiplicity; *b*-vetoed (BV); *b*-tagged (BT); and 3B, as shown in Table 6.4. The customers of these categories are respectively the models in Table 2.5, 2.6 and 2.7 in Sec. 2.5.3, which are referred as “BV”, “BT” and “3B” benchmark models from now on. The *b*-jet multiplicity for the reference signal models and the background at the pre-selection level is shown in Figure 6.4. Note that despite a fraction of signal events falling into other categories than the benchmarked one, they will not be wasted thanks to the combined fit performed in deriving the final result. As the *S/N* ratio and the background kinematics in BV/BT are found to be more or less similar, further kinematical selections in those categories are set to identical for simplicity. On the other hand, different selection strategy is adopted for the 3B categories since the background level is significantly lower and also the composition is very different.

Table 6.4: The definition of the “*b*-categories” and the main backgrounds.

Category	<i>b</i> -jet multiplicity	Main background
<i>B</i> -vetoed (BV)	0	$W + \text{jets}$
<i>B</i> -tagged (BT)	1-2	$t\bar{t}$
3B	≥ 3	$t\bar{t}, t\bar{t} + cc/bb$

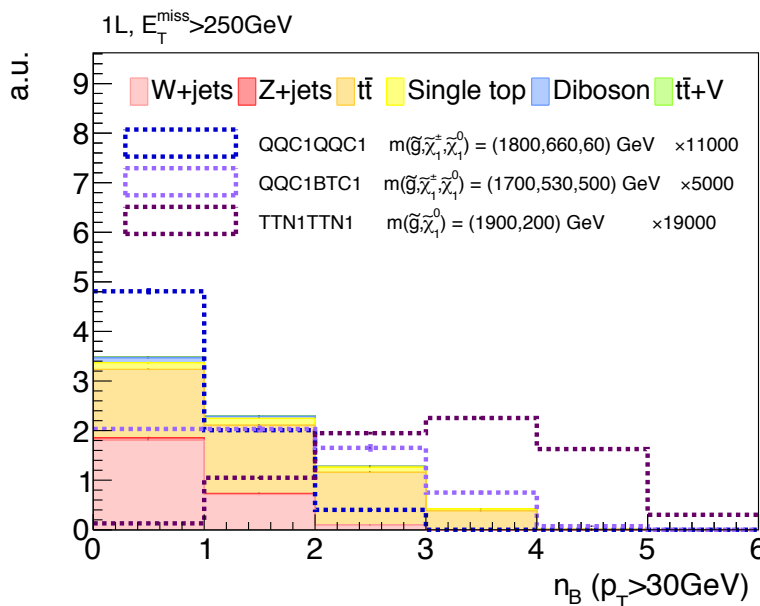


Figure 6.4: *B*-jet multiplicity for the standard model backgrounds (colored stack) and the reference signals after the 1-lepton pre-selection (dashed lines); **QQC1QQC1** for the BV; **QQC1BTC1** for the BT; and **TTN1TTN1** for the 3B category.

Towers

The BV/BT categories are further divided into 4 “towers”, to cope with the four representative configurations of the mass spectra in case of the 1-step decays. The four configurations and resultant observables are schematized in Figure 6.5 with the reference model **QQC1QQC1** being taken as an example, which is namely:

Intermediate EW gaugino is halfway between gluino and LSP ($x \sim 1/2$).¹

This is the most standard configuration where particles from both gluino and the intermediate EW gaugino decays are hard enough to pass the criteria of hard lepton (> 35 GeV) and jets ($p_T > 30$ GeV). As the signals targeted by the BV/BT categories typically result in 4 – 10 jets at the tree-level, a tower **6J** with $n_J \geq 6$ is defined.

Gluino and EW gauginos are all compressed.

From either trigger and background separation point of view, hard ISRs are indispensable for probing this type of signatures so that the $\tilde{g}\tilde{g}$ system gets kicked and resulting in large MET. On the other hand, as the kicked gluinos are typically enough heavy to be non-relativistic, the transverse momentum of the boosted $\tilde{g}\tilde{g}$ system is almost solely converted into MET. As a result the particles from gluino decays stay soft. The **2J** tower consisting of a soft lepton, at least two hard jets and large MET is defined for targeting the signature.

The intermediate EW gaugino and gluino or LSP are compressed ($x \sim 0, 1$).

There are also extreme cases where the intermediate EW gaugino mass is degenerate toward either of gluino or LSP and decoupled from the other. Two signal region towers: **High-x** and **Low-x** are employed to cover the scenarios. Note that the DM-oriented scenario is targeted by tower **Low-x**.

Direct gluino decay models are covered by the towers **2J** and **6J** i.e. **2J** deals with the scenario of compressed mass spectra between gluino and LSP while **6J** takes care of the other cases.

In contrast to the BV/BT category, the 3B does not undergo the additional classification in towers since the targeted signal models usually involve top quarks that can result in hard jets, hard leptons and MET. Therefore the kinematics does not dramatically vary between the mass configurations unless the top-quarks are on-shell. The only exception is when gluino and the intermediate EW gaugino get compressed, and the top-quarks turn to off-shell ending up in only soft particles. However, such events are then covered by the BV and BT towers instead, thanks to the dropped ≥ 3 b -jet acceptance according to the decreasing b -quarks’ p_T .

To summarize, 5 towers (**2J/6J/Low-x/High-x/3B**) are defined in total out of 3 categories (BV/BT/3B) as shown in Table 6.5.

¹ x is defined by Eq. (5.7)

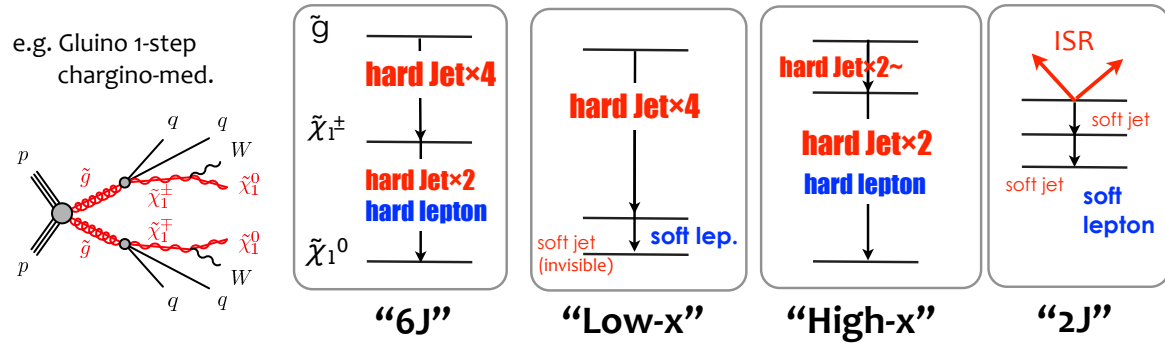


Figure 6.5: The four signal region towers for the BT/BV categories, and their targeted mass configuration.

Table 6.5: List of defined towers in each b -category and the kinematical selection required. **2J** and **6J** (or **Low-x** and **High-x**) are orthogonal to each other. **3B** are orthogonal to all the other towers.

b -category	Tower	Electron (muon) p_T [GeV]	n_J ($p_T > 30$ GeV)
BV/BT	2J	$\in [7(6), 35]$	≥ 2
	6J	> 35	≥ 6
	Low – x	$\in [7(6), 35]$	≥ 4
	High – x	> 35	≥ 4
3B	3B	> 15	≥ 7

m_{eff} -bins

Finally, the towers further experience the binning in terms of m_{eff} defined by the scalar sum of the transverse momenta of leptons and jets, and E_T^{miss} , in order to accommodate different scale of absolute mass splitting $\Delta m(\tilde{g}, \tilde{\chi}_1^0)$. The **2J/6J** and **3B** tower are segmented into 3 and 2 bins respectively, while **Low-x** and **High-x** stay a single bin as their low- m_{eff} -bins have too much overlap with **2J** and **6J**. The bin widths of m_{eff} are chosen to be 400 GeV – 500 GeV based on the width of m_{eff} distribution that targeted signals typical have. The **3B** tower enjoys an exceptionally wider bin width with 750 GeV, compromising with limited of statistics in corresponding control regions.

To conclude, the signal regions end up in 5 tower-structured bins as schematized as Figure 6.6, where 3×2 bins in $m_{\text{eff}} \times (\text{BV/BT})$ reside in the tower **2J** and **6J**; 1×2 bins in **Low-x** and **High-x**; and $2 m_{\text{eff}}$ -bins in **3B**. SRs bins in the towers are orthogonal each other except that **2J** (**6J**) and **Low-x** (**High-x**) are partially overlapped. Figure 6.7-6.8 schematize the mass regions in the signal grids that each tower or bin is supposed to address the sensitivity.

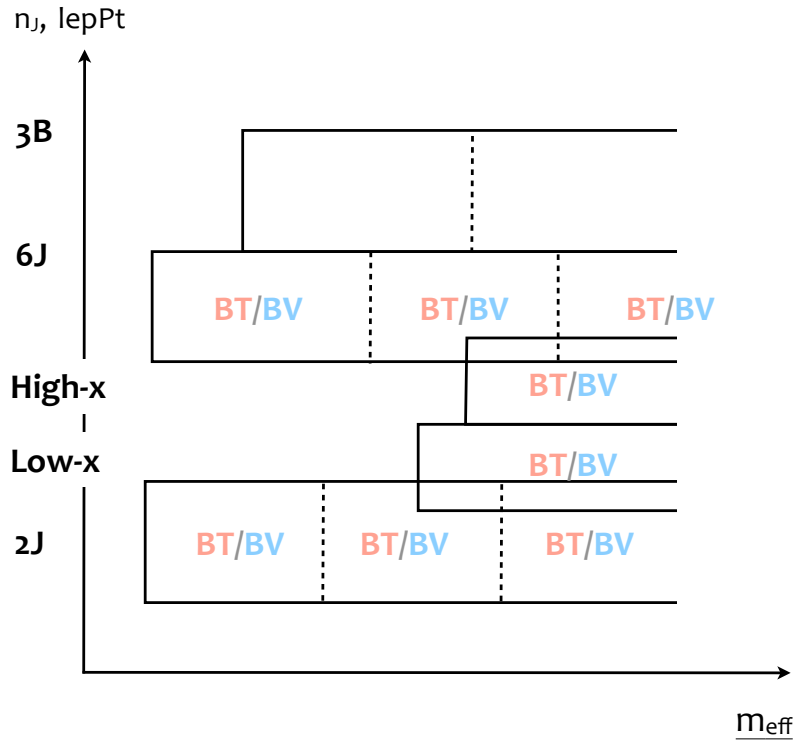


Figure 6.6: Tower structure and the m_{eff} -binning of the signal regions.

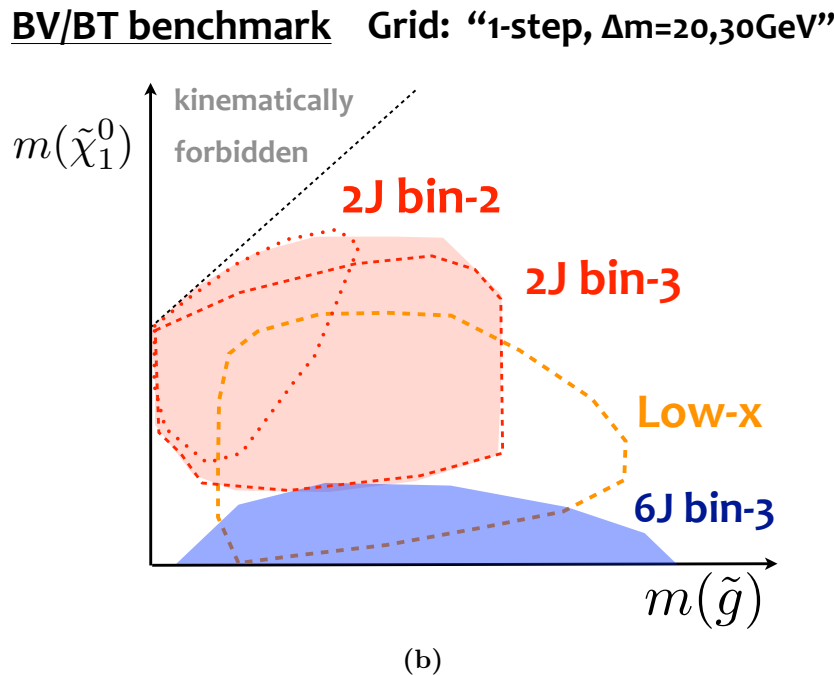
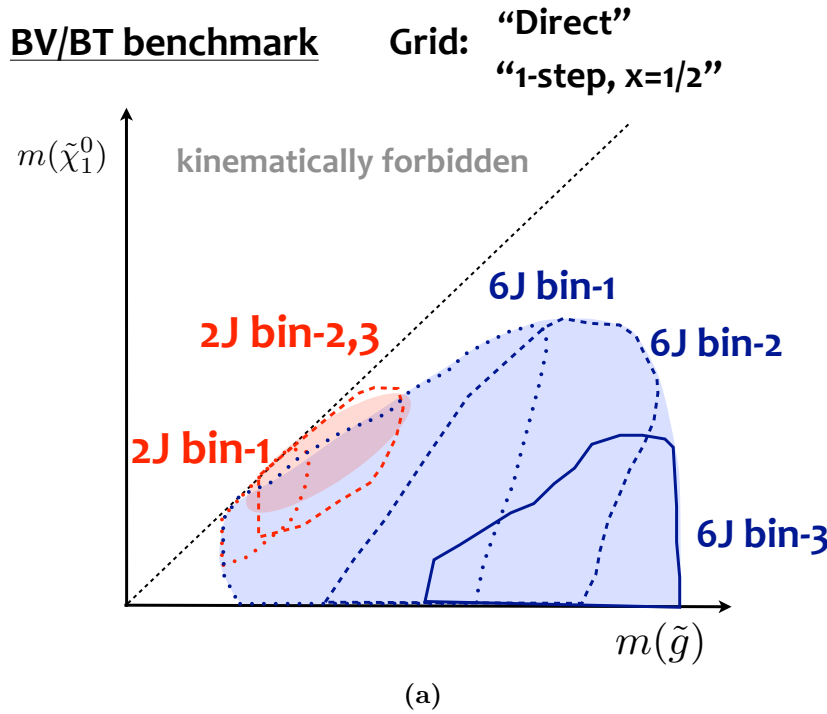


Figure 6.7: Sensitivity coverage by individual signal region towers (shades) or m_{eff} -bins (dashed contours) to the BT/BV benchmark models in the (a) **Direct** and **$x=1/2$** grid, and (b) **DM20**, **DM30** grid.

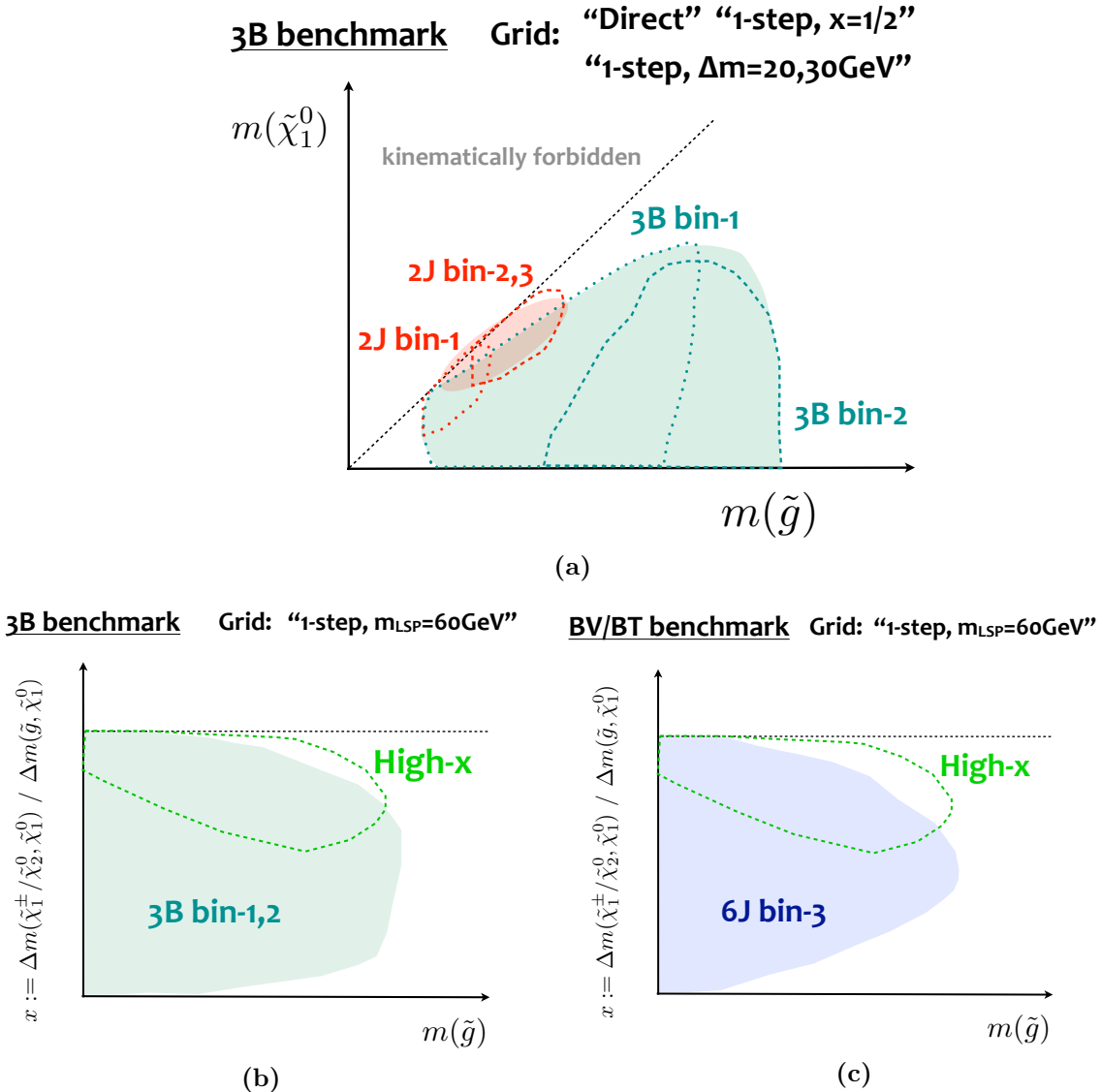


Figure 6.8: Sensitivity coverage by individual signal region towers (shades) or m_{eff} -bins (dashed contours) (a) to the 3B benchmark models in the **Direct**, **$x=1/2$** , **DM20** and **DM30** grids, (b) in the **LSP60** grid, and (c) to the BT/BV benchmark models in the **LSP60** grid.

6.3.2 Discriminating Variables for Background Rejection

While the signal region binning mainly focuses on the signal extraction, further kinematical cuts needs to be applied for dedicated background rejection. This sub-section overviews the kinematical variables used in the analysis for signal region definition. The distributions at the pre-selection are presented in Figure 6.10 - 6.11.²

n_J ($p_T > 30$ GeV) Jet multiplicity often shows a great discriminating power since the standard model processes suffer a sharp cut-off. However one should mind that the optimum cut is significantly dependent on gluino decay modes, and also that the aggressive cut will enhance the contribution from the higher-order effects, putting the background modeling at the risk of theoretical uncertainty. Therefore, the cut is kept moderated as means of background rejection.

E_T^{miss} Signal events with large E_T^{miss} reflects the presence of hard LSPs, therefore E_T^{miss} is very helpful in separation against the background when $\Delta m(\tilde{g}, \tilde{\chi}_1^0)$ is large. At analysis level, this is also true for the compressed case given that the MET via ISRs is nevertheless required for the trigger sake as described above.

m_{eff} m_{eff} is the best discriminating variable against the background. It is also notable that m_{eff} is highly correlated to the absolute mass splitting $\Delta m(\tilde{g}, \tilde{\chi}_1^0)$ irrespective to the relative mass splitting with respect to the intermediate EW gauginos, therefore the same binning can be used between different towers.

m_T($p_T(\ell), E_T^{\text{miss}}$) $m_T(p_T(\ell), E_T^{\text{miss}})$ is defined by the invariant mass between lepton transverse momentum and E_T^{miss} . Analogous to ordinary invariant mass peaking at the mass of the parent particle, the end point of m_T represents the parent mass. Since SM 1-lepton process is always with a leptonically decaying W -boson without additional hard missing particles, the bulk component experiences a sharp cut-off in m_T around $m_W = 81.4$ GeV, therefore the cut above m_W is tremendously effective in background rejection.

Aplanarity Aplanarity [135] is a variable characterizing the 3-dimensionality of an event in terms of the final state particles. It is defined by the third eigenvalue of the normalized momentum tensor S constructed from 3-momenta of jets and leptons:

$$\begin{aligned} S^{\alpha\beta} &:= \frac{\sum_{i \in j,\ell} p_i^\alpha p_i^\beta}{\sum_i |\mathbf{p}_i|^2}, \\ P^{-1}SP &= \begin{pmatrix} \lambda_1 & & \\ & \lambda_2 & \\ & & \lambda_3 \end{pmatrix}, \quad \lambda_1 > \lambda_2 > \lambda_3, \\ \text{Aplanarity} &:= \frac{3}{2} \times \lambda_3, \end{aligned} \tag{6.1}$$

²Some additional pre-selection is applied exceptionally; the soft lepton requirement ($p_T(\ell) \in [6, 35]$) for Figure 6.11 (b), $m_{\text{eff}} > 1500$ GeV for Figure 6.11 (b), and $n_B \geq 3$ $m_T > 125$ GeV are applied for Figure 6.11 (c) and (d).

where P stands for the 3×3 matrix diagonalizing S , and λ_i are the eigenvalues of S . It ranges from $0 < A < 1/2$. While $A = 0$ corresponds to an event with jets distributed in the common plain, $A = 1/2$ represents the isotropically distributed event topology. Aplanarity is an effective discriminator after requiring tight selection in m_{eff} or E_T^{miss} , where the remnant SM events (particularly $W + \text{jets}$) are typically heavily kicked by hard ISRs, leading to a linear event topology in their center-of-mass frame. These events end up in a planar topology in the lab frame once getting boosted toward the beam direction, as a result populating in low aplanarity region accordingly. On the other hand, the decay of gluino pairs keep relatively spherical thus the aplanarity distribution tends to be rather flat, which reflects the fact that gluino is too heavy to be boosted.

$E_T^{\text{miss}}/\mathbf{m}_{\text{eff}}$ $E_T^{\text{miss}}/m_{\text{eff}}$ separates the backgrounds and the signals targeted by the **2J** and **High-x** where jet activity is relatively low compared with the magnitude of MET required.

n_J/p_T(ℓ₁) Since the hardness of lepton and jets are positively correlated in normal processes in SM, it is relatively rare to end up in a soft lepton and hard jet activity simultaneously, while it is the case for the compressed gluino signature. A variable $n_J/p_T(\ell_1)$ helps visualize the different correlations, and used in the **2J** signal region towers to improve the sensitivity towards the compressed gluino signatures.

$\min_{i=1-4} \Delta\phi(\mathbf{j}_i, \mathbf{E}_T^{\text{miss}}) - \min_{i=1-4} \Delta\phi(j_i, E_T^{\text{miss}})$ is a variable intended to reject the remnant $t\bar{t}$ events after requiring tight selection of m_{eff} and E_T^{miss} . As such $t\bar{t}$ events typically have hard ISR jets to boost the $t\bar{t}$ system, the jets from $t\bar{t}$ decays and associated soft radiation tend to be collimated each other. Conversely, the jets from the gluino decays almost never get collimated due to the heavy mass of gluino.

Topness One of the most important background in 1-lepton analysis is di-leptonic $t\bar{t}$ events with a hadronically decaying tau lepton or a lepton that fails the baseline requirement. To reject those events, a χ^2 -based di-leptonic $t\bar{t}$ tagger “topness” has been designed in context of scalar-top search since Run1 [136]. The χ^2 function is defined as:

$$\begin{aligned}
S(p_W^x, p_W^y, p_W^z, p_\nu^z) \\
&= \chi^2(m_{t,1}^2) + \chi^2(m_{t,2}^2) + \chi^2(m_{W,1}^2) + \chi^2(\hat{s}(t\bar{t})) \\
&= \frac{(m_t^2 - (p_{b,1} + p_\ell + p_\nu)^2)^2}{a_t^4} \\
&\quad + \frac{(m_t^2 - (p_{b,2} + p_W)^2)^2}{a_t^4} \\
&\quad + \frac{(m_W^2 - (p_\ell + p_\nu)^2)^2}{a_W^4} \\
&\quad + \frac{(4m_t^2 - (p_\ell + p_\nu + p_{b,1} + p_{b,2} + p_W)^2)^2}{a_{t\bar{t}}^4},
\end{aligned} \tag{6.2}$$

assuming an event topology shown in Figure 6.9 where one of the leptons is totally undetected and the momentum does fully contribute to E_T^{miss} . It consists of four Gaussian constraints expressing

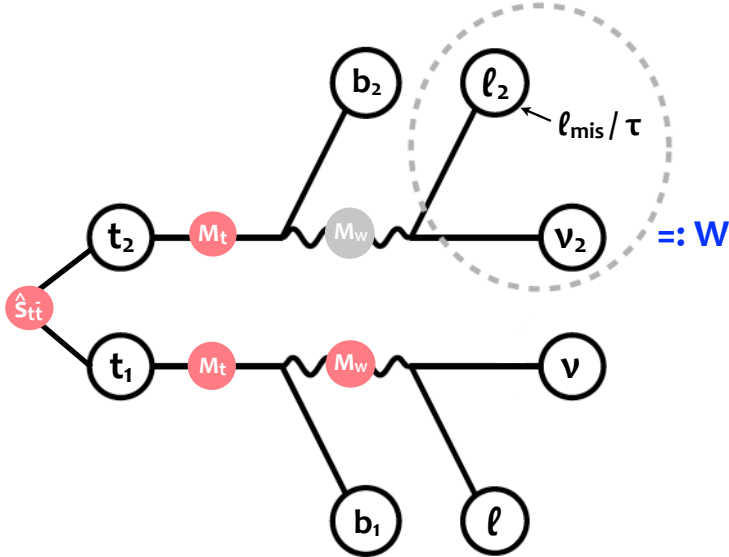


Figure 6.9: Di-leptonic $t\bar{t}$ topology assumed in the topness calculation where one lepton is tagged (ℓ_1) and the other lepton (ℓ_2) is “lost” with its momentum fully contributing to E_T^{miss} .

the mass constraint of a top-quark and a W -boson, and an approximate constraint on the center-of-mass for the $t\bar{t}$ system ($\hat{s}(t\bar{t})$) which peaks at $2m_t$. The width parameters are set to $(a_t, a_W, a_{t\bar{t}}) = (15, 5, 1000)$ GeV, accounting for the Breit-Wigner widths of top-quark and W -boson as well as the tail of $\hat{s}(t\bar{t})$ distribution. Although there are three missing particles in the topology, the number of unknown degree of freedom can be reduced into 4 by combining the missing lepton (ℓ_2) and the paired neutrino (ν_2) into a single on-shell W -boson and imposing the vectoral sum of transverse momenta of missing particles being equal to E_T^{miss} . Topness is then defined as the minimum χ^2 when scanning over the four DOFs (p_W and p_ν^z):

$$\text{Topness} := \min_{p_W^x, p_W^y, p_W^z, p_\nu^z} \ln[S]. \quad (6.3)$$

Events in the topology assumed are supposed to have solutions $(p_W^x, p_W^y, p_W^z, p_\nu^z)$ that satisfy the four constraints at the same time, however it is not necessarily the case for the other events. Figure 6.9 shows the typical separation between di-leptonic $t\bar{t}$ and signals, where the majority of di-leptonic $t\bar{t}$ resides on the lower pile while signals typically populate in the opposite one. Note that the di-leptonic $t\bar{t}$ in the higher pile are due to the fact that the energy of missing leptons or tau leptons does not entirely contribute to E_T^{miss} , violating the assumption made in Figure 6.9.

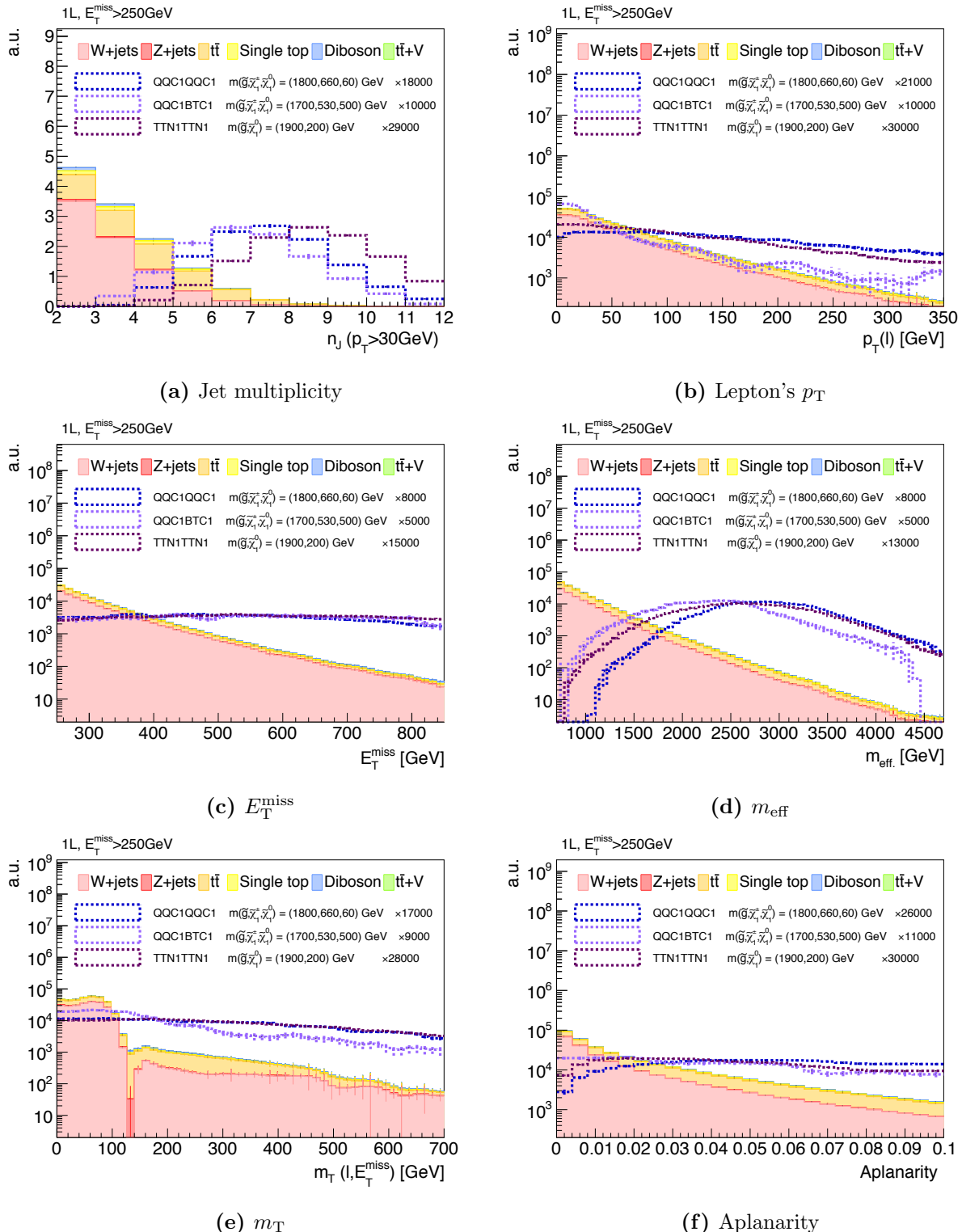


Figure 6.10: Distributions of discriminating variables for reference signal and background, at the pre-selection level.

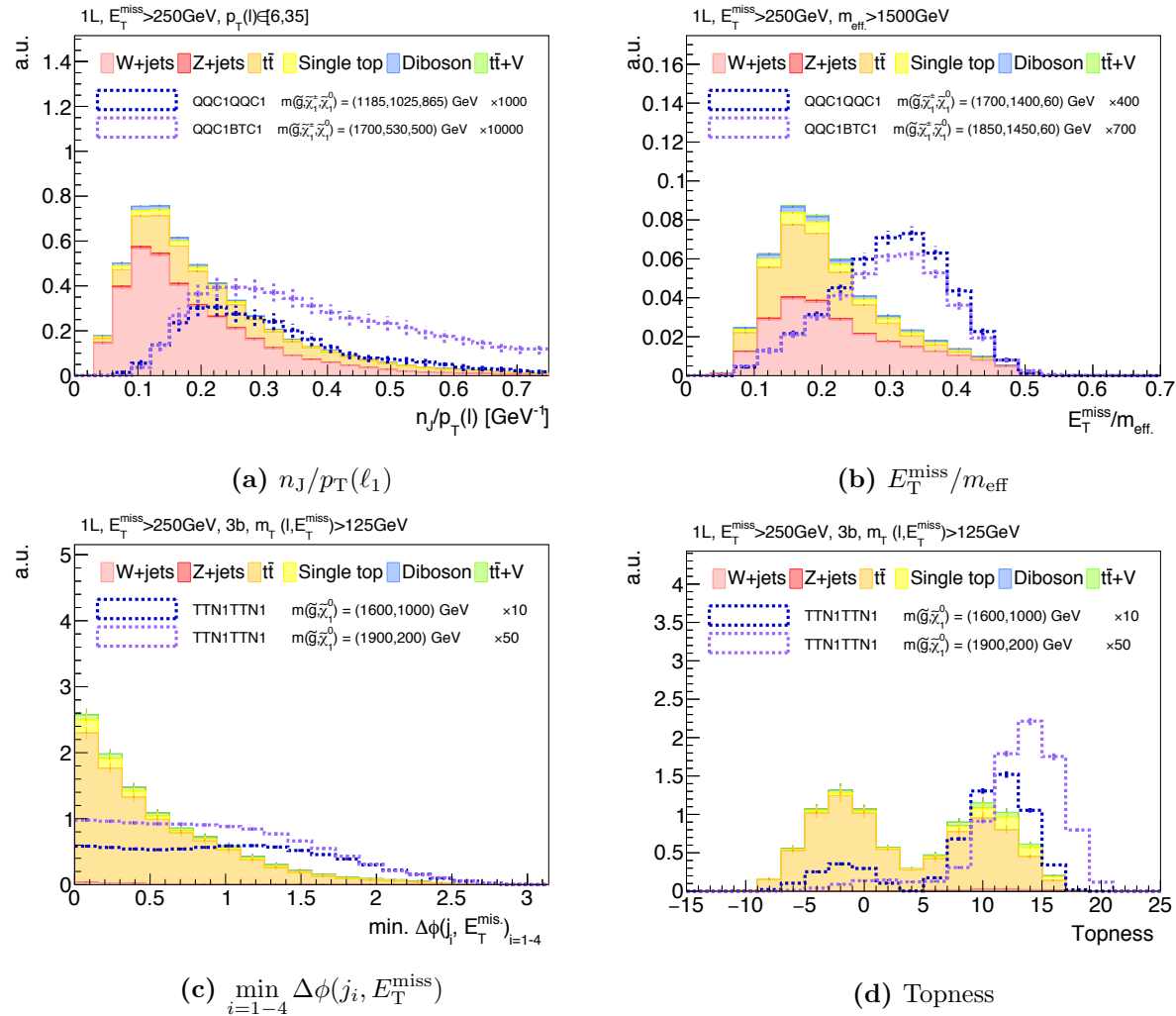


Figure 6.11: Distributions of discriminating variables at the pre-selection level. Soft lepton requirement: $p_T(\ell) \in [6, 35]$ is applied for (b), and $n_B \geq 3$ $m_T > 125$ GeV is applied for (c) additionally.

6.3.3 Cut Optimization

The cut values for the kinematic variables introduced above are optimized. Reference signal points are used for the optimization which are defined in Table 6.6. The optimization procedure proceeds as following:

1. The binning of m_{eff} is roughly decided so that the sensitivities for all the reference points in the same tower are well addressed.
2. Cuts values in other variables are then optimized by a simultaneous grid scan using machinery. The initial values are chosen based on the target mass regions of each signal region (as depicted by Figure 6.7-Figure 6.8), and the typical kinematics of such signals as shown in Figure B.1.1-B.1.4 in Appendix B.1. The sensitivity as the measure of the optimization is defined by the combined significance over the m_{eff} -bins such as:

$$Z_{N,\text{comb.}} = \sqrt{\sum_i Z_{N,i}^2} \quad (6.4)$$

(6.5)

where $Z_{N,i}$ is the significance that a single m_{eff} -bin addresses:

$$Z_{N,i} := S_i / \sqrt{B_i + \alpha^2 B_i^2}. \quad (6.6)$$

S_i , B_i are respectively the signal and background yields in the m_{eff} -bin i . α is relative uncertainty on the background expectation. This is fixed to 30% in the study, which is the typical level of systematic uncertainty. The cuts between BT and BV bins in the same tower and the same m_{eff} -bin are always set to common.

3. All the cuts including the m_{eff} -binning are re-optimized by perturbing the best cuts found in the previous step.
4. Another minor adjustment is done afterwards for sake of easier background estimation, where typically some of the cuts are loosened to facilitate the secure the control region statistics.

Finalized definition of signal regions are shown in Table 6.7-6.11. The m_{eff} distribution in the optimized signal regions are displayed in Figure 6.12-6.16 . The segmentation of m_{eff} -bin is found to successfully address the sensitivity in different mass region in the signal grid.

The optimized selection is also validated by checking the kinematic distributions in which one of the cuts is removed from the optimized signal region (“N-1 plots”). Figure B.2.1-B.2.9 in the appendix B.2 show the N-1 plots for each signal region, where the sensitivity is calculated as function of the cut position of the removed cut. The decided cut positions are indicated by the red arrows, which more or less accord with the optimum position for all the reference signals.

Table 6.6: The reference signal points for each signal region to which the cuts are optimized to.

Model	$(m_{\tilde{g}}, m_{\tilde{\chi}_1^\pm}, m_{\tilde{\chi}_1^0}), (m_{\tilde{g}}, m_{\tilde{\chi}_1^0})$ [GeV]
2J BV	
QQC1QQC1	(1550,580,550)
QQC1QQC1	(1065,1025,985)
TTN1TTN1	(1000,915)
2J BT	
QQC1BTC1	(1400,830,800)
QQC1BTC1	(1550,780,750)
6J BV	
QQC1QQC1	(1945,1105,265)
QQC1QQC1	(1850,1350,850)
QQC1QQC1	(1700,1300,900)
6J BT	
QQC1BTC1	(1850,1050,250)
QQC1BTC1	(1700,1300,900)
Low - x BV	
QQC1QQC1	(1700,460,60)
QQC1QQC1	(1600,260,60)
QQC1QQC1	(1700,530,500)
Low - x BT	
QQC1BTC1	(1700,730,700)
QQC1BTC1	(1700,530,500)
High - x BV	
QQC1QQC1	(1800,1600,60)
QQC1QQC1	(1800,1460,60)
QQC1QQC1	(1800,1260,60)
High - x BT	
QQC1BTC1	(1850,1750,60)
QQC1BTC1	(1850,1450,60)
3B	
TTN1TTN1	(2000,0)
TTN1TTN1	(1900,800)
TTN1TTN1	(1500,1000)

Table 6.7: Definition of signal/control/validation regions (SRs/CRs/VRs) for tower "2J"

	SR (BV/BT)	WR/TR	VR E_T^{miss}	VRb	VR QCD
$n_{\ell,\text{base.}}$	1	1	1	1	1
$n_{\ell,\text{sig.}}$	1	1	1	1	0
$p_T(\ell)$			[6, 35]		
$n_J (p_T > 30 \text{ GeV})$			≥ 2		
$n_B (p_T > 30 \text{ GeV})$	0/[1,2]	0/[1,2]	-	-	-
m_{eff}			[1100, 1500], [1500, 1900], > 1900		
E_T^{miss}	> 430	[250, 430]	[250, 430]	> 430	> 430
$m_T(p_T(\ell), E_T^{\text{miss}})$	> 100	[30, 100]	> 100	[30, 100]	> 100
$E_T^{\text{miss}}/m_{\text{eff}}$	> 0.25	> 0.15	> 0.1	> 0.2	> 0.25
$n_J/p_T(\ell)$		> 0.2	> 0.15		> 0.2
Topness	> 4	-	-	> 4	> 4

Table 6.8: Definition of signal/control/validation regions (SRs/CRs/VRs) for tower "6J"

	SR (BV/BT)	WR/TR	VRa	VRb	VR QCD
$n_{\ell,\text{base.}}$	1	1	1	1	1
$n_{\ell,\text{sig.}}$	1	1	1	1	0
$p_T(\ell)$			> 35		
$n_J (p_T > 30 \text{ GeV})$			≥ 6		
$n_B (p_T > 30 \text{ GeV})$	0/[1,2]	0/[1,2]	-	-	-
m_{eff}			[1100, 1600], [1600, 2100], > 2100		
E_T^{miss}	> 350	> 300	> 250	> 350	> 350
$m_T(p_T(\ell), E_T^{\text{miss}})$	> 175	[40, 125]	[125, 400]	[40, 125]	> 125
Aplanarity	> 0.06	< 0.06	< 0.04	> 0.06	> 0.06
Topness	> 4	-	-	> 4	> 4

Table 6.9: Definition of signal/control/validation regions (SRs/CRs/VRs) for tower "Lowx"

	SR (BV/BT)	WR/TR	VRa	VRb	VR QCD
$n_{\ell,\text{base.}}$	1	1	1	1	1
$n_{\ell,\text{sig.}}$	1	1	1	1	0
$p_T(\ell)$			[6, 35]		
$n_J (p_T > 30 \text{ GeV})$			≥ 4		
$n_B (p_T > 30 \text{ GeV})$	0/[1,2]	0/[1,2]	-	-	-
m_{eff}			> 1900		
$p_T(j_4)$			> 80		
E_T^{miss}	> 350	> 300	> 300	> 350	> 350
$m_T(p_T(\ell), E_T^{\text{miss}})$	> 100	[30, 100]	[100, 450]	[30, 100]	> 100
Aplanarity	> 0.02	< 0.02	< 0.02	> 0.02	> 0.02
Topness	> 4	-	-	> 4	> 4

Table 6.10: Definition of signal/control/validation regions (SRs/CRs/VRs) for tower "Highx"

	SR (BV/BT)	WR/TR	VRa	VRb	VR QCD
$n_{\ell,\text{base.}}$	1	1	1	1	1
$n_{\ell,\text{sig.}}$	1	1	1	1	0
$p_T(\ell)$			> 35		
$n_J (p_T > 30 \text{ GeV})$			≥ 4		
$n_B (p_T > 30 \text{ GeV})$	0/[1,2]	0/[1,2]	-	-	-
m_{eff}			> 2000		
E_T^{miss}	> 300	> 300	> 300	> 300	> 300
$m_T(p_T(\ell), E_T^{\text{miss}})$	> 300	[30, 125]	[125, 600]	[30, 125]	> 450
$E_T^{\text{miss}}/m_{\text{eff}}$	> 0.25	> 0.2	> 0.15	> 0.25	> 0.25
Aplanarity	> 0.01	< 0.01	< 0.01	> 0.01	> 0.01
Topness	> 4	-	-	> 4	> 4

Table 6.11: Definition of signal/control/validation regions (SRs/CRs/VRs) for tower "3B"

	SR	TR	VR m_T	VRb	VR QCD
$n_{\ell, \text{base.}}$	1	1	1	1	1
$n_{\ell, \text{sig.}}$	1	1	1	1	0
$p_T(\ell)$			> 15		
$n_J (p_T > 30 \text{ GeV})$			≥ 7		
$n_B (p_T > 30 \text{ GeV})$			≥ 3		
m_{eff}			[1000, 1750], > 1750		
E_T^{miss}	> 300	> 250	> 250	> 250	> 300
$m_T(p_T(\ell), E_T^{\text{miss}})$	> 175	[30, 125]	[125, 450]	[30, 125]	> 175
Aplanarity	> 0.01	-	-	> 0.01	> 0.01
$\min_{i=1-4} \Delta\phi(j_i, E_T^{\text{miss}})$	> 0.45	< 0.45	< 0.45	> 0.3	> 0.45
Topness	> 6	-	-	> 6	> 6

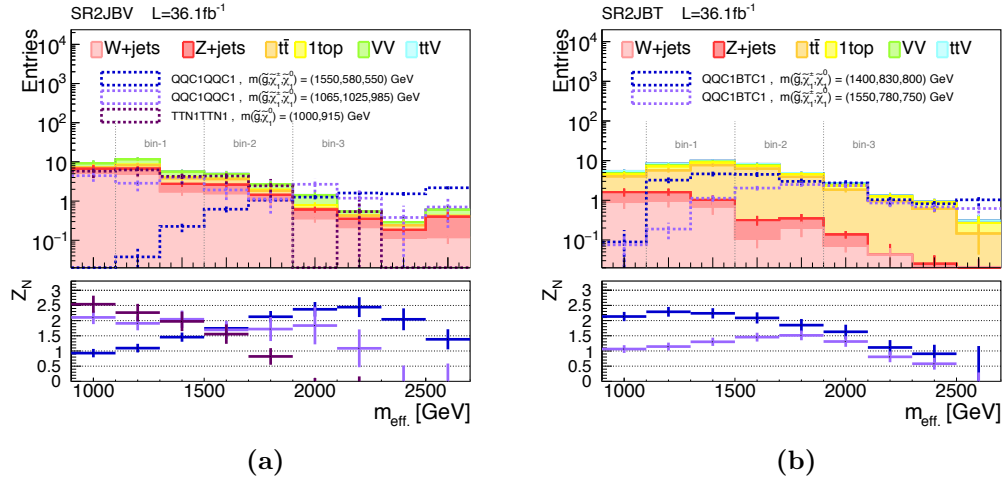


Figure 6.12: m_{eff} distribution in the (a) b-vetoed (BV) and (b) b-tagged (BT) slices of the optimized **2J** signal region. Bottom row display the sensitivity $Z_N := S/\sqrt{B + \alpha^2 B^2}$ for each reference signals.

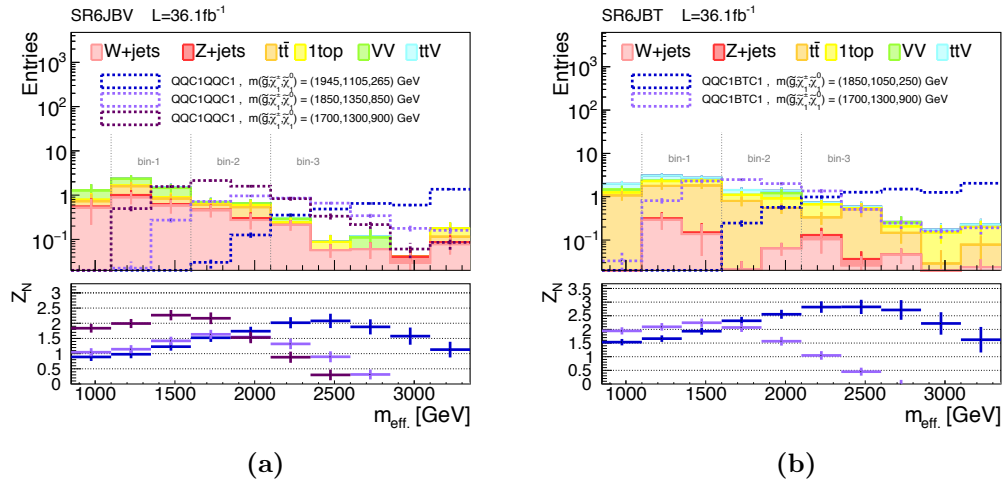


Figure 6.13: m_{eff} distribution in the (a) b-vetoed (BV) and (b) b-tagged (BT) slices of the optimized **6J** signal region. Bottom row display the sensitivity $Z_N := S/\sqrt{B + \alpha^2 B^2}$ for each reference signals.

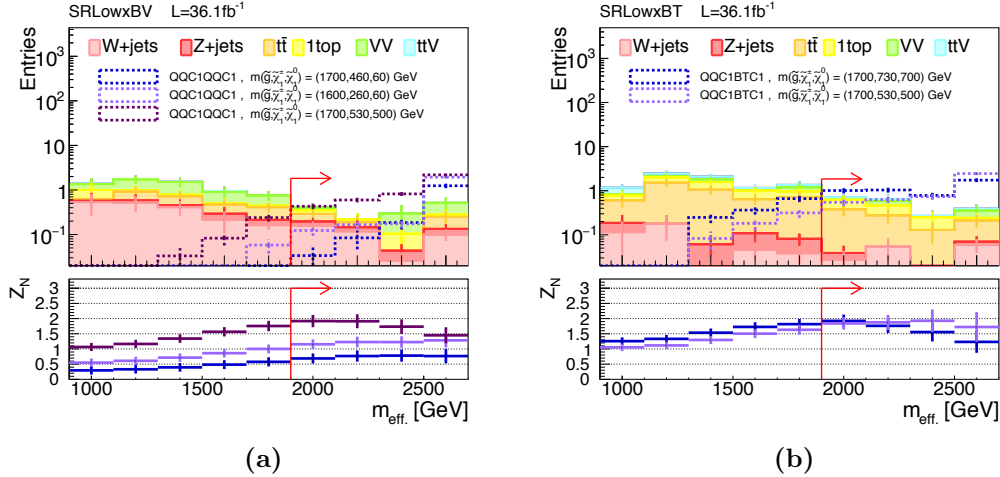


Figure 6.14: m_{eff} distribution in the (a) b-vetoed (BV) and (b) b-tagged (BT) slices of the optimized **Low-x** signal region. The red arrow indicates the cut position of m_{eff} . Bottom row display the sensitivity $Z_N := S/\sqrt{B + \alpha^2 B^2}$ for each reference signals.

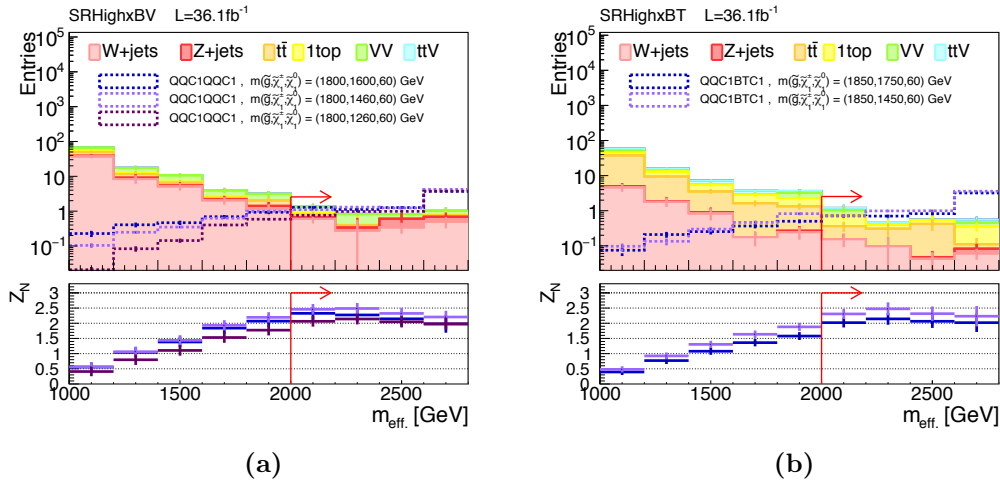


Figure 6.15: m_{eff} distribution in the (a) b-vetoed (BV) and (b) b-tagged (BT) slices of the optimized **High-x** signal region. The red arrow indicates the cut position of m_{eff} . Bottom row display the sensitivity $Z_N := S/\sqrt{B + \alpha^2 B^2}$ for each reference signals.

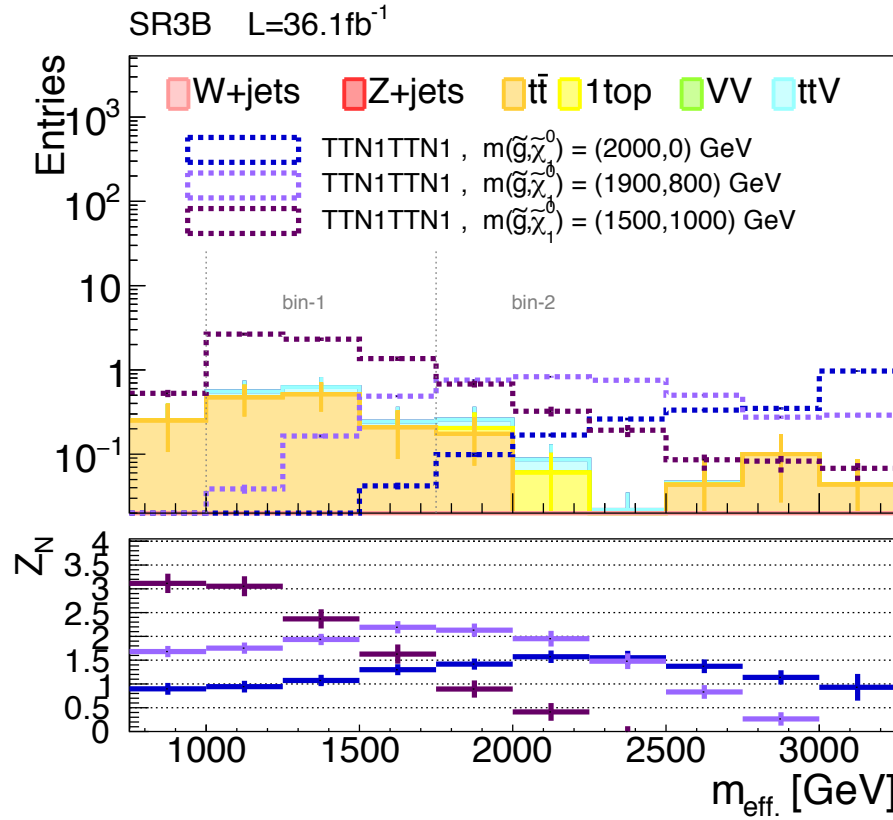


Figure 6.16: $m_{\text{eff.}}$ distribution in the (a) b-vetoed (BV) and (b) b-tagged (BT) slices of the optimized **3B** signal region. Bottom row display the sensitivity $Z_N := S/\sqrt{B + \alpha^2 B^2}$ for each reference signals.

6.3.4 Expected Sensitivity

The limits expected by the optimized signal regions are calculated for the reference models using the simulation normalized to an integrated luminosity of $L = 36.1\text{fb}^{-1}$. The expected exclusion limit for the **TTN1TTN1 Direct** grid is shown in 6.17. The dashed lines on the left plots indicate the exclusion provided by a single m_{eff} -bin, and the solid lines being the limit given by respective signal region towers with combined bins. The ultimately sensitivity provided by the combined towers are shown in the right plots. Since the all five towers are not completely orthogonal (**2J** and **Low-x**, **6J** and **High-x** are partially overlapped), there are four possible ways of combining orthogonal towers: **{2J, 6J, 3B}**, **{2J, High-x, 3B}**, **{Low-x, 6J, 3B}**, and **{Low-x, High-x, 3B}**. The final result is provided using the combination giving the best expected sensitivity. The expected sensitivity for **QQC1QQC1** and **QQC1BTC1** are presented in Figure 6.18 and Figure 6.19. Nice complementarity between the signal region towers and m_{eff} -bins are demonstrated. No suspicious structure indicating local over-optimization onto specific mass or decay models is found, ensuring the inclusive sensitivity of the analysis.

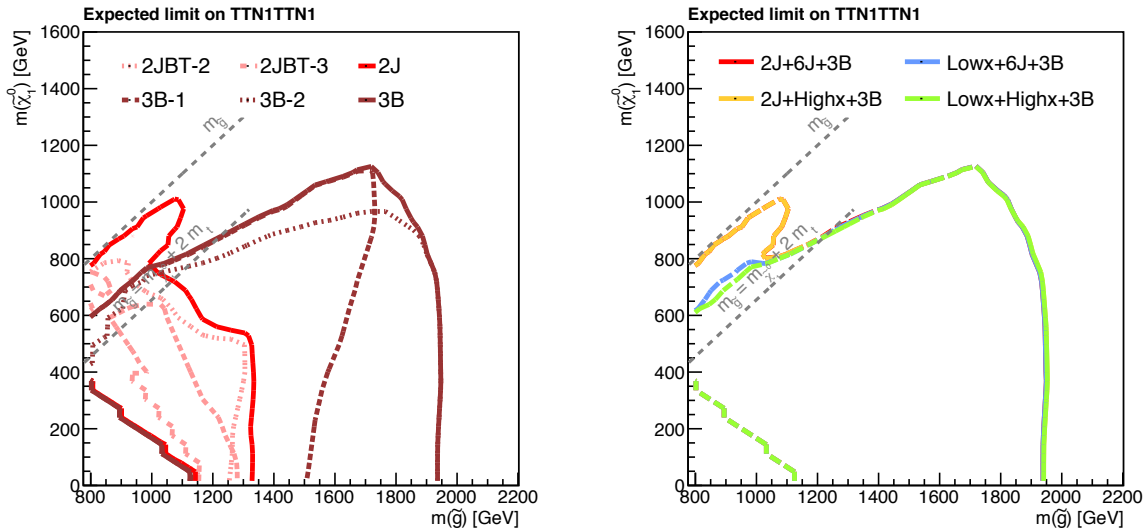


Figure 6.17: Expected exclusion (95%CL) for the benchmark model **TTN1TTN1**. The left plot shows the exclusion limits set by individual signal region m_{eff} -bin (dashed lines) or a tower (solid lines). The contours in the right plot display the ultimate sensitivity provided by the combined fit. The hypothetical test will be carried out using the best performed combination in deriving the final result.

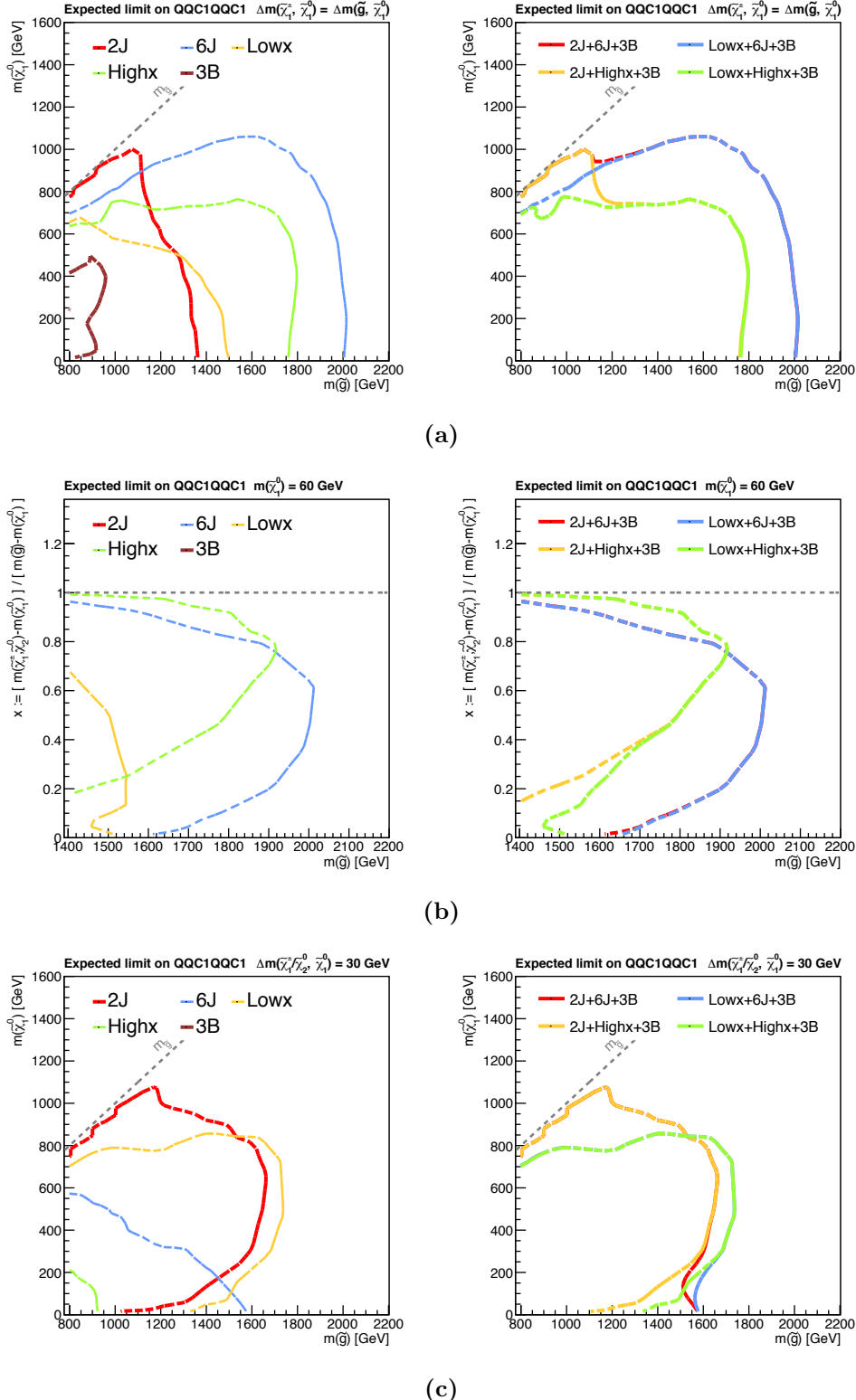


Figure 6.18: Projected expected exclusion (95%CL) for the benchmark model **QQC1QQC1** onto the (a) $x = 1/2$ (b) $m_{\tilde{\chi}_1^0} = 60$ GeV (c) $\Delta m(\tilde{\chi}_1^\pm, \tilde{\chi}_1^0) = 30$ GeV grid. The contours in the right plot display the ultimate sensitivity provided by the combined fit. The hypothetical test will be carried out using the best performed combination in deriving the final result.

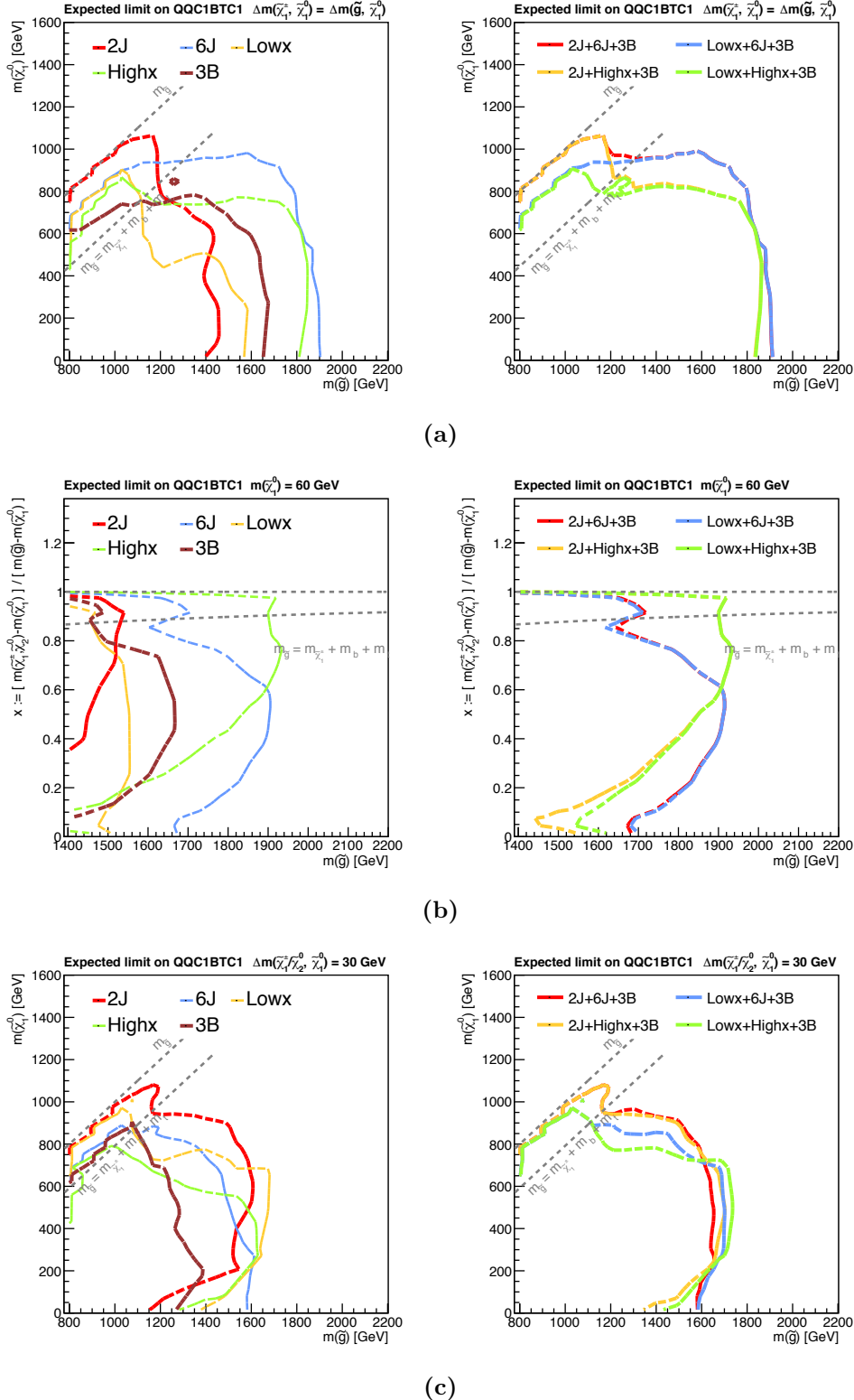


Figure 6.19: Projected expected exclusion (95%CL) for the benchmark model **QQC1BTC1** onto the (a) $x = 1/2$ (b) $m_{\tilde{\chi}_1^0} = 60$ GeV (c) $\Delta m(\tilde{\chi}_1^\pm, \tilde{\chi}_1^0) = 30$ GeV grid. The contours in the right plot display the ultimate sensitivity provided by the combined fit. The hypothetical test will be carried out using the best performed combination in deriving the final result.

Chapter 7

Background Estimation

Due to the enormously large cross-section of SM processes with respect to the signal, it is the fate for new physics searches to keep exploring the phase space with tight event selections. The consequence is the highly untypical kinematics for the remained SM backgrounds, and the modeling is usually challenging since the standard MC simulation is not necessarily accountable as seen in Sec. 7.2.1.

This is why (semi-)data-driven approach is remarkably motivated in search analyses. The most commonly done practice over the past analyses is to apply an in-situ correction to MC using the data events around the signal region (“control region”). The prediction in signal regions is then given by the corrected MC, assuming the modeling on the phase space between the control region and the signal region is correct. We refer this semi-data driven method as “**kinematical extrapolation method**”. The advantage of the kinematical extrapolation method is that the prediction does not suffer from severe statistical fluctuation, and often leading to relatively smaller total uncertainty. However the drawback is that it has to still rely on MC in the extrapolation from control regions to signal regions, which uncertainty is rather difficult to capture and quantify.

Since statistical error often dominates the uncertainty in the signal regions, it has no point in competing on a few percent precision in the estimation. Instead, it is more sensible to pursue the robustness avoiding risk to introducing unknown systematic effects, even if it will result in larger estimation uncertainty. A nearly fully data-driven method (“**object replacement method**”) is meant to that purpose, estimating particular background components by extrapolating from the 2-lepton control regions. In the study, the object replacement method is utilized as much as possible, while the rest of all is covered by the kinematical extrapolation method.

This section provides a complete description on the background estimation procedures employed in the analysis. After reviewing the breakdown in the signal regions and how they evade the event selection, both estimation methods will be described in detail. Finally, the performance is demonstrated using the data in a certain set of regions.

7.1 Background Breakdown in the Signal Regions

The breakdown of physics processes in the signal regions are shown in Figure 7.1. $W + \text{jets}$ and top backgrounds ($t\bar{t} + Wt$, mostly $t\bar{t}$) dominate over the b -tagged and b -vetoed regions respectively. The **3B** towers are completely dominated by $t\bar{t}$, where 60 % of them are with heavy flavor jets via radiative gluon splitting ($t\bar{t} + cc/bb$) while the rest are with one light flavor jet or hadronically decaying τ faking into b -tagged jet ($t\bar{t} + b_{\text{fake}}$).

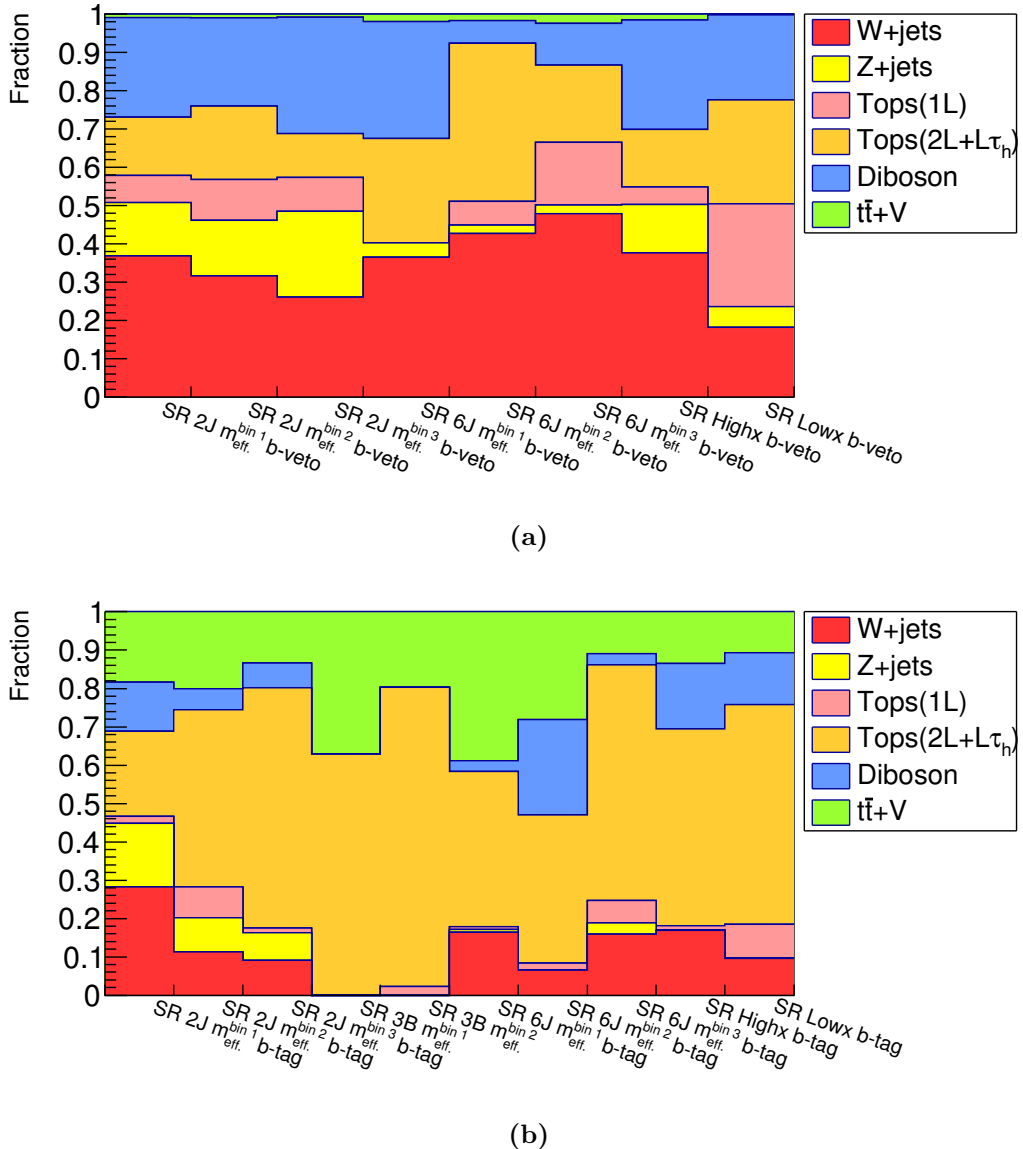


Figure 7.1: Background composition in terms of physics processes in the (a) BV, and (b) BT/3B signal regions. $t\bar{t}$ and single-top are merged as “Tops”, and the semi-leptonic and di-leptonic components are respectively labeled as “1L” and “ $2L + L\tau_h$ ”.

Backgrounds are also categorized depending on the mechanism they pass the selection, and different estimation methods are applied based on it. The categorization is shown in Table 7.1.

Table 7.1: Background classification in terms of the origin.

Category		Origin	Main physics process	Estimation method
“Semi-leptonic”		On-shell W with diluted m_T / High-mass Drell-Yan	$(W, t\bar{t}, VV) \rightarrow \ell\nu + \text{jets}$	Kine. extp. / MC
“Di-leptonic”	$\ell\ell_{\text{mis.}}$	“Out Acc.” “Mis. Reco.” “Mis. ID” “Mis. OR”	$(t\bar{t}, Wt, WW) \rightarrow \ell\nu\ell\nu + \text{jets}$	Kine. extp. Obj. rep. Obj. rep. Kine. extp.
	$\ell\tau_h$	1 real-lepton + τ_h	$t\bar{t}, Wt, WW \rightarrow \ell\nu\tau\nu + \text{jets}$	Obj. rep.
“Fake”		0 real-lepton + 1 fake-lepton.	$W \rightarrow \tau\nu, Z \rightarrow \nu\nu$	MC

The “**semi-leptonic**” category is defined by events with exactly one real light flavor lepton (e or μ). In the SM, these are uniquely provided by processes with leptonically decaying W-boson, such as from $W + \text{jets}$ and $t\bar{t}$. This is by far the dominant component at 1-lepton pre-selection level, however is drastically suppressed after a tight m_T cut since they are largely truncated at m_W . After the m_T cut, the remnant events are typically either: 1) Drell-Yan process with virtual heavy intermediate W boson, or 2) events with badly measured MET leading to prolonged tail in m_T . The former contribution is typically larger although the latter becomes addressing with increasing jet activity, as shown in Figure 7.2. In this category, the dominant processes $W + \text{jets}$ and $t\bar{t} + Wt$ are estimated by a semi-data driven approach referred as “kinematical extrapolation method” as detailed in following sub-section, while the other processes are taken from pure MC prediction since they are minor.

The “**di-leptonic**” category consists of processes with real two leptons including τ , mainly from di-leptonic decaying $t\bar{t}$, Wt and WW . The presence becomes highly significant with respect to the “semi-leptonic” after the m_T cut, since the source of missing transverse momentum is multiple thus they have no reason to cut-off at m_W . They fall into 1-lepton regions through two channels, namely 1) “ $\ell\ell_{\text{mis.}}$ ” (“missing lepton”): events with two real light flavor leptons and one of them fails the “baseline” requirement (See Sec. 4.10), and “ $\ell\tau_h$ ”: events with a real light flavor lepton and a hadronically decaying tau lepton. The origin of “missing lepton” is further four-fold and symbolized as follow:

“Out Acc.”

Leptons traveling outside the acceptance of “baseline” requirement i.e. $p_T > 7(6)$ GeV, $|\eta| < 2.47(2.5)$ for electrons (muons). ¹

“Mis. Reco”

Leptons within the (p_T, η) acceptance but failing the reconstruction.

“Mis. ID”

Reconstructed leptons within the (p_T, η) acceptance but failing the electron/muon ID.

¹Defined by the momenta of truth leptons in the MC.

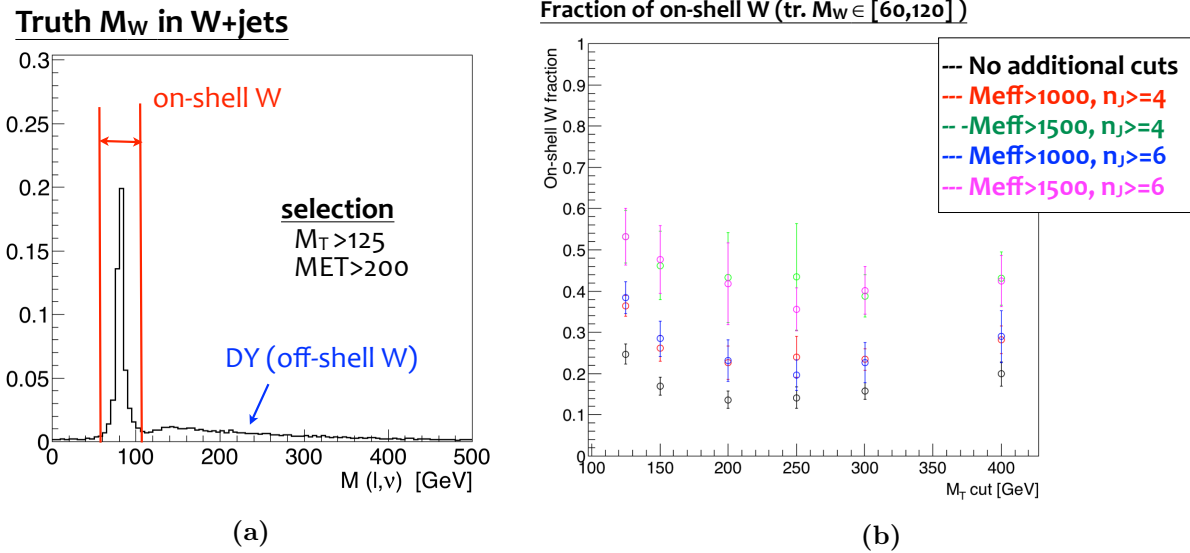


Figure 7.2: (a) Truth invariance mass $m(\ell, \nu)$ of high- m_T $W + \text{jets}$ events. Ideally there are only high-mass Drell-Yan type of events, however due to the finite detector resolution, a fraction of on-shell W events with badly measured MET sneak into regions with $m_T > m_W$. (b) The fraction of on-shell events defined by $m(\ell, \nu) \in [60, 125]$, as a function of the m_T cut. It is generally below 50 %, however increases with higher jet activity in the event.

“Mis. OR”

Reconstructed leptons within the (p_T, η) acceptance passing the ID, but overlapped with light-flavor jets by $\Delta R < 0.4$.² which are likely to be killed in the overlap removal (Sec. 4.7).

One nice thing about this “di-leptonic” component is that 2-lepton regions are available for control regions in the estimation. Since no signal regions are set there, exactly the same phase space with respect to SRs can be exploited. The estimation is done by the “object replacement method”, however the “Out Acc.” and “Mis. OR” events are estimated together with the “semi-leptonic” events due to some technical challenges. The third category “fake” involves events with a fake lepton, which is not negligible in regions dealing with soft leptons (**2J** and **Low-x**). The estimation fully relies the MC prediction. Dominant contribution is from $W \rightarrow \tau\nu$ and $Z \rightarrow \nu\nu$ which accompany a large MET from neutrinos. The contribution from the multi-jets process is supposed to be negligible, it is nevertheless dedicatedly cross-checked since the impact could be hazardous due to the huge cross-section. This is done using a series of validation regions referred as VRs-QCD, shown in Appendix C.3.

The background breakdown based on this categorization is summarized in Figure 7.3 where “semi-leptonic” and “di-leptonic” (particularly “ $\ell\tau_h$ ”) are shown to be overwhelmingly dominant in BV and BT/3B signal regions respectively.

²using the 85% b -tagging efficiency working point, in order to be consistent with the b -tagging used in the overlap removal 4.7.

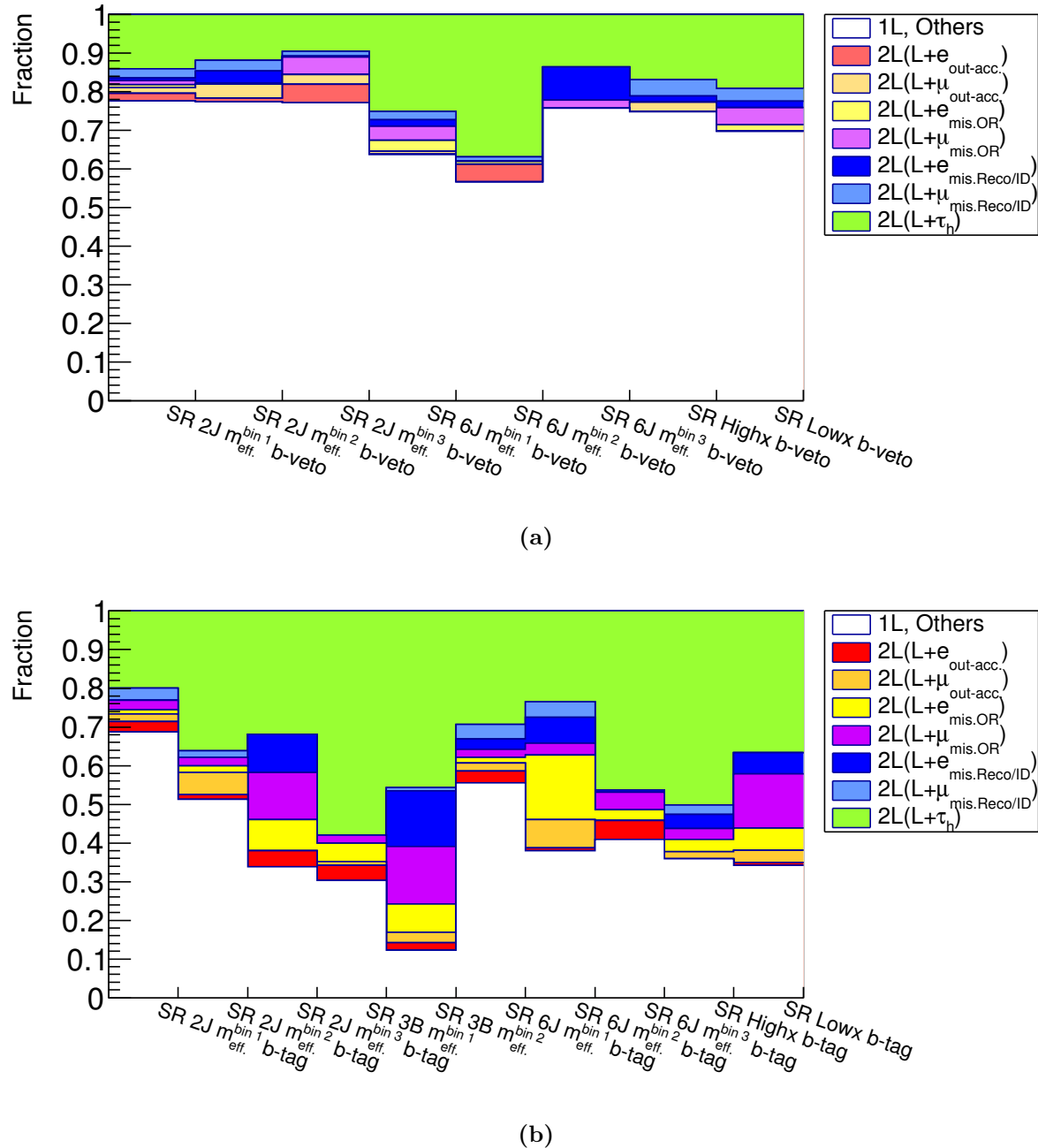


Figure 7.3: Background breakdown in the (a) BV, and (b) BT/3B signal regions based on the classification in Table 7.1. While the BV signal regions are dominated by the “semi-leptonic” category, BT/3B signal regions are mainly by “di-leptonic”, especially the “ $\ell\tau_h$ ” component.

7.2 The Kinematical Extrapolation Method

The main consideration in the kinematical extrapolation method is definition of control regions. It is basically a procedure of 1) specifying kinematical variables that are well-modeled by MC and suitable for the extrapolation from control regions (CRs) to signal regions (Sec. 7.2.1), and 2) deciding the selection of CRs (Sec. 7.2.2). MC is then normalized to data in the CRs. The measured normalization factors and yields in CRs are extensively discussed in Sec 7.2.3.

7.2.1 MC vs Data Comparison and the MC mis-modeling

The MC modeling of dominant background processes ($W + \text{jets}$ and $t\bar{t}$) is examined in pre-selection regions defined in Table 7.2. Each pre-selection region is intended to be dominated by the process being tested.

Table 7.2: Definition of pre-selection regions and corresponding tested physics processes. MET trigger requirement, event cleaning described Sec. 6.2, $n_J \geq 2$ and $E_T^{\text{miss}} > 250$ are applied as common selection.

Region name	$n_{\ell,\text{base.}}$	$n_{\ell,\text{sig.}}$	$p_T(\ell_1)$ [GeV]	n_B ($p_T > 30$ GeV)	Tested processes
1LBV	1	1	> 35	0	$W + \text{jets}$
1LBT	1	1	> 35	[1, 2]	$t\bar{t}/Wt (\rightarrow bqqb\ell\nu)$
2LBT	2	2	-	[1, 2]	$t\bar{t}/Wt (\rightarrow b\ell\nu b\ell\nu)$
1L3B	1	1	> 15	≥ 3	$t\bar{t} + cc/bb, t\bar{t} + b_{\text{fake}}$

W + jets :

Figure 7.4 - 7.5 show the kinematic distributions in the **1LBV** pre-selection region where $W + \text{jets}$ is enriched. While the bulk phase space is well-described by MC, there is generally a striking overestimation by MC in the tail regions. Discrepancy is mainly observed in distributions related to jet activity, particularly in jet multiplicity when it is above 3. Considering that the jets are all from ISRs or FSRs, and that the jet multiplicity in the event roughly corresponds to the number of QCD-order of the processes, this implies the mis-modeling is due to the truncated higher order contribution beyond NNLO in the simulation. This might not be surprising giving that the MC sample (generated by SHERPA 2.2) does not include loop diagrams beyond NLO and neither diagrams with more than 5 partons in the final state.

Variables that do not scale with transverse momenta of outgoing particles (“non-scaling” variables), such as m_T or aplanarity, keep relatively well-modeled up to the tails. Particularly, m_T is by construction insensitive to most of the kinematics since the tail is determined by the mass-line of W -boson or MET resolution. Aplanarity is also supposed to be robust since it takes a form of ratio of jet momenta. Therefore, these variables are decided to be used for the extrapolation from CRs to SRs. Note that the m_T cut-off ($m_T \sim m_W$) is slightly mis-modeled typically when tighter selections are applied, presumably due to the propagated effect from the ISR/FSR mis-modeling mentioned above. The effect becomes visible especially in CRs (e.g. Figure C.4.5) or b -vetoed SRs.

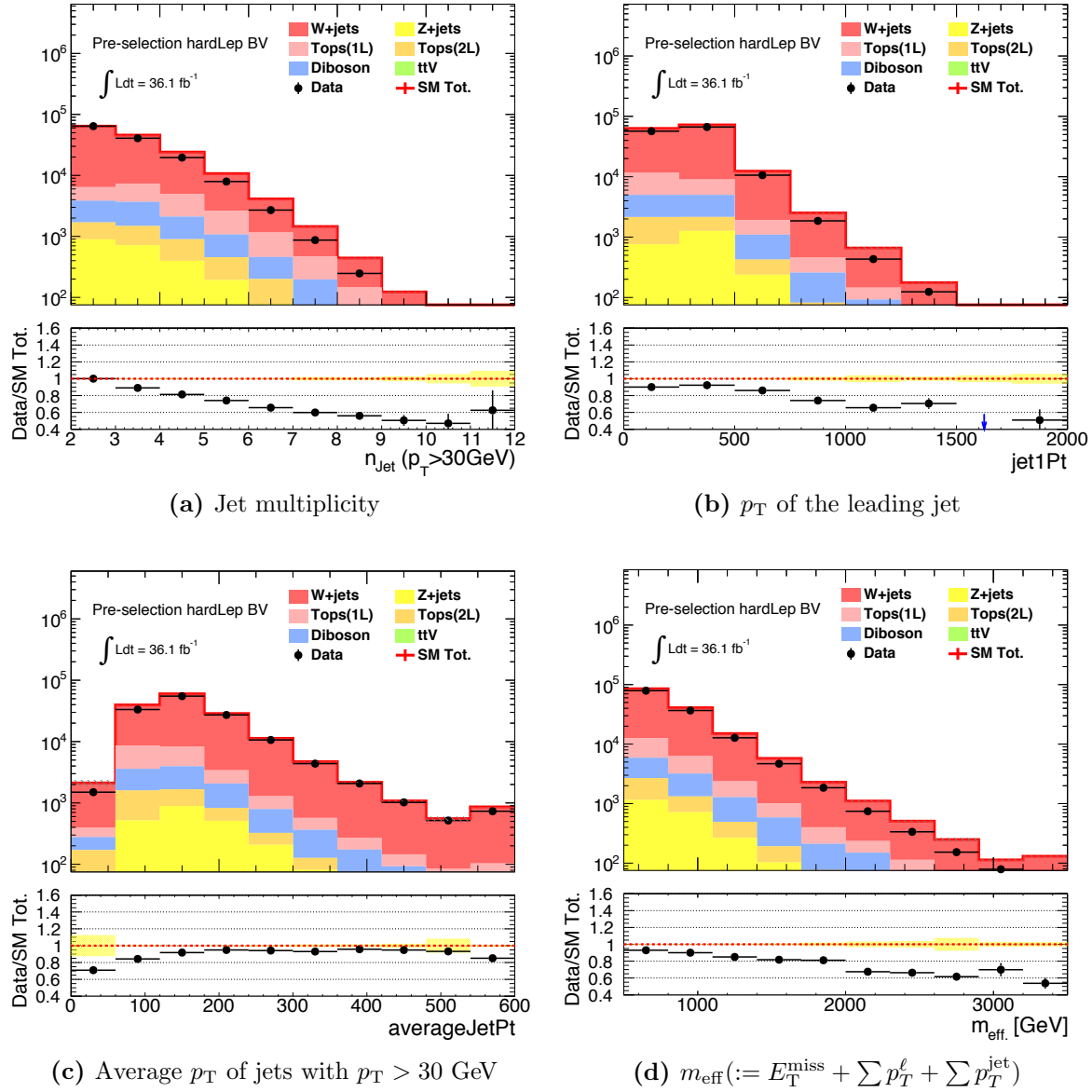


Figure 7.4: Kinematical distribution of data (black dots) and MC (colored stack) in the **1LBV** pre-selection region.

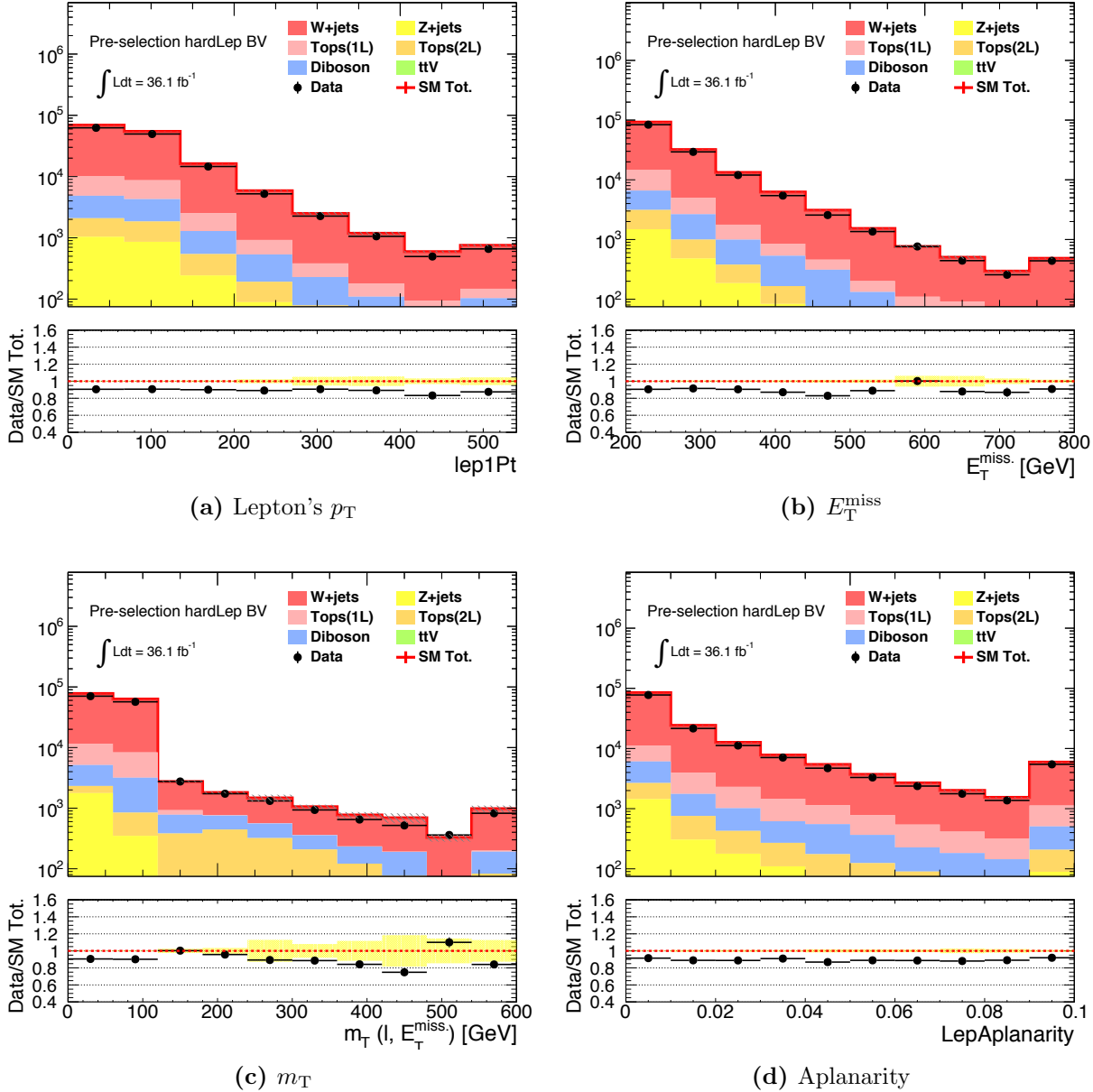


Figure 7.5: Kinematical distribution of data (black dots) and MC (colored stack) in the **1LBV** pre-selection region.

Semi-leptonic $t\bar{t}$:

Figure 7.6 - 7.7 are the kinematic distributions in the **1LBT** pre-selection region dominated by semi-leptonically decaying $t\bar{t}$. It is seen that MC is overshooting the data with increasing transverse momenta of outgoing particles such as jets, lepton and MET.

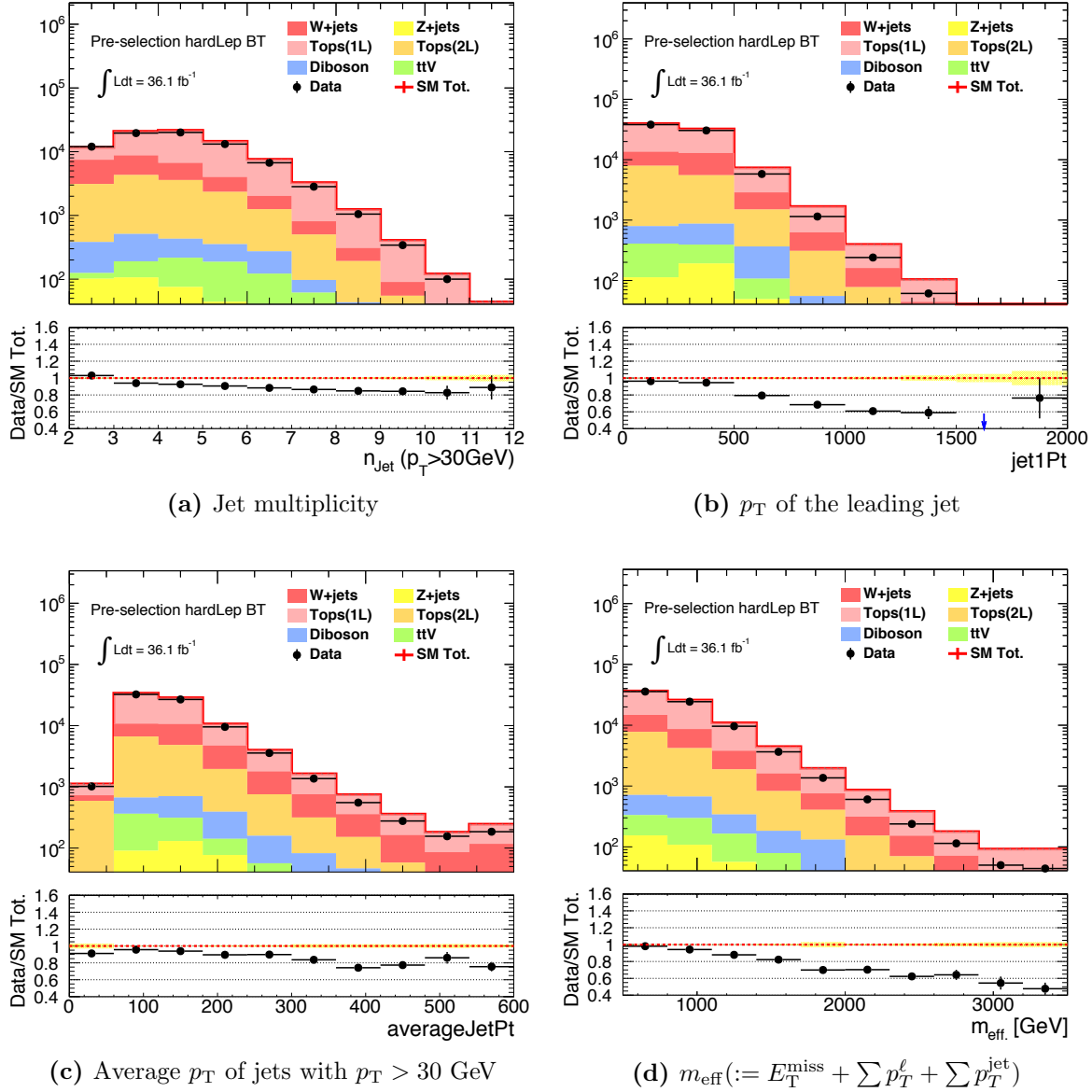


Figure 7.6: Kinematical distribution of data (black dots) and MC (colored stack) in the **1LBT** pre-selection region.

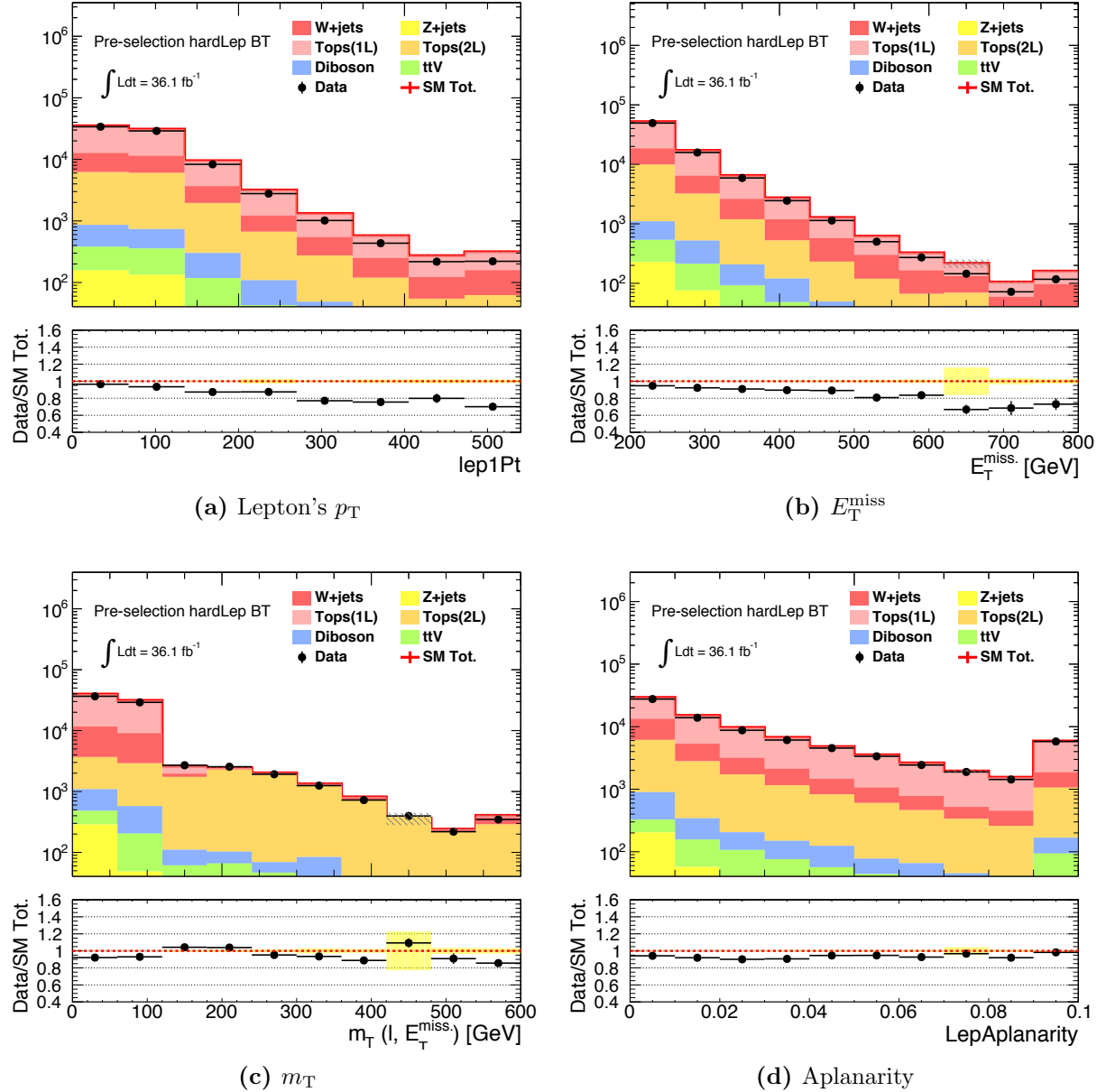


Figure 7.7: Kinematical distribution of data (black dots) and MC (colored stack) in the **1LBT** pre-selection region.

The mis-modeling in m_{eff} distribution is particularly concerning, given that the signal regions are designed to exploit its shape. The leading source of the mis-modeling is suspected to be in the description of ISR or FSR radiation. This is because hard jets ($p_T > 200 \text{ GeV}$) become more often non- $t\bar{t}$ origin in the tail of m_{eff} , as demonstrated by Figure 7.8, although $t\bar{t}$ does have 2-4 jets in its tree-level decay.

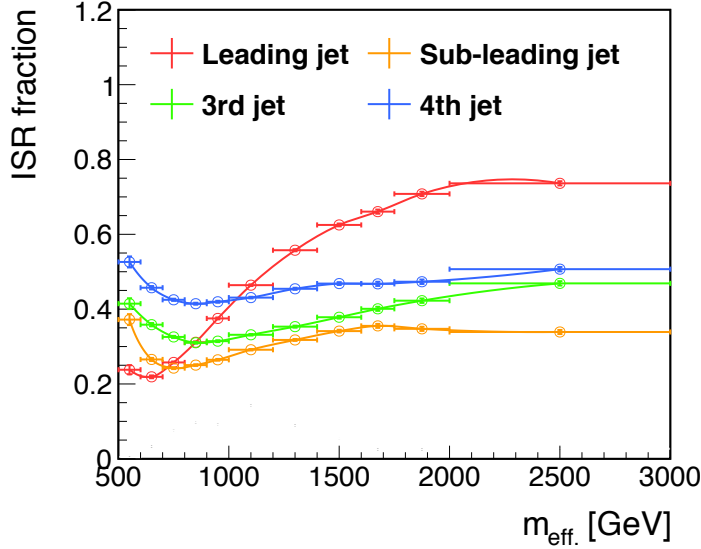


Figure 7.8: Fraction of ISR and FSR jets in the 4 leading jets with the largest transverse momenta, defined by the ratio of number of events where i -th leading jet does not match either jets from $t\bar{t}$ decay by $\Delta R < 0.2$ to all the events.

This is in fact also supported by a series of MC reweighting studies shown in Figure 7.9 where linear reweighting in various top kinematic variables is attempted to correct the slope of data/MC in m_{eff} . It turns that $p_T(t\bar{t})$ is the variable most sensitive to the mis-modeling, while reweighting in other variables can only change the normalization but the slope. This strongly indicates that the primary problem is in the radiation recoiling the $t\bar{t}$ rather than in the internal kinematics of the $t\bar{t}$ system. The discrepancies in other variables is also shown to be recovered by the same $p_T(t\bar{t})$ reweighting in Figure C.1.3-C.1.4 in appendix C.1).

In contrast, the “non-scaling” variables such as m_T and aplanarity look relatively well-modeled. Therefore, the same estimation strategy is taken as the case of $W + \text{jets}$ i.e. taking these as the extrapolating variables from CRs to SRs.

It is still acceptable though, note that the modeling of m_T is not perfect. For instance in Figure 7.6, there is a small bump-like structure in the ratio plot around $m_T = 100 \sim 200 \text{ GeV}$ corresponding the cut-off of the semi-leptonic $t\bar{t}$. This is suspected to be due to the interference between $t\bar{t} + Wt \rightarrow WWbb$ and other $WWbb$ diagrams which is not accounted by the generator, which effect is addressing in regions where bulk $t\bar{t}$ amplitude is suppressed. Corresponding uncertainty is evaluated in Sec. 8.2.1 and assigned as theory systematics.

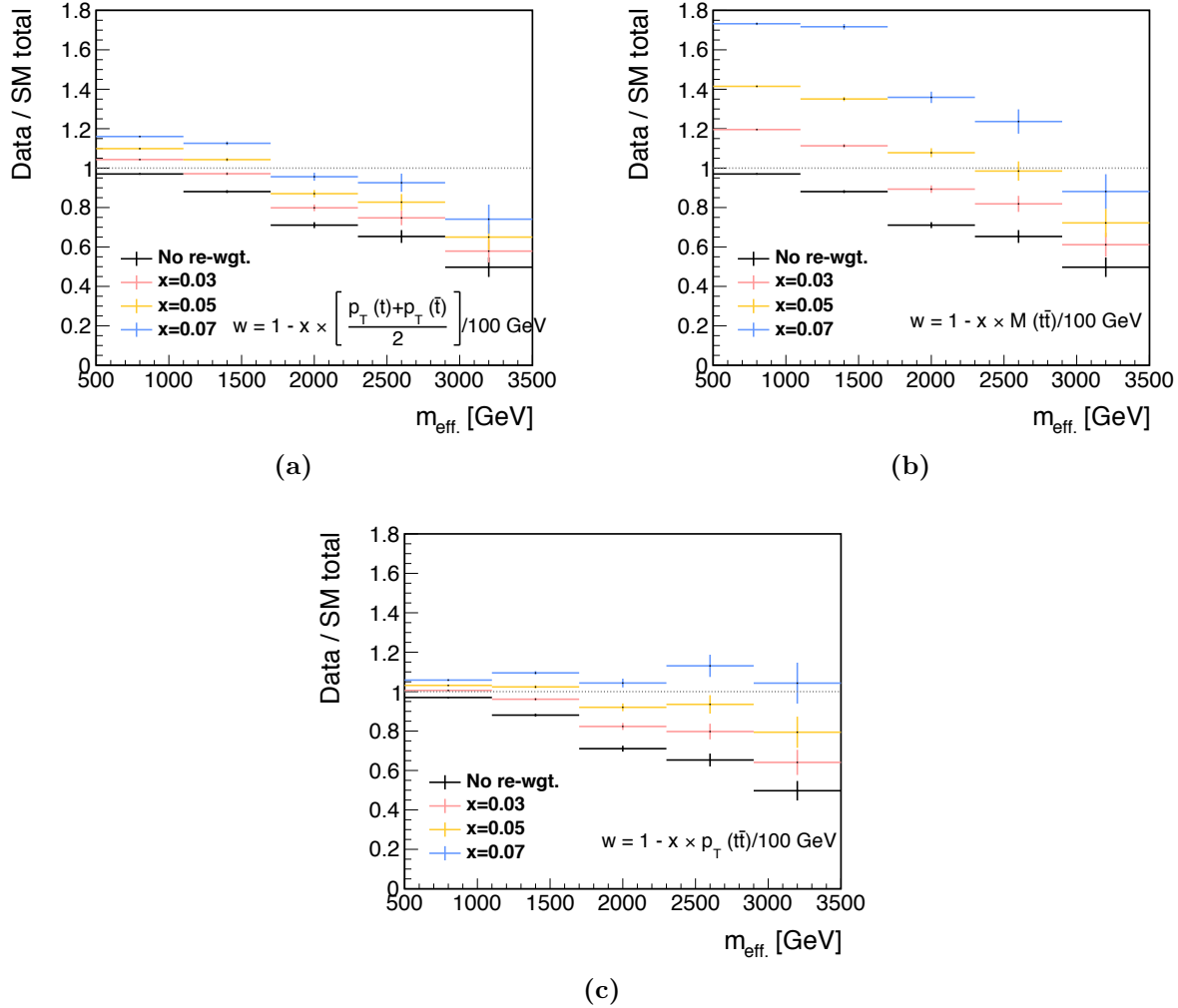


Figure 7.9: Response of data/MC in m_{eff} against a linear reweighting of $t\bar{t}$ events in terms of (a) average top transverse momentum ($(p_T(t) + p_T(\bar{t})) / 2$), (b) invariant mass of $t\bar{t}$ system ($m_{t\bar{t}}$) and (c) transverse momentum of $t\bar{t}$ system ($p_T(t\bar{t})$). $p_T(t\bar{t})$ is found to be sensitive to the slope of m_{eff} and improve the data/MC discrepancy, while the others are only capable of shifting the normalization.

Di-leptonic $t\bar{t}$:

Figure 7.10-7.11 plot the kinematic distributions in the 2-lepton b -tagged pre-selection region (**2LBT**) where di-leptonically decaying $t\bar{t}$ dominates.

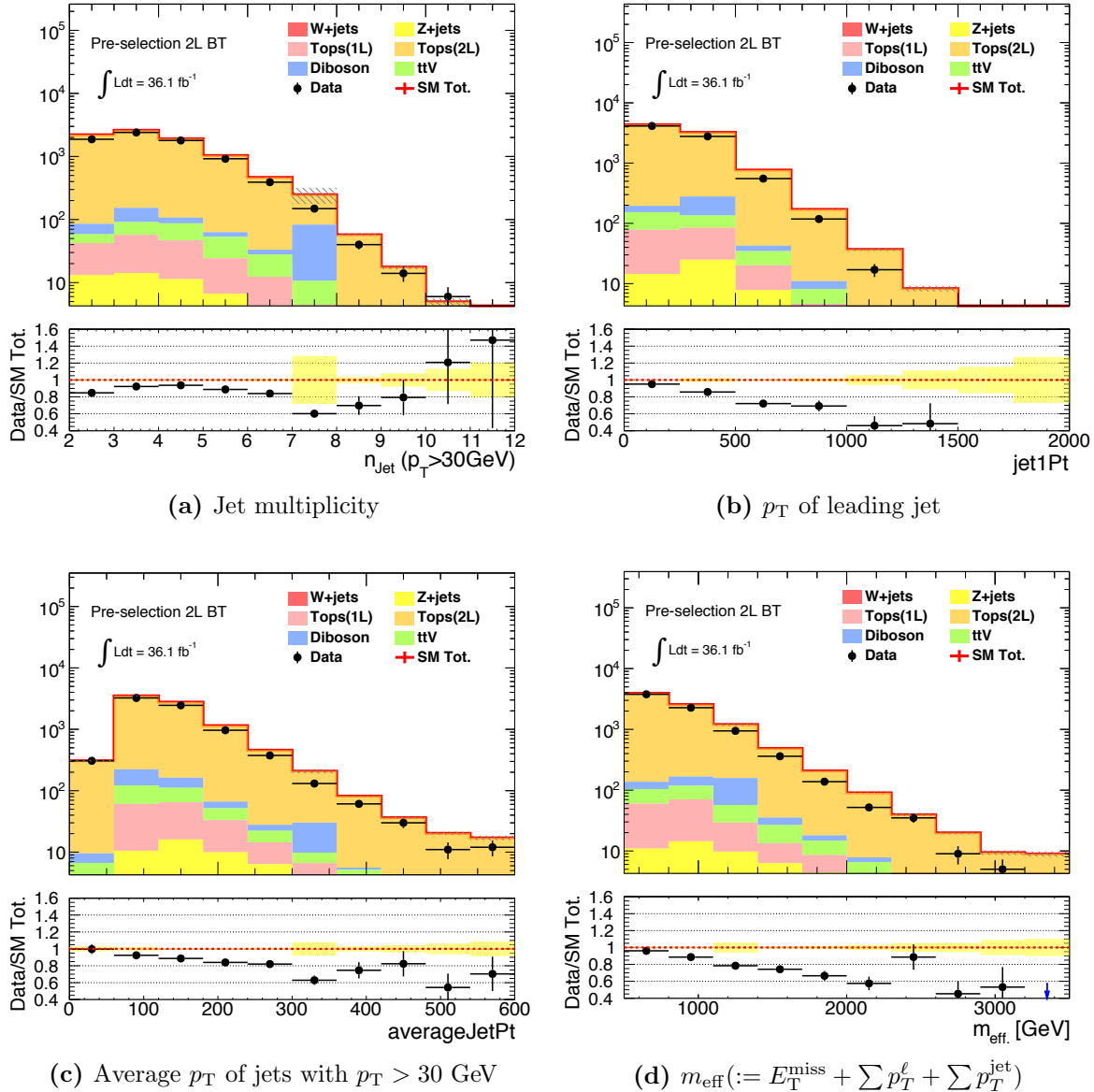


Figure 7.10: Kinematical distribution of data (black dots) and MC (colored stack) in the **2LBT** pre-selection region.

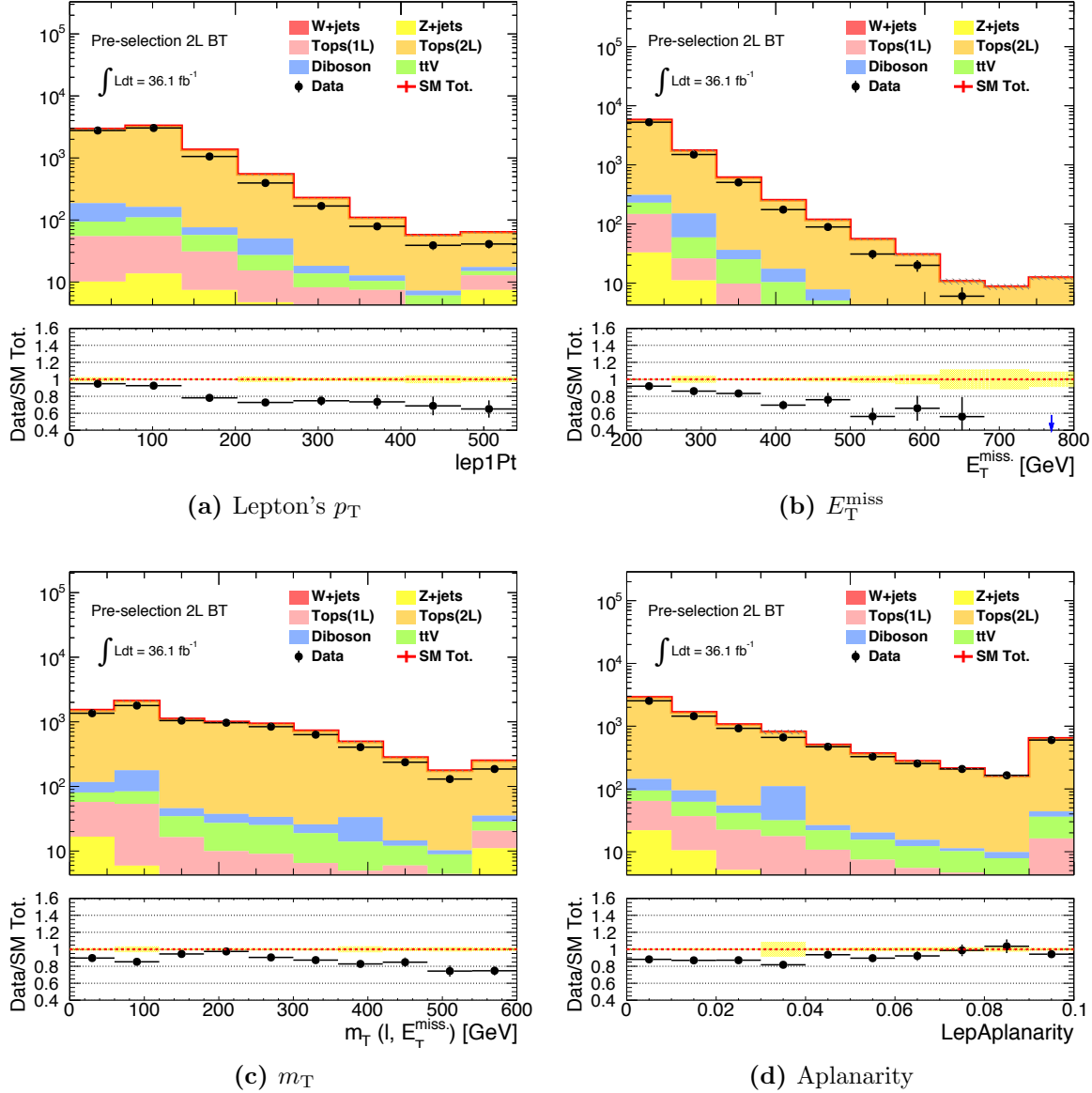


Figure 7.11: Kinematical distribution of data (black dots) and MC (colored stack) in the **2LBT** pre-selection region.

The same trend is observed also in the di-leptonic channel as well; constant slopes in data/MC are seen in variables related to the jet activity (jet transverse momenta, m_{eff} distributions or MET etc.); the other non-scaling variables (mt , aplanarity etc.) are relatively nicely modeled by MC. It might worth noting that the mis-modeling in jet variables can also be corrected by the same $p_T(t\bar{t})$ reweighting as the semi-leptonic case (Figure C.1.5-C.1.6 in appendix C.1). This universality strongly implies that the cause of mis-modeling in $t\bar{t}$ is likely in the kinematics before the W -bosons decay, which is an important underlying assumption for the object replacement method as described later.

The behavior of the “non-scaling” variables is also largely similar to the case of semi-leptonic $t\bar{t}$. The only exception is m_T that the m_T distribution for di-leptonic $t\bar{t}$ has no reason to cut-off at $m_T \sim m_W$, therefore it simply scales with lepton transverse momentum and MET. As a result, the m_T distribution of di-leptonic $t\bar{t}$ is affected by the mis-modeling of jet kinematics. The emerging data/MC discrepancy can be seen in Figure 7.11 (c). To avoid the impact by the mis-modeling in m_T , di-leptonic components are designed to be estimated by the other “object replacement” method as much as possible, and only small portion (“Out Acc.” and “Mis. OR” in Table 7.1) of them is covered by the kinematical extrapolation.

$t\bar{t}$ @3B:

Modeling of $t t + cc/bb$ and $t\bar{t} + b_{\text{fake}}$ are exclusively examined using a preselected region with 3 or more b -jets (**1L3B**). Figure 7.12 - 7.13 displays the data-MC comparison in the region. While the shapes seem to be affected by the same type of mis-modeling as observed in inclusive $t\bar{t}$ selection above, the normalization is also underestimated by about 30% which is thought to be due to the error of $t\bar{t} + cc/bb$ cross-section.

Despite the $t\bar{t}$ components in 3B regions suffer from such even more complex mis-modeling than the bulk, the impact on the final result is not dramatic since the majority of them are di-leptonic components in the SRs, therefore they are largely estimated by the object replacement method.

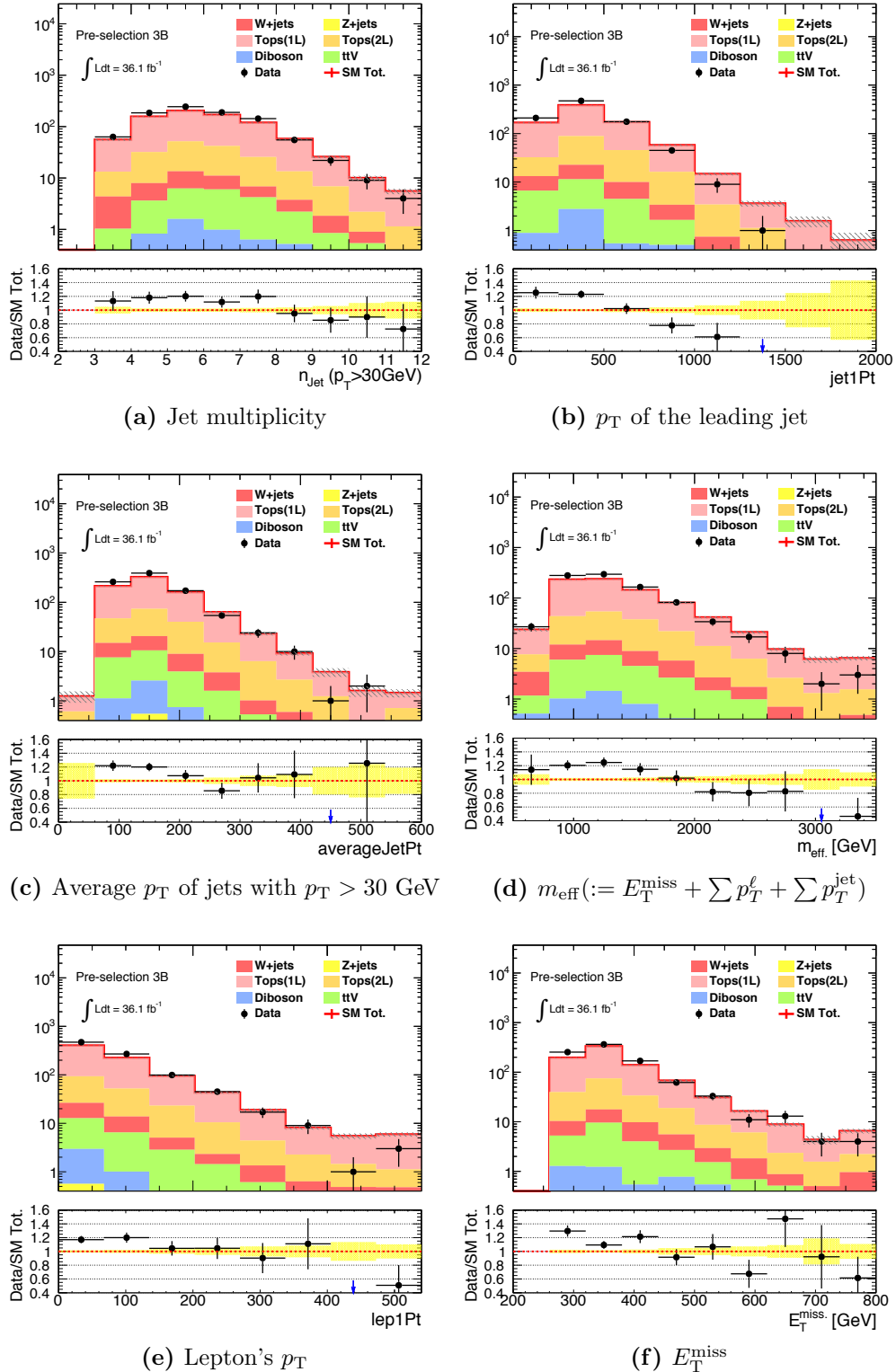


Figure 7.12: Kinematical distribution of data (black dots) and MC (colored stack) in the **1L3B** pre-selection region.

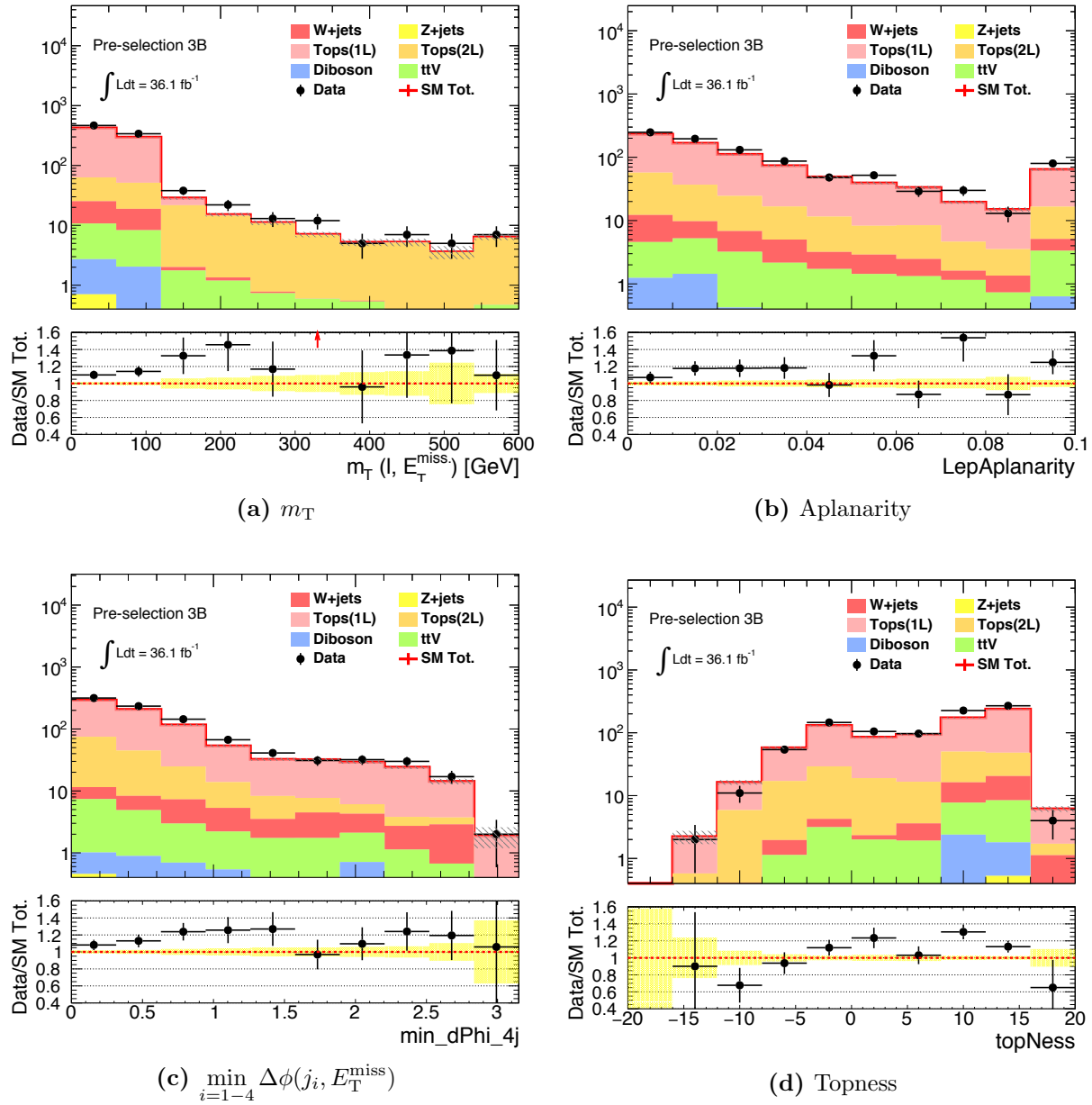


Figure 7.13: Kinematical distribution of data (black dots) and MC (colored stack) in the **1L3B** pre-selection region.

7.2.2 Definition of Control Regions and Validation Regions

The key assumption in this method is that the relative modeling of MC between CRs and SRs is correct. In other words, CRs and SRs need to suffer from the same extent of MC mis-modeling, so that the normalization in CRs can be compatible for SRs. Therefore, the most important requirement in CR definition is capturing the similar phase space with respect to the corresponding SR in terms of the mis-modeling.

The easiest realization of CR is to revert the SR cuts in kinematical variables well-modeled by MC. In this analysis, m_T , aplanarity and topness (and also $\min_{i=1-4} \Delta\phi(j_i, E_T^{\text{miss}})$ for the **3B** tower) are chosen as such variables. A exception is in the **2J** tower where E_T^{miss} is used instead of aplanarity, since aplanarity is not used in the signal region definition.

A couple of minor modifications follow based on the supplemental requirements below:

- CR statistics have to be sufficient.

Typically, about 10 times more data statistics in CRs with respect to SRs are desired for a stable correction particularly in cases where multiple components are corrected simultaneously (in this analysis, $W + \text{jets}$ and the top background i.e. $t\bar{t} + Wt$). For this sake, cuts in variables not fatally sensitive to the mis-modeling is loosened in some of the CRs. E_T^{miss} is for example always a good candidate to loosen for the large gain in statistics at a relatively low cost of the mis-modeling.³ $E_T^{\text{miss}}/m_{\text{eff}}$ is also loosened in **2J** and **High-x** since it is in a form of ratio which is relatively robust against the mis-modeling. On the other hand, it is promised that $n_J (p_T > 30 \text{ GeV})$ and m_{eff} are never touched since they are critical to the mis-modeling.

- A lower cut in m_T is needed to reduce the contribution from backgrounds with fake leptons. Low- m_T regions are typically more contaminated by events with fake leptons. As the MC modeling on the fake rate is generally less reliable, $m_T > 30 \sim 40 \text{ GeV}$ is applied in CRs.

CRs are defined for each SR bin independently, except that they are shared between b -tagged and b -vetoed SR bins. Instead, each CR is divided into b -tagged (“TR”) an b -vetoed bin (“WR”) in which different background components are controled. The correction is performed by normalizing the MC of $W + \text{jets}$ and the top background ($t\bar{t}$ and single-top) to the data in CRs, while raw MC prediction is quoted for the other minor backgrounds.

There are the third type of regions referred as “validation regions” designed to validate the estimation procedure by comparing with the data. They are typically set in between a SR and a CR, where at least one of the cuts in terms of the extrapolation variable is released with respect to the SR. Two types of VR is prepared; “VRa”, in which the m_T cut is relaxed validating the extrapolation in m_T ; “VRb”, where the other extrapolation variables (mainly aplanarity and topness. E_T^{miss} for **2J**) are validated. A upper cut in m_T is placed in some VRa to suppress the signal contamination. VRs-QCD are defined additionally to examine the contribution from QCD multi-jet processes in SRs which is supposedly negligible, which is detailed in Sec. C.3 in the appendix.

³Because the influence of the mis-modeling is diluted through the vectoral summation of them, instead of the scalar sum.

The finalized CRs and VRs are summarized together with the corresponding SRs in Table 6.7 - 6.11, which are graphically schematized by Figure 7.14. While SRs are carefully designed to be orthogonal to CRs and VRs, it is allowed to have overlap between CRs and VRs once the CRs are found to have much larger statistics than that of the VRs so that the overlapped events have no influence to the normalization. For instance, CR and VRa are overlapped in **3B**. This is intended to boost the CR statistics, while the number of events in VRa is small enough so that they are still nearly statistically independent.

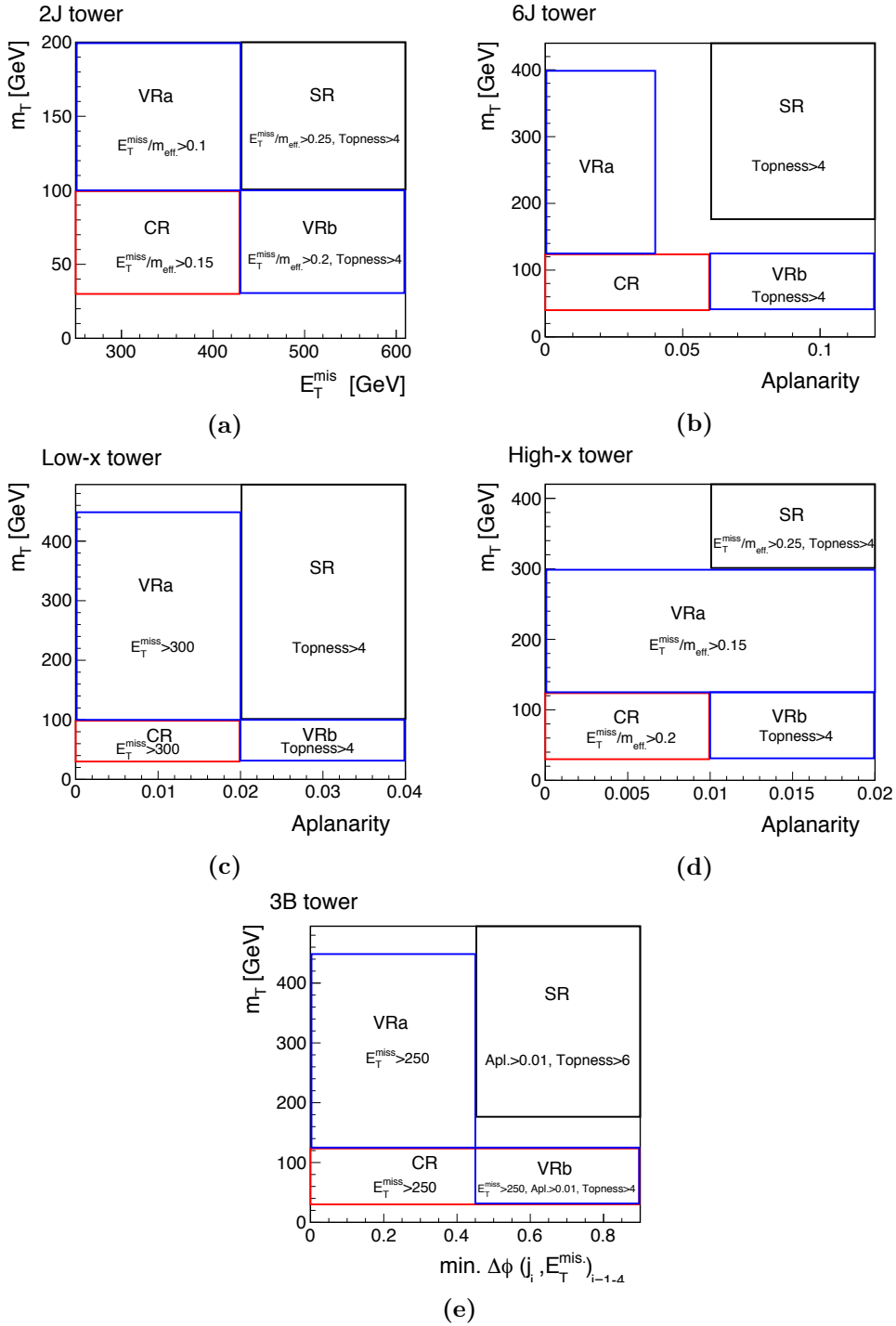


Figure 7.14: Schematics of CR/VR/SR in each signal region tower. Two major extrapolation variables are chosen as x - or y -axis to illustrate the difference between the regions. Extrapolation in the other variables are explicitly mentioned in the label. Note that each CR in the **3B** tower contains the VRa in it.

7.2.3 Result of the Normalization

The normalization factors are determined by a simultaneous fit on the WR and TR in which $W + \text{jets}$ and $t\bar{t}$ is dominant respectively. During the fit, all the normalization factors and nuisance parameters characterizing theoretical and experimental systematics are allowed to flow. The detail of the statistical procedure is described in Sec. 9.1.

The data yields in control regions are shown in Table 7.3 - 7.7, with the pre-fit and post-fit prediction by MC. Note that only $W + \text{jets}$ and top backgrounds ($t\bar{t}$ and single-top) are normalized while the yield of the other processes are kept constant during the fit. The effect of signal contamination in control regions is negligible.

Fitted normalization factors are summarized in Figure 7.15. Generally small normalization factors are observed in bins with high m_{eff} , reflecting the fact that MC is overpredicting in phase space with hard kinematics. The normalization factor is about 0.4 in the worst case, corresponding to an error of 150%, while the post-fit uncertainty is typically 20 \sim 40%, demonstrating a successful correction.

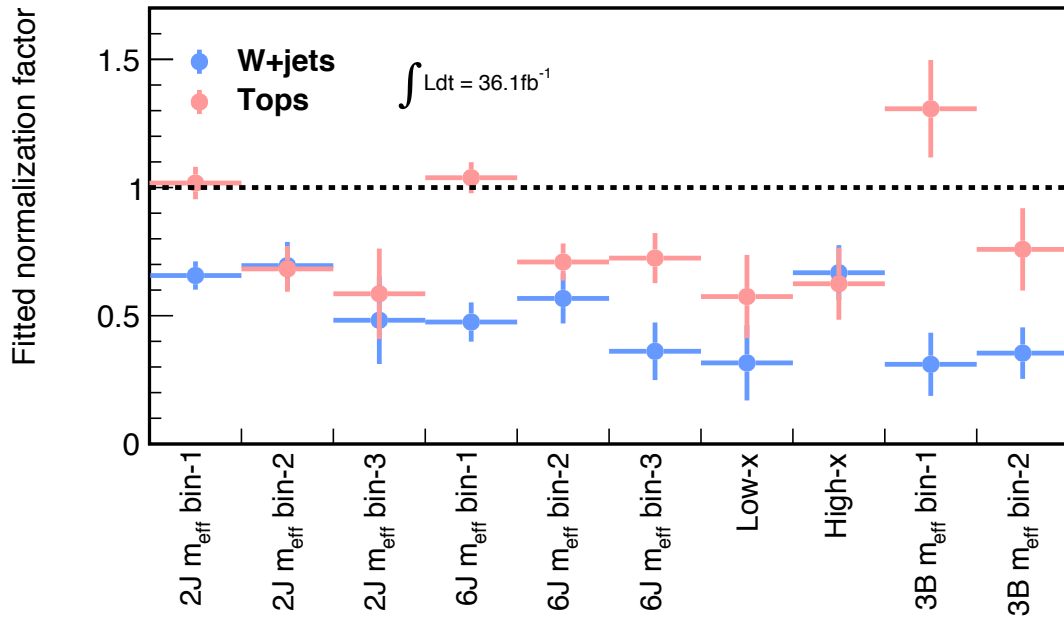


Figure 7.15: Fitted normalization factors for $W + \text{jets}$ and the top background ($t\bar{t}$ plus single-top). The error bars represent the combined systematic and statistical uncertainties.

The post-fit distributions for variables used in the extrapolation in each region are shown in Figure C.4.1-C.4.8 in the appendix.

Table 7.3: Number of observed data and the estimated background yields in the control regions in tower **2J**. Uncertainties include both systematic uncertainties discussed in chapter 8 and the uncertainties due to the limited data statistics in CR or the MC statistics. The uncertainties are symmetrised and truncated so that the yields remain positive.

WR 2J	$m_{\text{eff.}} \in [1100, 1500]$	$m_{\text{eff.}} \in [1500, 1900]$	$m_{\text{eff.}} > 1900$
Observed data	620	127	17
MC total (post-fit)	620.06 ± 24.93	126.89 ± 11.28	17.01 ± 4.14
$W + \text{jets}$	462.0 ± 34.1	99.7 ± 12.6	12.6 ± 4.4
$Z + \text{jets}$	14.3 ± 3.9	2.6 ± 0.7	0.5 ± 0.1
Tops	100.9 ± 17.1	14.9 ± 3.2	2.6 ± 0.9
Di-boson	41.7 ± 13.7	9.3 ± 3.6	1.3 ± 0.4
$t\bar{t} + V$	1.2 ± 0.3	0.3 ± 0.1	0.1 ± 0.0
MC total (pre-fit)	859.70 ± 30.91	177.49 ± 7.33	32.40 ± 1.67
$W + \text{jets}$	703.35 ± 19.15	143.40 ± 4.39	26.19 ± 1.22
$Z + \text{jets}$	14.26 ± 3.92	2.58 ± 0.72	0.45 ± 0.13
Tops	99.27 ± 13.32	21.88 ± 3.16	4.42 ± 0.75
Di-boson	41.63 ± 13.69	9.32 ± 3.55	1.26 ± 0.44
$t\bar{t} + V$	1.18 ± 0.25	0.30 ± 0.07	0.06 ± 0.02
TR 2J	$m_{\text{eff.}} \in [1100, 1500]$	$m_{\text{eff.}} \in [1500, 1900]$	$m_{\text{eff.}} > 1900$
Observed data	972	150	22
MC total (post-fit)	971.82 ± 31.18	150.01 ± 12.27	22.00 ± 4.71
$W + \text{jets}$	99.5 ± 35.0	23.2 ± 8.4	3.3 ± 1.7
$Z + \text{jets}$	3.9 ± 1.0	0.9 ± 0.2	0.2 ± 0.1
Tops	846.1 ± 48.2	120.2 ± 15.3	17.4 ± 5.2
Di-boson	11.9 ± 4.4	2.7 ± 0.9	0.7 ± 0.3
$t\bar{t} + V$	10.3 ± 1.8	3.1 ± 0.6	0.4 ± 0.1
MC total (pre-fit)	1009.13 ± 52.94	216.02 ± 11.81	37.88 ± 2.67
$W + \text{jets}$	151.50 ± 48.57	33.30 ± 10.57	6.91 ± 2.25
$Z + \text{jets}$	3.86 ± 1.05	0.85 ± 0.23	0.17 ± 0.05
Tops	831.49 ± 14.93	176.11 ± 4.06	29.70 ± 1.15
Di-boson	11.94 ± 4.35	2.67 ± 0.92	0.68 ± 0.27
$t\bar{t} + V$	10.34 ± 1.81	3.08 ± 0.58	0.43 ± 0.11

Table 7.4: Number of observed data and the estimated background yields in the control regions in tower **6J**. Uncertainties include both systematic uncertainties discussed in chapter 8 and the uncertainties due to the limited data statistics in CR or the MC statistics. The uncertainties are symmetrised and truncated so that the yields remain positive.

WR 6J	$m_{\text{eff.}} \in [1100, 1600]$	$m_{\text{eff.}} \in [1600, 2100]$	$m_{\text{eff.}} > 2100$
Observed data	248	120	53
MC total (post-fit)	248.06 ± 15.84	120.02 ± 11.21	52.98 ± 7.30
$W + \text{jets}$	147.5 ± 22.0	83.3 ± 13.9	30.6 ± 9.2
$Z + \text{jets}$	2.5 ± 1.0	1.1 ± 0.5	0.7 ± 0.3
Tops	71.7 ± 11.5	22.9 ± 4.4	14.3 ± 3.1
Di-boson	25.3 ± 7.5	12.1 ± 5.8	7.1 ± 3.8
$t\bar{t} + V$	1.1 ± 0.2	0.6 ± 0.2	0.3 ± 0.1
MC total (pre-fit)	408.20 ± 19.21	192.94 ± 10.30	112.45 ± 7.11
$W + \text{jets}$	310.29 ± 11.30	146.84 ± 5.42	84.62 ± 4.04
$Z + \text{jets}$	2.54 ± 1.03	1.10 ± 0.46	0.72 ± 0.33
Tops	69.12 ± 8.78	32.38 ± 4.37	19.72 ± 2.80
Di-boson	25.19 ± 7.45	12.05 ± 5.78	7.10 ± 3.80
$t\bar{t} + V$	1.06 ± 0.24	0.57 ± 0.17	0.29 ± 0.09
TR 6J	$m_{\text{eff.}} \in [1100, 1600]$	$m_{\text{eff.}} \in [1600, 2100]$	$m_{\text{eff.}} > 2100$
Observed data	647	232	117
MC total (post-fit)	646.88 ± 25.46	231.79 ± 15.24	116.91 ± 10.85
$W + \text{jets}$	43.2 ± 16.5	25.1 ± 9.7	11.6 ± 5.5
$Z + \text{jets}$	0.9 ± 0.4	0.6 ± 0.2	0.4 ± 0.2
Tops	586.2 ± 31.2	193.1 ± 18.7	98.8 ± 12.8
Di-boson	8.1 ± 2.5	8.2 ± 2.7	3.9 ± 1.7
$t\bar{t} + V$	8.5 ± 1.5	4.7 ± 1.1	2.3 ± 0.6
MC total (pre-fit)	672.53 ± 31.35	329.86 ± 16.23	174.76 ± 11.54
$W + \text{jets}$	90.62 ± 28.71	44.24 ± 14.02	31.99 ± 10.13
$Z + \text{jets}$	0.88 ± 0.36	0.58 ± 0.23	0.41 ± 0.20
Tops	564.43 ± 9.95	272.12 ± 5.74	136.21 ± 3.91
Di-boson	8.11 ± 2.51	8.21 ± 2.69	3.84 ± 1.69
$t\bar{t} + V$	8.48 ± 1.53	4.71 ± 1.14	2.30 ± 0.63

Table 7.5: Number of observed data and the estimated background yields in the control regions in tower **Low-x**. Uncertainties include both systematic uncertainties discussed in chapter 8 and the uncertainties due to the limited data statistics in CR or the MC statistics. The uncertainties are symmetrised and truncated so that the yields remain positive.

CR Low-x	WR	TR
Observed data	15	25
MC total (post-fit)	15.02 ± 3.89	24.97 ± 5.03
$W + \text{jets}$	9.3 ± 4.2	2.9 ± 1.8
$Z + \text{jets}$	0.4 ± 0.2	0.2 ± 0.1
Tops	2.7 ± 0.9	20.4 ± 5.7
Di-boson	2.6 ± 0.8	1.0 ± 1.0
$t\bar{t} + V$	0.0 ± 0.0	0.5 ± 0.1
MC total (pre-fit)	37.17 ± 2.56	46.38 ± 3.87
$W + \text{jets}$	29.51 ± 1.84	9.26 ± 3.05
$Z + \text{jets}$	0.38 ± 0.15	0.17 ± 0.07
Tops	4.62 ± 0.75	35.47 ± 1.52
Di-boson	2.61 ± 0.79	0.99 ± 0.98
$t\bar{t} + V$	0.05 ± 0.02	0.48 ± 0.11

Table 7.6: Number of observed data and the estimated background yields in the control regions in tower **High-x**. Uncertainties include both systematic uncertainties discussed in chapter 8 and the uncertainties due to the limited data statistics in CR or the MC statistics. The uncertainties are symmetrised and truncated so that the yields remain positive.

CR High-x	WR	TR
Observed data	92	73
MC total (post-fit)	91.91 ± 9.61	72.97 ± 8.57
$W + \text{jets}$	72.4 ± 11.1	17.0 ± 6.5
$Z + \text{jets}$	1.1 ± 0.4	0.3 ± 0.1
Tops	10.2 ± 2.9	52.0 ± 11.3
Di-boson	8.0 ± 3.5	2.7 ± 1.4
$t\bar{t} + V$	0.2 ± 0.1	1.0 ± 0.4
MC total (pre-fit)	134.04 ± 6.41	112.69 ± 9.52
$W + \text{jets}$	108.42 ± 3.88	25.52 ± 8.13
$Z + \text{jets}$	1.13 ± 0.39	0.29 ± 0.13
Tops	16.32 ± 2.19	83.19 ± 3.25
Di-boson	7.99 ± 3.50	2.70 ± 1.35
$t\bar{t} + V$	0.18 ± 0.08	0.99 ± 0.37

Table 7.7: Number of observed data and the estimated background yields in the control regions in tower **3B**. Uncertainties include both systematic uncertainties discussed in chapter 8 and the uncertainties due to the limited data statistics in CR or the MC statistics. The uncertainties are symmetrised and truncated so that the yields remain positive.

WR 3B	$m_{\text{eff.}} \in [1000, 1750]$	$m_{\text{eff.}} > 1750$
Observed data	368	107
MC total (post-fit)	368.18 ± 19.69	107.05 ± 10.56
$W + \text{jets}$	146.4 ± 59.3	58.3 ± 16.7
$Z + \text{jets}$	5.3 ± 1.5	2.4 ± 0.4
Tops	176.6 ± 52.2	33.1 ± 11.5
Di-boson	37.7 ± 9.9	12.5 ± 3.3
$t\bar{t} + V$	2.2 ± 0.5	0.8 ± 0.2
MC total (pre-fit)	651.86 ± 28.54	223.90 ± 10.02
$W + \text{jets}$	471.51 ± 7.38	164.58 ± 2.94
$Z + \text{jets}$	5.29 ± 1.45	2.39 ± 0.38
Tops	135.10 ± 21.31	43.59 ± 7.33
Di-boson	37.74 ± 9.93	12.53 ± 3.26
$t\bar{t} + V$	2.21 ± 0.52	0.80 ± 0.22
TR 3B	$m_{\text{eff.}} \in [1000, 1750]$	$m_{\text{eff.}} > 1750$
Observed data	234	47
MC total (post-fit)	233.97 ± 15.57	46.98 ± 6.95
$W + \text{jets}$	1.4 ± 1.0	0.9 ± 0.5
$Z + \text{jets}$	0.1 ± 0.1	0.1 ± 0.1
Tops	227.5 ± 15.8	44.1 ± 7.1
Di-boson	$0.2^{+0.3}_{-0.2}$	0.2 ± 0.1
$t\bar{t} + V$	4.7 ± 1.2	1.7 ± 0.4
MC total (pre-fit)	183.60 ± 23.01	62.71 ± 8.28
$W + \text{jets}$	4.54 ± 1.87	2.62 ± 1.00
$Z + \text{jets}$	0.12 ± 0.05	0.10 ± 0.06
Tops	174.00 ± 21.42	58.15 ± 7.43
Di-boson	$0.20^{+0.27}_{-0.20}$	0.18 ± 0.08
$t\bar{t} + V$	4.75 ± 1.17	1.66 ± 0.43

7.3 The Object Replacement Method

There are several potential concerns over extrapolating in m_T when estimating the “di-leptonic” background:

- The MC modeling itself is questionable.

As seen in Figure 7.11 (c) and discussed in 7.2.1 (Di-leptonic $t\bar{t}$), m_T of “di-leptonic” component seems to mis-modeled by MC since it does scale with the lepton momentum and MET for which MC is confirmed to be mis-modeling.

- Applying the same selection between CRs and SRs in the other variables no longer helps.

The extrapolation in m_T is essentially an extrapolation between the “semi-leptonic” components and the “di-leptonic” ones, since CRs are dominated by the “semi-leptonic” while SRs (VRs) are by “di-leptonic”. The outstanding issue for it is that different particles contribute to observables between the “semi-leptonic” and “di-leptonic processes”, and different phase spaces are chosen even when applying the same selection (see Table 7.8). For instance, MET is sourced by a single neutrino in the semi-leptonic channel while it is by a vectoral sum of two neutrinos in the di-leptonic one. More seriously, the number of ISR (FSR) jets is different under the same requirement in terms of jet multiplicity, for instance in $t\bar{t}$, the semi-leptonic channel yields 4 jets by its decay while the di-leptonic channel can only yield 2 (or 3 if hadronic decay product from τ is tagged as a jet). Therefore, applying the same selection between CRs and SRs no longer guarantee that CRs grasp the same phase space as SRs.

Table 7.8: Comparison of constituents of MET (E_T^{miss}) and jet multiplicity (n_J) between the semi-leptonic $t\bar{t}$ and di-leptonic $t\bar{t}$ as example. “1LCR” refers to the default control regions used in the kinematical extrapolation method, and “2LCR” is the 2-lepton version with the same kinematical selection. Note that the other composite variables using jet and MET (e.g. m_{eff} and m_T etc.) are also affected by the difference accordingly.

	SR	1LCR	2LCR
Dominant $t\bar{t}$ mode	$t\bar{t} \rightarrow b\ell\nu_1 b\tau\nu_2, \tau \rightarrow \tau_h\nu_\tau$	$t\bar{t} \rightarrow bqq\ell\nu$	$t\bar{t} \rightarrow b\ell\nu_1 b\ell\nu_2$
n_J	$\sim 2(3) + n_{\text{ISR/FSR}}$	$\sim 4 + n_{\text{ISR/FSR}}$	$\sim 2 + n_{\text{ISR/FSR}}$
E_T^{miss}	$ \mathbf{p}_T(\nu_1) + \mathbf{p}_T(\nu_2) + \mathbf{p}_T(\nu_\tau) $	$ \mathbf{p}_T(\nu) $	$ \mathbf{p}_T(\nu_1) + \mathbf{p}_T(\nu_2) $

The use of 2-lepton control regions (2LCRs) is then naturally motivated which does not require neither the extrapolation in m_T nor in the decay modes. Although this does improve the simulation a bit, there is still difference between the kinematics of the “di-leptonic” components in SRs and CRs, as shown in Table 7.8. The problem is found generic to the approach of MC normalization itself, since it can not accommodate the behavior of taus or missing leptons that differ event-by-event .

Instead, the approach of event-by-event can deal with the problem. The object replacement method is an example of it, which is an integrated method consisting of:

- "missing lepton replacement" to estimate a part of $\ell\ell_{\text{mis.}}$ events ("Mis. Reco." and "Mis. ID"),
- "tau replacement" to estimate $\ell\tau_h$,

where one of the lepton of data events in 2LCR (seed event) is replaced into a virtual missing lepton or a simulated hadronic tau decay respectively, as schematized in Figure 7.16. The detector responses and behavior in object reconstruction of those replaced objects are carefully emulated so that the replaced event can directly mimic the events in the signal regions.

The object replacement method is a nearly full data-driven method where the use of MC is limited in an area of tau decays and the modeling of instrumental effects around the lepton identification. The MC modeling is highly reliable, ensuring the extrapolation much more robust, compared with the kinematical extrapolation method where the mis-modeling in kinematic tail is always critical. For instance, the discrepancies with data are typically a few percent level and the cause are also mostly well-understood.

Note that the whole method relies on the orthogonality between kinematics and object properties:

$$\frac{d\sigma(\ell\ell)}{dx} \propto \frac{d\sigma(\ell\ell_{\text{ID}})}{dx} \propto \frac{d\sigma(\ell\ell_{\text{mis.}})}{dx} \quad (7.1)$$

and the lepton universality:

$$\frac{d\sigma(\ell\ell)}{dx} \propto \frac{d\sigma(\ell\tau)}{dx}, \quad (7.2)$$

where $\ell\ell_{\text{ID}}$ represents events with both two leptons are identified, and $\ell\ell_{\text{mis.}}$ denotes events with one of them is missed. x symbolizes kinematical variables. Particularly, the kinematics-object orthogonality (Eq. 7.1) is of paramount importance, since it allows to extrapolate the object properties measured in a very inclusive region into any arbitrary phase space. As long as the lepton reconstruction and identification is concerned, the statement is more or less true because they generally obeys the statistical behavior of detector responses such as fluctuating number of hits or energy deposit, which does not depend on global event kinematics, but rather on the nature of the particle itself (usually only on its momentum) as well as the local material configuration in the detector. Therefore, it is usually enough to parameterize the efficiency of reconstruction or identification simply by the momentum (p_T, η, ϕ) of the particles. This is however not the case when coming to the estimation of lepton being outside the (p_T, η) acceptance ("Out-Acc") or being dropped in the overlap removal ("Mis. OR"), since the probabilities do depend on the momentum of parent particle or the proximity to the nearest jet. Hence, the seed events do not fully represent the kinematics of "Out-Acc" and "Mis. OR", and this is the reason why these events can not be accounted by the object replacement method.

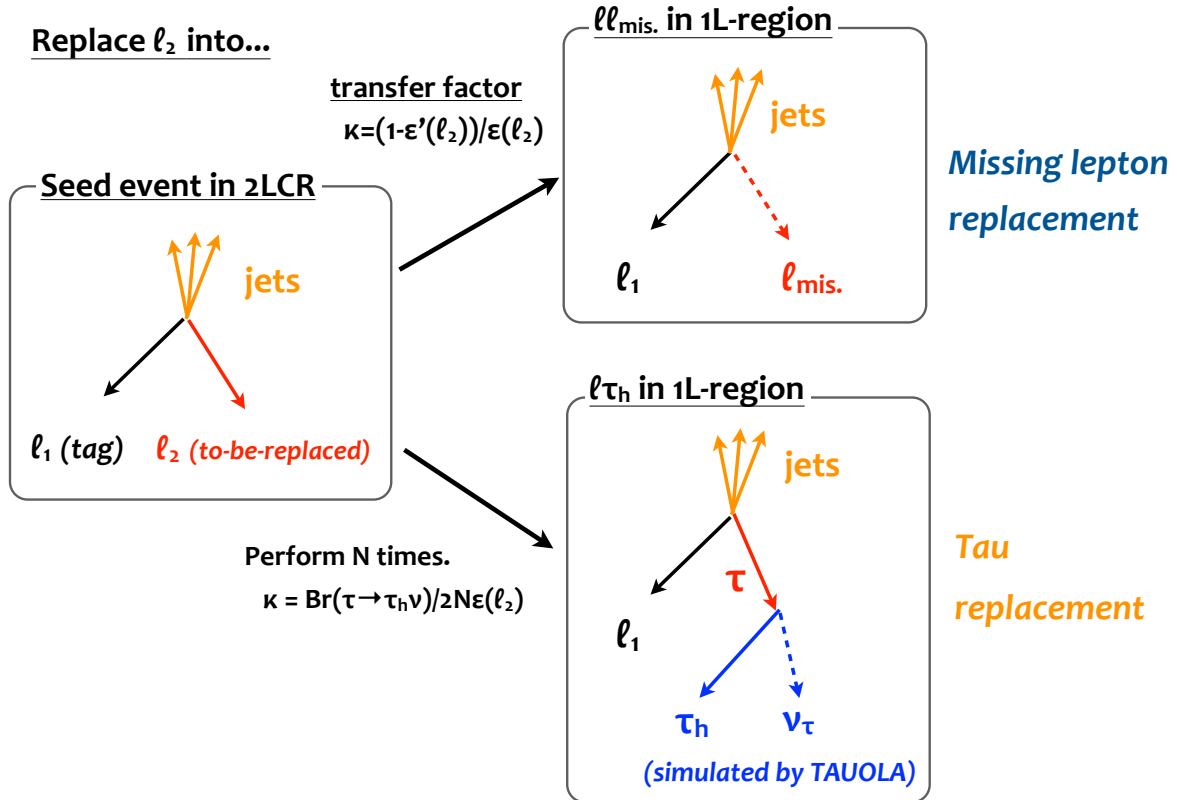


Figure 7.16: Schematic of the object replacement method. One of the leptons in the seed event is replaced into either a virtual missing lepton or a simulated hadronic tau decay. A weight κ is assigned to the replaced event (sub-event) to account for the different rate of occurrence between the seed events and the sub-event (e.g. probability of a lepton being identified and missed). More detail is found in Sec. 7.3.1.

7.3.1 The Replacement Procedure and the Per-event Logic

Figure 7.17 is the schematic of the work flow for the replacement procedure for a single seed event, which follows as below:

1. Pick up a 2LCR event ("seed event").
2. Replace a lepton of the seed event into a virtual missing lepton or a simulated hadronic decay of tau lepton, if the two leptons satisfy a certain criteria. This replaced event is called "sub-event".
3. (For tau replacement) Apply the calibration for the hadronic tau.
4. Re-calculate the event-level kinematics such as E_T^{miss} or m_{eff} etc.
5. Assign a weight κ for each sub-event as the transfer factor from 2LCR to 1-lepton regions.
6. (For tau replacement) Repeat the step 2-5 by $N = 50$ times and take the average, in order to accommodate the statistical nature of tau decay. Note that the number of iteration N only dictates the level of "smoothing" thus has no essential impact on the final result. The average is taken by scaling the κ by $1/N$.
7. Change the roles (tagged/replaced) between the two leptons and repeat 2-6.
8. Apply the analysis level selection (e.g. signal region selection) and post-selection to reject singal contamination for the generated sub-events.
9. Collect the accepted sub-events and fill them into an "event-level histogram". 100% of statistical uncertainty is assigned for each bin of the event-level histogram, accounting for all the sub-events are generated from the common seed event.
10. Loop over all seed events and sum up all the event-level histograms with ordinary statistical treatment where the uncertainty is quadratically summed for each bin of the histogram.

More detail and caveats about each step is provided below:

Seed event selection and trigger

For seed event selection, looser kinematical selection is generally preferred, to collect the necessary seed events as completely as possible. In particular, as MET and m_T change their values the most during the replacement, those cuts have to be drastically relaxed with respective to regions that one wants to estimate. For instance, Figure 7.18 shows the MET distribution of seed events when the MET after the replacement above 250 GeV is required. About 40% of seeds are with seed MET below 250 GeV, indicating that it will be underestimated by about 40% if naively requiring the same MET for seed events as the estimated regions.

While MET trigger is available for collecting the bulk events above its off-line threshold $E_T^{\text{miss}} > 250$ GeV, the single-lepton trigger (SLT) is introduced to complement the seeds events with $E_T^{\text{miss}} < 250$ GeV. In spite of its relatively low efficiency (70% – 90%) and the tight off-line

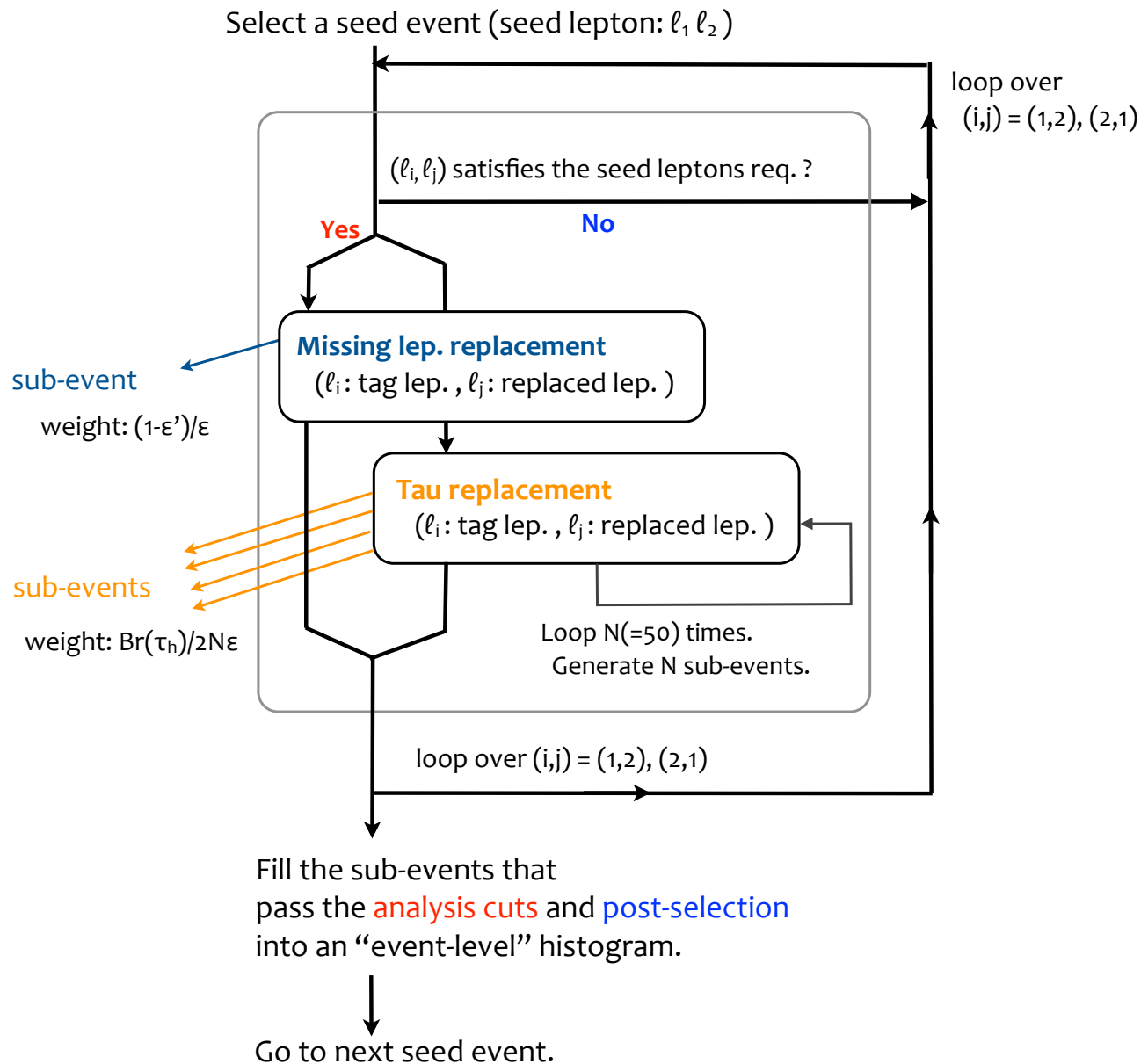


Figure 7.17: Work flow of the replacement procedures for a single seed event. Sub-events are generated through both the mis-lepton replacement

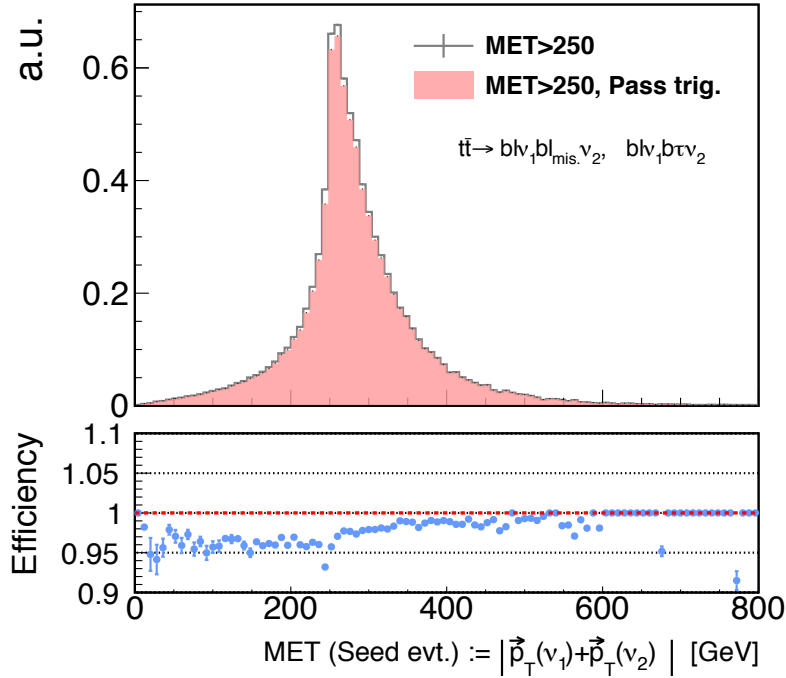


Figure 7.18: Seed MET distribution (gray) for the $\ell\ell_{\text{mis.}}$ and $\ell\tau_h$ events from $t\bar{t}$ resulting in $E_T^{\text{miss}} > 250$ GeV. The seed MET is defined by the vectorial sum of neutrinos from top decays: $|\vec{p}_T(\nu_1) + \vec{p}_T(\nu_2)|$, which is roughly equivalent to the MET in corresponding seed events ($t\bar{t} \rightarrow b\bar{b}\nu_1\bar{b}\bar{b}\nu_2$). Over 95% of the seed events are shown to be accepted by the combined trigger strategy defined in Table 7.9 (pink).

threshold of $p_T > 28(26)$ GeV for the single-electron (single-muon) trigger, SLT is still fully efficient for the seed events since there are two leptons being the candidate to fire the trigger. Eventually, as shown in Figure 7.18, more than 95% of the overall trigger efficiency can be maintained.

Although the enhanced backgrounds due to the lowered MET selection for 2LCR does not impact as much on the final result since most of them are skimmed out at the analysis-level selection applied after the replacement, the decent cut $E_T^{\text{miss}} > 100$ is required to suppress the bulk background components in 2LCR (Z+jets, 1L+fake lepton etc.) and make sure avoiding the large uncertainty from MC subtraction. The seed event loss due to the selection $E_T^{\text{miss}} > 100$ is negligible when estimating SRs/VRs. Table 7.9 shows the definition of common 2LCR.

Table 7.9: Definition of 2-lepton control region (2LCR).

$n_{\ell, \text{baseline}} = 2, n_{\ell, \text{signal}} \geq 1$
MET trigger, $E_T^{\text{miss}} > 250$ GeV
or
At least 1 signal lepton with $p_T > 28$ GeV firing the single-lepton trigger, $E_T^{\text{miss}} > 100$ GeV

Requirement on seed leptons for the replacement

A seed event with lepton ℓ_1, ℓ_2 have two choices for the replacement namely 1) keeping ℓ_1 and replacing ℓ_2 or 2) keeping ℓ_2 and replacing ℓ_1 . The replacement is proceeded only if the lepton to-be-replaced (“replaced lepton”) and the lepton to-be-kept (“tag lepton”) satisfy a certain condition shown in Table 7.10. As the tag lepton eventually corresponds to the single lepton used in the analysis in 1-lepton regions, it has to be in a consistent object definition in defining the signal regions (Table 4.3). On the other hand, generally looser requirement is preferred for the replaced lepton, instead from the CR statistics point of view. Therefore, it is loosened to “baseline”, except when estimating b -vetoed regions where it is kept to “signal” since the impact of fake lepton background in 2LCR is relatively large otherwise.

Note that the replacement can happen twice from the identical seed event if the both combinations (tag, rep.)= (ℓ_1, ℓ_2) , (ℓ_2, ℓ_1) are eligible.

Table 7.10: Lepton definition used for tag and replaced lepton versus the type of regions to be estimated.

	b -tagged, b -inclusive	b -vetoed
Tag lepton	signal	signal
Replaced lepton	baseline	signal

Treatment of virtual missing lepton

As mentioned in Sec. 4.7, electrons are usually also identified as jets. The doubly-counted object, either an electron or a jet, is discarded during the overlap removal. Therefore, electrons failing the reconstruction or identification will simply recognized as jets without experiencing the overlap removal. To emulate this effect, in case of replacing an electron in a seed event, the record that the electron is reconstructed as a jet candidate is retrieved, and the 4-vector of electron is replaced into the that of the jet candidate. As the jet candidate is fully calibrated in the hadronic scale, no correction is needed additionally. In an occasion where electrons do not have corresponding jet candidates, which typically happens when the transverse momentum is too low, the electron is replaced into a missing particle with the 4-momentum of the original electron.

Muons failing the reconstruction or identification are almost never identified as any other objects. Instead, they are included in the track soft term in the MET calculation, and in principle this needs to be emulated in the missing muon replacement. This is technically possible, however the bottleneck is that the muon track quality is totally different between well-identified muons and unidentified ones, and particularly it is difficult to reproduce the resolution of bad muon track from good one with a meaningful correction. As it turns that simply including the 4-momentum replaced muon into the soft term even leads to worse performance than not (as demonstrated in Figure 7.34), replaced muons are decided to be simply treated as a virtual missing particle in the same momentum, and added into MET. Although this rough treatment causes a non-zero error in the estimation as one will see in Sec. 7.3.2, fortunately the impact on final estimation is marginal because the rate of missing muon events are generally very low, compared with the other components (missing electron events or $\ell\tau_h$) due to the very high efficiency of muon reconstruction

and identification.

Simulation of tau decays and the τ_h -to-jet calibration

Tau decays are simulated by TAUOLA [137–139] assuming the taus are unpolarized. This assumption is incorrect given the parent W -bosons are left-handed, however the impact on the final result is found to be marginal. This is discussed in Sec. 7.3.2. Branching for leptonic decay is set to zero to reduce the number of loops.

Given that the analysis is free from explicit tau selections, hadronic taus within the p_T - η acceptance most likely undergo the jet clustering, as well as b -tagging and the jet calibration once they pass the JVT cut (Sec. 4.6.4). On the other hand, the output of TAUOLA is merely a 4-vector of truth level hadronic tau. Therefore, following pseudo-calibration is applied for the truth-level τ_h , to emulate the effect either of the detector response, jet calibration, and the b -tagging.

1. Scale the transverse momentum of truth τ_h .

The scale of a truth τ_h to an anti- k_T jets is derived using the $t\bar{t}$ MC samples, by comparing the transverse momenta of truth hadronic taus and that of ΔR -matched reconstructed jet by $\Delta R < 0.2$. It is defined by the mean value of the residual distribution (Figure 7.19) and parameterized in terms of p_T and η of truth hadronic taus (Figure 7.20). The scale is always positive and rises significantly in the low- p_T limit, due to the fact that the anti- k_T jet contains extra underlying tracks inside that become the pedestal. The difference in the calibration between light jets and b -tagged jets are ignored.

2. Smear the p_T of the hadronic tau.

After applying the scale above, smearing is subsequently adopted to account for the detector resolution. The resolution is taken from the Gaussian-fitted RMS of the residual distribution on which the scale above is defined as well (Figure 7.19), and parameterized as function of p_T and η of truth hadronic taus (Figure 7.21). The smearing is applied based on the Gaussian profile with RMS being the resolution.

3. Emulation of the JVT cut and b -tagging.

After the p_T -scaling and smearing, hadronic taus with $p_T > 30$ GeV, $|\eta| < 2.8$ are identified as jet candidates. Some of them are then randomly dropped to emulate the effect of the JVT cut, based on the calculated efficiency of JVT cut using the simulated $t\bar{t}$ sample (Figure 7.22). A random b -tagging is further performed on the remained jets, by assigning a random b -tagging score (MV2c10) following according to the profile obtained from the ΔR -matched reconstructed jets in the $t\bar{t}$ MC (Figure 7.23). While the JVT efficiency is mapped as a function of p_T and η of the jet candidates, the b -tagging score profile is only separated in terms of tau decay modes (1-prong and 3-prong).

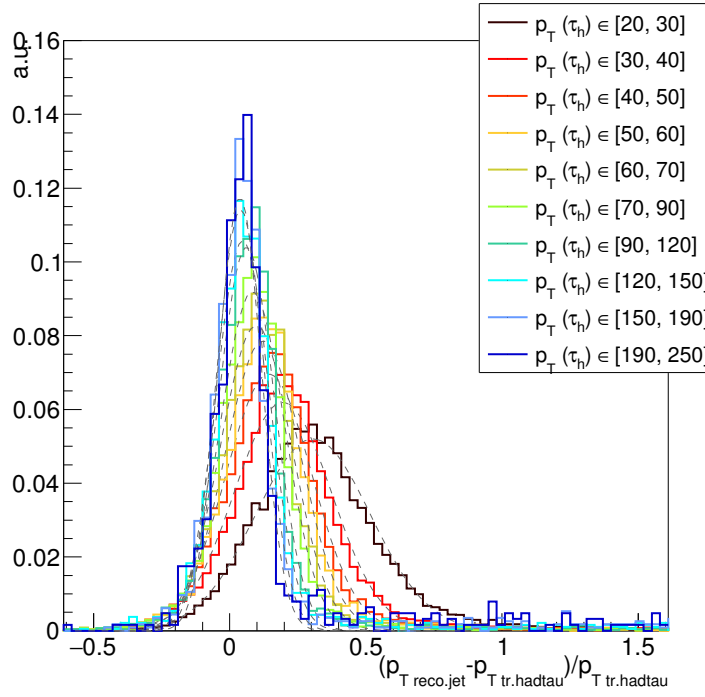


Figure 7.19: The residual of tau momentum measurement: $[p_{\text{T}}(\text{reco.}\tau - \text{jet}) - p_{\text{T}}(\text{tr.}\tau_h)] / p_{\text{T}}(\text{tr.}\tau_h)$ calculated using the simulated $t\bar{t}$ sample. $p_{\text{T}}(\text{tr.}\tau_h)$ is the transverse momentum of truth-level hadronic tau defined as $|\mathbf{p}(\tau) - \mathbf{p}(\nu_{\tau})|$ and $p_{\text{T}}(\text{reco.}\tau - \text{jet})$ is the corresponding reconstructed anti- k_{T} jet matched by $\Delta R < 0.2$.

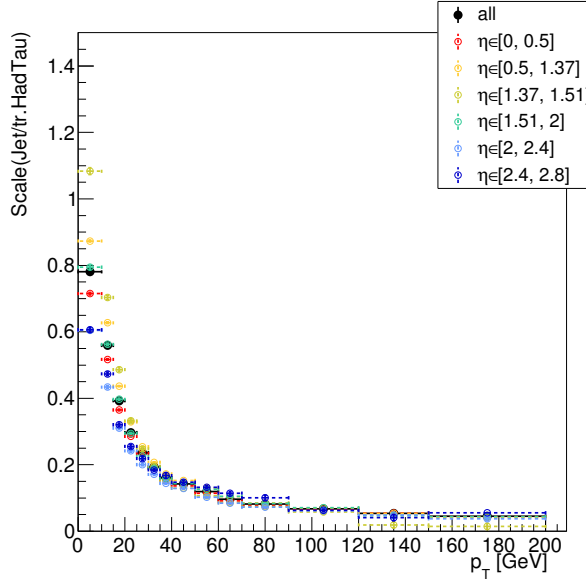


Figure 7.20: Scale of anti- k_{T} jets for truth hadronic taus, defined as the mean of the residual distribution Figure 7.19.

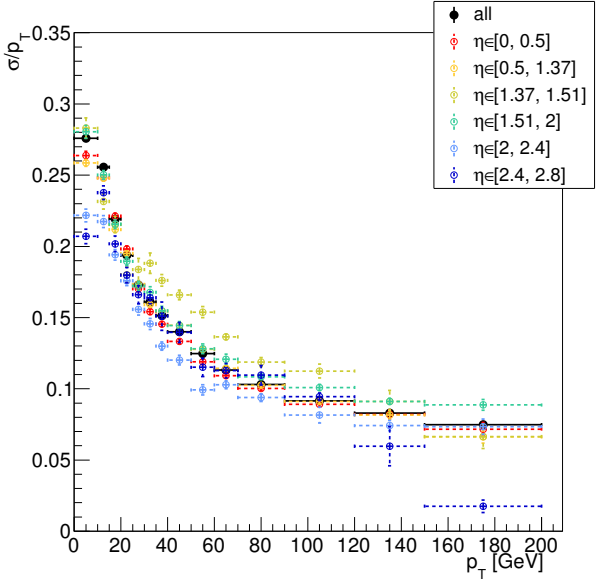


Figure 7.21: Resolution of hadronic tau, defined by the Gaussian-fitted RMS of the residual distribution Figure 7.19.

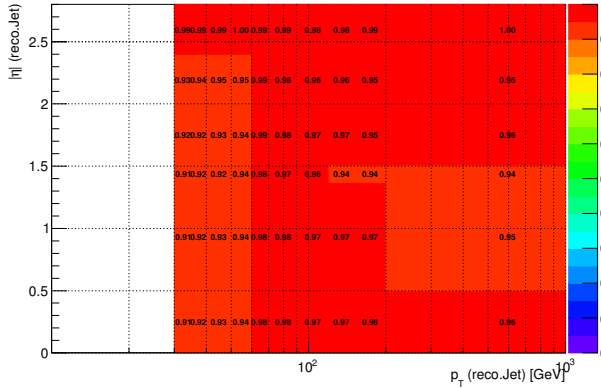


Figure 7.22: The efficiency map for the JVT cut for a reconstructed hadronic tau jet as function of its p_T and η , calculated using the $t\bar{t}$ MC sample. The efficiency is defined by the fraction of jets passing the JVT cuts and matched to truth hadronic taus by $\Delta R < 0.2$ that pass $p_T > 30$ GeV, $|\eta| < 2.8$.

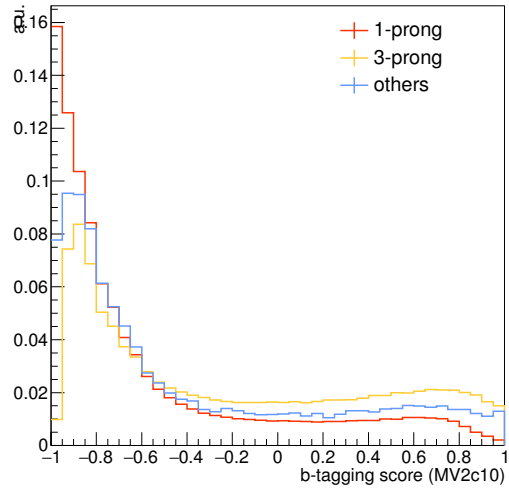


Figure 7.23: Profile of b -tagging score (MV2c10) for signal jets originated from hadronic tau decays. Only the dependency on the decay modes (1-prong or 3-prong) is taken into account. The threshold for the b -tagging is at 0.44. The 3-prong events result in a higher fake rate into b -tagged jets, reflecting the fact that the secondary vertex structure more resembles to that of b -hadrons. The simulated $t\bar{t}$ MC sample is used to derive the profiles.

Transfer factor

A weight κ is assigned to each sub-event, to account for the different probability of occurrence between the seed event and the replaced sub-event. For instance, in the missing lepton replacement, this corresponds to the difference between probability of a lepton being identified and being failed i.e. the inefficiency over the efficiency:

$$\kappa = \frac{1 - \epsilon_{\text{baseline}}(\ell_{\text{rep.}})}{\epsilon_{\text{rep.}}(\ell_{\text{rep.}})}. \quad (7.3)$$

Note that the efficiencies used in the numerator and the denominator is different; that in the enumerator for the working point used in second lepton veto (namely “baseline”); that in the denominator is for the working point that the replaced lepton is required, which can be either “baseline” and “signal” depending on cases (see Table 7.10).

As for the tau replacement, the transfer factor is

$$\kappa = \frac{\text{Br}(\tau \rightarrow \tau_h \nu)}{2N\epsilon_{\text{rep.}}(\ell_{\text{rep.}})}, \quad (7.4)$$

where N is number of iterations per replacement (set to 50 in this study), and $\epsilon_{\text{rep.}}$ the efficiency for working point used for requiring replaced lepton. The factor 2 in the denominator originates

from the fact that two channels ($e\ell$ and $\mu\ell$) are available as seeds for estimating a single channel $\tau\ell$ (see Table 7.11).

Table 7.11: Correspondence between the seed events and the generated sub-events, in terms of charge and lepton flavor. One finds that the sub-events generated by tau replacement need to be weighted by 1/2 otherwise will be double-counted.

Seed	Replaced lepton	sub-evt. by mis. lep. rep.	sub-evt. by tau rep.
e^+e^-	e^-	$e^+e_{\text{mis}}^-$	$e^+\tau^-$
	e^+	$e_{\text{mis}}^+e^-$	τ^+e^-
$e^+\mu^-$	μ_-	$e^+\mu_{\text{mis}}^-$	$e^+\tau^-$
	e^+	$e_{\text{mis}}^+\mu^-$	$\tau^+\mu^-$
μ^+e^-	e^+	$\mu^+e_{\text{mis}}^-$	$\mu^+\tau^-$
	μ^+	$\mu_{\text{mis}}^+e^-$	τ^+e^-
$\mu^+\mu^-$	μ^-	$\mu^+\mu_{\text{mis}}^-$	$\mu^+\tau^-$
	μ^+	$\mu_{\text{mis}}^+\mu^-$	$\tau^+\mu^-$

By its definition, $\alpha := 1/N_{\text{acc.}}\kappa$ roughly gives the ratio of expected effective statistics in CR with respect to the SR, where $N_{\text{acc.}}$ is average number of accepted sub-events after the kinematical cuts. α is typically $3 \sim 5$ for the missing lepton replacement, and about 1.4 ($\sim 1/\text{Br}(\tau \rightarrow \tau_h\nu)$) for the tau replacement at the pre-selection level. It is typically enhanced by about factor of 2 when $m_T(\ell_{\text{tag.}}, E_T^{\text{miss}}) > m_W$ is required (corresponding to $m_T > m_W$ in 1-lepton regions, which is always the case for VRa and SR). This is due to the fact that most of the di-leptonic SM processes follow⁴:

$$\min[m_T(\ell_1, E_T^{\text{miss}}), m_T(\ell_2, E_T^{\text{miss}})] < m_W, \quad (7.5)$$

in other words, either of the m_T must be below m_W . Given that both leptons in the seed event have the chance to be replaced, nearly half of the generated sub-events will be discarded by requiring $m_T(\ell_{\text{tag.}}, E_T^{\text{miss}}) > m_W$. Accordingly, together with the fact that the contribution from the tau replacement is dominant, the effective CR statistics for the object replacement method is constantly about 3 times more than that in SR. This factor of 3 gain in statistics is in fact subtle; given that the expected yields in SRs are typically a few events, it immediately leads to 20%–50% statistical uncertainty by itself. Therefore CR statistic is always the biggest source of uncertainty in this method.

Lepton efficiency

The lepton efficiency used in the transfer factor calculation is calculated using $t\bar{t}$ MC sample. The efficiency of ID/baseline/signal lepton requirement is respectively defined as the fraction of truth leptons that are matched with reconstructed leptons passing the ID / identified / signal lepton requirement by $\Delta R < 0.2$. Leptons overlapped with jets (if the nearest jet closer than $\Delta < 0.4$) are excluded since their efficiency is biased. The efficiencies are parameterized as a function of

⁴This holds when the event contains exactly two semi-leptonically W -bosons, and the two leptons and MET are only supplied from their decays. More detail found in [140].

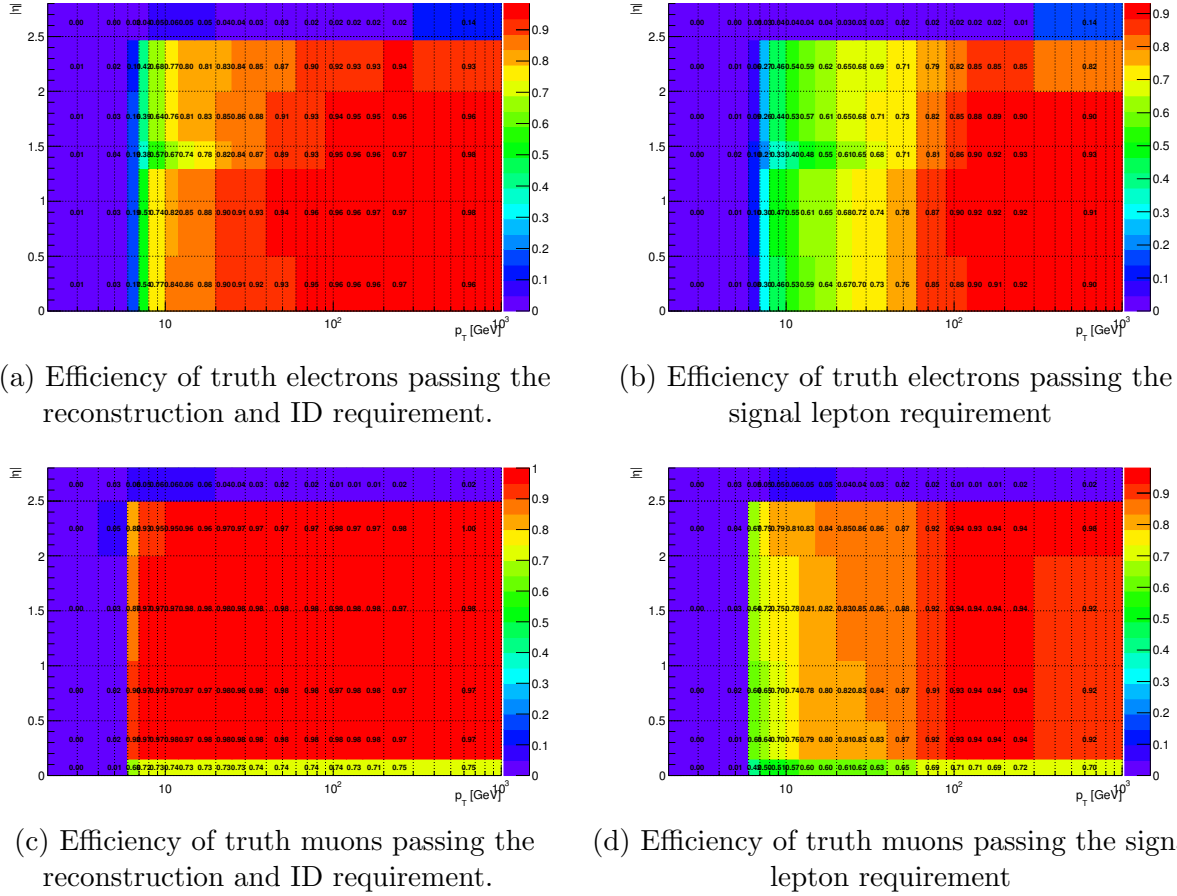


Figure 7.24: Off-line lepton selection efficiency used in the transfer factor calculation. The efficiency is defined by the fraction of truth leptons to match with reconstructed leptons passing the ID / identified / signal lepton requirement by $\Delta R < 0.2$.

lepton flavor (e/μ), p_T and η of truth leptons. The data/MC scale factor measured using the $Z \rightarrow ee/\mu\mu$ events are applied. The resultant efficiency maps are shown in Figure 7.24.

Post-selection for rejecting signal contamination

Signal contamination is generally not negligible when estimating SR-like regions in this method, since there are a class of benchmark models that result in $3 \sim 4$ W -bosons giving comparable di-leptonic branching as the semi-leptonic one. The contamination is generally disfavored since it will elevate the expected background level, causing the deterioration of either discover and exclusion sensitivity.

A post-selection in terms of $m_T(\ell_{\text{rep.}}, E_T^{\text{miss}})$ shown in Table 7.25 is applied for sub-events passing the kinematical selections, to get rid such the signal contamination. The key observation is that only SM processes follow the condition Eq. (7.5), therefore have a sharp cut-off in $m_T(\ell_{\text{rep.}}, E_T^{\text{miss}}) \sim m_W$ when $m_T(\ell_{\text{tag}}, E_T^{\text{miss}}) > m_W$, as shown in Figure 7.25.

The cut is designed to maintain the efficiency greater than 90% in SRs. The efficiency drop will be eventually compensated. On the other hand, signal contamination is largely suppressed typically to $y_{\text{contami.}}/y_S = 0.05 \sim 0.15$ in SRs after the post selection, where $y_{\text{contami.}}$ (y_S) is the expected increase of expected background due to the contamination (expected signal yield) in the region.

Table 7.12: Post-selection applied for signal contamination rejection. Inclusive efficiency of sub-events from SM background seeds are calculated using MC, shown in the rightest column. The efficiency drop is corrected based on the inverse efficiency.

Region	$m_T(\ell_{\text{rep.}}, E_T^{\text{miss}})$ [GeV]	SM efficiency
SR	< 250	0.9 ~ 0.98
VRa	< 300	> 0.97
VRb	—	1

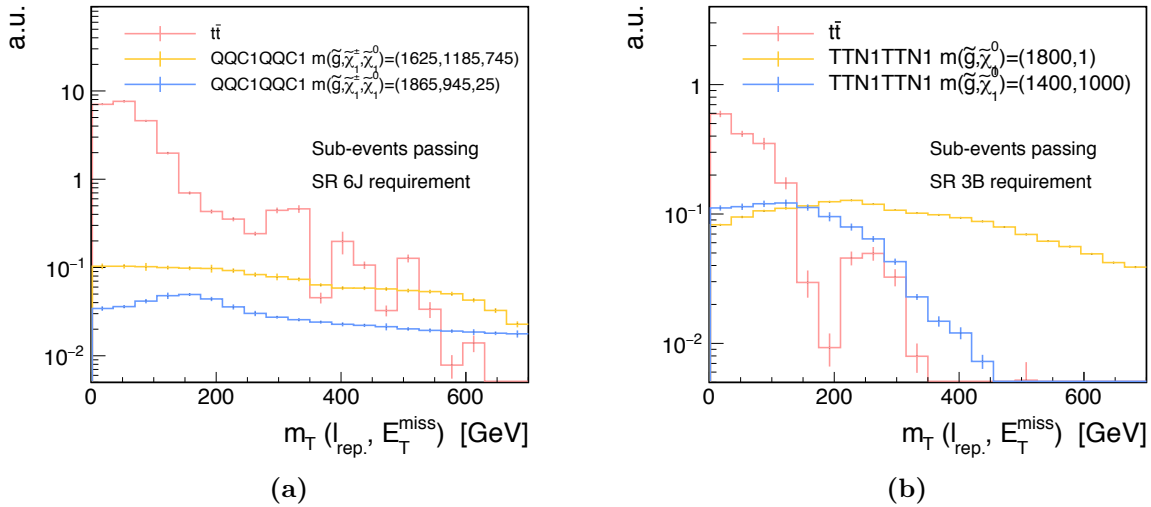


Figure 7.25: $m_T(\ell_{\text{rep.}}, E_T^{\text{miss}})$ distribution of sub-events passing the (a) SR 6J m_{eff} -inclusive selection, and (b) SR 3B m_{eff} -inclusive selection.

Event-level histogram and the statistical treatment

Multiple sub-events are generated by both the missing lepton replacement and the tau replacement from a single seed event. Those passing the analysis selections are collected and filled into a common histogram, referred as an “event-level histogram”. To account for their full statistical correlation between the filled sub-events, 100% error is then assigned to each bin of the event-level histogram. The summed event-level histograms over all seed events will be the desired distribution. While the statistical error on each bin is simply the quadratic sum of those over the all event-level histograms, there is generally also the inter-bin correlation since the bins of event-level histograms are not statistically independent between each other. This correlated uncertainty in fact needs to be modeled when performing the combined fit with multiple signal bins, which is examined and summarized in Sec. 8.3.

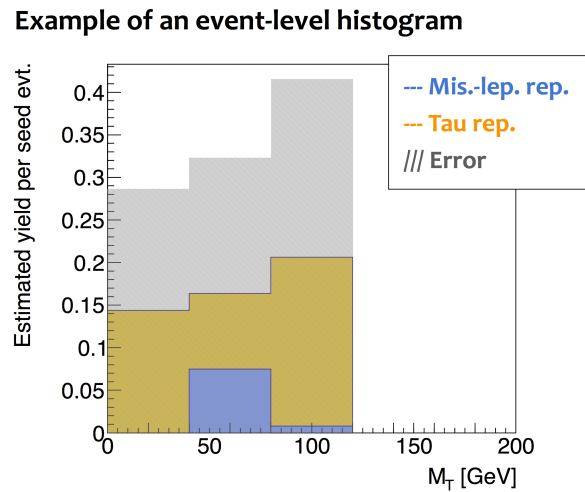


Figure 7.26: An example of event-level histogram. 100% uncertainty is assigned for each bin to account for the fact that all the entries are from the same seed. The final estimation is given by the sum of the event-level histograms over all seed events.

7.3.2 Closure Test using $t\bar{t}$ MC Samples

The methodologies are tested by comparing yields in regions with exactly one baseline lepton, between the estimation using the seed events in 2LCR and the actual $\ell\ell_{\text{mis.}}$ or $(\ell\tau_h)$ events. The test is referred as “closure test” where the level of disagreement (non-closure) indicates the generic accuracy about the method. The evaluated non-closure is assigned as systematics uncertainty. In the MC closure test, simulated $t\bar{t}$ sample is used in both seed events and the tested $\ell\ell_{\text{mis.}}$ ($\ell\tau_h$) events; the sample of seed events is provided by $t\bar{t} \rightarrow b\ell\nu b\ell\nu$ and that of the tested events are by $t\bar{t} \rightarrow b\ell\nu b\ell_{\text{mis.}}\nu$ and $t\bar{t} \rightarrow b\ell\nu b\tau\nu, \tau \rightarrow \tau_h\nu_\tau$. All irrelevant processes are excluded thus no subtraction is needed. The common 2LCR selection as defined in Table 7.9 is applied for seed events selection, except that the MET cut is removed in order to boost the statistics.

Figure 7.27-7.29 show the result with $p_T > 35$ GeV is required for the tag lepton. The test result for the case with a soft lepton ($p_T \in [6, 35]$ GeV) is displayed in the Appendix C.2.

Good closure is seen in overall kinematics. Non-closure generally stay within 10% (5%), and never exceeds 30% (10%) significantly for the missing lepton replacement (the tau replacement). Although the closure of missing lepton replacement is worse than that of tau replacement, it is not worrisome since the contribution of $\ell\ell_{\text{mis.}}$ is typically ~ 5 times smaller than $\ell\tau_h$.

Closure tests are also performed in phase space close to signal regions. Figure 7.30-7.31 are the btag/bveto-splitted closure in various regions requiring high MET, m_T , m_{eff} etc. The non-closure stay within 10% with respect to the overall estimation.

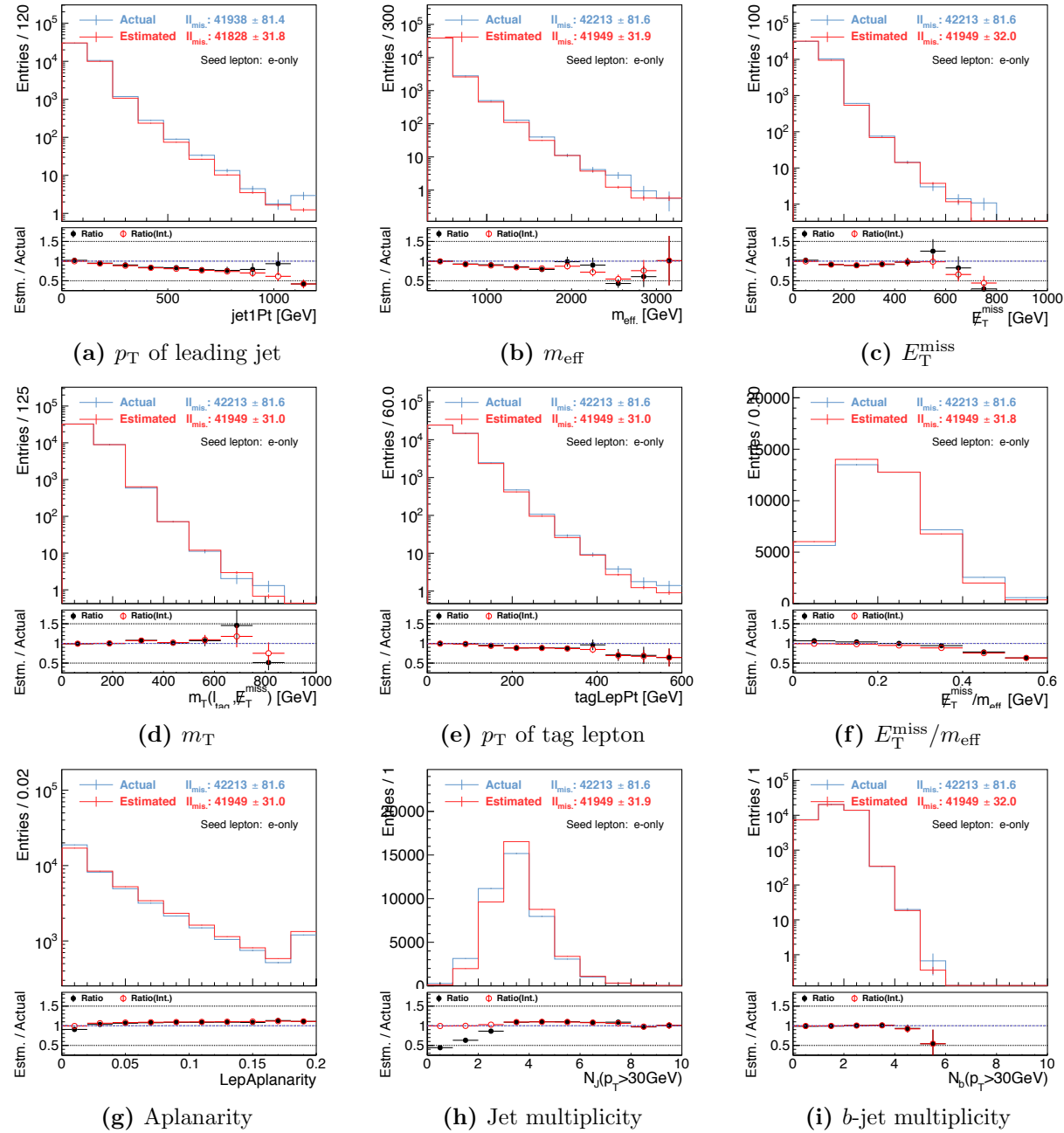


Figure 7.27: MC closure test for **missing lepton replacement** using $t\bar{t}$ MC sample. Seed events are collected by the single-lepton trigger. $p_T > 35$ GeV for the leading lepton is required. **Only electrons in the seed events are replaced.** Red points in the bottom plots show the ratio of integrated yields for the two histograms above the x-position that the point indicates.

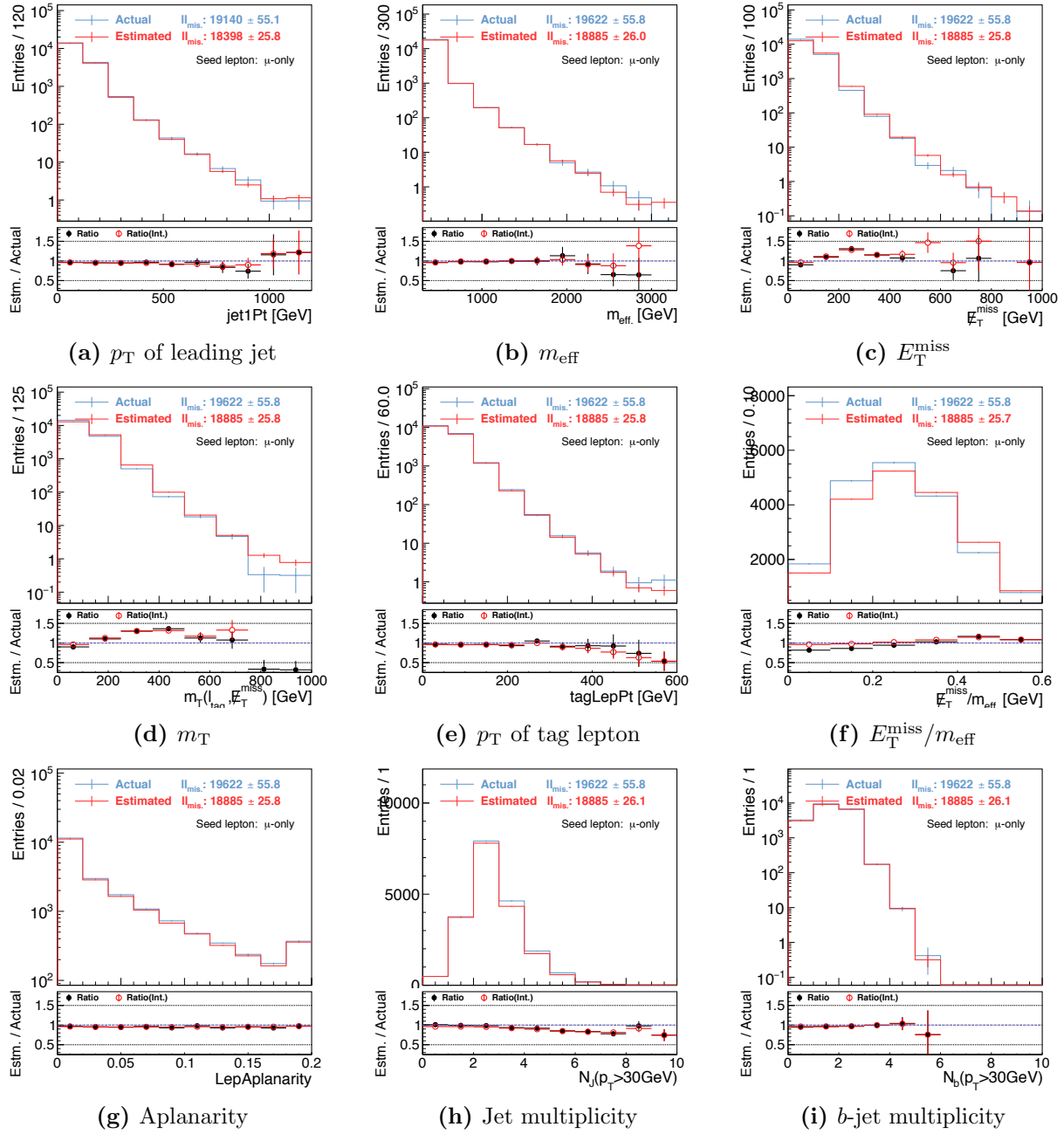


Figure 7.28: MC closure test for **missing lepton replacement** using $t\bar{t}$ MC sample. Seed events are collected by the single-lepton trigger. $p_T > 35$ GeV for the leading lepton is required. **Only muon in the seed events are replaced.** Red points in the bottom plots show the ratio of integrated yields for the two histograms above the x-position that the point indicates.

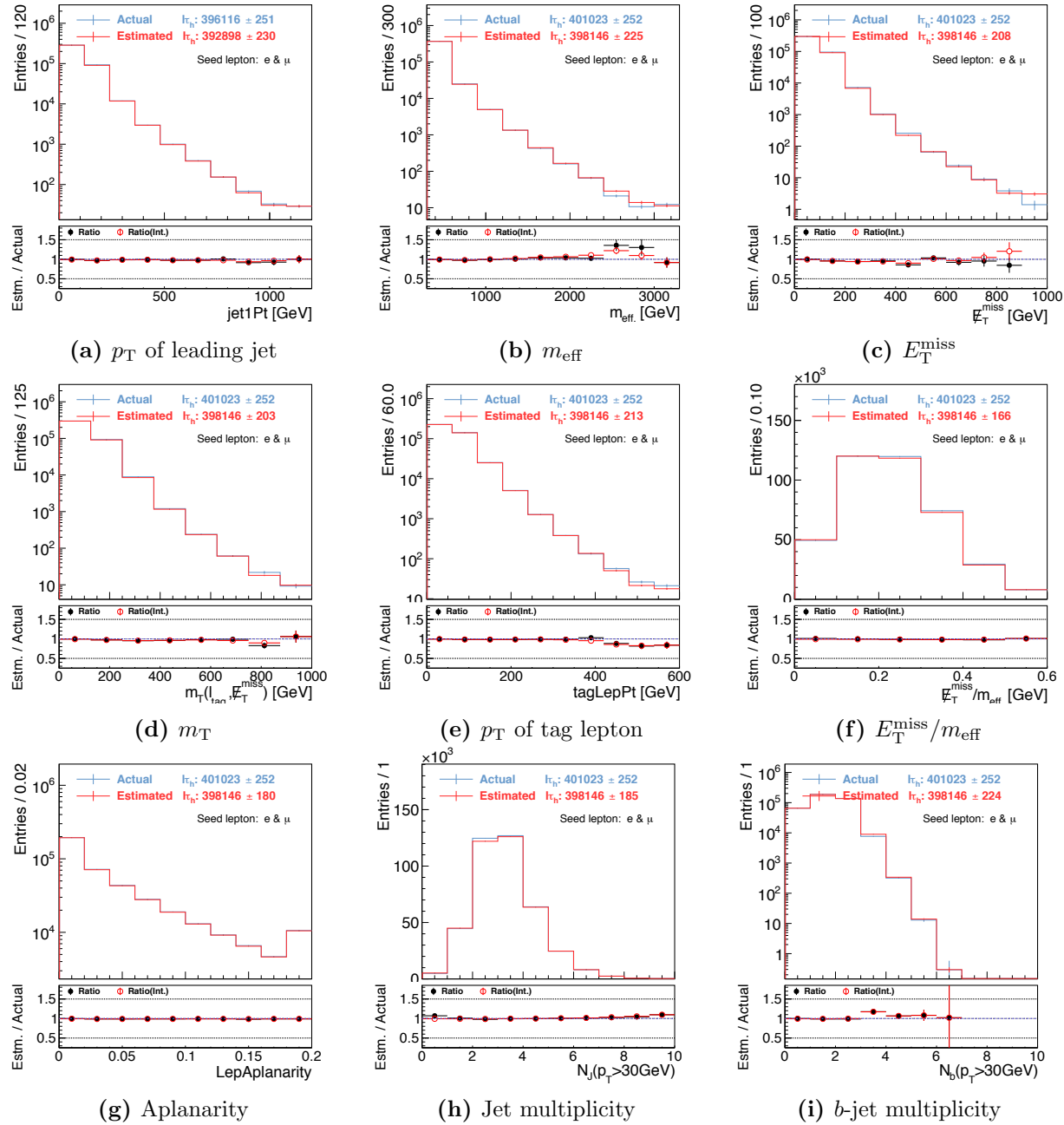


Figure 7.29: MC closure test for tau replacement using $t\bar{t}$ MC sample. Seed events are collected by the single-lepton trigger. $p_T > 35$ GeV for the leading lepton is required. **Both electrons and muons in the seed events are replaced.** Red points in the bottom plots show the ratio of integrated yields for the two histograms above the x-position that the point indicates.

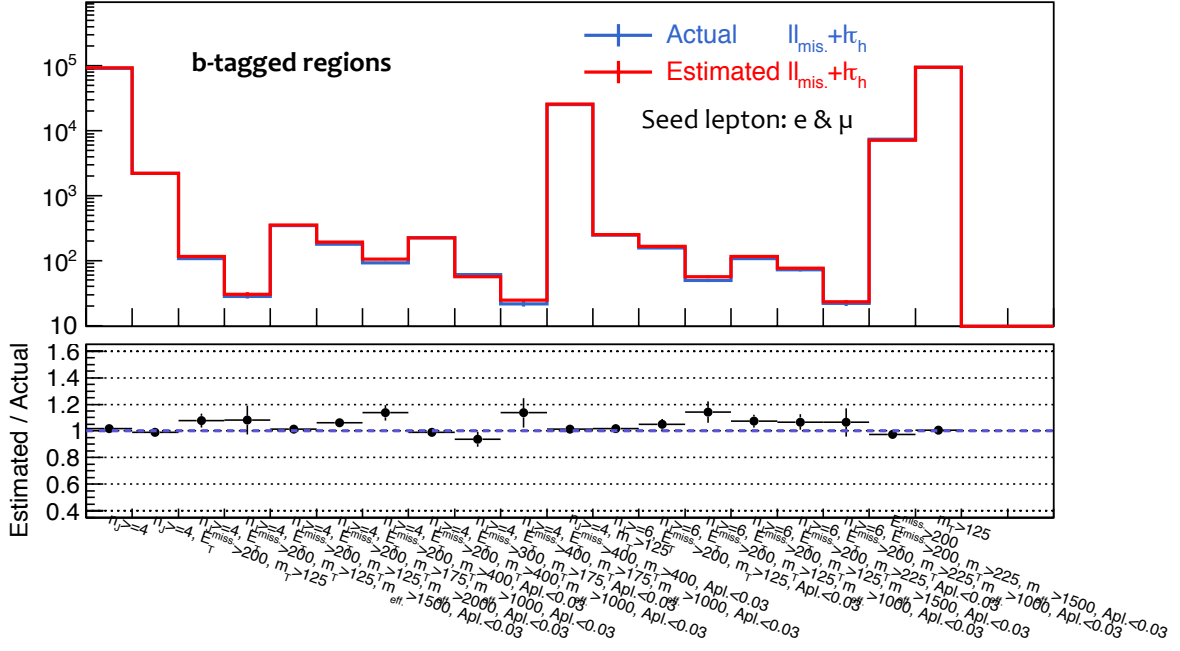


Figure 7.30: MC closure test for **combined estimation of missing lepton replacement and tau replacement** in various **b-tag** regions. Pre-selection $p_T(\ell_1) > 35$ GeV is applied on top of the cuts noted by the labels.

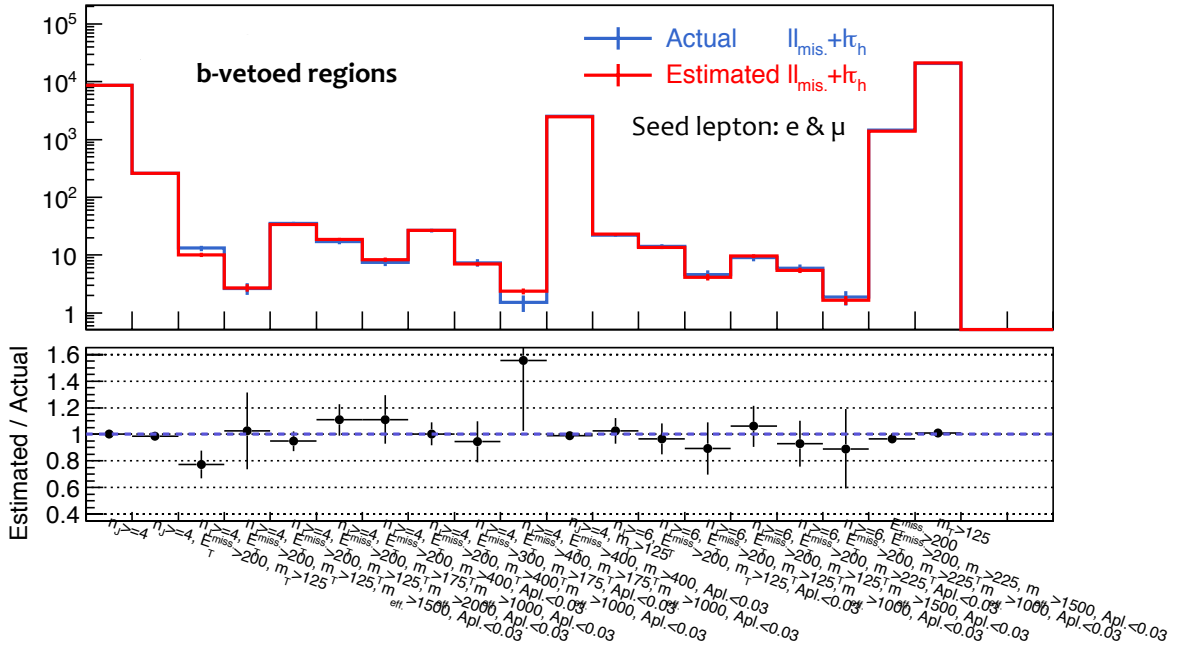


Figure 7.31: MC closure test for **combined estimation of missing lepton replacement and tau replacement** in various **b-vetoed** regions. Pre-selection $p_T(\ell_1) > 35$ GeV is applied on top of the cuts noted by the labels.

Visible non-closures are found in some distributions such as MET and jet transverse momentum, and the cause is nailed down as following:

Kinematical bias triggered by the two-lepton requirement in seed event selection

Though the orthogonality between kinematics and object properties (Eq. 7.1) generally hold as a good approximation, there is still some exception. The most notable example is when the parent particles of the two leptons in a seed event are heavily boosted, and the leptons get collimated and overlapped each other. This leads to deteriorated reconstruction/ID efficiency, therefore selecting events with exactly two leptons will discard part of such type of seed events automatically. The estimated spectra is biased and generally become softer. Electrons address more severe effect because the efficiency drop in the boosted environment is more striking than the case of muons.

Wrong assumption on tau polarization (for tau replacement)

For technical simplicity, tau decays are performed based on the unpolarized tau assumption, which is not true given that tau leptons here are mostly generated through weak decays of W -bosons. This can be seen in the non-closure observed in the visible tau fraction $x_\tau := E(\tau_h)/E(\tau)$ as shown in Figure 7.32 (a), and the non-closure found in the tails of the MET or m_T distribution is mainly ascribed to the propagated effect, given that those non-closure can be recovered by the ad hoc reweighting in terms of x_τ (see Figure 7.33). ⁵ Since the impact of this non-closure is marginal in estimating VRs and SRs (< 5%) fortunately, it is decided to be left as it is.

⁵This x_τ -reweighting correction is not brought into practice in the estimation, because the x_τ -profile varies by the physics processes (e.g. $t\bar{t}$, Wt or WW etc.) and the information of their relative breakdown needs to be provided from MC which uncertainty is not easy to evaluate.

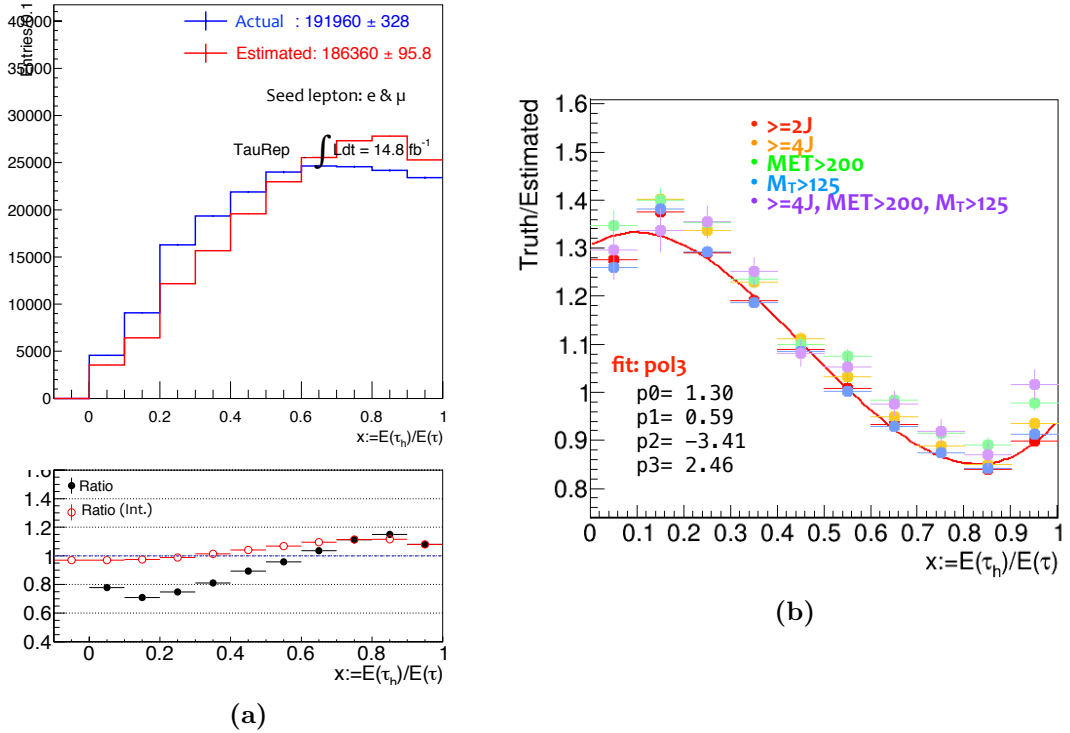


Figure 7.32: (a) Closure test in terms $x_\tau := E(\tau_h)/E(\tau)$. (b) Non-closure in terms of x_τ in various phase spaces. The non-closure can be well-modeled by a common third polynomial function, largely irrespective to phase space.

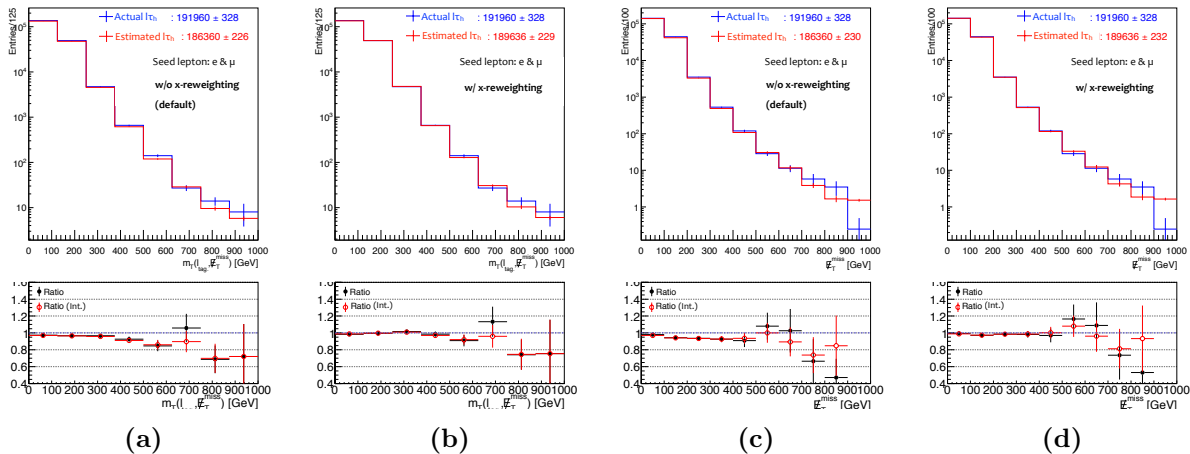


Figure 7.33: (a) m_T and (c) MET distribution before the reweighting in x_τ , and (b)(d) after the reweighting. The reweighting function is given by Figure 7.32 (b)

Treatment of missing muon (for missing muon replacement)

While the emulated missing muons are completely regarded as invisible particles in the replacement algorithm, the momenta of real unidentified muons do contribute to MET since their tracks are often included in the track soft term. This imperfect emulation leads to a non-closure around MET-related variables in the missing muon replacement. Naively thinking, this can be improved by simply stopping adding the missing muons momenta into MET. However, this is unfortunately not the case, as shown in Figure 7.34 where the improvement is limited in bulk region of the MET spectrum and the closure in the tail gets even worse. This is mainly because the poor momentum resolution of high pt unidentified muons is not emulated in the replacement. As the implementation of the full emulation is too costly compared with the small portion of missing muons backgrounds in the estimated regions, it is decided to keep the original treatment. Instead, the 30% of non-closure error is assigned to the estimation of the missing muon background.

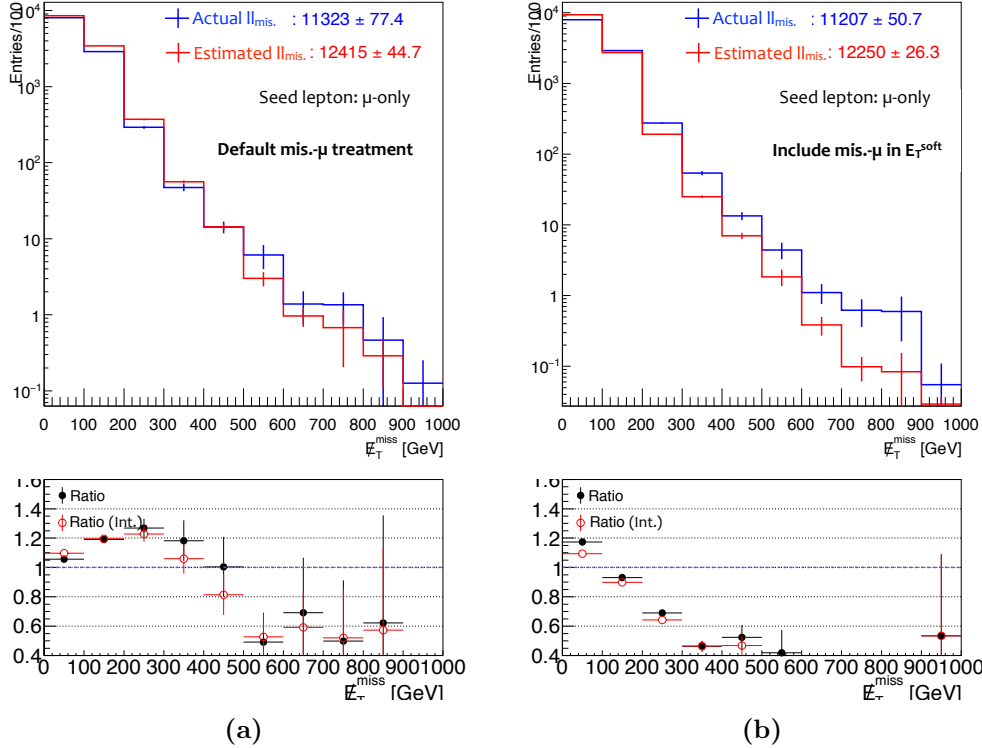


Figure 7.34: The MC closure of MET distribution for the missing muon sub-events, with missing muons are fully regarded (a) as invisible particles (default treatment), or (b) as visible particles.

7.3.3 Subtraction of Bogus Sub-events

One of the merits about the object replacement method is that the “di-leptonic” background can be inclusively estimated with a complete coverage regardless of the physics processes.⁶ The replacement of seed leptons from W -decays are totally valid, since the replaced sub-events do represent part of existing events in 1-lepton regions. On the other hand, the generated sub-events are not always sensible depending on the origin of the seed leptons:

- Seed leptons from Z -boson decays requests attention i.e. the sub-events of tau replacement will lead to a bogus topology of $Z \rightarrow \tau_h \ell$ ($\ell = e, \mu$) which never happens, thus these sub-events (bogus sub-events) are need to be subtracted.
- Likewise, seed leptons from leptonic tau decays ($\tau \rightarrow \ell \nu \bar{\nu}$) have the same issue that tau replacement leads to bogus sub-event where tau decays into tau again.
- Replacing a fake lepton can only end up in bogus sub-events. While the sub-traction takes place on sub-event basis, if can be only done statistically i.e. evaluate total contribution from bogus sub-events and subtract once.

The summary of legal and illegal replacement is given in Table 7.13 where bogus sub-events are label as “ \times ”. Note that the decision is made at the sub-event level (not at the seed event level), therefore even $W(\rightarrow \ell \nu) + \ell_{\text{fake}}$ can be seed events as long as one replaces ℓ rather than ℓ_{fake} .

The largest source of bogus sub-events are seed events with $\tau \rightarrow \ell \nu \bar{\nu}$ (denoted as τ_ℓ). The contribution is quite large, accounting for $10\% \sim 20\%$ of the estimated yields by the tau replacement. Therefore, a naive MC subtraction could introduce culprits from the MC mis-modeling, for example on $t\bar{t}$ as overviewed in Sec. 7.2.1. Instead, to avoid the impact, the subtraction is done in a form of ratio, such as:

$$y_\ell^{\text{Data}} = y_{\ell+\tau_\ell}^{\text{Data}} \times \frac{y_\ell^{\text{MC}}}{y_\ell^{\text{MC}} + y_{\tau_\ell}^{\text{MC}}} \quad (7.6)$$

where y_ℓ^{Data} ($y_{\ell+\tau_\ell}^{\text{Data}}$) denote the total yield estimated by tau replacement using data before (after) the subtraction, and y_ℓ^{MC} ($y_{\tau_\ell}^{\text{MC}}$) the contribution from legal (bogus) sub-events of tau replacement estimated by MC.

The subtraction of the $\ell \ell_{\text{fake}}$ is a little sensitive as MC modeling on fake leptons is less reliable in general. Therefore, relatively more aggressive suppression is applied at the stage of seed selection (Table 7.10) by requiring tighter isolation, in case that it could be addressing.

⁶The main contribuition is from $t\bar{t}$, Wt and WW , while minor contribution is found from $t\bar{t} + W/Z$ and WZ etc.

Table 7.13: Correspondence between origin of seed lepton and estimated components by the missing lepton replacement or the tau replacement. X represents any arbitrary particles. “ \times ” indicates that the generated sub-events represent non-existing processes (“bogus sub-events”) that requires the subtraction. The subscripts mis. denote missing leptons (leptons categorized in “Mis. Reco” and “Mis. ID” defined in Table 7.1).

Parent of seed lepton	sub-events of mis. lep. rep.	sub-events of tau rep.
$W(\rightarrow \ell\nu)$	$W + X, W \rightarrow \ell_{\text{mis.}}\nu$	$W + X, W \rightarrow \tau_h\nu$
$Z(\rightarrow \ell\ell)$	$Z + X, Z \rightarrow \ell_{\text{mis.}}\ell$	\times
$\tau(\rightarrow \tau_\ell\nu)$	$\tau_{\ell,\text{mis.}} + X$	\times
Fake	\times	\times

7.3.4 Closure Test using Data

In order to demonstrate the procedures beyond the ideal MC closure tests done in Sec. 7.3.2 such as the bogus sub-event subtraction (Sec. 7.3.3), another validation study is done using the data events.

Since the nominal VRs (Table 6.7 - 6.11) tends to have too tight selections resulting in small data statistics, a set of high- m_T regions “VRs-objRep” with relatively loose selections are deliberately defined, in which the object replacement estimation and data is compared. Nine complementary bins are defined as shown in Table 7.14.

It is populated by $\ell\ell_{\text{mis.}} + \ell\tau_h$ events with the purity of $\sim 30 \sim 60\%$, and the rest of backgrounds that are not covered by the object replacement (namely the “semi-leptonic”, “2L-Out. Acc” and “2L-Mis. OR” components) are estimated by a kinematics extrapolation where the MC of $W + \text{jets}$ and the top background is normalized to data in the corresponding control region bins (“CRs-objRep”) defined in Table 7.14 which are only different in the m_T cut with respect to VRs-objRep. An upper cut in aplanarity is placed in both VRs-objRep and CRs-objRep so that the signal contamination is reasonably subdued. Statistical uncertainty from the control region statistics, and a flat 5% non-closure error is assigned for the object replacement estimation in all the VR bins.

The result is presented in Figure 7.35. Nice agreement is observed where data is consistent with expectations within the uncertainty.

Table 7.14: Definition of VRs(CRs)-objRep. MC of $W + \text{jets}$ and the top background are normalized in corresponding CR-objRep.

	$n_J (p_T > 30 \text{ GeV})$	$E_T^{\text{miss}} [\text{GeV}]$	$m_T [\text{GeV}] (\text{CR-objRep})$	$m_{\text{eff}} [\text{GeV}]$	Aplanarity
bin-1	≥ 4	> 200	$> 125 (\in [60, 125])$	> 1500	< 0.03
bin-2	≥ 4	> 200	$> 125 (\in [60, 125])$	> 2000	< 0.03
bin-3	≥ 4	> 200	$> 175 (\in [60, 125])$	> 1000	< 0.03
bin-4	≥ 4	> 200	$> 400 (\in [60, 125])$	—	< 0.03
bin-5	≥ 4	> 200	$> 400 (\in [60, 125])$	> 1000	< 0.03
bin-6	≥ 4	> 300	$> 175 (\in [60, 125])$	—	< 0.03
bin-7	≥ 4	> 400	$> 175 (\in [60, 125])$	> 1000	< 0.03
bin-8	≥ 6	> 400	$> 400 (\in [60, 125])$	—	< 0.03
bin-9	≥ 6	> 200	$> 125 (\in [60, 125])$	> 1500	< 0.03

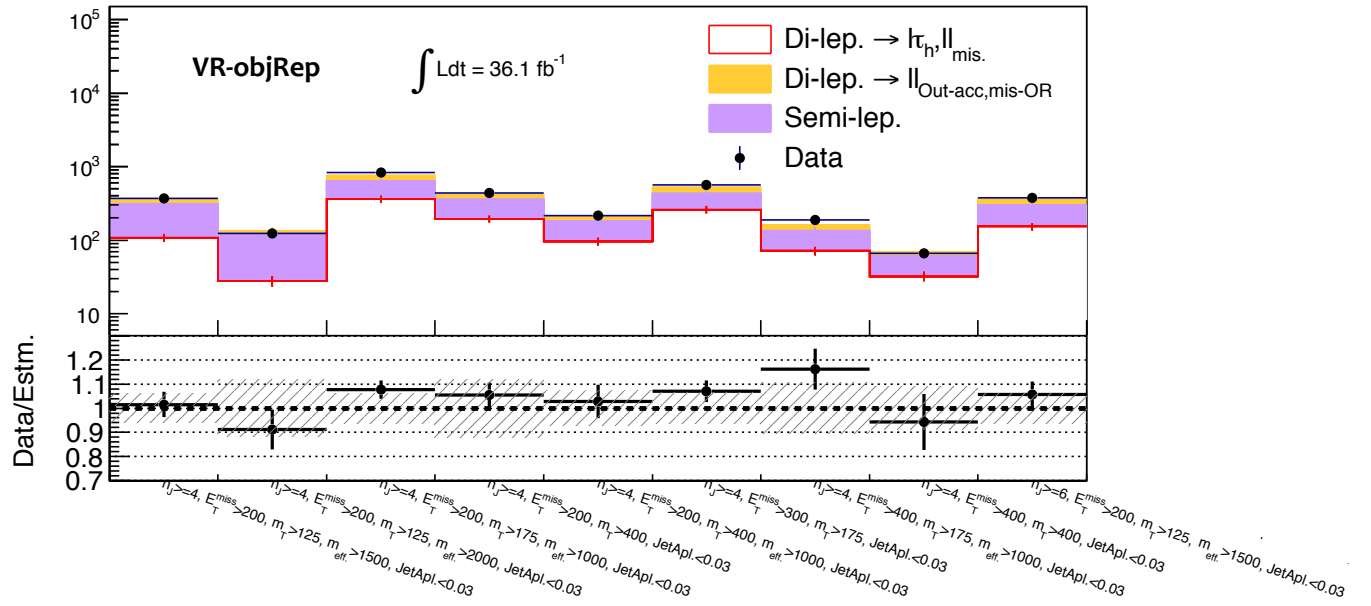


Figure 7.35: Closure test in VR-objRep bins. The white component is the yield of the $\ell\ell_{\text{mis}} + \ell\tau_h$ events that are estimated by the object replacement, while the colored stack represents the “semi-leptonic” (purple) and rest of the “di-leptonic” component (“2L-Out. Acc / Mis. OR”, orange) respectively. The bottom row plots the ratio between the estimated yield and the actual number of data. The gray dashed band shows the uncertainty in the estimation, including statistical error due to the CR statistics and a flat 5% non-closure for the object replacement.

7.4 Unblinded Validation Regions

The background estimation is inclusively tested in validation regions VR_a and VR_b defined in Table 6.7 - 6.11, where the phase space are close enough to the signal regions, giving the sensible demonstration of the estimation.

Table 7.15 - 7.19 show the data yields compared with the expected backgrounds together with the breakdown. The components estimated by the object replacement are merged and denoted as “Di-leptonic” in the tables, while the yields for the other components provided by the kinematical extrapolation are exclusively listed for each physic process. The attached errors are all post-fit uncertainty obtained by profiling the nuisance parameters (detail can be found in Sec. 9.1).

The visualized comparison between data and background expectation is illustrated in 7.36, together with the pulls defined by the number of gaussian-equivalent deviation. The tension with respect to data never exceeds 2σ , which can still be ascribed to the effects that the systematic uncertainties assigned mainly in the kinematical extrapolation. For instance, the trend of underestimation on $W + \text{jets}$ in some of the VR_b (in particular 2J) is expected by the correlation between extrapolating variables and the ill-modeled variables, which will be discussed in detail in Sec. 7.2. 15% of uncertainty is in fact assigned for this effect (based on Figure D.1.7, with the mis-modeling parameter w to be at ~ 0.1).

Another source of systematical underestimation is understood by the potential MC mis-modeling in the m_T shape as mentioned in Sec. 7.2.1; for $W + \text{jets}$, the cut-off at $m_T \sim m_W$ in MC is sharper than that in the data. No theoretical uncertainties are dedicatedly assigned for this effect, however it could still be explained by other theoretical uncertainties given the $\sim 1\sigma$ discrepancy; for $t\bar{t} + Wt$, lack of full description of interference between the non-top $WWbb$ diagrams is the potential reason for the underestimation for which 5% \sim 30% of systematics is assigned for the portion that the kinematical extrapolation estimates. All in all, underestimation upto 1σ is expected therefore we don't regard this as an issue.

The post-fit kinematical distributions in VRs are presented in Figure C.4.9-C.4.12 in the appendix.

Table 7.15: Number of observed data and the estimated background yields in the validation regions in tower **2J**. The component estimated by the object replacement method is symbolized as “Di-leptonic”, while the others are estimated by the kinematical extrapolation method. Uncertainties include both systematic uncertainties discussed in chapter 8 and the uncertainties due to the limited data statistics in CR or the MC statistics. The uncertainties are symmetrised and truncated so that the yields remain positive.

VRa 2J	$m_{\text{eff.}} \in [1100, 1500]$	$m_{\text{eff.}} \in [1500, 1900]$	$m_{\text{eff.}} > 1900$
Observed data	222	46	23
Expected background	209.88 ± 21.80	38.67 ± 5.51	17.28 ± 3.25
Di-leptonic	91.5 ± 11.1	11.7 ± 2.6	5.7 ± 1.6
$W + \text{jets}$	20.9 ± 3.8	8.0 ± 2.6	3.2 ± 1.3
$Z + \text{jets}$	2.6 ± 0.7	0.8 ± 0.2	0.3 ± 0.1
Tops	85.6 ± 18.0	15.6 ± 3.8	6.9 ± 2.8
Di-boson	6.0 ± 2.2	1.5 ± 0.5	0.8 ± 0.3
$t\bar{t} + V$	3.2 ± 0.5	0.9 ± 0.2	0.4 ± 0.1
VRb 2J	$m_{\text{eff.}} \in [1100, 1500]$	$m_{\text{eff.}} \in [1500, 1900]$	$m_{\text{eff.}} > 1900$
Observed data	390	113	52
Expected background	314.33 ± 36.92	104.33 ± 13.80	41.34 ± 8.95
Di-leptonic	10.5 ± 2.4	3.0 ± 1.1	3.7 ± 1.3
$W + \text{jets}$	219.5 ± 34.9	76.8 ± 13.0	24.9 ± 9.2
$Z + \text{jets}$	5.1 ± 1.3	2.0 ± 0.6	0.8 ± 0.2
Tops	56.7 ± 14.1	15.7 ± 4.5	8.1 ± 3.2
Di-boson	21.3 ± 7.4	6.3 ± 4.5	3.5 ± 1.1
$t\bar{t} + V$	1.2 ± 0.2	0.5 ± 0.1	0.4 ± 0.1

Table 7.16: Number of observed data and the estimated background yields in the validation regions in tower **6J**. The component estimated by the object replacement method is symbolized as “Di-leptonic”, while the others are estimated by the kinematical extrapolation method. Uncertainties include both systematic uncertainties discussed in chapter 8 and the uncertainties due to the limited data statistics in CR or the MC statistics. The uncertainties are symmetrised and truncated so that the yields remain positive.

VRa 6J	$m_{\text{eff.}} \in [1100, 1600]$	$m_{\text{eff.}} \in [1600, 2100]$	$m_{\text{eff.}} > 2100$
Observed data	130	60	31
Expected background	134.22 ± 18.17	48.27 ± 7.79	28.71 ± 4.57
Di-leptonic	71.9 ± 15.2	24.7 ± 6.8	11.5 ± 3.5
$W + \text{jets}$	7.6 ± 1.8	4.0 ± 1.0	2.5 ± 0.9
$Z + \text{jets}$	0.6 ± 0.2	0.3 ± 0.1	0.2 ± 0.1
Tops	45.7 ± 9.8	16.0 ± 3.7	12.0 ± 2.9
Di-boson	4.6 ± 1.5	2.1 ± 0.7	1.6 ± 0.7
$t\bar{t} + V$	3.8 ± 0.7	1.2 ± 0.3	0.9 ± 0.2
VRb 6J	$m_{\text{eff.}} \in [1100, 1600]$	$m_{\text{eff.}} \in [1600, 2100]$	$m_{\text{eff.}} > 2100$
Observed data	99	53	26
Expected background	84.21 ± 10.42	43.22 ± 5.50	25.15 ± 3.89
Di-leptonic	0.9 ± 0.4	1.0 ± 0.8	0.5 ± 0.4
$W + \text{jets}$	32.9 ± 6.5	21.8 ± 4.7	8.6 ± 2.9
$Z + \text{jets}$	0.4 ± 0.2	0.3 ± 0.1	0.2 ± 0.1
Tops	43.1 ± 9.0	16.3 ± 3.8	13.0 ± 3.4
Di-boson	5.6 ± 2.6	2.9 ± 1.8	2.3 ± 1.1
$t\bar{t} + V$	1.3 ± 0.3	0.9 ± 0.2	0.5 ± 0.2

Table 7.17: Number of observed data and the estimated background yields in the control regions in tower **Low-x**. Uncertainties include both systematic uncertainties discussed in chapter 8 and the uncertainties due to the limited data statistics in CR or the MC statistics. The uncertainties are symmetrised and truncated so that the yields remain positive.

VR Low-x	VRa	VRb
Observed data	20	23
Expected background	14.91 ± 2.09	15.77 ± 3.31
Di-leptonic	6.5 ± 1.2	0.6 ± 0.3
$W + \text{jets}$	1.5 ± 0.8	6.9 ± 3.3
$Z + \text{jets}$	0.5 ± 0.2	0.5 ± 0.2
Tops	5.0 ± 1.7	6.1 ± 2.1
Di-boson	1.0 ± 0.3	1.4 ± 0.4
$t\bar{t} + V$	0.4 ± 0.1	0.4 ± 0.1

Table 7.18: Number of observed data and the estimated background yields in the control regions in tower **High-x**. Uncertainties include both systematic uncertainties discussed in chapter 8 and the uncertainties due to the limited data statistics in CR or the MC statistics. The uncertainties are symmetrised and truncated so that the yields remain positive.

VR High-x	VRa	VRb
Observed data	66	119
Expected background	49.33 ± 8.80	102.12 ± 13.40
Di-leptonic	18.9 ± 5.4	0.0 ± 0.0
$W+jets$	8.8 ± 1.8	70.6 ± 13.3
$Z+jets$	0.4 ± 0.1	0.7 ± 0.3
Tops	16.0 ± 6.8	21.5 ± 7.5
Di-boson	4.2 ± 1.6	8.5 ± 3.2
$t\bar{t} + V$	1.1 ± 0.4	0.8 ± 0.3

Table 7.19: Number of observed data and the estimated background yields in the validation regions in tower **3B**. The component estimated by the object replacement method is symbolized as “Di-leptonic”, while the others are estimated by the kinematical extrapolation method. Uncertainties include both systematic uncertainties discussed in chapter 8 and the uncertainties due to the limited data statistics in CR or the MC statistics. The uncertainties are symmetrised and truncated so that the yields remain positive.

VRa 3B	$m_{\text{eff.}} \in [1000, 1750]$	$m_{\text{eff.}} > 1750$
Observed data	11	8
Expected background	12.46 ± 5.81	5.31 ± 1.58
Di-leptonic	7.3 ± 5.5	2.7 ± 1.3
$W+jets$	$0.0^{+0.0}_{-0.0}$	0.0 ± 0.0
$Z+jets$	0.0 ± 0.0	0.0 ± 0.0
Tops	4.8 ± 1.7	2.4 ± 0.9
Di-boson	$0.1^{+0.1}_{-0.1}$	0.0 ± 0.0
$t\bar{t} + V$	0.2 ± 0.1	0.2 ± 0.0
VRb 3B	$m_{\text{eff.}} \in [1000, 1750]$	$m_{\text{eff.}} > 1750$
Observed data	69	12
Expected background	60.09 ± 15.83	9.55 ± 2.77
Di-leptonic	3.3 ± 1.4	0.8 ± 0.6
$W+jets$	0.8 ± 0.5	0.4 ± 0.2
$Z+jets$	0.1 ± 0.0	0.0 ± 0.0
Tops	54.1 ± 15.7	7.8 ± 2.7
Di-boson	0.1 ± 0.1	0.2 ± 0.1
$t\bar{t} + V$	1.7 ± 0.4	0.4 ± 0.1

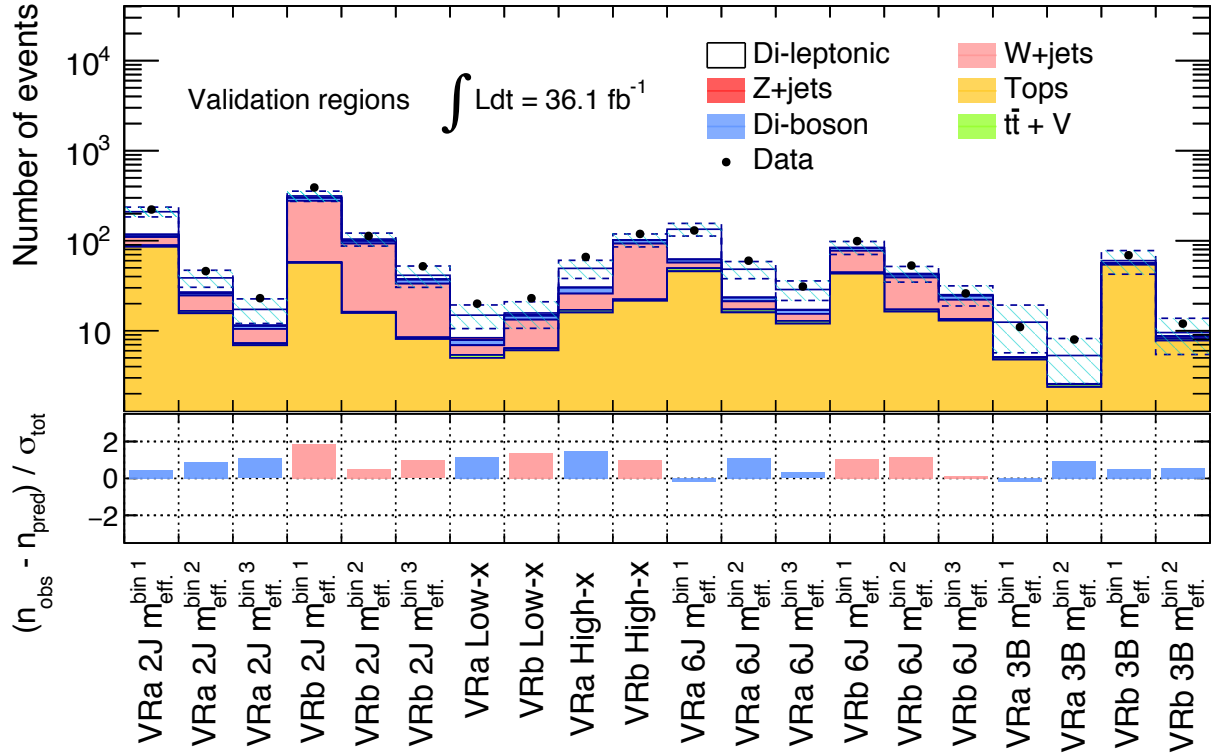


Figure 7.36: (Top) Number of observed data (black dots) and the estimated background yields (histogram) in the nominal validation regions (VRa/VRb). The white component is the backgrounds estimated by the object replacement method, while the colored ones are by the kinematical extrapolation method. The dashed band represents the combined statistical and systematic uncertainties on the total estimated backgrounds. (Bottom) Pull between the data and the estimation. Pulls in regions dominated by $W + \text{jets}$ and tops are painted by pink and blue respectively.

Chapter 8

Systematic Uncertainties

Uncertainties associated with background estimations and the signal modeling is dedicatedly discussed in this section. They are largely three-fold: instrumental uncertainties, theoretical uncertainties and the generic uncertainties for the background estimation methods. This chapter overviews the sources and discusses the evaluation.

8.1 Instrumental Uncertainty

Instrumental uncertainties are the systematic uncertainty regarding to the experiment, including the imperfection of calibration and mis-modeling of detector response and so on.

Jets

Despite the dedicated calibration procedures as described in Sec. 4.6, the residual uncertainty on the jet energy scale (JES) is often the largest source of instrumental uncertainty, since a slight shift in jet energy can cause a drastically change in the tail of the distributions. 87 independent uncertainties are modeled from each step in the calibration, including the MC uncertainty and observed discrepancy between MC and data. In the analysis, those with similar behavior are statistically combined, reducing into 8 independent uncertainties.

The sub-leading jet uncertainty is on the energy resolution (JER). JER measurement is done by the same dataset used in the in-situ JES calibration (see Sec. 4.6.2), using the balanced well-measured objects in di-jet or Z/γ^*+ jets events [84]. The uncertainty is quoted from the data/MC discrepancy, as well as the magnitude of the noise term reflecting our imperfect understanding of the origin. Figure 8.1 show the measured total uncertainty on JES and JER.

Systematics associated with flavor tagging are also important since the analysis deeply relies on the classification in terms of b -jet multiplicity. The uncertainty on the efficiency of b -jets and wrongly tagged light-flavor jets is separately evaluated by varying the training samples for each sub-algorithm, as well as the training configuration of the combining algorithm MV2. The resultant uncertainty is typically in a range of 5% \sim 10%.

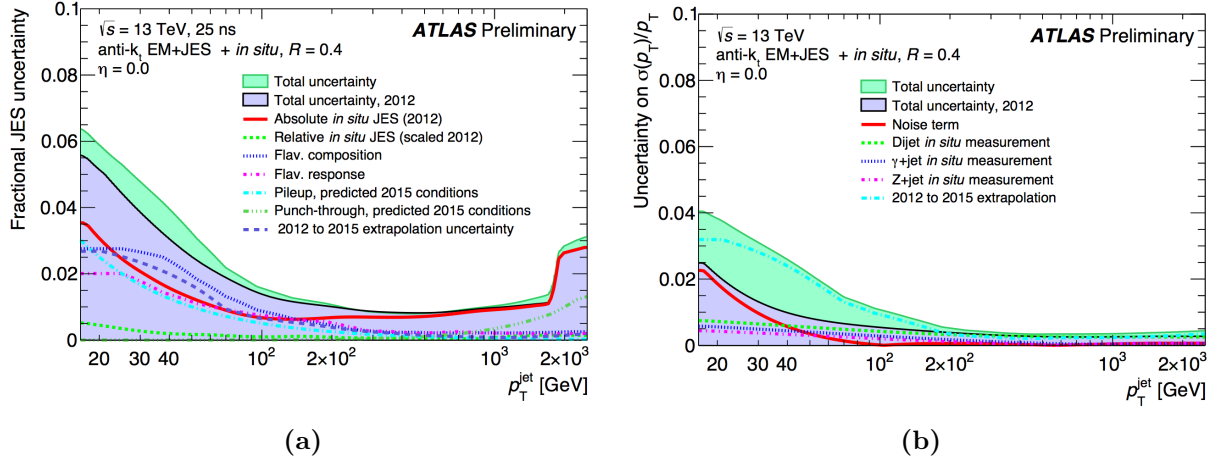


Figure 8.1: Measured uncertainty on (a) jet energy scale (JES), and (b) the relative resolution, with the breakdown of the sources [84].

Other uncertainties are qupted regarding to the angular position determination (η -calibration uncertainty) or JVT (Jet Vertex Tagger, Sec. 4.6) modeling.

Electrons

Electrons involve three efficiency uncertainties i.e. reconstruction, identification and isolation. These are mainly evaluated by the observed differences between the efficiencies measured using the $Z \rightarrow ee$ events from data and from the simulation. The uncertainties on the energy scale and resolution modeling are also taken into account. They are evaluated based on the discrepancy between simulated and observed response of the EM calorimeter in Run2.

Muons

Four efficiency uncertainties and two separated scale uncertainties are associated to muons. All the uncertainties are derived from the differences between the MC expectation and observed measurement outcome using the $Z \rightarrow \mu\mu$ events. The efficiency uncertainties involve the reconstruction, identification, isolation and TTVA (Tracks-To-Vetex-Association), while the two scale uncertainties corresponds to the statistical and systematic uncertainty in the measurement.

Missing Transverse Energy

On top of the propagated uncertainties on the scales and resolutions of the reconstructed objects, MET suffers from additional uncertainty regarding to the modeling of the soft term defined in Sec. 4.9. This is measured using the $Z(\rightarrow \ell\ell) + \text{jets}$ events, by comparing the expected momentum profile of soft terms and the observed ones.

8.2 Theoretical Uncertainty

Uncertainties associated with the generated events in simulation subject to theoretical uncertainty. This is the main uncertainty for the kinematical extrapolation and signal modeling, while the object replacement suffers from negligible impact. The sources of such uncertainties are as follow:

Cross-section uncertainty

The primary source contributing to it is the missing higher-order terms in the calculation, such as terms beyond NNLO for the NLO calculation, or the absence of soft gluon resummation. The other typical sources are from PDF, and measurement precision on standard model parameters, particularly in strong coupling constant and quark masses for higher order QCD correction. Since this uncertainty only affects the global normalization of each physics processes, those of $W + \text{jets}$ and top background will vanish during the normalization in CRs.

Choice of renormalization scales

The renormalization scale ($\mu_{\text{renom.}}$) is a non-physical theory parameter known to have no impact on observables when all the terms in the perturbation series is taken into account. However, it is not the case when considering a fixed-order calculation truncating part of the higher-order terms, leaving a non-physical dependency. This is commonly regarded as the generic precision that the calculation can address. The variation due to the different choice of $\mu_{\text{renom.}}$ is quoted as systematics in this analysis, which is evaluated by shifting $\mu_{\text{renom.}}$ from the default scale by factor of 2 or 0.5. There have been claims that the choice of scales appearing in factorization and resummation can be independent of $\mu_{\text{renom.}}$. The dependencies on those scale are additionally evaluated in the same recipe in case of SHERPA where those scales are separately parametrized.

Parton shower (PS)

The modeling dependence on parton showering schemes or setup is quoted as systematics. For top backgrounds, this is done by directly comparing the default scheme using PYTHIA 6.428 with the alternative using HERWIG. The difference is taken as 1σ variation. For the other backgrounds generated by SHERPA, the dependency on the matching scale in the CKKW matching is quoted for the parton shower systematics. While the default matching scale is set to $\mu_{\text{CKKW}} = 20$ GeV, the up (down) variation is generated by shifting it to $\mu_{\text{CKKW}} = 15(30)$ GeV. For SUSY signals, 5 variations are generated by tuning the internal parameters in PYTHIA 8.186. The uncertainties are evaluated by the variance with respect to the nominal one, and added in quadrature.

Interference between $WWbb$ diagrams (for top background)

The diagrams of $t\bar{t} + Wt$ and the other $WWbb$ diagrams do interfere each other since they are in the common final states. This is actually missed in the MC description as the involvement of top-quarks is explicitly required in the sample generation of top backgrounds. The impact is known to be significant after a high m_T cut is applied where the bulk $t\bar{t}$ component is suppressed (see Figure 8.2). It is then evaluated by comparing two truth-level MadGraph samples: one with the only diagrams of $t\bar{t} + Wt$, and the other with inclusive $WWbb$ diagrams. The difference is taken as 1σ variation.

Hard process description (for $t\bar{t} + W/Z/WW$)

As $t\bar{t} + W/Z/WW$ have not dedicatedly measured in precision using data yet, there is no particular generator favored by data i.e. the prediction by MADGRAPH5_aMC@NLO (nominal) and SHERPA (alternative) are equivalent. An envelope calculation is then done by comparing the modeling of MG5_aMC@NLO and SHERPA, and the difference is quoted as a systematics in terms of the hard process description.

While the envelope calculations are done all using MC, the limited MC statistics becomes an issue in quantifying $5\% \sim 10\%$ level difference. Therefore, some of the cuts are loosened, and different recipes are employed depending on the type of samples, which will be detailed as following sections.

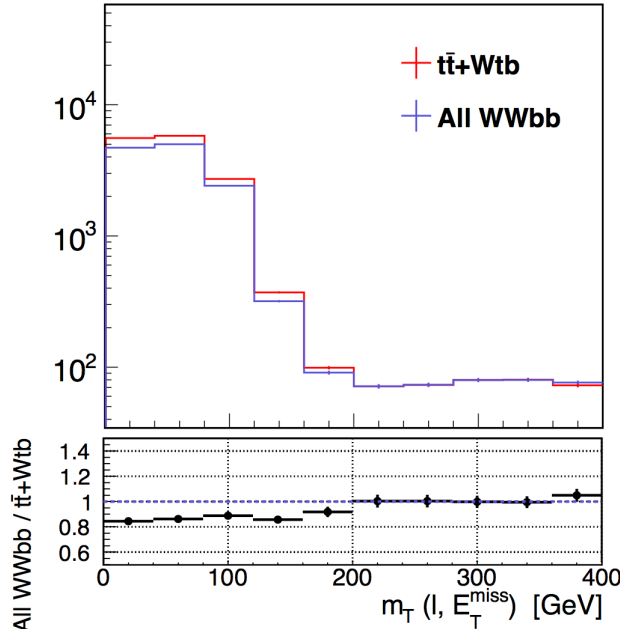


Figure 8.2: Comparison of the m_T shape between $t\bar{t} + Wt \rightarrow WWbb$ (red) and all $WWbb$ (blue).

8.2.1 Normalized Backgrounds: $W + \text{jets}$ and Tops

The uncertainties for the normalized backgrounds ($W + \text{jets}$ and top background) are essentially the MC modeling uncertainties on the extrapolation variables (mt , aplanarity and topness etc.). They are evaluated by computing the variation in the ratio of MC yields between in a CR and a SR (or VR) when the systematical variations are applied. Some of the cuts are released to suppress the statistical fluctuation in MC to a reasonable level. b -jet requirement is first removed, based on the fact that it is generally orthogonal to kinematics. The m_{eff} cut is also removed in addition to it, based on the concept that the shape variation in terms of the extrapolation variables are tested. Therefore, the evaluated systematics are common to all the bins in the same tower eventually. Table 8.2a (8.2b) summarizes the evaluated uncertainties for $W + \text{jets}$ (top background). Systematics contributing below 5% or 5 times less than that of the leading uncertainty in the region are ignored (labeled as "-").

Table 8.1: Assigned theory uncertainties for (a) $W + \text{jets}$ and (b) top background [%]. The uncertainties are all shared by the m_{eff} -bins in the same tower. The symbols stand for; $\mu_{\text{fact.}}$: systematic variation in factorization scale, $\mu_{\text{resum.}}$: resummation scale, $\mu_{\text{ren.}}$: renormalization scale, “PS”: Parton shower, “INTF”: interference between $t\bar{t} + Wtb$ and other $WWbb$ diagrams.

(a) $W + \text{jets}$					(b) Top background			
	$\mu_{\text{fact.}}$	$\mu_{\text{resum.}}$	$\mu_{\text{ren.}}$	PS		$\mu_{\text{fact.}}, \mu_{\text{ren.}}$	INTF.	PS
SR 2J	-	7	7	9	SR 2J	22	17	8
SR 6J	9	-	23	-	SR 6J	21	24	25
SR Low-x	-	11	-	6	SR Low-x	15	13	10
SR High-x	19	7	-	-	SR High-x	15	17	28
SR 3B	36	15	-	19	SR 3B	27	25	13
VRa 2J	-	8	12	-	VRa 2J	12	5	10
VRa 6J	13	11	-	-	VRa 6J	15	7	9
VRa Low-x	9	-	8	8	VRa Low-x	10	12	6
VRa High-x	-	6	-	9	VRa High-x	17	10	-
VRa 3B	20	16	7	6	VRa 3B	13	26	8
VRb 2J	-	4	3	7	VRb 2J	-	21	10
VRb 6J	5	-	5	6	VRb 6J	-	19	5
VRb Low-x	-	5	6	5	VRb Low-x	-	18	5
VRb High-x	5	-	-	5	VRb High-x	-	23	8
VRb 3B	-	5	5	5	VRb 3B	-	25	7

8.2.2 Non-normalized Backgrounds: $Z + \text{jets}$, di-bosons and $t\bar{t} + W/Z/WW$

The cross-section uncertainty for $Z + \text{jets}$, di-bosons and $t\bar{t} + W/Z/WW$ amounts upto level of 5% [141], 6% [128] and 13% [114] respectively. The other uncertainties affecting the shape are evaluated in SRs/VRs with the cuts in m_T , aplanarity and topness are removed, as well as the b -tagging requirement. This is because that the impact of systematics is dominantly seen in spectra regarding to jet activity, in particular jet-multiplicity and m_{eff} . The uncertainties derived for each m_{eff} -bin of SR and VR are summarized in Table 8.3. Systematics contributing below 5% or 5 times less than that of the leading uncertainty in the region are ignored.

Table 8.3: Assigned theory uncertainties for $Z + \text{jets}$, di-bosons and $t\bar{t} + W/Z/WW$ [%]. The symbols stand for; $\mu_{\text{fact.}}$: systematic variation in factorization scale, $\mu_{\text{resum.}}$: resummation scale, $\mu_{\text{ren.}}$: renormalization scale, “PS”: Parton shower, “Hard proc.”: systematics assigned based on the generator comparison.

	$Z + \text{jets}$			Di-bosons			$t\bar{t} + W/Z/WW$	
	$\mu_{\text{fact.}}$	$\mu_{\text{ren.}}$	PS	$\mu_{\text{fact.}}$	$\mu_{\text{resum.}}$	$\mu_{\text{ren.}}$	$\mu_{\text{fact.}}, \mu_{\text{ren.}}$	Hard proc.
2J $m_{\text{eff}}^{\text{bin}1}$	-	23	7	-	-	16	-	9
2J $m_{\text{eff}}^{\text{bin}2}$	-	25	-	21	-	21	5	10
2J $m_{\text{eff}}^{\text{bin}3}$	-	25	-	-	-	23	-	16
6J $m_{\text{eff}}^{\text{bin}1}$	-	35	-	8	9	19	-	8
6J $m_{\text{eff}}^{\text{bin}2}$	10	35	-	8	7	26	-	17
6J $m_{\text{eff}}^{\text{bin}3}$	-	39	15	9	11	37	-	22
Low-x	-	33	10	13	-	22	-	16
High-x	-	32	-	-	12	34	-	33
3B $m_{\text{eff}}^{\text{bin}1}$	-	-	-	-	7	29	5	5
3B $m_{\text{eff}}^{\text{bin}2}$	-	-	-	13	-	35	-	13

8.2.3 SUSY Signals

The cross-section uncertainty of gluino pair production amounts up-to 15% \sim 35%, as shown in Figure 5.3 in Sec. 5.3.1. The other uncertainties affecting the shape are evaluated over the signal points in the **x=1/2** grid of the model **QQC1QQC1**, and found to be typically marginal compared with the cross-section uncertainty. This is because the jet activity is predominantly sourced by gluino decays rather than the ISRs and FSRs for most of the cases. The only exception is found in low m_{eff} -bins in SR **2J** where the target signals are with highly compressed mass splitting between gluino and LSP ($\Delta m(\tilde{g}, \tilde{\chi}_1^0) < 50$ GeV) that have to rely on the additional radiation to enter the signal regions. In such case, the acceptance can vary upto by 20% by the theoretical variation. Table 8.4 presents the assigned shape uncertainties, which are common to all the signal models and mass points.

Table 8.4: Shape uncertainties assigned for SUSY signal processes [%]. The uncertainties are common to all the signal models. The symbols stand for; $\mu_{\text{fact.}}$: systematic variation in factorization scale, $\mu_{\text{ren.}}$: renormalization scale, “PS”: Parton shower.

	$\mu_{\text{fact.}}, \mu_{\text{ren.}}$	PS
SR 2J $m_{\text{eff}}^{\text{bin}1}$	15	20
SR 2J $m_{\text{eff}}^{\text{bin}2}$	10	10
SR 2J $m_{\text{eff}}^{\text{bin}3}$	-	5
The other regions	-	-

8.3 Other Uncertainties

8.3.1 Generaic Uncertainty on the BG Estimation Methods

Kinematical extrapolation method

Though all theoretical uncertainties that are already known are assigned on the extrapolation, one has to notice that none of them can explain the mis-modeling observed in the pre-selection region (Sec. 7.2.1). Therefore, there obviously exists unknown theoretical uncertainties, and in principle it can also affect the extrapolation.

It is seemingly impossible to know the impact of “unknown systematics” though, remember that we can largely cure the mis-modeling by a ad hoc kinematical reweighting:

$$\begin{cases} y = 1 - 0.1 \times (n_J - 2) & (W + \text{jets}) \\ y = 1.05 \times [1 - 0.061 \times p_T(t\bar{t})] & (t\bar{t}, @1L, 2L) \\ y = 1.4 \times [1 - 0.061 \times p_T(t\bar{t})] & (t\bar{t}, @3B). \end{cases}$$

Reweighted distributions are shown in appendix C.1. The idea is to emulate the “unknown systematic” by these reweighting, and quote the variation in the extrapolation as the systematics. Although this is not trivial how good the reweighting approximation is, this is the current best thing one could do. Figures in appendix D.1 show the extrapolation variation against the magnitude of mis-modeling generated by reweighting the MC events with:

$$\begin{aligned} y &= 1 - w \times (n_J - 2), & w \in [0, 0.18] && (W + \text{jets}) \\ y &= 1 - w \times p_T(t\bar{t})/100 \text{ GeV}, & w \in [0, 0.09] && (t\bar{t}). \end{aligned} \quad (8.1)$$

The vertical axis on the top panels in the plots show the amount of variation that a CR and corresponding SR(VR) experience by the MC reweighting as a function of w . The relative variation in CR (orange) is equivalent to the normalization factor actually obtained via the fit to data, while that in SR (blue) to the ideal normalization factor need to fully correct the SR(VR). The bottom panels display the ratio, namely the resultant extrapolation variation. B -tagging requirement is removed to maintain sufficient MC statistics, assuming the kinematics are invariant with it. For the $t\bar{t}$ process, component estimated by the object replacement method is excluded from the test.

The assigned uncertainty to each SR and VR are decided as Table 8.5, quoting the extrapolation error at $w = 0.1$ and $w = 0.07$ for $W + \text{jets}$ and $t\bar{t}$ respectively. As single-top is assumed to suffer from the same uncertainty as $t\bar{t}$, they are collectively noted as “Tops”.

Table 8.5: Uncertainty on the kinematical extrapolation by the accounted theoretical uncertainties, for $W + \text{jets}$ and top background respectively [%].

	$W + \text{jets}$	Tops		$W + \text{jets}$	Tops		$W + \text{jets}$	Tops
SR 2J $m_{\text{eff}}^{\text{bin}1}$	15	5	VRa 2J $m_{\text{eff}}^{\text{bin}1}$	-	10	VRb 2J $m_{\text{eff}}^{\text{bin}1}$	10	5
SR 2J $m_{\text{eff}}^{\text{bin}2}$	15	-	VRa 2J $m_{\text{eff}}^{\text{bin}2}$	5	10	VRb 2J $m_{\text{eff}}^{\text{bin}2}$	5	10
SR 2J $m_{\text{eff}}^{\text{bin}3}$	15	20	VRa 2J $m_{\text{eff}}^{\text{bin}3}$	-	20	VRb 2J $m_{\text{eff}}^{\text{bin}3}$	5	10
SR 6J $m_{\text{eff}}^{\text{bin}1}$	-	5	VRa 6J $m_{\text{eff}}^{\text{bin}1}$	-	5	VRb 6J $m_{\text{eff}}^{\text{bin}1}$	-	-
SR 6J $m_{\text{eff}}^{\text{bin}2}$	-	10	VRa 6J $m_{\text{eff}}^{\text{bin}2}$	-	5	VRb 6J $m_{\text{eff}}^{\text{bin}2}$	5	5
SR 6J $m_{\text{eff}}^{\text{bin}3}$	-	-	VRa 6J $m_{\text{eff}}^{\text{bin}3}$	-	5	VRb 6J $m_{\text{eff}}^{\text{bin}3}$	5	10
SR Low-x	10	-	VRa Low-x	-	5	VRb Low-x	10	5
SR High-x	-	10	VRa High-x	-	30	VRb High-x	5	10
SR 3B $m_{\text{eff}}^{\text{bin}1}$	-	5	VRa 3B $m_{\text{eff}}^{\text{bin}1}$	30	-	VRb 3B $m_{\text{eff}}^{\text{bin}1}$	20	10
SR 3B $m_{\text{eff}}^{\text{bin}2}$	-	10	VRa 3B $m_{\text{eff}}^{\text{bin}2}$	30	5	VRb 3B $m_{\text{eff}}^{\text{bin}2}$	30	15

Object replacement method

For the object replacement method, the observed non-closure error discussed in Sec. 7.3.2 are included as systematics as listed in Table 8.6.

Table 8.6: Summary of non-closure errors in the object replacement method [%].

	BV/BT	3B
Tau replacement	5	20
Missing electron replacement	15	
Missing muon replacement	30	

8.3.2 Control region statistics

In both of the background estimation methods, reflecting the (semi-)data driven nature, the statistical error in CRs often becomes the primary uncertainty in the estimation. This typically occurs in case of the high m_{eff} bins, for instance the yields in the CRs for the kinematical extrapolation can end up in about 15 events in the worst case, immediately resulting in 20% – 30% of uncertainty. The tendency is more striking concerning to the object replacement method where the uncertainty is solely dominated by the statistical error in terms of seed event statistics that amounts 20% – 60% in SRs depending on the tightness of selection. Furthermore, one has to mind that the statistical error in the object replacement method is not independent between the regions given that the sub-events from a single seed event can fall into different regions. The correlated statistical error between each of the two signal regions is then evaluated by identifying the fraction of common seed events between their estimation. Table 8.3 shows the correlation coefficient in the estimated yields between SR_i and SR_j defined as:

$$\rho := \frac{\sum_e \sqrt{w_e^i w_e^j}}{\sqrt{\sum_e w_e^i} \sqrt{\sum_e w_e^j}}$$

where e runs over all seed events, and w_e^i denotes the sum of weighted sub-events falling into SR_i generated by the seed event e . Correlation is mainly found in adjacent m_{eff} -bins, between high m_{eff} BT and 3B bins, and between high m_{eff} hard-lepton and soft-lepton bins. The effect of overlapped sub-events is taken into account in the final fitting. Though a large inter-bin correlation can potentially spoil the sensitivity of the shape fit, the impact on the final result to this analysis is limited, since the signal points rarely lay over multiple bins with equal abundance.

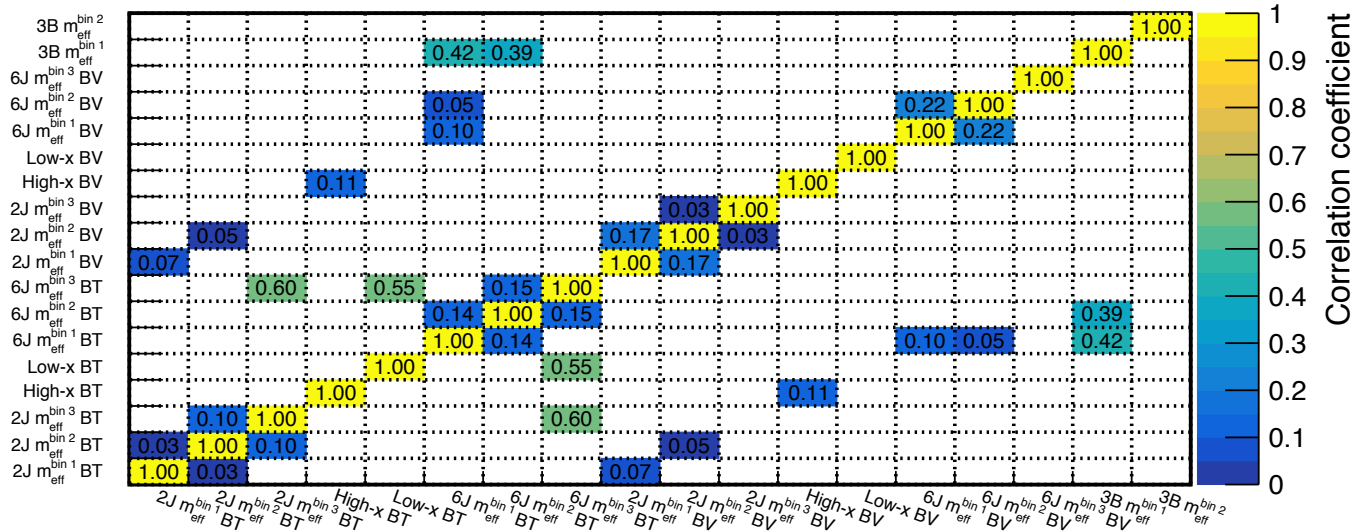


Figure 8.3: The correlation coefficient in the estimated yields between each of the two signal regions, indicating the level of correlated statistical fluctuation.

8.3.3 MC statistics

Limited MC statistics lead to a non-negligible uncertainty in signal and background yields in regions with tight selection. The largest impact is found in SR 3B $m_{\text{eff}}^{\text{bin}2}$ amounting upto 15%, which is still minor compared with the other systematics sources. The statistical behavior is carefully taken into account in the fit, as detailed in the Sec. 9.1.

Chapter 9

Result

After fixing the background estimation algorithm, the data in the signal regions are unblinded. The yields are compared with either the background-only hypothesis or various signal hypothesis, testing the compatibility. The statistical result is finally interpreted into physics results, in a form of exclusion limit in terms of the SUSY masses either the cross-section upper limits.

This chapter begins with describing the statistical procedure employed in deriving the background expectation (i.e. deciding the normalization factors in the kinematical extrapolation) and the hypothesis tests. Unblinded data in the signal regions are then shown, and the statistical result and the interpretation are discussed in the end of this chapter.

9.1 Statistical Analysis and Hypothetical Test

Profile likelihood and treatment of systematics Statistical tests are performed to examine the consistency of observed data with respect to the SM background expectation or that with specific signal being overlaid. This is implemented via a likelihood function based on the probability density distribution (PDF) in terms of number of observed events in each signal region bin. The full representation of the likelihood is given by Eq. (9.1):

$$\begin{aligned}
\mathcal{L}(\mu; \mu_W^i, \mu_{\text{Top}}^i, \boldsymbol{\theta}) &= \mathcal{L}(\mathbf{n}^{\text{SR}}, \mathbf{n}^{\text{WR}}, \mathbf{n}^{\text{TR}} | \mu, \mu_W^i, \mu_{\text{Top}}^i, \boldsymbol{\theta}) \\
&= \mathcal{P}_{\text{SR}} \times \mathcal{P}_{\text{CR}} \times \prod_{k \in \text{syst.}} \rho(\theta_k), \\
\mathcal{P}_{\text{SR}} &= \prod_{i \notin \mathbf{3B}} \left[\prod_{b \in \text{BT,BV}} \text{Pois}(n_{i,b}^{\text{SR}} | \mu s_{i,b}^{\text{SR}}(\boldsymbol{\theta}) + \mu_W^i w_{i,b}^{\text{SR}}(\boldsymbol{\theta}) + \mu_{\text{Top}}^i t_{i,b}^{\text{SR}}(\boldsymbol{\theta}) + b_{i,b}^{\text{SR}}(\boldsymbol{\theta})) \right] \\
&\quad \times \prod_{i \in \mathbf{3B}} \text{Pois}(n_i^{\text{SR}} | \mu s_i^{\text{SR}}(\boldsymbol{\theta}) + \mu_W^i w_i^{\text{SR}}(\boldsymbol{\theta}) + \mu_{\text{Top}}^i t_i^{\text{SR}}(\boldsymbol{\theta}) + b_i^{\text{SR}}(\boldsymbol{\theta})) \\
\mathcal{P}_{\text{CR}} &= \prod_i \text{Pois}(n_i^{\text{TR}} | \mu s_i^{\text{WR}}(\boldsymbol{\theta}) + \mu_W^i w_i^{\text{WR}}(\boldsymbol{\theta}) + \mu_{\text{Top}}^i t_i^{\text{WR}}(\boldsymbol{\theta}) + b_i^{\text{WR}}(\boldsymbol{\theta})) \\
&\quad \times \text{Pois}(n_i^{\text{WR}} | \mu s_i^{\text{TR}}(\boldsymbol{\theta}) + \mu_W^i w_i^{\text{TR}}(\boldsymbol{\theta}) + \mu_{\text{Top}}^i t_i^{\text{TR}}(\boldsymbol{\theta}) + b_i^{\text{TR}}(\boldsymbol{\theta}))
\end{aligned} \tag{9.1}$$

where \mathbf{n}^{SR} , \mathbf{n}^{WR} and \mathbf{n}^{TR} are respectively the numbers of observed events in SRs, corresponding CRs such as WRs and TRs, with the vector indices running over regions ; s_r is the expected signal yield in region r in the signal model to be tested; w_r and t_r are respectively the expected yields of $W + \text{jets}$ and the top background in region r before the normalization, with the components derived by the object replacement method being excluded; b_r are the expected yields of the other backgrounds in region r ; $\boldsymbol{\theta}$ is the vector of nuisance parameters for each systematic uncertainty; μ_W^i and μ_{Top}^i are the normalization factors for $W + \text{jets}$ and the top background which are allowed to vary between i ; and μ is the signal strength, a parameter describing the relative normalization with respect to the signal model to be tested i.e. $\mu = 0$ corresponds to a background-only hypothesis and $\mu = 1$ to a hypothesis with the nominal signal level expected by the signal model. Index i runs along signal region bins joining the combination that are orthogonal to each other s.t. :

$$\begin{aligned} i \in & \{ \mathbf{2J}, \mathbf{6J}, \mathbf{3B} \} \\ \text{or } & \{ \mathbf{2J}, \mathbf{High-x}, \mathbf{3B} \} \\ \text{or } & \{ \mathbf{Low-x}, \mathbf{6J}, \mathbf{3B} \} \\ \text{or } & \{ \mathbf{Low-x}, \mathbf{High-x}, \mathbf{3B} \} \end{aligned} \quad (9.2)$$

where

$$\begin{aligned} \mathbf{2J} &= \{ 2J-m_{\text{eff}}^{\text{bin}1}, 2J-m_{\text{eff}}^{\text{bin}2}, 2J-m_{\text{eff}}^{\text{bin}3} \} \\ \mathbf{6J} &= \{ 6J-m_{\text{eff}}^{\text{bin}1}, 6J-m_{\text{eff}}^{\text{bin}2}, 6J-m_{\text{eff}}^{\text{bin}3} \} \\ \mathbf{Low-x} &= \{ \text{Low-x} \} \\ \mathbf{High-x} &= \{ \text{High-x} \} \\ \mathbf{3B} &= \{ 3B-m_{\text{eff}}^{\text{bin}1}, 3B-m_{\text{eff}}^{\text{bin}2} \} \end{aligned} \quad (9.3)$$

The normalization factors for $W + \text{jets}$ and the top background backgrounds are simultaneously determined, in order to correlate the behavior of systematics. Therefore the CRs terms are also placed in the common likelihood with an identical representation as SRs.

The statistical behavior of the PDFs is fully characterized by a product of Poisson distributions for each SR or CR:

$$\text{Pois}(n|\nu) := \frac{\nu^n}{n!} e^{-\nu}$$

where ν and n are the expected yield and observed number respectively.

The effect of a systematics (indexed by k) are then incorporated by shifting the Poisson mean ν , via a corresponding nuisance parameter θ_k so as: $\nu(0)$ corresponds to the nominal expectation and $\nu(\pm 1)$ to that with $\pm 1\sigma$ variation due to the systematics. While $\nu(0)$ and $\nu(\pm 1)$ are calculated explicitly, the whole function $\nu(\theta_k)$ is obtained by interpolating or extrapolating the three points using a polynomial or an exponential function, providing a continuous functional form of \mathcal{L} in terms of $\boldsymbol{\theta}$.

What is here intend to do is to perform a global fit on data, simultaneously determining μ , μ_W^i , μ_{Top}^i and $\boldsymbol{\theta}$ by minimizing the likelihood \mathcal{L} (Eq. 9.1). While μ , μ_W^i and μ_{Top}^i are allowed to flow based on our total ignorance, the shifts of the nuisance parameters $\boldsymbol{\theta}$ need to be restricted reflecting the level of our confidence. This is implemented by the last terms in the likelihood $\prod_{k \in \text{syst.}} \rho(\theta_k)$ known as the “penalty terms” serving as the prior constraints for the likelihood. The form of the penalty terms depends on the statistical nature of each systematics:

- A Gaussian PDF is commonly assumed for most systematic uncertainties:

$$\rho(\theta) = \frac{1}{\sqrt{2\pi}\sigma} \exp\left(-\frac{\theta^2}{2\sigma^2}\right) \quad (9.4)$$

- The Gamma PDF is used to describe uncertainties following according to Poisson distribution, typically associated with the number of data events in control regions, or selected MC events:

$$\rho(a) = \frac{\nu^a}{a!} e^{-\nu} \quad (9.5)$$

where a is related with θ using the symmetrized uncertainty σ by

$$\theta = \frac{a - \nu}{\sigma}$$

A multi-dimensional minimization over the parameter spaces of all the normalization factors, nuisance parameters and signal strength ¹ is performed by the **Minuit2** algorithm [142], interfaced by a number wrapper packages; **HistFitter** [143], **HistFactory** [144] and **RooFit** [145]. Signal strength and the background normalization factors are allowed to range $0 \sim 5$, while nuisance parameters are to moved by $-5\sigma \sim 5\sigma$ during the fit. Systematics found to have tiny enough impact on the yields in the SR or CR bins (evaluated by the Kolmogorov-Smirnov test) are excluded from the fit to reduce the redundant dimensions of the scan (“pruning”).

Hypothetical testing A hypothetical test against a hypothesis H is done by examining the compatibility with observation, via p-value. The p-value for testing hypothesis H is commonly defined as the probability to find even rarer outcome than the observation under H . For the simplest one bin counting experiment where signal is manifested as an data excess, the p-value is then:

$$p_\mu := \sum_{n=n_{\text{obs}}}^{\infty} L(n|\mu) \quad (9.6)$$

using the number of observed events n_{obs} as the test static. One would claim a discovery against the null hypothesis H_0 if the p_0 is significantly low that the observation can be hardly ascribed to statistical fluctuation of H_0 . In the field of high energy physics experiment, this is usually set to one corresponding to 5σ gaussian standard deviation ($\sim 10^{-7}$ in p-value).

¹Remind that we have $8 - 16$ normalization factors and ~ 150 nuisance parameters in case of the combination over all SR towers.

On the other hand, one can claim the exclusion of a signal hypothesis H_1 when p_1 is reasonably low. $p_1 < 0.05$ is conventionally used as the threshold, equivalent to an exclusion at 95% confidence level. There are circumstances where observation does not agree with either H_0 and H_1 due to statistical fluctuation or more seriously poor understanding to the backgrounds, and result in strong exclusion power typically when data undershoots the expectation. In LHC, in order to prevent such potentially unreasonably strong exclusion, a modified measure CL_s is used:

$$\text{CL}_s := \frac{p_1}{p_0}, \quad (9.7)$$

and $\text{CL}_s < 0.05$ is accepted as the equivalence of an exclusion at 95% confidence level.

In presence of multiple test statics (\mathbf{n}^{SR}) together with bunches of nuisance parameters, it is not trivial how to define the “rareness” on the multi-dimension of space. In such cases, the likelihood itself is often chosen as the test static projecting from n -dimension into 1-dimension, providing a well-defined measure of “rareness” by definition. In LHC analyses, a normalized likelihood test static λ_μ is commonly used:

$$\lambda_\mu = \begin{cases} \frac{\mathcal{L}(\mu, \hat{\theta}(\mu))}{\mathcal{L}(\hat{\mu}, \hat{\theta})} & (\hat{\mu} > 0) \\ \frac{\mathcal{L}(\mu, \hat{\theta}(\mu))}{\mathcal{L}(0, \hat{\theta}(0))} & (\hat{\mu} < 0) \end{cases} \quad (9.8)$$

where $\hat{\theta}(\mu)$ denotes the best-fit nuisance parameters with fixed μ , while $\hat{\mu}$ and $\hat{\theta}$ the best-fit parameters with μ is allowed to float. $\mathcal{L}(\mu, \hat{\theta}(\mu))$ presents the conditional likelihood normalized by the μ -agonistic denominator $\mathcal{L}(\hat{\mu}, \hat{\theta})$, forcing the range of λ_μ to $0 < \lambda_\mu < 1$.

The p-value is finally defined as:

$$p_\mu := \int_{q_{\mu, \text{obs}}}^{\infty} f(q_\mu | \mu) dq_\mu \quad (9.9)$$

where q_μ is defined by:

$$q_\mu = \begin{cases} -2 \log \lambda_\mu & (\hat{\mu} < \mu) \\ 0 & (\hat{\mu} > \mu) \end{cases} \quad (9.10)$$

conserving a 1-to-1 correspondence with λ_μ . $f(q_\mu)$ is the PDF that q_μ obeys, describing the fluctuation of q_μ against the statistical fluctuation of \mathbf{n}^{SR} as well as the variation due to the systematics. Unlike the PDF in the simplest counting experiment Eq. (9.6), $f(q_\mu)$ is in generally not known neither modeled analytically thus needs a bunch of toy experiments to determine; scanning from $\mu = 0$ upto $\mu = 5$ with a finite step, on each of which a number of the likelihood fits are performed with different fluctuating data statistics and systematic variation applied. This is an incredibly crazy course of computation, and we have to go relying on some analytical approximation after all².

²Each likelihood fit takes approximately 8-15 minutes.

Fortunately, there are a couple of powerful approximation formula such as Wald's approximation [146]:

$$q_\mu = -2 \log \lambda(\mu) = \frac{\mu - \hat{\mu}}{\sigma^2} + O(1/\sqrt{N}) \quad (9.11)$$

and the asymptotic formula based on the Asimov dataset [147]:

$$\begin{aligned} f(q_\mu, \mu) &= \frac{1}{\sqrt{q_\mu}} \frac{1}{\sqrt{2\pi}} \left[\exp\left(-\frac{1}{2}(\sqrt{q_\mu} + \sqrt{R})\right) + \exp\left(-\frac{1}{2}(\sqrt{q_\mu} - \sqrt{R})\right) \right], \\ R &:= \frac{(\mu - \hat{\mu})^2}{\sigma^2}, \end{aligned} \quad (9.12)$$

with Wald's approximation (Eq. (9.11)) being applied. σ is the fitting error on $\hat{\mu}$ and N symbolizes the magnitude of number of events in signal regions, with which the PDF $f(q_\mu)$ can be determined by only one fit.

Note that the approximation is essentially ignoring the $O(1/\sqrt{N})$ terms, which may not be fully justified given that the signal regions typically contain number of events less than 5. In the thesis, the result for background-only hypothesis (Sec. 9.2) is derived using the rigid toy experiments, however the Asimov's formula (Eq. 9.12) is used for limit setting avoiding the unrealistic computing time required for the toy experiments.³

9.2 Unblinded Signal Regions with Background-only Hypothesis

The background expectation in signal regions for null signal hypothesis are determined tower-by-tower, by performing a simultaneous fit on the normalization factors (μ_W , μ_{Top}) as well as all the nuisance parameters associated to systematics uncertainties, onto the data in all the relevant bins of control regions and signal regions. The post-fit uncertainties are summarized in Figure 9.1, determined by the range of nuisance parameters giving $\mathcal{L} < \mathcal{L}_{\min} + 1/2$. For the low m_{eff} -bins, typically the estimation precision is at 20% level where theory systematics is the main source. The signal region bins with the tightest m_{eff} selection end up in 40% \sim 60% of total uncertainty, dominated by the control region statistics.

The unblinded yields of observed data together with the expected backgrounds in the signal regions are shown in Table 9.1 - 9.3. Observed data are found to be consistent in general, with no signal regions exhibiting deviation more than 3σ . The pulls between data and expectation is shown in Figure 9.2.

Figure 9.3-9.9 show the kinematical distributions of either data and prediction in unblinded signal regions. The slight data excess found (in SR 2J- $m_{\text{eff}}^{\text{bin}1}$ BV, SR 2J- $m_{\text{eff}}^{\text{bin}3}$ BV and SR High-x BT) turns to be not very much favored by the targeted models in the signal regions bins, though the data statistics is too low to conclude.

³This is in fact how ATLAS and CMS provide the result, based on the notion that this is the best thing one could afford to do.

Table 9.1: Observed yields and backgrounds expectation in the signal region bins in tower **2J** and **6J**. Background component estimated by the object replacement are denoted as “Di-leptonic”, while the others are derived from the kinematical extrapolation method.

SR 2J <i>b</i> -tag	$m_{\text{eff.}} \in [1100, 1500]$	$m_{\text{eff.}} \in [1500, 1900]$	$m_{\text{eff.}} > 1900$
Observed data	8	2	1
Expected background	7.20 ± 1.40	2.46 ± 0.60	2.31 ± 0.77
Di-leptonic	2.4 ± 1.0	0.8 ± 0.4	1.7 ± 0.7
$W + \text{jets}$	1.0 ± 0.5	$0.1^{+0.2}_{-0.1}$	0.0 ± 0.0
$Z + \text{jets}$	0.6 ± 0.2	0.2 ± 0.0	0.1 ± 0.0
Tops	2.1 ± 0.7	0.8 ± 0.3	0.4 ± 0.2
Di-boson	0.4 ± 0.1	0.2 ± 0.2	0.1 ± 0.0
$t\bar{t} + V$	0.8 ± 0.2	0.3 ± 0.1	0.1 ± 0.0
SR 2J <i>b</i> -veto	$m_{\text{eff.}} \in [1100, 1500]$	$m_{\text{eff.}} \in [1500, 1900]$	$m_{\text{eff.}} > 1900$
Observed data	25	8	6
Expected background	13.33 ± 2.59	6.84 ± 1.44	2.53 ± 0.66
Di-leptonic	2.4 ± 1.8	2.3 ± 1.1	0.7 ± 0.6
$W + \text{jets}$	4.2 ± 1.1	1.6 ± 0.4	0.4 ± 0.2
$Z + \text{jets}$	2.3 ± 0.7	1.0 ± 0.3	0.6 ± 0.2
Tops	1.1 ± 0.4	0.3 ± 0.1	0.2 ± 0.1
Di-boson	3.2 ± 1.1	1.6 ± 0.5	0.7 ± 0.2
$t\bar{t} + V$	0.1 ± 0.0	0.1 ± 0.0	0.0 ± 0.0
SR 6J <i>b</i> -tag	$m_{\text{eff.}} \in [1100, 1600]$	$m_{\text{eff.}} \in [1600, 2100]$	$m_{\text{eff.}} > 2100$
Observed data	7	3	0
Expected background	5.09 ± 1.04	2.14 ± 0.65	2.46 ± 0.89
Di-leptonic	2.6 ± 0.8	1.1 ± 0.6	1.5 ± 0.8
$W + \text{jets}$	0.4 ± 0.2	0.1 ± 0.1	0.1 ± 0.1
$Z + \text{jets}$	$0.0^{+0.0}_{-0.0}$	0.0 ± 0.0	$0.0^{+0.0}_{-0.0}$
Tops	1.0 ± 0.4	0.5 ± 0.2	0.6 ± 0.3
Di-boson	0.2 ± 0.1	0.1 ± 0.1	$0.1^{+0.1}_{-0.1}$
$t\bar{t} + V$	0.8 ± 0.2	0.3 ± 0.1	0.1 ± 0.0
SR 6J <i>b</i> -veto	$m_{\text{eff.}} \in [1100, 1600]$	$m_{\text{eff.}} \in [1600, 2100]$	$m_{\text{eff.}} > 2100$
Observed data	5	0	1
Expected background	3.93 ± 0.88	1.28 ± 0.36	0.65 ± 0.18
Di-leptonic	1.5 ± 0.6	$0.2^{+0.2}_{-0.2}$	0.0 ± 0.0
$W + \text{jets}$	1.1 ± 0.5	0.6 ± 0.3	0.3 ± 0.1
$Z + \text{jets}$	0.2 ± 0.1	0.0 ± 0.0	0.0 ± 0.0
Tops	0.3 ± 0.1	0.1 ± 0.1	0.1 ± 0.1
Di-boson	0.7 ± 0.2	0.3 ± 0.1	0.2 ± 0.1
$t\bar{t} + V$	0.1 ± 0.0	0.0 ± 0.0	0.0 ± 0.0

Table 9.2: Observed yields and backgrounds expectation in the signal region bins in tower **Low-x** and **High-x**. Background component estimated by the object replacement are denoted as “Di-leptonic”, while the others are derived from the kinematical extrapolation method.

SR Low-x	<i>b</i> -tag	<i>b</i> -veto
Observed data	0	3
Expected background	2.04 ± 0.70	1.46 ± 0.59
Di-leptonic	1.2 ± 0.7	0.6 ± 0.5
$W+jets$	0.1 ± 0.0	0.2 ± 0.1
$Z+jets$	0.0 ± 0.0	0.1 ± 0.0
Tops	0.6 ± 0.2	0.4 ± 0.2
Di-boson	0.1 ± 0.0	0.2 ± 0.1
$t\bar{t} + V$	0.1 ± 0.0	0.0 ± 0.0

SR High-x	<i>b</i> -tag	<i>b</i> -veto
Observed data	6	4
Expected background	2.35 ± 0.59	4.27 ± 0.94
Di-leptonic	0.8 ± 0.5	0.8 ± 0.5
$W+jets$	0.3 ± 0.1	1.7 ± 0.5
$Z+jets$	$0.0^{+0.0}_{-0.0}$	0.5 ± 0.2
Tops	0.5 ± 0.2	0.1 ± 0.1
Di-boson	0.4 ± 0.2	1.1 ± 0.5
$t\bar{t} + V$	0.3 ± 0.1	0.1 ± 0.0

Table 9.3: Observed yields and backgrounds expectation in the signal region bins in tower **3B**. Background component estimated by the object replacement are denoted as “Di-leptonic”, while the others are derived from the kinematical extrapolation method.

SR 3B	$m_{\text{eff.}} \in [1000, 1750]$	$m_{\text{eff.}} > 1750$
Observed data	2	1
Expected background	2.06 ± 0.68	1.00 ± 0.52
Di-leptonic	1.3 ± 0.5	0.8 ± 0.5
$W+jets$	0.0 ± 0.0	0.0 ± 0.0
$Z+jets$	0.0 ± 0.0	0.0 ± 0.0
Tops	0.6 ± 0.4	0.2 ± 0.1
Di-boson	0.0 ± 0.0	0.0 ± 0.0
$t\bar{t} + V$	0.2 ± 0.1	0.1 ± 0.0

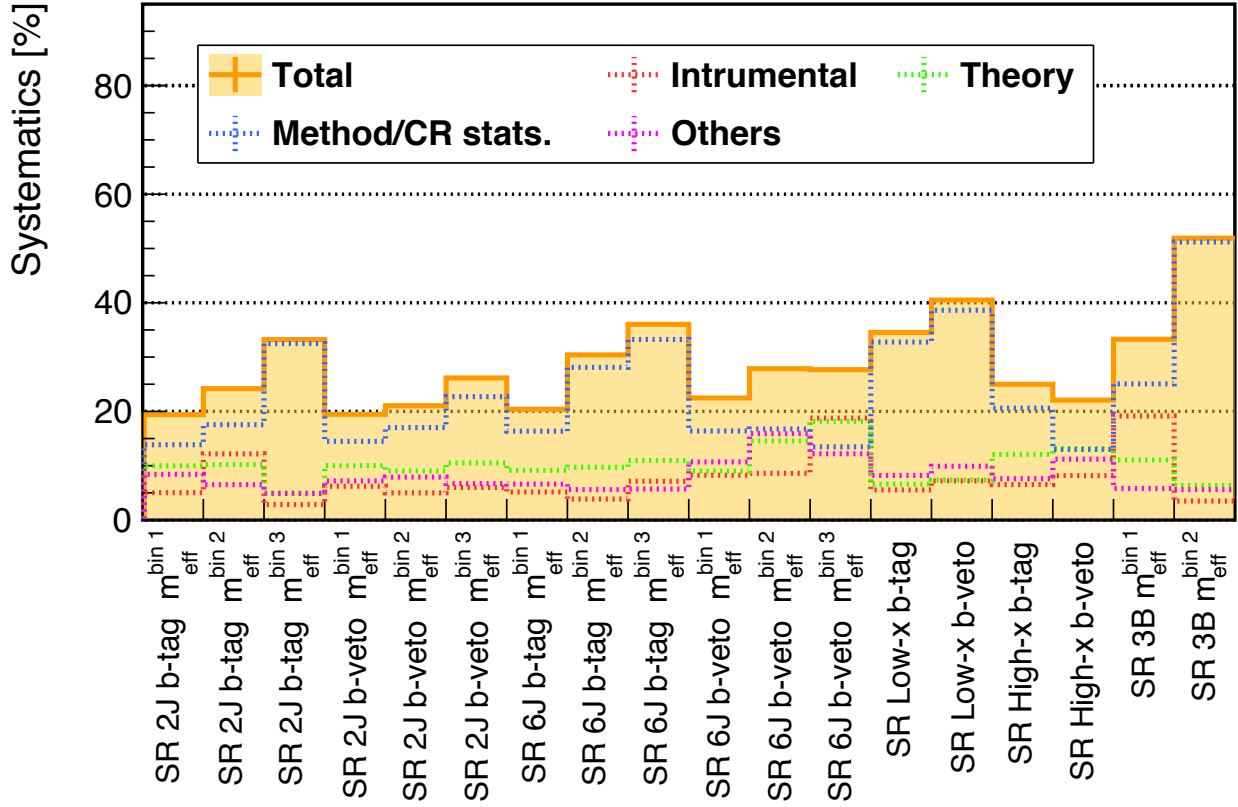


Figure 9.1: Systematic uncertainty in the signal regions with respect to the expected yields. The total systematics uncertainty is shown by the filled orange histogram, and the breakdowns are by the dashed lines. While the systematics in BT/3B bins are purely dominated by control region statistics, it is comparable to the other sources in the BV bins. The overall uncertainty ranges between 20% ~ 50%.

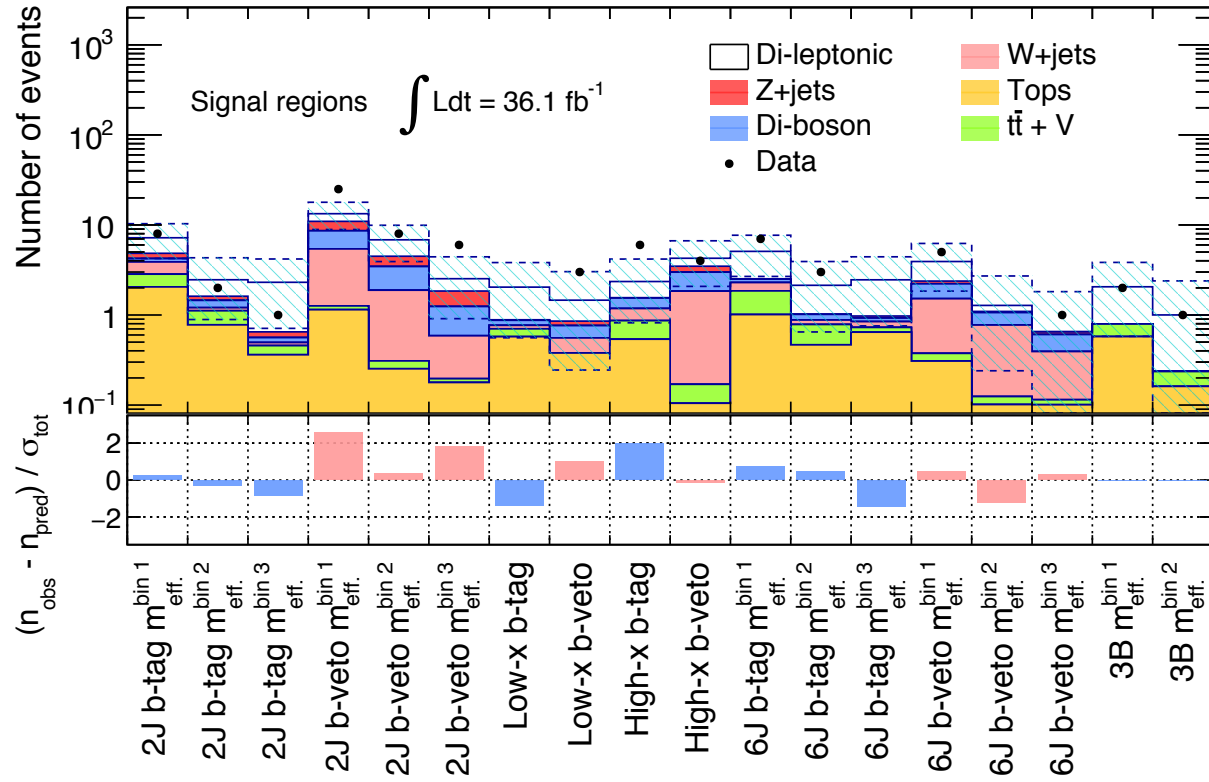


Figure 9.2: (Top) Observed data yields (black dots) and the background expectation (histogram) in the signal regions. The white component is the backgrounds estimated by the object replacement method, while the colored ones are by the kinematical extrapolation method. The dashed band represents the combined statistical and systematic uncertainty on the total estimated backgrounds. (Bottom) Pull between the observed data and the expectation. No significant deviation from expectation exceeding 3σ .

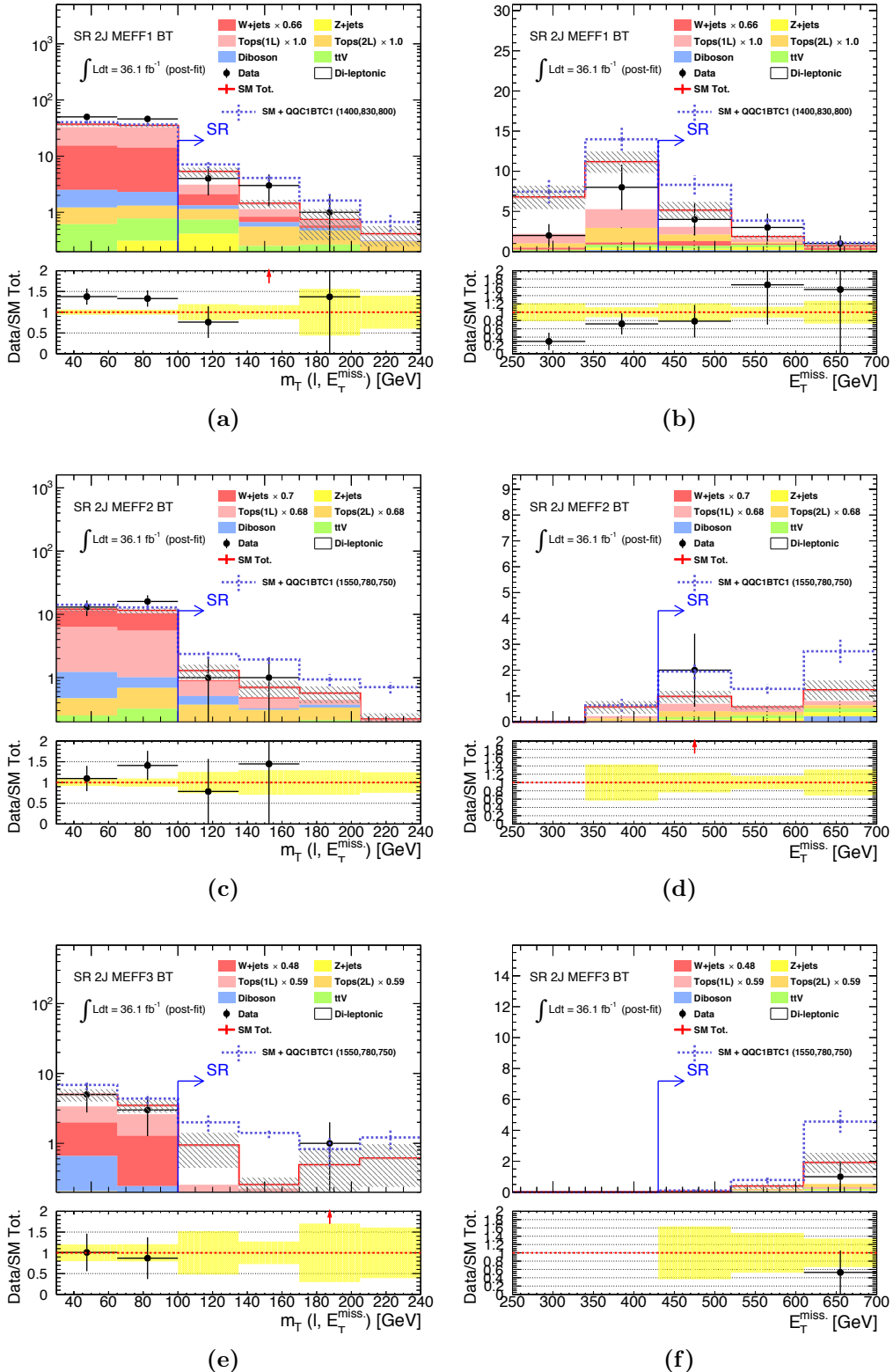


Figure 9.3: Post-fit distributions of (left column) m_T , and (right column) E_T^{miss} . (a,b) SR 2J- $m_{\text{eff}}^{\text{bin}1}$ BT. (c,d) SR 2J- $m_{\text{eff}}^{\text{bin}2}$ BT. (e,f) SR 2J- $m_{\text{eff}}^{\text{bin}3}$ BT. The yellow bands in the bottom panel indicate the uncertainty due to the CR statistics. The overflow is included in the highest bin. Dashed lines represent the expected distributions of total background plus the typical signal targeted in the signal region bin.

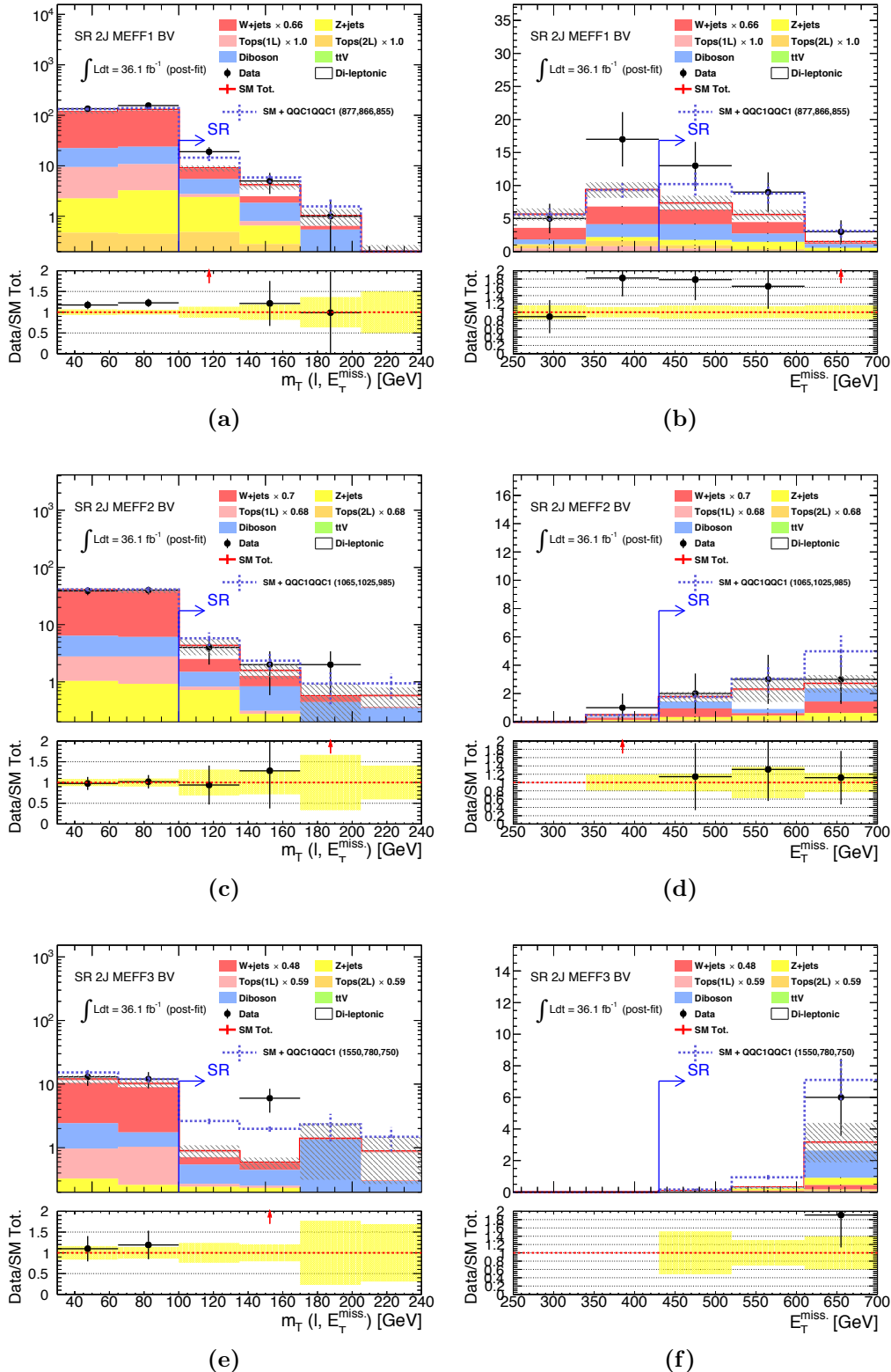


Figure 9.4: Post-fit distributions of (left column) m_T , and (right column) E_T^{miss} . (a,b) SR 2J- $m_{\text{eff}}^{\text{bin}1}$ BV. (c,d) SR 2J- $m_{\text{eff}}^{\text{bin}2}$ BV. (e,f) SR 2J- $m_{\text{eff}}^{\text{bin}3}$ BV. The yellow bands in the bottom panel indicate the uncertainty due to the CR statistics. The overflow is included in the highest bin. Dashed lines represent the expected distributions of total background plus the typical signal targeted in the signal region bin.

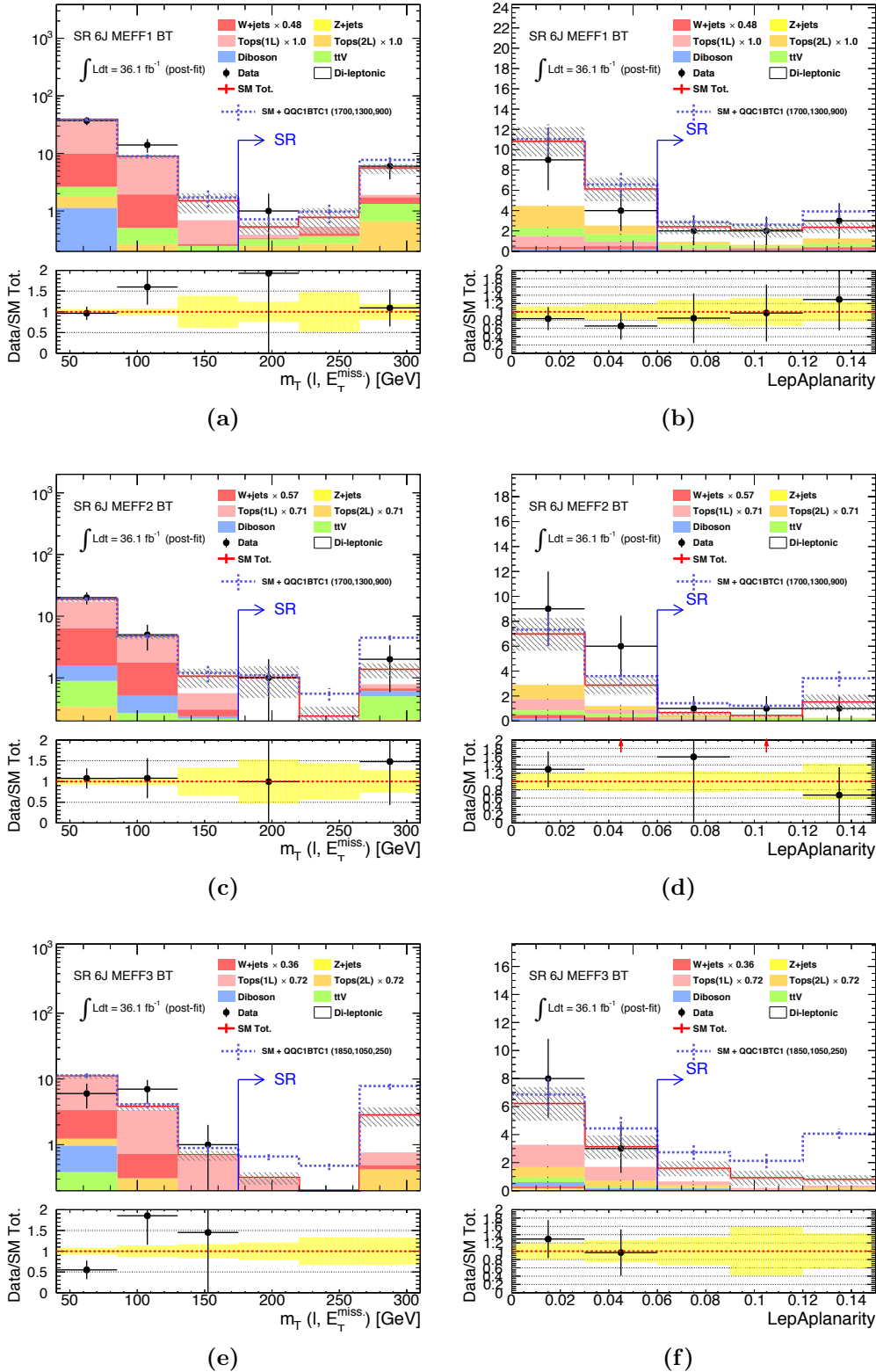


Figure 9.5: Post-fit distributions of (left column) m_T , and (right column) aplanarity. (a,b) SR 6J- $m_{\text{eff}}^{\text{bin}1}$ BT. (c,d) SR 6J- $m_{\text{eff}}^{\text{bin}2}$ BT. (e,f) SR 6J- $m_{\text{eff}}^{\text{bin}3}$ BT. The yellow bands in the bottom panel indicate the uncertainty due to the CR statistics. The overflow is included in the highest bin. Dashed lines represent the expected distributions of total background plus the typical signal targeted in the signal region bin.

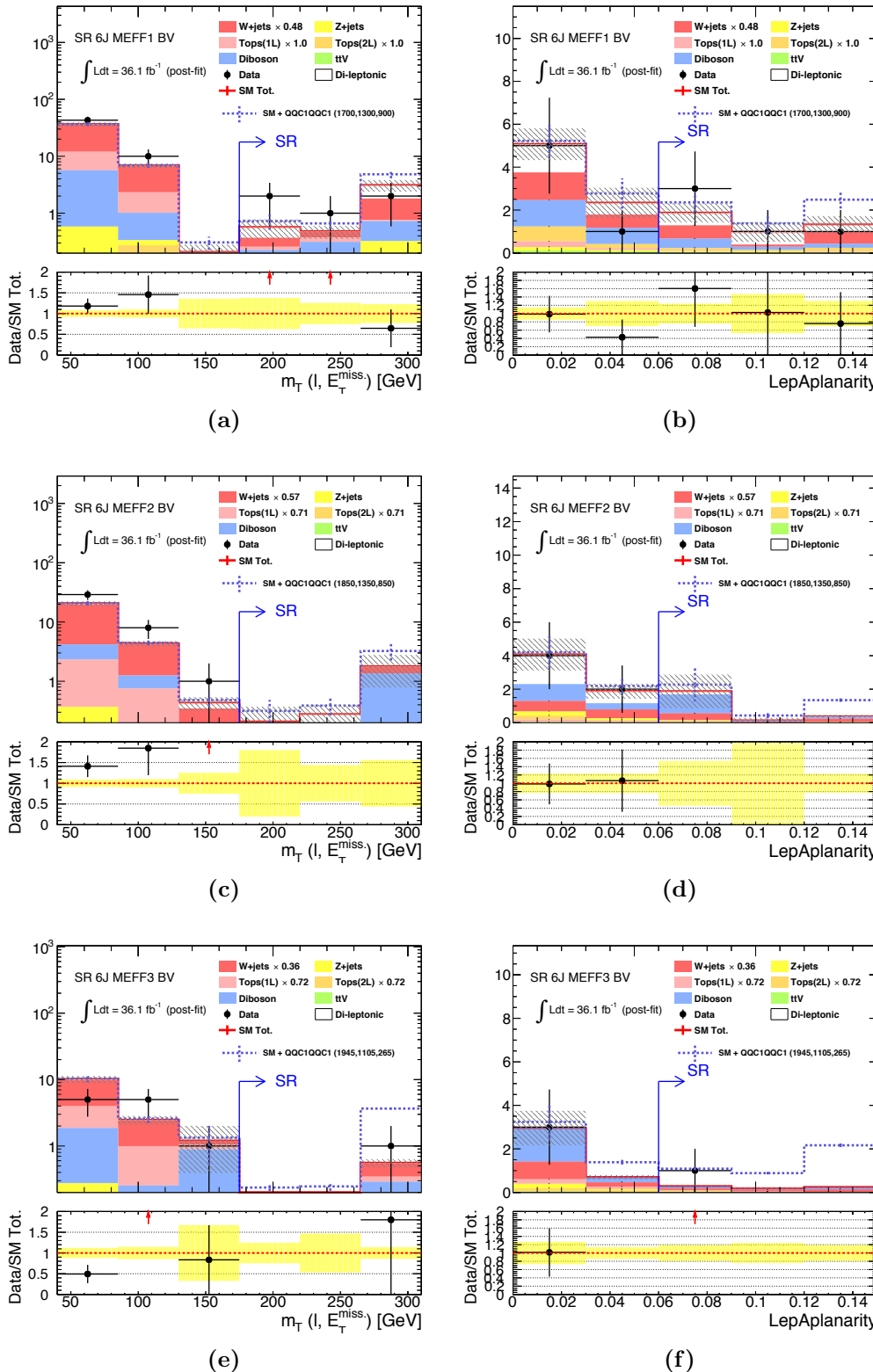


Figure 9.6: Post-fit distributions of (left column) m_T , and (right column) aplanarity. (a,b) SR 6J- $m_{\text{eff}}^{\text{bin}1}$ BV. (c,d) SR 6J- $m_{\text{eff}}^{\text{bin}2}$ BV. (e,f) SR 6J- $m_{\text{eff}}^{\text{bin}3}$ BV. The yellow bands in the bottom panel indicate the uncertainty due to the CR statistics. The overflow is included in the highest bin. Dashed lines represent the expected distributions of total background plus the typical signal targeted in the signal region bin.

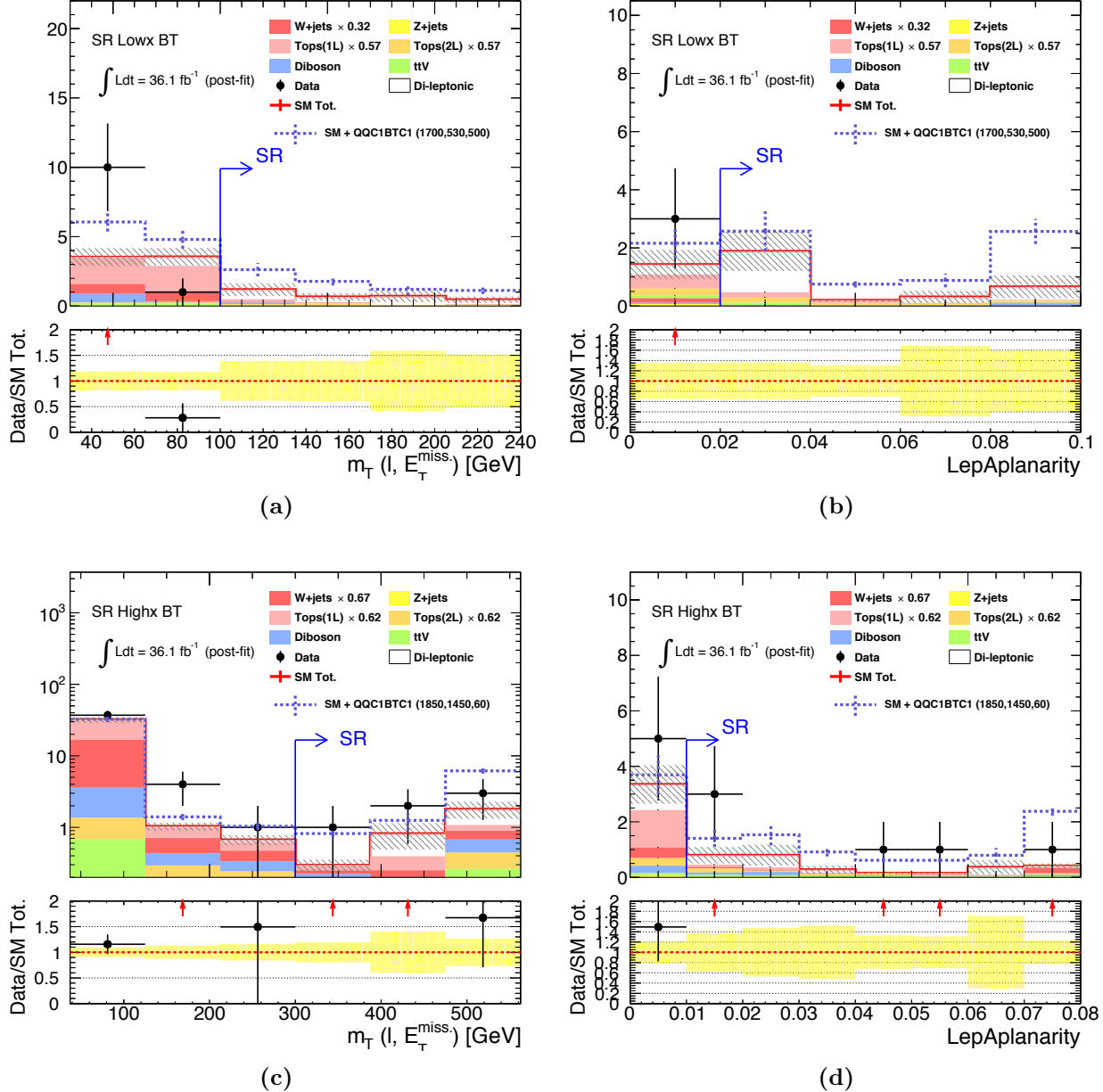


Figure 9.7: Post-fit distribution of (left column) m_T and (right column) aplanarity. (a,b) SR Low-x BT. (c,d) SR High-x BT. The yellow bands in the bottom panel indicate the uncertainty due to the CR statistics. The overflow is included in the highest bin. Dashed lines represent the expected distributions of total background plus the typical signal targeted in the signal region bin.

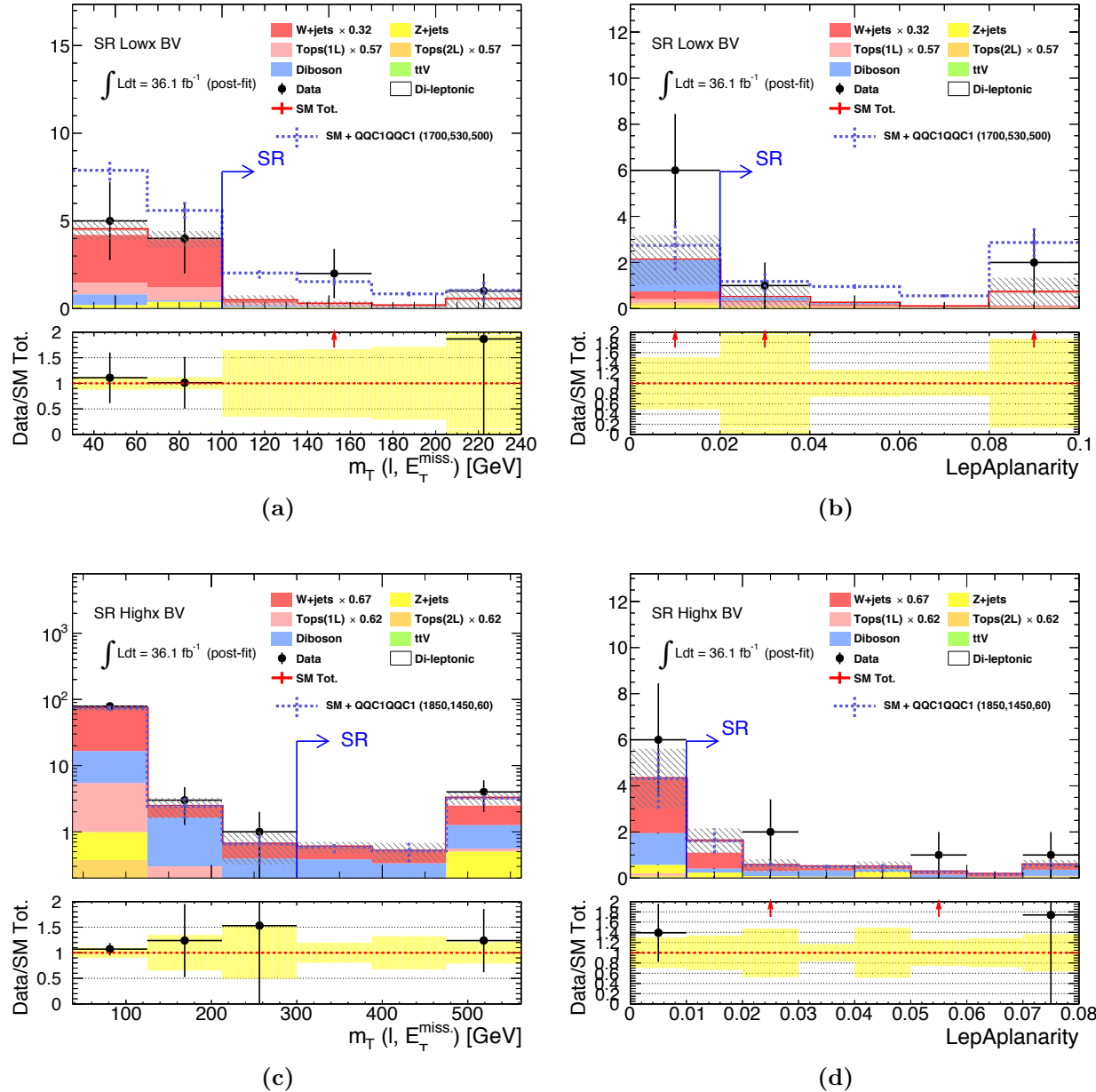


Figure 9.8: Post-fit distribution of (left column) m_T and (right column) aplanarity. (a,b) SR Low-x BV. (c,d) SR High-x BV. The yellow bands in the bottom panel indicate the uncertainty due to the CR statistics. The overflow is included in the highest bin. Dashed lines represent the expected distributions of total background plus the typical signal targeted in the signal region bin.

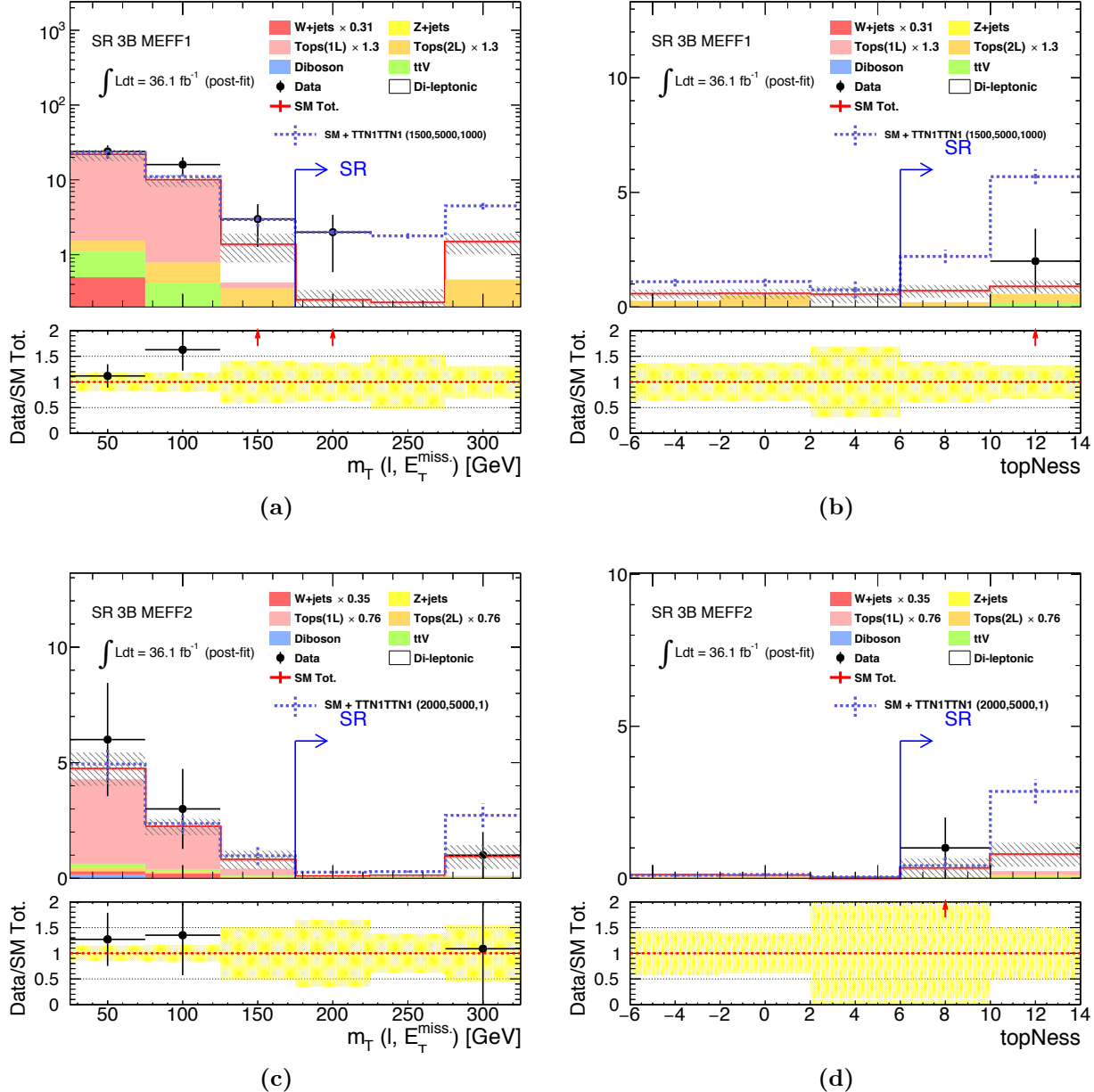


Figure 9.9: Post-fit distributions of (left column) m_T , and (right column) topness. (a,b) SR 3B- $m_{\text{eff}}^{\text{bin}1}$. (c,d) SR 3B- $m_{\text{eff}}^{\text{bin}2}$. The yellow bands in the bottom panel indicate the uncertainty due to the CR statistics. The overflow is included in the highest bin. Dashed lines represent the expected distributions of total background plus the typical signal targeted in the signal region bin.

9.3 Constraints on the Benchmark Models

The observed results are then interpreted into the constraints on the benchmark models listed in Table 2.5 - 2.7. The obtained limits are also compared with the previous ATLAS results with integrated luminosity of 14.8 fb^{-1} or 36.1 fb^{-1} .

QQC1QQC1

Figure 9.10 presents the exclusion limit on **QQC1QQC1**, the reference model for BV benchmarks (Table 2.5). Hypothetical tests are done with each signal point using the combination of signal regions that gives the best expected sensitivity. The excluded region is defined by areas with $\text{CL}_s < 0.05$, corresponding to 95% confidence level. The associated expected limit is represented by a blue line with a yellow 1σ band defined by the range of observed limit if observation is consistent with expectation within $\pm 1\sigma$. Observed limits are typically worse than the expected ones in the mass region where sensitivity is primarily driven by SR **2J** and SR **High-x**, namely the diagonal region in the **x=1/2** grid, and the high- x region in the **LSP60** grid respectively, reflecting the observed excess there which weakens the exclusion power.

Exclusion limits driven by the previous 1-lepton search in ATLAS with 14.8 fb^{-1} [148] are shown by the shaded areas. While the magenta areas are the exclusion limit directly quoted from the reference [148], the cyan ones indicate the potential exclusion that could have achieved by the SRs in the previous search, calculated based on the observed yields in the signal regions, since no interpretation has been made with the grids.

For grids **x=1/2** and **LSP60** that has been the main target in previous analyses, the exclusion limits are pushed forward by about $100 \text{ GeV} \sim 400 \text{ GeV}$ in gluino mass at the same mass splitting. The merit of the improved analysis can be clearly acknowledged, given that the cross-section of gluino pair production rapidly falls with respect to increased gluino mass which is about $1/3$ by every 200 GeV (i.e. the limit improvement by the increased data statistics is $\sim 100 \text{ GeV}$). Upto 2 TeV of gluino mass is excluded with the nearly massless LSP scenario, while it also reaches about 1.9 TeV of gluino mass for case with $m_{\tilde{\chi}_1^0} < 1 \text{ TeV}$. More radical improvement is seen in the **DM20** and **DM30** grids, since no analysis has been provided dedicatedly sensitivity to the scenario before. The sensitivity improvement is about $200 \text{ GeV} \sim 450 \text{ GeV}$ in gluino mass with the same mass splitting, and the $1.2 \text{ TeV} - 1.6 \text{ TeV}$ is excluded by this study.

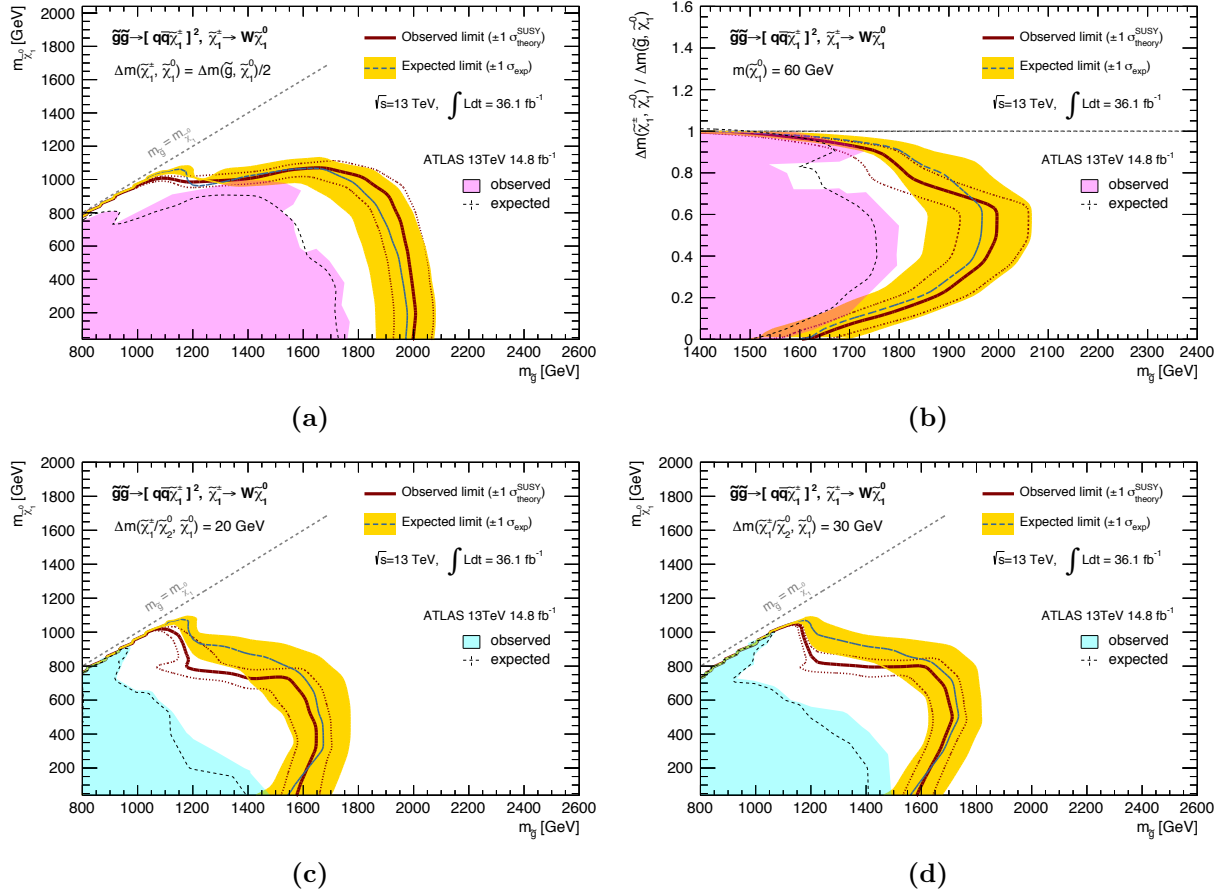


Figure 9.10: Exclusion limit for the benchmark model **QQC1QQC1** presented in the (a) **x=1/2** (b) **LSP60** (c) **DM20** (d) **DM30** grids. Observed limits are shown by the solid red lines, while the expected limit are expressed by the dashed blue lines with yellow 1σ bands. The previous 1-lepton search result by ATLAS with 14.8 fb^{-1} [148] are overlayed (observed limit: shaded area, expected limit: black dashed line). The magenta areas are the exclusion limit directly quoted from the reference [148], while the cyan ones are the calculated potential achievable exclusion by the previous search using the same SRs. All limits correspond to 95% CL.

QQC1BTC1

Figure 9.11 exhibits the limits for model **QQC1BTC1**, the reference model for BT benchmarks (Table 2.5). As the sensitivity is mainly driven by the BT bins for this model, it is relatively more affected by the $\sim 2\sigma$ excess observed in the SR High-x BT, which drastically weakens the limit in part of the **LSP60** grid. Nevertheless, the overall exclusion reach is comparable to that of the **QQC1QQC1** model, amounting to 1.9 TeV \sim 2 TeV in gluino mass for $m_{\tilde{\chi}_1^0} < 1$ TeV. As the asymmetric decays of gluino have never been interpreted before, this is the first explicit constraints put on such class of models.

Potential exclusion that could have been addressed by the previous 1-lepton search in ATLAS with 14.8 fb^{-1} [148] are shown by the cyan shaded areas. The sensitivity improvement is similar to the case of **QQC1QQC1**, except for **DM20** and **DM30** grids that are relatively easy to explore even without dedicate soft-lepton selections since top-quarks decay can emit hard leptons.

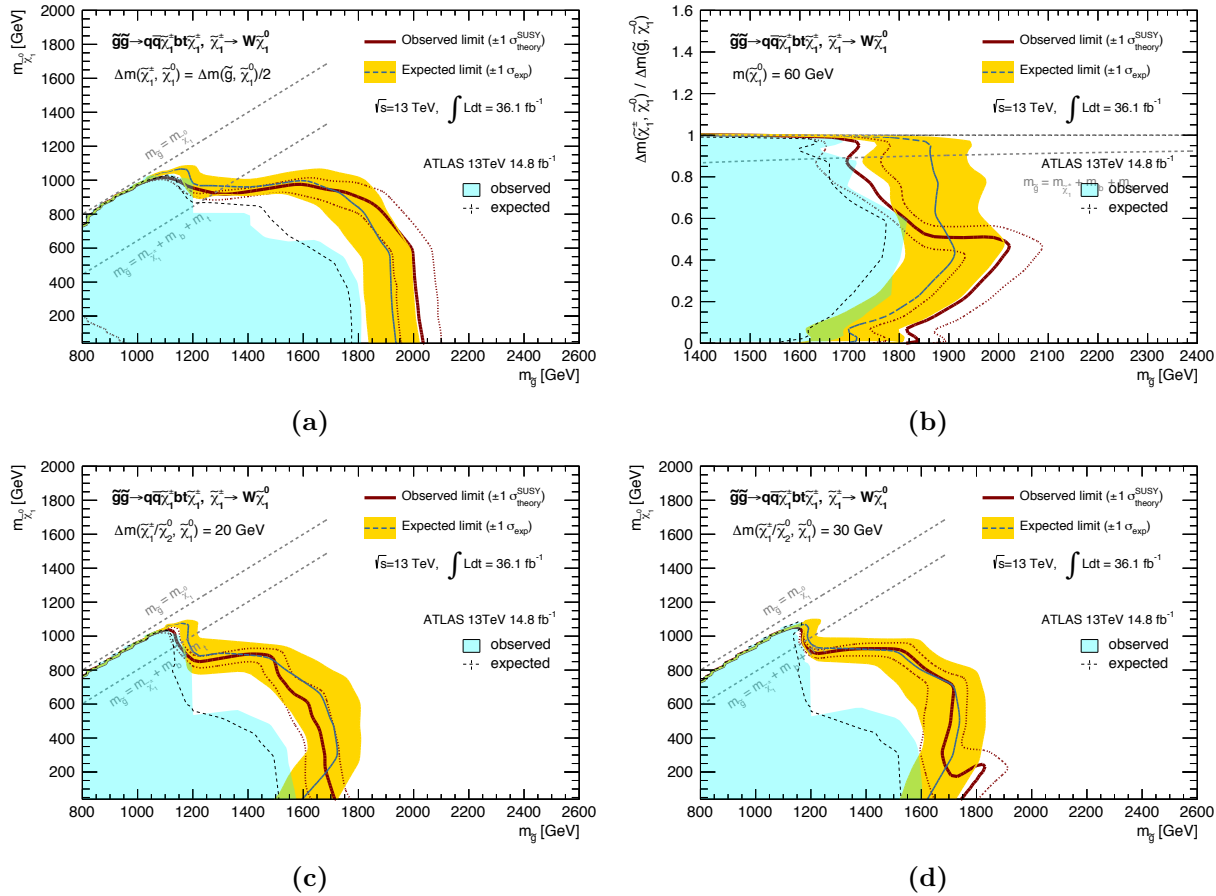


Figure 9.11: Projected exclusion limit (95% CL) for benchmark model **QQC1BTC1** presented in (a) **x=1/2** (b) **LSP60** (c) **DM20** (d) **DM30**. Observed limits are shown by the solid red lines, while the expected limit are expressed by the dashed blue lines with yellow 1σ bands. Potential achievable exclusion by the previous 1-lepton search in ATLAS (14.8 fb^{-1}) [148] are shown by the cyan shaded areas. All limits correspond to 95% CL.

TTN1TTN1

The exclusion limit for the model **TTN1TTN1**, the reference model for the 3B benchmarks (Table 2.5) is shown in Figure 9.12. The observed and expected limits largely agree reflecting that the observed data yields in **3B** SRs are fairly consistent with the expectation.

The exclusion limit provided by the previous ATLAS analyses (multi-*b*: [149], same-sign leptons or three leptons: [150]) are displayed by the shade area. The most prominent update is around the diagonal region with the mass splitting $\Delta m(\tilde{g}, \tilde{\chi}_1^0)$ below 200 GeV, where the explicit limit is set for the first time. On the other hand, there is seemingly no improvement in the direction toward higher gluino mass. This is because the compared past limit is provided by the multi-*b* analysis where the combination of both 0-lepton and 1-lepton channel is performed, drastically enhancing the sensitivity.

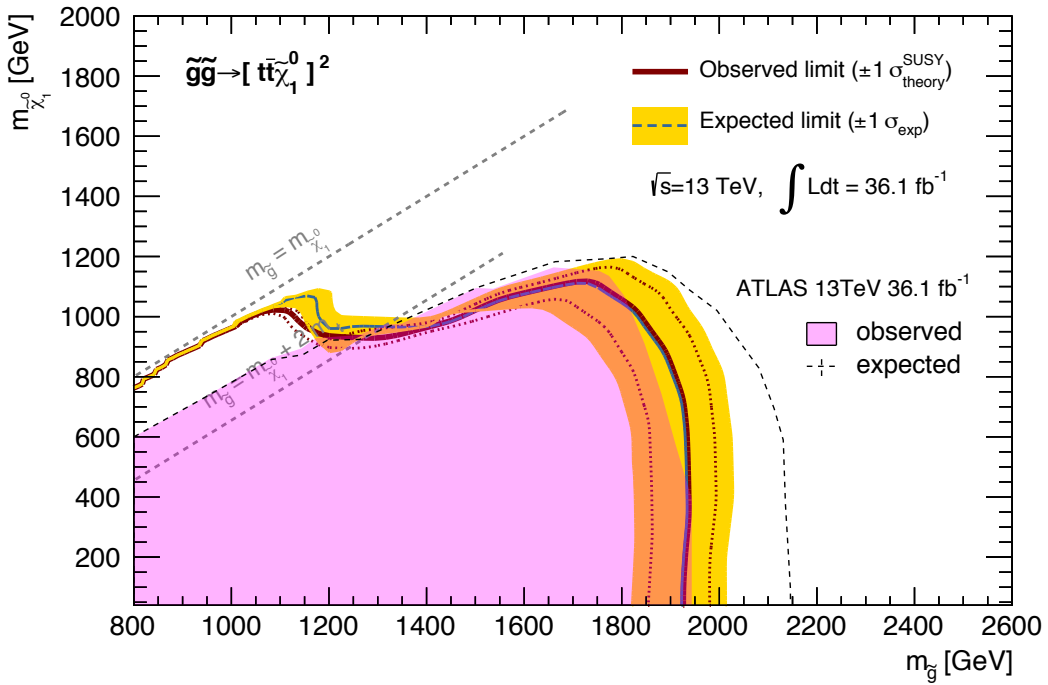


Figure 9.12: Exclusion limit for benchmark model **TTN1TTN1**. Observed limit is shown by the solid red line, while the expected limit are expressed by the dashed blue line with a yellow 1σ band. The past result provided by ATLAS (multi-*b*: [149], same-sign leptons or three leptons: [150]) is overlayed (observed limit: magenta shade, expected limit: black dashed line), which is mostly given by the multi-*b* analysis where the combination of 0-lepton and 1-lepton channel is performed. All limits correspond to 95% CL.

Other benchmark models

The exclusion limits for all the 45 models and grids are calculated similarly. Observed limits are compared in Figure 9.13-9.17. BV/BT/3B benchmark models (defined respectively by Table 2.5 - 2.7) are overlaid in the same plot respectively. Though the acceptance after the 1-lepton pre-selection are similar between them, the final sensitivity does vary depending on the branching into the 1-lepton final state which has a relatively wide variety. This ends up in $300 \text{ GeV} \sim 400 \text{ GeV}$ of difference in gluino mass at the largest. On the other hand, this implies that the models with less sensitivity can be fully recovered by the combination with 0-lepton final state. Aside such several models with the small 1-lepton branches, the variation is typically $100 \text{ GeV} \sim 200 \text{ GeV}$, which confirms the inclusiveness of the analysis.

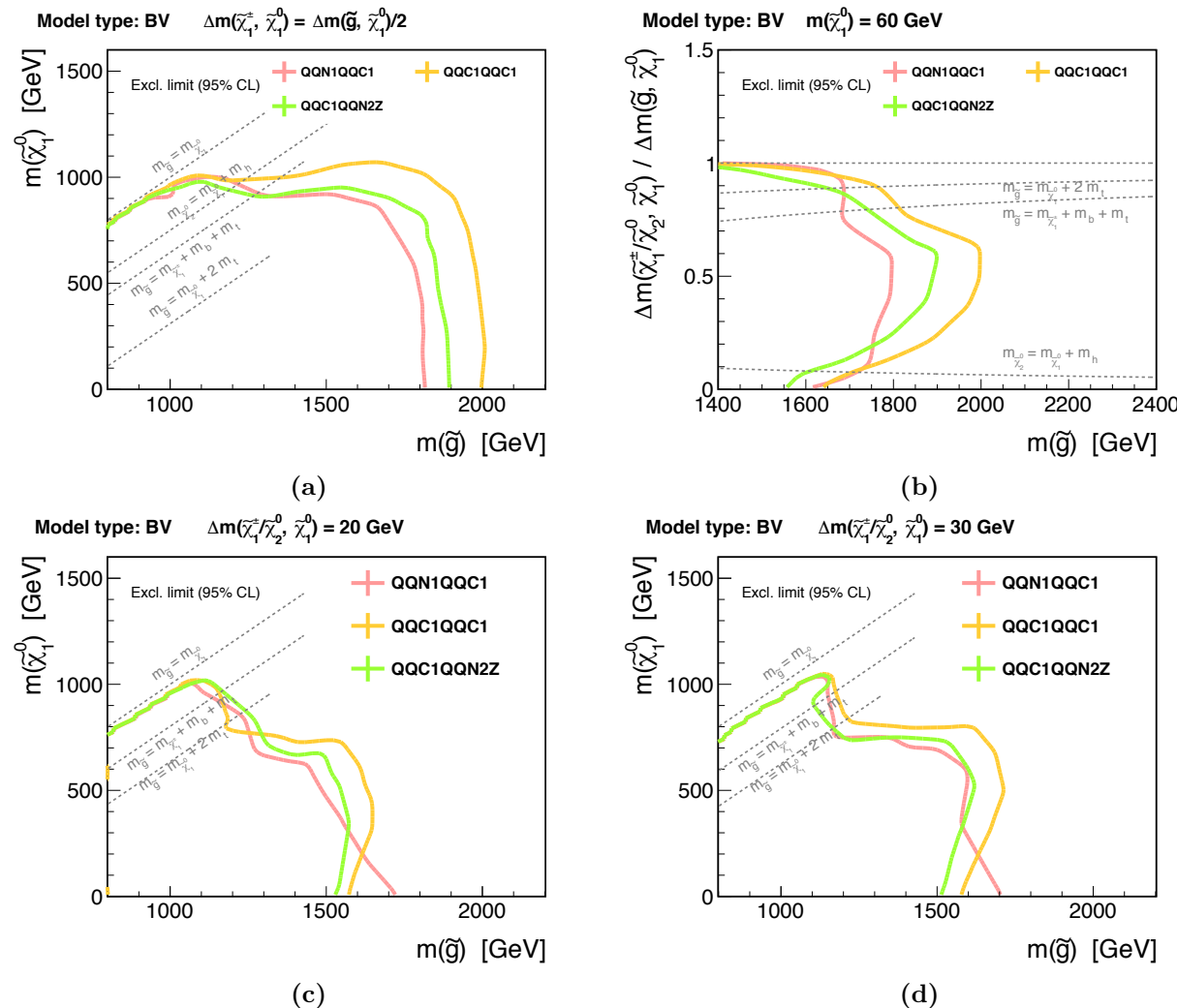


Figure 9.13: Observed limit for BV benchmark models (defined in Table 2.5) presented in grid (a) **x=1/2** (b) **LSP 60** (c) **DM20** (d) **DM30**.

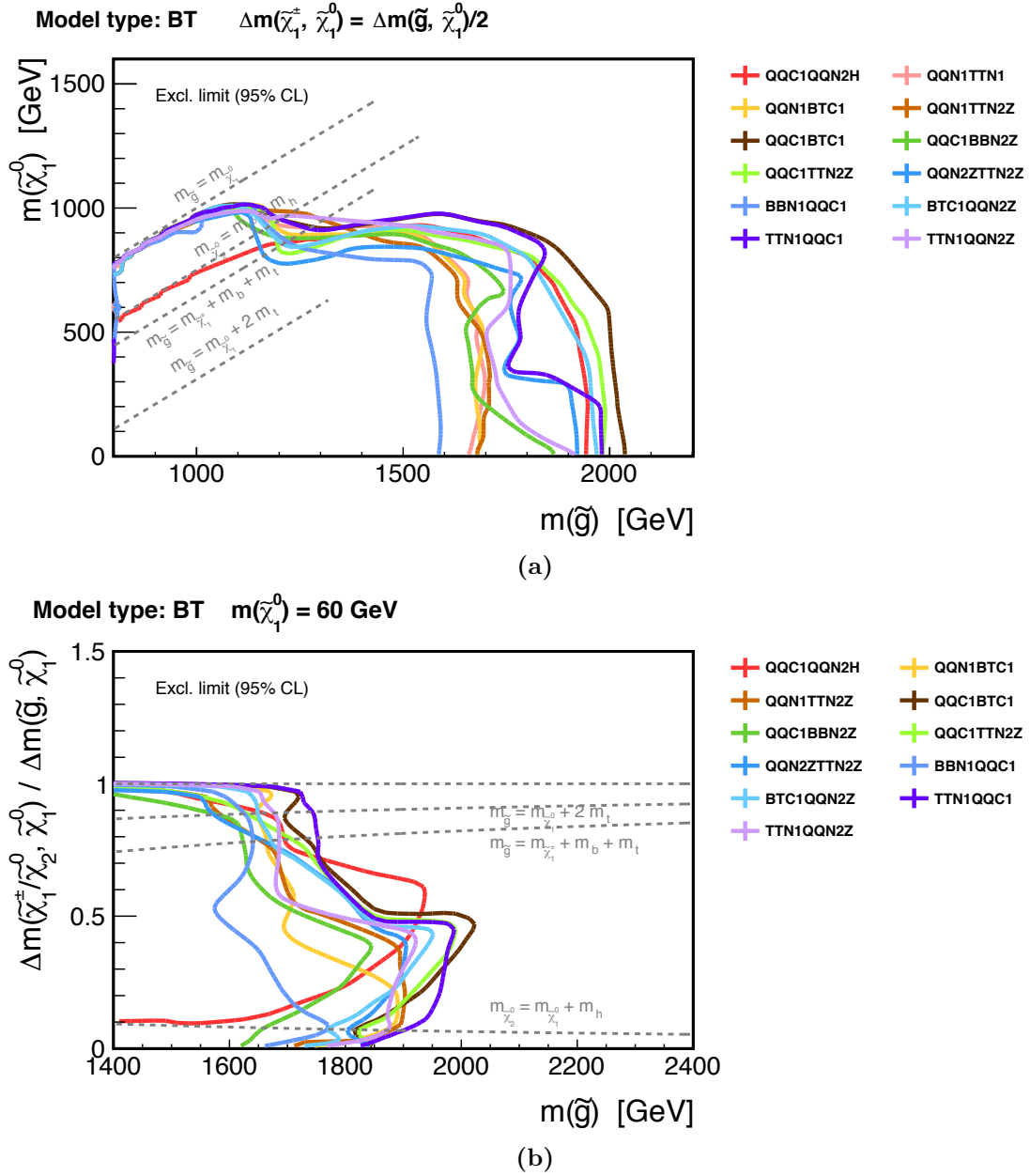


Figure 9.14: Observed limit for BT benchmark models (defined in Table 2.6) presented in grid (a) **x=1/2** (b) **LSP 60**.

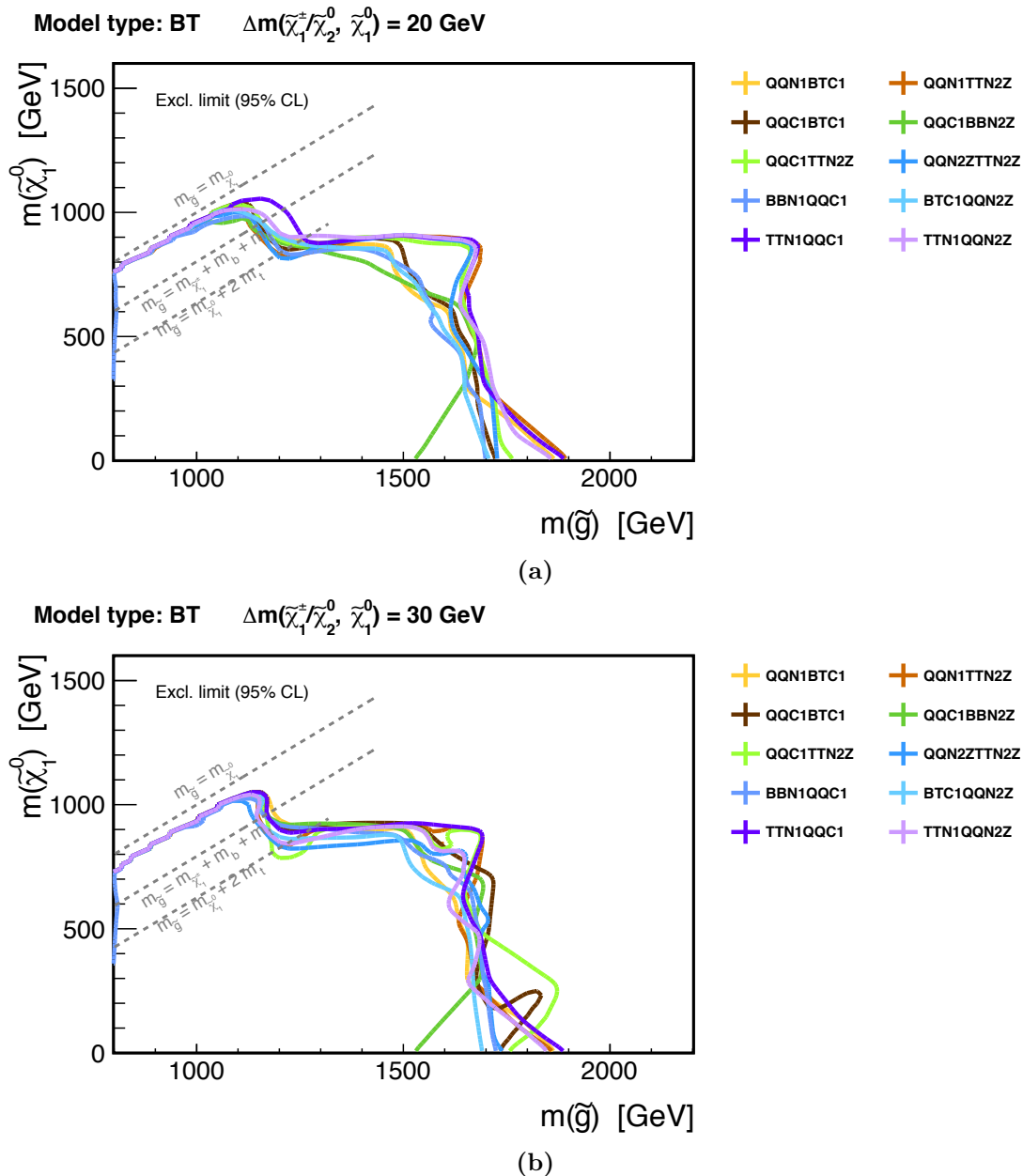


Figure 9.15: Observed limit for BT benchmark models (defined in Table 2.6) presented in grid (a) **DM20** (b) **DM30**.

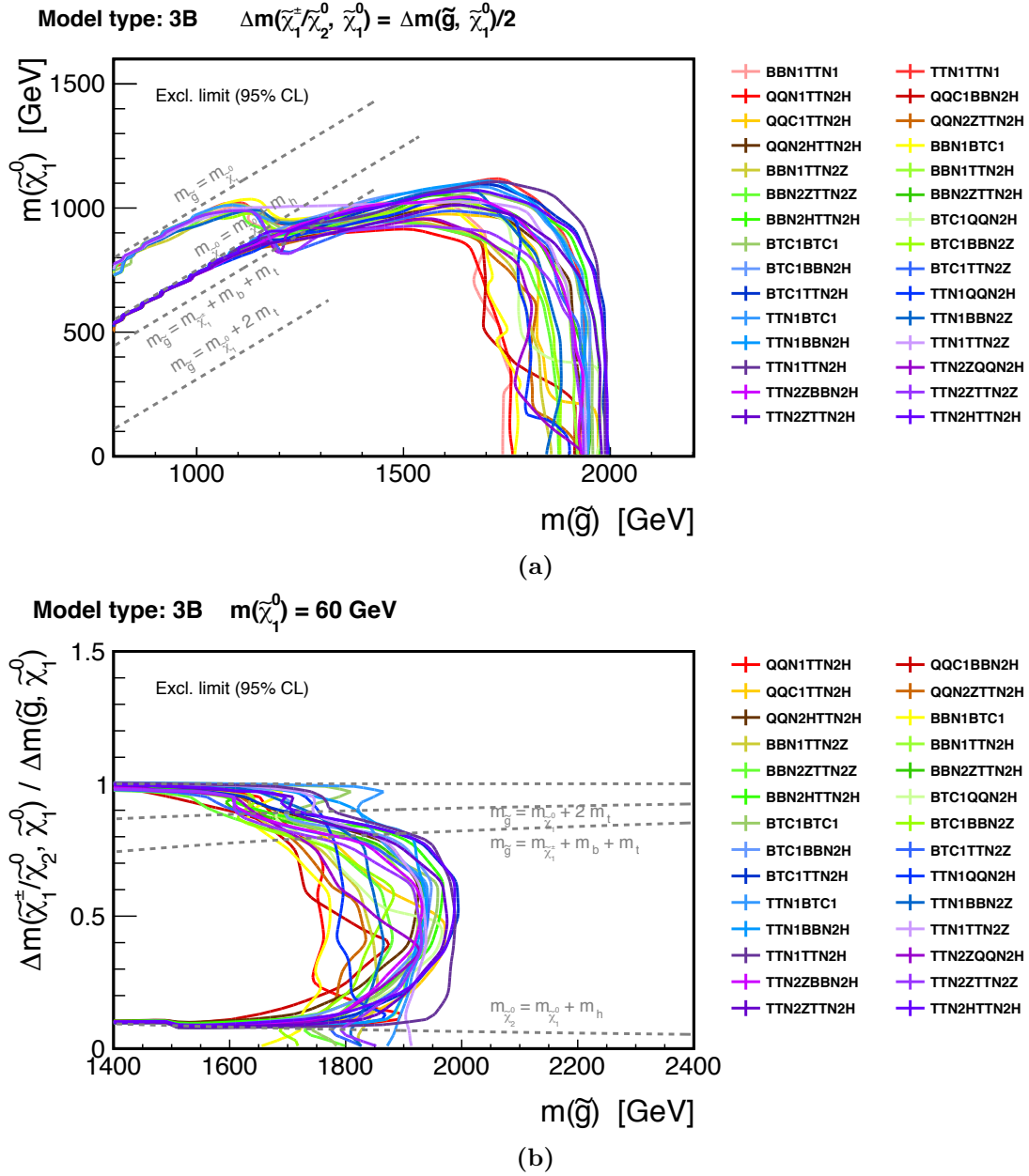


Figure 9.16: Observed limit for 3B benchmark models (defined in Table 2.7) presented in grid (a) **x=1/2** (b) **LSP 60**.

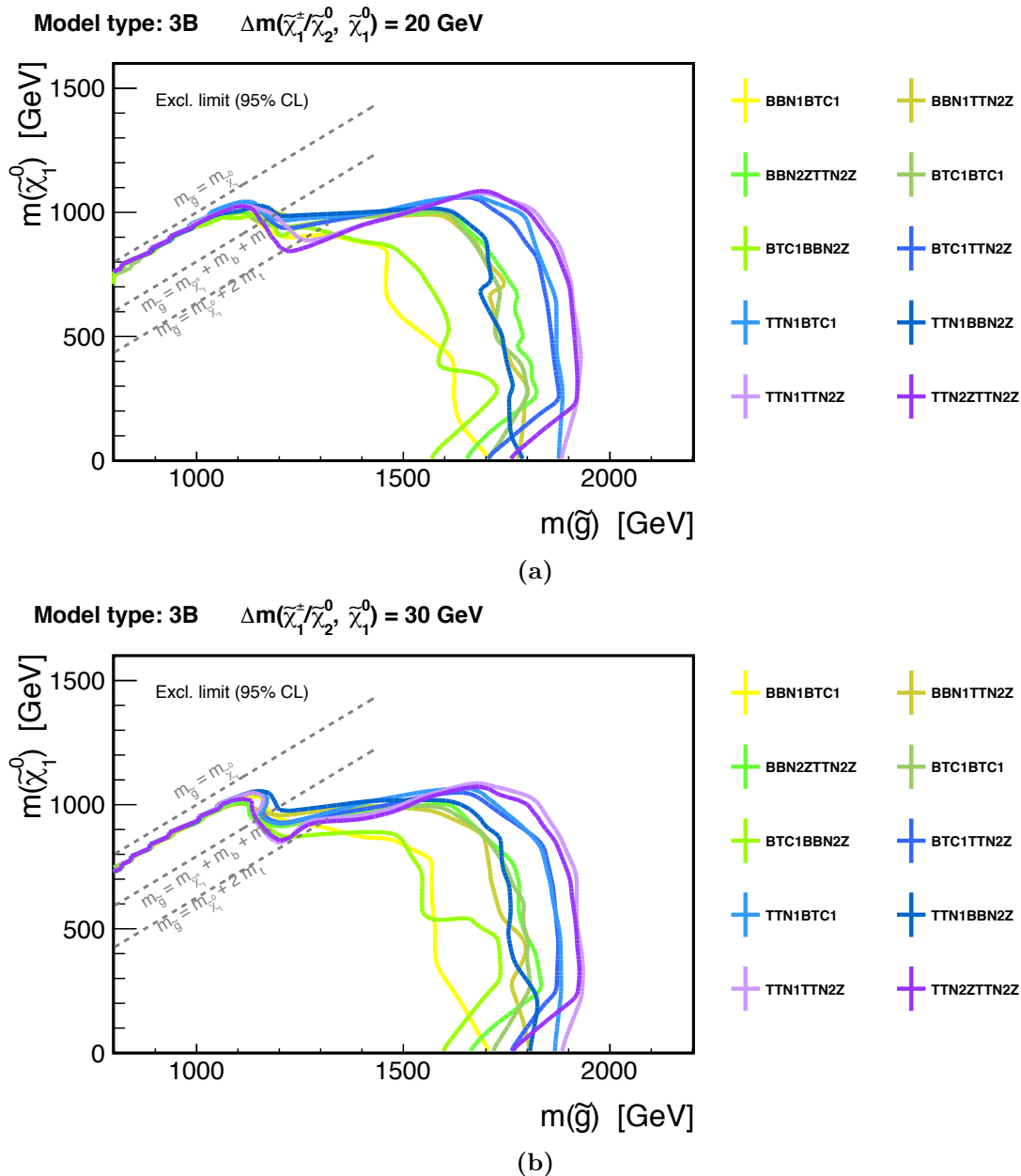


Figure 9.17: Observed limit for 3B benchmark models (defined in Table 2.7) presented in grid (a) **DM20** (b) **DM30**.

9.4 Obtained Cross-section Upper-limit

CL_s value is calculated as the function of the signal strength μ ($\in [0, 5]$) in the hypothetical test. Therefore, the upper limit on μ can be determined as:

$$\mu_{95\text{CL}} := \mu(\text{CL}_s = 0.05). \quad (9.13)$$

This can be straightforwardly interpreted into the upper limit on the excluded cross-section ($\sigma_{95\text{CL}}$), and it is a completely model-independent presentation of the result once the decay chain and the masses of gluino and EW-gauginos are specified. Figure 9.18–9.20 present the results for the reference models **QQC1QQC1**, **QQC1BTC1** and **TTN1TTN1**.

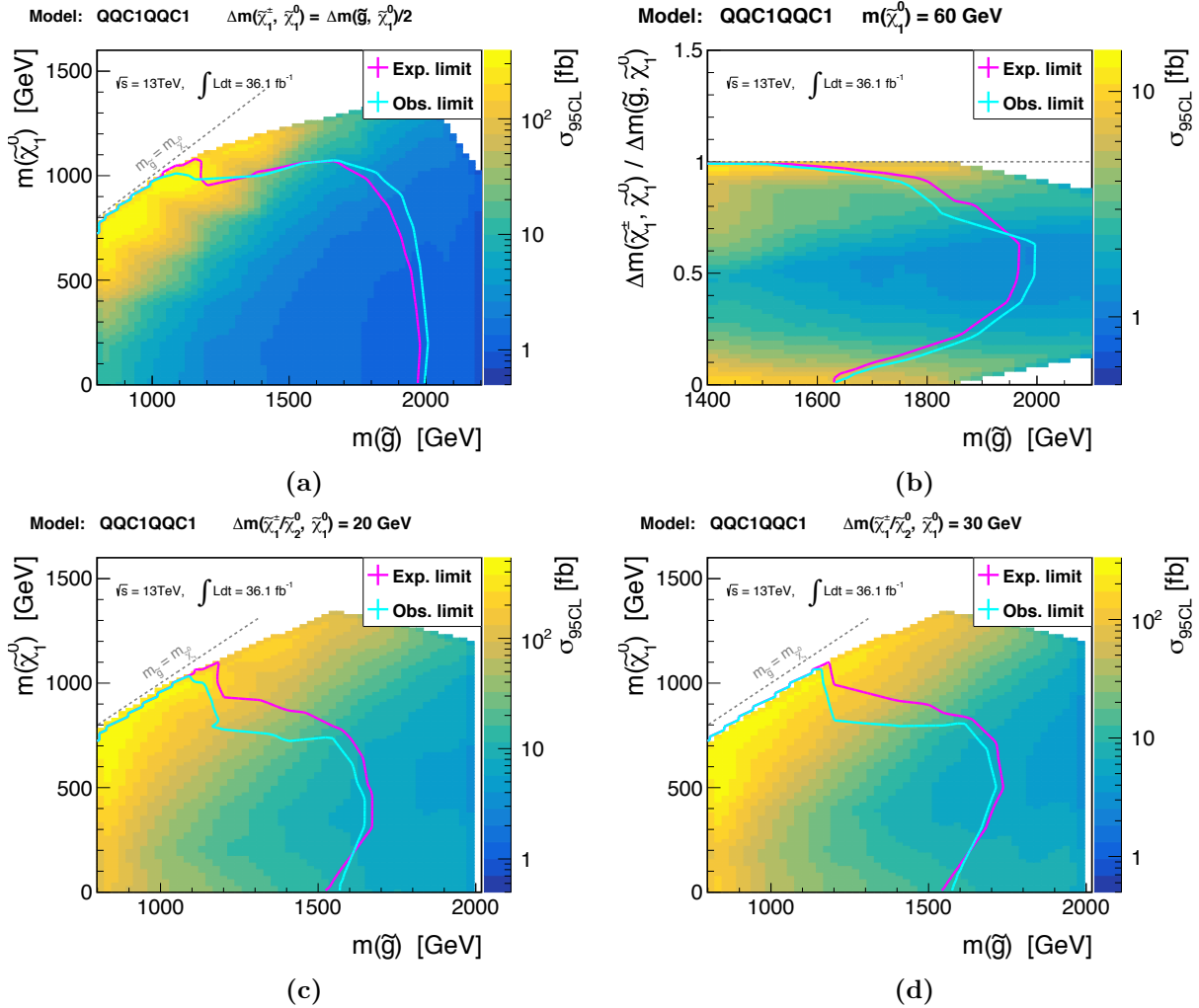


Figure 9.18: Upper limit of excluded cross-section (95%CL) as the function of the SUSY masses, for the reference model **QQC1QQC1**, presented in grids (a) **x=1/2** (b) **LSP60** (c) **DM20** (d) **DM30**.

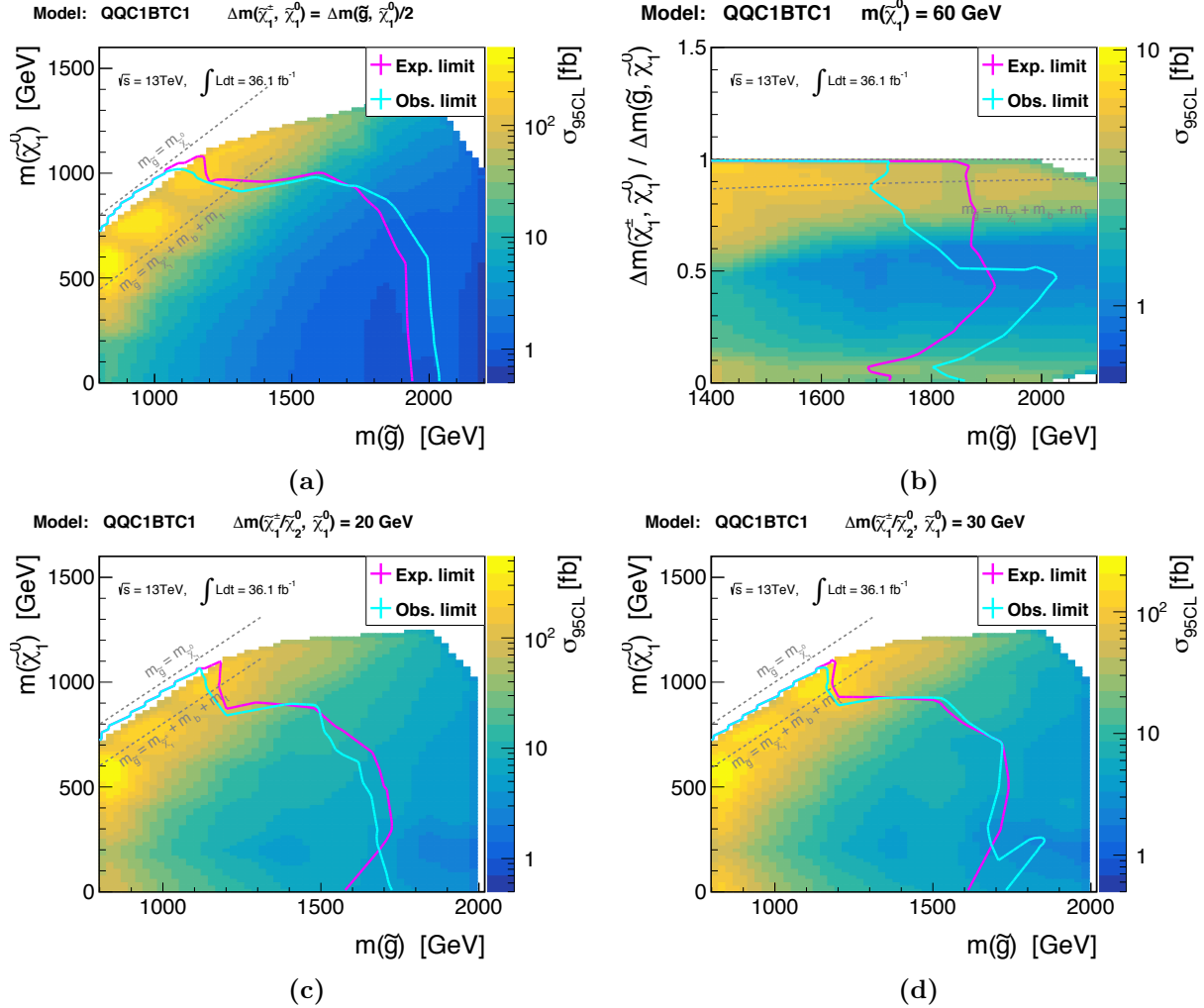


Figure 9.19: Upper limit of excluded cross-section (95%CL) as the function of the SUSY masses, for the reference model **QQC1BTC1**, presented in grids (a) **x=1/2** (b) **LSP60** (c) **DM20** (d) **DM30**.

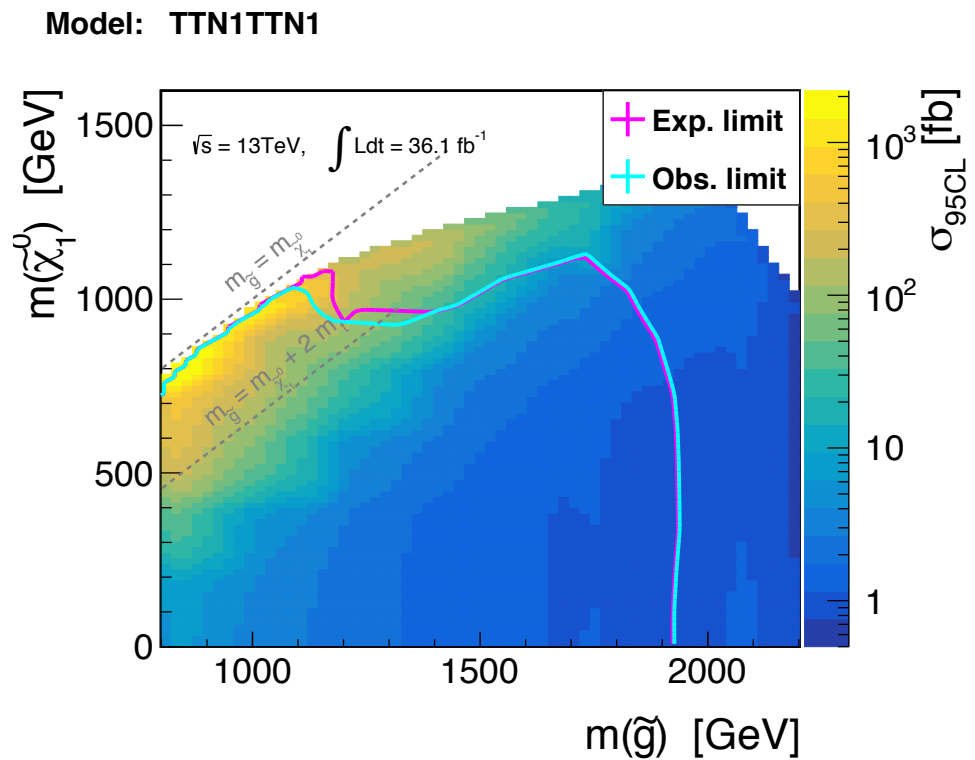


Figure 9.20: Upper limit of excluded cross-section (95%CL) as the function of the SUSY masses, for the reference model **TTN1TTN1**.

Chapter 10

Discussion

In this chapter, the impact and implication of the result is discussed, particularly about the comparison with the other gluino search analyses using the similar dataset as mentioned in [2.4.3](#), as well as the unique achievements done by the study. A short remark about the future outlook is attached concluding the chapter.

10.1 Comparison with the Other Up-to-date LHC Searches

Figure [10.1](#) show the obtained limits by the study on (a) **QQC1QQC1 ($x=1/2$ grid)** and (b) **TTN1TTN1** which are the conventionally studied gluino decay chains in the 1-lepton final, together with those provided by the other ATLAS/CMS searches appearing in the Figure [2.9-2.10](#) in chapter [2.4.3](#).

Sensitivity to decay chain **QQC1QQC1 ($x=1/2$ grid)**

Compared with the ATLAS 0-lepton analysis [\[151\]](#), the result of this thesis addresses a comparable sensitivity in the massless LSP limit, and outperforms in the massive LSP scenario as the 1-lepton final state is generally advantageous in the additional background rejection power by m_T . Quite similar sensitivities are seen between the thesis analysis and the CMS 1-lepton one [\[152\]](#), except for the region with heavy LSP where the kinematics is not very hard and therefore benefited by the combined multi-bin fit the most. The CMS SUSY analyses do much better job in this front as they often employ an incredibly large number of signal region bins (30-160). Note that the absence of limit in the diagonal region by CMS is because it only considers the on-shell W -boson emission in the interpretation.

Sensitivity to decay chain **TTN1TTN1**

The ATLAS multi- b analysis [\[153\]](#) is quite advantageous in sensitivity for high mass gluino scenario, since it exploits the statistical combination between 0-lepton and 1-lepton signal regions as mentioned in previous chapter, though the observed limit is much worse due to the $\sim 2\sigma$ excess found in 0-lepton signal regions. The sensitivity driven by the 1-lepton signal regions are quite comparable between the three cases.

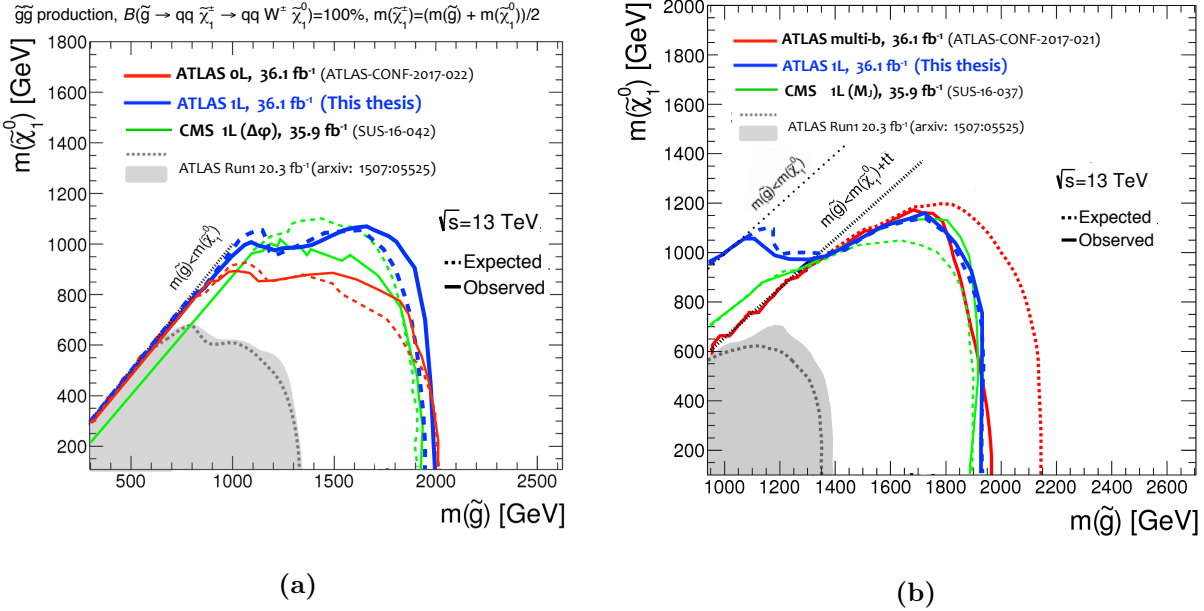


Figure 10.1: Constraints set by this analysis (blue) and other up-to-date ATLAS/CMS analyses (red/green) on (a) **QQC1QQC1** with the chargino mass is set to the midmost between the masses of gluino and the LSP (**x=1/2** grid), and on (b) **TTN1TTN1**.

Sensitivity to other decay chains

Although the other gluino decay chains (e.g. asymmetric decaying gluinos) have never been explicitly interpreted into limit before, those signatures could still be captured by the ordinary signal regions. For instance, the CMS analyses are suppose to address reasonable sensitivity to most of the decay chains with typical mass configuration, giving the wide phase space coverage of the signal regions and the large number of signal bins. However, an exception is expected in the case of the DM-oriented scenario where LSP and NLSP EW gauginos are compressed, which requires particular consideration in event selection. One of the nice thing about this thesis is that it provides optimized sensitivity to such scenario.

10.2 What is Unique/Important in This Study?

Design of dedicated event selection for the DM oriented scenario.

In the previous ATLAS 1-lepton analyses [148][154], there has been a signal region indeed targeting scenarios with compressed NLSP and LSP (“Low-x”). However, it was only optimized to the case with massless LSP (low- x region in the **LSP60** grid) where the soft lepton selection was not applied since the emitted lepton can be hard due to the heavily boosted NLSP. Giving that the massless LSP is no longer realistic for many reasons (see Sec. 2.4.2), the focus is shifted to the massive LSP scenario in this analysis where the soft lepton selection is explicitly applied. Similarly, the CMS analyses do not contain the soft lepton selection in their signal region. Therefore, the DM-oriented grids are likely to have the optimized sensitivity for the first time in this study.

Establishment of a refined background estimation technique.

The most important achievement of this study may be the establishment of the object replacement method; from the refinement of the previous studies, to the implementation in the analysis with the conventional kinematical extrapolation method working together. The dependency on simulation is then dramatically reduced as a result, enhancing the confidence in our background estimation by replacing the main systematic uncertainty from the theoretical uncertainty (which evaluation is in fact often questionable) to the statistical uncertainty regarding to the control region statistics. This is a highly helpful aspect towards claiming the discovery once excesses are found, since the uncertainty can be reduced just by adding data statistics. In a longer term, the object replacement method is supposed to benefit even more, as heavier gluino will be targeted with tighter selections in the future analyses in which more extreme phase space will be explored where MC is supposed to be even more unreliable.

There is one thing that has to be remarked that the idea of object replacement itself is not original to this work. One of the most famous example of such type of estimation in the past might be the “tau embedding” performed in the Higgs analysis ($h \rightarrow \tau\tau$) in ATLAS Run1 [155]. This is to estimate the $Z \rightarrow \tau\tau$ background from $Z \rightarrow \mu\mu$ data events, by replacing muons into simulated tau decays. Replaced events are re-input in the detector simulation, in order to reduce the instrumental systematics. This is however too computationally costly for search analyses where instrumental systematics has little impact in general. Therefore, a simplified version has been proposed where detector effect is emulated instead of simulated (“tau replacement”) [156]. The first implementation in the published analysis is done by CMS in Run1 [157] (0-lepton, $\mathcal{L} = 20.3 \text{ fb}^{-1}$). The author has been working on the refinement and implementation into the ATLAS analysis which is done for the first time in this work. The main difference between the CMS implementation is the use of MC; while it is carefully designed to ensure the object-kinematics orthogonality (Eq. 7.1) (i.e. lepton’s efficiency is parameterized only by the feature of the lepton such as p_T and η etc.) in this analysis, CMS takes an opposite philosophy where lepton efficiency is parameterized by as many event-level kinematical variables as possible. This might lead to some difference in estimation in highly extreme phase space.

An small improvement is also made in the context of the kinematical extrapolation method, with a liitle more complete assignment of theoretical uncertainty. Conventionally, it is assigned based only on the known effects, even if an unaccountable mis-modeling is found on top of those since it had been supposed to be the best thing one can do. This study makes one more step forward; the effects from “unknown theory systematics” is approximately expressed through a course of kinematic reweightings (see Sec. 8.3.1), and impact is evaluated quantitatively. Although since the method is not first-principle thus is still a sort of “the best thing one can do”, it is the first time that the uncertainty due to “unknown systematics” is assigned in the analysis, reducing the risk of being hit by unaccounted effects.

First interpretation on a comprehensive classes of the gluino decay chains.

The poor variety in decay chains considered in ATLAS/CMS SUSY searches has been always an one of the most outstanding issue. As for gluino pair production, only 6 decay scenarios have been targeted and interpreted so far. This is not comprehensive at all, and it is hard for one to judge if the provided mass reaches are general or not.

The full-model oriented approach is then gradually attempted recently. The most popular study is done with the phenomenological MSSM (pMSSM), a simplified framework of MSSM in which only 18 kinematically important parameters are set free. It is basically a parameter scan in a 18-dimensional space, generating a bunch of points of signal models with inclusive decay patterns (ATLAS Run1: [158][159], CMS Run1: [160]). Though much more comprehensive, it in turn suffers from a couple of presentational problems; the limit is hardly expressed by the mass reach hence non-intuitive; the result is so model dependent that it is impossible to re-interpreted to the other models.

On the other hand, the presentation in this study largely addresses all of the problem; this is the first study explicitly testing each direct/1-step gluino decay chain that can be targeted by 1-lepton final state; limits are presented in terms of mass reach; model-independent upper limit on the excluded cross-section is also provided so that any model can be tested based on the result.

10.3 Future Prospect

The future LHC run schedule is schematized in Figure 10.2. After the current Run2 ($\mathcal{L} \sim 150 \text{ fb}^{-1}$) and following phase-1 upgrade, Run3 is planned to take place in which another 150 fb^{-1} is expected in 4-year of the operation. The HL-LHC project (High-Luminosity LHC) [161] is then planned after Run3, with a large scale upgrade both in terms of the accelerator to boost the luminosity and the detectors to cope with more severe radiation environment (phase-2 upgrade). The HL-LHC physics runs are planned to be operated with a center-of-mass energy of 14 TeV, accumulating $\mathcal{L} \sim 3000 \text{ fb}^{-1}$ of data in about 10 years.

Gluino seach will keep interesting as it has no experimental or phenomenologically implied upper limit in its mass. The limit can be easily extended by keep applying tighter selection, as the background separation becomes easier with exploring heavier gluinos. The search sensitivity is expected to extend upto 2.5 TeV ~ 3 TeV in gluino mass with $\mathcal{L} \sim 3000 \text{ fb}^{-1}$ (Figure 10.3).

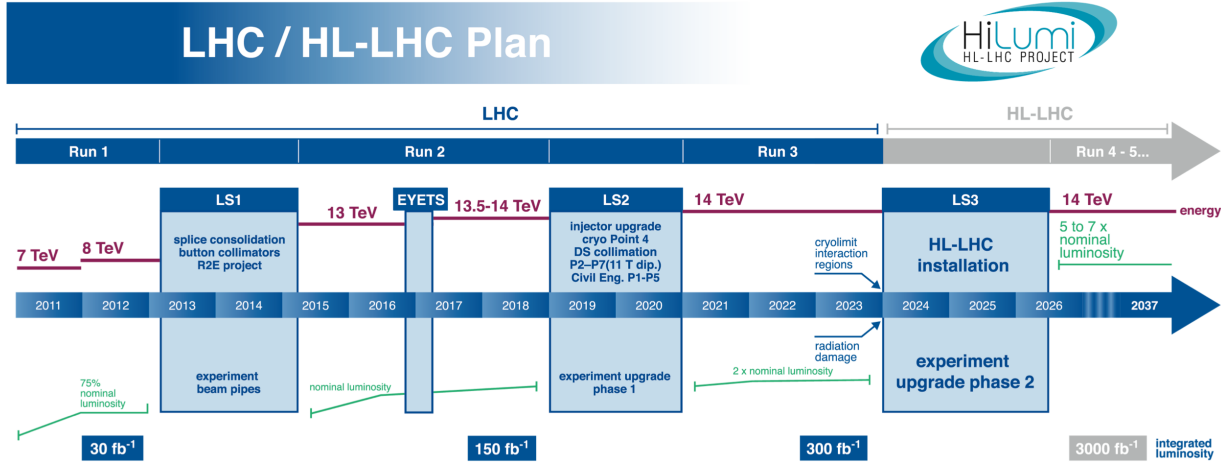


Figure 10.2: The time-scale of current LHC and foreseen HL-LHC project [161].

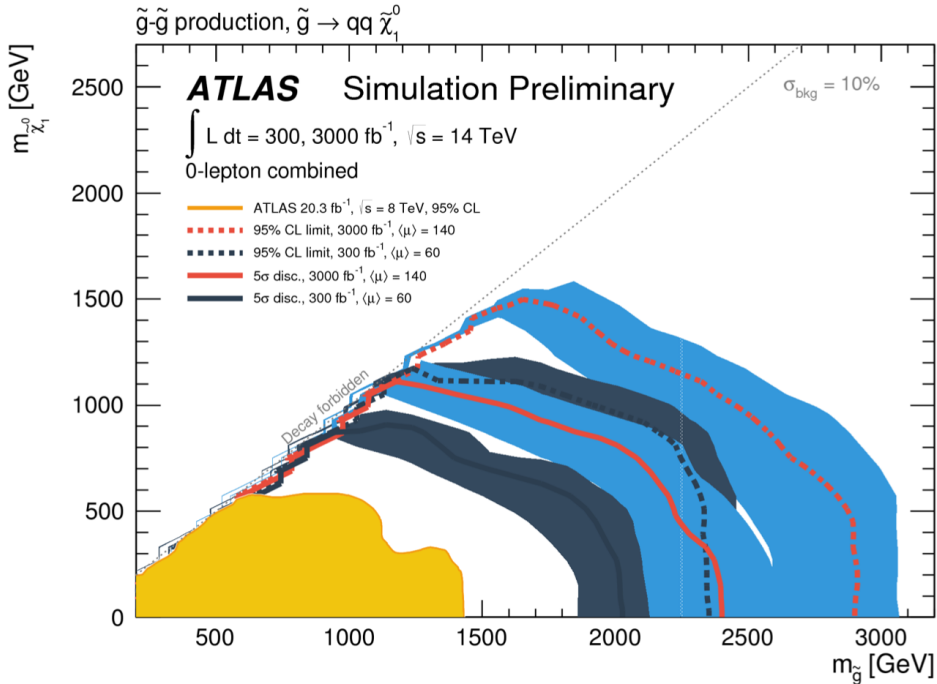


Figure 10.3: Expected discovery reach (5σ) and exclusion limit (95% CL) with the whole Run2-3 dataset ($\mathcal{L} \sim 300 \text{ fb}^{-1}$) and HL-LHC dataset ($\mathcal{L} \sim 3000 \text{ fb}^{-1}$) [162].

Chapter 11

Conclusion

This thesis presents the search for gluinos using proton-proton collisions in the Large Hadron Collider (LHC) at the center-of-mass energy of $\sqrt{s} = 13$ TeV. Focusing on the final state with one leptons, all relevant 45 decay chains for pair produced gluinos are explored, together with various scenarios of the mass spectra, aiming to provide the most general result achievable in principle.

The highlight of the analysis is designing a dedicated data-driven background estimation method, reinforce the confidence on the estimation by reducing the reliance on simulation which typically less performing in an extreme phase space.

The analysis is performed with the data recorded by the ATLAS detector with an integrated luminosity of 36.1 fb^{-1} . In the unblinded signal regions, no significant excess is found. Constraints are set on each of the 45 models of gluino decay chain. Exclusion upto 1.7 TeV – 2.0 TeV in gluino mass and upto ~ 1 TeV in the lightest neutralino mass is widely confirmed with typical mass spectra of gluino and EW gauginos, while upto 1.5 TeV – 1.9 TeV in gluino mass is excluded in case of the compressed EW gauginos which is motivated by the dark matter relic observation.

Acknowledgement

The appreciation from the author to people for the contribution of this work is summarized in Table 11.1-11.2.

Table 11.1: List of guys I want to thank.

Name	Relation with the author	The author thanks for ...
Tokyo Group		
Sachio Komamiya	Supervisor	Encouraging the author to jump in the field, reviewing this thesis.
Yoshio Kamiya	Semi-boss	Providing initial how-tos (programing, DAQ, statistics etc.) at the beginning of master
Daniel Jeans	Semi-boss	Teaching physics and software while in master. Proof reading of CV.
Junping Tian	Neighbor desk	Discussing the prospect of China.
Tokyo Computing Team	Host	Maintaining the incredibly efficient server.
Kono-san	Secretary	Handling paper works of trips and contact to JPS.
Shiota-san	Secretary	Handling paper works of trips.
Chihiro Kozakai	Colleague	Sharing the tough feeling of Ph.D.
Yusuke Suda	Colleague	Sharing the tough feeling of Ph.D.
Yuya Kano	Colleague	Instruct the author why US people like to say “t’sup” instead of “hello”.

Table 11.2: List of guys I want to thank.

Name	Relation with the author	The author thanks for ...
People in CERN		
Shoji Asai	Local Supervisor in CERN	Suggestion on topics for the Ph.D project.
Junichi Tanaka	Local Supervisor in CERN	Secretly generating samples exerting the privilege of MC coordinator. Maintaining the server for Tokyo group in CERN.
Takashi Yamanaka	Supervising role in the analysis	Answering every technical question from the author, discussing physics in deep, polishing many new/preliminary ideas.
Tomoyuki Saito	Supervising role in the analysis	Constant consultant on plans in analysis, co-developer of the object replacement.
Shimpei Yamamoto	Staff of ICEPP (-2015)	Comprehensive assistance in the initiation of the analysis. Maintaining the server for Tokyo group in CERN.
Yohei Yamaguchi		Teaching the author how to fish.
Yuji Enari	Staff of ICEPP, kebab mate	Providing keen comments to the analysis. Promoting eating kebabs as the dessert of a dinner to the community.
Yasu Okumura	Staff of ICEPP	Consultant on post-doc app., proof reading of CV and research proposals.
Keisuke Yoshihara	Foreseen colleague in UPenn	Secure author's life after the Ph. D.
Till Eifert	SUSY convener	Encouraging aggressive ideas. Teaching the author that the life does not end even if SUSY is not found.
Stefano Zambito		
Moritz Backe		
Jeanette Lorentz	Analysis Contact	Cool coordination.
Da Xu		
Nikolai Hartmann		
Huajie Cheng	Colleague	Closely working together in the analysis.
Valentina Tudorache		
Masahiro Morinaga	Room mate	Cooking 10 kg Bolongese per week. Throwing mushrooms from window.
K. Onogi	Room mate	Keep the rooms comfortable. Suggesting interesting comics to the author.
Chikuma Kato	Hiking mate	Sharing the tough feeling of Ph.D.
K. Motohashi and		
D. Kobayashi	Iceland mate (2015)	Running on the icelandic terrain.
Shadachi and		
Y. Minegishi	Iceland mate (2016)	Crossing a river by car, chasing icelandic sheep.
T. Nobe	Famous hip-hopper in Japan	Preaching a notion that money is all.
T. Nitta	Famous climber in Japan	Teaching basic movement of climbing.
Others		
Chun Chen / Ying Chen	Parents	Feeding the author for > 25 years.
Maya Okawa	Life-time partner	Making my life awesome.

Appendix

A Auxiliary Materials for MC Simulation

A.1 Detail Configuration of Event Generation

$W/Z + \text{jets}$

Events involving a leptonically decaying W/Z boson with associated jets are simulated using the SHERPA 2.2.1 generator [115]. The matrix elements are calculated up to two partons at NLO and four partons at LO using the Comix [163] and OpenLoops [164] generators. Parton showers are generated by the internal algorithm of SHERPA 2.2.1 [165] and merged based on the ME+PS@NLO prescription [166]. The CKKW scheme is used for ME/PS matching with matching scale set to 30 GeV. Hadronic decay modes of W/Z are not included in the sample.

Tops ($t\bar{t}/\text{single-top}$)

The events are generated using the POWHEG-BOX generator, explicitly designating diagrams involving top-quarks. The generator parameters are set to well-accounting for the data in LHC Run1 [167]. The interference between $t\bar{t}$ and $Wt + b$ is taken into account by the Diagram Removal scheme [168]. The EvtGen v1.2.0 program [169] is used to correct the bottom and charm hadron decays (“after burner”). Parton shower and underlying events are simulated using the interfaced PYTHIA 6.

Di-bosons: WW/WZ/ZZ

All samples are simulated by the SHERPA 2.2.1 generator. Full leptonic processes are simulated with five final states ($\ell\ell\ell\ell$, $\ell\ell\ell\nu$, $\ell\ell\nu\nu$, $\ell\nu\nu\nu$, $\nu\nu\nu\nu$). The intermediated states are not specified therefore the contribution from Drell-Yan-like off-shell diboson and the interference between different diboson processes (e.g. $WW \rightarrow \ell\ell\nu\nu$ and $WZ \rightarrow \ell\ell\nu\nu$) are taken into account. The semi-leptonic diboson processes ($WW/WZ \rightarrow \ell\nu qq$, $WZ/ZZ \rightarrow \ell\ell qq$) are simulated with explicitly designating the intermediated states (W or Z), therefore no interference amplitude between them is accounted. Full hadronic diboson events are not included in the sample.

$t\bar{t} + W/Z/WW$

All processes are simulated by MG5_aMC@NLO2.2.3 at LO interfaced to the PYTHIA 8.186 parton shower model, with up to two ($t\bar{t} + W$), one ($t\bar{t} + Z$) or no ($t\bar{t} + WW$) extra partons included in the matrix element.

SUSY signals

Decay of EW gauginos are done in PYTHIA, based on phase space with no consideration of the spin. The CKKW-L matching scheme [170] is applied for the matching of the matrix element and the parton shower, with the corresponding scale parameter set to 1/4 of the gluino mass. The cross-section uncertainty are taken from an envelope of cross-section predictions using different PDF sets and factorization and renormalisation scales, as described in Ref. [171], considering only the four light-flavor left-handed squarks (\tilde{u}_L , \tilde{d}_L , \tilde{s}_L , and \tilde{c}_L). Figure 5.3 shows the calculated cross-section and the associated error. Model parameters irrelevant to SUSY masses are fixed to arbitrary reasonable values, since presumably they do not change the kinematics as discussed in Sec. 2.5.2. The mixing parameters are set so that LSP and NLSP are bino- and wino-like.

A.2 Fast Simulation vs Detector Emulation

In order to save the computing resources, only a few signal models are generated with detector simulation (✓ in Table 2.5-2.7). The detector response for the samples of the other models are then emulated, using the parametrized efficiency functions (in terms of electron identification, muon identification, isolation cut, JVT cut and b -tagging) and smearing fucntions (in terms of energy resolution of objects and E_T^{miss}) from full-simulated $t\bar{t}$ samples. The emulation is validated by comparing the kinematics of signals with the samepls of fast-simulation. 3 reference mass points for **QQC1QQC1** and one reference point for **TTN1TTN1** are chosen, and results are shown in Figure A.2.1-A.2.4. In the bulk phase space, the difference is within 10% which is sufficient with respect to the signal cross-section uncertainty (15% ~ 35%). The emulation is sometimes not perfect in the tail of the distributions, however it does not matter for most of the cases since such region does not address any signal sensitivity.

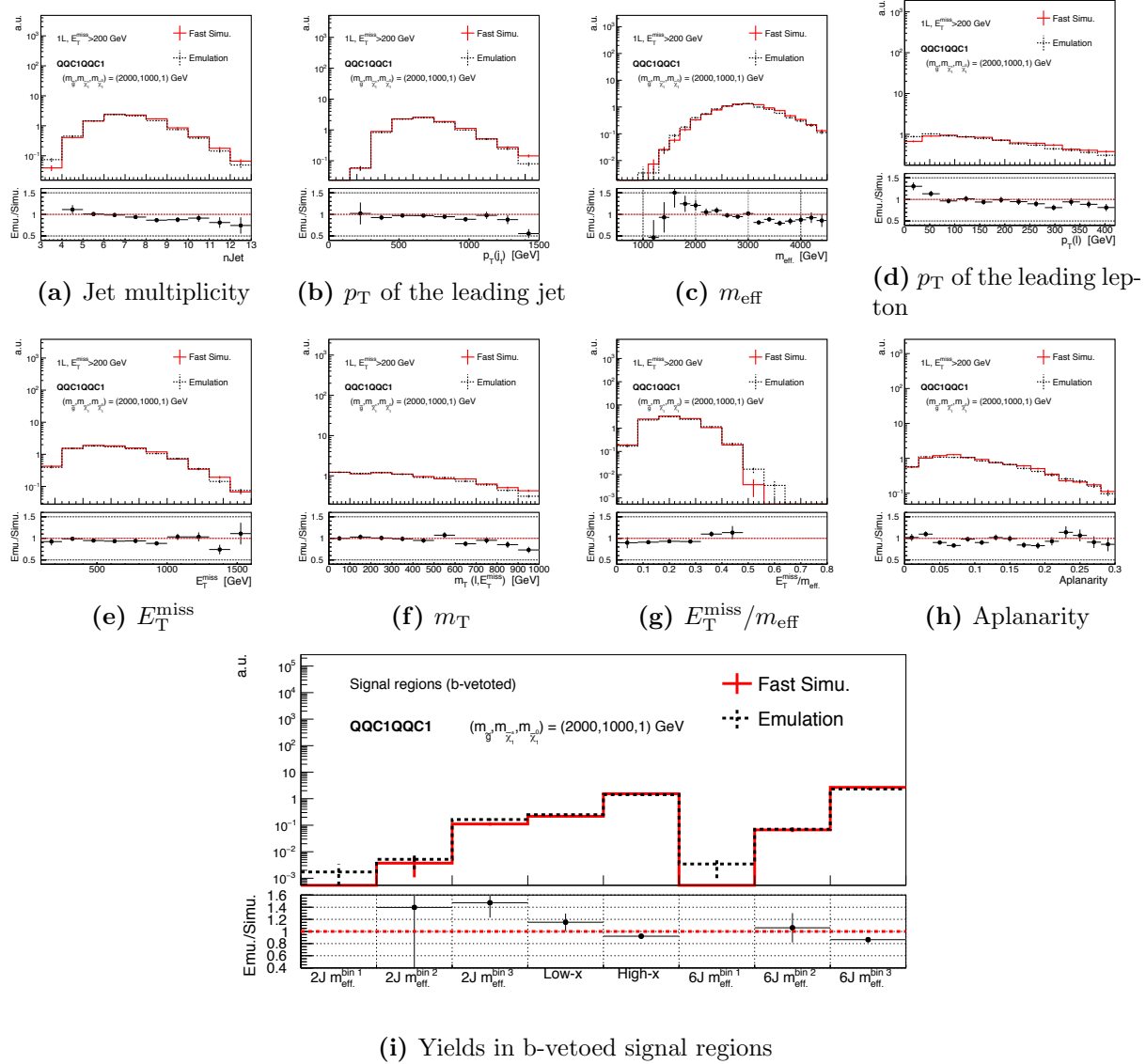
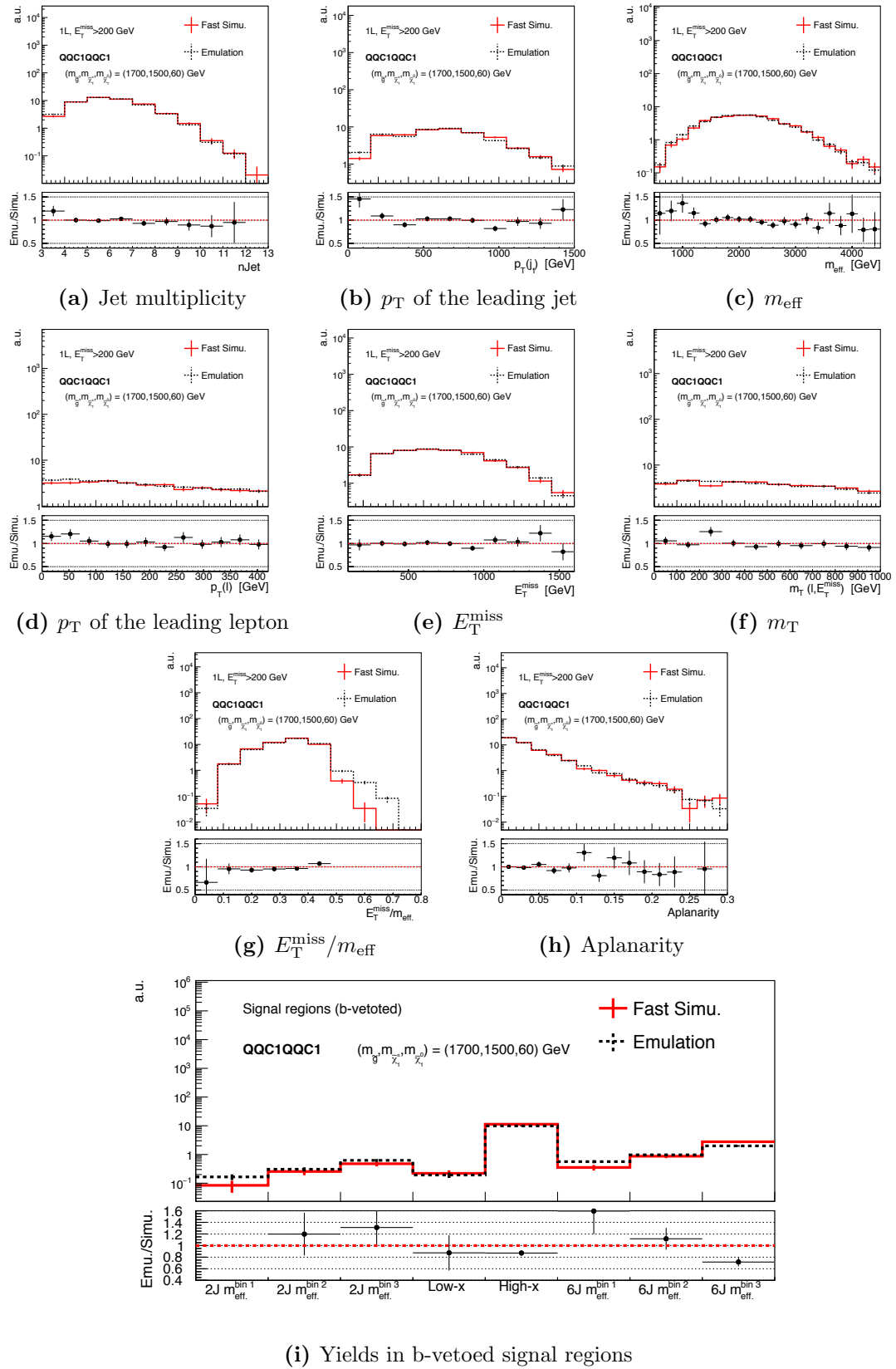


Figure A.2.1: **QQC1QQC1**, $(m_{\tilde{g}}, m_{\tilde{\chi}_1^\pm}, m_{\tilde{\chi}_2^0}) = (2000, 1000, 0)$ GeV



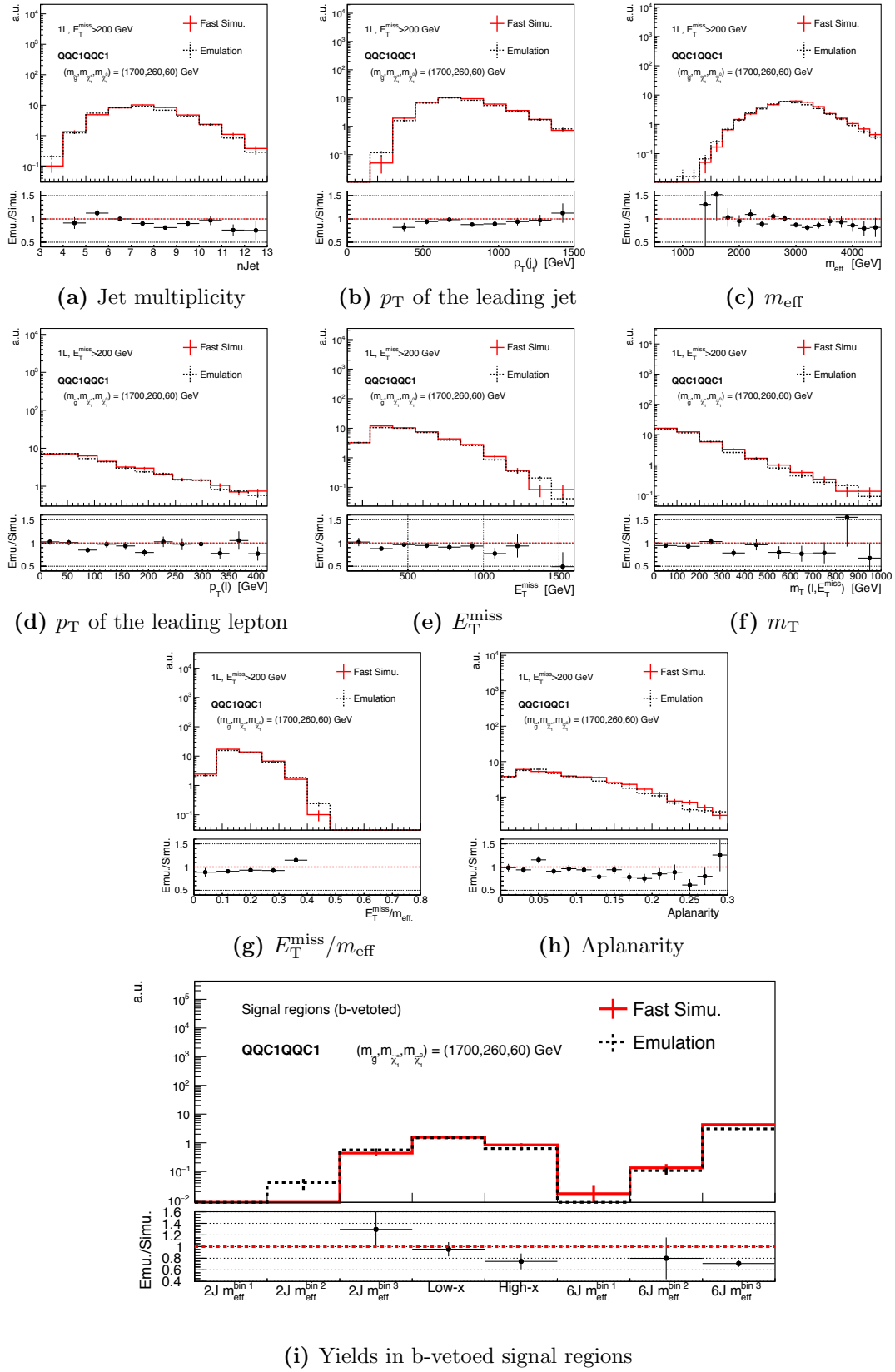


Figure A.2.3: QQC1QQC1, $(m_{\tilde{g}}, m_{\tilde{\chi}_1^\pm}, m_{\tilde{\chi}_2^0}) = (1700, 260, 60)$ GeV

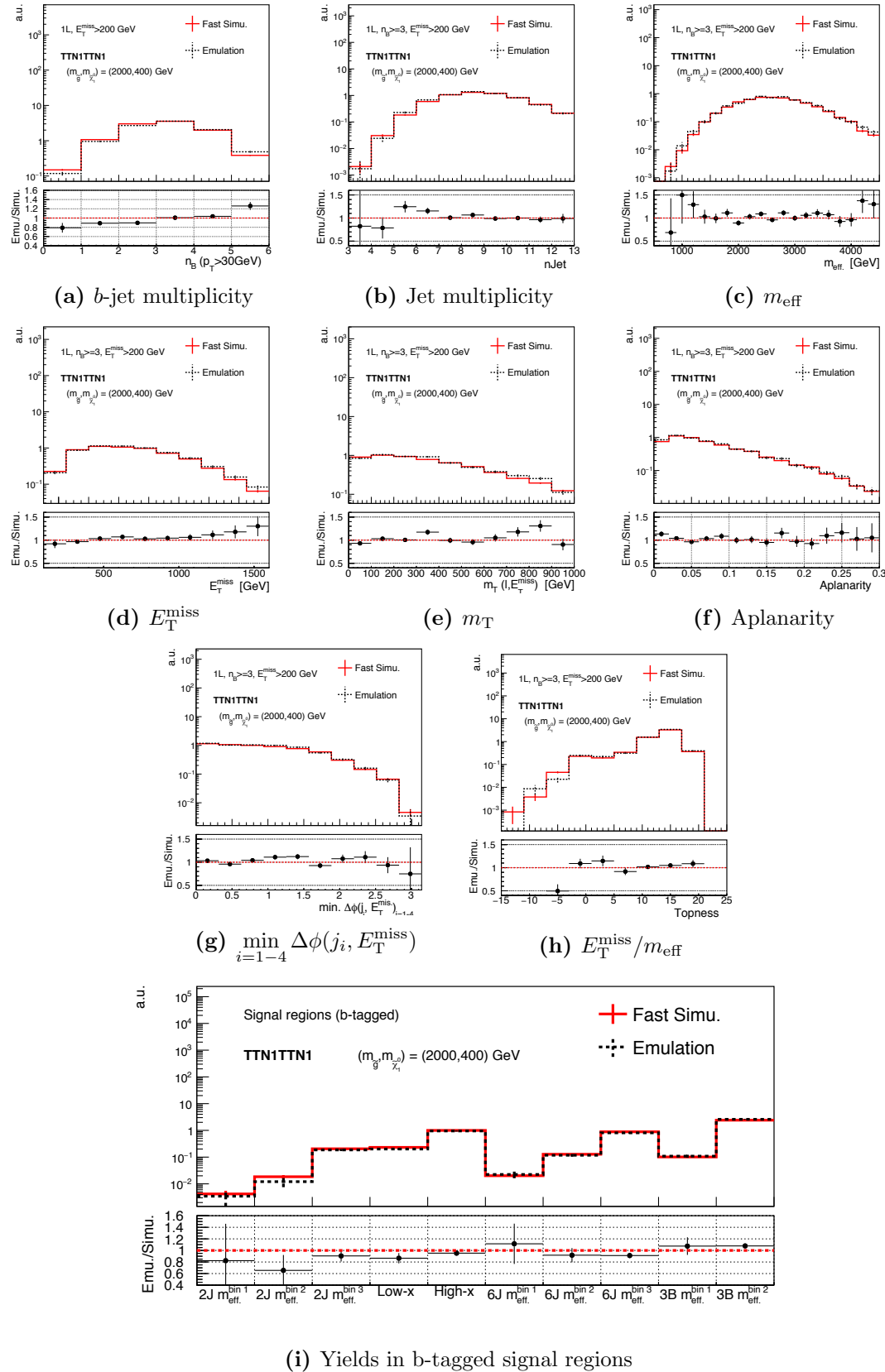


Figure A.2.4: TTN1TTN1, $(m_{\tilde{g}}, m_{\tilde{\chi}_2^0}) = (2000, 400)$ GeV

B Auxiliary Materials for Event Selection

B.1 Kinematics vs SUSY Masses

The trend of the kinematical variables over the mass grids are shown in Figure B.1.1-B.1.4. The color scale (z-axis) indicates the mean of the distribution of the variable that the signal events in the mass point result in. The examples of three **QQC1QQC1** grids (**x=1/2**, **LSP60**, **DM30**) and one **TTN1TTN1** grid are shown. While the variables related to transverse momenta of outgoing particles such as m_{eff} , $p_T(\ell)$ and E_T^{miss} simply scale with the mass splitting, the other variables (e.g. aplanarity, $E_T^{\text{miss}}/m_{\text{eff}}$ etc.) typically vary depending on the relative mass splitting, the cuts in which are therefore helpful for segmenting the signal region towers. These are used in deciding the initial cuts for the signal regions optimization.

QQC1QQC1 (x=1/2 grid)

The initial selection for tower **2J** and **6J** are decided based on the profile below. Lepton p_T and $E_T^{\text{miss}}/m_{\text{eff}}$ are found to be helpful for **2J** targeting the diagonal region, while requiring hard kinematics as well as high aplanarity is useful for scenarios with high-mass gluino which **6J** is targeting.

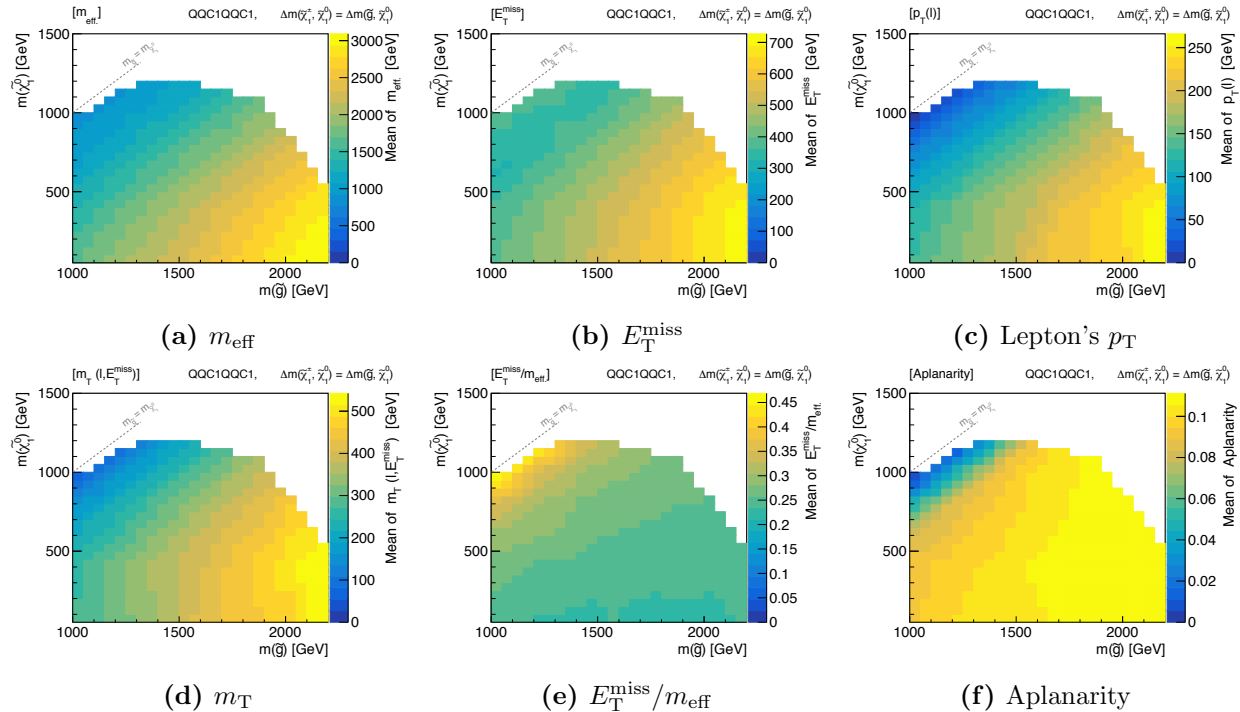


Figure B.1.1: Mean value of kinematical variables after the 1-lepton pre-selection (Table 6.3) as function of $m_{\tilde{g}}$ and $m_{\tilde{\chi}_1^\pm}$ for the reference model **QQC1QQC1** in the **x=1/2** grid.

QQC1QQC1 (LSP60 grid)

The initial selection for tower **High-x** is designed based on the profile below. Note that the low- x region of this grid is not dedicatedly targeted by the analysis since the assumption of nearly massless LSP is supposed to be obsolete, and instead the **Low-x** tower targets the DM-oriented grids in which LSP is generally massive. High leptonic activity including m_T and relatively low jet activity is favored for the mass region that is targeted by **High-x**. Moderated aplanarity cut (~ 0.02) is also found helpful.

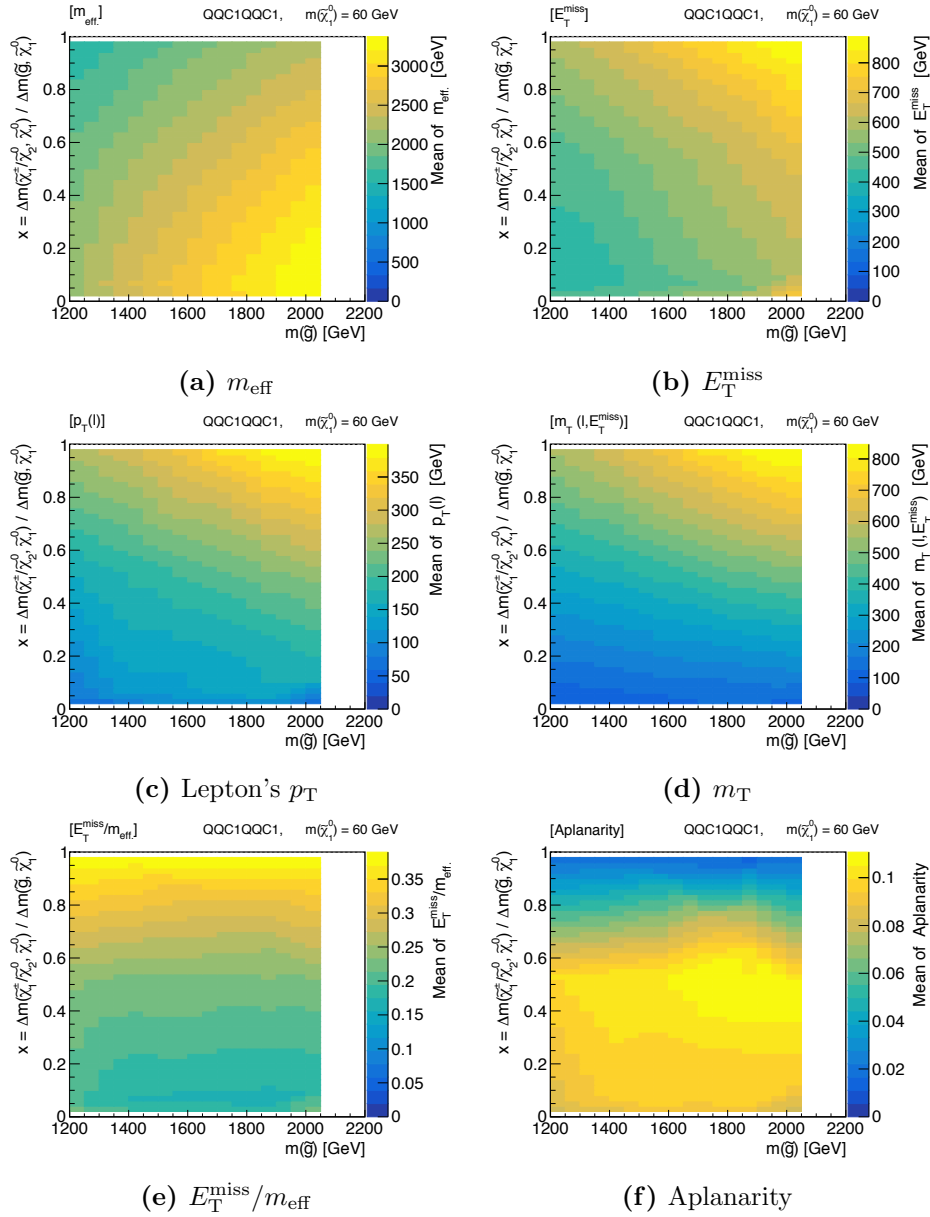


Figure B.1.2: Mean value of kinematical variables after the 1-lepton pre-selection (Table 6.3) as function of $m_{\tilde{g}}$ and x ($:= \Delta m(\tilde{\chi}_1^\pm, \tilde{\chi}_1^0) / \Delta m(\tilde{g}, \tilde{\chi}_1^0)$) for the reference model **QQC1QQC1** in the **LSP60** grid.

QQC1QQC1 (DM30 grid)

The initial selection for tower **Low-x** is designed based on the profile below. Note that only scenarios with massive LSP and with non-degenerated gluino and LSP are dedicatedly followed. A combination of soft lepton and high jet activity is generally favored.

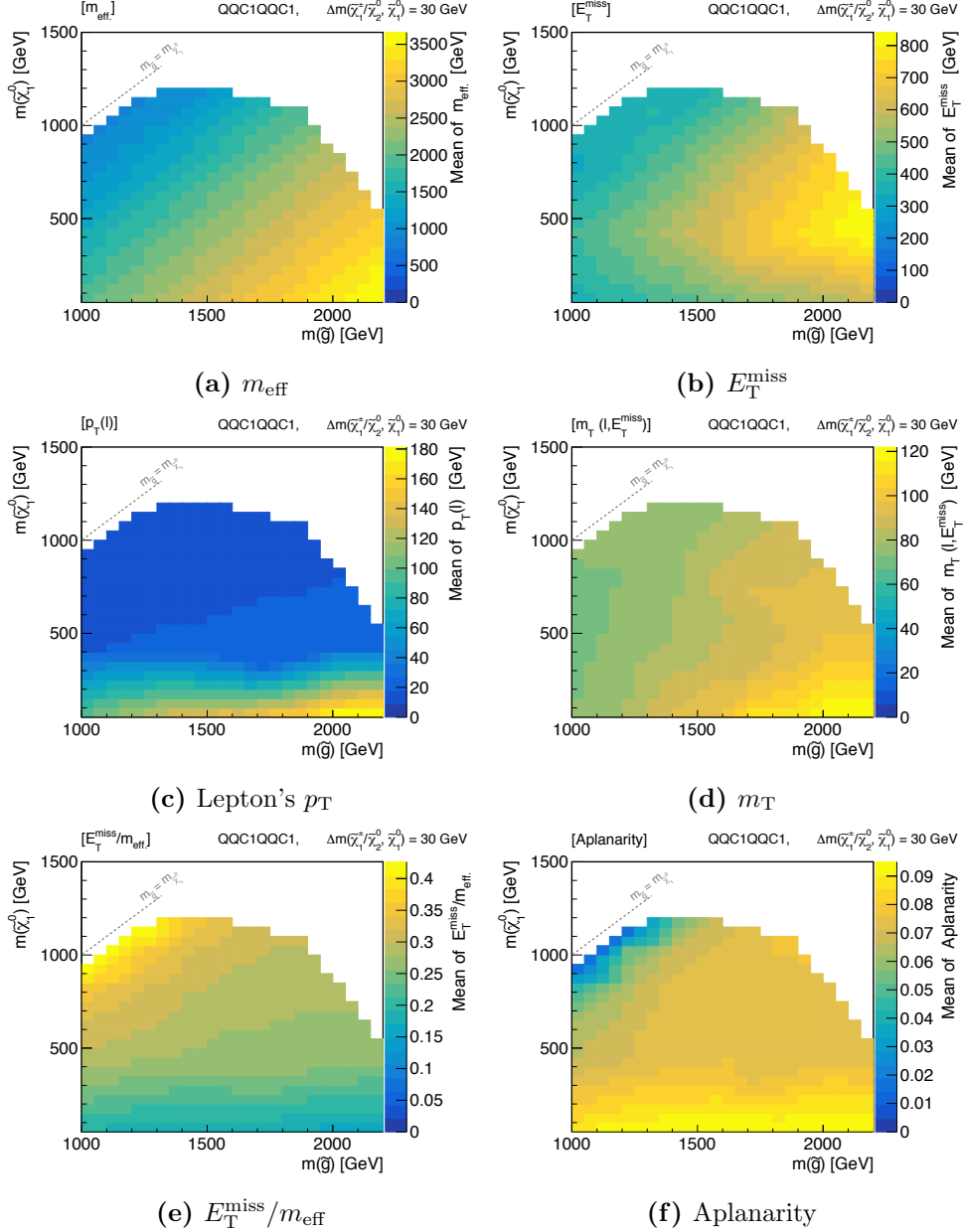


Figure B.1.3: Mean value of kinematical variables after the 1-lepton pre-selection (Table 6.3) as function of $m_{\tilde{g}}$ and $m_{\tilde{\chi}_1^0}$ for the reference model **QQC1QQC1** in the **DM30** grid.

TTN1TTN1

The initial selection for tower **3B** is decided based on the profile below. Note that the diagonal region where the off-shell tops result in soft b -jets that are not tagged in the analysis is not covered by **3B** but by **2J**. While almost all variables display nice separation power for scenarios with large mass splitting, aplanarity, $\min_{i=1-4} \Delta\phi(j_i, E_T^{\text{miss}})$ and topness are found to be the key variables for moderated mass splitting cases.

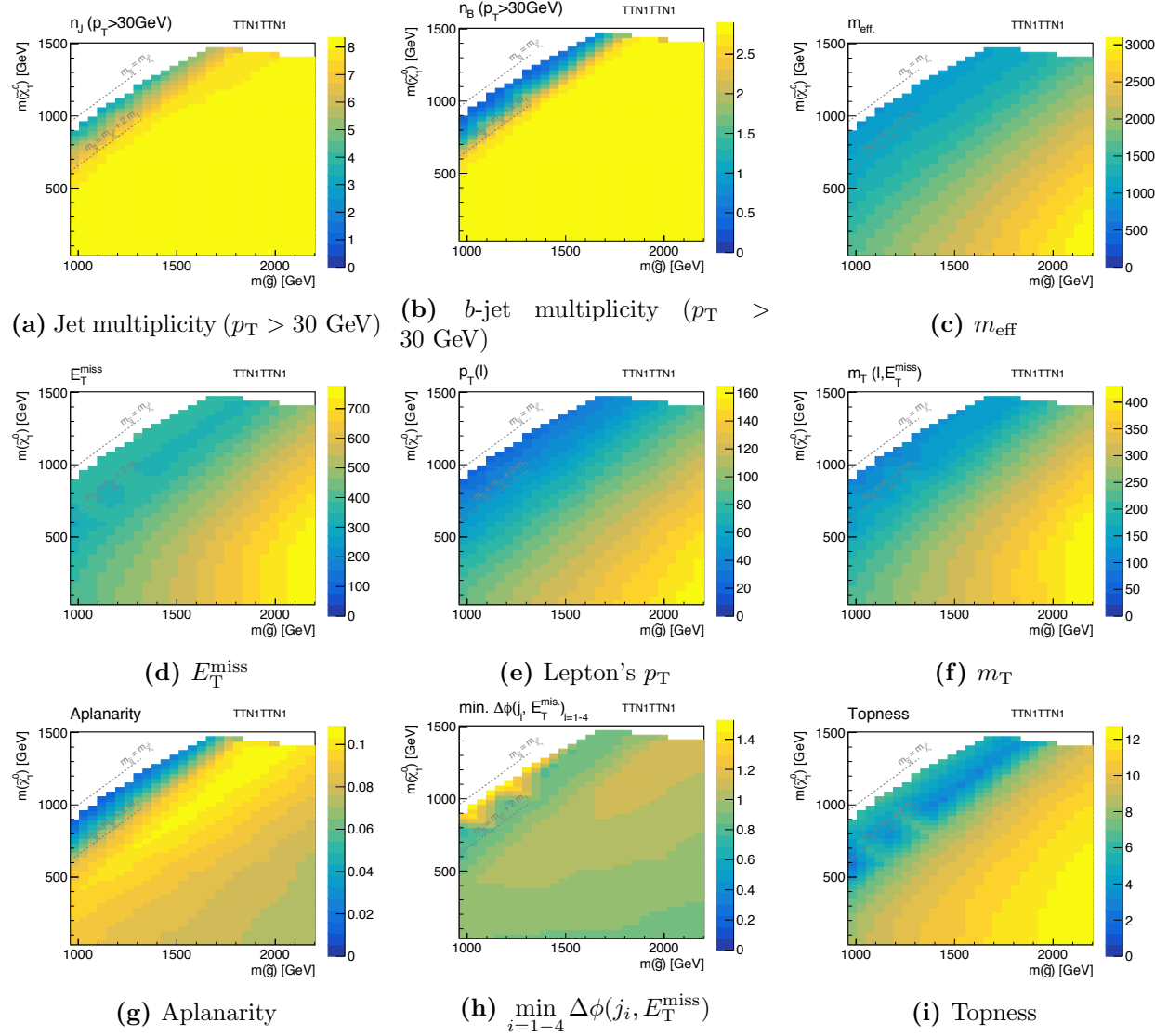


Figure B.1.4: Mean value of kinematical variables after the 1-lepton pre-selection (Table 6.3) as function of $m_{\tilde{g}}$ and $m_{\tilde{\chi}_1^0}$ for the reference model **TTN1TTN1**.

B.2 N-1 Plots for the Optimized Signal Regions

Figure B.2.1-B.2.9 are the “N-1” plots, the kinematical distributions in regions where one of the cuts is removed from the optimized signal region. The sensitivity is calculated as function of the position of the removed cut. The decided cut positions are indicated by the red arrows, which more or less accord with the optimum position for all the reference signals.

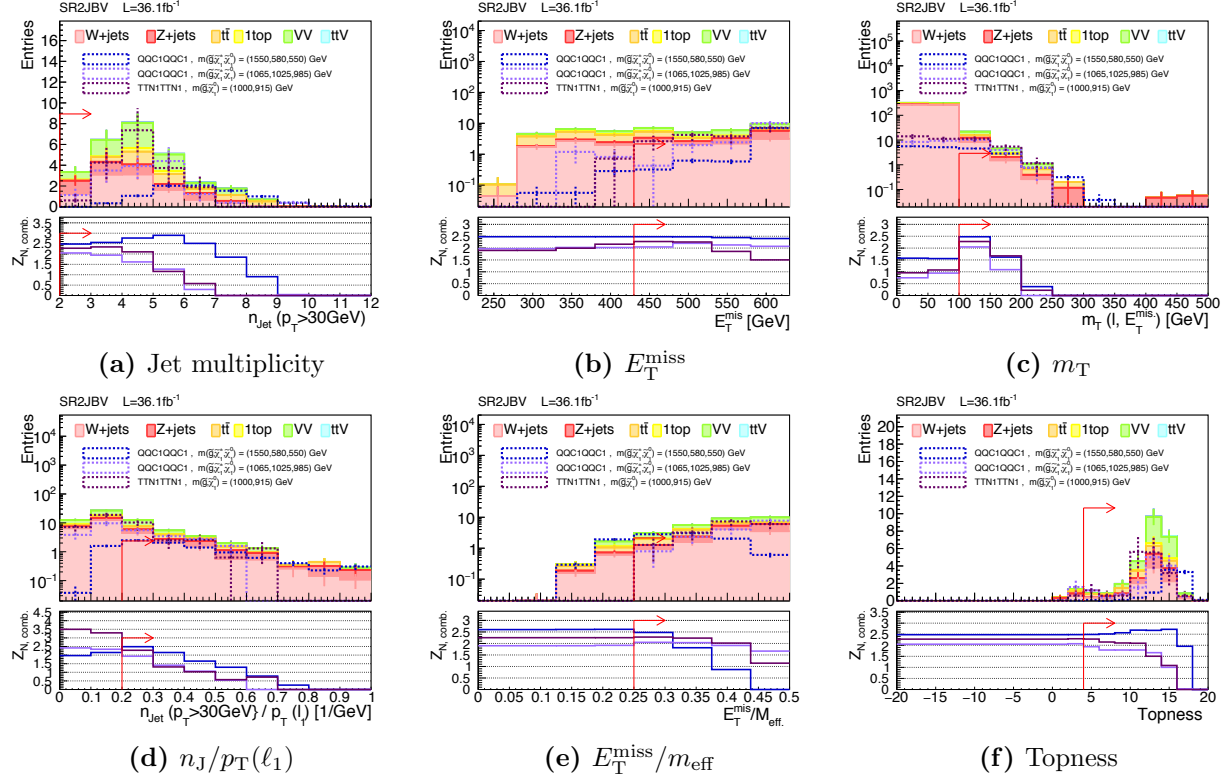


Figure B.2.1: N-1 plots for the b-vetoed (BV) slices of the optimized **2J** signal regions. Bottom row presents the combined significance over the m_{eff} -bins defined in Eq. (6.4). The position of SR cut is indicated by the red arrow.

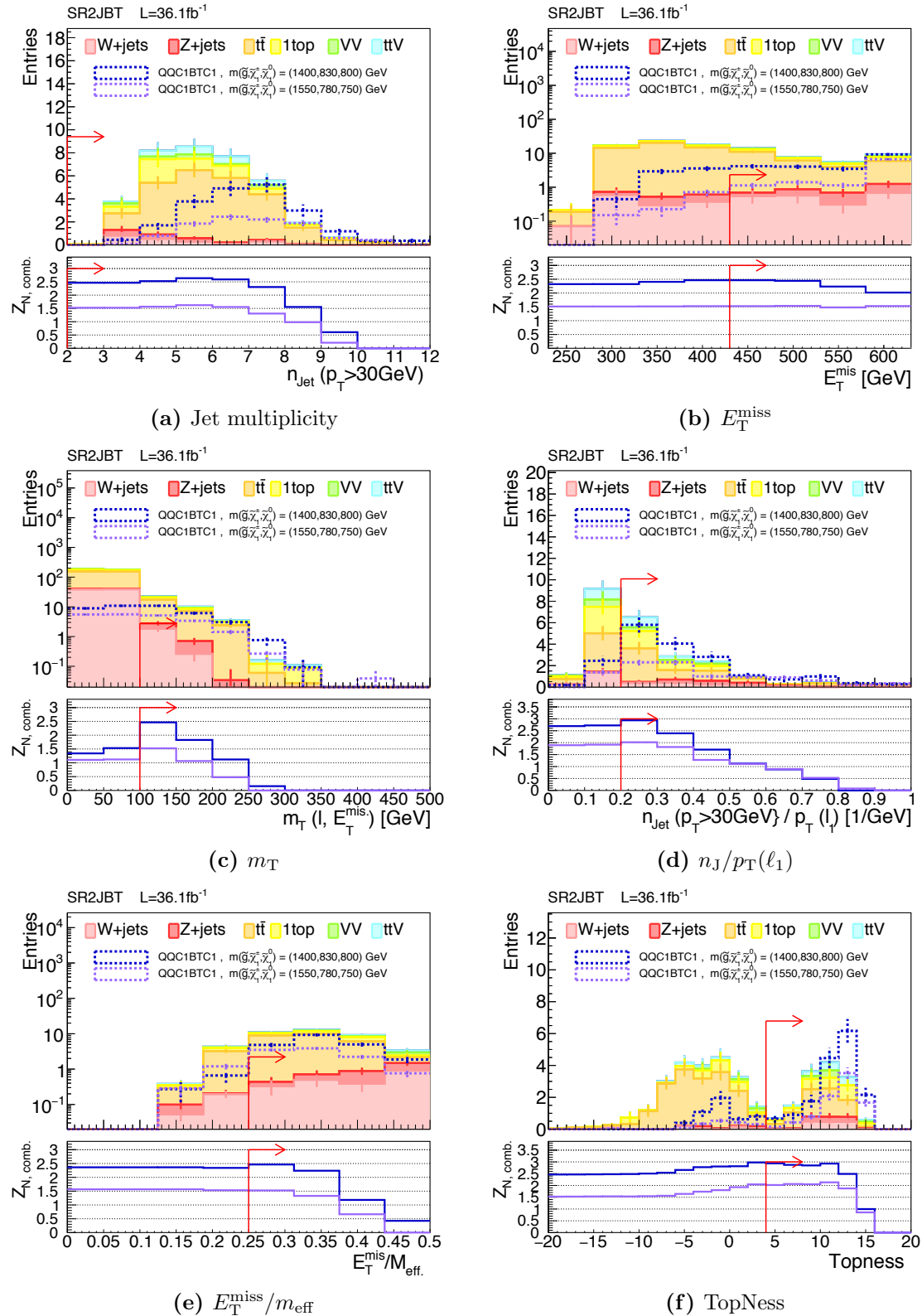


Figure B.2.2: N-1 plots for the b-tagged (BT) slices of the optimized **2J** signal regions. Bottom row presents the combined significance over the m_{eff} -bins defined in Eq. (6.4). The position of SR cut is indicated by the red arrow.

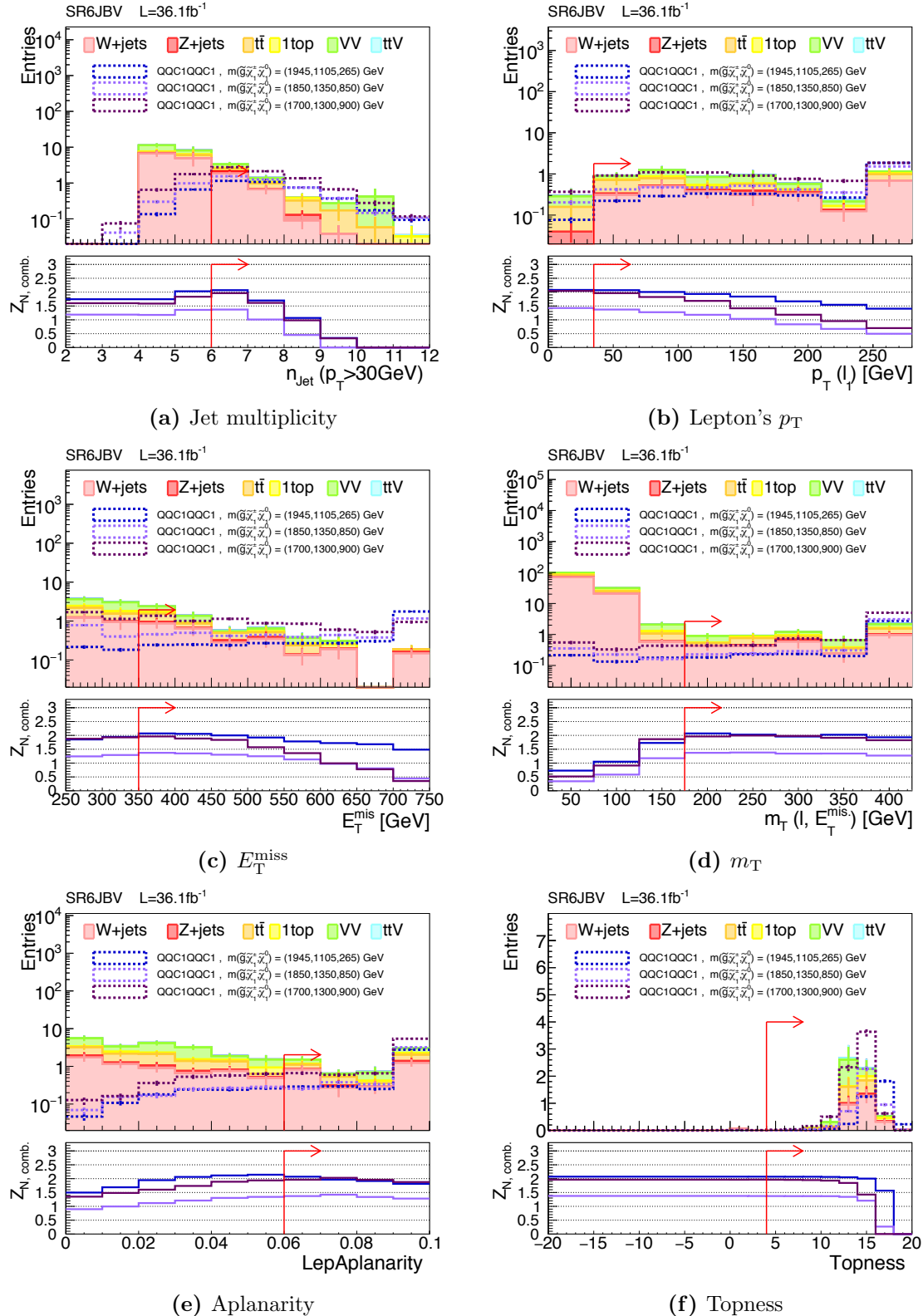


Figure B.2.3: N-1 plots for the b-vetoed (BV) slices of the optimized **6J** signal regions. Bottom row presents the combined significance over the m_{eff} -bins defined in Eq. (6.4). The position of SR cut is indicated by the red arrow.

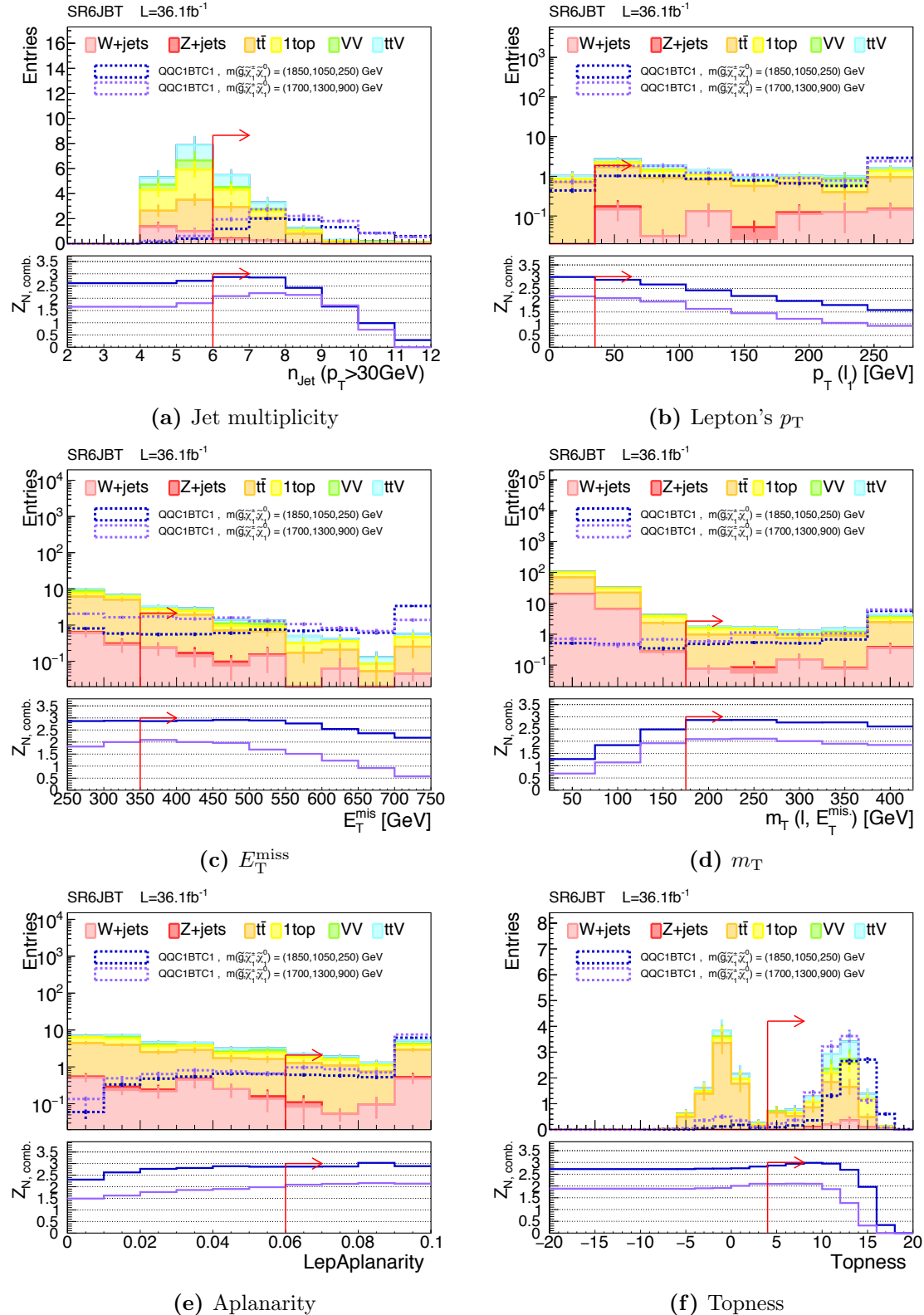


Figure B.2.4: N-1 plots for the b-tagged (BT) slices of the optimized **6J** signal regions. Bottom row presents the combined significance over the m_{eff} -bins defined in Eq. (6.4). The position of SR cut is indicated by the red arrow.

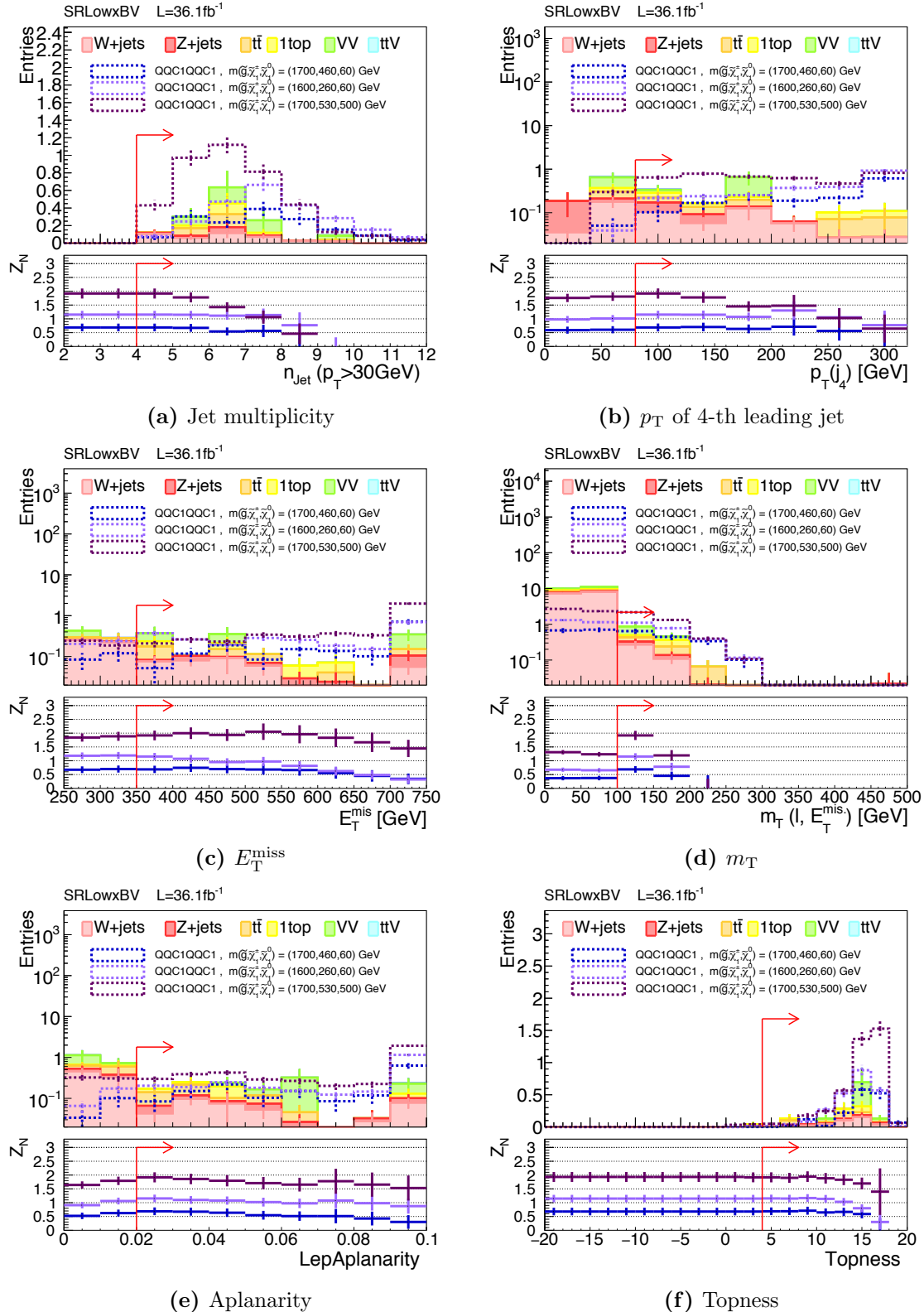


Figure B.2.5: N-1 plots for the b-vetoed (BV) slices of the optimized **Low-x** signal region. Bottom row presents the significace defined in Eq. (6.6). The position of SR cut is indicated by the red arrow.

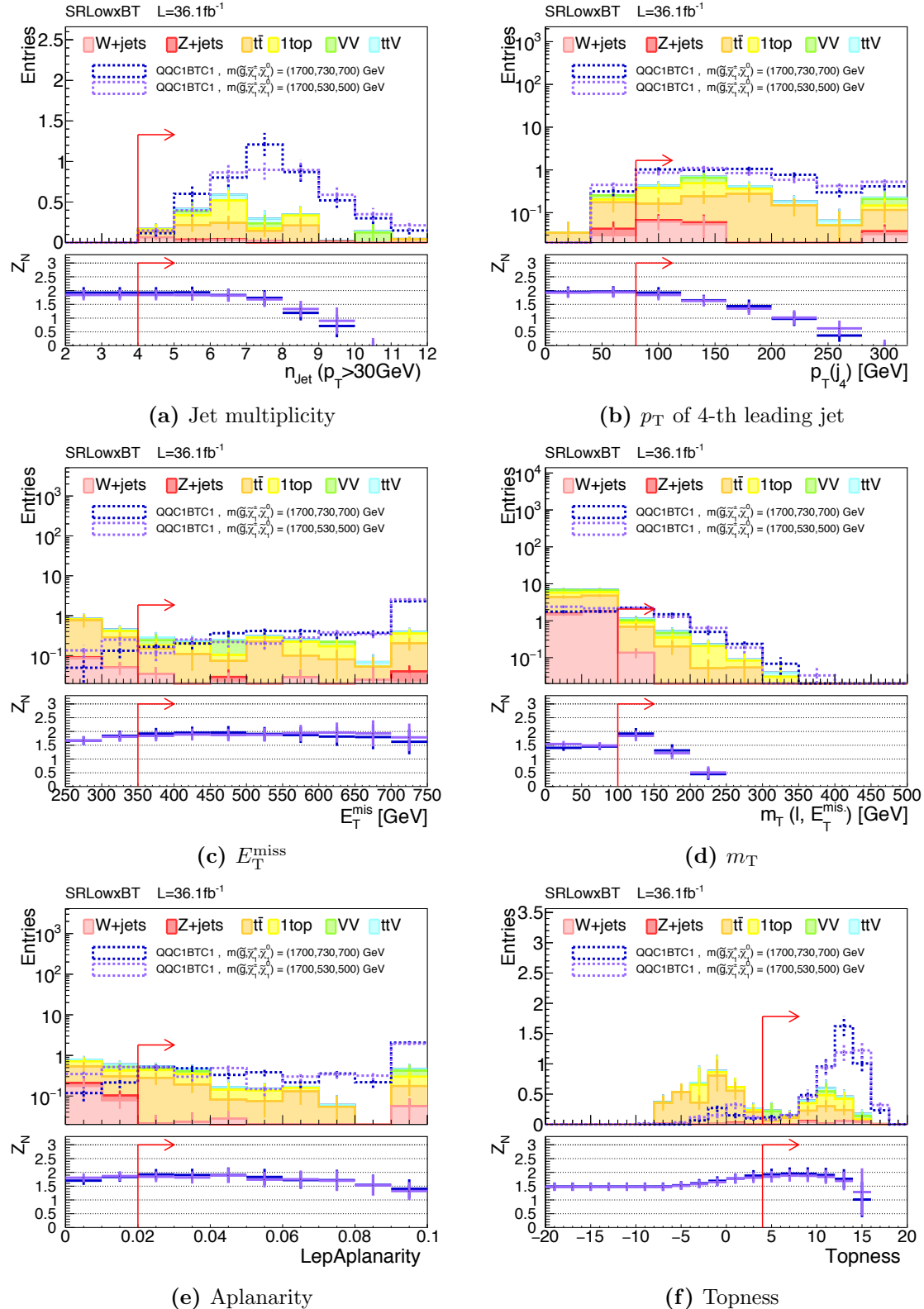


Figure B.2.6: N-1 plots for the b-tagged (BT) slices of the optimized **Low-x** signal region. Bottom row presents the significace defined in Eq. (6.6). The position of SR cut is indicated by the red arrow.

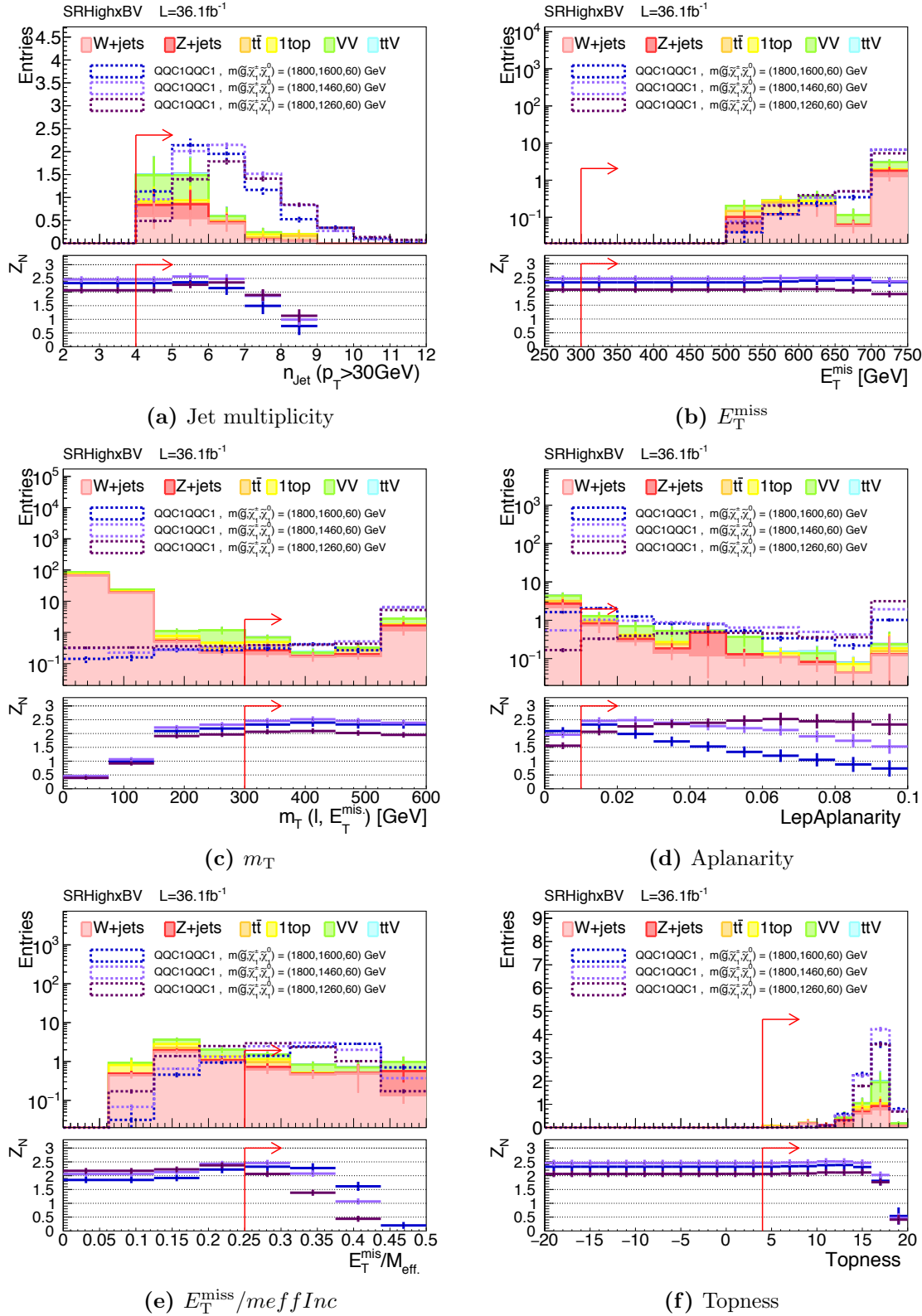


Figure B.2.7: N-1 plots for the b-vetoed (BV) slices of the optimized **High-x** signal region. Bottom row presents the significace defined in Eq. (6.6). The position of SR cut is indicated by the red arrow.

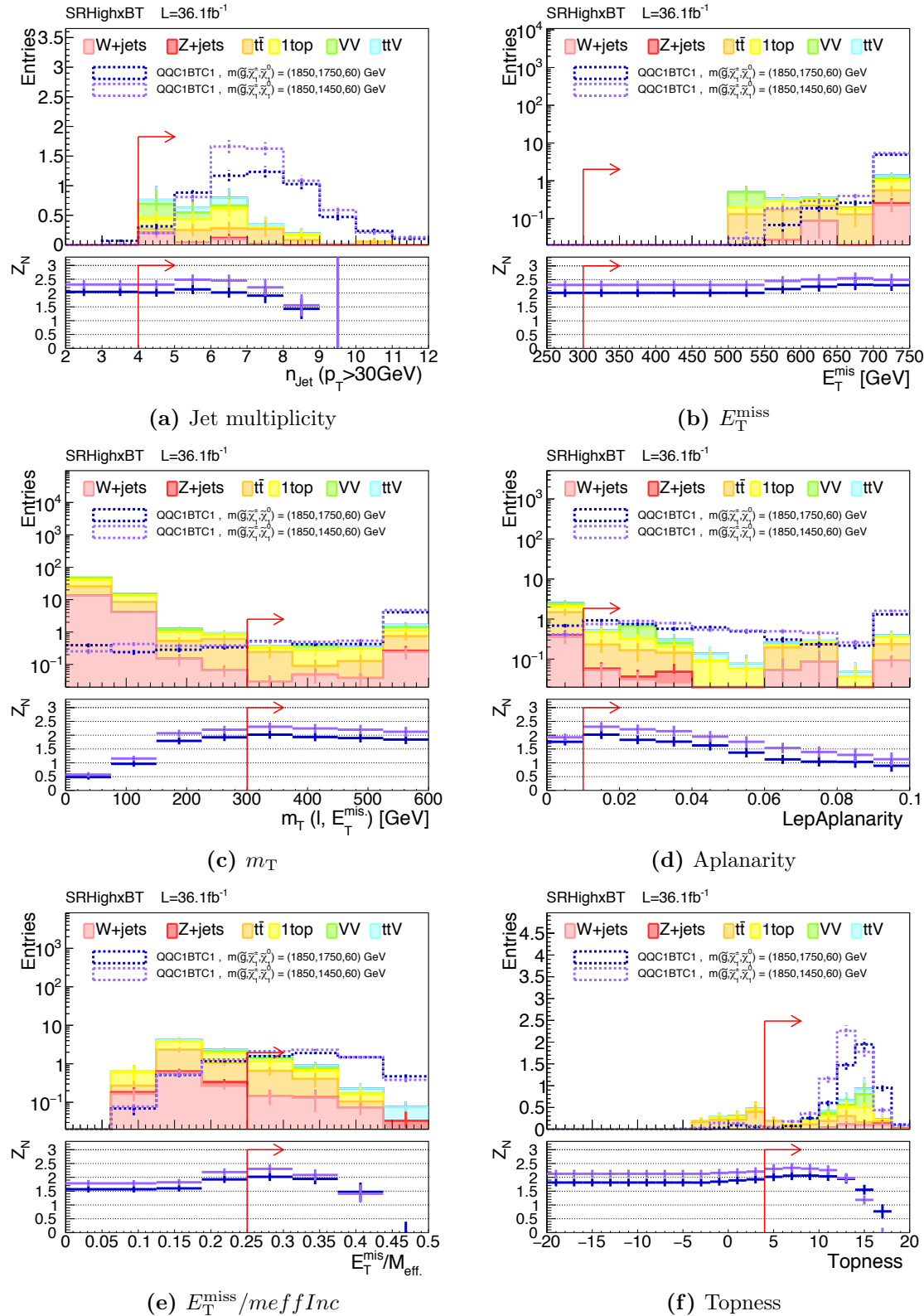


Figure B.2.8: N-1 plots for the b-tagged (BT) slices of the optimized **High-x** signal region. Bottom row presents the significace defined in Eq. (6.6). The position of SR cut is indicated by the red arrow.

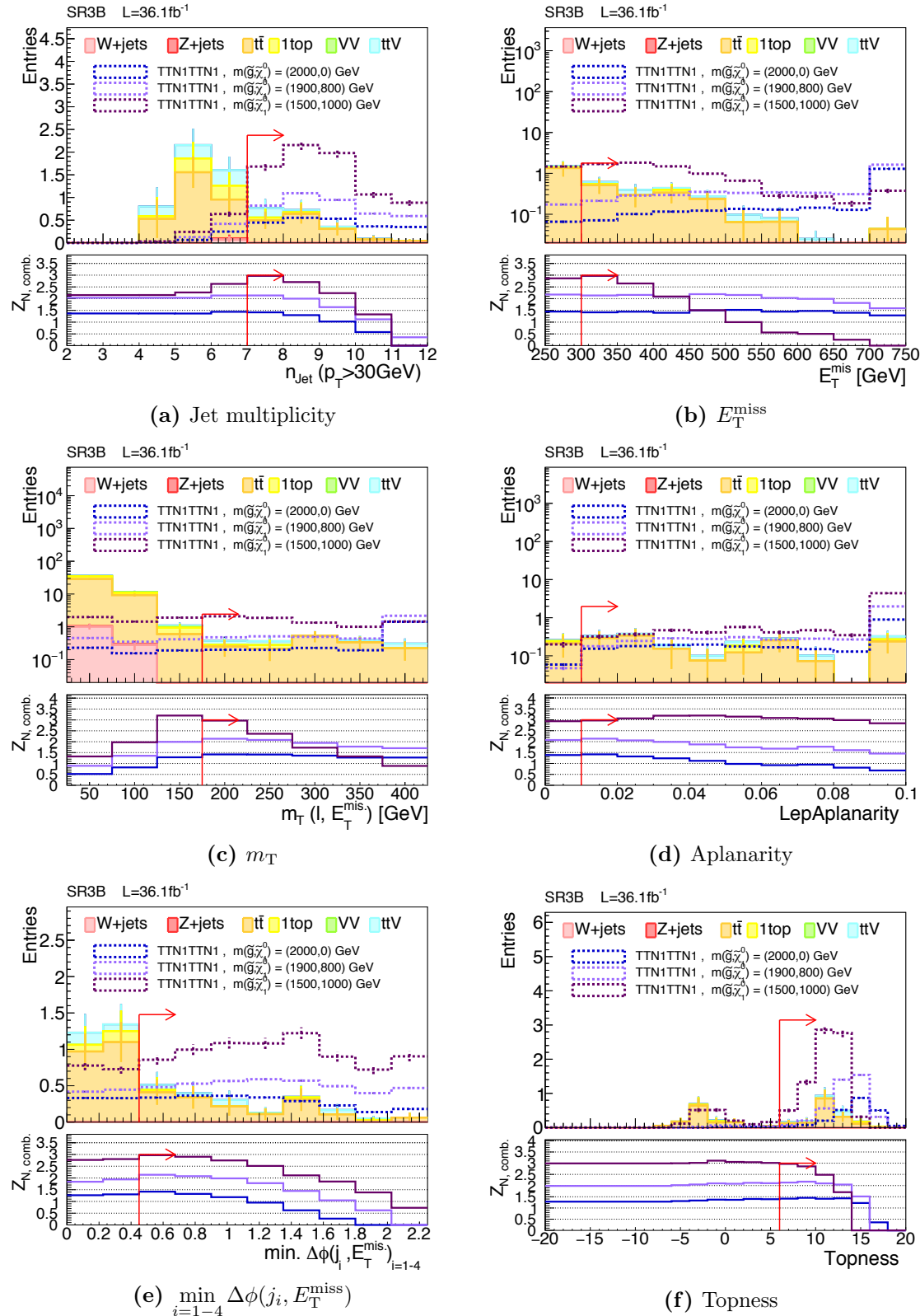


Figure B.2.9: N-1 plots for the optimized 3B signal regions. Bottom row presents the combined significance over the m_{eff} -bins defined in Eq. (6.4). The position of SR cut is indicated by the red arrow.

C Auxiliary Materials for Background Estimation

C.1 Data vs Reweighted MC in the Pre-selection Regions

Following plots (Figure C.1.1-C.1.8) present the data/MC comparison in the pre-selection regions that are shown in Sec. 7.2.1, with the MC events of $W + \text{jets}$ and $t\bar{t}$ are reweighted event-by-event by:

$$\begin{cases} y = 1 - 0.1 \times (n_J - 2) & (W + \text{jets}) \\ y = 1.05 \times [1 - 0.061 \times p_T(t\bar{t})] & (t\bar{t}, @1L, 2L \text{ pre-selection regions}) \\ y = 1.4 \times [1 - 0.061 \times p_T(t\bar{t})] & (t\bar{t}, @3B \text{ pre-selection regions}). \end{cases} \quad (\text{C.1.1})$$

The MC mis-modeling discussed in Sec. 7.2.1, primarily in terms of jet activity (jet p_T or m_{eff}), is shown to be largely recovered by the reweighting, supporting the conjecture that the mis-modeling is mainly around the ISR/FSR radiation. The linear coefficients in Eq. (C.1.1) are chosen so that the mis-modeling is maximally cured. Note that these optimal coefficients vary depending on the selection, which is the main reason why this reweighting is not seriously employed as the correction in the estimation. Instead, the reweighting is used in the envelope calculation of the extrapolation uncertainty due to the MC mis-modeling (Sec. 8.3.1).

1LBV pre-selection region

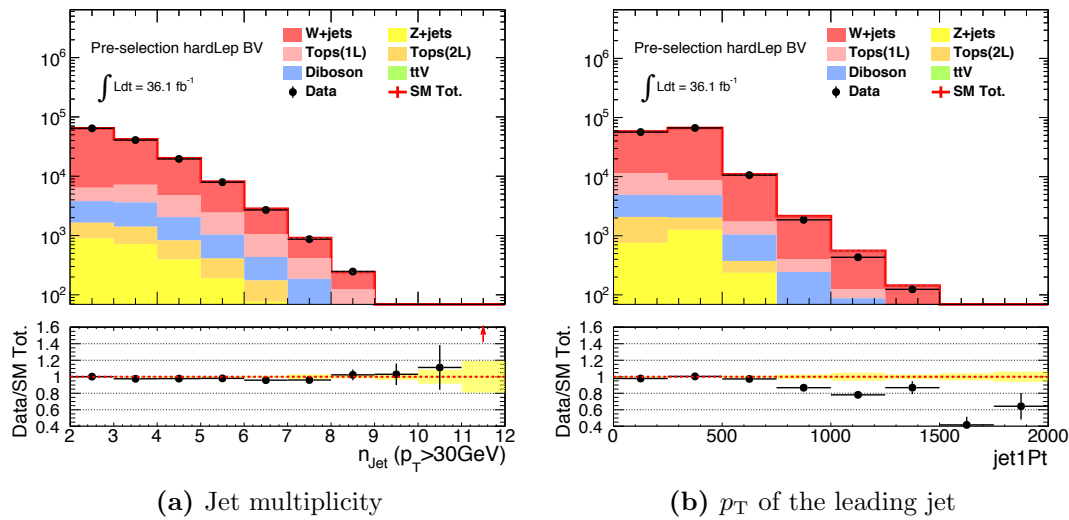


Figure C.1.1: Kinematical distribution of data (black dots) and MC (colored stack) in the **1LBV** pre-selection region, with the reweighting $w = 1 - 0.1 \times (n_J - 2)$ being applied for $W + \text{jets}$ MC.

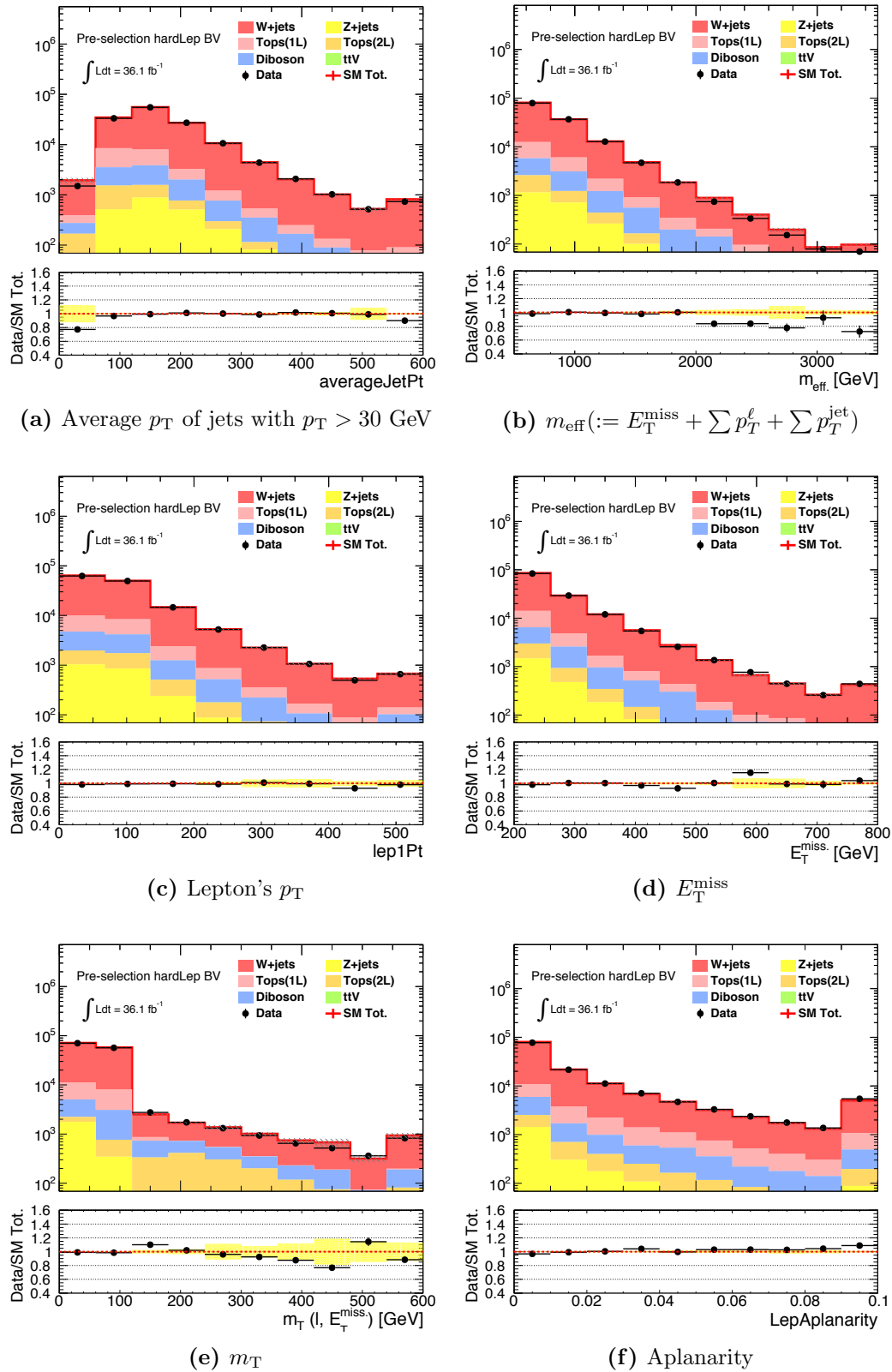


Figure C.1.2: Kinematical distribution of data (black dots) and MC (colored stack) in the **1LBV** pre-selection region, with the reweighting $w = 1 - 0.1 \times (n_J - 2)$ being applied for $W + \text{jets}$ MC.

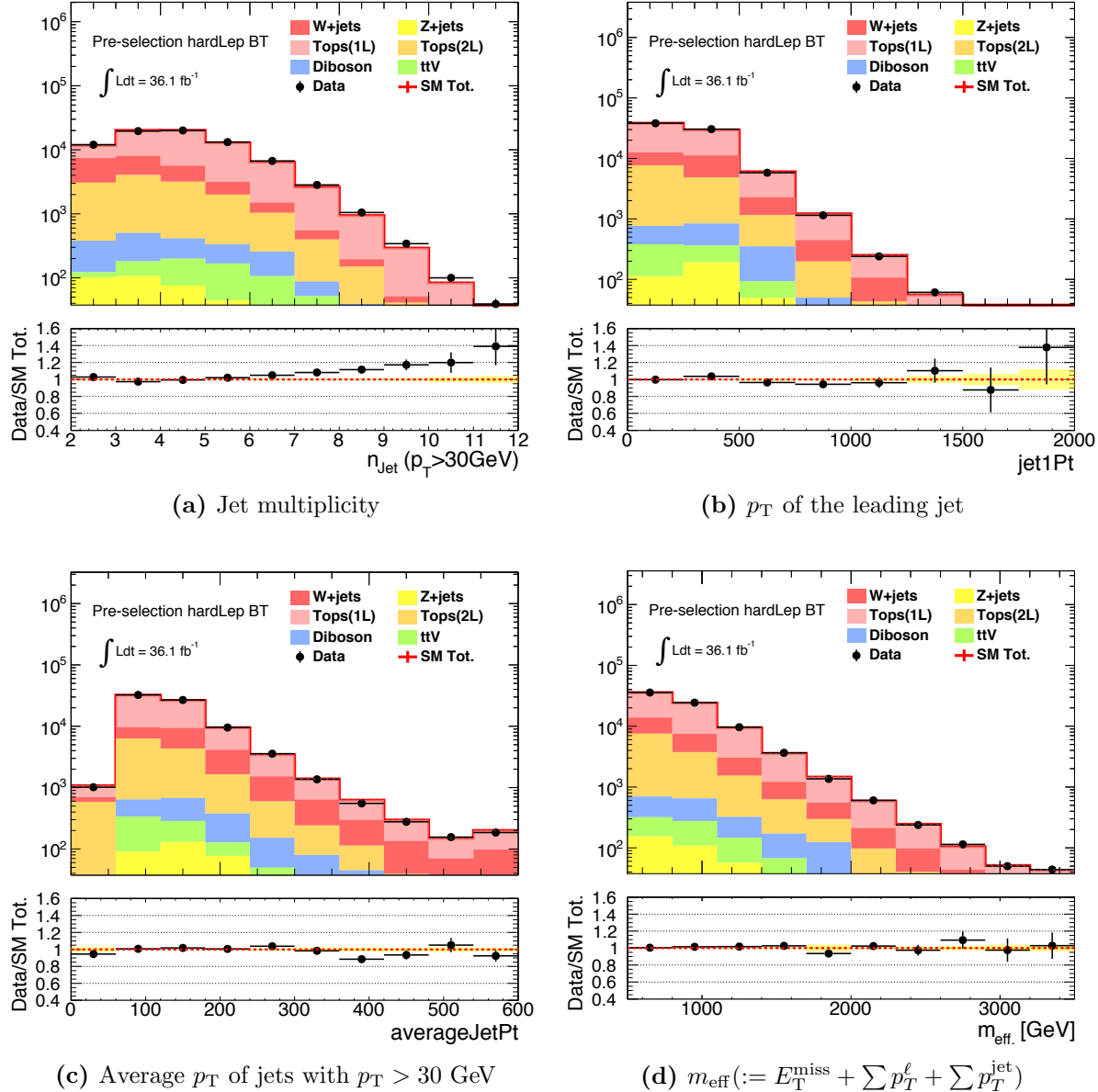
1LBT pre-selection region

Figure C.1.3: Kinematical distribution of data (black dots) and MC (colored stack) in the **1LBT** pre-selection region, reweighting $w = 1.05 \times [1 - 0.061 \times p_T(t\bar{t})]$ being applied for $t\bar{t}$ MC.

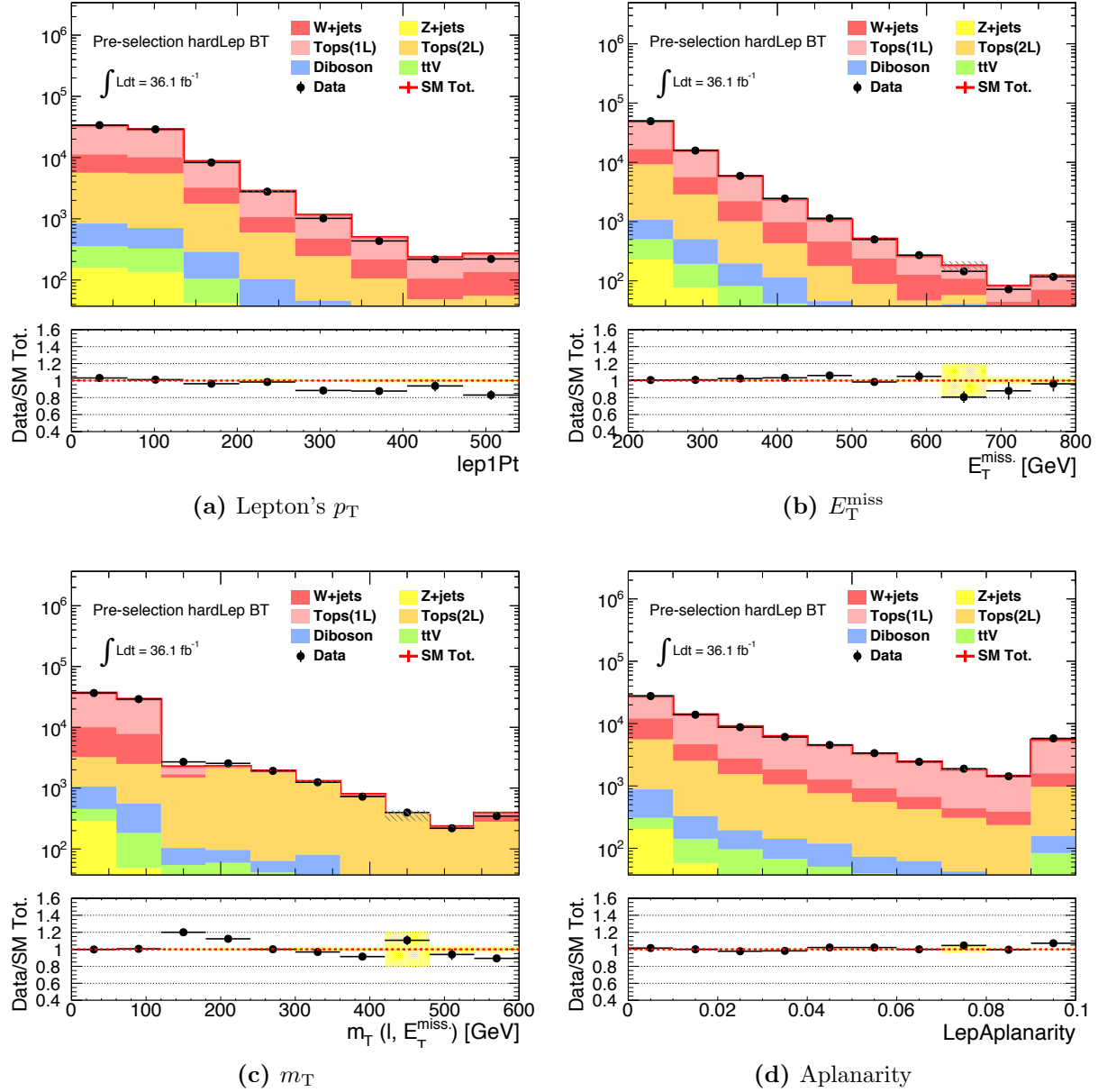


Figure C.1.4: Kinematical distribution of data (black dots) and MC (colored stack) in the **1LBT** pre-selection region, with the reweighting $w = 1.05 \times [1 - 0.061 \times p_T(t\bar{t})]$ being applied for $t\bar{t}$ MC.

2LBT pre-selection region

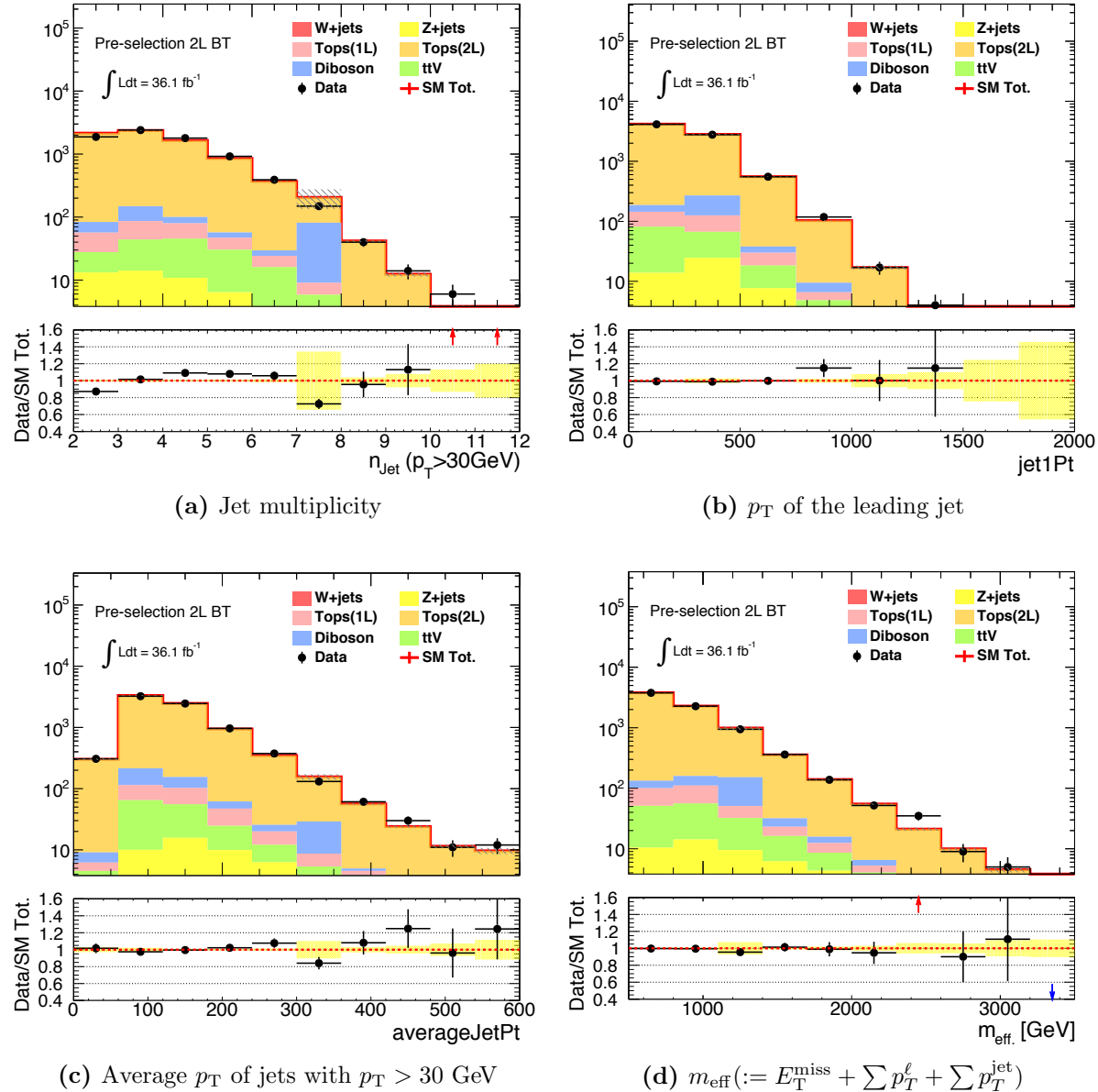


Figure C.1.5: Kinematical distribution of data (black dots) and MC (colored stack) in the **2LBT** pre-selection region, reweighting $w = 1.05 \times [1 - 0.061 \times p_T(t\bar{t})]$ being applied for $t\bar{t}$ MC.

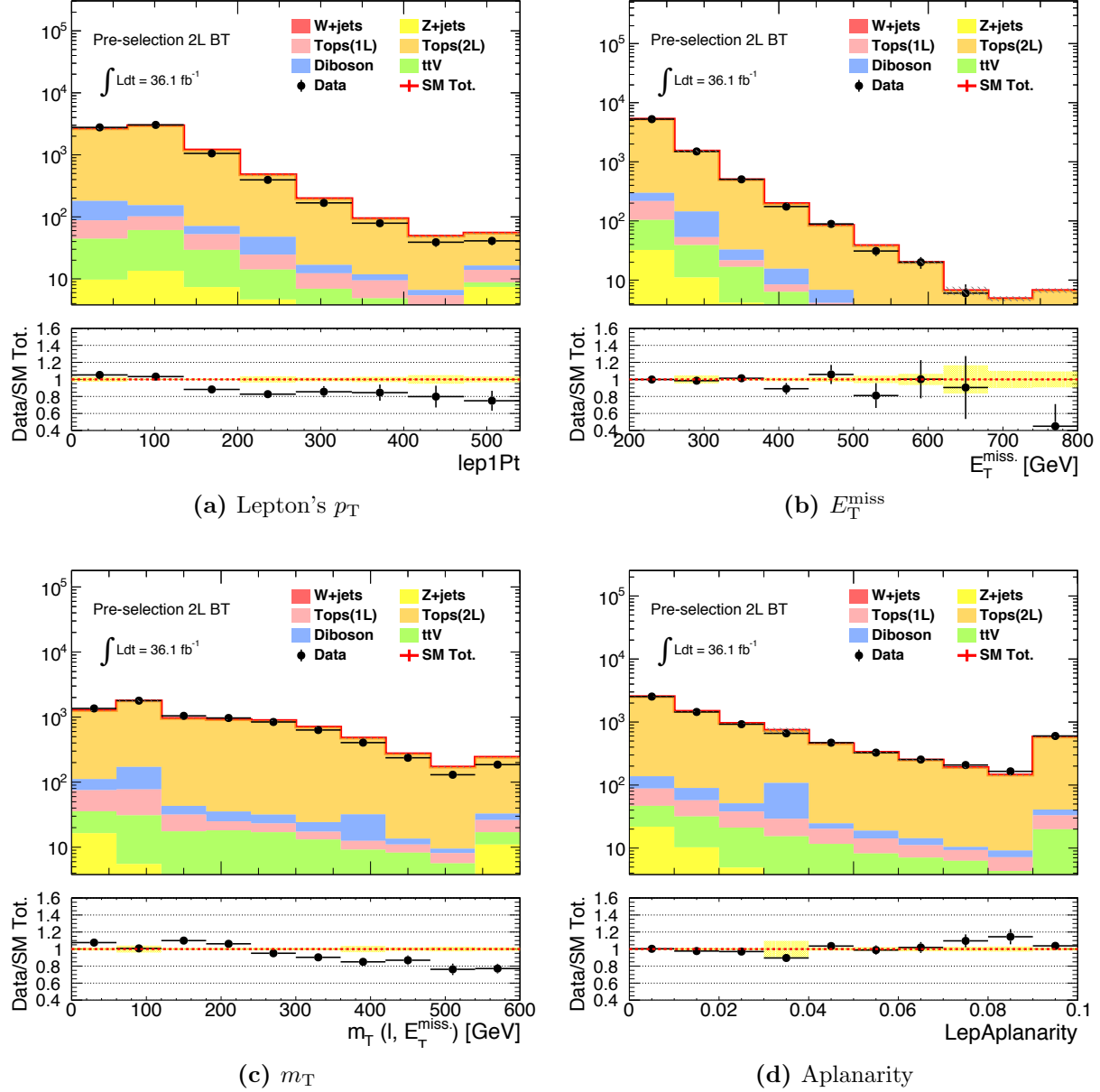


Figure C.1.6: Kinematical distribution of data (black dots) and MC (colored stack) in the **2LBT** pre-selection region, with the reweighting $w = 1.05 \times [1 - 0.061 \times p_T(t\bar{t})]$ being applied for $t\bar{t}$ MC.

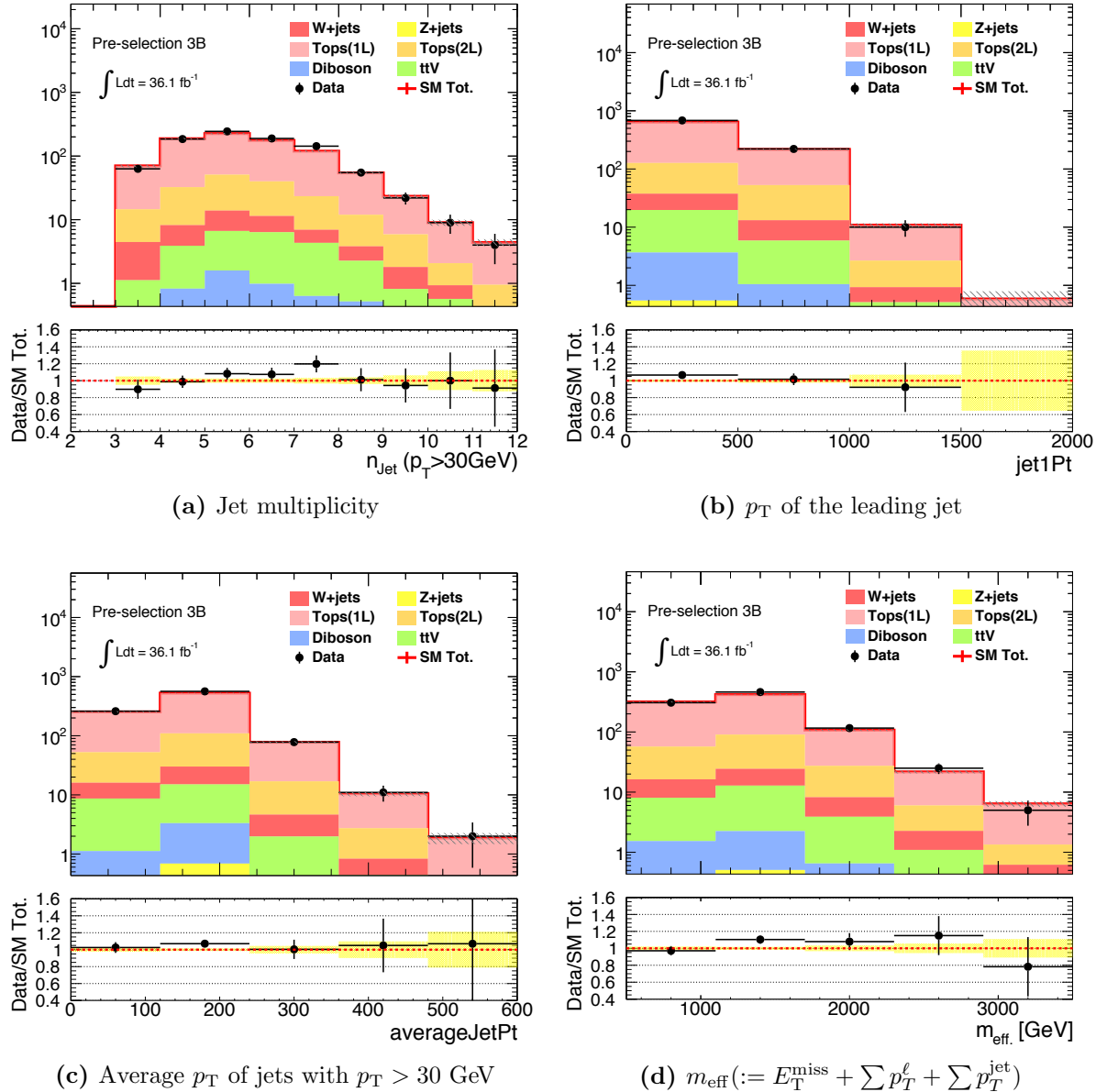
1L3B pre-selection region

Figure C.1.7: Kinematical distribution of data (black dots) and MC (colored stack) in the **1L3B** pre-selection region, with the reweighting $w = 1.4 \times [1 - 0.061 \times p_T(t\bar{t})]$ being applied for $t\bar{t}$ MC.

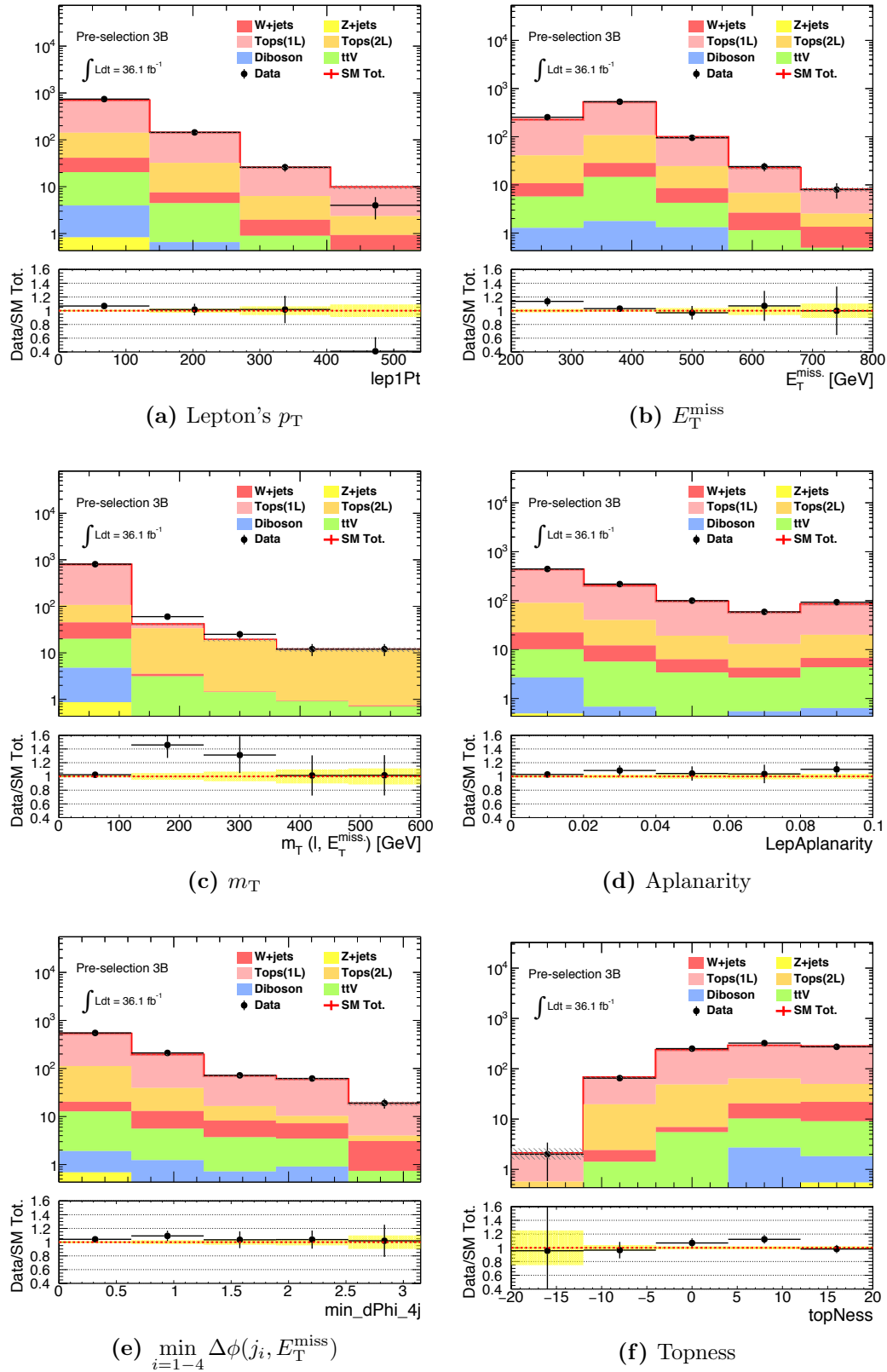


Figure C.1.8: Kinematical distribution of data (black dots) and MC (colored stack) in the **1L3B** pre-selection region, with the reweighting: $w = 1.4 \times [1 - 0.061 \times p_T(t\bar{t})]$ being applied for $t\bar{t}$ MC.

C.2 MC Closure Test for the Object Replacement Method Estimating the Soft-Lepton Regions

While the closure test estimating hard lepton regions are shown in Sec. 7.3.2, this section presents the case of soft-lepton regions. Figure C.2.1, C.2.2 and C.2.3 respectively illustrate the closure of missing-electron, missing-muon replacement, and the tau replacement in which the tag lepton is soft ($p_T \in [6, 35]$ GeV). The common 2LCR selection is used as the case in Sec. 7.3.2. Though it is sometimes a bit subtle due to the limited MC statistics, good agreement is seen in general.

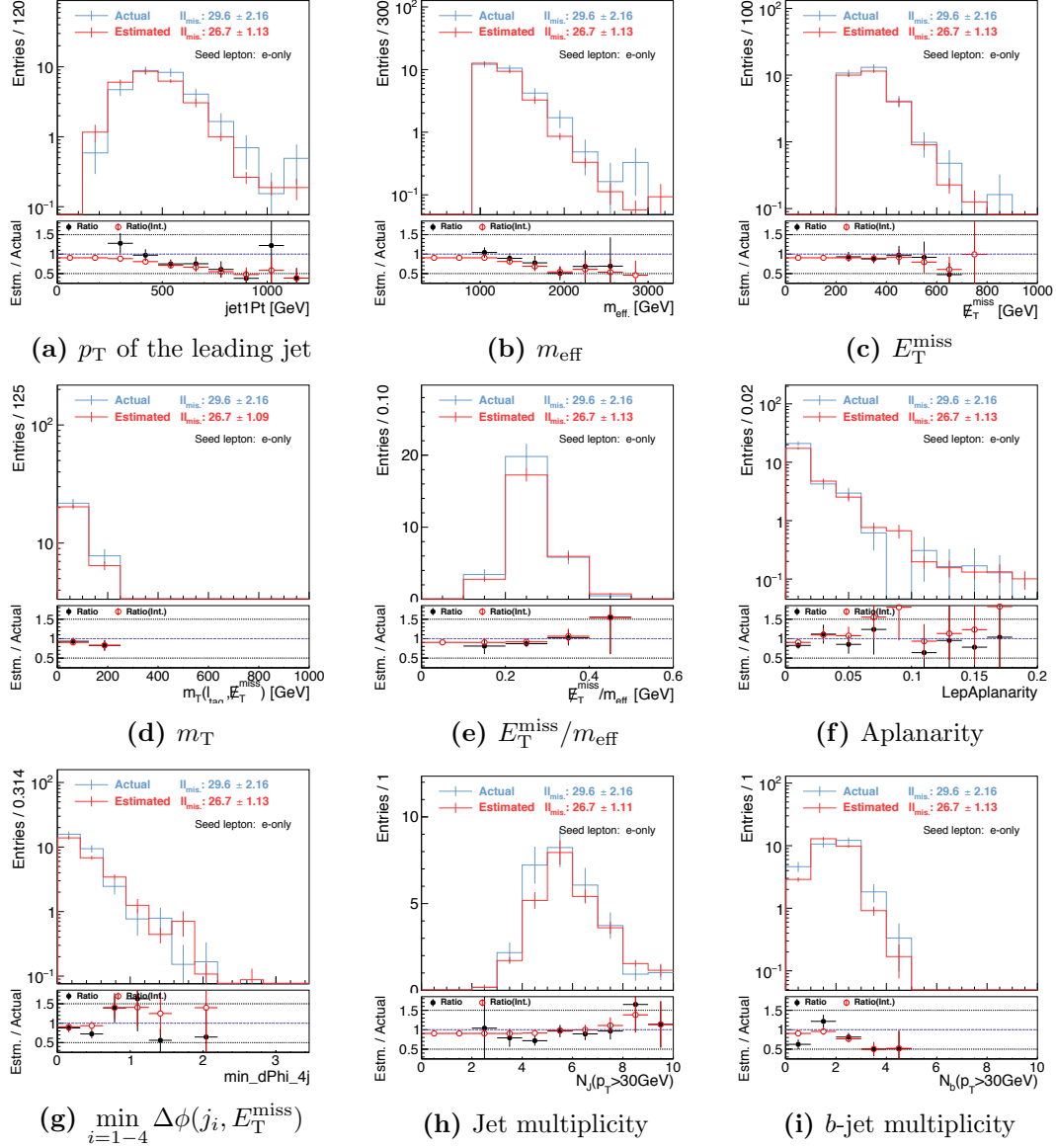


Figure C.2.1: MC closure test for **missing lepton replacement** using $t\bar{t}$ MC sample. Seed events are collected by the use of MET trigger. $p_T < 35$ GeV for the leading lepton is required. **Only electrons in the seed events are replaced.** Red points in the bottom plots show the ratio of integrated yields for the two histograms above the x-position that the point indicates.

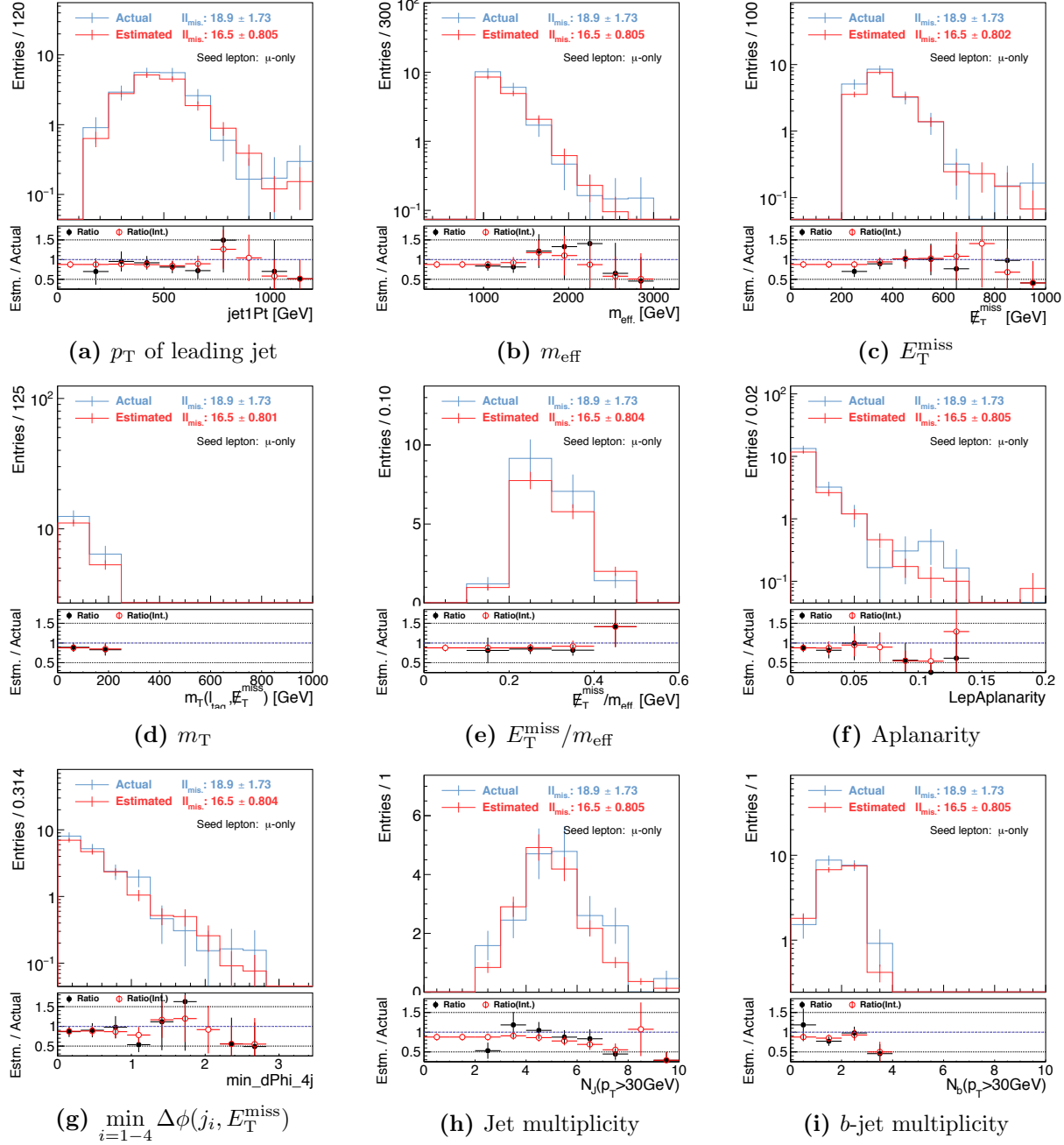


Figure C.2.2: MC closure test for **missing lepton replacement** using $t\bar{t}$ MC sample. Seed events are collected by the use of MET trigger. $p_T < 35$ GeV for the leading lepton is required. **Only muon in the seed events are replaced.** Red points in the bottom plots show the ratio of integrated yields for the two histograms above the x-position that the point indicates.

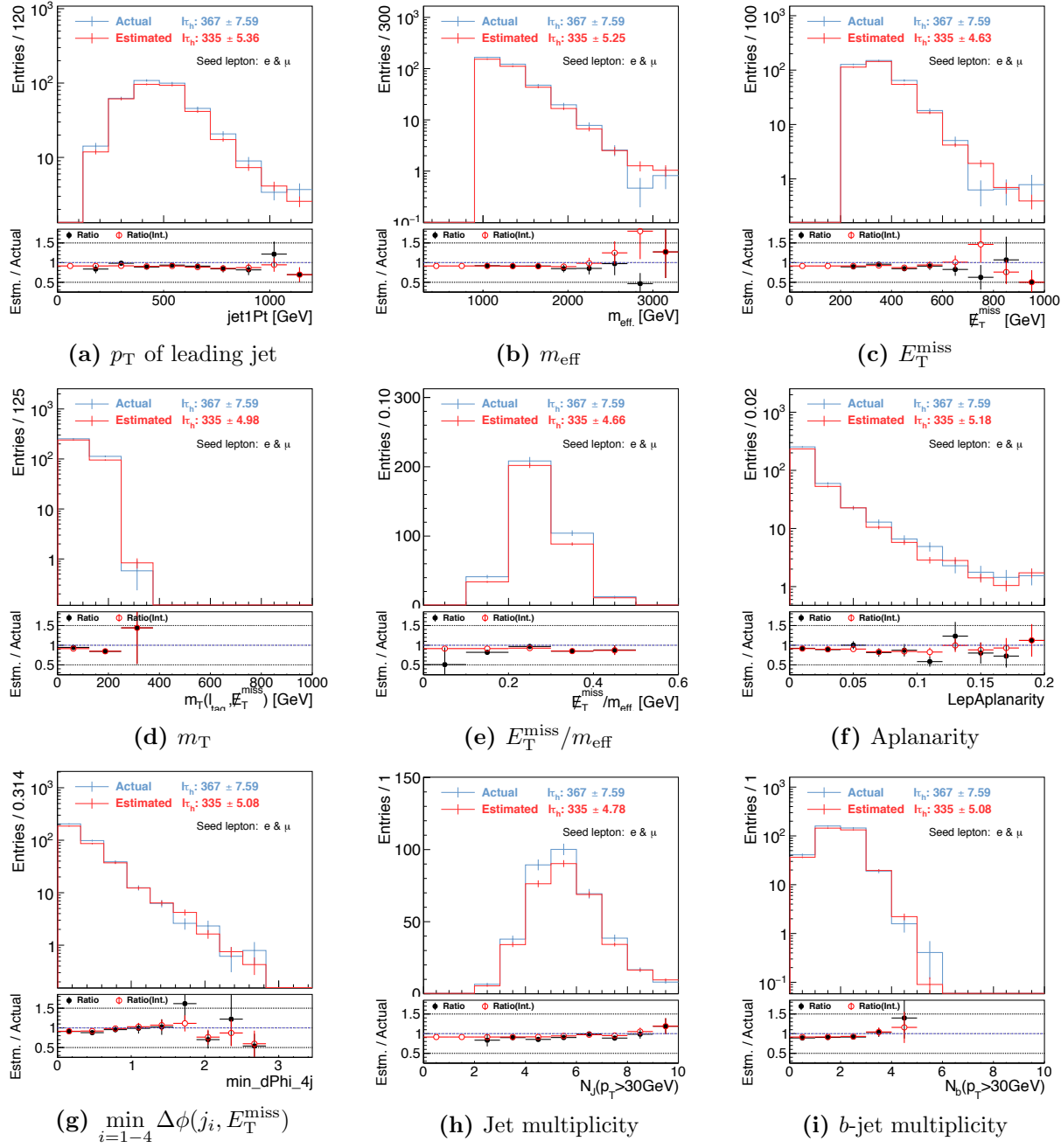


Figure C.2.3: MC closure test for tau replacement using $t\bar{t}$ MC sample. Seed events are collected by the use of MET trigger. $p_T < 35$ GeV for the leading lepton is required. **Both electrons and muons in the seed events are replaced.** Red points in the bottom plots show the ratio of integrated yields for the two histograms above the x-position that the point indicates.

C.3 Validation of Fake-Lepton Background Estimation

The “fake” background (defined in Table 7.1) involves two types of component:

- Multi-jets background

This includes the QCD di-jet events and full-hadronic decays of $V + \text{jets}$, which is ignored in the estimation since it is supposed to be negligible after requiring one signal lepton and $E_T^{\text{miss}} > 250$ in the events, based on the MC study and the past Run2 ATLAS 1-lepton analyses [148][154]. However, it always needs caution since the impact could be fatal once it turns to contribute because of its huge cross-section.

- Leptonical $V + \text{jets}$

The dominating component in the “fake” events is $W \rightarrow \tau\nu$ and $Z \rightarrow \nu\nu$. These are included in the $V + \text{jets}$ MC thus accounted in the estimation via the kinematical extrapolation method. However, the modeling on the fake rate of lepton candidates is very complicated and the MC description is known to be sometimes unreliable (often under-estimating).

Therefore, a data-driven validation is motivated to make sure the estimation is not really underestimating, using a set of specific validation regions (VRs-QCD) listed in Table 6.7 - 6.11. VR-QCDs are defined by inverting the isolation requirement on the final state lepton with respect to the SRs. The abundance of “fake” components is enhanced by about a factor of $5 \sim 10$ with respect to the SRs, due to the high “fake” rejection power of the isolation requirement. Figure C.3.1 presents the result. Note that the normalization factors (Figure 7.15) are applied for $W + \text{jets}$ and the top background. No particular data excess is found, implying a reasonable MC modeling on fake lepton.

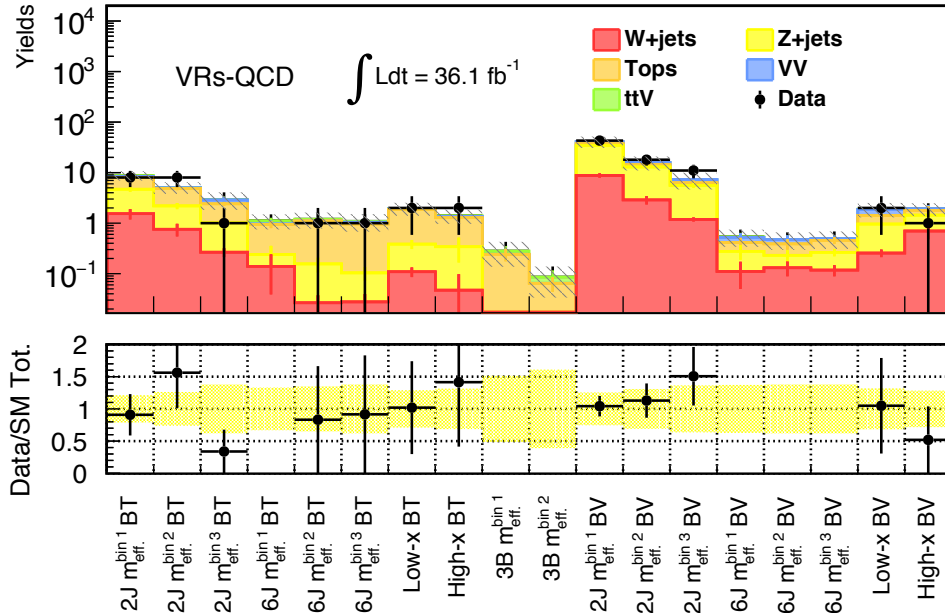


Figure C.3.1: Observed yields (black dots) and background expected by the kinematical extrapolation (colored stack) in VRs-QCD. The error bands include both statistical and systematic (the same theory systematics is quoted as the SRs) uncertainty.

C.4 Post-fit Distributions in CRs and VRs

Control Regions

Figure C.4.1-C.4.8 show the kinematical distribution in after the MC normalization. Blue arrows indicate the CRs that the MC is normalized.

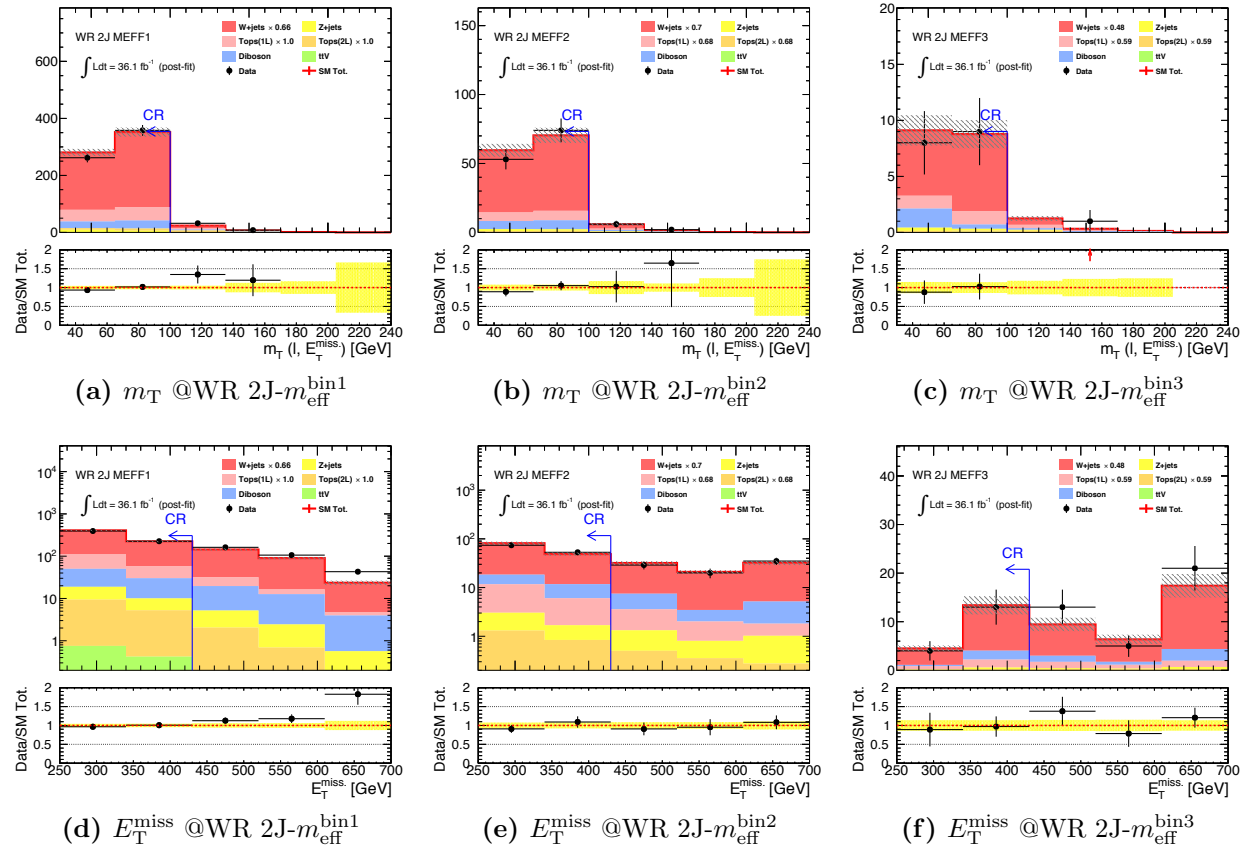


Figure C.4.1: Distribution of m_T and E_T^{miss} in WR 2J after the MC normalization in CRs. The yellow band in the bottom panel represents only statistical error. The overflow is included in the highest bin.

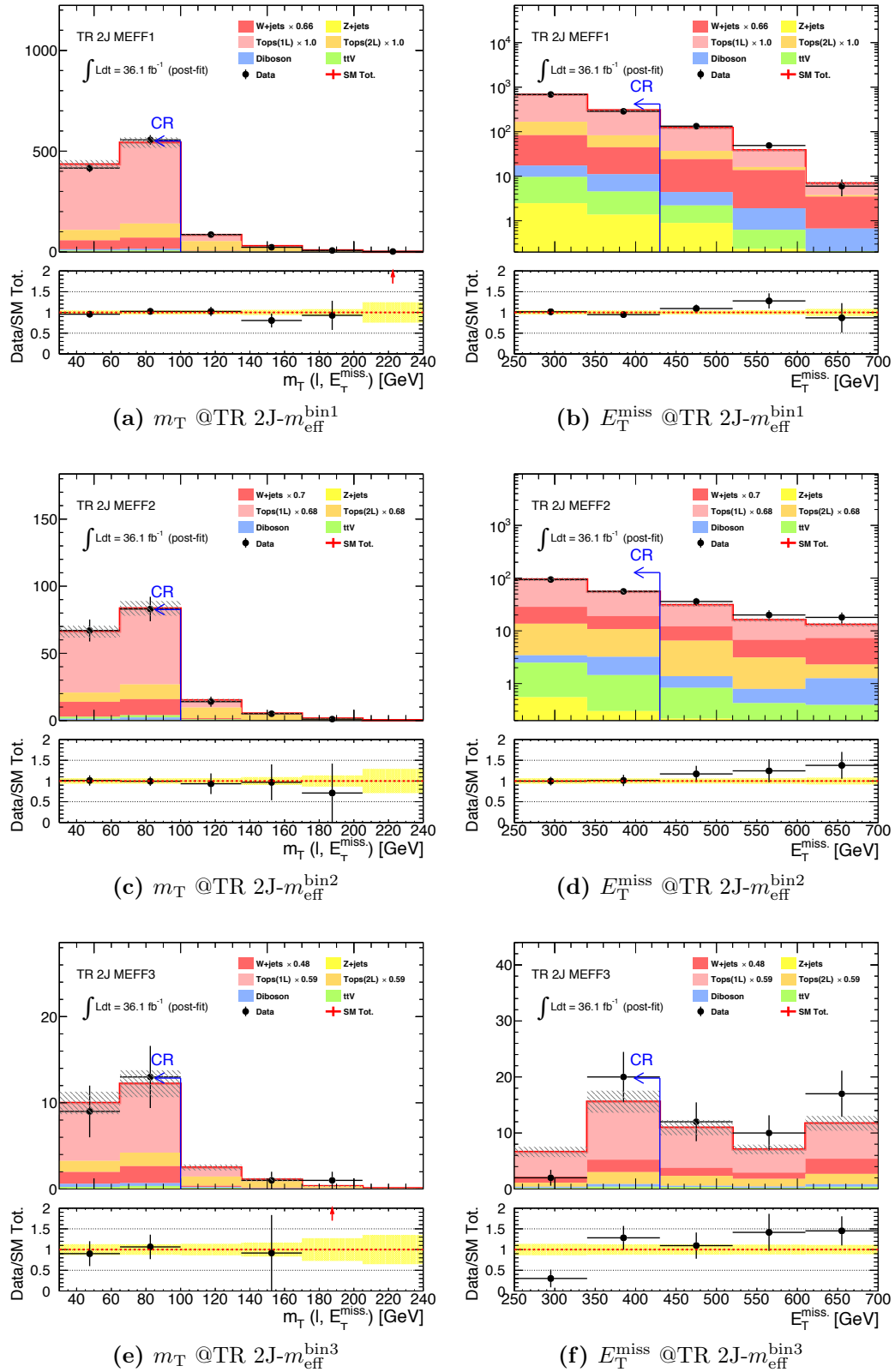


Figure C.4.2: Distribution of m_T and E_T^{miss} in TR 2J after the MC normalization in CRs. The yellow band in the bottom panel represents only statistical error. The overflow is included in the highest bin.

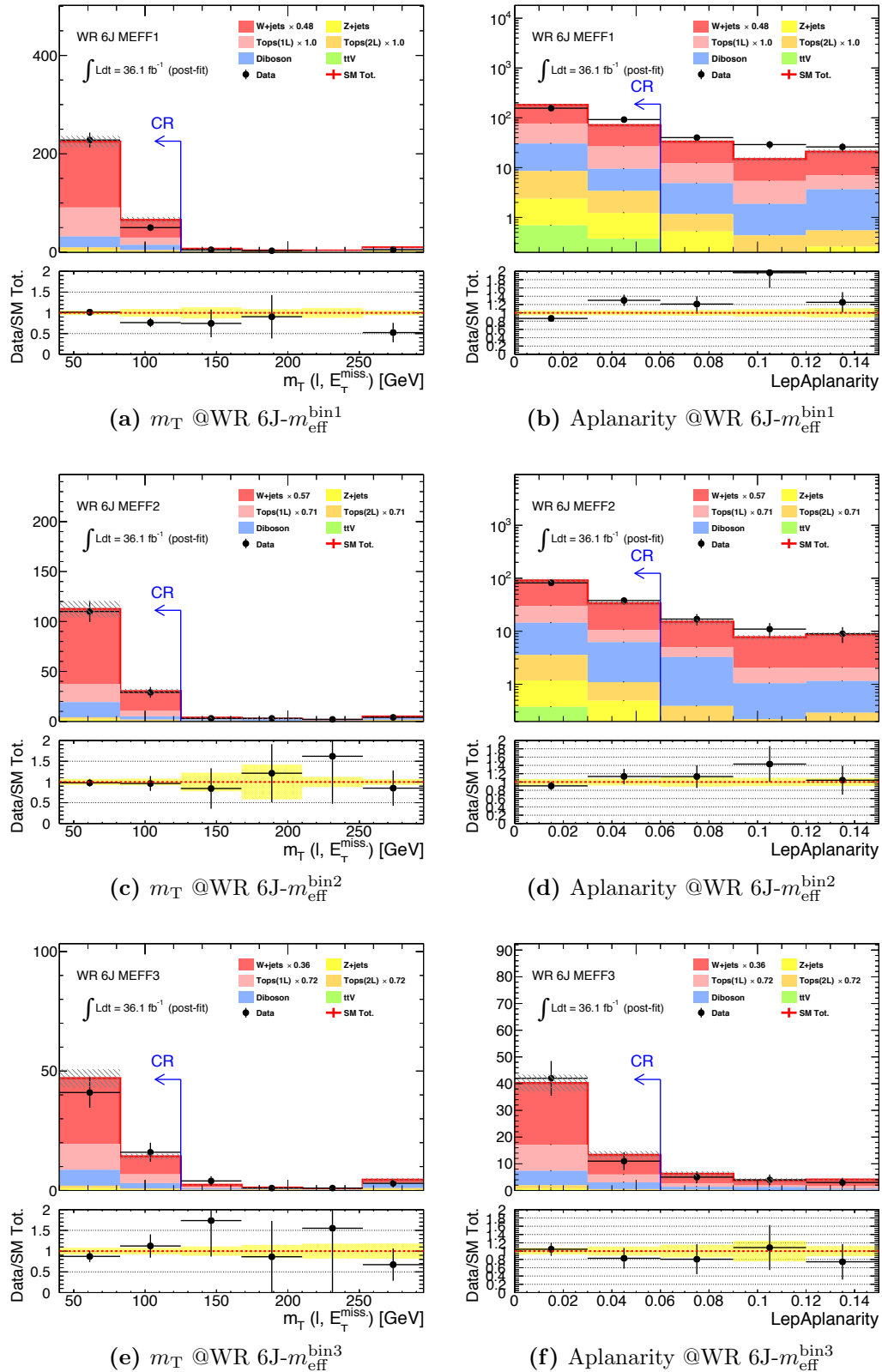


Figure C.4.3: Distribution of m_T and aplanarity in WR 6J after the MC normalization in CRs. The yellow band in the bottom panel represents only statistical error. The overflow is included in the highest bin.

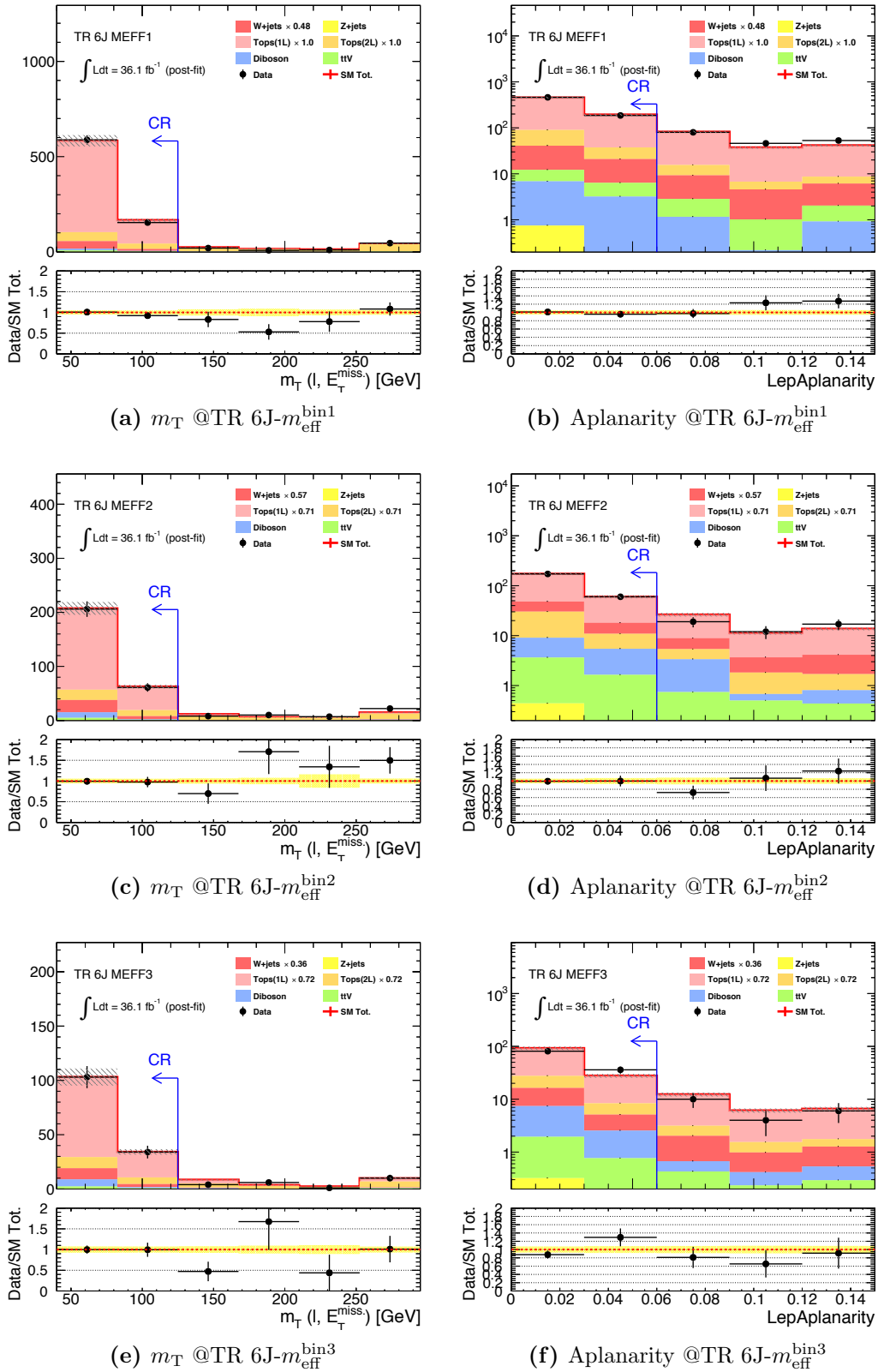


Figure C.4.4: Distribution of m_T and aplanarity in TR 6J after the MC normalization in CRs. The yellow band in the bottom panel represents only statistical error. The overflow is included in the highest bin.

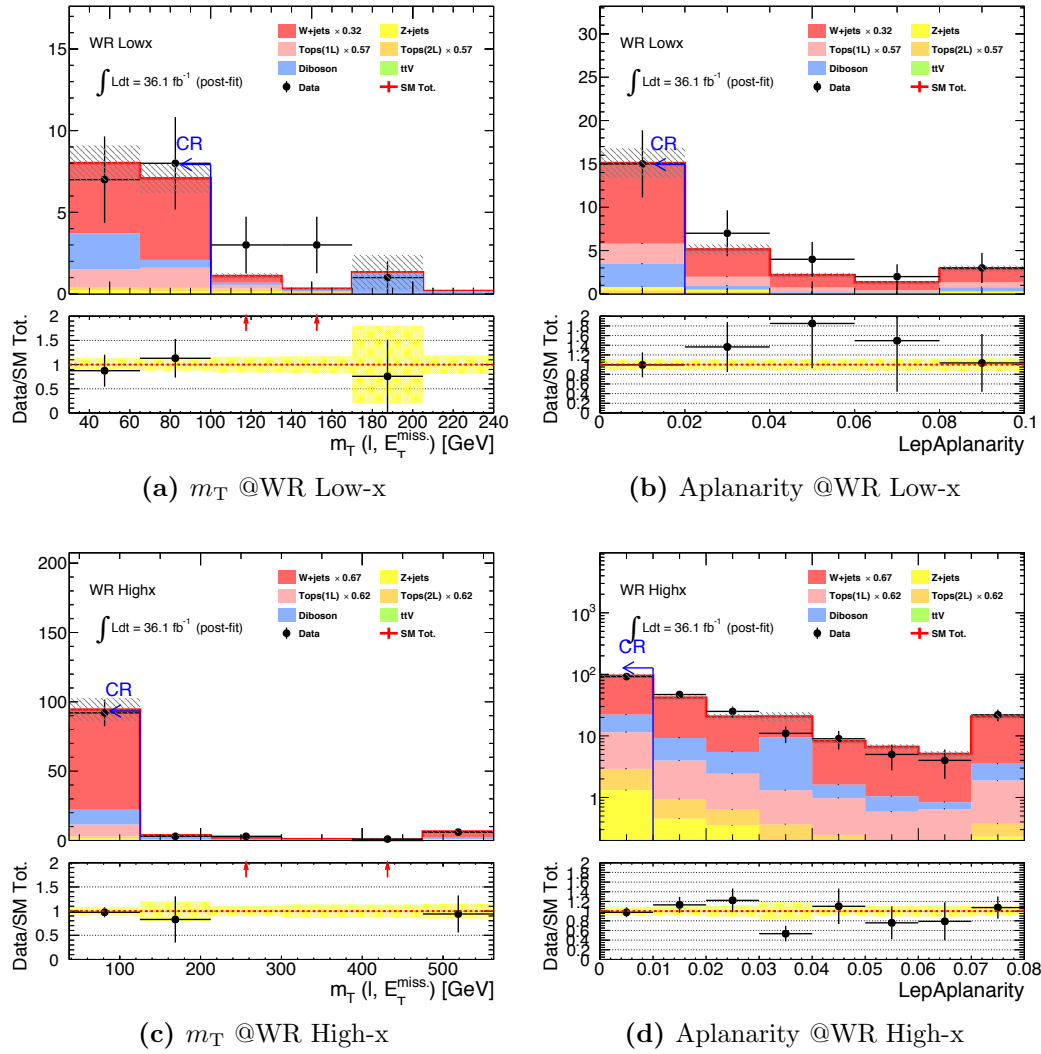


Figure C.4.5: Distribution in m_T , aplanarity and topness in WR **Low-x** and WR **High-x** after the MC normalization in CRs. The yellow band in the bottom panel represents only statistical error. The overflow is included in the highest bin.

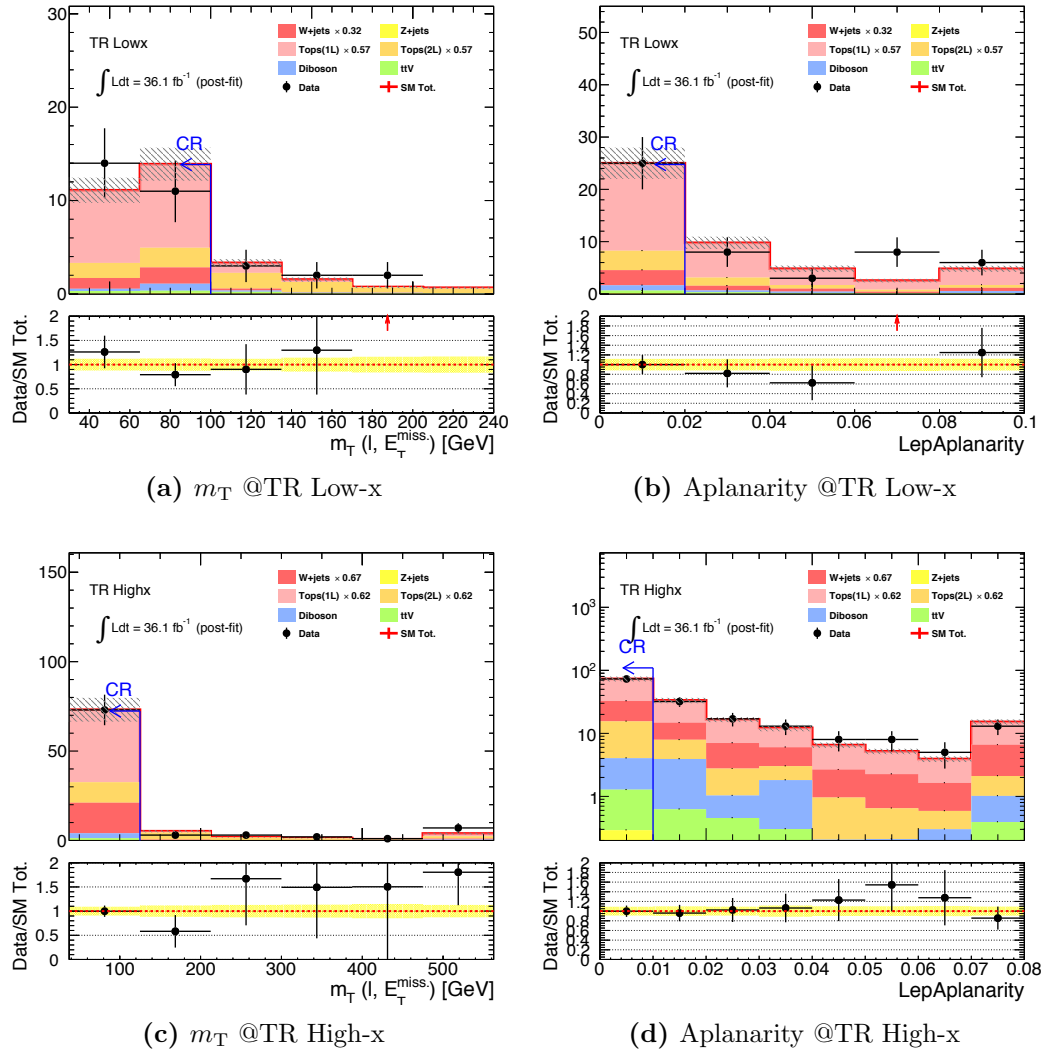


Figure C.4.6: Distribution in m_T , aplanarity and topness in TR **Low-x** and TR **High-x** after the MC normalization in CRs. The yellow band in the bottom panel represents only statistical error. The overflow is included in the highest bin.

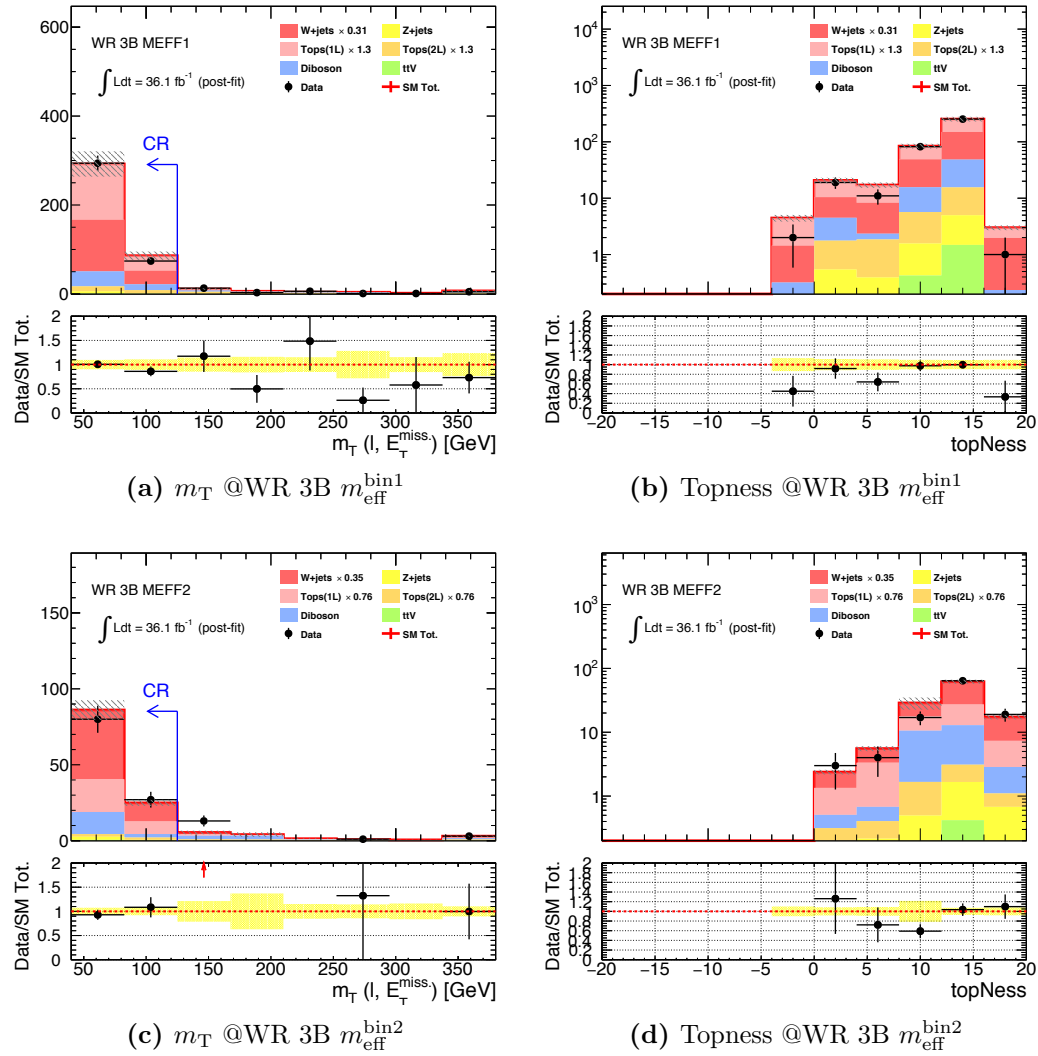


Figure C.4.7: Distribution in m_T , aplanarity and topness in WR 3B after the MC normalization in CRs. The yellow band in the bottom panel represents only statistical error. The overflow is included in the highest bin.

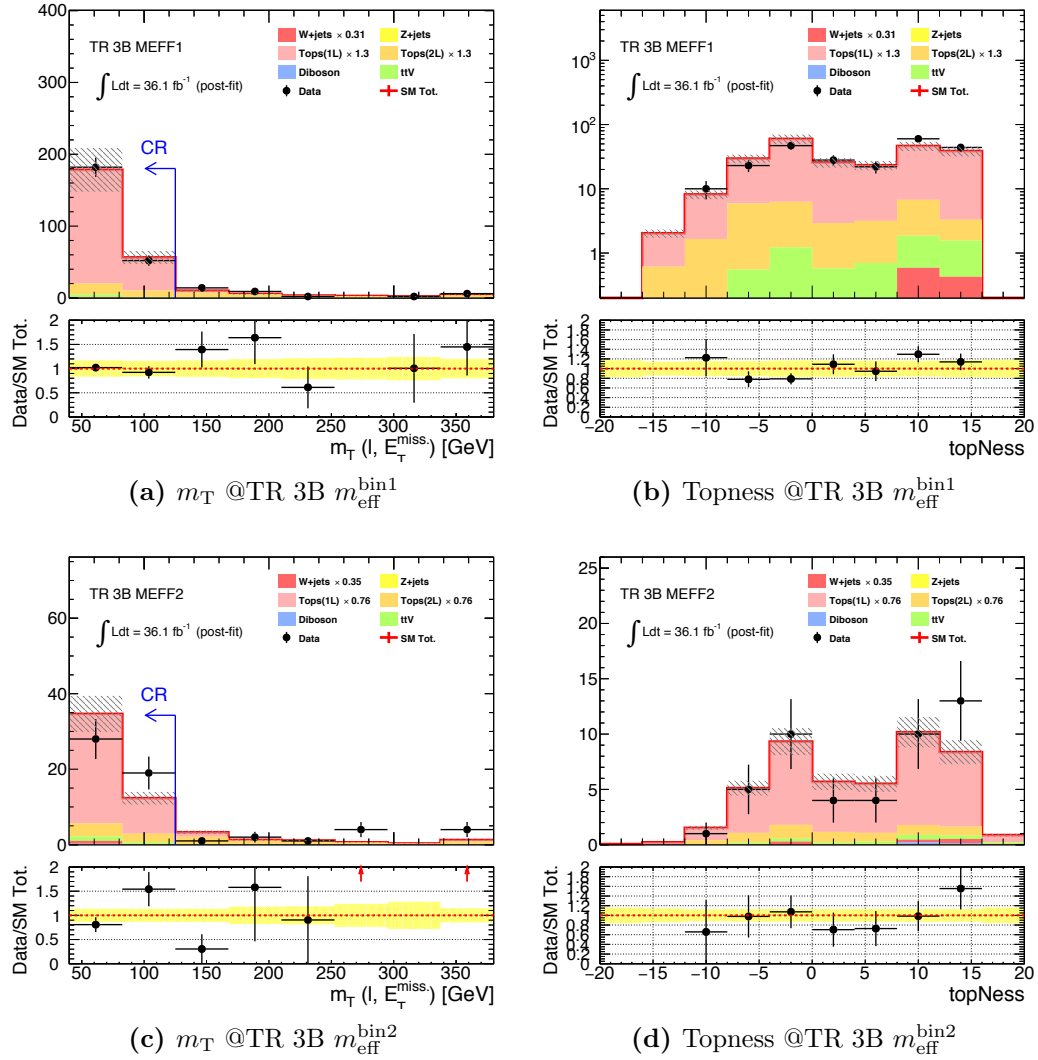


Figure C.4.8: Distribution in m_T , aplanarity and topness in TR 3B after the MC normalization in CRs. The yellow band in the bottom panel represents only statistical error. The overflow is included in the highest bin.

Validation Regions

Figure C.4.9-C.4.12 display the distribution of data and the estimated background in VRs, in terms of the kinematical variables which VRs are designed to test i.e. m_T for VRa and aplanarity/topness etc. for VRb. The white component is the background estimated by the object replacement while the colored ones are by the kinematical extrapolation. Blue arrows indicate the cut position with which the VRs are defined.

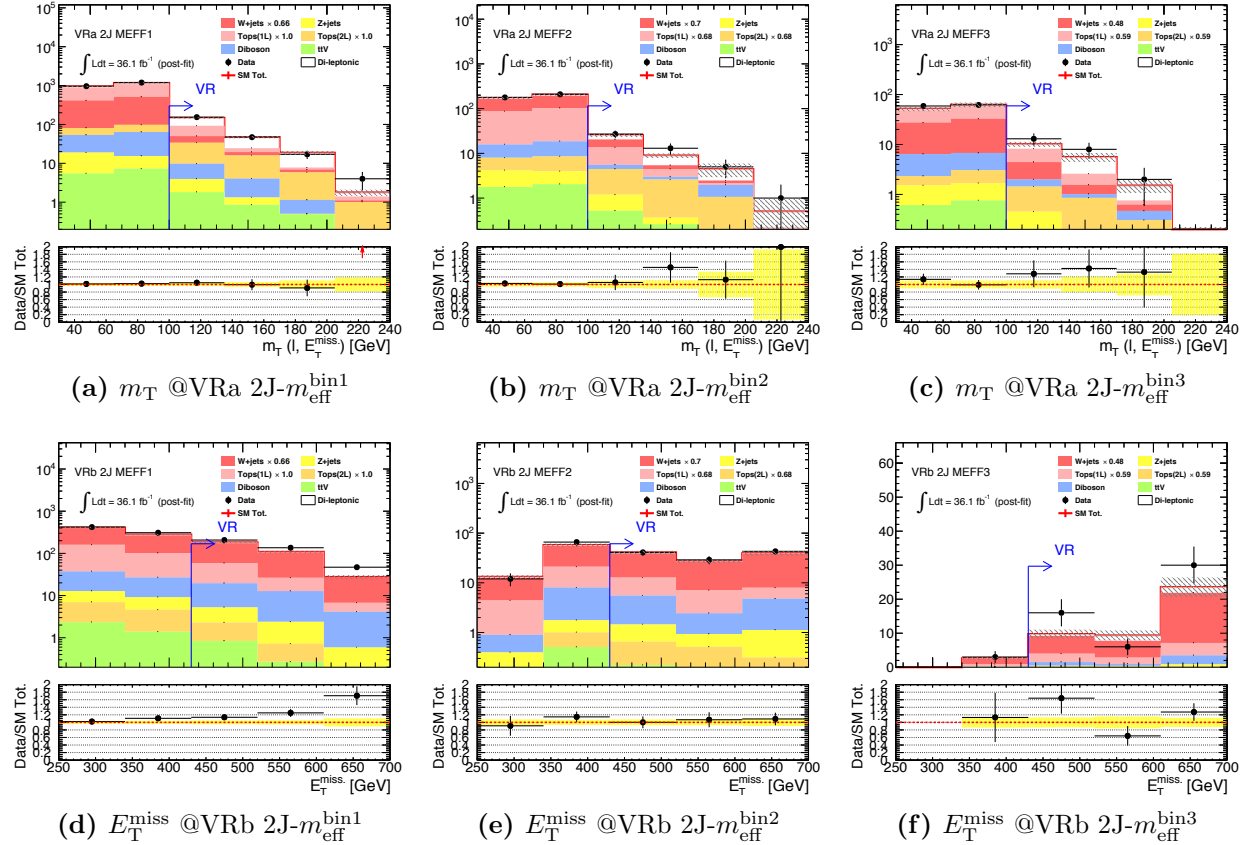


Figure C.4.9: Distribution of data and the estimated background in VR **2J**. The yellow band in the bottom panel represents statistical error. The overflow is included in the highest bin.

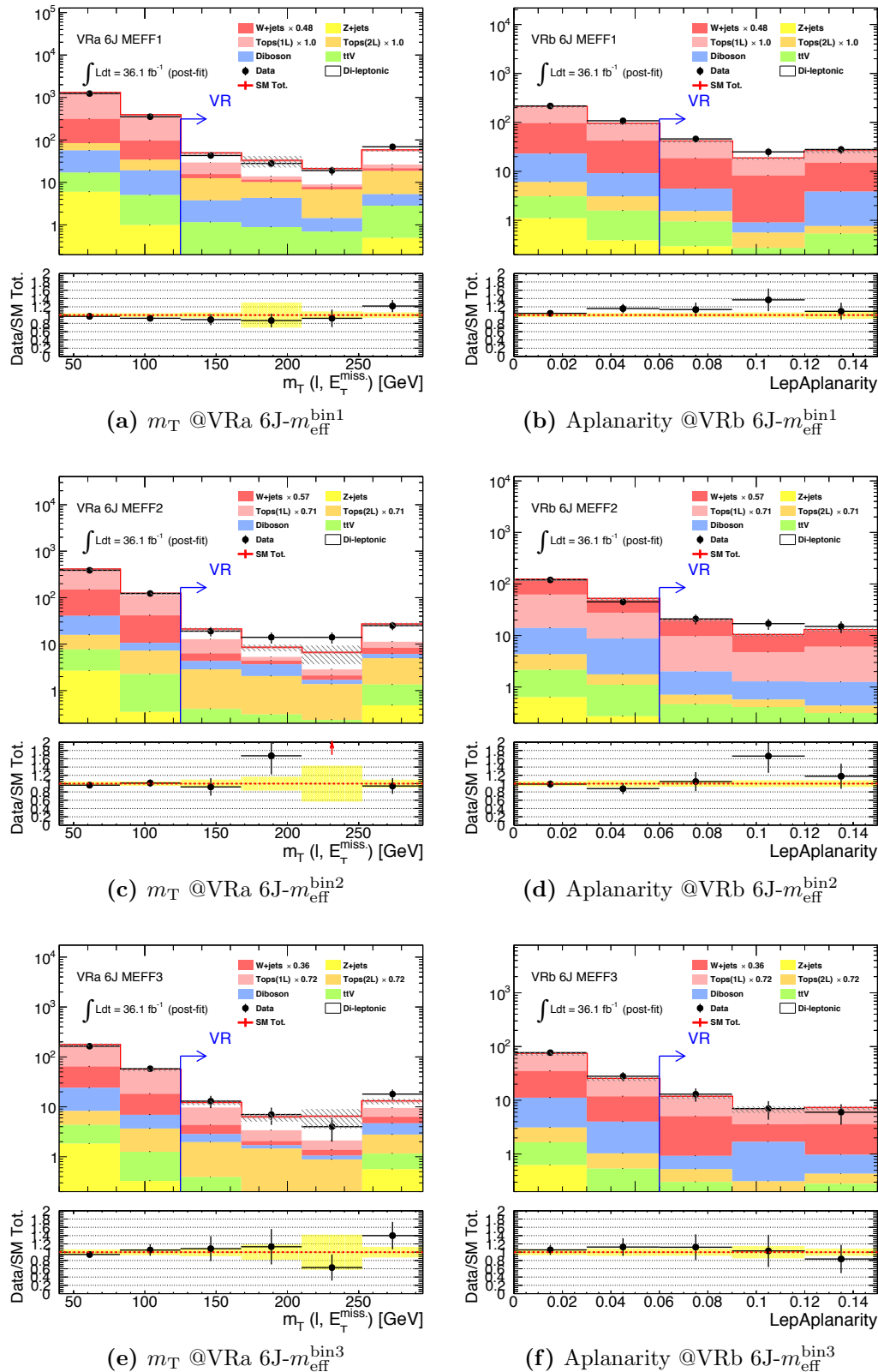


Figure C.4.10: Distribution of data and the estimated background in VR **6J**. The yellow band in the bottom panel represents statistical error. The overflow is included in the highest bin.

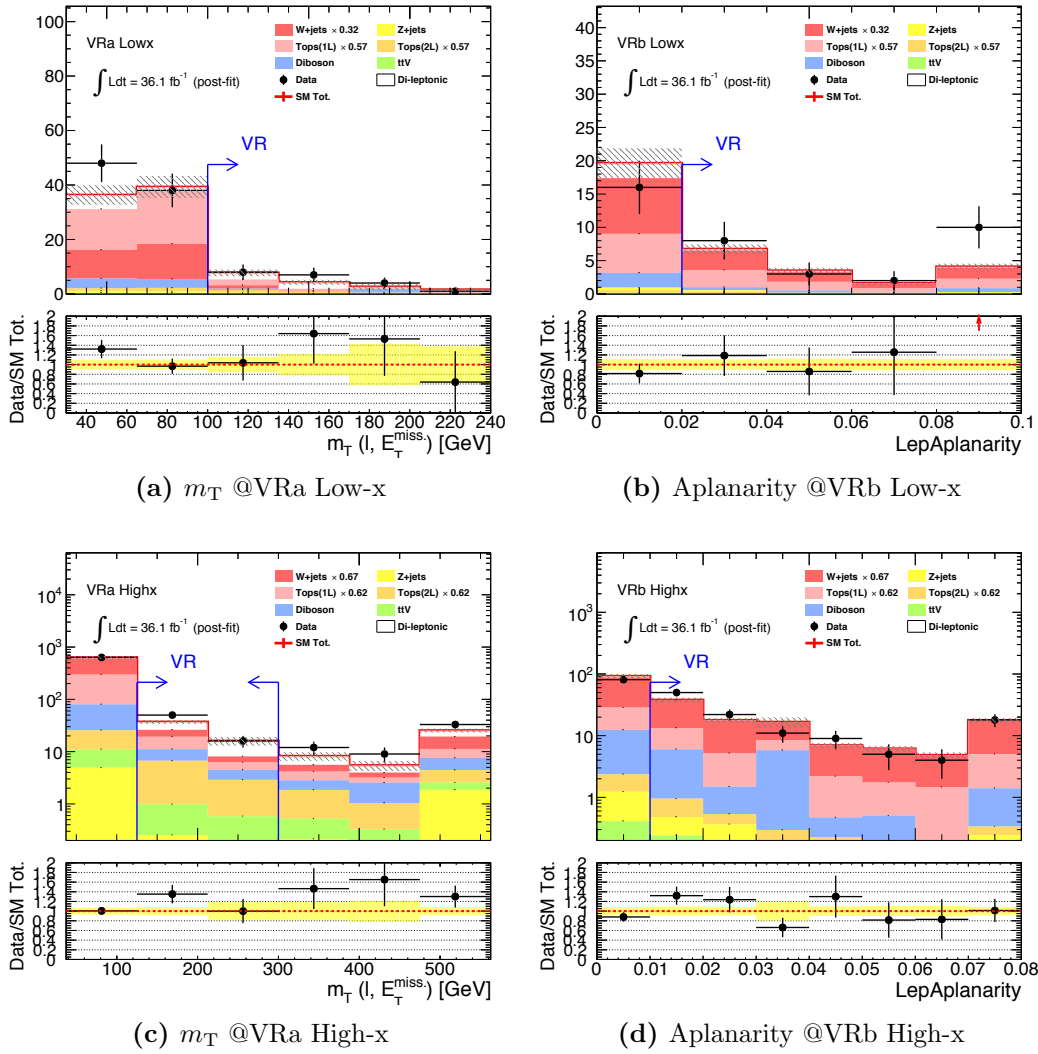


Figure C.4.11: Distribution of data and the estimated background in VR **Low-x** and VR **High-x**. The yellow band in the bottom panel represents only statistical error. The overflow is included in the highest bin.

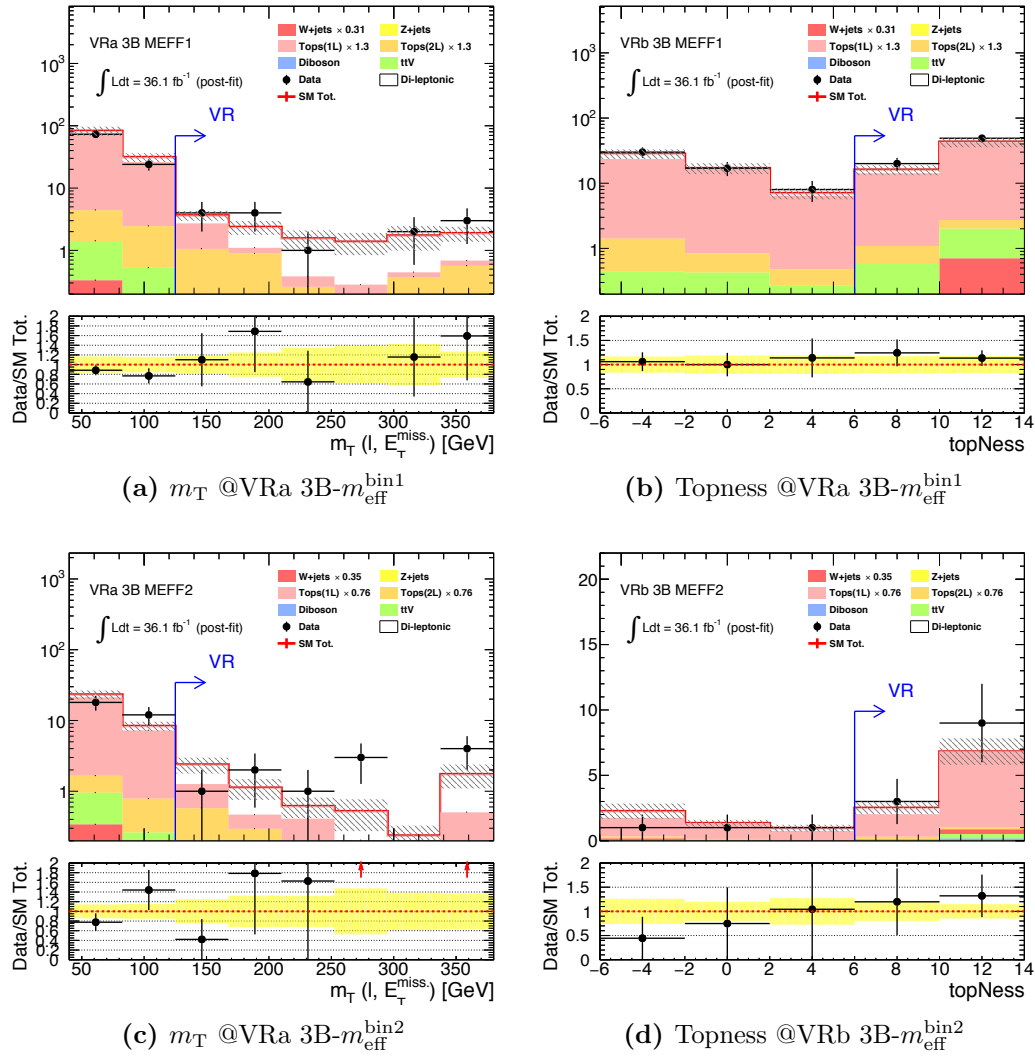
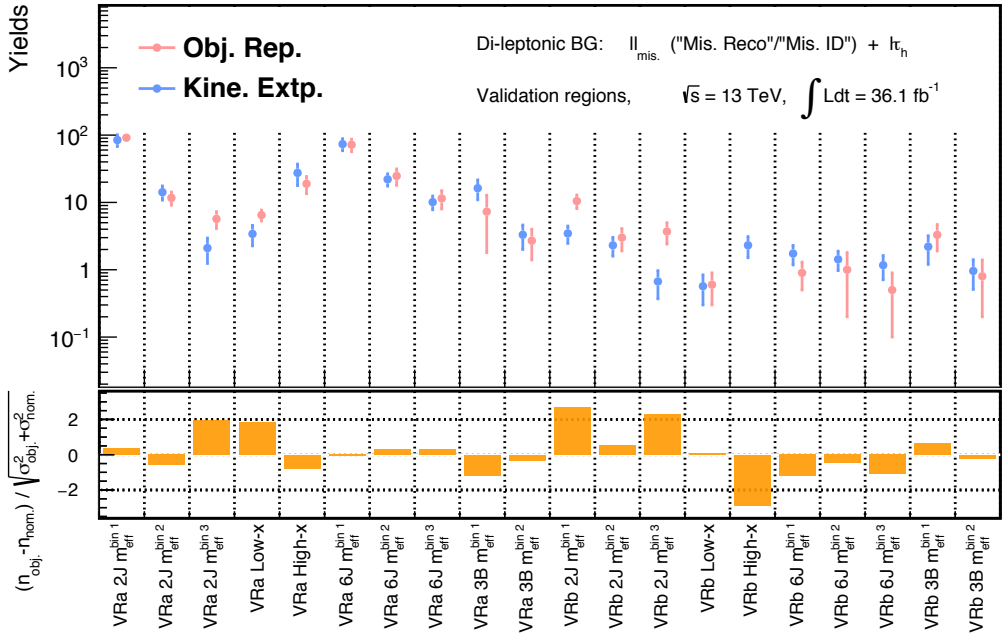


Figure C.4.12: Distribution of data and the estimated background in VR 3B. The yellow band in the bottom panel represents only statistical error. The overflow is included in the highest bin.

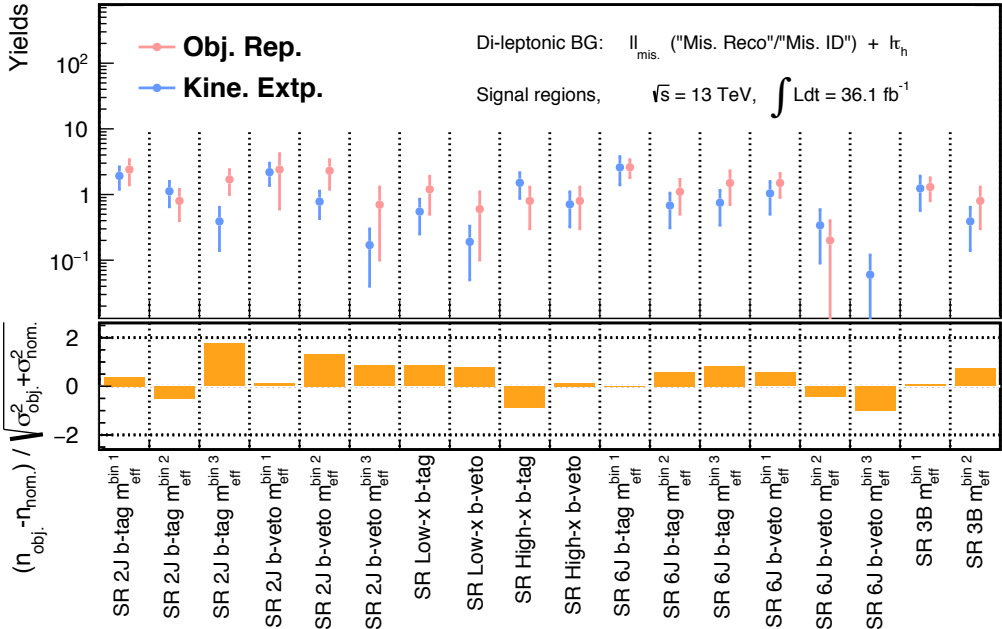
C.5 Comparison between Kinematical Extrapolation and Object Replacement

For the cross-check of “di-leptonic” background estimation, it is also estimated by the kinematical extrapolation method and compared with the nominal prediction provided by the object replacement. Figure C.5.1 show the direct comparison in the predicted yields in SRs (VRs) between the two methods. Note that the same normalization factors are obtained in Sec. 7.2.3 are used in case of the kinematical extrapolation. While they are found to be consistent in most of the regions, object replacement tends to predict a bit higher yields in high- m_T regions where kinematical extrapolation is known to under-estimate due to the potential MC mis-modeling m_T cut-off as mentioned in Sec. 7.4.

Figure C.5.3 show the comparison of total background expectation and the pulls in VRs (SRs) between the two methods, where fairly consistent results are obtained. On the other hand, the source of uncertainty on the estimation is in contrast between the two estimation methods. Figure C.5.4 summarizes the total uncertainty and the breakdown for the two methods. Though the total uncertainty is comparable with each other, the leading source is theory uncertainty for the kinematical extrapolation while the CR statistics is the dominant source for the object replacement.

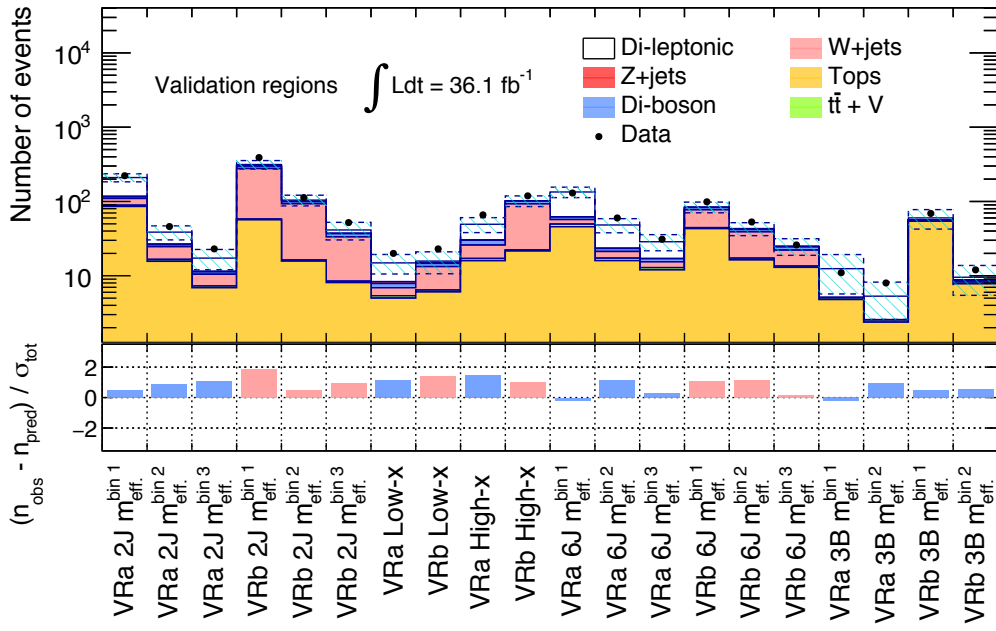


(a) Comparison of predicted “di-leptonic” yields in VRs between the two methods.

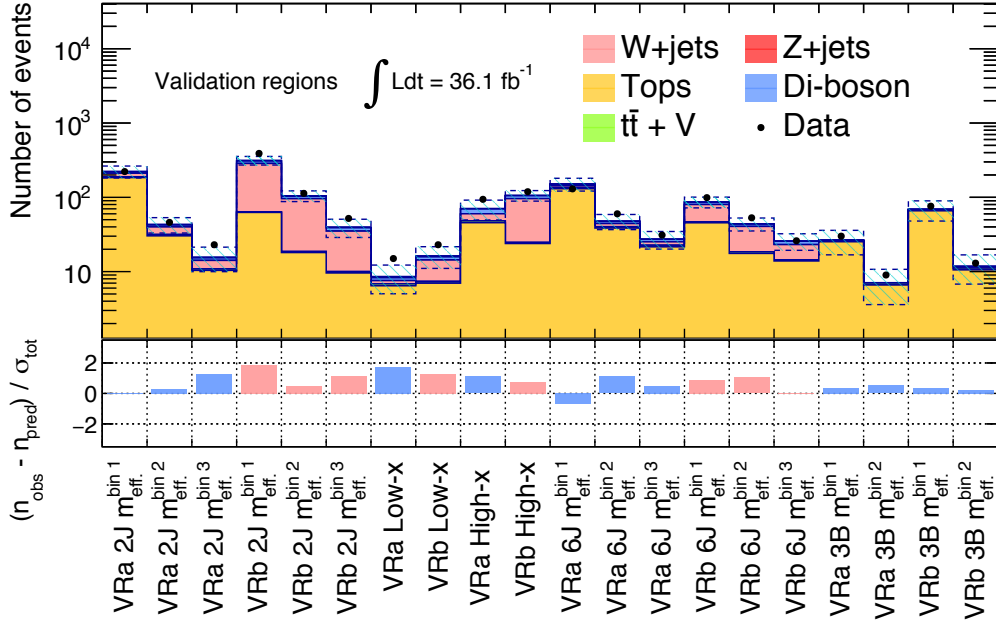


(b) Comparison of predicted “di-leptonic” yields in SRs between the two methods.

Figure C.5.1: (Top pannels) Estimated yields of the di-leptonic components (“Mis-Reco”, “Mis-ID” and “ $\ell\tau_h$ ”) in (a) VRs or in (b) SRs by the nominal method (pink) and the kinematical extrapolation method (blue). Error bars included both statistical and systematic uncertainty. (Bottom pannels) Pull between the two estimations.

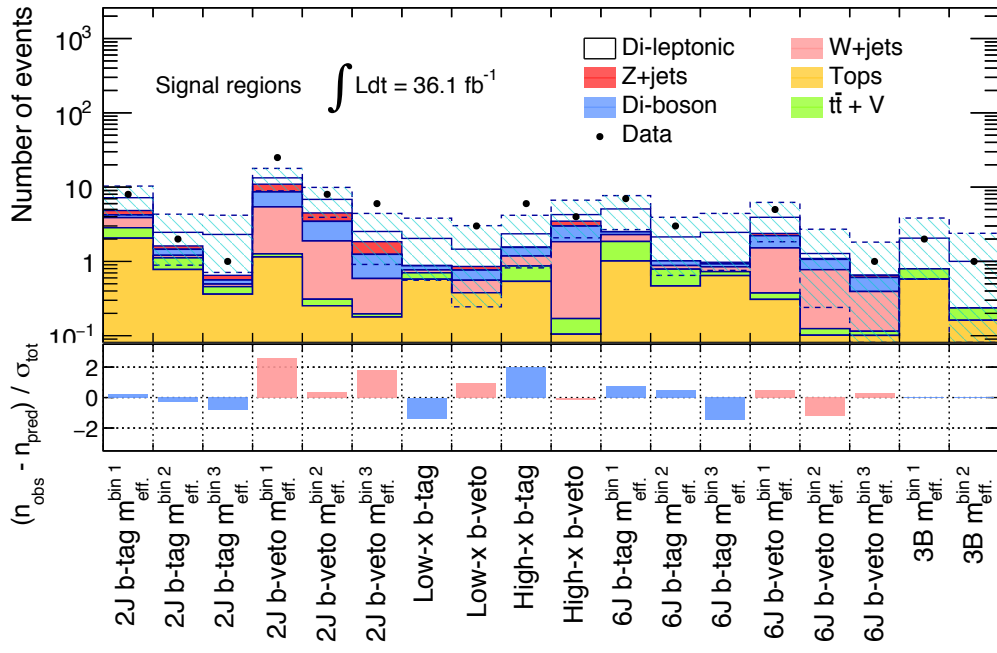


(a) Estimated yields and pulls in VRs with the **nominal** estimation (same as Figure 7.36).

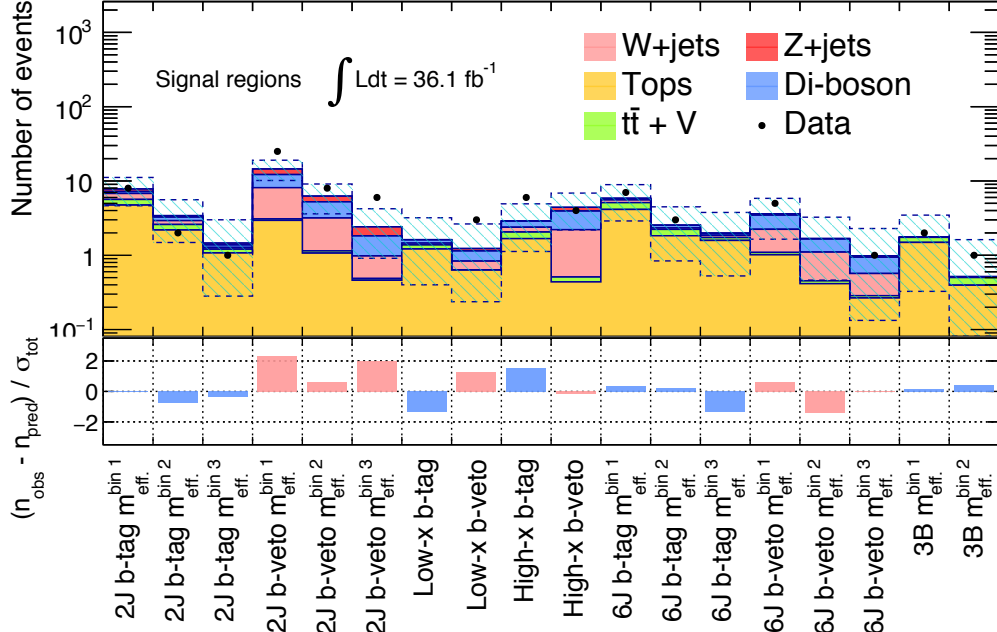


(b) Estimated yields and pulls in VRs with the **alternative** estimation in which all the background are estimated by the kinematical extrapolation.

Figure C.5.2: Total background expectation and the observed pulls in VRs. The dashed band represents uncertainty on the background estimation including both statistical and systematical uncertainty.



(a) Estimated yields and pulls in SRs with the **nominal** estimation (same as Figure 9.2).



(b) Estimated yields and pulls in SRs with the **alternative** estimation in which all the background are estimated by the kinematical extrapolation.

Figure C.5.3: Total background expectation and the observed pulls in SRs. The dashed band represents uncertainty on the background estimation including both statistical and systematical uncertainty.

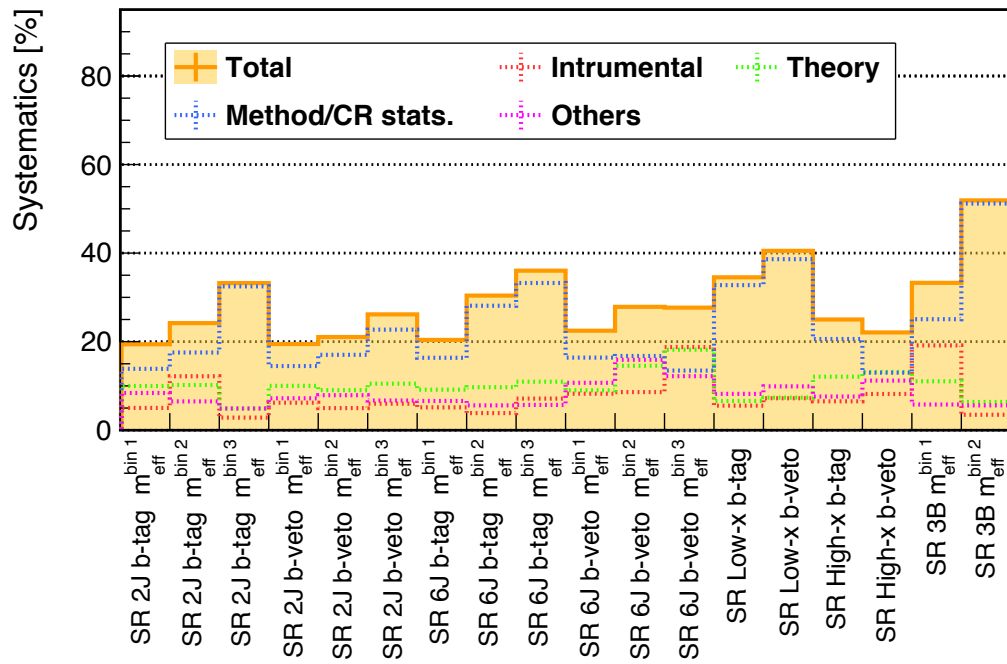
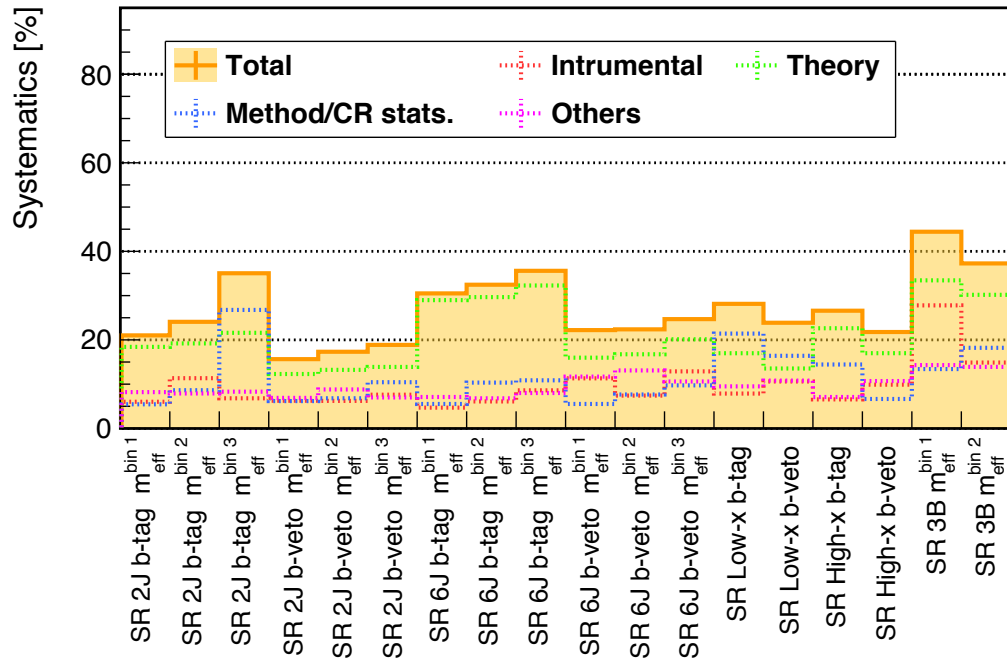
(a) Uncertainty associated with the **nominal** estimation (same as Figure 9.1)(b) Uncertainty associated with the **alternative** estimation in which all the background is estimated by the kinematical extrapolation method.

Figure C.5.4: Post-fit systematic uncertainty with respect to the expected yield in the signal regions. Total systematics uncertainty is shown by the filled orange histogram, and the breakdowns are by dashed lines.

D Auxiliary Materials for Systematic Uncertainties

D.1 Extrapolation Error due to the MC Mis-modeling

The impact of the unaccounted MC mis-modeling found in the pre-selection (see Sec. 7.2.1) on the extrapolation from CRs to SRs (VRs) is evaluated by the procedure described in Sec. 8.3.1 (“Kinematical extrapolation method”). Figure D.1.1-D.1.8 display the result as function of the linear coefficient x in Eq. (8.1); The top pannels show the yield variation of $W + \text{jets}$ (left) and $t\bar{t}$ (right) when the MC events are reweighted by Eq. (8.1) as function of the coefficient w ; Bottom rows are the relative difference in their response against the injected variation, namely the extrapolation error.

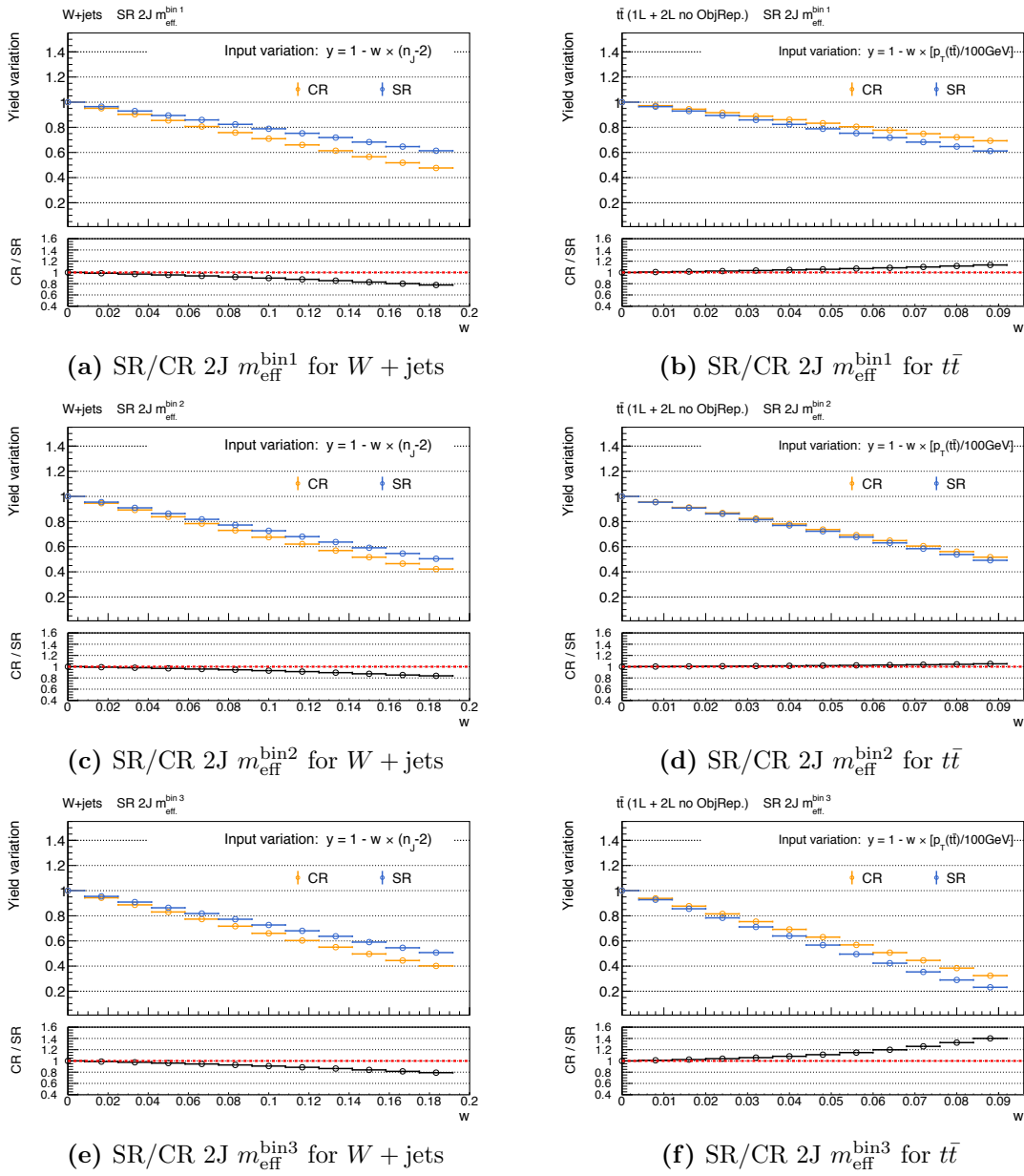


Figure D.1.1: Extrapolation error in SR/CR 2J evaluated by reweighting the MC with Eq. (8.1).

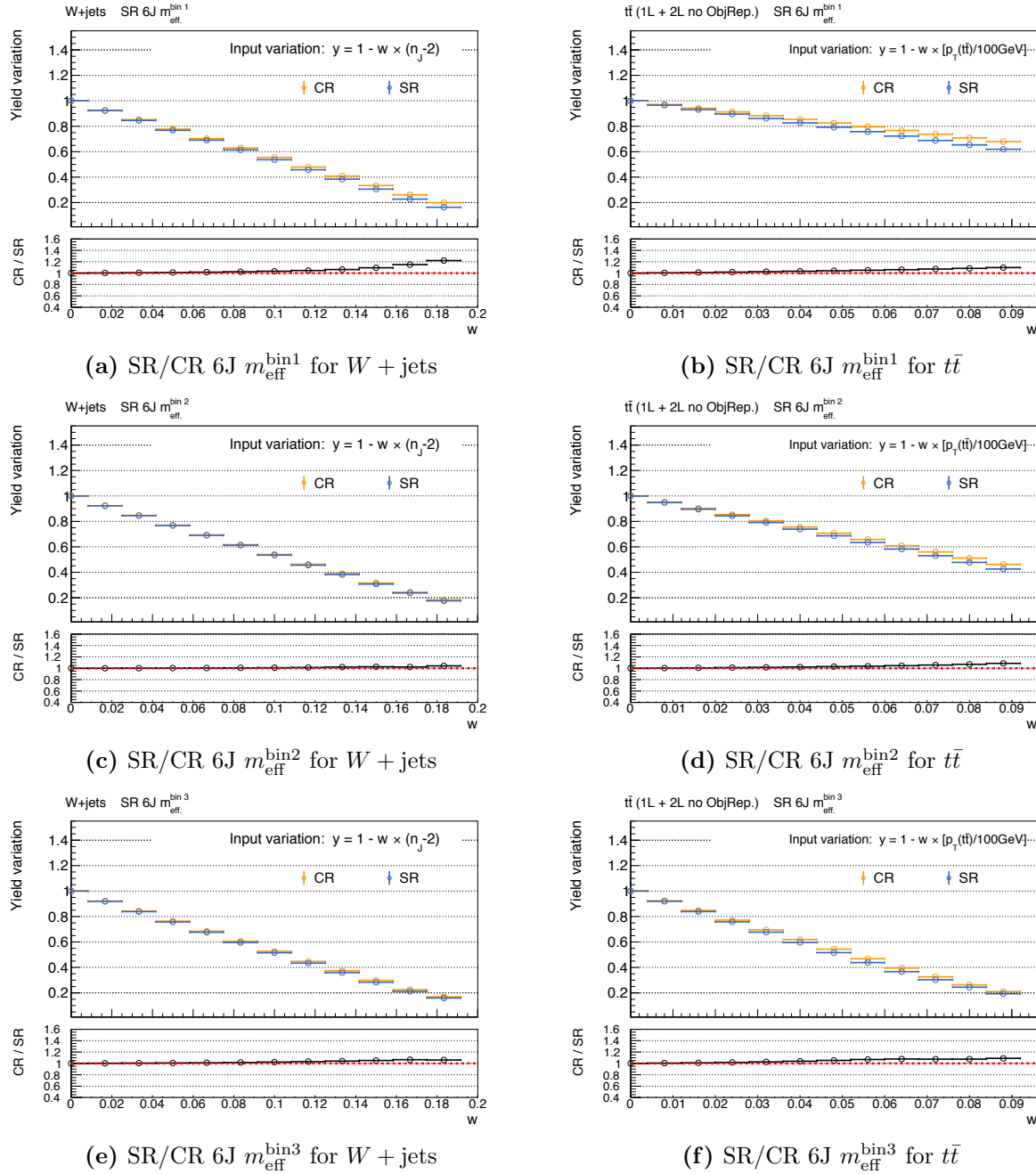


Figure D.1.2: Extrapolation error in SR/CR 6J evaluated by reweighting the MC with Eq. (8.1).

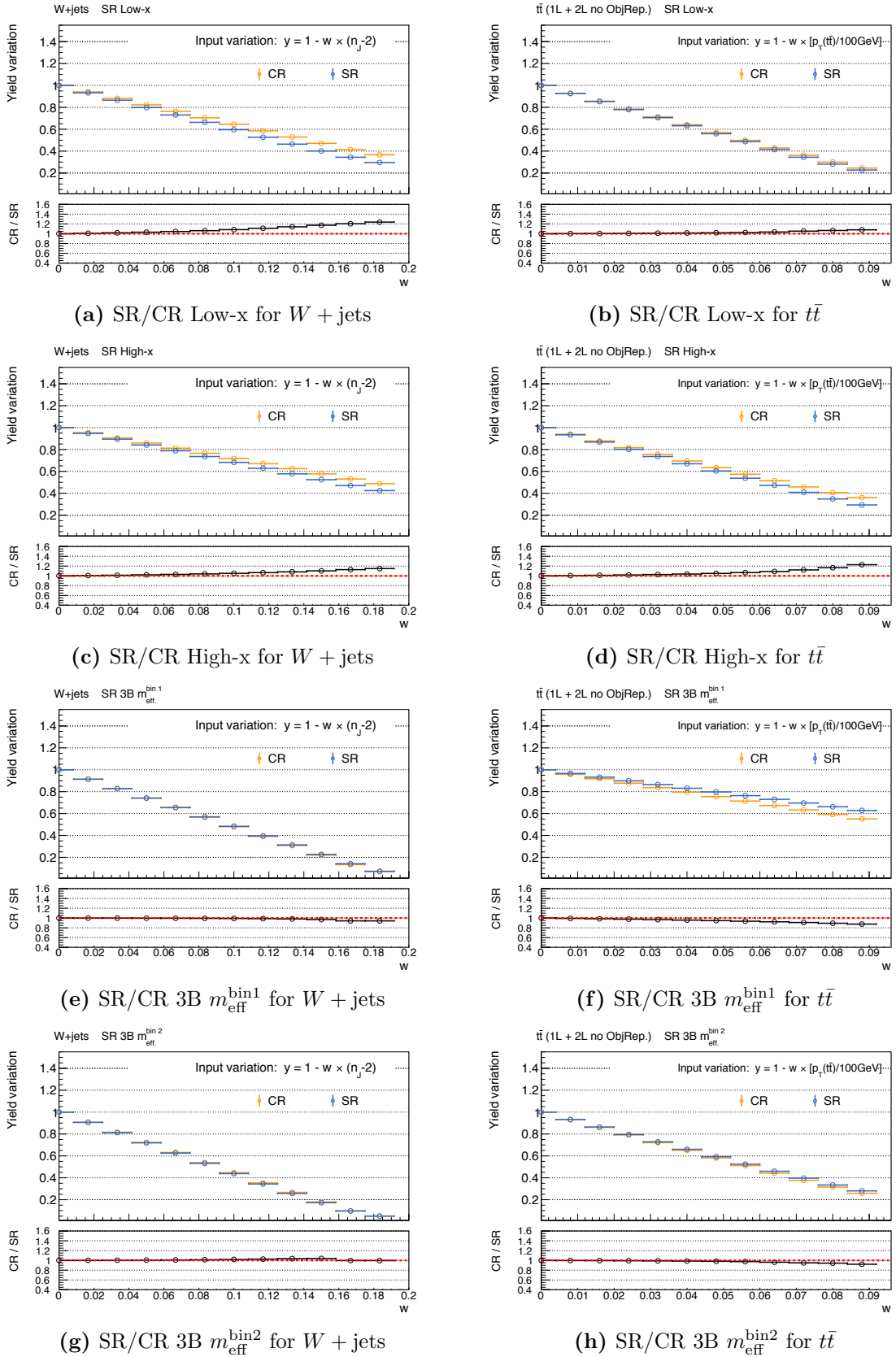


Figure D.1.3: Extrapolation error in SR/CR (a)(b) **Low-x**, (c)(d) **High-x** and (e-h) **3B** evaluated by reweighting the MC with Eq. (8.1).

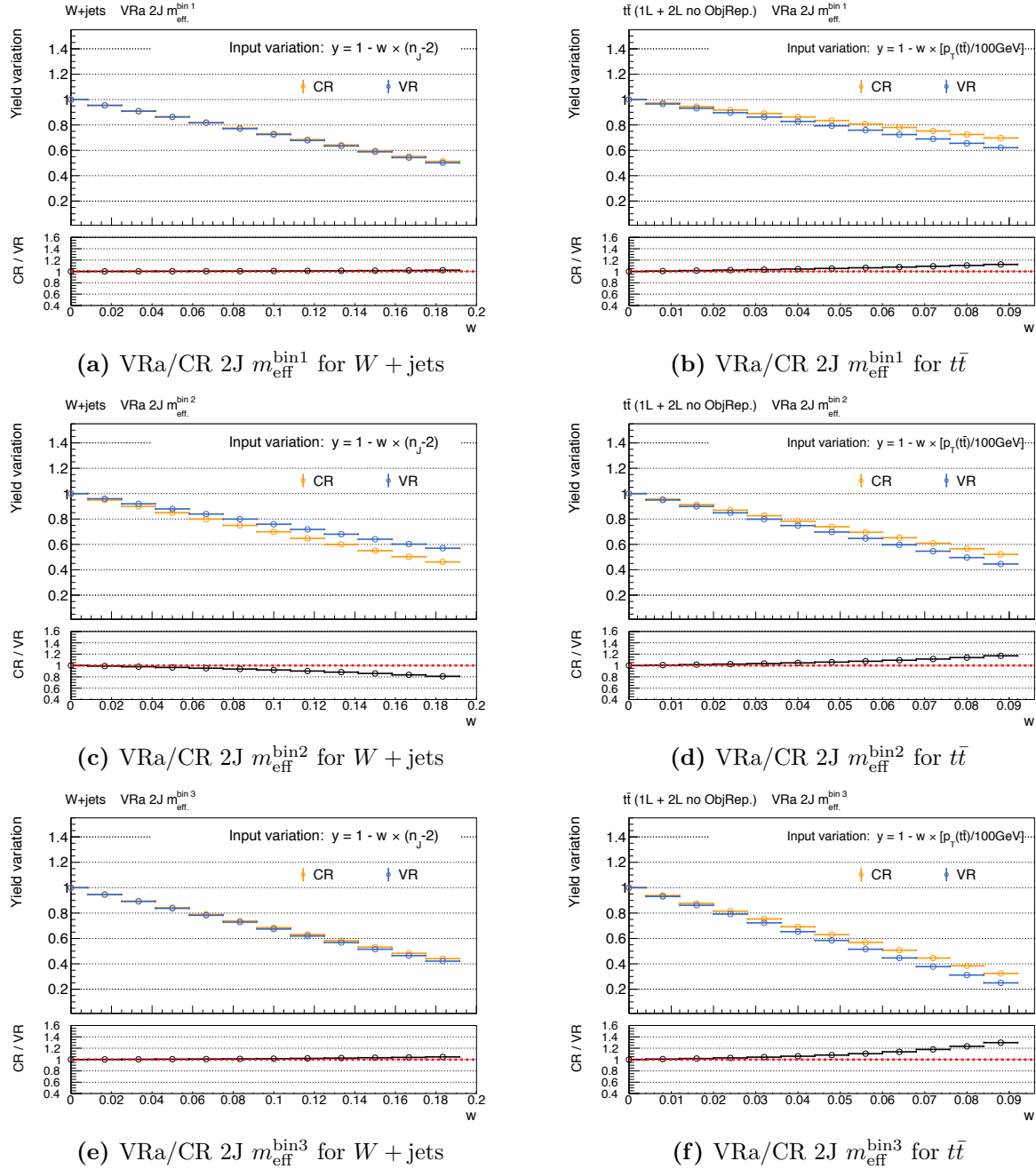


Figure D.1.4: Extrapolation error in VRa/CR 2J evaluated by reweighting the MC with Eq. (8.1).

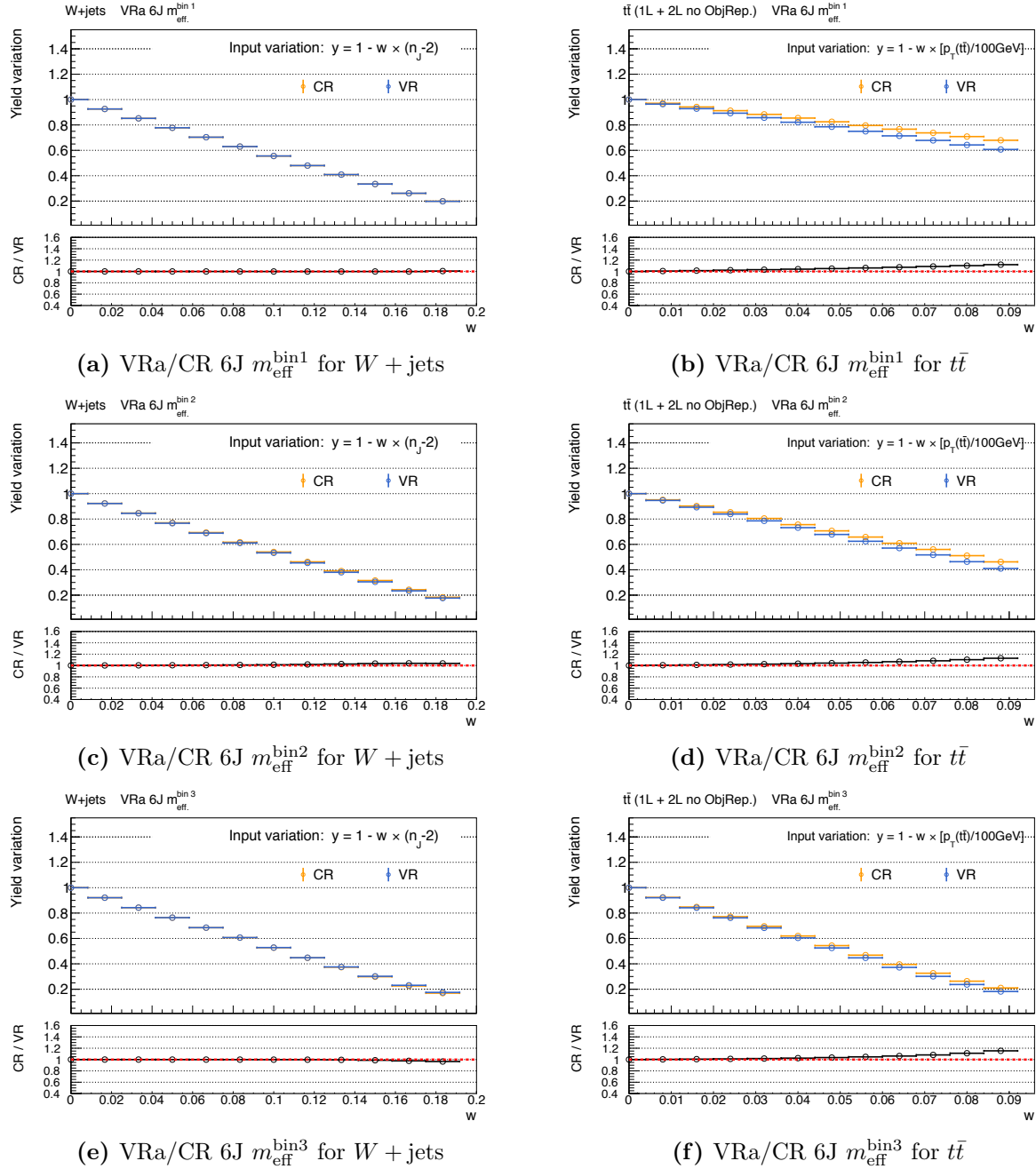


Figure D.1.5: Extrapolation error in VRa/CR 6J evaluated by reweighting the MC with Eq. (8.1).

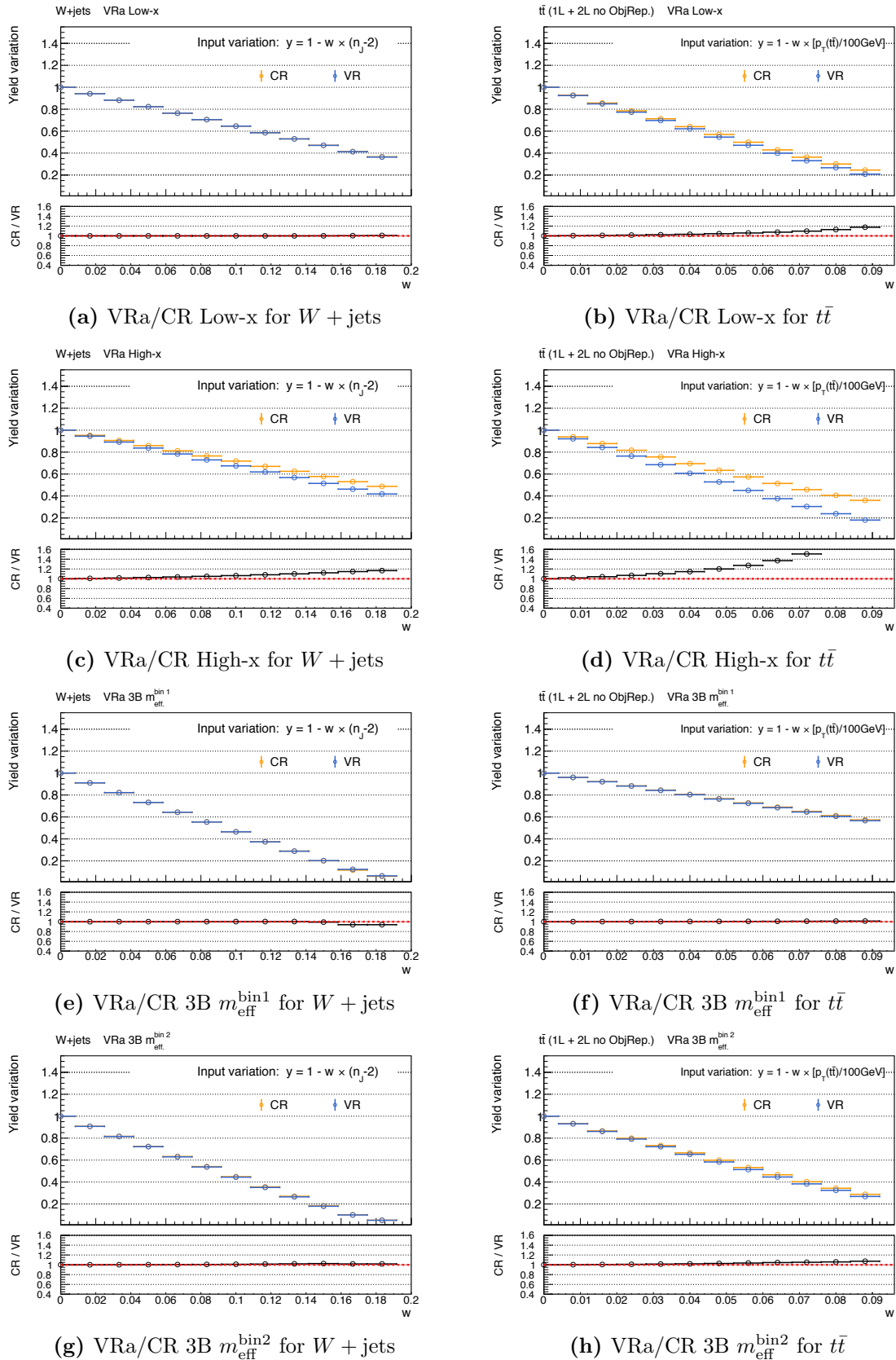


Figure D.1.6: Extrapolation error in VRa/CR (a)(b) **Low-x**, (c)(d) **High-x** and (e-h) **3B** evaluated by reweighting the MC with Eq. (8.1).

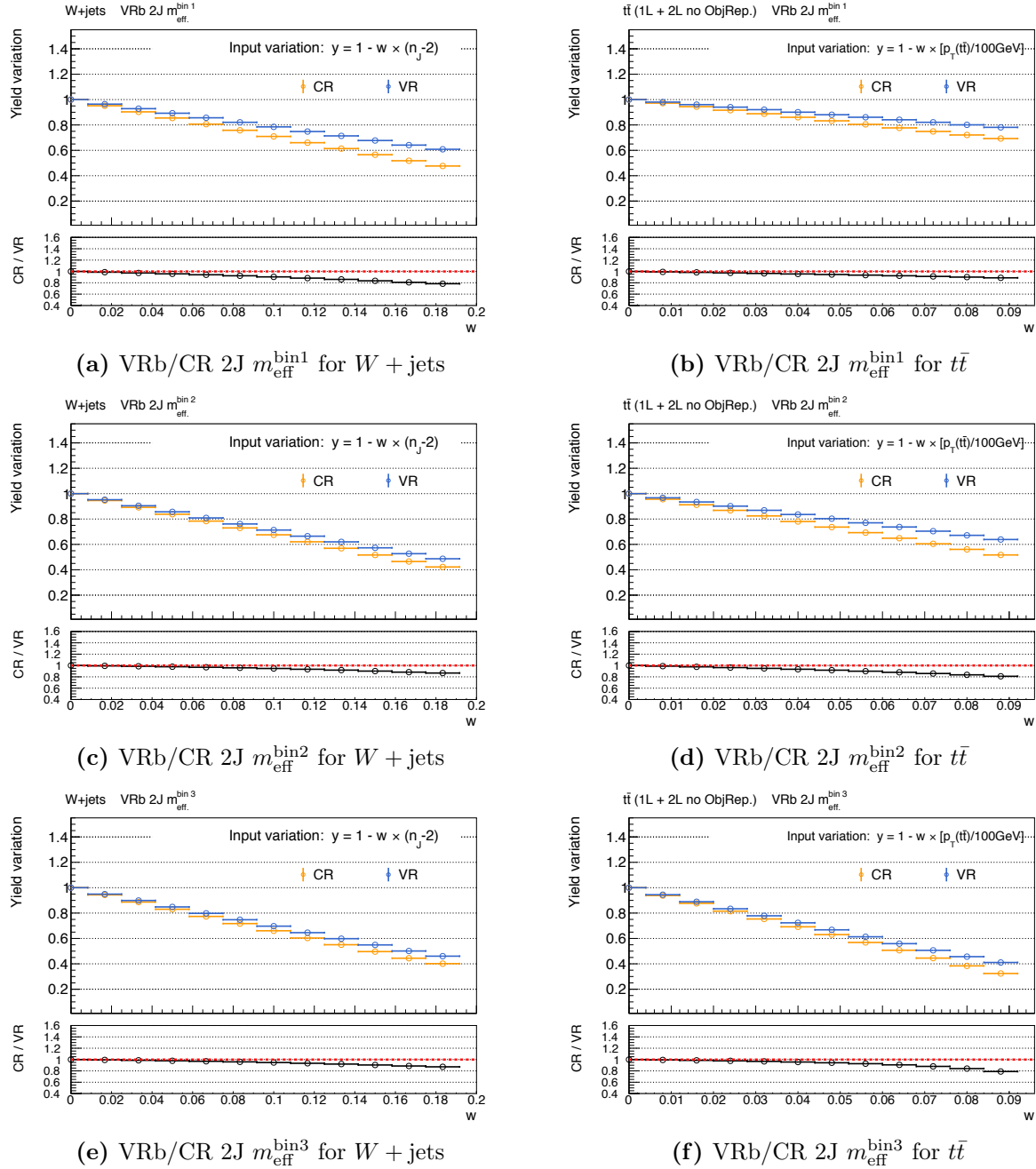


Figure D.1.7: Extrapolation error in VRb/CR **2J** evaluated by reweighting the MC with Eq. (8.1).

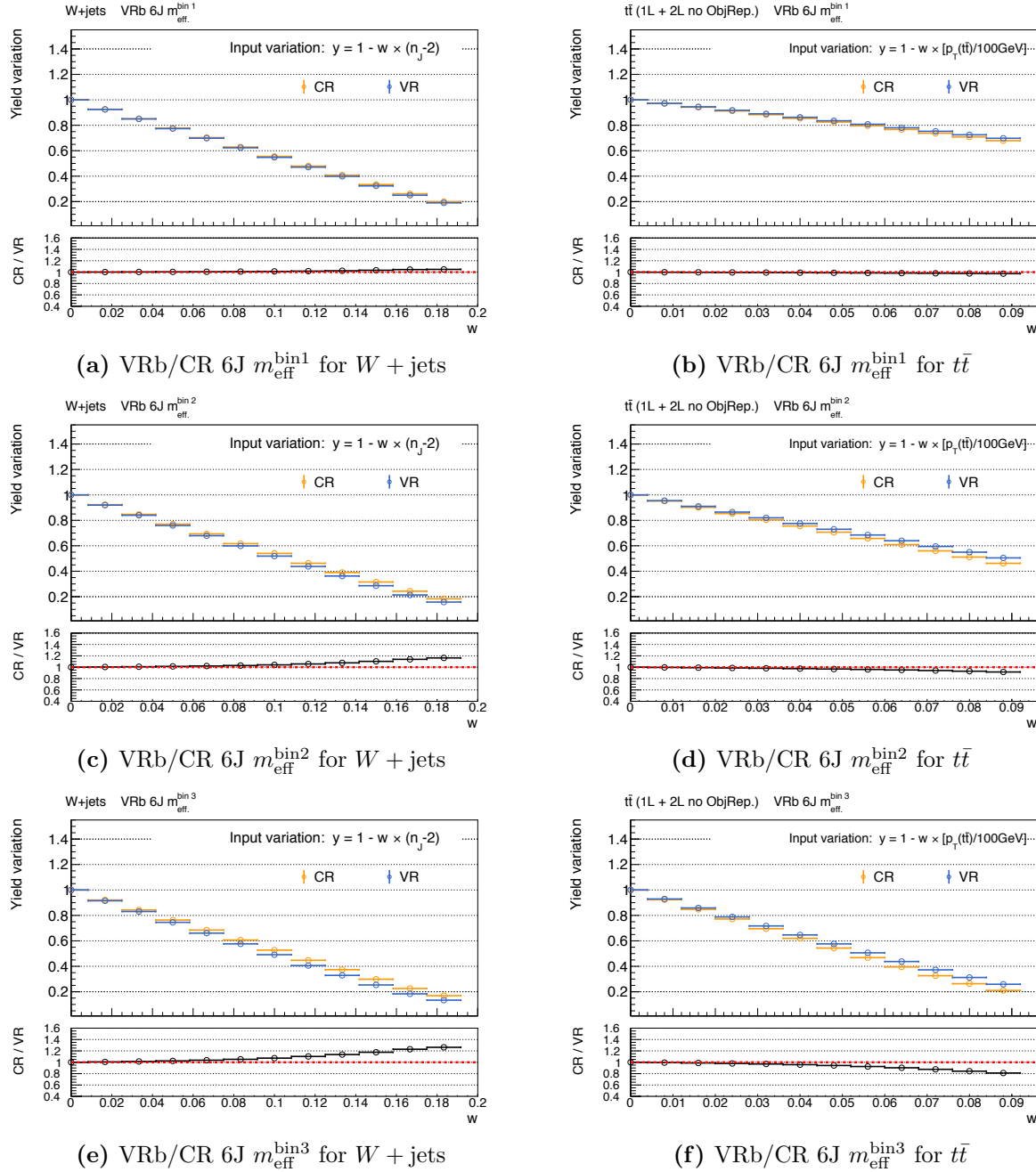


Figure D.1.8: Extrapolation error in VRb/CR **6J** evaluated by reweighting the MC with Eq. (8.1).

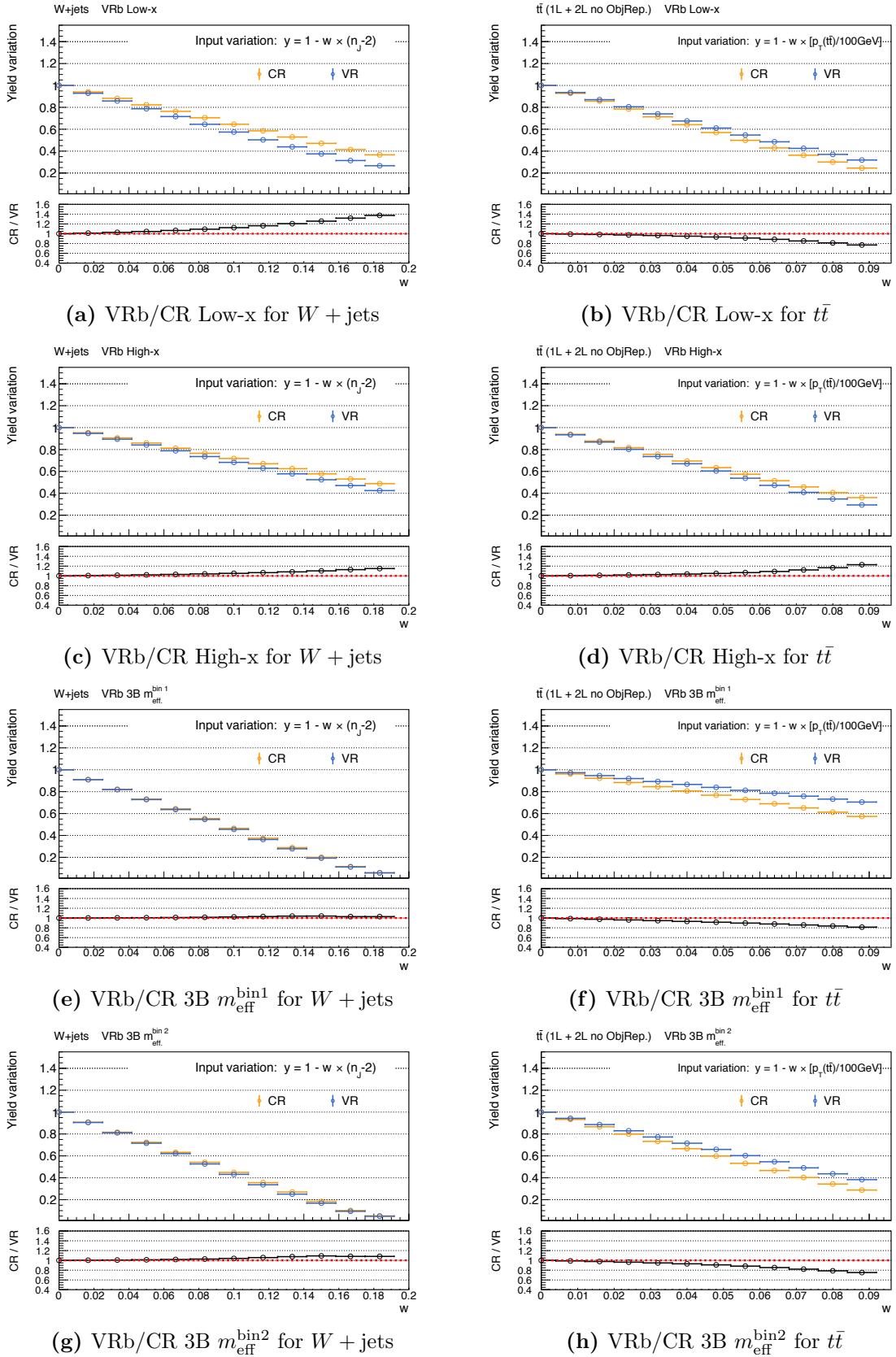


Figure D.1.9: Extrapolation error in VRb/CR (a)(b) **Low-x**, (c)(d) **High-x** and (e-h) **3B** evaluated by reweighting the MC with Eq. (8.1).

E Tips

Naming Convention of the Side of ATLAS Detector



Figure E.0.1: It is said that the A- and C-side of ATLAS are named after the direction to “Airport” (Geneva Cointrin airport) and “Charlie’s pub” (a pub in St. Genis-Pouilly, France) from ATLAS respectively.

Bibliography

- [1] V. Voltolina, *Cat Facts: What Does it Mean When a Cat Wags Its Tail?*, PET MD () .
- [2] M. Peskin and D. V. Schröder, *An introduction to Quantum Filed Theory*, Boulder, CO: Westview Press, 1995, URL: <https://cds.cern.ch/record/257493>.
- [3] F. Halzen and A. D. Martin,
Quarks & Leptons: An Introductory Course in Modern Particle Physics, Wiley; 1st edition, 1984, ISBN: 0471887412, 9780471887416.
- [4] F. Englert and R. Brout, *Broken symmetry and the mass of gauge vector mesons*, Physical Review Letters **13** (1964) p. 321.
- [5] P. W. Higgs, *Broken symmetries, massless particles and gauge fields*, Physics Letters **12** (1964) p. 132.
- [6] J. C. Ward, *An Identity in Quantum Electrodynamics*, Physical Review **78** (1950) p. 182, ISSN: 0031-899X.
- [7] Y. Takahashi, *On the generalized ward identity*, Il Nuovo Cimento **6** (1957) p. 371, ISSN: 00296341.
- [8] G. 'tHooft and M. Veltman, *Regulariation and Renormalization of Gauge Fields*, Nuclear Physics B **44** (1972) p. 189.
- [9] S. L. Glashow, *Partial-symmetries of weak interactions*, Nuclear Physics **22** (1961) p. 579.
- [10] S. Weinberg, *A model of leptons*, Physical review letters **19** (1967) p. 1264.
- [11] A. Salam and J. C. Ward, *Electromagnetic and weak interactions*, Physics Letters **13** (1964) p. 168.
- [12] T.-D. Lee and C.-N. Yang, *Question of parity conservation in weak interactions*, Physical Review **104** (1956) p. 254.
- [13] C.-S. Wu et al., *Experimental test of parity conservation in beta decay*, Physical review **105** (1957) p. 1413.
- [14] M. Kobayashi and T. Maskawa,
CP-Violation in the Renormalizable Theory of Weak Interaction, Progress of Theoretical Physics **49** (1973) p. 652, ISSN: 0033-068X.
- [15] ATLAS Collaboration, *Observation of a new particle in the search for the Standard Model Higgs boson with the ATLAS detector at the LHC*, Physics Letters, Section B: Nuclear, Elementary Particle and High-Energy Physics **716** (2012) p. 1, ISSN: 03702693, arXiv: [1207.7214 \[hep-ex\]](https://arxiv.org/abs/1207.7214).

- [16] CMS Collaboration, *Observation of a new boson at a mass of 125 GeV with the CMS experiment at the LHC*, Physics Letters, Section B: Nuclear, Elementary Particle and High-Energy Physics **716** (2012) p. 30, ISSN: 03702693, arXiv: [1207.7235](#).
- [17] A. Collaboration et al., *Evidence for the spin-0 nature of the Higgs boson using ATLAS data*, Physics Letters B **726** (2013) p. 120.
- [18] V. Khachatryan et al., *Constraints on the spin-parity and anomalous H V V couplings of the Higgs boson in proton collisions at 7 and 8 TeV*, Physical Review D **92** (2015) p. 012004.
- [19] ATLAS Collaboration, *Measurements of the Higgs boson production and decay rates and coupling strengths using pp collision data at $\sqrt{s} = 7$ and 8 TeV in the ATLAS experiment*, European Physical Journal C **76** (2016) p. 1, ISSN: 14346052, arXiv: [1507.04548](#).
- [20] CMS Collaboration, *Precise determination of the mass of the Higgs boson and tests of compatibility of its couplings with the standard model predictions using proton collisions at 7 and 8 TeV*, European Physical Journal C **75** (2015), ISSN: 14346052, arXiv: [1412.8662 \[hep-ex\]](#).
- [21] S. Weinberg, *Implications of dynamical symmetry breaking*, Physical Review D **13** (1976) p. 974.
- [22] S. Weinberg, *Implications of dynamical symmetry breaking: an addendum*, Physical Review D **19** (1979) p. 1277.
- [23] E. Gildener, *Gauge-symmetry hierarchies*, Physical Review D **14** (1976) p. 1667.
- [24] L. Susskind, *Dynamics of spontaneous symmetry breaking in the Weinberg-Salam theory*, Physical Review D **20** (1979) p. 2619.
- [25] S. P. Martin, *A Supersymmetry Primer*, Adv. Ser. Direct. High Energy Phys **21** (1997), ISSN: 09205632, arXiv: [9709356 \[hep-ph\]](#).
- [26] V. C. Rubin and W. K. Ford Jr, *Rotation of the andromeda nebula from a spectroscopic survey of emission regions*, The Astrophysical Journal **159** (1970) p. 379.
- [27] V. C. Rubin, W. K. Ford Jr, and N. Thonnard, *Rotational properties of 21 SC galaxies with a large range of luminosities and radii, from NGC 4605/R= 4kpc/to UGC 2885/R= 122 kpc*, The Astrophysical Journal **238** (1980) p. 471.
- [28] P. Agrawal et al., *Make dark matter charged again*, Journal of Cosmology and Astroparticle Physics **5** (2017), ISSN: 1475-7516, arXiv: [1610.04611](#).
- [29] C. L. Bennett et al., *Nine-Year Wilkinson Microwave Anisotropy Probe (WMAP) Observations: Final Maps and Results*, The Astrophysical Journal Supplement Series **208** (2012), ISSN: 0067-0049, arXiv: [1212.5225](#).
- [30] Planck Collaboration, *Astrophysics Special feature Planck 2015 results*, Astronomy & Astrophysics **594** (2016), arXiv: [1502.01589](#).
- [31] G. F. Giudice and R Rattazzi, *Theories with gauge-mediated supersymmetry breaking*, Physics Reports **322** (1999) p. 419, arXiv: [9801271 \[hep-ph\]](#).

- [32] G. F. Giudice et al., *Gaugino mass without singlets*, Journal of High Energy Physics **1998** (1998) p. 027, ISSN: 1029-8479, arXiv: 9810442 [hep-ph].
- [33] L. Randall and R. Sundrum, *Out of this world supersymmetry breaking*, Nuclear Physics B **557** (1999) p. 42, ISSN: 05503213, arXiv: 9810155 [hep-th].
- [34] J. Wess and J. Bagger, *Supersymmetry and supergravity*, Princeton university press, 1992.
- [35] The Super-Kamiokande Collaboration, *Search for proton decay via $p \rightarrow e+(pi0)$ and $p \rightarrow \mu+(pi0)$ in a large water cherenkov detector*, Physical Review Letters **102** (2009) p. 2, ISSN: 00319007, arXiv: 0903.0676 [hep-ex].
- [36] L. J. Hall, D. Pinner, and J. T. Ruderman, *A natural SUSY Higgs near 125 GeV*, Journal of High Energy Physics **2012** (2012) p. 131, ISSN: 11266708, arXiv: 1112.2703.
- [37] N. Arkani-Hamed, A. Delgado, and G. Giudice, *The Well-Tempered Neutralino*, Nuclear Physics B **741** (2006) p. 108, arXiv: 0601041 [hep-ph].
- [38] H. Baer et al., *Exploring the BWCA (Bino-Wino Co-Anihilation) Scenario for Neutralino Dark Matter*, Journal of High Energy Physics **2005** (2005), arXiv: 0511034 [hep-ph].
- [39] J. Bramante et al., *Towards the final word on neutralino dark matter*, Physical Review D **93** (2016), ISSN: 15502368, arXiv: 1510.03460.
- [40] ATLAS Collaboration, “Summary plots from the ATLAS Supersymmetry physics group”, 2017, URL: <https://atlas.web.cern.ch/Atlas/GROUPS/PHYSICS/CombinedSummaryPlots/SUSY/index.html>.
- [41] CMS Collaboration, “CMS Supersymmetry Physics Results”, 2017, URL: <https://twiki.cern.ch/twiki/bin/view/CMSPublic/PhysicsResultsSUS>.
- [42] ATLAS Collaboration, *Search for electroweak production of supersymmetric particles in the two and three lepton final state at $\sqrt{s} = 13$ TeV with the ATLAS detector*, ATLAS-CONF-2017-039 (2017), URL: <https://cds.cern.ch/record/2267406>.
- [43] CMS Collaboration, *Search for electroweak production of charginos and neutralinos in multilepton final states in pp collision data at $\sqrt{s} = 13$ TeV*, CMS PAS SUS-16-039 (2017), URL: <https://cds.cern.ch/record/2256434>.
- [44] ATLAS Collaboration, *Search for long-lived charginos based on a $\sqrt{s} = 13$ TeV with the ATLAS detector*, ATLAS-CONF-2017-017 (2017), URL: <https://cds.cern.ch/record/2258131>.
- [45] CMS Collaboration, *Search for disappearing tracks in proton-proton collisions at $\sqrt{s} = 8$ TeV*, Journal of High Energy Physics **2015** (2015), arXiv: 1411.6006.
- [46] L. S. W. Group, “Combined LEP Chargino Results, up to 208 GeV for low DM”, 2002, URL: http://lepsusy.web.cern.ch/lepsusy/www/inoslowdmsummer02/charginolowdm_pub.html.
- [47] W. Beenakker et al., *Squark and gluino production at hadron colliders*, Nuclear Physics B **492** (1997) p. 51.
- [48] C. Patrignani et al. (Particle Data Group), *Review of Particle Physics*, Chinese Physics C **40** (2016) p. 100001, ISSN: 1674-1137, arXiv: 0402007 [gr-qc].

- [49] ATLAS Collaboration, *The simulation principle and performance of the ATLAS fast calorimeter simulation FastCaloSim*, ATL-PHYS-PUB-2010-013 (2010), URL: <http://cds.cern.ch/record/1300517>.
- [50] L. Evans and P. Bryant, *LHC Machine*, *Journal of Instrumentation* **3** (2008) S08001, ISSN: 1748-0221.
- [51] ATLAS Collaboration, *The ATLAS Experiment at the CERN Large Hadron Collider*, *J. Instrum.* **3** (2008) S08003.
- [52] CMS Collaboration, *The CMS experiment at the CERN LHC*, *J. Instrum.* **3** (2008) p. 285, ISSN: 1748-0221.
- [53] ALICE Collaboration, *The ALICE experiment at the CERN LHC*, *J. Instrum.* **3** (2008).
- [54] ATLAS Collaboration, *The LHCb Detector at the LHC*, *Journal of Instrumentation* **3** (2008) S08005, ISSN: 1748-0221.
- [55] CERN, “CERN Media Archive Photo”, URL: <https://mediastream.cern.ch/MediaArchive/Photo/Public/2008/0812015/0812015/0812015-A4-at-144-dpi.jpg>.
- [56] ATLAS Collaboration, “ATLAS Data Preparation Summary 2016”, URL: <https://atlas.web.cern.ch/Atlas/GROUPS/DATAPREPARATION/DataSummary/2016/>.
- [57] ATLAS Collaboration, “ATLAS Luminosity Public Results Run2”, URL: <https://twiki.cern.ch/twiki/bin/view/AtlasPublic/LuminosityPublicResultsRun2>.
- [58] ATLAS Collaboration, *ATLAS detector and physics performance: Technical Design Report, 1*, CERN/LHCC 99-14 (1999), URL: <http://cdsweb.cern.ch/record/391176/files/cer-0317330.pdf>.
- [59] ATLAS Collaboration, *Studies of the performance of the ATLAS detector using cosmic-ray muons*, *Eur. Phys. J. C* **71** (2011), arXiv: [1011.6665](https://arxiv.org/abs/1011.6665).
- [60] ATLAS Collaboration, “ATLAS TRT Public Result”, URL: <https://twiki.cern.ch/twiki/bin/view/AtlasPublic/TRTPublicResults>.
- [61] ATLAS Collaboration, *Liquid Argon Technical Design Report*, CERN-LHCC-96-041 (1996), URL: <https://cds.cern.ch/record/331061>.
- [62] ATLAS Collaboration, *Tile Calorimeter Technical Design Report*, CERN-LHCC-96-042 (1996), URL: <https://cds.cern.ch/record/331062>.
- [63] S. van der Meer, *Calibration of the Effective Beam Height in the ISR*, ISR-PO/68-31 (1968), URL: <https://cds.cern.ch/record/296752>.
- [64] ATLAS Collaboration, *Improved luminosity determination in pp collisions at $\sqrt{s} = 7 \text{ TeV}$ using the ATLAS detector at the LHC*, *Eur. Phys. J. C* **73** (2013) p. 2, ISSN: 14346052, arXiv: [1302.4393](https://arxiv.org/abs/1302.4393).
- [65] ATLAS Collaboration, *Performance of the ATLAS Trigger System in 2015*, *Eur. Phys. J. C* **77** (2017), ISSN: 1434-6044, arXiv: [1611.09661](https://arxiv.org/abs/1611.09661).
- [66] ATLAS Collaboration, “ATLAS Trigger operation public results”, URL: <https://twiki.cern.ch/twiki/bin/view/AtlasPublic/TriggerOperationPublicResults>.

- [67] ATLAS Collaboration, *The Optimization of ATLAS Track Reconstruction in Dense Environments*, ATL-PHYS-PUB-2015-006 (2015), URL: <https://cds.cern.ch/record/2002609>.
- [68] A. Osenfeld and J. P. L., *Sequential Operations in Digital Picture Processing*, Journal of the ACM **13** (1966) p. 471.
- [69] ATLAS Collaboration, *A neural network clustering algorithm for the ATLAS silicon pixel detector*, J. Instrum. **9** (2014), arXiv: [1406.7690 \[hep-ex\]](https://arxiv.org/abs/1406.7690).
- [70] R. Frühwirth, *Aplication of Kalman Filtering to track and vertex fitting*, Nuclear Inst. and Methods in Physics Research, A **262** (1987) p. 444.
- [71] G. Cerati, P. Elmer, and S. Lantz, “Advances in tracking and trigger concepts”, International Conference on Computing in High Energy and Nuclear Physics, 2008.
- [72] ATLAS Collaboration, *Performance of primary vertex reconstruction in proton-proton collisions at $\sqrt{s} = 7$ TeV in the ATLAS experiment*, ATLAS-CONF-2010-069 (2010), URL: <https://cds.cern.ch/record/1281344>.
- [73] ATLAS Collaboration, *Performance of the ATLAS Inner Detector Track and Vertex Reconstruction in the High Pile-Up LHC Environment*, ATLAS-CONF-2012-042 (2012), URL: <https://cds.cern.ch/record/1435196>.
- [74] W. Waltenberger, R. Frühwirth, and P. Vanlaer, *Adaptive vertex fitting*, J. Phys. G: Nucl. Part. Phys. **34** (2007) p. 343.
- [75] ATLAS Collaboration, *Topological cell clustering in the ATLAS calorimeters and its performance in LHC Run1*, CERN-PH-EP-2015-304 (2016), arXiv: [arXiv:1603.02934v2](https://arxiv.org/abs/1603.02934v2).
- [76] ATLAS Collaboration, *Electron efficiency measurements with the ATLAS detector using the 2015 LHC proton-proton collision data*, ATLAS-CONF-2016-024 (2016), URL: <https://cds.cern.ch/record/2157687>.
- [77] ATLAS Collaboration, *Improved electron reconstruction in ATLAS using the Gaussian Sum Filter-based model for bremsstrahlung*, ATLAS-CONF-2012-047 (2012), URL: <https://cds.cern.ch/record/1449796>.
- [78] ATLAS Collaboration, *Electron and photon energy calibration with the ATLAS detector using LHC Run 1 data*, Eur. Phys. J. C **74** (2013), arXiv: [1407.5063](https://arxiv.org/abs/1407.5063).
- [79] N. Neyman and E. S. Pearson, *On the Problem of the most Efficient Tests of Statistical Hypotheses*, Philosophical Transactions of the Royal Society of London Series A **231** (1933).
- [80] ATLAS Collaboration, *Electron and photon energy calibration with the ATLAS detector using data collected in 2015 at $\sqrt{s} = 13$ TeV*, ATL-PHYS-PUB-2016-015 (2016), URL: <https://cds.cern.ch/record/2203514>.
- [81] ATLAS Collaboration, *Measurement of the muon reconstruction performance of the Measurement of the muon reconstruction performance of the ATLAS detector using 2011 and 2012 LHC proton – proton collision data*, CERN-PH-EP-2014-151 (2014), arXiv: [arXiv:1407.3935v2](https://arxiv.org/abs/1407.3935v2).

- [82] ATLAS Collaboration, *Muon reconstruction performance of the ATLAS detector in proton–proton collision data at $\sqrt{s} = 13$ TeV*, *Eur. Phys. J. C* **76** (2016), arXiv: [1603.05598](#).
- [83] M. Cacciari, G. P. Salam, and G. Soyez, *The anti- k_t jet clustering algorithm*, *Journal of High Energy Physics* **2008** (2008), arXiv: [0802.1189 \[hep-ph\]](#).
- [84] ATLAS Collaboration, *Jet energy scale measurements and their systematic uncertainties in proton–proton collisions at $\sqrt{s} = 13$ TeV with the ATLAS detector*, ATL-PHYS-PUB-2015-015 (2016), arXiv: [arXiv:1703.09665v1](#), URL: <https://cds.cern.ch/record/2257300>.
- [85] ATLAS Collaboration, *Jet energy measurement and its systematic uncertainty in proton–proton collisions at $\sqrt{s} = 7$ TeV with the ATLAS detector*, *Eur. Phys. J. C* **75** (2015), arXiv: [arXiv:1406.0076v3](#).
- [86] M. Cacciari and G. P. Salam, *Pileup subtraction using jet areas*, *Physics Letters B* **659** (2007) p. 119, arXiv: [0707.1378](#).
- [87] G. P. Salam, *Towards Jetography*, *Eur. Phys. J. C* **67** (2010) p. 637, arXiv: [0906.1833](#).
- [88] ATLAS Collaboration, *Jet energy measurement with the ATLAS detector in proton-proton collisions at $\sqrt{s} = 7$ TeV*, *Eur. Phys. J. C* **73** (2013), arXiv: [1112.6426](#).
- [89] ATLAS Collaboration, *Expected performance of the ATLAS b-tagging algorithms in Run-2*, ATL-PHYS-PUB-2015-022 (2015), URL: <https://cds.cern.ch/record/2037697>.
- [90] ATLAS Collaboration, *Optimisation of the ATLAS b-tagging performance for the 2016 LHC Run*, ATL-PHYS-PUB-2016-012 (2016), URL: <https://cds.cern.ch/record/2160731>.
- [91] ATLAS Collaboration, *Performance of b-jet identification in the ATLAS experiment*, *Journal of Instrumentation* **11** (2016) P04008, ISSN: 1748-0221, arXiv: [1512.01094](#).
- [92] ATLAS Collaboration, *Commissioning of the ATLAS high-performance b-tagging algorithms in the 7 TeV collision data*, *Europhysics Conference on High Energy Physics* (2011), URL: <https://cds.cern.ch/record/1369219>.
- [93] G. Pauletta, F. Simonetto, and M. Witek, *A new inclusive secondary vertex algorithm for b-jet tagging in ATLAS*, *International Conference on Computing in High Energy and Nuclear Physics* (2008).
- [94] ATLAS Collaboration, *Tagging and suppression of pileup jets with the ATLAS detector*, ATLAS-CONF-2014-018 (2014), URL: <https://cds.cern.ch/record/1700870>.
- [95] C. W. Miller, A. Schwartzman, and D. Su, *Jet-Vertex Association Algorithm*, ATL-COM-PHYS-2008-008 (2008), URL: <https://cds.cern.ch/record/1082880>.
- [96] ATLAS Collaboration, *Performance of missing transverse momentum reconstruction with the ATLAS detector in the first proton-proton collisions at $\sqrt{s} = 13$ TeV*, ATL-PHYS-PUB-2015-027 (2015), URL: <https://cds.cern.ch/record/2037904>.
- [97] ATLAS Collaboration, “Missing Transverse Momentum Distribution and Performance in 2016 data”, 2016, URL: <https://atlas.web.cern.ch/Atlas/GROUPS/PHYSICS/PLOTS/JETM-2016-008/>.

- [98] A. Buckley et al., *General-purpose event generators for LHC physics*, Physics Reports **504** (2011) p. 145, arXiv: [1101.2599](https://arxiv.org/abs/1101.2599).
- [99] P. Skands, *QCD for Collider Physics*, CERN-TH-2011-080 (2011), arXiv: [1104.2863](https://arxiv.org/abs/1104.2863), URL: <http://arxiv.org/abs/1104.2863>.
- [100] J. C. Collins, D. E. Soper, and G. Sterman, *Factorization of hard processes in QCD*, Adv. Ser. Direct. High Energy Phys **5** (1989) p. 1.
- [101] J. Butterworth et al., *PDF4LHC recommendations for Run II*, J. Phys. G: Nucl. Part. Phys. **43** (2016), ISSN: 18248039, arXiv: [1510.03865](https://arxiv.org/abs/1510.03865).
- [102] R. D. Ball et al., *Parton distributions for the LHC run II*, Journal of High Energy Physics **2015** (2015), ISSN: 10298479, arXiv: [1410.8849](https://arxiv.org/abs/1410.8849).
- [103] S. Dulat et al., *New parton distribution functions from a global analysis of quantum chromodynamics*, Physical Review D **93** (2016), ISSN: 15502368, arXiv: [1506.07443](https://arxiv.org/abs/1506.07443).
- [104] A. D. Martin et al., *Heavy-quark mass dependence in global PDF analyses and 3- and 4-flavour parton distributions*, Eur. Phys. J. C **70** (2010) p. 51, ISSN: 14346044, arXiv: [1007.2624](https://arxiv.org/abs/1007.2624).
- [105] Y. L. Dokshitzer, *Calculation of the Structure Functions for Deep Inelastic Scattering and e+ e- Annihilation by Perturbation Theory in Quantum Chromodynamics*, Sov. Phys. JETP **46** (1977).
- [106] V. N. G. Lipatov and L. N., *Deep inelastic e-p scattering in perturbation theory*, Sov. J. Nucl. Phys. **15** (1972) p. 438.
- [107] G. Altarelli and G. Parisi, *Asymptotic freedom in parton language*, Nuclear Physics B **126** (1977) p. 298, ISSN: 05503213.
- [108] V. V. Sudakov, *Vertex parts at very high-energies in quantum electrodynamics*, Sov. Phys. JETP **3** (1965).
- [109] S. Catani et al., *QCD Matrix Elements + Parton Showers*, Journal of High Energy Physics **2001** (2001), ISSN: <null>, arXiv: [0109231 \[hep-ph\]](https://arxiv.org/abs/0109231).
- [110] M. J. Alwall, S. Höche, F. Krauss, N. Lavesson, L. Lönnblad, F. Maltoni, M.L. Mangano, M. Moretti, C.G. Papadopoulos, F. Piccinini, S. Schumann, M. Treccani, J. Winter, *Comparative study of various algorithms for the merging of parton showers and matrix elements in hadronic collisions*, Eur. Phys. J. C **53** (2008) p. 473, arXiv: [0706.2569 \[hep-ph\]](https://arxiv.org/abs/0706.2569).
- [111] B. Andersson et al., *Parton fragmentation and string dynamics*, Physics Reports **97** (1983) p. 31, ISSN: 03701573.
- [112] R. D. Ball et al., *Parton distributions for the LHC Run II*, JHEP **04** (2015) p. 040, arXiv: [1410.8849 \[hep-ph\]](https://arxiv.org/abs/1410.8849).
- [113] H.-L. Lai et al., *New parton distributions for collider physics*, Phys. Rev. **D82** (2010) p. 074024, arXiv: [1007.2241 \[hep-ph\]](https://arxiv.org/abs/1007.2241).
- [114] J. Alwall et al., *The automated computation of tree-level and next-to-leading order differential cross sections, and their matching to parton shower simulations*, JHEP **07** (2014) p. 079, arXiv: [1405.0301 \[hep-ph\]](https://arxiv.org/abs/1405.0301).
- [115] T. Gleisberg et al., *Event generation with SHERPA 1.1*, JHEP **02** (2009) p. 007, arXiv: [0811.4622 \[hep-ph\]](https://arxiv.org/abs/0811.4622).

- [116] S. Alioli et al., *A general framework for implementing NLO calculations in shower Monte Carlo programs: the POWHEG BOX*, JHEP **06** (2010) p. 043, arXiv: [1002.2581 \[hep-ph\]](#).
- [117] T. Sjöstrand, S. Mrenna, and P. Z. Skands, *A Brief Introduction to PYTHIA 8.1*, Comput.Phys.Commun. **178** (2008) p. 852, arXiv: [0710.3820 \[hep-ph\]](#).
- [118] T. Sjöstrand, S. Mrenna, and P. Z. Skands, *PYTHIA 6.4 Physics and Manual*, JHEP **05** (2006) p. 026, arXiv: [hep-ph/0603175](#).
- [119] W. Beenakker et al., *Squark and gluino production at hadron colliders*, Nucl. Phys. B **492** (1997) p. 51, arXiv: [hep-ph/9610490](#).
- [120] A. Kulesza and L. Motyka,
Threshold resummation for squark-antisquark and gluino-pair production at the LHC, Phys. Rev. Lett. **102** (2009) p. 111802, arXiv: [0807.2405 \[hep-ph\]](#).
- [121] A. Kulesza and L. Motyka, *Soft gluon resummation for the production of gluino-gluino and squark-antisquark pairs at the LHC*, Phys. Rev. D **80** (2009) p. 095004, arXiv: [0905.4749 \[hep-ph\]](#).
- [122] W. Beenakker et al., *Soft-gluon resummation for squark and gluino hadroproduction*, JHEP **12** (2009) p. 041, arXiv: [0909.4418 \[hep-ph\]](#).
- [123] W. Beenakker et al., *Squark and gluino hadroproduction*, Int. J. Mod. Phys. A **26** (2011) p. 2637, arXiv: [1105.1110 \[hep-ph\]](#).
- [124] R. Gavin et al.,
FEWZ 2.0: A code for hadronic Z production at next-to-next-to-leading order, Comput. Phys. Commun. **182** (2011) p. 2388, arXiv: [1011.3540 \[hep-ph\]](#).
- [125] M. Czakon and A. Mitov,
Top++: A Program for the Calculation of the Top-Pair Cross-Section at Hadron Colliders, Comput. Phys. Commun. **185** (2014) p. 2930, arXiv: [1112.5675 \[hep-ph\]](#).
- [126] N. Kidonakis, *Two-loop soft anomalous dimensions for single top quark associated production with a W- or H-*, Phys.Rev. D **82** (2010) p. 054018, arXiv: [1005.4451 \[hep-ph\]](#).
- [127] P. Kant et al., *HATHOR for single top-quark production: Updated predictions and uncertainty estimates for single top-quark production in hadronic collisions*, Comput. Phys. Commun. **191** (2015) p. 74, arXiv: [1406.4403 \[hep-ph\]](#).
- [128] ATLAS Collaboration, *Multi-Boson Simulation for 13 TeV ATLAS Analyses*, ATL-PHYS-PUB-2016-002 (2016), URL: <http://cds.cern.ch/record/2119986>.
- [129] A. Lazopoulos et al., *Next-to-leading order QCD corrections to $t\bar{t}Z$ production at the LHC*, Phys. Lett. **B666** (2008) p. 62, arXiv: [0804.2220 \[hep-ph\]](#).
- [130] J. M. Campbell and R. K. Ellis, *$t\bar{t}W^{+-}$ production and decay at NLO*, JHEP **07** (2012) p. 052, arXiv: [1204.5678 \[hep-ph\]](#).
- [131] ATLAS Collaboration, *Summary of ATLAS Pythia 8 tunes*, ATL-PHYS-PUB-2012-003 (2012), URL: <http://cds.cern.ch/record/1474107>.
- [132] ATLAS Collaboration, *The ATLAS Simulation Infrastructure*, Eur. Phys. J. C **70** (2010) p. 823, arXiv: [1005.4568 \[physics.ins-det\]](#).
- [133] S. Agostinelli et al., *GEANT4: A Simulation toolkit*, Nucl. Instrum. Meth. A **506** (2003) p. 250.

- [134] ATLAS Collaboration, *Selection of jets produced in 13 TeV proton-proton collisions with the ATLAS detector*, ATLAS-CONF-2015-029 (2015), URL: <http://cdsweb.cern.ch/record/2037702>.
- [135] J. M. Campbell, M. A. Cullen, and E. W. N. Glover, *Four jet event shapes in electron-positron annihilation*, Eur. Phys. J. C **9** (1999) p. 245, arXiv: [9809429 \[hep-ph\]](#).
- [136] M. L. Graesser and J. Shelton, *Hunting mixed top squark decays*, Physical Review Letters **111** (2013), ISSN: 00319007, arXiv: [1212.4495 \[hep-ph\]](#).
- [137] S. Jadach, J. H. Kühn, and Z. Was, *TAUOLA - a library of Monte Carlo programs to simulate decays of polarized τ leptons*, Computer Physics Communications **64** (1991) p. 275, ISSN: 00104655.
- [138] P. Golonka et al., *The tauola-photos-F environment for the TAUOLA and PHOTOS packages, release II*, Computer Physics Communications **174** (2006) p. 818, ISSN: 00104655, arXiv: [arXiv:1301.7105v1](#).
- [139] N. Davidson et al., *Universal interface of TAUOLA: Technical and physics documentation*, Computer Physics Communications **183** (2012) p. 821, ISSN: 00104655, arXiv: [1002.0543](#).
- [140] C. G. Lester and D. J. Summers, *Measuring masses of semi-invisibly decaying particles pair produced at hadron colliders*, Physics Letters B (1999) p. 8, ISSN: 03702693, arXiv: [9906349 \[hep-ph\]](#).
- [141] ATLAS Collaboration, *Measurement of the inclusive W^\pm and Z/γ^* cross sections in the e and μ decay channels in pp collisions at $\sqrt{s} = 7$ TeV with the ATLAS detector*, Physical Review D **85** (2012) p. 072004, ISSN: 1550-7998, arXiv: [1109.5141 \[hep-ex\]](#).
- [142] F James and M Roos, *Minuit: A System for Function Minimization and Analysis of the Parameter Errors and Correlations*, Computer Physics Communications **10** (1975) p. 343.
- [143] M Baak et al., *HistFitter software framework for statistical data analysis*, Eur. Phys. J. C **75** (2015), arXiv: [1410.1280](#).
- [144] K. Cranmer et al., “HistFactory; A tool for creating statistical models for use with RooFit and RooStats”, 2012, URL: <https://cds.cern.ch/record/1456844/>.
- [145] W. Verkerke and D. Kirkby, *The RooFit toolkit for data modeling*, arxiv (2003), arXiv: [0306116 \[arXiv:physics\]](#).
- [146] A. Wald, *Tests of Statistical Hypotheses Concerning Several Parameters When the Number of Observations is Large*, American Mathematical Society, **54** (1943) p. 426.
- [147] G. Cowan et al., *Asymptotic formulae for likelihood-based tests of new physics*, Eur. Phys. J. C **71** (2011), arXiv: [1007.1727](#).
- [148] ATLAS Collaboration, *Search for squarks and gluinos in events with an isolated lepton, jets and missing transverse momentum at $\sqrt{s} = 13$ TeV with the ATLAS detector*, ATLAS-CONF-2016-054 (2016), URL: inspirehep.net/record/1410169.
- [149] ATLAS Collaboration, *Search for pair production of gluinos decaying via top or bottom squarks in events with b-jets and large missing transverse momentum in $p\ p$ collisions at $\sqrt{s} = 13$ TeV with the ATLAS detector*, ATLAS-CONF-2016-052 (2016), URL: <https://cds.cern.ch/record/2206134>.

- [150] ATLAS Collaboration, *Search for supersymmetry p with two same-sign leptons or three by the ATLAS detector*, ATLAS-CONF-2016-037 (2016) p. 1, URL: <https://cds.cern.ch/record/2205745>.
- [151] ATLAS Collaboration, *Search for squarks and gluinos in final states with jets and missing transverse momentum using 36 fb^{-1} of $\sqrt{s} = 13 \text{ TeV}$ pp collision data with the ATLAS detector*, ATLAS-CONF-2017-022 (2017), URL: <https://cds.cern.ch/record/2258145>.
- [152] CMS Collaboration, *Search for supersymmetry in events with one lepton and multiple jets in proton-proton collisions at $\sqrt{s} = 13 \text{ TeV}$ with 2016 data*, CMS PAS SUS-16-042 (2017), URL: <https://cds.cern.ch/record/2257294>.
- [153] ATLAS Collaboration, *Search for production of supersymmetric particles in final states with missing transverse momentum and multiple b-jets at $s = 13 \text{ TeV}$ proton-proton collisions with the ATLAS detector*, ATLAS-CONF-2017-021 (2017), URL: <https://cds.cern.ch/record/2258143>.
- [154] ATLAS Collaboration, *Search for gluinos in events with an isolated lepton, jets and missing transverse momentum at $\sqrt{s} = 13 \text{ TeV}$ with the ATLAS detector*, Eur. Phys. J. C **76** (2016), ISSN: 14346052, arXiv: [1605.04285 \[hep-ex\]](https://arxiv.org/abs/1605.04285).
- [155] ATLAS Collaboration, *Modelling $Z \rightarrow \tau\tau$ processes in ATLAS with τ -embedded $Z \rightarrow \mu\mu$ data*, Journal of High Energy Physics **10** (2015).
- [156] ATLAS Collaboration, *Data-Driven Determination of $t\bar{t}$ Background to Supersymmetry Searches*, ATL-PHYS-PUB-2009-083 (2009), URL: <https://cds.cern.ch/record/1190215>.
- [157] CMS Collaboration, *Search for new physics in the multijet and missing transverse momentum final state in proton-proton collisions at $\sqrt{s} = 8 \text{ TeV}$* , Journal of High Energy Physics **2014** (2014) p. 55, ISSN: 10298479, arXiv: [1402.4770](https://arxiv.org/abs/1402.4770).
- [158] ATLAS Collaboration, *Summary of the ATLAS experiment's sensitivity to supersymmetry after LHC Run 1 — interpreted in the phenomenological MSSM*, Journal of High Energy Physics **10** (2015).
- [159] ATLAS Collaboration, *Dark matter interpretations of ATLAS searches for the electroweak production of supersymmetric particles in $\sqrt{s} = 8 \text{ TeV}$ proton-proton collisions*, Journal of High Energy Physics **9** (2016), ISSN: 10298479.
- [160] CMS Collaboration, *Phenomenological MSSM interpretation of the CMS 7 and 8 TeV results*, CMS PAS SUS-13-020 (2014), ISSN: 1098-5530, arXiv: [1606.03577](https://arxiv.org/abs/1606.03577), URL: <https://cds.cern.ch/record/1693148>.
- [161] CERN, ““The HL-LHC project””, URL: <http://hilumilhc.web.cern.ch/about/hl-lhc-project..>
- [162] A. Cakir and On behalf of the CMS and ATLAS Collaborations, *Prospects of New Physics searches using High Lumi - LHC*, CMS CR-2014/382 (2014), arXiv: [1412.8503](https://arxiv.org/abs/1412.8503), URL: [http://arxiv.org/abs/1412.8503](https://arxiv.org/abs/1412.8503).
- [163] T. Gleisberg and S. Höche, *Comix, a new matrix element generator*, JHEP **12** (2008) p. 039, arXiv: [0808.3674 \[hep-ph\]](https://arxiv.org/abs/0808.3674).
- [164] F. Caccioli, P. Maierhofer, and S. Pozzorini, *Scattering Amplitudes with Open Loops*, Phys. Rev. Lett. **108** (2012) p. 111601, arXiv: [1111.5206 \[hep-ph\]](https://arxiv.org/abs/1111.5206).

- [165] S. Schumann and F. Krauss,
A Parton shower algorithm based on Catani-Seymour dipole factorisation,
JHEP **03** (2008) p. 038, arXiv: [0709.1027 \[hep-ph\]](#).
- [166] S. Höche et al., *QCD matrix elements + parton showers: The NLO case*,
JHEP **04** (2013) p. 027, arXiv: [1207.5030 \[hep-ph\]](#).
- [167] ATLAS Collaboration, *Comparison of Monte Carlo generator predictions for gap fraction and jet multiplicity observables in ttbar events*, ATL-PHYS-PUB-2014-005 (2014),
ISSN: 1434-6044, arXiv: [arXiv:1012.1792](#).
- [168] C. D. White et al., *Isolating Wt production at the LHC*,
Journal of High Energy Physics **2009** (2009), ISSN: 1029-8479, arXiv: [0908.0631](#).
- [169] D. J. Lange, *The EvtGen particle decay simulation package*,
Nucl. Instrum. Meth. A **462** (2001) p. 152.
- [170] L. Lönnblad and S. Prestel,
Matching Tree-Level Matrix Elements with Interleaved Showers, JHEP **03** (2012) p. 019,
arXiv: [1109.4829 \[hep-ph\]](#).
- [171] C. Borschensky et al., *Squark and gluino production cross sections in pp collisions at $\sqrt{s} = 13, 14, 33$ and 100 TeV*, Eur. Phys. J. C **74** (2014) p. 3174,
arXiv: [1407.5066 \[hep-ph\]](#).